

Biological and Medical Physics, Biomedical Engineering

Vasily Astratov *Editor*

# Label-Free Super- Resolution Microscopy

 Springer

# Biological and Medical Physics, Biomedical Engineering

# BIOLOGICAL AND MEDICAL PHYSICS, BIOMEDICAL ENGINEERING

---

This series is intended to be comprehensive, covering a broad range of topics important to the study of the physical, chemical and biological sciences. Its goal is to provide scientists and engineers with textbooks, monographs, and reference works to address the growing need for information. The fields of biological and medical physics and biomedical engineering are broad, multidisciplinary and dynamic. They lie at the crossroads of frontier research in physics, biology, chemistry, and medicine.

Books in the series emphasize established and emergent areas of science including molecular, membrane, and mathematical biophysics; photosynthetic energy harvesting and conversion; information processing; physical principles of genetics; sensory communications; automata networks, neural networks, and cellular automata. Equally important is coverage of applied aspects of biological and medical physics and biomedical engineering such as molecular electronic components and devices, biosensors, medicine, imaging, physical principles of renewable energy production, advanced prostheses, and environmental control and engineering.

## Editor-in-Chief

Bernard S. Gerstman, Department of Physics, Florida International University, Miami, FL, USA

## Editorial Board

Masuo Aizawa, Tokyo Institute Technology, Tokyo, Japan

Robert H. Austin, Princeton, NJ, USA

James Barber, Wolfson Laboratories, Imperial College of Science Technology, London, UK

Howard C. Berg, Cambridge, MA, USA

Robert Callender, Department of Biochemistry, Albert Einstein College of Medicine, Bronx, NY, USA

George Feher, Department of Physics, University of California, San Diego, La Jolla, CA, USA

Hans Frauenfelder, Los Alamos, NM, USA

Ivar Giaever, Rensselaer Polytechnic Institute, Troy, NY, USA

Pierre Joliot, Institute de Biologie Physico-Chimique, Fondation Edmond de Rothschild, Paris, France

Lajos Keszthelyi, Biological Research Center, Hungarian Academy of Sciences, Szeged, Hungary

Paul W. King, Biosciences Center and Photobiology, National Renewable Energy Laboratory, Lakewood, CO, USA

Gianluca Lazzi, University of Utah, Salt Lake City, UT, USA

Aaron Lewis, Department of Applied Physics, Hebrew University, Jerusalem, Israel

Stuart M. Lindsay, Department of Physics and Astronomy, Arizona State University, Tempe, AZ, USA

Xiang Yang Liu, Department of Physics, Faculty of Sciences, National University of Singapore, Singapore, Singapore

David Mauzerall, Rockefeller University, New York, NY, USA

Eugenie V. Mielczarek, Department of Physics and Astronomy, George Mason University, Fairfax, USA

Markolf Niemz, Medical Faculty Mannheim, University of Heidelberg, Mannheim, Germany

V. Adrian Parsegian, Physical Science Laboratory, National Institutes of Health, Bethesda, MD, USA

Linda S. Powers, University of Arizona, Tucson, AZ, USA

Earl W. Prohofsky, Department of Physics, Purdue University, West Lafayette, IN, USA

Tatiana K. Rostovtseva, NICHD, National Institutes of Health, Bethesda, MD, USA

Andrew Rubin, Department of Biophysics, Moscow State University, Moscow, Russia

Michael Seibert, National Renewable Energy Laboratory, Golden, CO, USA

Nongjian Tao, Biodesign Center for Bioelectronics, Arizona State University, Tempe, AZ, USA

David Thomas, Department of Biochemistry, University of Minnesota Medical School, Minneapolis, MN, USA

More information about this series at <http://www.springer.com/series/3740>

Vasily Astratov  
Editor

# Label-Free Super-Resolution Microscopy

 Springer

*Editor*  
Vasily Astratov  
University of North Carolina at Charlotte  
Charlotte, NC, USA

ISSN 1618-7210                      ISSN 2197-5647 (electronic)  
Biological and Medical Physics, Biomedical Engineering  
ISBN 978-3-030-21721-1              ISBN 978-3-030-21722-8 (eBook)  
<https://doi.org/10.1007/978-3-030-21722-8>

© Springer Nature Switzerland AG 2019

This work is subject to copyright. All rights are reserved by the Publisher, whether the whole or part of the material is concerned, specifically the rights of translation, reprinting, reuse of illustrations, recitation, broadcasting, reproduction on microfilms or in any other physical way, and transmission or information storage and retrieval, electronic adaptation, computer software, or by similar or dissimilar methodology now known or hereafter developed.

The use of general descriptive names, registered names, trademarks, service marks, etc. in this publication does not imply, even in the absence of a specific statement, that such names are exempt from the relevant protective laws and regulations and therefore free for general use.

The publisher, the authors and the editors are safe to assume that the advice and information in this book are believed to be true and accurate at the date of publication. Neither the publisher nor the authors or the editors give a warranty, expressed or implied, with respect to the material contained herein or for any errors or omissions that may have been made. The publisher remains neutral with regard to jurisdictional claims in published maps and institutional affiliations.

This Springer imprint is published by the registered company Springer Nature Switzerland AG  
The registered company address is: Gewerbestrasse 11, 6330 Cham, Switzerland

# Preface

*The clear winner was light microscopy, which has remained the most popular microscopy technique in the life sciences.*  
Stefan W. Hell, Nobel Lecture “Nanoscopy with Focused Light” 2014

*Based on these results, it is generally agreed that the Rayleigh limit to resolution represents a practical limit to resolution that can be achieved with a conventional imaging system.*  
Joseph W. Goodman, Introduction to Fourier Optics 2005

The diffraction limit was introduced at the end of the nineteenth century by several prominent scientists, including Abbe, Helmholtz, and Raleigh, and it stated that the far-field resolution of optical systems is limited at  $\lambda/(2n)$  level, where  $\lambda$  is the operating wavelength in a medium with the refractive index  $n$ . At the beginning of twentieth century, it may seem almost impossible that the diffraction limit would be overcome. The onset of a super-resolution era was manifested by a proposal in 1928 by E. H. Synge who was encouraged by Albert Einstein. He proposed “a miniature aperture, whose diameter is approximately  $10^{-6}$  cm, has been constructed in an opaque plate or film and that this is illuminated intensely from below, and is placed immediately beneath the exposed side of the biological section, so that the distance of the minute hole from the section is a fraction of  $10^{-6}$  cm” [E. H. Synge, *Phil Mag.* **6**, 356–362 (1928)] and suggested that the use of such miniature aperture can in principle result in resolutions better than 10 nm. This principle underlies the invention in 1984 of the near-field scanning optical microscope (NSOM) by Dieter Pohl, Aaron Lewis, and coworkers. The race to improve the spatial resolution of optical microscopes was one of the frontiers of science and technology in the twentieth century. This story of success became possible due to a synergistic interplay of new physical principles used in these instruments and new discoveries in Physics, Chemistry, and Biology made by these devices with ever increasing spatiotemporal resolution.

The range of applications of light microscopy is extraordinary wide, from the observation of nanometer-sized gold particles by Adolf Zsigmondy in the beginning of twentieth century (1925 Nobel Prize in Chemistry) to the discovery of green

fluorescent (FL) protein in the 1960s, which allowed to “highlight” the structures inside living cell, the achievement which heralded a new era in cell biology. In the 1990s, it was shown that certain optical nonlinear and single-molecule FL detection properties allow achieving extraordinary high, nanometer-scale resolutions in methods such as stimulated emission depletion (STED) and localization microscopies. Due to very strong contrast mechanism and extreme sensitivity up to a single-molecule level, these techniques became a method of choice in biomedical studies. The development of super-resolved FL microscopy was recognized by the 2014 Nobel Prize in Chemistry awarded jointly to the pioneers of these methods, Eric Betzig, Stefan W. Hell, and William E. Moerner. Although the resolutions available in these methods go far beyond the classical diffraction limit, these methods also have drawbacks. The speed of FL imaging can be rather slow because of the relatively weak signals. The FL intensity dims over time because the fluorophore is being degraded by light (*photobleaching*). In addition, FL labeling may induce undesirable effects like phototoxicity. Besides, labeling itself may be difficult for some specimens.

The label-free microscopy (LFM), which does not require sample staining, is a desirable option and it is in a high demand for even wider range of applications than FL microscopy. However, the development of LFM methods took longer time compared to a rapid progress of FL microscopy since the LFM mechanisms rely on subtler light-scattering processes in nanoscale objects, resulting in lower effective image contrasts. The pursuit of super-resolution in LFM is also somewhat complicated since we cannot rely on nonlinear and localization properties offered by individual dye molecules. It should be also noted that the resolution quantification can be a controversial issue in the case of LFM performed using coherent or partly coherent illumination schemes compared to more straightforward resolution quantification in the case of incoherent FL imaging.

The turning point in the LFM development can be dated to the 1950s when the phase-contrast microscopy (PCM) was introduced by Frits Zernike (1953 Nobel Prize in Physics). It was followed by the development of a large family of interferometric detection techniques such as differential interference contrast (DIC), reflection, and Mirau interference microscopy, as well as more modern digital holographic microscopy (DHM). Although being diffraction-limited, these methods demonstrated the best spatiotemporal resolution among regular microscopy techniques for various biomedical samples. On a somewhat separate note, the development of electron microscopy with unsurpassed subnanometer spatial resolution in the 1960s was an extraordinarily important achievement; however, the light microscopy has remained the most widely used method for biomedical imaging. As it was already stated, a powerful impact on the development of LFM techniques was produced by the invention of NSOM in the 1980s, which can offer a nanometer-scale resolution, but by the expense of being relatively slow point-by-point scanning technology. One more important development was structured illumination microscopy (SIM) introduced around the year 2000 providing a twofold increase in resolution compared to the diffraction limit. A new momentum for LFM imaging was produced in the past two decades with the advent of

nanoplasmonics and metamaterials. The super-resolution imaging proposals stemmed from the John Pendry's idea of "perfect lens" in 1999. Since that time, this field has truly flourished with the proposals of far-field superlens, hyperlens, localized plasmonic structured illumination, and microspherical nanoscopy.

Thus, the super-resolution LFM is a rapidly developing interdisciplinary area that fuses physics, engineering, novel photonic, plasmonic and metamaterials designs, microscopy hardware, imaging software, and biomedical applications. The importance of super-resolution LFM is evident in its truly explosive growth and in the number of papers and patents in this area as well as in the number of citations to these papers (from few dozen in 2008 to more than a thousand in 2018). However, these studies evolved separately in the physics and biomedical optics communities, and the most important results have not been presented in a single place. The purpose of this book is not only to fill this gap, but also to serve as a reference point for students and researches interested in this field.

The organizational structure of the book is imposed by the several principles of obtaining high-resolution imaging in LFM. The first five chapters of this book illustrate the state of the art of the modern interference detection techniques. Although the lateral resolution is usually diffraction-limited in these methods (unless combined with the additional techniques), they offer an unsurpassed precision of axial resolution combined with high temporal resolution that explains the widespread and high popularity of these methods in biomedical imaging applications. In some sense, these first five chapters are genetically connected to the phase-contrast microscopy pioneered by Frits Zernike and show the modern level of development of the interferometric methods. These include Chap. 1 on quantitative phase imaging (QPI), Chap. 2 on interferometric scattering (iSCAT) microscopy and related techniques, Chap. 3 on coherent brightfield (COBRI) microscopy, Chap. 4 on tomographic diffractive microscopy (TDM), and Chap. 5 on a combination of NSOM with digital holography.

Another super-resolution imaging concept is based on using nonlinear optics approaches. These ideas flourished in developing nonlinear LFM methods and applications, as illustrated in Chaps. 6–12. Although the resolution advantage of these methods is achieved by the expense of higher excitation levels, they have many applications for imaging photonic and plasmonic nanostructures, semiconductor nanoscale devices, nanoparticles, and novel materials such as graphene. These methods are represented in Chap. 6 by absorption-based far-field super-resolved LFM, in Chap. 7 by pump-probe LFM, in Chap. 8 by Raman microscopy and related methods, in Chap. 9 by the use of silicon for super-resolved imaging, in Chap. 10 by super-resolution based on nonlinear plasmonic scattering, in Chap. 11 by super-resolution based on nonlinear photomodulated reflectivity, and in Chap. 12 by a combination of nonlinear LFM with structured illumination.

One more route to achieving super-resolution imaging is represented by far-field super-lenses and hyperlenses made from advanced plasmonic and metamaterials with engineered dispersion relations as illustrated in Chaps. 13 and 14. Examples are represented by 2D *plasmonic microscope* using image magnification inside the media with much shorter plasmonic wavelengths compared to that in air, *far-field*

*superlens* involving amplification of the object's near fields in a thin layer of metal followed by the diffraction in air, and different types of *hyperlenses* using metamaterials with the hyperbolic dispersion relations including an example of hyperstructured illumination presented in Chap. 14.

The last three chapters of the book describe imaging of nanoscale objects through contact dielectric microlenses, namely dielectric microspheres. A detailed review of such methods can be found in Chap. 15. A review of corresponding theoretical mechanisms is presented in Chap. 16. A combination of these methods with interferometric detection schemes is represented in Chap. 17. The resolution of these methods is expected to be limited by the solid immersion lens concept, but, in fact, the use of nanoplasmonic objects or plasmonic metasurfaces resonantly coupled to such objects can increase the resolution beyond the solid immersion lens limit. The applications of such methods are stimulated by their simplicity combined with the easiness of their integration with the whole arsenal of other super-resolution techniques, leading to even higher resolution values which can be obtained in future studies.

Although the scope of this book is rather broad, some of the super-resolution LFM methods related to information theory used in combination with novel ways of illumination of samples and/or collection of the optical information are not included in this book. The method with a significant application in ophthalmology is represented by ultrahigh-resolution optical coherence tomography (OCT) where the lateral resolution is diffraction-limited, but the axial resolution can be very high since it is determined by the bandwidth of the source. Another important area of applications is represented by imaging through strongly scattering media. Such approaches as ghost imaging, wavefront shaping, speckle imaging using time reversal of light, and sparse imaging were developed in this field. One more approach to super-resolution LFM imaging is offered by a superoscillation lens. All these approaches are relevant to the subject of this book, but they are not included in this book.

Due to its logical organizational structure, this book can be used as a teaching tool in the graduate and upper division undergraduate-level courses devoted to super-resolved microscopy, nanoscale imaging, microscopy instrumentation, and biomedical imaging. In addition, this book can be used as a text for a seminar course on this subject where particular chapters can be selected for focused presentations by students aimed at understanding the super-resolution mechanisms and corresponding microscopy tools. In a wider sense, this book provides a snapshot of this rapidly evolving field and it can be used by students and researchers who would like to learn about the main advancements in this area in their historical perspective. The introductions to all chapters are particularly useful in this regard.

This book naturally stemmed from a series of special sessions and workshops on Label-Free Super-Resolution Microscopy, which I organized at PQE-2016 and 2017, IEEE Photonics-2017, and ICTON-2017, 2018, and 2019 conferences. I would like to thank all the authors who submitted their chapters, including participants of these sessions as well as the authors who did not participate in these

conferences. This is a collective effort of all coauthors contributing to this book, and I am extremely grateful to every author for their time and commitment to this book.

I hope that this book will generate even more momentum to this rapidly developing area, which progresses in parallel with the remarkably successful super-resolved FL microscopy and continues to be a frontier of nanoscale science and technology in the twenty-first century.

Charlotte, NC, USA

Vasily Astratov

# Contents

|          |  |           |
|----------|--|-----------|
| <b>1</b> | <b>Quantitative Phase Imaging: Principles and Applications</b> . . . . .                             | <b>1</b>  |
|          | Chenfei Hu and Gabriel Popescu   |           |
| 1.1      | Introduction . . . . .   | 1         |
| 1.2      | Physical Interpretation of Phase Imaging in Transmission<br>Versus Reflection Measurements . . . . . | 2         |
| 1.3      | Principles of Full-Field QPI . . . . .   | 6         |
| 1.3.1    | Off-axis Methods . . . . .   | 8         |
| 1.3.2    | Phase-Shifting Methods . . . . .   | 10        |
| 1.4      | Applications . . . . .   | 12        |
| 1.4.1    | Medical Applications . . . . .   | 13        |
| 1.4.2    | Cellular Dynamics . . . . .  | 14        |
| 1.4.3    | Tomography . . . . .   | 14        |
| 1.5      | Important Concepts in QPI . . . . .  | 15        |
| 1.5.1    | Effects of Spatial Coherence . . . . .   | 15        |
| 1.5.2    | Defining Resolution . . . . .  | 16        |
| 1.6      | Summary and Outlook . . . . .  | 17        |
|          | References . . . . .   | 18        |
| <b>2</b> | <b>Interferometric Scattering (iSCAT) Microscopy and Related<br/>Techniques</b> . . . . .            | <b>25</b> |
|          | Richard W. Taylor and Vahid Sandoghdar   |           |
| 2.1      | Introduction . . . . .   | 25        |
| 2.2      | Historical Perspective . . . . .   | 27        |
| 2.3      | Interferometric Scattering Microscopy (iSCAT) . . . . .  | 32        |
| 2.3.1    | Foundations . . . . .  | 32        |
| 2.3.2    | Detection Sensitivity and Signal-to-Noise Ratio<br>(SNR) . . . . .                                   | 36        |
| 2.3.3    | Background Removal . . . . .   | 37        |
| 2.3.4    | Long Measurements: Indefinite Photostability . . . . .   | 39        |
| 2.3.5    | Fast Measurements: No Saturation . . . . .   | 39        |

|          |  |            |
|----------|--|------------|
| 2.3.6    | Exquisite Lateral and Axial Resolution . . . . .   | 40         |
| 2.3.7    | Illumination and Detection Schemes . . . . .   | 41         |
| 2.4      | iSCAT Showcase . . . . .   | 43         |
| 2.4.1    | Detection and Sensing of Nanoparticles . . . . .   | 43         |
| 2.4.2    | Dynamics in Nanobiology . . . . .  | 51         |
| 2.5      | Summary and Outlook . . . . .  | 56         |
|          | References . . . . .   | 57         |
| <b>3</b> | <b>Label-Free, Ultrahigh-Speed, Direct Imaging and Tracking of Bionanoparticles in Live Cells by Using Coherent Brightfield Microscopy . . . . .</b> | <b>67</b>  |
|          | Chia-Lung Hsieh  |            |
| 3.1      | Introduction to Label-Free Imaging in Live Cells Through Linear Scattering . . . . .   | 67         |
| 3.2      | COBRI Microscopy . . . . .   | 69         |
| 3.3      | Scattering Background Estimation and Correction . . . . .  | 74         |
| 3.4      | Label-Free, Ultrahigh-Speed Imaging and Tracking of a Single Bionanoparticle in Live Cells . . . . .   | 77         |
| 3.4.1    | Single Virus Dynamics on Cell Membrane . . . . .   | 78         |
| 3.4.2    | Nanosopic Dynamics of a Cell Vesicle During Active Transportation . . . . .  | 79         |
| 3.5      | Conclusions and Future Perspectives . . . . .  | 79         |
|          | References . . . . .   | 82         |
| <b>4</b> | <b>Tomographic Diffractive Microscopy: Principles, Implementations, and Applications in Biology . . . . .</b>  | <b>85</b>  |
|          | Bertrand Simon and Olivier Haeberlé  |            |
| 4.1      | Introduction . . . . .   | 85         |
| 4.2      | Digital Holographic Microscopy . . . . .   | 86         |
| 4.3      | TDM with Illumination Rotation . . . . .   | 90         |
| 4.4      | Multiwavelength TDM . . . . .  | 94         |
| 4.5      | TDM with Sample Rotation . . . . .   | 96         |
| 4.6      | Combined Approaches . . . . .  | 99         |
| 4.7      | Conclusion and Perspectives . . . . .  | 102        |
|          | References . . . . .   | 104        |
| <b>5</b> | <b>Near-Field Scanning Optical Microscope Combined with Digital Holography for Three-Dimensional Electromagnetic Field Reconstruction . . . . .</b>  | <b>113</b> |
|          | Nancy Rahbany, Ignacio Izeddin, Valentina Krachmalnicoff, Rémi Carminati, Gilles Tessier and Yannick De Wilde  |            |
| 5.1      | Introduction to Near-Field Scanning Optical Microscopy (NSOM) . . . . .  | 114        |
| 5.2      | Principles of Digital Holography . . . . .   | 116        |

|          |   |            |
|----------|---|------------|
| 5.3      | Near-Field Scanning Optical Microscopy Combined with Digital Holography . . . . .           | 119        |
| 5.3.1    | Experimental Setup . . . . .  | 121        |
| 5.3.2    | 3D Reconstructed EM Field Through Different Media . . . . .                                 | 122        |
| 5.3.3    | Characterization of the Angular Scattering . . . . .  | 125        |
| 5.4      | Possible Applications . . . . .   | 128        |
| 5.4.1    | Coupled Nanoantennas . . . . .  | 128        |
| 5.4.2    | Brownian Nanoparticles as Stochastic Optical Probes . . . . .                               | 131        |
| 5.4.3    | Scattering Through Disordered Media . . . . .   | 132        |
| 5.5      | Conclusion . . . . .  | 133        |
|          | References . . . . .  | 134        |
| <b>6</b> | <b>Absorption-Based Far-Field Label-Free Super-Resolution Microscopy . . . . .</b>          | <b>137</b> |
|          | Chen Li and Ji-Xin Cheng  |            |
| 6.1      | Introduction to Absorption-Based Far-Field Label-Free Super-Resolution Microscopy . . . . . | 137        |
| 6.2      | Breaking the Diffraction Limit in IR Microscopy Through Photothermal Detection . . . . .    | 140        |
| 6.2.1    | Laser-Induced Photothermal Lens Effect: The Origin of the Photothermal Contrast . . . . .   | 140        |
| 6.2.2    | Improvement of Detection Sensitivity of Photothermal Spectroscopy . . . . .                 | 140        |
| 6.2.3    | Beat the Diffraction Limit of the Pump Beam . . . . .                                       | 142        |
| 6.2.4    | Visible Beam Excited Photothermal Microscopy . . . . .                                      | 146        |
| 6.2.5    | Mid-IR Excited Photothermal Microscopy . . . . .  | 149        |
| 6.2.6    | Applications of Super-Resolution Photothermal Microscopy . . . . .                          | 152        |
| 6.3      | Super-Resolution Transient Absorption Microscopy . . . . .                                  | 156        |
| 6.3.1    | Transient Absorption Microscopy . . . . .   | 157        |
| 6.3.2    | Spatially Controlled Saturated Transient Absorption . . . . .                               | 158        |
| 6.3.3    | Super-Resolution Stimulated Raman Microscopy . . . . .                                      | 161        |
| 6.4      | Conclusion and Outlook . . . . .  | 162        |
|          | References . . . . .  | 162        |
| <b>7</b> | <b>Label-Free Pump-Probe Nanoscopy . . . . .</b>  | <b>171</b> |
|          | Paolo Bianchini, Giulia Zanini and Alberto Diaspro  |            |
| 7.1      | Nonlinear Optical Interactions . . . . .  | 171        |
| 7.1.1    | Nonlinear Absorption . . . . .  | 172        |
| 7.2      | Pump-Probe Microscopy . . . . .   | 174        |
| 7.2.1    | Pump-Probe Microscope Design . . . . .  | 175        |

|           |  |            |
|-----------|--|------------|
| 7.2.2     | Pump–Probe Signal Information . . . . .  | 179        |
| 7.2.3     | State-of-the-Art of Pump–Probe Microscopy . . . . .  | 180        |
| 7.3       | Breaking the Diffraction Limit in Pump–Probe Microscopy . . . . .  | 182        |
| 7.3.1     | The Generalized RESOLFT Concept . . . . .  | 183        |
| 7.3.2     | Saturated Pump–Probe Nanoscopy . . . . .   | 184        |
| 7.3.3     | Other Super-Resolution Approaches in Pump–Probe<br>Microscopy . . . . .  | 186        |
| 7.4       | Summary and Future Perspectives . . . . .  | 188        |
|           | References . . . . .   | 188        |
| <b>8</b>  | <b>Super-Resolution Imaging in Raman Microscopy . . . . .</b>  | <b>195</b> |
|           | Katsumasa Fujita   |            |
| 8.1       | Introduction . . . . .   | 195        |
| 8.2       | Point Spread Function (PSF) Engineering . . . . .  | 196        |
| 8.2.1     | Nonlinear Techniques . . . . .   | 197        |
| 8.2.2     | Linear Techniques . . . . .  | 203        |
| 8.3       | Structure Illumination Microscopy . . . . .  | 205        |
| 8.4       | Localization Microscopy . . . . .  | 207        |
| 8.5       | Conclusions . . . . .  | 209        |
|           | References . . . . .   | 210        |
| <b>9</b>  | <b>Use of Silicon for Label-Free Super-Resolved Imaging . . . . .</b>  | <b>213</b> |
|           | Hadar Pinhas, Yossef Danan, Amihai Meiri, Omer Wagner,<br>Asaf Shahmoon, Tali Ilovitsh, Yehonatan Ramon, Dror Malka,<br>Meir Danino, Moshe Sinvani and Zeev Zalevsky |            |
| 9.1       | Introduction . . . . .   | 214        |
| 9.2       | Theoretical Background . . . . .   | 215        |
| 9.3       | Usage of Silicon-Coated Nanostructures . . . . .   | 217        |
| 9.4       | Enhancement of the Effect . . . . .  | 222        |
| 9.5       | Feasibility Experimental Results . . . . .   | 225        |
| 9.6       | Silicon Wafers Imaging . . . . .   | 228        |
| 9.7       | Conclusions . . . . .  | 234        |
|           | References . . . . .   | 235        |
| <b>10</b> | <b>Super-Resolution Imaging Based on Nonlinear Plasmonic<br/>Scattering . . . . .</b>  | <b>239</b> |
|           | Tushar C. Jagadale and Shi-Wei Chu   |            |
| 10.1      | Introduction . . . . .   | 240        |
| 10.1.1    | Why Label-Free Super-Resolution Light<br>Microscopy? . . . . .   | 240        |
| 10.1.2    | Plasmonic Nanostructures for Super-Resolution<br>Microscopy . . . . .  | 243        |

|           |   |            |
|-----------|---|------------|
| 10.2      | Principle of Super-Resolution Based on Nonlinear Absorption and Emission . . . . .                | 246        |
| 10.2.1    | Saturation of Emission + Temporal Modulation: SAX . . . . .                                       | 246        |
| 10.2.2    | All-Optical Switching + Spatial Modulation + Saturation: STED . . . . .                           | 247        |
| 10.3      | Discovery of Nonlinear Plasmonic Scattering . . . . .   | 248        |
| 10.3.1    | Nonlinear Scattering of Au Nanospheres . . . . .  | 248        |
| 10.3.2    | Nonlinear Scattering in Various Plasmonic Structures . . . . .                                    | 250        |
| 10.3.3    | All-Optical Switch on a Plasmonic (Au) Nanospheres . . . . .                                      | 251        |
| 10.4      | Super-Resolution Based on Nonlinear Scattering . . . . .  | 253        |
| 10.4.1    | Super Resolution Based on Reverse Saturation of Scattering . . . . .                              | 253        |
| 10.4.2    | Super-Resolution Based on Combination of Saturation of Plasmonic Scattering and SAX . . . . .     | 254        |
| 10.4.3    | Super-Resolution Based on Optical Suppression of Scattering Imaging (SUSI) . . . . .              | 256        |
| 10.5      | Summary . . . . .   | 257        |
|           | References . . . . .  | 258        |
| <b>11</b> | <b>Label-Free Super-Resolution Microscopy by Nonlinear Photo-modulated Reflectivity . . . . .</b> | <b>261</b> |
|           | Omer Tzang, Dror Hershkovitz and Ori Cheshnovsky  |            |
| 11.1      | Introduction . . . . .  | 262        |
| 11.1.1    | Pump and Probe with Large Difference in Wavelengths for SR . . . . .                              | 262        |
| 11.2      | Nonlinear Photo-modulated Reflectivity . . . . .  | 263        |
| 11.2.1    | Photo-Induced Reflectivity Changes . . . . .  | 263        |
| 11.2.2    | The Principles of Nonlinear Photo-Modulated Reflectivity . . . . .                                | 264        |
| 11.2.3    | Timescales of the Experiment . . . . .  | 266        |
| 11.2.4    | The Relation Between High Harmonics Detection and SR . . . . .                                    | 266        |
| 11.2.5    | The Need for Pure Sinusoidal Excitation . . . . .   | 267        |
| 11.3      | Experimental System . . . . .   | 268        |
| 11.4      | Examples of NPMR . . . . .  | 269        |
| 11.4.1    | Silicon on Sapphire . . . . .   | 269        |
| 11.4.2    | Gold on Sapphire . . . . .  | 270        |
| 11.4.3    | Vanadium Oxide on Silicon . . . . .   | 270        |
| 11.5      | Modality Variations to Improve and Simplify NPMR . . . . .  | 273        |
| 11.5.1    | Spatial Modulation . . . . .  | 273        |

|           |   |            |
|-----------|---|------------|
| 11.5.2    | Pump and Probe with a Single Laser . . . . .  | 274        |
| 11.5.3    | Resolution Improvement via Beam Apodization . . . . .   | 276        |
| 11.6      | Using Nonlinear Response in Other Label-Free<br>Microscopy Modalities . . . . .                           | 277        |
| 11.6.1    | Temperature-Dependent Raman Scattering for SR . . . . .   | 277        |
| 11.6.2    | Nonlinear Photo-acoustic Feedback Signal<br>for Focusing Through Scattering Media . . . . .               | 280        |
| 11.7      | Conclusions . . . . .   | 282        |
|           | Appendix: Pure Sinusoidal Photo-Modulation Using<br>an Acousto-optic Modulator . . . . .                  | 282        |
|           | References . . . . .  | 285        |
| <b>12</b> | <b>Nonlinear Label-Free Super-Resolution Microscopy<br/>Using Structured Illumination . . . . .</b>       | <b>289</b> |
|           | Mikko J. Huttunen and Antti Kiviniemi   |            |
| 12.1      | Introduction . . . . .  | 289        |
| 12.2      | Structured Illumination Microscopy . . . . .  | 291        |
| 12.3      | Laser-Scanning SIM Implementations . . . . .  | 294        |
| 12.4      | Nonlinear Optical Processes . . . . .   | 296        |
| 12.5      | Super-Resolution Using Nonlinear Processes<br>and Structured Illumination . . . . .                       | 297        |
| 12.5.1    | Super-Resolution Using Incoherent Nonlinear<br>Processes . . . . .  | 297        |
| 12.5.2    | Super-Resolution Using Coherent Nonlinear<br>Processes . . . . .  | 299        |
| 12.6      | Current Applications of Nonlinear Microscopy . . . . .  | 303        |
| 12.7      | Future Directions and Challenges . . . . .  | 305        |
| 12.8      | Conclusion . . . . .  | 307        |
|           | References . . . . .  | 307        |
| <b>13</b> | <b>Super-Resolution Microscopy Techniques Based on Plasmonics<br/>and Transformation Optics . . . . .</b> | <b>313</b> |
|           | Igor I. Smolyaninov and Vera N. Smolyaninova  |            |
| 13.1      | Introduction . . . . .  | 313        |
| 13.2      | Surface Plasmon Microscopy . . . . .  | 316        |
| 13.3      | Hyperlenses Based on 2D Hyperbolic Metamaterials . . . . .  | 321        |
| 13.4      | Super-Resolution Microscopy Based on Photon Tunneling . . . . .   | 326        |
| 13.5      | Microscopy Techniques Based on 2D Transformation<br>Optics . . . . .                                      | 329        |
| 13.5.1    | Microdroplet-Based Transformation Optics . . . . .  | 329        |
| 13.5.2    | Lithographically Defined Transformation Optics<br>Devices . . . . .                                       | 334        |
| 13.6      | Conclusion . . . . .  | 339        |
|           | References . . . . .  | 342        |

**14 Label-Free Super-Resolution Imaging with Hyperbolic Materials** . . . . . 345  
 Emroz Khan and Evgenii Narimanov

14.1 Introduction . . . . . 345

14.2 Super-Resolution Microscopy . . . . . 346

14.3 Metamaterials-Based Super-Resolution . . . . . 347

14.4 Hyperbolic Media . . . . . 349

14.5 The Hyperlens . . . . . 352

    14.5.1 Hyperlens: The Concept . . . . . 352

    14.5.2 Hyperlens: The Experimental Demonstration . . . . . 356

    14.5.3 Hyperlens: The Limitations . . . . . 356

14.6 Hyperstructured Illumination . . . . . 358

    14.6.1 HSI: The Concept . . . . . 359

    14.6.2 HSI: Theoretical Description . . . . . 361

    14.6.3 HSI Performance . . . . . 362

    14.6.4 HSI: The Effect of Disorder . . . . . 362

    14.6.5 HSI: Experimental Demonstration . . . . . 363

14.7 Conclusions . . . . . 366

References . . . . . 367

**15 Super-Resolution Imaging and Microscopy by Dielectric Particle-Lenses** . . . . . 371  
 Zengbo Wang and Boris Luk'yanchuk

15.1 Introduction . . . . . 371

    15.1.1 Background . . . . . 371

    15.1.2 Microsphere Super-Resolution Imaging . . . . . 373

    15.1.3 From Microsphere to Metamaterial Particle-Lens . . . . . 375

15.2 Super-Resolution Mechanisms: Photonic Nanojet, Super-Resonance and Evanescent Jets . . . . . 376

    15.2.1 Microsphere and Microcylinder . . . . . 376

    15.2.2 Dielectric Nanoparticle-Based Metamaterial Superlens . . . . . 383

15.3 Microsphere Nanoscopy: Key Progresses . . . . . 386

    15.3.1 Confocal Imaging and Resolution Quantification . . . . . 386

    15.3.2 Scanning Microsphere Super-Resolution Imaging . . . . . 387

    15.3.3 Endoscopy Application . . . . . 391

    15.3.4 3D Interferometry and Optical Profiling . . . . . 392

15.4 Metamaterial Dielectric Superlens . . . . . 393

    15.4.1 mSIL . . . . . 393

    15.4.2 Nanohybrid Lens . . . . . 395

15.5 Biological Superlens . . . . . 397

|           |  |            |
|-----------|--|------------|
| 15.6      | Devices with Integrated Microsphere Superlens . . . . .  | 398        |
| 15.7      | Outlook and Conclusions . . . . .  | 400        |
|           | References . . . . .   | 401        |
| <b>16</b> | <b>Theoretical Foundations of Super-Resolution in Microspherical Nanoscopy</b> . . . . .   | <b>407</b> |
|           | Alexey V. Maslov and Vasily N. Astratov  |            |
| 16.1      | Introduction . . . . .   | 408        |
|           | 16.1.1 Experimental Results . . . . .  | 408        |
|           | 16.1.2 Theoretical Modeling . . . . .  | 412        |
| 16.2      | Geometrical Optics of Contact Microspheres . . . . .   | 413        |
| 16.3      | Diffractive Optics of Contact Microspheres . . . . .   | 415        |
|           | 16.3.1 Wave Scattering and Focusing . . . . .  | 415        |
|           | 16.3.2 Point-Source Emission and Field Distribution . . . . .  | 417        |
| 16.4      | Microsphere as a Solid Immersion Lens: Resolution Analysis . . . . .   | 418        |
|           | 16.4.1 Imaging of a Point Source . . . . .   | 418        |
|           | 16.4.2 Coherent Versus Incoherent Imaging . . . . .  | 421        |
| 16.5      | Beyond Solid Immersion Lens: Plasmonic Contributions . . . . .   | 422        |
|           | 16.5.1 Principles of SIM, PSIM, and LPSIM . . . . .  | 424        |
|           | 16.5.2 Plasmon-Coupled Leakage Radiation (PCLR) . . . . .  | 428        |
|           | 16.5.3 Microspherical Nanoscopy Based on Short-Period Arrays with Small Gaps: Super-Resolution Without Post-imaging Processing . . . . . | 430        |
| 16.6      | Conclusion . . . . .   | 434        |
|           | References . . . . .   | 436        |
| <b>17</b> | <b>Microsphere-Assisted Interference Microscopy</b> . . . . .  | <b>443</b> |
|           | Stephane Perrin, Sylvain Lecler and Paul Montgomery  |            |
| 17.1      | Optical Microscopy and Its Advances for Super-Resolution . . . . .   | 443        |
|           | 17.1.1 From Diffraction-Limited Optical Microscopy . . . . .   | 444        |
|           | 17.1.2 To Super-Resolution Optical Microscopy . . . . .  | 446        |
| 17.2      | Microsphere-Assisted Microscopy for 2D Imaging . . . . .   | 451        |
|           | 17.2.1 Principle . . . . .   | 451        |
|           | 17.2.2 Performance . . . . .   | 452        |
|           | 17.2.3 Image Formation . . . . .   | 455        |
|           | 17.2.4 Applications . . . . .  | 457        |
| 17.3      | Three-Dimensional Microsphere-Assisted Microscopy . . . . .  | 458        |
|           | 17.3.1 Interference Methods . . . . .  | 458        |
|           | 17.3.2 Super-Resolution Interference Methods . . . . .   | 459        |
| 17.4      | Conclusion . . . . .   | 463        |
|           | References . . . . .   | 464        |
|           | <b>Index</b> . . . . .   | <b>471</b> |

# Contributors

**Vasily N. Astratov** Department of Physics and Optical Science, Center for Optoelectronics and Optical Communication, University of North Carolina at Charlotte, Charlotte, NC, USA

**Paolo Bianchini** Istituto Italiano di Tecnologia, Genoa, Italy

**Rémi Carminati** Institut Langevin, ESPCI Paris, CNRS, PSL University, Paris, France

**Ji-Xin Cheng** Boston University Photonics Center, Boston, MA, USA

**Ori Cheshnovsky** The Raymond and Beverly Sackler, Faculty of Exact Sciences, School of Chemistry, Tel Aviv University, Tel Aviv, Israel

**Shi-Wei Chu** Department of Physics, Molecular Imaging Centre, National Taiwan University, Taipei, Taiwan (R.O.C.)

**Yossef Danan** Faculty of Engineering, The Bar-Ilan Institute of Nanotechnology and Advanced Materials, Bar-Ilan University, Ramat-Gan, Israel

**Meir Danino** Faculty of Engineering, Bar-Ilan University, Ramat-Gan, Israel

**Yannick De Wilde** Institut Langevin, ESPCI Paris, CNRS, PSL University, Paris, France

**Alberto Diaspro** Istituto Italiano di Tecnologia, Genoa, Italy

**Katsumasa Fujita** Department of Applied Physics, Osaka University, Suita, Osaka, Japan

**Olivier Haeberlé** Laboratoire Photonique Numérique et Nanosciences (LP2N - UMR 5298), Institut d'Optique Graduate School, Université de Bordeaux, CNRS, Bordeaux, France;

Institut de Recherche en Informatique, Mathématiques, Automatique et Signal (IRIMAS - EA7499), Université de Haute-Alsace, Mulhouse, France

**Dror Hershkovitz** School of Chemistry, The Raymond and Beverly Sackler, Faculty of Exact Sciences, Tel Aviv University, Tel Aviv, Israel

**Chia-Lung Hsieh** Institute of Atomic and Molecular Sciences (IAMS), Academia Sinica, Taipei, Taiwan

**Chenfei Hu** Quantitative Light Imaging Laboratory, Electrical and Computer Engineering, Beckman Institute for Advanced Science and Technology, University of Illinois at Urbana-Champaign, Urbana, IL, USA

**Mikko J. Huttunen** Faculty of Engineering and Natural Sciences, Tampere University, Tampere, Finland

**Tali Ilvitch** Faculty of Engineering, The Bar-Ilan Institute of Nanotechnology and Advanced Materials, Bar-Ilan University, Ramat-Gan, Israel

**Ignacio Izeddin** Institut Langevin, ESPCI Paris, CNRS, PSL University, Paris, France

**Tushar C. Jagadale** Department of Physics, National Taiwan University, Taipei, Taiwan (R.O.C.);  
Technical Physics Division, Bhabha Atomic Research Centre, Mumbai, India

**Emroz Khan** Department of Electrical and Computer Engineering, Birck Nanotechnology Center, Purdue University, West Lafayette, IN, USA

**Antti Kiviniemi** Faculty of Engineering and Natural Sciences, Tampere University, Tampere, Finland

**Valentina Krachmalnicoff** Institut Langevin, ESPCI Paris, CNRS, PSL University, Paris, France

**Sylvain Lecler** ICube, University of Strasbourg - CNRS, Illkirch, France

**Chen Li** Department of Chemistry, Purdue University, West Lafayette, IN, USA

**Boris Luk'yanchuk** Division of Physics and Applied Physics, School of Physical and Mathematical Sciences, Nanyang Technological University, Singapore, Singapore;  
Faculty of Physics, Lomonosov Moscow State University, Moscow, Russia

**Dror Malka** Faculty of Engineering, Bar-Ilan University, Ramat-Gan, Israel;  
Faculty of Engineering, Holon Institute of Technology, Holon, Israel

**Alexey V. Maslov** University of Nizhny Novgorod, Nizhny Novgorod, Russia

**Amihai Meiri** Faculty of Engineering, The Bar-Ilan Institute of Nanotechnology and Advanced Materials, Bar-Ilan University, Ramat-Gan, Israel

**Paul Montgomery** ICube, University of Strasbourg - CNRS, Illkirch, France

**Evgenii Narimanov** Department of Electrical and Computer Engineering, Birck Nanotechnology Center, Purdue University, West Lafayette, IN, USA

**Stephane Perrin** ICube, University of Strasbourg - CNRS, Illkirch, France

**Hadar Pinhas** Faculty of Engineering, The Bar-Ilan Institute of Nanotechnology and Advanced Materials, Bar-Ilan University, Ramat-Gan, Israel

**Gabriel Popescu** Quantitative Light Imaging Laboratory, Electrical and Computer Engineering, Beckman Institute for Advanced Science and Technology, University of Illinois at Urbana-Champaign, Urbana, IL, USA

**Nancy Rahbany** Institut Langevin, ESPCI Paris, CNRS, PSL University, Paris, France

**Yehonatan Ramon** Faculty of Engineering, The Bar-Ilan Institute of Nanotechnology and Advanced Materials, Bar-Ilan University, Ramat-Gan, Israel

**Vahid Sandoghdar** Max Planck Institute for the Science of Light, Erlangen, Germany

**Asaf Shahmoon** Faculty of Engineering, The Bar-Ilan Institute of Nanotechnology and Advanced Materials, Bar-Ilan University, Ramat-Gan, Israel

**Bertrand Simon** Laboratoire Photonique Numérique et Nanosciences (LP2N - UMR 5298), Institut d'Optique Graduate School, Université de Bordeaux, CNRS, Bordeaux, France;  
Institut de Recherche en Informatique, Mathématiques, Automatique et Signal (IRIMAS - EA7499), Université de Haute-Alsace, Mulhouse, France

**Moshe Sinvani** Faculty of Engineering, Bar-Ilan University, Ramat-Gan, Israel

**Igor I. Smolyaninov** Department of Electrical and Computer Engineering, University of Maryland, College Park, MD, USA;  
Saltenna LLC, McLean, VA, USA

**Vera N. Smolyaninova** Department of Physics Astronomy and Geosciences, Towson University, Towson, MD, USA

**Richard W. Taylor** Max Planck Institute for the Science of Light, Erlangen, Germany

**Gilles Tessier** Sorbonne Université, CNRS, INSERM, Institut de La Vision, Paris, France

**Omer Tzang** School of Chemistry, The Raymond and Beverly Sackler, Faculty of Exact Sciences, Tel Aviv University, Tel Aviv, Israel

**Omer Wagner** Faculty of Engineering, The Bar-Ilan Institute of Nanotechnology and Advanced Materials, Bar-Ilan University, Ramat-Gan, Israel

**Zengbo Wang** School of Computer Science and Electronic Engineering, Bangor University, Bangor, UK

**Zeev Zalevsky** Faculty of Engineering, The Bar-Ilan Institute of Nanotechnology and Advanced Materials, Bar-Ilan University, Ramat-Gan, Israel

**Giulia Zanini** Istituto Italiano di Tecnologia, Genoa, Italy

# Chapter 1

## Quantitative Phase Imaging: Principles and Applications



Chenfei Hu and Gabriel Popescu

**Abstract** Quantitative phase imaging (QPI) is an emerging label-free imaging approach. QPI measures the optical phase delay associated with the object, and the resulting image provides an objective measure of morphology and dynamics, in the absence of contrast agents. As tremendous advances have been made in the past one–two decades, the QPI field continues expanding and gaining popularity. It has found applications in many different fields, especially in biomedicine. In this chapter, we provide a review of the principles associated with this exciting field, with discussion focused on optical physics, experimental principles, and applications.

### 1.1 Introduction

The phase of a scattered field is of great interest, as it carries information about the internal structure of the specimen under investigation [1, 2]. In microscopy, biological samples (e.g., cells and tissue slices) exhibit low absorption in the visible spectrum. Thus, it is the phase change rather than the amplitude of the field that provides an intrinsic contrast mechanism. Zernike and Nomarski are the pioneers exploiting the phase imaging concept. Their inventions, phase-contrast microscopy (PCM), and differential interference contrast (DIC) microscopy, respectively, reveal the inner details of transparent specimen without exogenous staining or fluorescent tagging, which has been widely used in biological laboratories worldwide [3–5]. However, these early methods only produce intensity images, where the complex field information, i.e., the amplitude and phase, cannot be retrieved uniquely. On the other hand, in the 1940s, Gabor proved the concept that a complex optical field can be stored and reconstructed by using principles of holography [6, 7].

---

C. Hu · G. Popescu (✉)

Quantitative Light Imaging Laboratory, Electrical and Computer Engineering, Beckman Institute for Advanced Science and Technology, University of Illinois at Urbana-Champaign, Urbana, IL 61801, USA

e-mail: [gpopescu@illinois.edu](mailto:gpopescu@illinois.edu)

© Springer Nature Switzerland AG 2019

V. Astratov (ed.), *Label-Free Super-Resolution Microscopy*,

Biological and Medical Physics, Biomedical Engineering,

[https://doi.org/10.1007/978-3-030-21722-8\\_1](https://doi.org/10.1007/978-3-030-21722-8_1)

Combing these pioneer works, quantitative phase imaging (QPI) appears and has become a powerful label-free imaging modality for studying biospecimens [1, 8–11]. In general, QPI produces a map of optical pathlength shift associated with the specimen, and thus, reports information about both the local thickness as well as the refractive index, which are directly related to a sample’s biophysical properties. In addition, because it employs interferometry, QPI exhibits nanoscale sensitivity to morphological and dynamic changes of transparent features. Since the early demonstrations in the 1990s [12–15], multiple QPI imaging platforms have been proposed, which enable 2D, 3D, and 4D investigation capabilities [16–19]. These instruments provide the remarkable performance of QPI in a range of applications in biomedicine and material science.

In this chapter, we overview several important aspects of QPI, from basic physics to system instrumentation. The material is organized as follows. Section 1.2 presents the physical interpretation of the QPI data in transmission versus backscattering, using the first-order Born approximation. Section 1.3 focuses on the typical QPI configurations, phase retrieval methods and novel QPI systems. Section 1.4 presents QPI applications in a few aspects. Section 1.5 discusses concepts related to the phase measurability and resolution. We summarize and discuss future directions in Sect. 1.6.

## 1.2 Physical Interpretation of Phase Imaging in Transmission Versus Reflection Measurements

Let us consider the physics meaning of the measurable *phase* associated with an optical field interacting with a weakly scattering medium. Given an inhomogeneous medium, the scattered field,  $U_1$ , satisfies the inhomogeneous Helmholtz equation [20–24]

$$\nabla^2 U_1(\mathbf{r}) + n_0^2 \beta_0^2 U_1(\mathbf{r}) = -\beta_0^2 \chi(\mathbf{r}) U(\mathbf{r}) \quad (1.1)$$

where  $\mathbf{r}$  is the spatial coordinate,  $n_0$  the refractive index in the background,  $\beta_0 = 2\pi/\lambda$  with  $\lambda$  the wavelength, and  $\chi(\mathbf{r}) = n^2(\mathbf{r}) - n_0^2$  the scattering potential. The total field,  $U$ , is the sum of the incident field ( $U_0$ ) and the linear scattering component ( $U_1$ ), i.e.,  $U = U_0 + U_1$ . Let us consider the object is illuminated by a monochromatic plane wave traveling in z-axis,  $U_0 = Ae^{i\beta_0 z}$  with  $A$  the amplitude. Under the first-order Born approximation, which assumes the incident wave is dominant in the medium, (1.1) becomes

$$\nabla^2 U_1(\mathbf{r}) + \beta^2 U_1(\mathbf{r}) = -\beta_0^2 \chi(\mathbf{r}) Ae^{i\beta_0 z} \quad (1.2)$$

In (1.2),  $\beta = n_0 \beta_0$ . Performing a Fourier transform with respect to  $\mathbf{r}$ , the scattering field can be easily obtained in the spatial frequency ( $\mathbf{k}$ ) space [25, 26] as

$$U_1(\mathbf{k}) = -\beta_0^2 A \chi(k_\perp, k_z - \beta) \frac{1}{2\gamma} \left[ \frac{1}{\gamma - k_z} + \frac{1}{\gamma + k_z} \right] \quad (1.3)$$

where  $\gamma = \sqrt{\beta^2 - k_\perp^2}$ . Here, we use the same symbol but different variables to distinguish a function and its frequency representation, e.g.,  $f(\mathbf{r}) \leftrightarrow f(\mathbf{k})$ , with  $\leftrightarrow$  indicating the Fourier transform operation. The two terms on the right-hand side of (1.3) correspond to the components of the scattered field traveling along  $+z$  (forward scattering) and  $-z$  (backscattering) direction, respectively. We perform an inverse Fourier transform with respect to  $k_z$  and bring the scattering field in the  $(k_\perp, z)$  domain, resulting in

$$U_1(k_\perp, z) = \left[ -i\beta_0^2 A \left. \frac{\chi(k_\perp, z) e^{i\beta z}}{2\gamma} \right|_{z \geq 0} \right] \textcircled{v}_z e^{i\gamma z} + \left[ i\beta_0^2 A \left. \frac{\chi(k_\perp, -z) e^{-i\beta z}}{2\gamma} \right|_{z < 0} \right] \textcircled{v}_z e^{-i\gamma z} \quad (1.4)$$

where  $\textcircled{v}_z$  represents a convolution operation with respect to  $z$ , and the  $+i$  and  $-i$  factors indicate a wave advanced or delayed by  $\pi/2$ , respectively. Invoking the Fourier transform property,  $e^{i\gamma z} \textcircled{v}_z f(z) = e^{i\gamma z} f(\gamma)$ , the expression in (1.4) can be simplified to

$$\begin{aligned} U_1(k_\perp, z) &= -i\beta_0^2 A \frac{e^{i\gamma z}}{2\gamma} \chi(k_\perp, \gamma - \beta) + i\beta_0^2 A \frac{e^{-i\gamma z}}{2\gamma} \chi(k_\perp, -\gamma - \beta) \\ &= U^+(k_\perp, z) + U^-(k_\perp, z) \end{aligned} \quad (1.5)$$

Here, we use  $U^+$  and  $U^-$  to denote the forward and backscattering fields. For smooth samples, the  $k_\perp$  is mostly restricted in a small region close to 0, and  $\gamma = \sqrt{\beta^2 - k_\perp^2} \approx \beta$ . This approximation applies for low-NA imaging, but the physical insights can be extended to broader situations. As a result, the expression in (1.5) can be further simplified to

$$U^+(k_\perp, z) = -\frac{i}{2n_0} \beta_0 A e^{i\beta z} \chi(k_\perp, 0) \quad (1.6a)$$

$$U^-(k_\perp, z) = \frac{i}{2n_0} \beta_0 A e^{-i\beta z} \chi(k_\perp, -2\beta) \quad (1.6b)$$

Equation (1.6a)–(1.6b) point one significant difference between forward and backscattering field: while the former depends on the axial scattering potentials evaluated at zero (central) axial frequency,  $\chi(k_\perp, 0)$ , the latter depends on  $\chi$  evaluated at frequency  $k_z = -2\beta$ . Taking an inverse Fourier transform with respect to  $k_\perp$ , we obtain its spatial domain expression as

$$U^+(r_\perp, z) = -\frac{i}{2n_0}\beta_0 A e^{i\beta z} \chi(r_\perp, 0) \quad (1.7a)$$

$$U^-(r_\perp, z) = \frac{i}{2n_0}\beta_0 A e^{-i\beta z} \chi(r_\perp, -2\beta) \quad (1.7b)$$

Next, in order to extract the phase delay associated with the *transmission* imaging field, the scattered fields must be mixed with the incident field. In reflection, however, this incident wave is not present. For straightforward comparison, we add and then subtract the incident field, whose amplitude is the same as  $U_0$  but propagates in the  $-z$  direction. Therefore, the detected field in transmission and reflection can be written as

$$U_f(r_\perp, z, \omega) = A e^{i\beta z} - \frac{i}{2n_0}\beta_0 A e^{i\beta z} \chi(r_\perp, 0) \quad (1.8a)$$

$$U_b(r_\perp, z) = A e^{-i\beta z} + \frac{i}{2n_0}\beta_0 A e^{-i\beta z} \chi(r_\perp, -2\beta) - A e^{-i\beta z} \quad (1.8b)$$

Using the central ordinate theorem of the Fourier transform to express  $\chi(r_\perp, 0)$  and  $\chi(r_\perp, -2\beta)$ , we have

$$U_f(r_\perp, z) = A e^{i\beta z} - \frac{i}{2n_0}\beta_0 A e^{i\beta z} \int_{-L/2}^{L/2} [n^2(r_\perp, z) - n_0^2] e^{-ik_z z} dz \Big|_{k_z=0} \quad (1.9a)$$

$$U_b(r_\perp, z) = A e^{-i\beta z} + \frac{i}{2n_0}\beta_0 A e^{-i\beta z} \int_{-L/2}^{L/2} [n^2(r_\perp, z) - n_0^2] e^{-ik_z z} dz \Big|_{k_z=-2\beta} - A e^{-i\beta z} \quad (1.9b)$$

In (1.9a)–(1.9b), the integral limit accounts for the sample thickness,  $L$ . For cell and thin tissue slices, the scattering potential satisfies low refractive index condition, i.e.,  $n^2 - n_0^2 \approx 2n_0(n - n_0)$ , and simpler expressions of (1.9a)–(1.9b) are obtained

$$U_f(r_\perp, z) = A e^{i\beta z} \{1 - i\beta_0[\bar{n}(r_\perp) - n_0]L\} \quad (1.10a)$$

$$U_b(r_\perp, z) = A e^{-i\beta z} \left\{ 1 + i\beta_0 \int_{-L/2}^{L/2} [n(r_\perp, z) - n_0] e^{i2\beta z} dz \right\} - A e^{-i\beta z} \quad (1.10b)$$

In (1.10a),  $\bar{n}(r_\perp)$  is the longitudinally averaged refractive index,  $\bar{n}(r_\perp) = \frac{1}{L} \int_{-L/2}^{L/2} n(r_\perp, z) dz$ . For small phase shifts, using the approximation,  $e^{ix} \approx 1 + ix$ , we reach the final expressions of the fields as

$$U_f(r_\perp, z) = A e^{i\beta z} e^{-i\beta_0[\bar{n}(r_\perp) - n_0]L} \quad (1.11a)$$

$$U_b(r_{\perp}, z) = Ae^{-i\beta z} e^{i\beta_0 \int_{-L/2}^{L/2} [n(r_{\perp}, z) - n_0] e^{i2\beta z} dz} - Ae^{-i\beta z} \quad (1.11b)$$

Equation (1.11a)–(1.11b) reveals the fundamental difference of the phase values measured in transmission and backscattering geometry. For weakly scattering specimens, the transmitted field contains the conventional defined phase delay,  $\phi = \beta_0(\bar{n} - n_0)L$  (Fig. 1.1a). However, the backscattering field contains the axial projection of the refractive index contrast weighted by the plane wave  $e^{i2\beta z}$ . Ignoring transverse features in the object, this expression indicates that the field detected in backscattering consists of a superposition of backpropagating plane waves originating at various depths,  $z$ , with respective phases  $2\beta z$  (Fig. 1.1b). What confounds matter further is the fact that the phase imaged in backscattering is not  $\phi^- = \beta_0 \int_{-L/2}^{L/2} [n(r_{\perp}, z, \omega) - n_0] e^{i2\beta z} dz$ , but the phase of field difference, i.e.,  $e^{i\phi^-} - 1$  according to (1.11b). Thus, the forward and backscattering phase shifts have the form

$$\varphi_f(x, y) = \beta_0 \Delta n L \quad (1.12a)$$

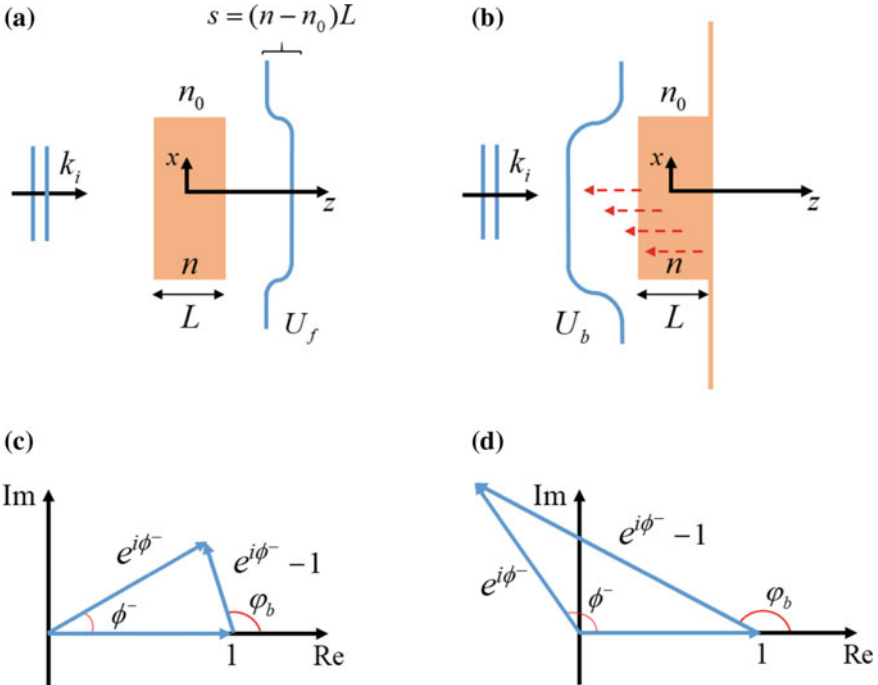


**Fig. 1.1** Transmission field (a) versus reflection field (b). **c–d** Phasor representation of the backscattering field from (1.11b): for  $\phi^-$  smaller (c) or larger (d) than  $\pi/2$  (Reprinted from [26])

$$\varphi_b(x, y) = \arg\left(e^{i\phi^-} - 1\right) \quad (1.12b)$$

The physical significance of  $\varphi_b$  can be well appreciated by using a phasor diagram in Fig. 1.1c–d. The two phases are related by trigonometry,

$$\varphi_b \approx 90^\circ + \frac{\phi^-}{2} \quad (1.13)$$

Thus, it is challenging to infer topological information of 3D transparent samples from a single backscattering measurement [26, 27].

In order to illustrate the interpretation of the phase image measured in backscattering versus transmission, we performed a numerical simulation. First, a 3D refractive index contrast map of a live neuron was obtained in an earlier study, shown in Fig. 1.2a, and a forward (Fig. 1.2b) and backscattering phase (Fig. 1.2c) can be, therefore, calculated as an averaged  $z$  projection with a different weighting factor. The insets in Fig. 1.2b–c represent the zoomed-in areas of a dendrite. Figure 1.2c shows both these areas next to each other demonstrating how vastly different the forward and backscattering phase measurements of the same cell region are. Furthermore, Fig. 1.2d plots the phase values along the same length of a dendrite indicated by the white solid lines in Fig. 1.2b–c. Clearly, the two signals are completely different. Note that, while it is true that the backscattering measurement consists of higher spatial frequencies from the object, the backscattering phase is not simply the high-pass version of the transmission phase. These results make it apparent that the phase signals obtained in backscattering and their statistics cannot be immediately related to the object structure. In fact, the backscattering phase maps appear as random speckle patterns. The contour of the object can be identified from the background only because the speckle statistics is different from that of the background.

### 1.3 Principles of Full-Field QPI

Following the conclusion derived in Sect. 1.2, the image field in transmission microscopy can be modeled as a function of time and space

$$U_i(x, y, t) = |U_i(x, y)|e^{-i[\langle\omega\rangle t - \langle\mathbf{k}\rangle \cdot \mathbf{r} + \varphi(x, y)]} \quad (1.14)$$

where  $|U_i(x, y)|$  the magnitude of the field,  $\langle\omega\rangle$  the central frequency,  $\langle\mathbf{k}\rangle$  the central wavevector,  $\varphi$  the phase of interest defined in (1.12a). Since a conventional photodetector only detects the intensity distribution, i.e., the modulus squared of the field, QPI employs an interferometer, whereby a *reference field* is mixed with the *image field* to generate an interferogram that incorporates phase information. Let  $U_R$  be the reference field such that the resulting interferogram at the detector plane can be expressed as

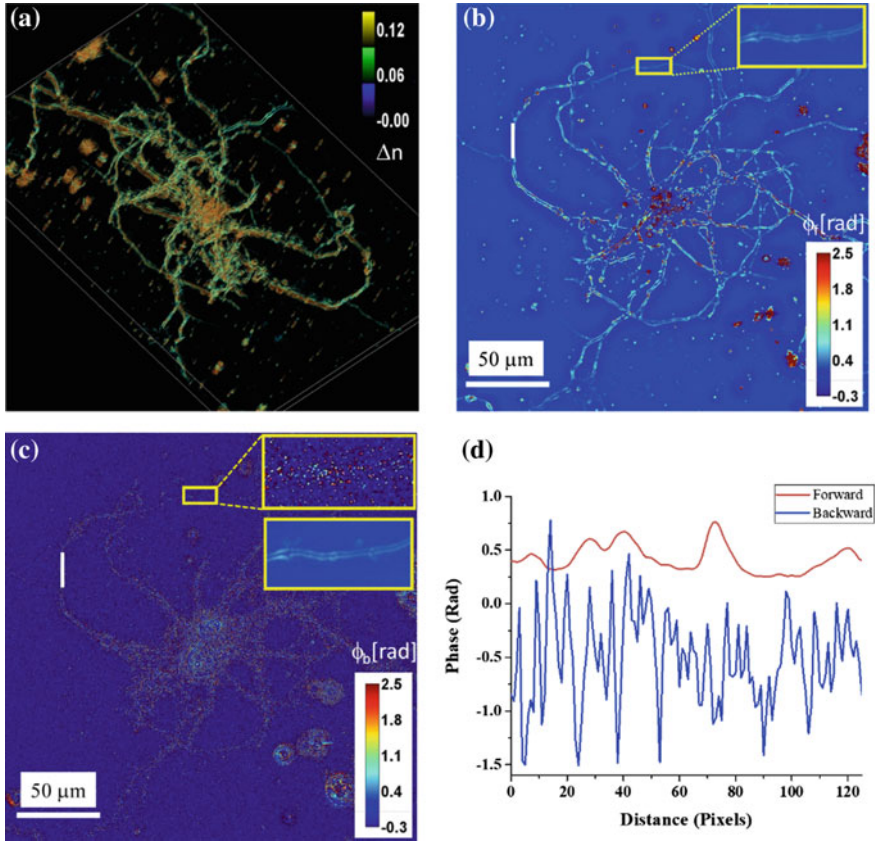


**Fig. 1.2** Comparison of measured phase image of transmission versus backscattering field. **a** 3D refractive index contrast map; simulated forward **(b)** and backscattering **(c)** phase; **d** phase values along the white solid lines in **(b)** and **(c)** (Reprinted from [26])

$$I(x, y, t) = |U_i(x, y)|^2 + |U_R|^2 + 2|U_i(x, y)||U_R| \cos[\langle\omega\rangle(t - t_R) - (\langle\mathbf{k}\rangle - \mathbf{k}_R) \cdot \mathbf{r} + \varphi(x, y)] \quad (1.15)$$

where  $|U_R|$ ,  $t_R$ , and  $\mathbf{k}_R$  are the amplitude, time delay, and wavevector of the reference field, respectively. In general,  $\mathbf{k}_R$  and  $t_R$  describe the two main QPI configurations: (1) *off-axis* interferometry uses a  $\mathbf{k}_R$  in a different direction than the image field (Fig. 1.3a), and (2) *phase-shifting* interferometry modulates the  $t_R$  to change the phase delay between image and the reference field (Fig. 1.3b). Now, let us describe the phase retrieval algorithm and instrumentation for each configuration.

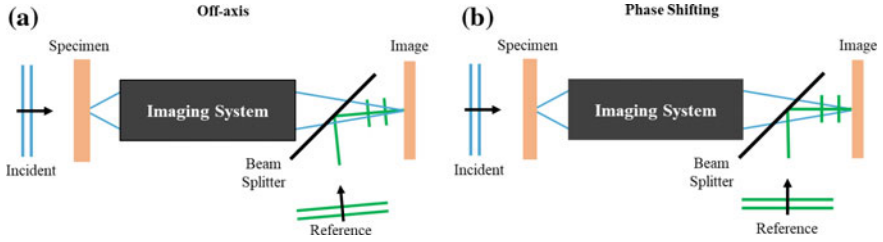


**Fig. 1.3** Main configurations of QPI: **a** off-axis and **b** phase shifting methods (Reprinted from [92] with permission)

### 1.3.1 Off-axis Methods

In off-axis schemes, the tilted reference field and the sample field go through a different path and reach the image plane at the same time ( $t - t_R = 0$ ), and the resulting irradiance of this interferogram is given by

$$I(x, y) = |U_i(x, y)|^2 + |U_R|^2 + 2|U_i(x, y)||U_R| \cos[\Delta kx + \varphi(x, y)] \quad (1.16)$$

In (1.16),  $\Delta k = |\mathbf{k} - \mathbf{k}_R|$  is the magnitude of the wavevector difference between the image and reference field, which is assumed to be along the  $x$ -axis, acting as the carrier frequency. The recorded image is essentially interference fringes, whose shapes are perturbed by the phase delay (inset in Fig. 1.4a). The procedure of phase reconstruction is illustrated in Fig. 1.4. An implementation of spatial Hilbert transform takes the input interferogram (Fig. 1.4a), performs a Fourier transform (Fig. 1.4b), selects only one side of the Fourier spectrum (red continuous circle in Fig. 1.4b), shifts this selection to the center (dotted circle in Fig. 1.4b), and Fourier transform this signal back to the spatial domain, where the argument provides the

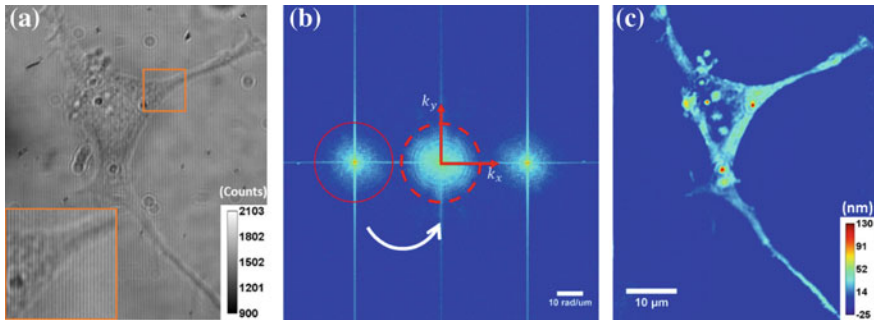


**Fig. 1.4** Procedure of phase reconstruction of off-axis QPI. **a** A raw interferogram. **b** Fourier transform of the raw interferogram selects one side of the Fourier spectrum and shifts this selection to the center. **c** A phase map is obtained by performing an inverse Fourier transform (Reprinted from [43] with permission)

phase map,  $\varphi$  (Fig. 1.4c). Other reconstruction methods are discussed elsewhere [28–32].

The off-axis method reconstructs a phase map from one raw measurement, and the speed of this imaging modality is only limited by the photodetector, which makes it widely adopted [33–40]. However, the high time-bandwidth product comes at the expense of the space-bandwidth product, as the interferogram period must be sampled by a sufficient number of pixels as described in [28].

Most off-axis methods use physically separated beams, specific to traditional interferometers, e.g., Michelson and Mach–Zehnder, which results in noisy measurements. One of the successful demonstrations of common-path, off-axis QPI is called diffraction phase microscopy (DPM) [41–43], which is realized by attaching an additional module to the camera port of an existing microscope system (Fig. 1.5). At the output of a bright-field microscope, a transmission grating is placed at the image plane, and then multiple diffraction orders are produced with each containing the full spatial information about the sample. All diffraction orders are blocked, except the zeroth- and first-order beam. At the Fourier plane, using a physical pinhole or an amplitude spatial light modulator (SLM), one diffraction beam is spatially low passed to create a DC reference field, while it leaves the other beam intact to form the sample field. After the second Fourier lens, the two beams recombine and form an interferogram on the detector, and a phase shift is retrieved used the method shown in Fig. 1.4. DPM is designed in common-path geometry, where the sample and reference field propagate in close vicinity to each other, and the two interference beams suffer the same background disturbance. As a result, the system noise is greatly canceled out in the resulting interferogram, which significantly improves the temporal-phase stability. This standalone module is compatible with reflection measurement, which enables imaging topological structures of reflective surfaces, such as semiconductors [44–47]. In addition, by modulating the wavelength of illumination, the spectroscopic off-axis method has the potential of providing chemical or functional information about the specimen [48–51].

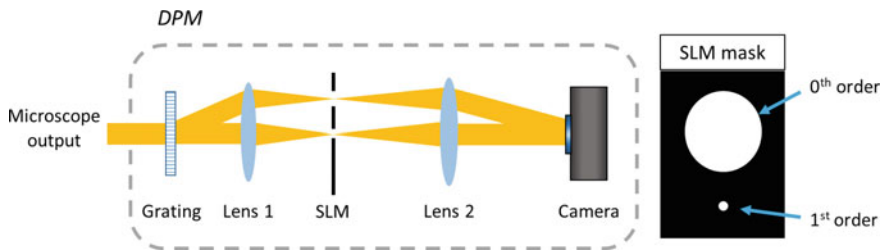


**Fig. 1.5** System schematic of DPM. The grating is placed at the output image plane of the microscope. Under a 4-f configuration, the first lens takes a Fourier transform creating a Fourier plane. A spatial filter is placed in the Fourier plane, which allows the full zeroth order to pass, and the first order is filtered down using a small pinhole such that after the second lens takes a Fourier transform, the field becomes a uniform plane wave and serves as the reference to the interferometer (Adapted from [43] with permission)

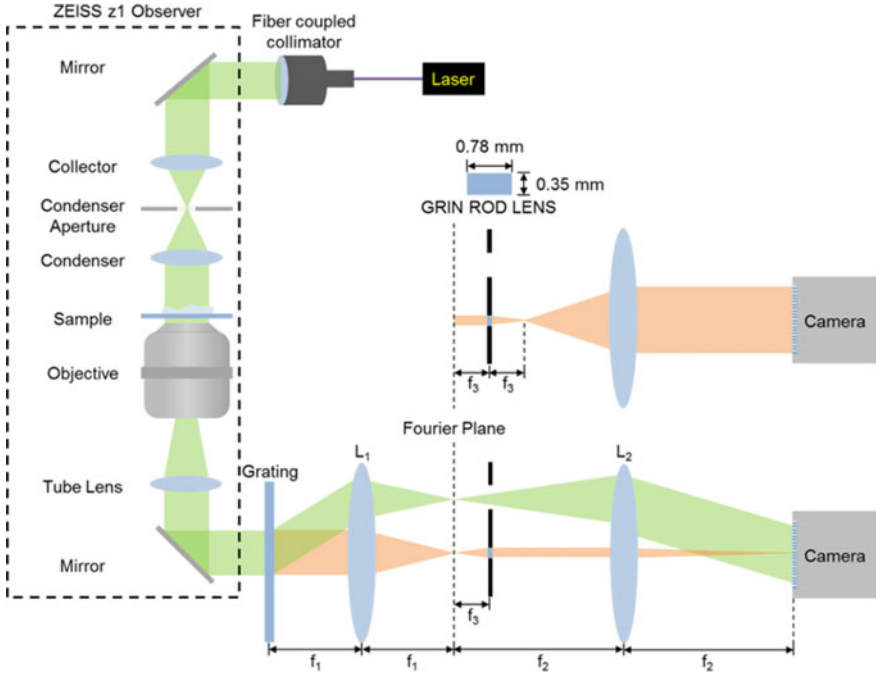


Fig. 1.6 Optical setup of MISS (Reprinted from [52])

Built upon the success of DPM, magnified image spatial spectrum (MISS) microscopy has been demonstrated recently [52]. A system schematic is shown in Fig. 1.6. Briefly, MISS replaces a pinhole with a gradient index (GRIN) lens with a very short focal length. This GRIN lens,  $L_3$ , is placed on the optical axis at close proximity to the Fourier plane. As a result,  $L_3$  and  $L_2$  form another 4-f system and magnify the image of zeroth diffraction beam with a factor of 500, and this makes the camera only detect the DC component of the zeroth-order beam, which becomes the reference field. The authors in [52] demonstrated that this MISS design achieves an acquisition speed as fast as 833 frames per second, making it possible to study fast dynamic phenomena in living samples.

### 1.3.2 Phase-Shifting Methods

Phase-shifting QPI makes use of a phase SLM or similar device to introduce additional phase delay between sample and the reference light, and it records a collection of images to retrieve the associated phase [53–57]. Let  $\delta = \langle \omega \rangle (t - t_R)$ , the image irradiance in this configuration takes the form as

$$I(x, y, \delta) = |U_i(x, y)|^2 + |U_R|^2 + 2|U_i(x, y)||U_R| \cos[\varphi(x, y) + \delta] \quad (1.17)$$

In general, a phase map could be easily obtained using 4 intensity measurements, each with an increment phase delay of  $\pi/2$ , as

$$\varphi(x, y) = \arg(I_0 - I_\pi, I_{3\pi/2} - I_{\pi/2}) \quad (1.18)$$

Spatial light interference microscopy (SLIM) [53] is a phase-shifting, but also common-path QPI system. Based on an existing Zernike microscope, SLIM combines advantages of phase-contrast microscopy and Gabor's holography to obtain quantitative phase shift across the sample. A system schematic of SLIM is shown in Fig. 1.7. At the output of a phase-contrast microscope, two Fourier lens, compose a 4-f system and relay the image plane to the camera plane. A reflection SLM is placed at the back focal plane of the first Fourier lens to provide additional phase shift between scattered (sample) field and unscattered (reference) field, by increments of  $\pi/2$ . The projected pattern on the SLM is precisely calculated to match the size and position of the phase ring in the objective. As a result, 4 intensity images, each with a different delay, are acquired, and then the phase delay of the object is uniquely determined using (1.18). By employing a broadband white light as the illumination

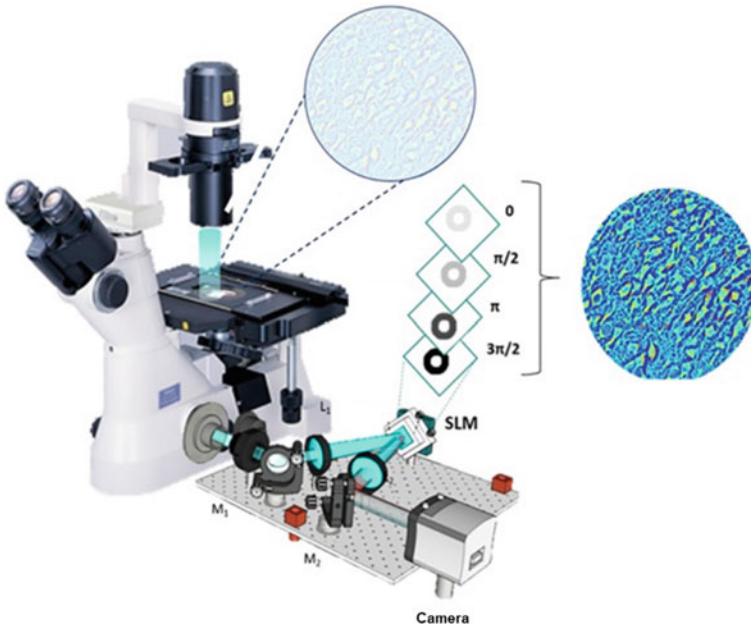


**Fig. 1.7** SLIM combines conventional phase contrast microscopy and an external module. The SLIM module consists of a 4-f lens system and an SLM, which produces phase modulation. Four intensity images, corresponding to  $0, \pi/2, \pi,$  and  $3\pi/2$  phase shift, are recorded to create one phase map (Reprinted from [94] with permission)

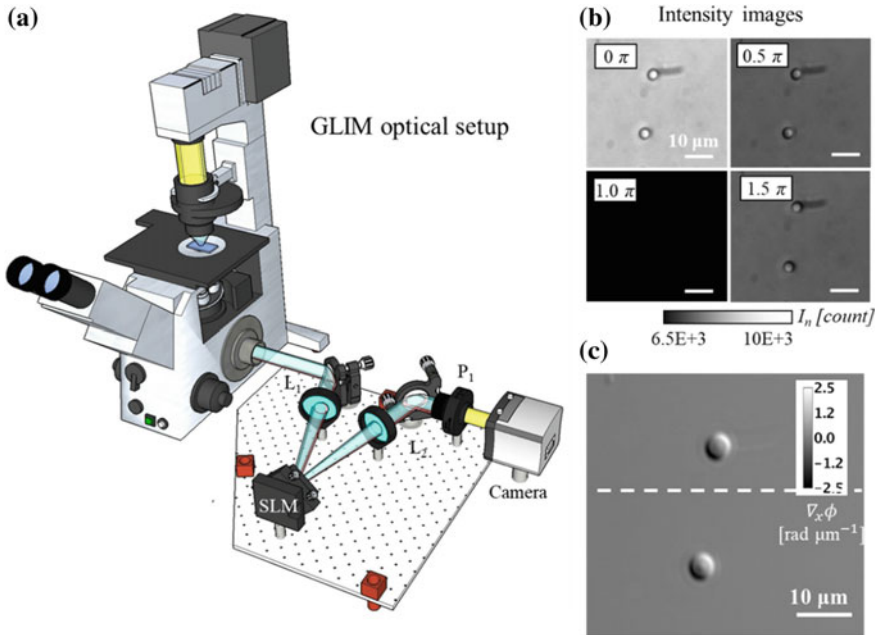


**Fig. 1.8** Principle of GLIM (Reprinted from [24])

source, SLIM provides speckle-free phase maps with exceptionally high sensitivity and stability.

Recently, a novel phase-shifting QPI system, referred as gradient light interference microscopy (GLIM), has been developed to extend QPI to thick, strongly scattering specimens [24]. The GLIM optical setup is shown in Fig. 1.8. GLIM combines the phase resolving power in DIC microscopy and holography to extract the gradient of phase map. Similar to the principle of SLIM, GLIM modulates the phase delay between the two interfering fields and reconstruct phase shift using 4 intensity images. Except for a tiny transverse shift, the two interfering beams experience identical degradation, and therefore, GLIM significantly rejects the multiple scattering, which makes it suitable to image thick samples. Furthermore, with a fully opened condenser, GLIM also exhibits strong tomographic capabilities.

## 1.4 Applications

In the past decade, accompanied by the advances in system design, the QPI field has continued growing and become a powerful approach for imaging biospecimens, which allows applications in a variety of fields, e.g., cell pathophysiology [58–68], cell dynamics and growth [61, 69–75], cell tomography [17, 19, 23, 24, 76, 77], tissue

optics [30, 49, 78–83], medical diagnosis [84–91], and neuroscience [52, 92–97]. Due to its capabilities for label-free imaging, high sensitivity, stability, and objective information, QPI allows investigating a sample's structure and dynamics at broad spatial and temporal scale [1].

### 1.4.1 Medical Applications

An important medical application for QPI is in pathological studies. Traditionally, this is mostly achieved by histological methods, where one uses multiple stains to render colors at different tissue structures and observes the sample under a conventional intensity-based microscope. The conventional methods only provide qualitative information on tissue morphology and the diagnosis outcome suffers from inter-observer variability [98]. Using QPI, however, the intrinsic phase contrast accurately maps the morphological features of sample, and more importantly, it can pick up structures that cannot be observed in stained tissue due to the staining error (see Fig. 1.9 for a QPI image of brain slice). Past studies have shown QPI's capabilities for diagnosing [99–101] and monitoring disease progression [102]. Furthermore, using scattering-phase theorem [103], one can extract scattering parameters associated with the specimen, which describes alterations in diseased tissue [82, 103–108]. For instance, measuring morphologies of blood cell (cell volume and surface area) has shown potential for hematology such as sickle cell disease [33, 109], diabetes

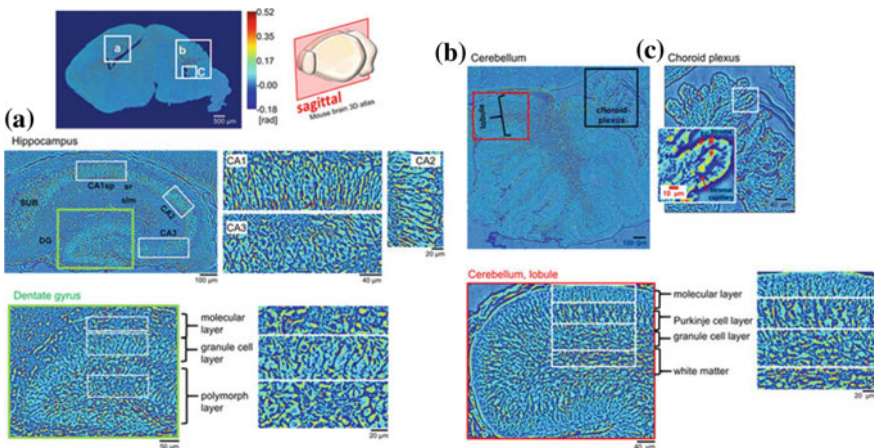


**Fig. 1.9** A brain slice imaging by a QPI tissue scanner. Regions **a** hippocampus, **b** cerebellum, and **c** choroid plexus are shown at increasing magnification. The green box in **(a)** shows the area of the dentate gyrus. The red box in **(b)** shows a cerebellum lobule. The layered structure for each region is analyzed in terms of phase value. The red arrows in **(c)** are pointing to stromal capillaries within the choroid plexus (Reprinted from [108])

[110], and malaria infection [111]. Combining with artificial intelligence, QPI-based tissue imager opens new directions for achieving automated diagnosis [112–114].

### 1.4.2 Cellular Dynamics

The cell growth and proliferation is a complicated process, which involves various activities such as producing proteins, communication with neighboring cells, interacting with the extracellular matrix, and migration [115]. Accurately recording and monitoring these phenomena, in general, is challenging. Since QPI reports the non-aqueous content within the sample referred to as *dry mass*, this label-free imaging modality offers an alternative means to measure cellular-level mass production in a noninvasive manner [61, 116, 117]. The local dry mass,  $\rho$ , is calculated as

$$\rho = \frac{\lambda\varphi}{2\pi\gamma} \quad (1.19)$$

where  $\lambda$  is the central wavelength of illumination light,  $\varphi$  the measured phase shift, and  $\gamma = 0.2 \text{ ml/g}$  the refractive increment of protein. Thus, the total mass of a region of interest is then calculated by integrating over the area. This simple math operation allows quantitative investigation of dynamics at cellular level, e.g., cell growth and division, emergence of neuronal network [61, 118–121]. In addition, by fitting the QPI data to a diffusion equation, biophysical features, e.g., advection and diffusion, can also be extracted to interpret the mass transport capabilities of the studied sample [43, 73, 122–126]. Recently, we have seen that several other models are invented to probe a sample’s biophysical properties, further expanding the scope of QPI applications.

### 1.4.3 Tomography

Tomographic imaging is an invaluable method for understanding the internal structure and dynamics in biological cells and tissue. In the past, 3D live cell imaging was mostly done by fluorescent-based techniques, such as confocal microscopy, which have limitations due to photobleaching and phototoxicity [127]. QPI tomography produces refractive index distribution in 3D and directly offers chemical composition and structural information of a sample, which is complementary to conventional methods [40, 128, 129]. For example, spiculated red blood cell structure was visualized by a white-light diffraction tomography [130]. A time-lapse tomogram of a chimeric antigen receptor T cell killing a leukemic B cell was obtained using optical diffraction tomography [1]. More recently, QPI tomography has been extended to measure thick specimen such as embryos, brain slices and organoids. Figure 1.10 shows 3D structural changes in a bovine embryo over several days [24].

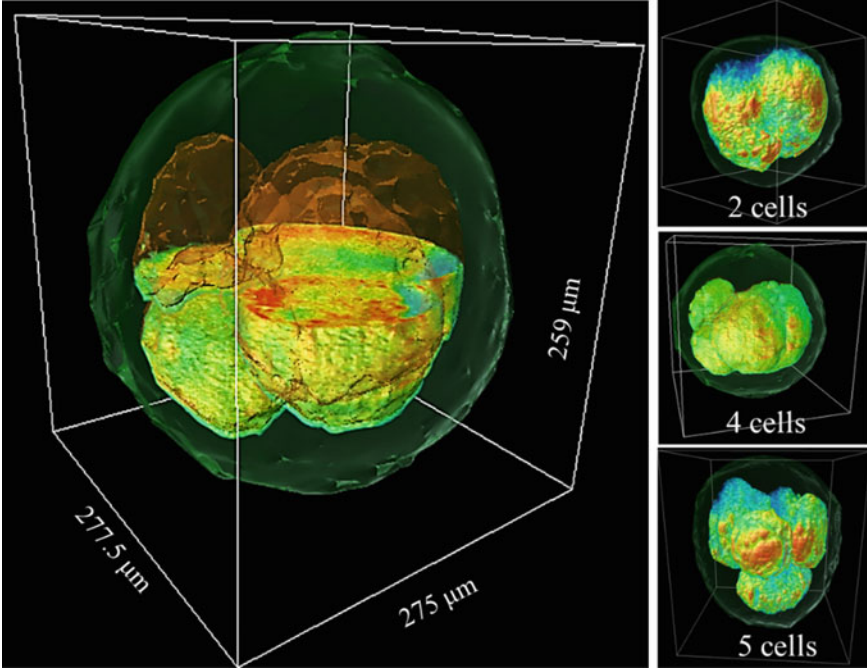


**Fig. 1.10** Time-lapse tomographic imaging of a bovine embryo with GLIM (Reprinted from [24])

## 1.5 Important Concepts in QPI

### 1.5.1 Effects of Spatial Coherence

In QPI, the accuracy of the phase retrieval depends on the spatial coherence of the light source. Building on the principles of interferometry, the phase is retrieved from the phase shifting and off-axis methods, via the cross-correlation function between the total field and a reference field, i.e.,  $\varphi(\mathbf{r}) = \arg[J_{t,r}(\mathbf{r}, \mathbf{r})]$ , where  $J_{t,r}(\mathbf{r}, \mathbf{r}) = \langle U_t(\mathbf{r}, t)U_r^*(\mathbf{r}, t) \rangle_t$  with \* indicating the complex conjugate. As discussed in [131–133], the measured phase is subject to the spatial correlation of the illumination field through the relation

$$\varphi(\mathbf{r}) \approx \varphi_0(\mathbf{r}) \odot_r [\delta(\mathbf{r}) - h_i(\mathbf{r})] \quad (1.20)$$

where  $\varphi_0$  the diffraction-limited phase measured in the conditions of full coherence,  $\delta(\mathbf{r})$  the 3D Dirac delta-function, and  $h_i(\mathbf{r})$  the normalized spatial correlation function associated with the illuminating field. Assume the object of interest in an extremely

small point,  $\varphi_0$  and  $\varphi$  are essentially the ideal PSF and measured PSF, respectively. Equation 1.20 states that the high-pass filtered version of the ideal phase is due to the partial spatial coherence from the source. The phase information is completely lost when the source is incoherent, meaning, when  $h_i(\mathbf{r})$  reduces to  $\delta(\mathbf{r})$ . Though methods have been developed to mitigate these artifacts [83, 134, 135], this partial spatial coherence essentially affects the measurement accuracy, and furthermore, brings into question whether the conventional resolution definition can be applied to characterize QPI and coherent imaging in general.

### 1.5.2 Defining Resolution

In microscopy, imaging contrast and spatial resolution are typical metrics to characterize the performance of an imaging system. The definition of magnification and contrast are well understood, the meaning of spatial resolution, however, appears to be ambiguous, especially for coherent imaging. The resolution of intensity-based imaging system, fluorescence for instance, is relatively straightforward. Due to the linear response between the optical intensity emitted from the object and those detected at the image plane, the resolution for incoherent imaging system is well characterized by its point spread function (PSF). The criteria for resolution include the maximum spatial frequency (Abbe criterion) [136] or the distance to the PSF's first root (Rayleigh criterion) [137]. However, a measurability issue arises when switched to the case of coherent imaging, due to the fact that the system has a linear response in the optical field but not its intensity, which is the measured quantity [138, 139]. Consider the case where two point sources are imaged by a microscope. Let us assume the two sources produce mutually incoherent light, and they are spatially separated by a distance larger than the diffraction limit, which makes them resolvable using an incoherent microscope. However, under the same microscope, if generating coherent light with 0 phase delay, these two point sources become fully unresolved (see, e.g., Chap. 8 in [2]). This simple illustration suggests that measuring and reporting its intensity profile is not a suitable means to characterize resolution.

With this context in mind, a practical unambiguous resolution standard is highly desirable to reliably assess the merits of coherent microscopic techniques. Several theoretical and practical methods have been proposed [138, 140, 141]. Here, we briefly discuss the resolution problem from the perspective of uncertainty relation. For an arbitrary field, the accuracy in defining the  $\mathbf{k}$ -vector and position cannot be both arbitrarily high. In 1927, Heisenberg stated this uncertainty principle in the context of quantum mechanics [142]. For an arbitrary field, the standard deviation of the  $\mathbf{k}$ -vector and its spatial spread along an axis satisfy the inequality

$$\Delta x \Delta k_x \geq \frac{1}{2}, \quad (1.21)$$

where the equality holds for Gaussian distributions. This uncertainty principle does not place a bound on the ability to make a measurement, but rather on the accuracy with which we can *define* the field distribution as well as its frequency representation. Equation 1.21 has direct consequences for imaging and scattering events, as it states that the minimum resolvable feature on the object is governed by the “spreading” in its  $\mathbf{k}$ -vector domain, instead of the maximum value,

$$R \propto \frac{2\pi}{\Delta k} \quad (1.22)$$

Thus, a generalized resolution definition can be achieved as inverse spatial bandwidth, in all three directions.

## 1.6 Summary and Outlook

As we have seen here, QPI adds essential value to microscopy. The intrinsic phase signal measured by QPI provides novel parameters to investigate physiological processes in biological samples. As discussed in the previous sections, tremendous progress has been made to improve the spatial and temporal resolution of QPI systems. Temporally, since no exogenous labeling is needed, QPI enables live sample measurements, lasting from the millisecond scale to days, even weeks. QPI could measure samples at different spatial scales, ranging from sub-cellular structures below the resolution limit, to thick tissues, 100s of micrometers thick. These advances in instrument development offer exciting possibilities for numerous applications in biology and medicine. Looking ahead, we foresee a few directions of potential interest. Firstly, the benefit of imaging unlabeled specimens comes at the cost of losing *specificity*. Most existing QPI systems rely on correlative fluorescent tagging to identify the structure of interest. One potential solution is to replace the fluorescent markers with scattering particles. By labeling structures of interest with nanoparticles with high refractive index, QPI would become an ideal imaging tool with high specificity, but without photobleaching. Secondly, the possibility of endoscopic QPI is another interesting avenue [36]. While most existing QPI systems measure samples *in vitro* or *ex vivo*, the study of *in vivo* or deep tissue imaging with QPI is rarely explored [143, 144]. Thirdly, label-free super-resolution imaging remains a significant technical goal. The existing super-resolution methods are typically involving fluorophores. Finally, we anticipate that combining QPI and artificial intelligence approaches will lead to advances in objective diagnosis. In the years to come, we anticipate that QPI will continue gaining popularity as it transfers from engineering to biomedical laboratories [1].

## References

1. Y. Park, C. Depeursinge, G. Popescu, Quantitative phase imaging in biomedicine. *Nat. Photonics* **12**, 578–589 (2018)
2. G. Popescu, *Quantitative Phase Imaging of Cells and Tissues*, McGraw-Hill biophotonics (McGraw-Hill, New York, 2011), p. 385
3. F. Zernike, Phase contrast, a new method for the microscopic observation of transparent objects Part II. *Physica* **9**, 974–986 (1942)
4. J. Mertz, *Introduction to Optical Microscopy*, vol. 138 (Roberts, 2010)
5. R.D. Allen, G.B. David, G. Nomarski, The zeiss-Nomarski differential interference equipment for transmitted-light microscopy. *Z. Wiss. Mikrosk.* **69**, 193–221 (1969)
6. D. Gabor, A new microscopic principle. *Nature* **161**, 777–778 (1948)
7. R. Collier, *Optical Holography* (Elsevier, 2013)
8. G. Popescu, *Quantitative Phase Imaging of Cells and Tissues* (McGraw Hill Professional, 2011)
9. Coherent light microscopy: imaging and quantitative phase analysis, in *Springer Series in Surface Sciences*, vol. 46 (2011), pp. 1–372
10. F. Merola, B. Mandracchia, L. Miccio, P. Memmolo, V. Bianco, M. Mugnano, P.L. Maffettone, M. Villone, E. Di Maio, V. Ferraro, Z. Wang, V. Pagliarulo, S. Grilli, P. Ferraro, Recent advancements and perspective about digital holography: a super-tool in biomedical and bioengineering fields, in *Advancement of Optical Methods & Digital Image Correlation in Experimental Mechanics*, vol. 3 (Springer International Publishing, 2019), pp. 235–241
11. M. Mir, B. Bhaduri, R. Wang, R. Zhu, G. Popescu, Quantitative phase imaging. *Prog. Opt.* **57**, 133–217 (2012)
12. G.A. Dunn, D. Zicha, Dynamics of fibroblast spreading. *J. Cell Sci.* **108**, 1239–1249 (1995)
13. D. Zicha, G.A. Dunn, An image-processing system for cell behavior studies in subconfluent cultures. *J. Microsc.* **179**, 11–21 (1995)
14. K.A. Nugent, T.E. Gureyev, D.F. Cookson, D. Paganin, Z. Barnea, Quantitative phase imaging using hard x rays. *Phys. Rev. Lett.* **77**, 2961–2964 (1996)
15. A. Barty, K.A. Nugent, D. Paganin, A. Roberts, Quantitative optical phase microscopy. *Opt. Lett.* **23**, 817–819 (1998)
16. P. Marquet, B. Rappaz, P.J. Magistretti, E. Cuche, Y. Emery, T. Colomb, C. Depeursinge, Digital holographic microscopy: a noninvasive contrast imaging technique allowing quantitative visualization of living cells with subwavelength axial accuracy. *Opt. Lett.* **30**, 468–470 (2005)
17. K. Kim, K.S. Kim, H. Park, J.C. Ye, Y. Park, Real-time visualization of 3-D dynamic microscopic objects using optical diffraction tomography. *Opt. Express* **21**, 32269–32278 (2013)
18. B. Kemper, G. von Bally, Digital holographic microscopy for live cell applications and technical inspection. *Appl. Opt.* **47**, A52–A61 (2008)
19. W. Choi, C. Fang-Yen, K. Badizadegan, S. Oh, N. Lue, R.R. Dasari, M.S. Feld, Tomographic phase microscopy. *Nat. Methods* **4**, 717–719 (2007)
20. M. Born, E. Wolf, *Principles of Optics: Electromagnetic Theory of Propagation, Interference and Diffraction of Light* (Elsevier, 2013)
21. D. Jin, R. Zhou, Z. Yaqoob, P.T.C. So, Tomographic phase microscopy: principles and applications in bioimaging [Invited]. *J. Opt. Soc. Am. B* **34**, B64–B77 (2017)
22. R.J. Zhou, T. Kim, L.L. Goddard, G. Popescu, Inverse scattering solutions using low-coherence light. *Opt. Lett.* **39**, 4494–4497 (2014)
23. T. Kim, R.J. Zhou, M. Mir, S.D. Babacan, P.S. Carney, L.L. Goddard, G. Popescu, White-light diffraction tomography of unlabeled live cells. *Nat. Photonics* **8**, 256–263 (2014)
24. T.H. Nguyen, M.E. Kandel, M. Rubessa, M.B. Wheeler, G. Popescu, Gradient light interference microscopy for 3D imaging of unlabeled specimens. *Nat. Commun.* **8**, 210 (2017)
25. M. Lee, E. Lee, J. Jung, H. Yu, K. Kim, J. Yoon, S. Lee, Y. Jeong, Y. Park, Label-free optical quantification of structural alterations in Alzheimer’s disease. *Sci Rep* **6**, 31034 (2016)
26. C. Hu, G. Popescu, Physical significance of backscattering phase measurements. *Opt. Lett.* **42**, 4643–4646 (2017)

27. C. Yang, A. Wax, I. Georgakoudi, E.B. Hanlon, K. Badizadegan, R.R. Dasari, M.S. Feld, Interferometric phase-dispersion microscopy. *Opt. Lett.* **25**, 1526–1528 (2000)
28. B. Bhaduri, C. Edwards, H. Pham, R.J. Zhou, T.H. Nguyen, L.L. Goddard, G. Popescu, Diffraction phase microscopy: principles and applications in materials and life sciences. *Adv. Opt. Photonics* **6**, 57–119 (2014)
29. S.K. Debnath, Y. Park, Real-time quantitative phase imaging with a spatial phase-shifting algorithm. *Opt. Lett.* **36**, 4677–4679 (2011)
30. Y. Lin, L. Dong, H. Chen, S. Huang, Phase distribution analysis of tissues based on the off-axis digital holographic hybrid reconstruction algorithm. *Biomed. Opt. Express* **9**, 1–13 (2018)
31. B. Bhaduri, G. Popescu, Derivative method for phase retrieval in off-axis quantitative phase imaging. *Opt. Lett.* **37**, 1868–1870 (2012)
32. H. Pham, N. Ding, N. Sobh, M. Do, S. Patel, G. Popescu, Off-axis quantitative phase imaging processing using CUDA: toward real-time applications. *Biomed. Opt. Express* **2**, 1781 (2011)
33. N.T. Shaked, L.L. Satterwhite, M.J. Telen, G.A. Truskey, A. Wax, Quantitative microscopy and nanoscopy of sickle red blood cells performed by wide field digital interferometry. *J. Biomed. Opt.* **16**, 030506 (2011)
34. S. Chowdhury, W.J. Eldridge, A. Wax, J. Izatt, Refractive index tomography with structured illumination. *Optica* **4**, 537–545 (2017)
35. T. Ikeda, G. Popescu, R.R. Dasari, M.S. Feld, Hilbert phase microscopy for investigating fast dynamics in transparent systems. *Opt. Lett.* **30**, 1165–1167 (2005)
36. C. Hu, S. Zhu, L. Gao, G. Popescu, Endoscopic diffraction phase microscopy. *Opt. Lett.* **43**, 3373–3376 (2018)
37. V. Mico, Z. Zalevsky, J. Garcia, Common-path phase-shifting digital holographic microscopy: a way to quantitative phase imaging and superresolution. *Opt. Commun.* **281**, 4273–4281 (2008)
38. S. Chen, C. Li, C. Ma, T.C. Poon, Y. Zhu, Phase sensitivity of off-axis digital holography. *Opt. Lett.* **43**, 4993–4996 (2018)
39. L. Liu, M. Shan, Z. Zhong, B. Liu, G. Luan, M. Diao, Y. Zhang, Simultaneous dual-wavelength off-axis flipping digital holography. *Opt. Lett.* **42**, 4331–4334 (2017)
40. F. Merola, P. Memmolo, L. Miccio, R. Savoia, M. Mugnano, A. Fontana, G. D’Ippolito, A. Sardo, A. Iolascon, A. Gambale, P. Ferraro, Tomographic flow cytometry by digital holography. *Light-Sci. Appl.* **6** (2017)
41. G. Popescu, T. Ikeda, R.R. Dasari, M.S. Feld, Diffraction phase microscopy for quantifying cell structure and dynamics. *Opt. Lett.* **31**, 775–777 (2006)
42. B. Bhaduri, H. Pham, M. Mir, G. Popescu, Diffraction phase microscopy with white light. *Opt. Lett.* **37**, 1094–1096 (2012)
43. C. Hu, R. Sam, M. Shan, V. Nastasa, M. Wang, T. Kim, M. Gillette, P. Sengupta, G. Popescu, Optical excitation and detection of neuronal activity. *J. Biophotonics*, e201800269 (2018)
44. C. Edwards, B. Bhaduri, B.G. Griffin, L.L. Goddard, G. Popescu, Epi-illumination diffraction phase microscopy with white light. *Opt. Lett.* **39**, 6162–6165 (2014)
45. M. Finkeldey, L. Goring, C. Brenner, M. Hofmann, N.C. Gerhardt, Depth-filtering in common-path digital holographic microscopy. *Opt. Express* **25**, 19398–19407 (2017)
46. R.J. Zhou, C. Edwards, A. Arbabi, G. Popescu, L.L. Goddard, Detecting 20 nm wide defects in large area nanopatterns using optical interferometric microscopy. *Nano Lett.* **13**, 3716–3721 (2013)
47. C. Edwards, A. Arbabi, G. Popescu, L.L. Goddard, Optically monitoring and controlling nanoscale topography during semiconductor etching. *Light-Sci. Appl.* **1** (2012)
48. H. Pham, B. Bhaduri, H. Ding, G. Popescu, Spectroscopic diffraction phase microscopy. *Opt. Lett.* **37**, 3438–3440 (2012)
49. E. Min, S. Ban, Y. Wang, S.C. Bae, G. Popescu, C. Best-Popescu, W. Jung, Measurement of multispectral scattering properties in mouse brain tissue. *Biomed. Opt. Express* **8**, 1763–1770 (2017)
50. J. Jung, K. Kim, H. Yu, K. Lee, S. Lee, S. Nahm, H. Park, Y. Park, Biomedical applications of holographic microscopy [invited]. *Appl. Opt.* **53**, G111–G122 (2014)

51. M. Rinehart, Y. Zhu, A. Wax, Quantitative phase spectroscopy. *Biomed. Opt. Express* **3**, 958–965 (2012)
52. H. Majeed, L. Ma, Y.J. Lee, M. Kandel, E. Min, W. Jung, C. Best-Popescu, G. Popescu, Magnified Image Spatial Spectrum (MISS) microscopy for nanometer and millisecond scale label-free imaging. *Opt. Express* **26**, 5423–5440 (2018)
53. Z. Wang, L. Millet, M. Mir, H.F. Ding, S. Unarunotai, J. Rogers, M.U. Gillette, G. Popescu, Spatial light interference microscopy (SLIM). *Opt. Express* **19**, 1016–1026 (2011)
54. H. Iwai, C. Fang-Yen, G. Popescu, A. Wax, K. Badizadegan, R.R. Dasari, M.S. Feld, Quantitative phase imaging using actively stabilized phase-shifting low-coherence interferometry. *Opt. Lett.* **29**, 2399–2401 (2004)
55. D.S. Mehta, V. Srivastava, Quantitative phase imaging of human red blood cells using phase-shifting white light interference microscopy with colour fringe analysis. *Appl. Phys. Lett.* **101** (2012)
56. Y. Wang, X.A. Qiu, J.X. Xiong, B.B. Li, L.Y. Zhong, S.D. Liu, Y.F. Zhou, J.D. Tian, X.X. Lu, General spatial phase-shifting interferometry by optimizing the signal retrieving function. *Opt. Express* **25**, 7170–7180 (2017)
57. N.T. Shaked, Y. Zhu, M.T. Rinehart, A. Wax, Two-step-only phase-shifting interferometry with optimized detector bandwidth for microscopy of live cells. *Opt. Express* **17**, 15585–15591 (2009)
58. K. Lee, K. Kim, J. Jung, J. Heo, S. Cho, S. Lee, G. Chang, Y. Jo, H. Park, Y. Park, Quantitative phase imaging techniques for the study of cell pathophysiology: from principles to applications. *Sensors (Basel)* **13**, 4170–4191 (2013)
59. M. Mir, A. Bergamaschi, B.S. Katzenellenbogen, G. Popescu, Highly sensitive quantitative imaging for monitoring single cancer cell growth kinetics and drug response. *PLoS ONE* **9**, e89000 (2014)
60. Y.K. Park, M. Diez-Silva, G. Popescu, G. Lykotrafitis, W. Choi, M.S. Feld, S. Suresh, Refractive index maps and membrane dynamics of human red blood cells parasitized by *Plasmodium falciparum*. *Proc. Natl. Acad. Sci. U.S.A.* **105**, 13730 (2008)
61. G. Popescu, Y. Park, N. Lue, C. Best-Popescu, L. Deflores, R.R. Dasari, M.S. Feld, K. Badizadegan, Optical imaging of cell mass and growth dynamics. *Am. J. Physiol. Cell Physiol.* **295**, C538–C544 (2008)
62. K. Park, L. Millet, J. Huan, N. Kim, G. Popescu, N. Aluru, K. J. Hsia, Bashir, Measurement of adherent cell mass and growth. *Proc. Nat. Acad. Sci.* (2010)
63. S. Ceballos, M. Kandel, S. Sridharan, H. Majeed, F. Monroy, G. Popescu, Active intracellular transport in metastatic cells studied by spatial light interference microscopy. *J. Biomed. Opt.* **20**, 111209–111209 (2015)
64. S. Sridharan Weaver, Y. Li, L. Foucard, H. Majeed, B. Bhaduri, A.J. Levine, K.A. Kilian, G. Popescu, Simultaneous cell traction and growth measurements using light. *J. Biophotonics* **0**, e201800182
65. Y.K. Park, C.A. Best, T. Auth, N. Gov, S.A. Safran, G. Popescu, S. Suresh, M.S. Feld, Metabolic remodeling of the human red blood cell membran. *Proc. Natl. Acad. Sci.* **107**, 1289 (2010)
66. R. Pandey, R. Zhou, R. Bordett, C. Hunter, K. Glunde, I. Barman, T. Valdez, C. Finck, Integration of diffraction phase microscopy and Raman imaging for label-free morpho-molecular assessment of live cells. *J. Biophotonics*, e201800291 (2018)
67. K. Kim, H. Yoon, M. Diez-Silva, M. Dao, R.R. Dasari, Y. Park, High-resolution three-dimensional imaging of red blood cells parasitized by *Plasmodium falciparum* and in situ hemozoin crystals using optical diffraction tomography. *BIOMEDO* **19** (2014)
68. G. Di Caprio, M.A. Ferrara, L. Miccio, F. Merola, P. Memmolo, P. Ferraro, G. Coppola, Holographic imaging of unlabelled sperm cells for semen analysis: a review. *J. Biophotonics* **8**, 779–789 (2015)
69. G. Popescu, K. Badizadegan, R.R. Dasari, M.S. Feld, Observation of dynamic subdomains in red blood cells. *J. Biomed. Opt. Lett.* **11**, 040503 (2006)

70. N. Lue, W. Choi, G. Popescu, R.R. Dasari, K. Badizadegan, M.S. Feld, Quantitative phase imaging of live cells using fast Fourier phase microscopy. *Appl. Opt.* **46**, 1836 (2007)
71. R. Gannavarpu, B. Bhaduri, K. Tangella, G. Popescu, Spatiotemporal characterization of a fibrin clot using quantitative phase imaging. *PLoS ONE* **9** (2014)
72. M.E. Kandel, K.W. Teng, P.R. Selvin, G. Popescu, Label-free imaging of single microtubule dynamics using spatial light interference microscopy. *ACS Nano* (2016)
73. R. Wang, Z. Wang, L. Millet, M.U. Gillette, A.J. Levine, G. Popescu, Dispersion-relation phase spectroscopy of intracellular transport. *Opt. Express* **19**, 20571–20579 (2011)
74. B. Kemper, D. Carl, J. Schnekenburger, I. Bredebusch, M. Schafer, W. Domschke, G. von Bally, Investigation of living pancreas tumor cells by digital holographic microscopy. *J. Biomed. Opt.* **11**, 34005 (2006)
75. B. Rappaz, P. Marquet, E. Cuche, Y. Emery, C. Depeursinge, P.J. Magistretti, Measurement of the integral refractive index and dynamic cell morphometry of living cells with digital holographic microscopy. *Opt. Express* **13**, 9361–9373 (2005)
76. F. Charriere, N. Pavillon, T. Colomb, C. Depeursinge, T.J. Heger, E.A.D. Mitchell, P. Marquet, B. Rappaz, Living specimen tomography by digital holographic microscopy: morphometry of testate amoeba. *Opt. Express* **14**, 7005–7013 (2006)
77. F. Merola, P. Memmolo, L. Miccio, R. Savoia, M. Mugnano, A. Fontana, G. D’Ippolito, A. Sardo, A. Iolascon, A. Gambale, P. Ferraro, Tomographic flow cytometry by digital holography. *Light. Sci. Appl.* **6**, e16241 (2017)
78. R.Y. Zhu, S. Sridharan, K. Tangella, A. Balla, G. Popescu, Correlation-induced spectral changes in tissues. *Opt. Lett.* **36**, 4209–4211 (2011)
79. T. Kim, R.J. Zhou, L.L. Goddard, G. Popescu, Breakthroughs in photonics 2013: quantitative phase imaging: metrology meets biology. *IEEE Photonics J.* **6** (2014)
80. M. Shan, M.E. Kandel, H. Majeed, V. Nastasa, G. Popescu, White-light diffraction phase microscopy at doubled space-bandwidth product. *Opt. Express* **24**, 29033–29039 (2016)
81. M. Shan, M.E. Kandel, G. Popescu, Refractive index variance of cells and tissues measured by quantitative phase imaging. *Opt. Express* **25**, 1573–1581 (2017)
82. S. Ban, E. Min, S. Baek, H.M. Kwon, G. Popescu, W. Jung, Optical properties of acute kidney injury measured by quantitative phase imaging. *Biomed. Opt. Express* **9**, 921–932 (2018)
83. M.E. Kandel, M. Fanous, C. Best-Popescu, G. Popescu, Real-time halo correction in phase contrast imaging. *Biomed. Opt. Express* **9**, 623–635 (2018)
84. H. Majeed, S. Sridharan, M. Mir, L. Ma, E. Min, W. Jung, G. Popescu, Quantitative phase imaging for medical diagnosis. *J. Biophotonics* **10**, 177–205 (2017)
85. M. Mir, M. Ding, Z. Wang, J. Reedy, K. Tangella, G. Popescu, Blood screening using diffraction phase cytometry. *J. Biomed. Opt.*, 027016-027011-027014 (2010)
86. S. Sridharan, V. Macias, K. Tangella, J. Melamed, E. Dube, M.X. Kong, A. Kajdacsy-Balla, G. Popescu, Prediction of prostate cancer recurrence using quantitative phase imaging: validation on a general population. *Sci. Rep.* **6** (2016)
87. M.E. Kandel, S. Sridharan, J. Liang, Z. Luo, K. Han, V. Macias, A. Shah, R. Patel, K. Tangella, A. Kajdacsy-Balla, G. Guzman, G. Popescu, Label-free tissue scanner for colorectal cancer screening. *J. Biomed. Opt.* **22**, 066016–066016 (2017)
88. T.H. Nguyen, S. Sridharan, V. Macias, A. Kajdacsy-Balla, J. Melamed, M.N. Do, G. Popescu, Automatic Gleason grading of prostate cancer using quantitative phase imaging and machine learning. *J. Biomed. Opt.* **22**, 036015–036015 (2017)
89. H. Majeed, T.H. Nguyen, M.E. Kandel, A. Kajdacsy-Balla, G. Popescu, Label-free quantitative evaluation of breast tissue using Spatial Light Interference Microscopy (SLIM). *Sci. Rep.* **8**, 6875 (2018)
90. M. Takabayashi, H. Majeed, A. Kajdacsy-Balla, G. Popescu, Disorder strength measured by quantitative phase imaging as intrinsic cancer marker in fixed tissue biopsies. *PLoS ONE* **13**, e0194320 (2018)
91. D. Roitshtain, L. Wolbromsky, E. Bal, H. Greenspan, L.L. Satterwhite, N.T. Shaked, Quantitative phase microscopy spatial signatures of cancer cells. *Cytometry A* **91**, 482–493 (2017)

92. C. Hu, G. Popescu, Quantitative phase imaging (QPI) in neuroscience. *IEEE J. Sel. Top. Quantum Electron.* **25**, 1–9 (2019)
93. Z. Wang, I.S. Chun, X.L. Li, Z.Y. Ong, E. Pop, L. Millet, M. Gillette, G. Popescu, Topography and refractometry of nanostructures using spatial light interference microscopy. *Opt. Lett.* **35**, 208–210 (2010)
94. P. Cintora, J. Arikath, M. Kandel, G. Popescu, C. Best-Popescu, Cell density modulates intracellular mass transport in neural networks. *Cytometry A* **91**, 503–509 (2017)
95. M.E. Kandel, D. Fernandes, A.M. Taylor, H. Shakir, C. Best-Popescu, G. Popescu, Three-dimensional intracellular transport in neuron bodies and neurites investigated by label-free dispersion-relation phase spectroscopy. *Cytometry Part A*, n/a–n/a (2017)
96. Y.J. Lee, P. Cintora, J. Arikath, O. Akinsola, M. Kandel, G. Popescu, C. Best-Popescu, Quantitative assessment of neural outgrowth using spatial light interference microscopy. *BIOMEDO* **22**, 066015–066015 (2017)
97. P. Marquet, C. Depeursinge, P.J. Magistretti, Review of quantitative phase-digital holographic microscopy: promising novel imaging technique to resolve neuronal network activity and identify cellular biomarkers of psychiatric disorders. *Neurophotonics* **1**, 020901 (2014)
98. C.R. Taylor, R.M. Levenson, Quantification of immunohistochemistry—issues concerning methods, utility and semiquantitative assessment II. *Histopathology* **49**, 411–424 (2006)
99. H. Majeed, M.E. Kandel, K. Han, Z.L. Luo, V. Macias, K. Tangella, A. Balla, G. Popescu, Breast cancer diagnosis using spatial light interference microscopy. *BIOMEDO* **20** (2015)
100. I. Barnea, L. Karako, S.K. Mirsky, M. Levi, M. Balberg, N.T. Shaked, Stain-free interferometric phase microscopy correlation with DNA fragmentation stain in human spermatozoa. *J. Biophotonics* **11**, e201800137 (2018)
101. Z. Wang, K. Tangella, A. Balla, G. Popescu, Tissue refractive index as marker of disease. *BIOMEDO* **16** (2011)
102. S.A. Yang, J. Yoon, K. Kim, Y. Park, Measurements of morphological and biophysical alterations in individual neuron cells associated with early neurotoxic effects in Parkinson's disease. *Cytometry Part A* **91a**, 510–518 (2017)
103. Z. Wang, H. Ding, G. Popescu, Scattering-phase theorem. *Opt. Lett.* **36**, 1215 (2011)
104. M. Lee, E. Lee, J. Jung, H. Yu, K. Kim, J. Yoon, S. Lee, Y. Jeong, Y. Park, Label-free optical quantification of structural alterations in Alzheimer's disease. *Sci. Rep. UK* **6**, 31034 (2016)
105. S. Sridharan, V. Macias, K. Tangella, A. Kajdacsy-Balla, G. Popescu, Prediction of prostate cancer recurrence using quantitative phase imaging. *Sci. Rep. UK* **5** (2015)
106. H. Ding, Z. Wang, F. Nguyen, S.A. Boppart, G. Popescu, Fourier transform light scattering of inhomogeneous and dynamic structures. *Phys. Rev. Lett.* **101**, 238102 (2008)
107. H. Ding, Z. Wang, X. Liang, S.A. Boppart, K. Tangella, G. Popescu, Measuring the scattering parameters of tissues from quantitative phase imaging of thin slices. *Opt. Lett.* **36**, 2281–2283 (2011)
108. E. Min, M.E. Kandel, C.J. Ko, G. Popescu, W. Jung, C. Best-Popescu, Label-free, multi-scale imaging of ex-vivo mouse brain using spatial light interference microscopy. *Sci. Rep. UK* **6** (2016)
109. B. Javidi, A. Markman, S. Rawat, T. O'Connor, A. Anand, B. Andemariam, Sickle cell disease diagnosis based on spatio-temporal cell dynamics analysis using 3D printed shearing digital holographic microscopy. *Opt. Express* **26**, 13614–13627 (2018)
110. S. Lee, H. Park, K. Kim, Y. Sohn, S. Jang, Y. Park, Refractive index tomograms and dynamic membrane fluctuations of red blood cells from patients with diabetes mellitus. *Sci. Rep.* **7**, 1039 (2017)
111. M.T. Rinehart, H.S. Park, K.A. Walzer, J.T. Chi, A. Wax, Hemoglobin consumption by *P. falciparum* in individual erythrocytes imaged via quantitative phase spectroscopy. *Sci. Rep.* **6**, 24461 (2016)
112. H. Majeed, T.H. Nguyen, M.E. Kandel, A. Kajdacsy-Balla, G. Popescu, Label-free quantitative evaluation of breast tissue using Spatial Light Interference Microscopy (SLIM). *Sci. Rep. UK* **8** (2018)

113. H.S. Park, M. Rinehart, K.A. Walzer, J.T.A. Chi, A. Wax, Automated detection of *P. falciparum* using machine learning algorithms with quantitative phase images of unstained cells. *PLoS ONE* **11**(2016)
114. T.H. Nguyen, S. Sridharan, V. Macias, A. Kajdacsy-Balla, J. Melamed, M.N. Do, G. Popescu, Automatic Gleason grading of prostate cancer using quantitative phase imaging and machine learning. *BIOMEDO* **22** (2017)
115. A. Tzur, R. Kafri, V.S. LeBleu, G. Lahav, M.W. Kirschner, Cell growth and size homeostasis in proliferating animal cells. *Science* **325**, 167–171 (2009)
116. R. Barer, Interference microscopy and mass determination. *Nature* **169**, 366–367 (1952)
117. R. Barer, Determination of dry mass, thickness, solid and water concentration in living cells. *Nature* **172**, 1097–1098 (1953)
118. M. Mir, T. Kim, A. Majumder, M. Xiang, R. Wang, S.C. Liu, M.U. Gillette, S. Stice, G. Popescu, Label-free characterization of emerging human neuronal networks. *Sci. Rep.* **4**, 4434 (2014)
119. M. Mir, Z. Wang, Z. Shen, M. Bednarz, R. Bashir, I. Golding, S.G. Prasanth, G. Popescu, Optical measurement of cycle-dependent cell growth. *Proc. Natl. Acad. Sci. U.S.A.* **108**, 13124–13129 (2011)
120. Y. Park, C.A. Best, T. Auth, N.S. Gov, S.A. Safran, G. Popescu, S. Suresh, M.S. Feld, Metabolic remodeling of the human red blood cell membrane. *Proc. Natl. Acad. Sci. U.S.A.* **107**, 1289–1294 (2010)
121. B. Mandracchia, O. Gennari, A. Bramanti, S. Grilli, P. Ferraro, Label-free quantification of the effects of lithium niobate polarization on cell adhesion via holographic microscopy. *J. Biophotonics* **11**, e201700332 (2018)
122. W.J. Eldridge, A. Sheinfeld, M.T. Rinehart, A. Wax, Imaging deformation of adherent cells due to shear stress using quantitative phase imaging. *Opt. Lett.* **41**, 352–355 (2016)
123. M. Balberg, M. Levi, K. Kalinowski, I. Barnea, S.K. Mirsky, N.T. Shaked, Localized measurements of physical parameters within human sperm cells obtained with wide-field interferometry. *J. Biophotonics* **10**, 1305–1314 (2017)
124. G. Popescu, T. Ikeda, K. Goda, C.A. Best-Popescu, M. Laposata, S. Manley, R.R. Dasari, K. Badizadegan, M.S. Feld, Optical measurement of cell membrane tension. *Phys. Rev. Lett.* **97**, 218101 (2006)
125. M. Zakerin, A. Novak, M. Toda, Y. Emery, F. Natalio, H.J. Butt, R. Berger, Thermal characterization of dynamic silicon cantilever array sensors by digital holographic microscopy. *Sensors (Basel)* **17** (2017)
126. H.F. Ding, Z. Wang, F. Nguyen, S.A. Boppart, G. Popescu, Fourier transform light scattering of inhomogeneous and dynamic structures. *Phys. Rev. Lett.* **101** (2008)
127. J. B. Pawley, *Handbook of Biological Confocal Microscopy*, 3rd ed. (Springer, New York, 2006), pp. xxviii, 985 p
128. Y. Sung, W. Choi, C. Fang-Yen, K. Badizadegan, R.R. Dasari, M.S. Feld, Optical diffraction tomography for high resolution live cell imaging. *Opt. Express* **17**, 266–277 (2009)
129. F. Merola, P. Memmolo, L. Miccio, M. Mugnano, P. Ferraro, Phase contrast tomography at lab on chip scale by digital holography. *Methods* **136**, 108–115 (2018)
130. T. Kim, R. Zhou, M. Mir, S.D. Babacan, P.S. Carney, L.L. Goddard, G. Popescu, White-light diffraction tomography of unlabelled live cells. *Nat. Photon* **8**, 256–263 (2014)
131. C. Edwards, B. Bhaduri, T. Nguyen, B.G. Griffin, H. Pham, T. Kim, G. Popescu, L.L. Goddard, Effects of spatial coherence in diffraction phase microscopy. *Opt. Express* **22**, 5133–5146 (2014)
132. T.H. Nguyen, C. Edwards, L.L. Goddard, G. Popescu, Quantitative phase imaging with partially coherent illumination. *Opt. Lett.* **39**, 5511–5514 (2014)
133. T.H. Nguyen, C. Edwards, L.L. Goddard, G. Popescu, Quantitative phase imaging of weakly scattering objects using partially coherent illumination. *Opt. Express* **24**, 11683–11693 (2016)
134. T.H. Nguyen, M. Kandel, H.M. Shakir, C. Best-Popescu, J. Arikath, M.N. Do, G. Popescu, Halo-free phase contrast microscopy. *Sci. Rep. UK* **7** (2017)

135. I. Vartiainen, R. Mokso, M. Stampanoni, C. David, Halo suppression in full-field x-ray Zernike phase contrast microscopy. *Opt. Lett.* **39**, 1601–1604 (2014)
136. E. Abbe, A contribution to the theory of the microscope and the nature of microscopic vision, in *Proceedings of the Bristol Naturalists' Society* (1874), pp. 200–261
137. A.J. den Dekker, A. van den Bos, Resolution: a survey. *J. Opt. Soc. Am. A* **14**, 547–557 (1997)
138. R. Horstmeyer, R. Heintzmann, G. Popescu, L. Waller, C.H. Yang, Standardizing the resolution claims for coherent microscopy. *Nat. Photonics* **10**, 68–71 (2016)
139. P. Bon, G. Maucort, B. Wattellier, S. Monneret, Quadriwave lateral shearing interferometry for quantitative phase microscopy of living cells. *Opt. Express* **17**, 13080–13094 (2009)
140. C. Park, S. Shin, Y. Park, Generalized quantification of three-dimensional resolution in optical diffraction tomography using the projection of maximal spatial bandwidths. *J. Opt. Soc. Am. A* **35**, 1891–1898 (2018)
141. C.J.R. Sheppard, Resolution and super-resolution. *Microsc. Res. Tech.* **80**, 590–598 (2017)
142. W. Heisenberg, Über den anschaulichen Inhalt der quantentheoretischen Kinematik und Mechanik. *Z. für Phys.* **43**, 172–198 (1927)
143. Y. Choi, C. Yoon, M. Kim, T.D. Yang, C. Fang-Yen, R.R. Dasari, K.J. Lee, W. Choi, Scanner-free and wide-field endoscopic imaging by using a single multimode optical fiber. *Phys. Rev. Lett.* **109** (2012)
144. T. Cizmar, K. Dholakia, Exploiting multimode waveguides for pure fibre-based imaging. *Nat. Commun.* **3** (2012)

# Chapter 2

## Interferometric Scattering (iSCAT) Microscopy and Related Techniques



Richard W. Taylor and Vahid Sandoghdar

**Abstract** Interferometric scattering (iSCAT) microscopy is a powerful tool for label-free sensitive detection and imaging of nanoparticles to high spatiotemporal resolution. As it was born out of detection principles central to conventional microscopy, we begin by surveying the historical development of the microscope to examine how the exciting possibility for interferometric scattering microscopy with sensitivities sufficient to observe single molecules has become a reality. We discuss the theory of interferometric detection and also issues relevant to achieving a high detection sensitivity and speed. A showcase of numerous applications and avenues of novel research across various disciplines that iSCAT microscopy has opened up is also presented.

### 2.1 Introduction

Super-resolving the position of nanoscopic objects to a precision better than the wavelength of light is an important and powerful technology in nanoscience and, in particular, in the rapidly growing field of nanobiology. The forebear to modern super-resolution microscopy, where typically one aims to resolve intricate extended cellular substructures, is fluorescence microscopy. With the advent of single-molecule fluorescent spectroscopy and microscopy in the early 1990s, it became possible to extend such measurements to fluorescent labels as small as single dye molecules, quantum dots or single fluorescent proteins [1]. Fluorescence as a contrast mechanism, however, brings about several restrictions. These include (1) the use of the label itself, which may introduce artifacts to the interpretation, (2) the limited photoemission, caused by photobleaching and photoblinking as well as (3) saturation which curtails the spatiotemporal resolution and duration of a measurement. Fluorescence-free alternatives are thus highly desirable to overcome these limitations.

---

R. W. Taylor · V. Sandoghdar (✉)  
Max Planck Institute for the Science of Light, 91058 Erlangen, Germany  
e-mail: [vahid.sandoghdar@mpl.mpg.de](mailto:vahid.sandoghdar@mpl.mpg.de)

© Springer Nature Switzerland AG 2019  
V. Astratov (ed.), *Label-Free Super-Resolution Microscopy*,  
Biological and Medical Physics, Biomedical Engineering,  
[https://doi.org/10.1007/978-3-030-21722-8\\_2](https://doi.org/10.1007/978-3-030-21722-8_2)

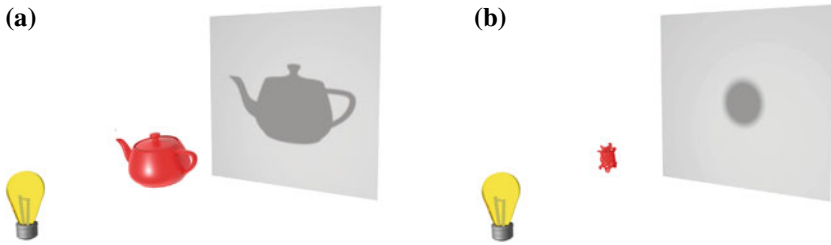


**Fig. 2.1** Detection of an object from its shadow: just as we may observe an everyday object from the shadow it casts—such as the teapot **(a)**, we may equally do so with an object much smaller than the wavelength of light, i.e., a nanoparticle or even a single protein **(b)**. Such a small object casts a shadow with no structure, instead, the shadow appears as a single spot with a minimum size given by the diffraction limit of light

The most familiar and common mode of fluorescence-free microscopy is when one detects the optical *shadow* cast by the object (see Fig. 2.1a). The size of the shadow is proportional to the size of the object, and its degree of darkness is a measure for its transparency. This detection principle serves as the foundation for the earliest developments in microscopy and continues to be the basis of any modern microscope. It turns out that this line of thought is also applicable for viewing subwavelength nanoscopic particles, and even single molecules. In this regime, the geometric shape and size of the object is no longer represented by the shadow, which collapses to the point-spread function (PSF) of the microscope. Nevertheless, the object imprints its signature in the faint *extinction* of the illuminating beam (see Fig. 2.1b). The challenge lies in reaching a high sensitivity in detection to observe the resulting *nano-shadow*, requiring discrimination of the minuscule changes in light intensity as well as oftentimes measures to separate the desired shadow from the accompanying background.

In this chapter, we shall show that successful detection of the shadow from nano-objects permits label-free localization with outstanding spatial and temporal resolution, made possible by a high signal-to-noise ratio (SNR). As we shall see, the resulting extinction nanoscopy can be seen as a very recent realization of an old contrast mechanism. It is thus instructive to take a retrospective look at some of the developments in light microscopy that have led us to this exciting possibility, which we summarize in Fig. 2.2.

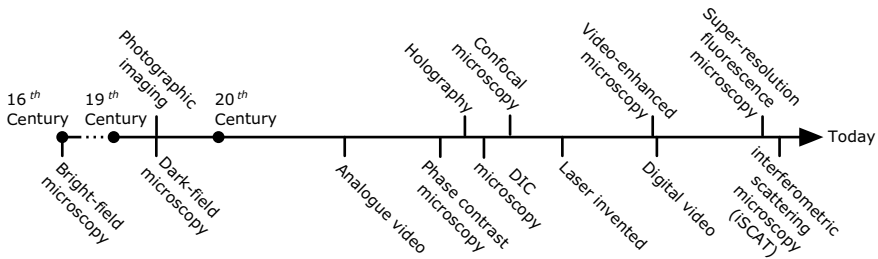


Fig. 2.2 Important milestones throughout the history of microscopy

## 2.2 Historical Perspective

One of the earliest documented examples of a microscope is attributed to Zacharias Jansen (1585–1638) who reportedly demonstrated a compound two-lens microscope as early as 1590. The microscope boasted a 20-fold magnification and was able to image sufficiently opaque samples when viewed with the eye. About half a century later, both Robert Hooke (1635–1703) and Antonie van Leeuwenhoek (1632–1723) would use microscopes as the foundation for their study into small organisms. Remarkably, the self-made microscopes of the latter reached a magnification one order of magnitude larger than his contemporaries—placing it on the level with current research-grade microscopes, permitting him to observe individual blood and yeast cells, as well as microscopic bacteria and protozoans. These efforts laid the foundations for the discipline of biological microscopy.

In the time following van Leeuwenhoek up to the turn of the twentieth century, the art of microscopy would mature into a rigorous scientific discipline following continuous refinement and innovation. For example, after 1820 it became possible to manufacture combinations of lenses small enough for high magnification objectives that could also include corrections for chromatic aberrations. In 1873 Ernst Abbe (1840–1905) published on his theory of the microscope [2], introducing strict mathematical definitions to the vocabulary of microscopy, which in turn led to a better understanding of the physical operation of the microscope and hence to better designed instruments. Thereafter, commercial availability of microscopes with superior performance led to their widespread adoption by scientists of that era. During this period, we also began to see a burgeoning diversity in the specimens which became the subject of microscopic investigation. The smallest specimens investigated, however, remained limited to that of micron-sized entities, something already observable since the seventeenth century. To appreciate why this limit was encountered, it is important to consider the sensitivity of the detector commonly used in these microscopies, namely, the eye.

The response of the human eye to light intensity is nonlinear, beginning with a detection threshold of around 2%. Our ability to sense changes in light intensity—which we call *contrast*, diminishes as the change becomes a smaller fraction of

the overall brightness [3]. In conventional bright-field microscopy this means that if small, thin or otherwise weakly interacting samples cannot cast a shadow of sufficient darkness then, to our eyes, it cannot be seen. An apt example of our limited contrast sensitivity is that of the spider web [4]; viewed against the bright sky the web is practically invisible, but when seen illuminated by the same sunlight against the darker surface of the ground, the web is now readily observed. In other words, we can circumvent the limitations of our visual sensitivity by diminishing the brightness of the background against which we wish to detect a shadow. This situation is also familiar to the astronomer, as favorable conditions for observing the faint light of distant stars occurs when the surrounding sky is as dark as possible.

In microscopic imaging, the deliberate removal of background illumination is known as dark-field imaging, with the first recorded instance of its implementation dating back as early as 1830 to Joseph Jackson Lister (1786–1869) [5]. Despite its effectiveness and advocates, dark-field microscopy initially failed to gain appreciation in the wider circles of microscopy, and was seen somewhat of a novelty. The technique remained largely overlooked [6] until the realization of the potential for dark-field to observe minute specimens that were otherwise invisible in bright-field. Austrian Chemist Richard Adolf Zsigmondy (1865–1929) would beautifully demonstrate this principle in 1902. Zsigmondy, along with Henry Siedentopf (1872–1940), presented the technique for the observation of nanometer-sized gold particles *by eye*. Consisting of an orthogonal objective and condenser, the “ultramicroscope”—as it was so named, allowed the observation of light scattered by the nanoparticles in the absence of a background [7]. This technique facilitated a more sensitive detection microscopy, which would enable, for example, the breakthroughs into identifying the microorganisms responsible for syphilis. In recognition of his achievements, Zsigmondy would be awarded the Chemistry Nobel Prize in 1925, the first of many Nobel Prizes to be awarded for advances in optical microscopy. It should be noted, however, that dark-field imaging becomes increasingly challenging for smaller objects, especially those in the presence of larger ones, as noise and incomplete removal of the background obscures detectability.

Where dark-field imaging seeks to better detection sensitivity through complete removal of the background, a more powerful approach to higher imaging contrast is to selectively shift the phase of the background illumination with respect to the incident light that interacts with the sample. This realization would be made in the decade following Zsigmondy’s Nobel Prize by Frits Zernike (1888–1966), who developed such wisdom from the study of aberrations and coherence in diffraction gratings and telescopic optics [8–10]. Phase Contrast Microscopy (PCM) [10–12], as it became to be known, involved the addition of a phase plate to the illumination path in the microscope with the effect of enhancing the bright-field contrast of specimens with refractive index similar to that of the surrounding media. Phase Contrast Microscopy represented a monumental advancement in microscopy, garnering Zernike the 1953 Physics Nobel Prize, with the successes brought about within the research of cancer being cited as one of the many advances enabled by PCM.

Arguably, Zernike’s greater impact was to bring interferometric principles to the fore of contemporary microscopy, specifically into biologically-orientated imaging,

where the early success of staining techniques had quashed the necessity to search for more elaborate means to improve contrast. Another interferometric modality that has since become popular is Differential Interference Contrast (DIC) microscopy, in which regions of differing optical paths in the sample, such as those occurring at edges, are shown with enhanced contrast through the interference of parallel sheared beams. The spatial displacement and angular deviation of the beams, on the order of half the airy disk diameter, is achieved through a special prism introduced by Georges Normanski (1919–1997) which bears his name [13]. Interestingly, the conceptual roots of DIC microscopy can be traced to the interferometer developed by Jules Jamin (1818–1886) in 1856 [14], and the first interference microscope from Jacobus Laurens Sirks (1837–1905) in 1893 [15]. Another important related invention was that of holography as proposed by Dennis Gabor (1900–1979) in 1947 [16], an accomplishment that would lead to Gabor being awarded the Physics Nobel Prize in 1971. As a new technique, Holography was mainly employed in macroscopic imaging, one of the first holographic microscopes was reported in 1966 [17], enabled by the commercial availability of the laser which was invented several years prior.

By the era of the late 1950s, interferometric microscopy was in its heyday, with a bewildering array of interferometric microscopes demonstrated, several of which found commercial release. A comprehensive review of these microscopes is provided in [18]. Popular categories of design for these interferometric microscopes include [19, 20]: (1) the beam-shearing type, (2) a two-arm design, and (3) the dual focus type in which the reference wave is focused to a different plane than that of the specimen. Unfortunately, interferometric microscopies witnessed a general decline after the 1950s, save for their application in surface profilometry, e.g., in precision engineering, and later for inspection in the microelectronics industry, where reflection-based Normanski DIC and the Mirau interferometer objective remain workhorses to this day [21]. The decline of interferometry as the principle imaging technique in the life sciences was the result of a series of innovations and developments in fluorescence microscopy [22, 23], such as the invention of immunolabeling in 1950, which led to a meteoric rise in fluorescence imaging, aided by the subsequent invention of confocal scanning microscopy in 1955 by Marvin Minsky (1927–2016) [24].

One interferometric technique that would thrive throughout the 1960–70s was Interferometric Reflection Microscopy (IRM). This simple technique, which in fact does not require an explicit interferometer, relies on the sample coverslip to provide the reference beam. The rise of IRM is widely accredited to Adam Curtis (1934–2017), who investigated and estimated the *nanometric* separation between glass and cell at sites of adhesion in living cultured fibroblasts [25]. The interferometric nature of the image provided nanometer-level information on the cell–substrate distances—a resolution unmatched by fluorescent methodologies of the time, enabling researchers using IRM to pioneer investigations into cell adhesion [26–30] as well as associated cytoskeletal components [31]. Johan Sebastiaan Ploem (born 1927) would later introduce instrumental refinements to better the sensitivity and performance of the technique under the alternative name Reflection Contrast Microscopy (RCM) [26]. Ultimately the failure to interpret quantitatively the interferometric content of the images, i.e., accounting for contributions from variations

in refractive index or path length [26, 32], would lead to declining interest in the method. Nevertheless, the technique would undergo a new lease of life in the late 1980s under the helm of Erich Sackmann (born 1934) who sought to implement greater quantitative rigor, initially studying cell membrane elasticity [33] and later the interaction of synthetic vesicle membranes to their substrates [34, 35].

Other interferometric methods would also find a revival in the 1980s, following the realization that analogue controls for camera gain and offset could be used to increase the dynamic range and contrast of microscopic images. This contrast enhancement facilitated real-time observations of structures that were previously too faint to see by the naked eye. Indeed, weak contrast variations composing an image are more easily detected by the video camera owing to its linear response to light intensity. While this fact was known since the invention of the video camera in the 1940s, the better resolution and historical success of photography cemented the latter as the dogma in microscopic documentation. It would not be until 1975 for this view to change [36], and another 6 years before the first implementations of this *analogue* contrast enhancement [37, 38].

The improvement in analogue contrast immediately precipitated a new problem of how to remove unwanted background signals such as *speckle* originating from uneven illumination or the presence of dust, etc. By digitizing the analogue video signal, these problems could be readily tackled because the live video signal could undergo in-line digital processing including static image subtraction, averaging and differential subtraction [39, 40]. This technique was referred to as *digital* contrast enhancement, and along with its analogue cousin, would collectively become known as *video-enhanced microscopy* [41, 42] and often paired with DIC imaging. Following its introduction in the early 1980s, video-enhanced microscopy quickly led to a flurry of efforts to explore previously hidden aspects of cellular architecture and function, including the network structure of cellular microtubules and actin filaments, or transport of particles and vesicles in and around the cell [43–47].

Following these demonstrations, the video-enhanced microscopy of the late 1980s and early 1990 quickly advanced efforts to monitor intracellular dynamics of specific proteins in living cells through introduction of sub-hundred nanometer colloidal particles. Michael Sheetz and colleagues pioneered this microscopy under the moniker *Nanovid-microscopy* (nanometer video-enhanced microscopy) and investigated *in vitro* mobility assays on microtubules, receptor-mediated endocytosis and single-protein diffusion in the plasma membrane of cells [48–53]—a body of work that serves as the foundation for single-particle tracking microscopy. In the latter half of the 1990s to early 2000s, Akihiro Kusumi and colleagues would use this technique to advance the study of single-protein diffusion in the plasma membrane of cells [54, 55].

It is worth noting that the challenge of detecting and analyzing micro- and sub-microscopic particulates were also confronted in the field of aerosol science, dating from the period of the 1970s. Whilst employing intensity-based detection, in 1982 Pettit and Peterson [56] introduced an interferometric scheme derived from the Jamin interferometer to detect the phase shift induced by microscopic particles upon the incident illuminating beam. By using phase a better estimate of the particle size was

demonstrated along with an improved detection sensitivity. This scheme would be refined further by Batchelder and Taubenblatt in 1989 [57].

The 1980s also saw the field of nanoscience emerge out of the collective invention of advanced scanning probe techniques, such as the Scanning Tunneling Microscope (STM) in 1981, Scanning Near-Field Optical Microscopy (SNOM) in 1984 [58], and the Atomic Force Microscope (AFM) in 1986 [59] as well as the discovery of new materials such as carbon nanotubes and fullerenes. Optical microscopy would similarly undergo great advances in performance following demonstration of the optical detection of single dye molecules in 1989 [60]. Complemented by the general political optimism at the end of the cold war, these developments launched a euphoria in accessing the *nano-world* at the turn of the 1990s, as had been imagined by Richard Feynman almost 30 years prior [61].

With the emergence of SNOM, optical microscopy experienced a revolutionary era as it was now freed of the century-long bounds of the diffraction limit, and brought promise of the detection and spectroscopy of individual molecules in contexts ranging from materials science to chemistry, physics and biology. As in conventional light microscopy, the main contrast mechanism in SNOM is based on the extinction of light, now exiting a scanning subwavelength aperture. However, the physical interaction at work in SNOM should be understood in the context of *scattering* rather than reflection or transmission as considered in far-field imaging. In practice, SNOM suffered from very weak signals stemming from faint illumination out of a nanometric aperture and weak scattering from nanoscopic features on the sample surface. One of the efforts in tackling the limited throughput were put forth in 1994 by the group of Wickramasinghe, who demonstrated interferometric (homodyne) detection of the field scattered from a sharp solid tip (apertureless SNOM) [62]. Interpretation of the SNOM signal in this mode and similar configurations presented a great challenge caused by spurious interference effects [63], which hampered adoption of this technique until they were overcome a few years later [64–66].

In this nascent era of nanoscience, reappraisal of the optical functionality of gold and silver nanoparticles and thin films, under the modern label of *Plasmonics*, led a new generation of scientists to explore the detection and spectroscopy of individual metallic nanoparticles. The first spectroscopy reported from single gold nanoparticles appeared in 1998 using SNOM [67]. Detection of individual gold nanoparticles was soon pursued by a number of methods, including conventional dark-field [68] and total internal reflection dark-field microscopy [69]. A particularly promising impetus was the biocompatibility of gold and its indefinite photostability, which prompted the use of colloidal nanoparticles as optical immunolabels for biology [68]. Interestingly, while just a few years earlier, the common wisdom would have been that Rayleigh scattering was too weak for the detection of individual nanoparticles, this techniques also found application in the detection of single nanoparticles such as carbon nanotubes [70].

By the end of the twentieth century, the achievements in detecting single nanoparticles with diameter on the order of 50 nm marked a milestone in detection sensitivity [67–69]. However, most applications, especially those concerning biology, wished to work with much smaller particles, e.g., 5 nm in diameter, corresponding to a

million-fold reduction in signal strength for dark-field microscopy. To address this huge challenge, other techniques such as lock-in enhanced photothermal detection [71, 72], interferometric scattering (iSCAT) [73] and lock-in enhanced transmission [74] were soon introduced. The success of these measurements showed that sensitive optical detection of nano-objects would indeed be possible through nonfluorescent means. In the decade that followed right up to the present day we see a broad array of research efforts, drawn from numerous communities, exploring interferometric detection of single nano-objects such as viruses, DNA, microtubules, exosomes, and proteins [75–91]. Interestingly, interferometric microscopies are also flourishing in the general context of label-free imaging of cells and membranes even if nanoparticles are not at the center of attention [75, 76, 90, 92–105]. The underlying physics of these methods remains the same although a plethora of acronyms such as interference reflectance imaging sensing (IRIS) [77], rotating coherent scattering (ROCS) [98], interference plasmonic imaging (iPM) [88], coherent bright-field imaging (COBRI) [106], stroboscopic interference scattering imaging (strobeSCAT) [107], interferometric scattering mass spectrometry (iSCAMS) [108] are on the rise. In what follows, we bring all these techniques under the umbrella of iSCAT, emphasizing the two central concepts and mechanisms of *interference* and *scattering* as the basis for recording the extinction signal (nano-shadow) generated by nanoparticles.

## 2.3 Interferometric Scattering Microscopy (iSCAT)

### 2.3.1 Foundations

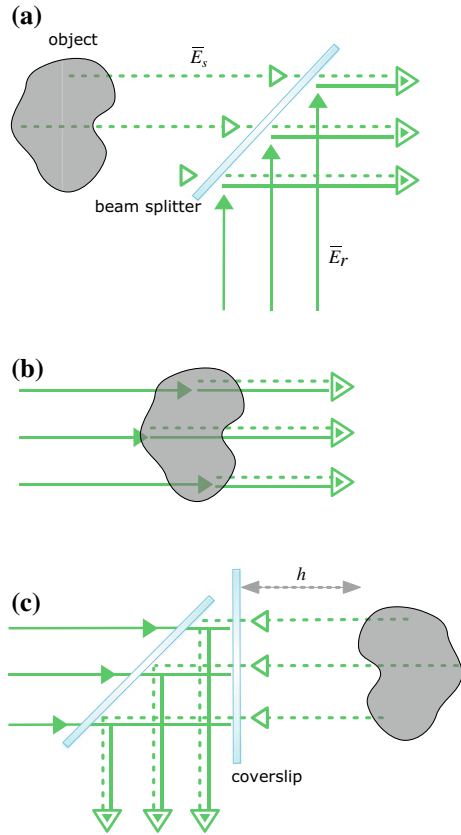
The principle concept in interferometric microscopy is to superpose a reference light beam with the response of the sample, as illustrated in Fig. 2.3a. Let us consider a field  $\bar{E}_s = E_s e^{i\phi_s}$  scattered from the object. The signal on the detector reads:

$$I_{\text{det}} \propto |\bar{E}_r + \bar{E}_s|^2 = I_r + I_s + 2E_r E_s \cos \phi, \quad (2.1)$$

where  $\bar{E}_r = E_r e^{i\phi_r}$  denotes the complex electric field of the reference arm. The three resulting components can be respectively identified as the contribution of the reference field ( $I_r = |\bar{E}_r|^2$ ), the pure scattering recorded from the object ( $I_s = |\bar{E}_s|^2$ ) and finally the cross-term ( $2E_r E_s \cos \phi$ ), wherein  $\phi = \phi_r - \phi_s$ . In general, this phase contains a component describing the sinusoidal modulation along the propagation path, a Gouy phase stemming from variations of wavevectors and the scattering phase imposed by the material properties of the object [109, 110].

As is common in holography, one can realize various iSCAT illumination and detection schemes, which are all essentially described by (2.1). The simplest, oldest and perhaps the most subtle version is shown in Fig. 2.3b, corresponding to conventional bright-field imaging. Although the intuitive explanation of this imaging modality is based on the concept of absorption and shadow, its mathematical essence is well

**Fig. 2.3** Different realizations of interferometric detection. **a** Principle of interferometry, where the signal of interest, here the scattered field  $\bar{E}_s$ , is superposed with a coherent reference  $\bar{E}_r$ . **b** Conventional bright-field imaging also consists of the superposing of reference (illumination) and scattered fields, and thus is also interferometric in nature. **c** An alternative back-reflection scheme for interferometric detection



described by (2.1) if one only replaces  $\bar{E}_r$  with an illuminating field  $\bar{E}_i = E_i e^{i\phi_i}$  incident upon the object. Here, it is important to remember that as formulated by the optical theorem, extinction (loss of light, i.e., shadow) is determined by the cross-term in (2.1) and can be expressed as the sum of absorption and scattering [111]. The latter two stem from imaginary and real parts of the complex extinction coefficient of the object, which are also implicitly encoded in  $\phi_s$ . As illustrated by the dashed and solid arrows in Fig. 2.3b, propagation phases are the same for  $\bar{E}_r$  and  $\bar{E}_s$  for each nanoscopic constituent of the object such that this imaging modality does not reveal any path dependence. Thus, the coherence length of the light source is not a parameter of concern. Another point of view that supports this picture is entailed in Abbe's theory on image formation and in Fourier optics, where an image results from the diffraction (and thus interference) of light from the sample.

An interesting simple extension of the scheme in Fig. 2.3b is shown in Fig. 2.3c, where a partially reflective surface is placed in the illumination path. In this configuration, a portion of the illumination is reflected and interferes with the light that is back-scattered by the object. Thus, in this case we can write  $\bar{E}_r = r\bar{E}_i$ , where  $r$

denotes the complex field reflectivity. In this instance, the detected signal depends sensitively on the displacement  $h$  above the surface or index modulations of the object.

Schemes such as phase contrast, differential interference contrast, reflection interference, or Mirau interference microscopy can all be described with the same underlying physics of (2.1) if one accounts for specific assignments of  $\bar{E}_r$  and  $\bar{E}_s$ . In the conventional realizations of these microscopies, the emphasis has been on visualization of edge contours or refractive index modulations in super-wavelength objects or features. It turns out, however, that interference microscopy can be even more important for the detection of very small nanoparticles and single molecules, which is particularly desirable within the context of nanoscience.

Let us take a spheroid with semiaxes  $a_1, a_2, a_3$  much smaller than the wavelength of light as a model nanoparticle. The response of this particle to light can be formulated as  $\bar{E}_s \propto \alpha \bar{E}_r$  where

$$\alpha_i = \epsilon_0 V \left( \frac{\epsilon_s - \epsilon_m}{\epsilon_m + L_i(\epsilon_s - \epsilon_m)} \right) \quad (2.2)$$

denotes the complex particle polarizability along the semiaxis  $a_i$ , and  $k$  signifies the wavenumber [111]. The quantity  $V$  is the volume of the particle, and  $L_i$  is the depolarization factor along  $a_i$ . For a sphere,  $a_1 = a_2 = a_3$  and  $L_i = 1/3$ . Complex parameters  $\epsilon_s$  and  $\epsilon_m$  are the dielectric functions of the scatterer and the embedding medium respectively, and  $\epsilon_0$  is the dielectric constant. The denominator in this expression can reach a minimum for metals such as silver and gold, thus enhancing their scattering response, but plasmonic enhancements only amount to about one order of magnitude for realistic materials in the visible domain. Thus, the chief factor responsible for the magnitude of  $\alpha_i$  is the particle volume  $V$ . The dependence on the volume results in the scattering field scaling as the third power of the particle dimension, and hence the scattering intensity ( $I_s = |\bar{E}_s|^2$ ) drops with the *sixth* power of the particle size.

When the particle is sufficiently small,  $I_s$  becomes much weaker than the cross-term  $2E_r E_s \cos \phi$  in (2.1) which is linearly proportional to the scattered field. As a result, interferometric detection of scattering seems more favorable over dark-field schemes. Indeed, (2.1) highlights the challenge in dark-field microscopy of detecting small particles: the difference between the signal of a 50 nm nanoparticle and one with 5 nm diameter is a factor of *one million!* We also remark that (2.1) describes both homodyne and heterodyne detection schemes [112], where the particle field is amplified by the larger field of the reference  $E_r$  in the cross-term. We present a more differentiated discussion on the comparison between the sensitivities of dark-field and iSCAT detection later in this section.

The first report of iSCAT microscopy and spectroscopy of *single* nanoparticles appeared in 2004 [73] using the configuration shown in Fig. 2.3c (see Sect. 2.4 for an additional historical anecdote). More precisely, a supercontinuum laser beam was focused on a glass substrate supporting gold nanoparticles (GNPs) as small as 5 nm covered by immersion oil. This was quite an impressive step toward optical detec-

tion of small nanoparticles since conventional methods such as dark-field microscopy were not able to reach this limit. The only other technique with appreciable sensitivity was reported just two years earlier based on photothermal detection [71]. In this technique, one heats the GNP through its enhanced absorption at the plasmon resonance and detects the heat-induced change of refractive index in its vicinity. Interestingly, however, this latter decisive step is also achieved via interferometry using a second laser beam.

In the following years, iSCAT was extended in our laboratory to different illumination and detection conditions [113, 114] and used to detect single unlabeled viruses [115, 116], semiconductor quantum dots [114], lipid vesicles [117, 118] and unlabeled proteins [119]. In more recent years, several other groups have also successfully applied different illumination/detection variants of iSCAT to detect single proteins [108, 120, 121], single viruses [83, 106], lipids [122, 123] and other nanoparticles [82], and even charge carriers [107].

Neglecting the scattering intensity ( $I_s$ ) which is vanishingly weak for very small particles, the iSCAT signal of interest, namely the interferometric cross-term, can be obtained by subtracting the reference intensity that acts as a background from the detected intensity,  $I_{\text{det}} - I_r \approx 2E_s E_r \cos \phi$ . Thus, the contrast obtained when comparing images with and without a nanoparticle becomes:

$$c = \frac{2E_s E_r \cos \phi}{I_r} = 2 \frac{E_s}{E_r} \cos \phi. \quad (2.3)$$

The final expression in (2.3) might prompt one to conclude that one can reach a better sensitivity through minimization of  $E_r$  in the denominator. Indeed, one can devise an optical scheme, where  $E_r$  is freely adjustable, e.g., by implementing a separate reference arm (see, e.g., scheme of Fig. 2.3a). However, the resulting increase in contrast is at the cost of a lower overall signal which leads to a smaller signal-to-noise ratio (SNR) in shot-noise-limited detection. Furthermore, a separate arm compromises sensitivity owing to the introduction of mechanical instabilities. We discuss the issue of SNR and other instrumental considerations in more detail below.

Before we begin the discussion of experimental issues, we take a moment to remark on the fundamental efficiency of interferometric detection of small objects, down to single atoms and molecules. When an ideal two-level atom is illuminated with monochromatic light at its resonance frequency, it undergoes a transition from the ground to the excited state. This process can lead to absorption and successive emission of light. The resulting fluorescence is incoherent because it follows a spontaneous process, thus not respecting the phase of the illumination field. However, in the weak excitation regime, the interaction of the incoming light with an atom can also be described by Rayleigh scattering [124]. It follows then that the interaction of the incoming light and the atom can equally be described in the same way as in (2.1), that is, via interference. Considering that the extinction cross section of an unperturbed atom can be as large as  $3\lambda^2/2\pi$ , where  $\lambda$  is the transition wavelength, and that light can be focused down to the diffraction limit in the order of  $(\lambda/2)^2$ , one ought to expect a single atom to be capable of casting a dark shadow on a laser beam.

Indeed, one can rigorously show that a single atom can extinguish a laser beam in entirety [125].

The most fundamental requirement for reaching full extinction is spatial mode matching: the wavefronts of the incident beam should match the dipolar emission pattern of the atom [125]. An alternative approach is to modify the radiation pattern of the atom by coupling it to an appropriate antenna [126]. In fact, a glass–water interface is known to act as a primitive planar antenna that modifies the radiation pattern of an oscillating dipole into one that is enhanced about the critical angle [127]. Optimization of the iSCAT contrast in recent efforts, where part of the reflected beam is blocked with a pinhole in the back focal plane, can indeed be understood as the result of a better mode matching [128–130]. A particularly compact antenna consists of a subwavelength waveguide (nanoguide), such as a thinned glass fiber [131], whereby the emission of an atom is efficiently coupled to the nanoguide mode, thus improving its interference with the field propagating within with high efficiency. Given the central role of spatial modes in this picture, these considerations are also of immediate relevance for iSCAT detection of nanoparticles, which radiate with a dipolar pattern. To our knowledge, this feature has not yet been explored although the nanoguide arrangement has been demonstrated to perform well in dark-field microscopy [132].

### ***2.3.2 Detection Sensitivity and Signal-to-Noise Ratio (SNR)***

Thus far, iSCAT has been successfully employed to detect individual unlabeled proteins as small as 50 kDa. An important question that arises is whether there exists a fundamental limit in detection sensitivity, and what might be the accompanying technical challenges. In what follows below, we give an overview of some of the pertinent issues.

The central restriction in any sensitive measurement is signal fluctuation. In their absence, arbitrarily small signals may be identified even on very large backgrounds. While slow fluctuations such as thermal or mechanical drifts can be directly or indirectly accounted for, fast random variations, which we call “noise” pose a serious challenge. Some of the main sources of noise in an iSCAT measurement are as follows:

Laser intensity noise: Even the best lasers have instrumental power fluctuations and beam instabilities. It is indeed not easy to have a freely running laser with power stability better than about  $10^{-3}$ . To detect iSCAT contrasts beyond this, one has to account for laser intensity fluctuations through referencing or normalization. In confocal imaging, a balanced photodiode pair employing common-mode rejection can be as good as  $1 \times 10^{-7}$  [133]. In wide-field camera-based detection, one can normalize the total power recorded within each frame to similarly reject intra-frame fluctuations. As the contrast signal is the ratio of two fields sharing the same laser noise, they naturally self-reference.

If one manages to deal with the instrumental laser intensity noise, one is still confronted with the fundamental limit of shot noise which is the noise associated with the fact that the number  $N$  of the photons in a laser beam varies according to a Poisson distribution, i.e., as  $\sqrt{N}$  for large  $N$  [124]. As a rule of thumb, the shot-noise-limited SNR improves by  $\sqrt{N}$  as  $N$  is increased.

Detector background noise: Any electronic device has an intrinsic noise, stemming from, for example, thermally generated electrons in the detector (referred to as dark noise) or errors introduced in the voltage reading circuitry. Modern cameras and photodiodes can be extremely quiet, and since iSCAT is typically performed on a high background level due to the reference field  $E_r$ , detector dark noise is not a major concern. Nevertheless, depending on the experimental arrangement, it might become a limiting factor.

Dynamic range and analogue-to-digital conversion noise: Realistic detectors have a limited working range on both sides of small and large signals. The limit for the largest signals is given by detector nonlinearities and saturation effects, while the lower limit often has to do with the fundamental sensitivity of the particular detector technology. The ratio between the largest and smallest signal values defines the dynamic range, and for imaging cameras the read noise level is often taken as the smallest signal quantity which is detectable. From the sensor dynamic range, an appropriate bit depth is selected for analogue-to-digital conversion. For example, an image rendered into 12-bit imposes a read-out resolution of 1 in 4096, i.e.,  $2 \times 10^{-4}$ .

Mechanical stability: Although iSCAT is an interferometric method, it can be extremely robust against mechanical instabilities if the reference and the scattering beams share identical paths (see Fig. 2.3). Nevertheless, lateral vibrations at the sample cause problems since even a few nanometers of motion could translate into fluctuations of the contrast when the background is subtracted (see section below) [134].

### 2.3.3 Background Removal

Fluorescence detection exploits highly efficient spectral filtering to eliminate spurious backgrounds caused by the illumination or unwanted fluorescence. Similarly, dark-field microscopy, including variants using total internal reflection, employ spatial filtering to reject background illumination in order to detect Rayleigh scattering. In iSCAT, however, one does not exclude the background but instead records it in an intense reference beam, just as in resonant extinction measurements of a quantum emitter [135].

As mentioned earlier, this would not pose any problem if one could subtract a constant background level from the measured signal, even if the signal were to be arbitrarily small. Figure 2.4a, which displays an iSCAT image of a coverslip supporting 10nm GNPs in water, shows that in practice, one is confronted with

lateral background modulations that make it difficult to identify the gold particles. These background features, however, should not be attributed to noise since they are fully reproducible: iSCAT is extremely sensitive to slightest changes in the optical path—down to the level of single small proteins—hence the background contains a high degree of a speckle-like patterns caused by any slight inhomogeneity of the refractive index or topography.

Background components that do not originate from the sample and its environment can be eliminated by measures such as lock-in-type detection. For example, wavefront inhomogeneities in wide-field illumination can be removed by mechanically modulating the sample [113, 119]. The most effective procedure, however, would involve modulations of properties that are specific to the nanoparticle of interest. For example, the wavelength dependence of plasmon spectra was used to separate the signal of GNPs from a dielectric background composed of microtubules to which they were bound [113].

A very powerful method for eliminating the background becomes available in dynamic studies, where the particle of interest appears on the detection scene at a given time or moves within it. In this case, differential treatment of consecutive images can eliminate the static part of the sample [114, 119], illustrated in Fig. 2.4b. This can be achieved by an assortment of methods, e.g., subtraction of a temporal median intensity [136], subtraction through an iterative-estimation algorithm [137] or employing rolling-window averaging across stacks of frames [108]. The method chosen should be based on the problem and equipment at hand regarding image acquisition speed and also the speed at which the nanoparticle moves. The situation becomes more challenging in the presence of a background with a fluctuating spatiotemporal dynamics, e.g., speckle features from live biological specimens. Nevertheless, more advanced computational tools can be employed for analyzing the obtained images as recently demonstrated for tracking GNP-labeled transmembrane proteins in live cells [138].

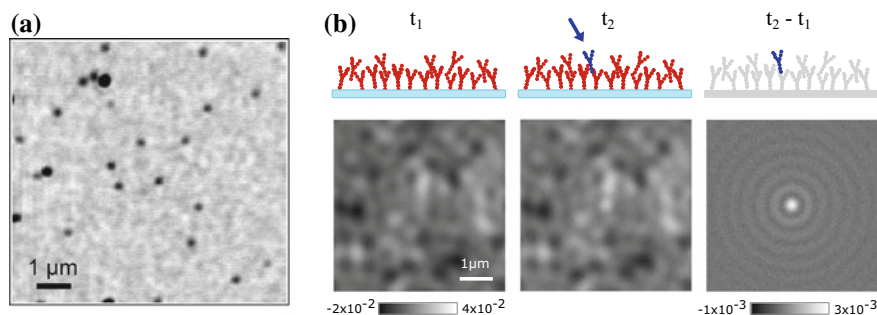


**Fig. 2.4** **a** Substrate roughness introduces modulations in the background of the image in accompaniment to imaging of gold nanoparticles of size 10 nm [113]. Reproduced with permission from the Optical Society of America. **b** Background subtraction through differential imaging. In wanting to image the arriving protein shown in blue, one subtracts the image of the substrate at a time before arrival ( $t_1$ ), and a time after ( $t_2$ ). The difference isolates the presence of the target protein

We remark that the background subtraction methods discussed above could also be equally well applied to dark-field microscopy [139]. Thus, one might wonder whether dark-field microscopy might not match the performance of iSCAT microscopy. Indeed, one can show that the shot-noise-limited advantage of interferometric (homodyne) over dark-field (scattering intensity) detection is only a factor of two. The practical implementation of ultrasensitive dark-field, however, is nontrivial because the very small dark-field signal proportional to the sixth power of the particle size (see (2.1)) puts higher demands on the detector technology.

### ***2.3.4 Long Measurements: Indefinite Photostability***

One of the key advantages of detecting scattering instead of fluorescence is that the former does not suffer from photobleaching. Whether one uses the inherent scattering of a bioparticle such as a virus or if one detects a GNP label, the scattering signal does not degrade over time. Thus, very long—in principle indefinite—measurements become possible. Such experiments might encounter technical difficulties such as the particle moving out of the field of view, but these can be easily overcome with more sophisticated instrumentation.

### ***2.3.5 Fast Measurements: No Saturation***

Another favorable feature of scattering contrast as compared to fluorescence is lack of saturation. A fluorophore is a quantum mechanical system with an inherent anharmonicity, implying that only one photon at a time can be absorbed. The fluorescence lifetime of the excited-state places a limit on how fast the photon can be emitted, imposing a bottleneck for the rate at which the fluorophore can radiate, and thus a limit to how fast one can image. A nanoparticle behaves like a classical oscillating dipole which does not suffer from saturation: the stronger the illumination, the higher the rate of scattering. Indeed, iSCAT imaging speeds up to about 1 MHz has been demonstrated [118]. The immediate limitation is currently a technological matter of availability of suitable cameras. A more fundamental limit is introduced when concerned over photodamage of the sample when using very strong illuminations since every realistic substance also absorbs light at every wavelength, even if very weakly. When performing iSCAT on biological samples, illumination intensities in the order of  $0.001\text{--}0.1\text{ mW}\mu\text{m}^{-2}$  have been reported for membranes [118, 138], with powers as high as  $5\text{ mW}\mu\text{m}^{-2}$  [118] for the fastest MHz imaging rates.

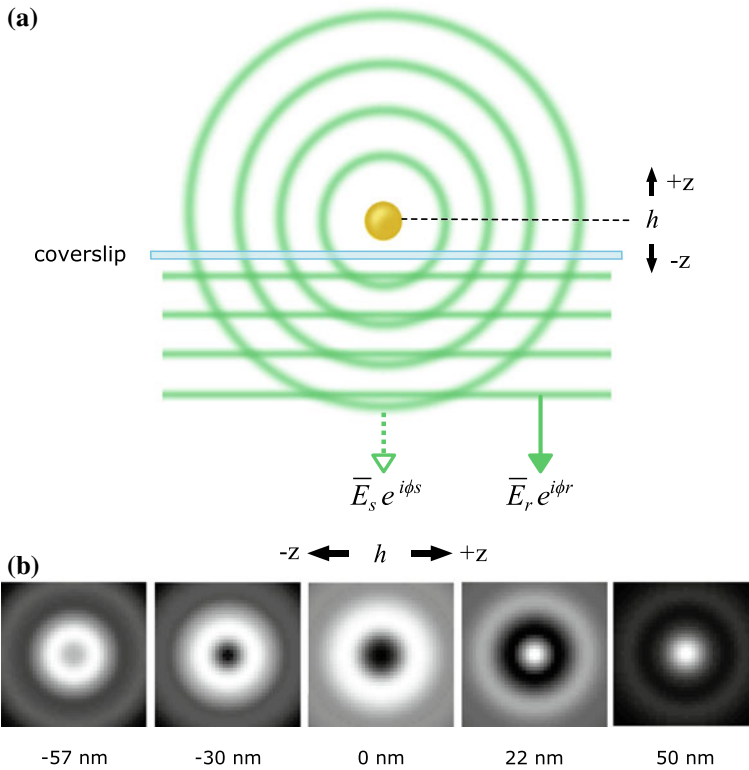


**Fig. 2.5** **a** Schematic view of the scattering specimen upon the coverslip in iSCAT imaging. **b** The interferometric point-spread function of the scatterer in reflection wide-field mode possesses a unique signature of ring radii and contrasts which vary as a function of the axial position  $h$  of the scatterer above the reflecting coverslip

### 2.3.6 Exquisite Lateral and Axial Resolution

The resolution attainable in iSCAT imaging is diffraction-limited. However, when investigating single nanoparticles, it is often the location and trajectory that is of interest. These can be obtained in an analogous fashion to fluorescence localization microscopy and particle tracking [140]. Lack of photobleaching and saturation provides strong iSCAT signals which, in turn, yield a higher localization precision within a shorter observation time than is achievable in fluorescence imaging.

The point-spread function (PSF) in iSCAT can take on different forms, depending on the illumination and detection modes. A particularly useful situation is encountered in wide-field illumination where plane waves and spherical waves interfere together, resulting in many rings around the main PSF spot (see Fig. 2.5) [84, 138, 141]. For most lateral tracking applications, a Gaussian fit to the central spot is sufficient although the radial symmetry of the overall PSF can be very helpful

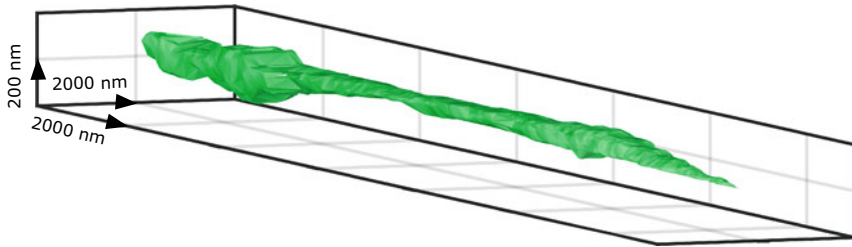


**Fig. 2.6** A reconstruction of the outer surface of a cellular filopodium, rendered from interpolation of approximately 800,000 three-dimensional trajectory positions as a GNP traverses the filopodium surface

in identifying small signals on a complicated feature-rich background. For example, GNPs have been tracked with spatial resolution of 2 nm within  $10\ \mu\text{s}$  on a live cell membrane [138].

A major asset of iSCAT imaging stems from its inherent interferometric nature, which makes the signal very sensitive to phase  $\phi$  in (2.1). Consequently, axial displacements of a nanoparticle in the order of nanometers can be put into evidence. The first accounts of this nano-holographic feature of iSCAT were presented in [113] and [117]. In these studies, however, one was limited to displacements below 100 nm by the ambiguity that is due to the periodicity of the iSCAT signal. More recently, we have shown that a quantitative PSF analysis in wide-field iSCAT gives access to nanometer axial resolution over several micrometers [138, 142]. Figure 2.6 presents an example of a three-dimensional surface map of an intercellular filament generated by the motion of a GNP that was bound to an epidermal growth factor receptor (EGFR). We note that the best axial resolution is attainable in the reflection mode iSCAT, where the scatterer can be located at a distance above the beam-splitting coverslip, and thus accumulate a traveling phase.

### 2.3.7 Illumination and Detection Schemes

Interferometric detection of light scattering can be realized through various flexible permutations of illumination and detection schemes. The first efforts used scanning confocal point illumination and detection [73] but this was soon extended to wide-field [113] and fast beam-scanning [116] illumination schemes in conjunction with camera-based detection. Of these, one additionally may place the detector in the forward direction or in the reverse (see Fig. 2.7), while keeping the inherent interferometric character of iSCAT.

In confocal point detection the reference consists of a focused Gaussian beam that is raster scanned across the sample. While this helps to discriminate unwanted scattering from the depth of the samples, a major hurdle is that temporal noise in the illumination light becomes translated into spatial noise in the image as each image

pixel is acquired sequentially in time. Another noteworthy feature of a scanning mode is better mode matching between the spherical scattered wave and the strongly focused reference beam wavefront, which renders the PSF without distinct ring features.

For applications requiring fast imaging, wide-field illumination with camera-based detection is the most popular modality. By measuring in reflection, higher contrasts are obtained than for transmission because of the lower amplitude of the reference field in the former ( $r = 0.06$  for the reflected beam, see (2.3)). This assists greatly with visual inspection of the raw iSCAT image. In the case where one wishes to better the contrast for real-time inspection, phase-masks that attenuate the reference field have been introduced (recalling Lister's dark-field stop, or the Zernike phase plate) [128–130]. In the absence of computational real-time background removal, such a physical contrast enhancement can serve a useful function.

The great advantage of reflection iSCAT is its sensitivity to the axial position of the nanoparticle. Transmission measurements, on the other hand, suffer less from the background since the disappearance of phase differences between  $E_r$  and  $E_s$  (see Fig. 2.3) minimizes speckle. This advantage was used in conjunction with index matching for detecting single small organic molecules [133, 143]. What is important to realize, however, is that while most iSCAT measurements are performed with a laser, this is not a necessity if the distance between the nanoparticle and the place where the reference is picked up is not larger than the coherence length of the source. In other words, measurements involving nanoparticles very close to a cover glass can be just as well done using incoherent sources such as LEDs [75, 83, 85, 144].

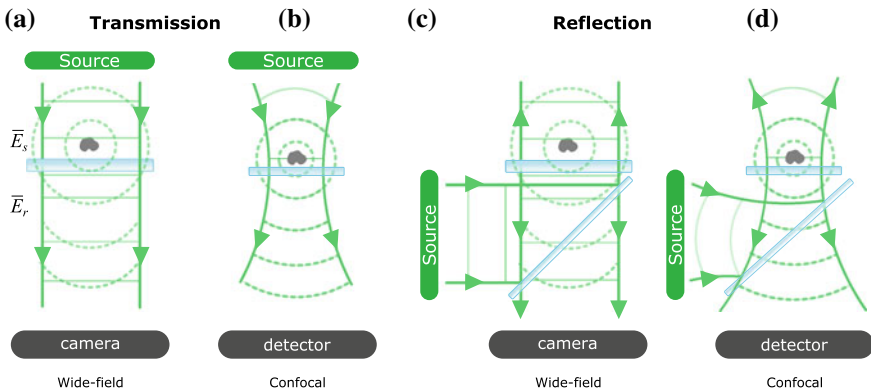


**Fig. 2.7** Modes of iSCAT microscopy, encompassing wide-field and confocal illumination and detection schemes performed in both the forward transmission or backward reflection geometry

## 2.4 iSCAT Showcase

### 2.4.1 *Detection and Sensing of Nanoparticles*

Since the debut of iSCAT in 2004, iSCAT and related techniques have revived interference and extinction microscopies in the context of detection and imaging of various nanoparticles. In this section, we provide a brief overview of some of the exciting application areas to which these methods have contributed.

#### 2.4.1.1 Gold Nanoparticles

Gold nanoparticles in the colloidal form have a wide range of applications due to key properties such as biocompatibility, inertness, ease of fabrication and possibility for functionalization with different molecules. The recent developments of nano-optics, and in particular plasmonics, have brought about a strong drive for studying and using these nanoparticles. Indeed, the first account of iSCAT was published on the direct far-field imaging of single GNPs, to size as small as 5 nm. This was a formidable task at the time as in dark-field imaging one begins to struggle to visualize gold colloids smaller than 40 nm. The GNPs, immobilized upon a coverslip, were imaged when index-matched with oil [73] and also under ambient conditions at the water–glass interface [113]—see Fig. 2.8a. The latter is especially important as it begins to match biological conditions wherein ultra-small GNPs serve as useful super-resolution probes (discussed later). The sensitivity limit on the size of the detectable GNPs in the early experiments was set by the speckle background that results from slightest variations in the refractive index and topography of the underlying glass substrate.

To date, GNPs as small as 2 nm in diameter [145], smaller than a protein, have been imaged and localized to a precision of 8 nm with short exposure times sufficient to function as a scattering label—cementing iSCAT as a powerful means to image and localize nanoscale colloids. At this point, it is perhaps interesting to mention that we had actually started exploiting iSCAT already in 2001 when investigating gold nanoparticles of diameter 100 nm [146]. In those studies, we detected individual gold nanoparticles at the glass–air interface as dark spots in a scanning confocal reflection measurement and were puzzled that particles which scattered well would actually appear dark. Further studies then led to the appreciation of the role of interference and the advent of iSCAT [73].

Given that iSCAT imaging intrinsically contains quantitative phase information about the sample, proper interpretation of the interferometric scattering PSF allows one to attain material and morphological features of the colloid. For example, calibration of the spherical colloid size from the extinction contrast has been demonstrated [147], as well as the orientation of anisotropic ellipsoidal nanorods through polarized detection [148]. Moreover, the complete complex dielectric function of a single

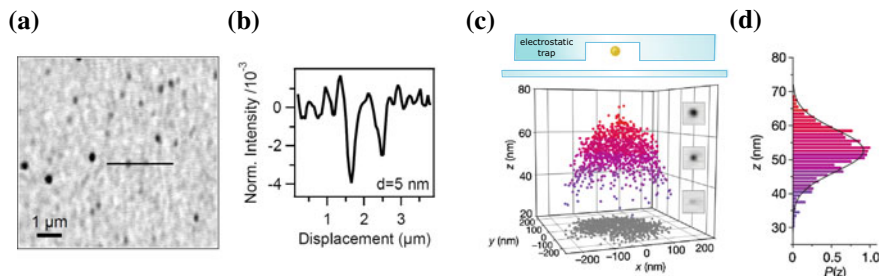


**Fig. 2.8** iSCAT microscopy on single nanoparticles of gold. **a** An early demonstration of iSCAT imaging of 5 nm GNP at the glass–water interface. **b** The intensity profile corresponding to the cross section marked in **(a)** [113]. Reproduced with permission from the Optical Society of America. **c** Three-dimensional localizations of a 100 nm gold particle within a 500 nm electrostatic trap potential (illustrated above), revealing the potential landscape of the trap pocket. **d** Histogram of axial positions from which trap stiffness can be discerned [117]. Reproduced with permission from the Nature Publishing Group

gold nanoparticle has been retrieved from colloids as small as 10 nm by performing iSCAT with a supercontinuum light source in a DIC configuration [149].

iSCAT tracking of GNPs has also been exploited to probe the three-dimensional landscape of electrostatic potential traps [117, 150]—shown in Fig. 2.8c, d. In a similar fashion, the height occupation probability, which provides a description of the free-energy landscape within a microfluidic slit channel, has been demonstrated for fast tracking of diffusing 60 nm GNPs [151]. Geometry-induced electrostatic potentials at the end of a nanopipette have also been used for local manipulation of plasmonic antennas observed by iSCAT [152]. In the following sections, we shall also discuss the application of GNPs as scattering labels for tracking lipids and proteins on synthetic and cellular membranes.

#### 2.4.1.2 Semiconductor Colloids and Dye Molecules

The first half of the early 1990s showed that single dye molecules could be detected via fluorescence microscopy at room temperature [153]. The key to the success of these endeavors was efficient spectral filtering, efficient collection and sensitive low-noise detection of the emitted photons on a very low background. Once the dogma surrounding the difficulty of single-molecule detection was overcome, other fluorescent entities such as semiconductor quantum dots and diamond color centers were also detected in the same fashion. Considering that very few species fluoresce, however, this method found limited use, prompting scientists to search for alternative ways to detect nanoscopic amount of matter via extinction rather than fluorescence.

A single molecule may possess an extinction cross section of  $\sigma = 10^{-16} - 10^{-15} \text{ cm}^2$  whereas a diffraction-limited beam can be focused down to an area of about  $A = 10^{-9} \text{ cm}^2$ . Thus a simple estimate of  $\sigma/A$  reveals the need for suppres-

sion of noise to the level of parts-per-million in order to overcome the challenge of detecting a single molecule in extinction. While several groups attempted absorption measurements in various configurations [154–156], it was iSCAT that demonstrated direct room temperature modulation-free extinction of single molecules and quantum dots [114, 133, 143].

The first important step in extending the sensitivity of iSCAT was taken with the detection of single semiconductor nanocrystals [114], shown in Fig. 2.9. Core–shell semiconductor nanocrystals such as CdSe/ZnS have been employed in many areas of photonics, optoelectronics and bio-imaging. By varying the material and size of the core and shell, one can tune their optical properties such as emission wavelength and photostability over a wide range.

The extinction cross sections of the quantum dots under study were on the order of  $10^{-15} \text{ cm}^{-2}$ . By using a thin sheet of mica as substrate, which can be locally atomically flat, the iSCAT background was reduced by about one order of magnitude. Furthermore, laser intensity fluctuations were accounted for by employing a second photodiode as a power reference. These measures turned out to be sufficient to detect different types of single core–shell colloidal dots. Simultaneous fluorescence and iSCAT measurements as well as iSCAT benchmarking with 10 nm gold nanoparticles provided a robust evidence for the success of iSCAT in detecting extinction from individual quantum emitters at room temperature. A very interesting example of study that became accessible with such measurements is the investigation of the quantum dot even during dark periods of photoblinking [114].

To extend extinction experiments to single organic molecules, it was necessary to improve the SNR further owing to the smaller extinction cross section of a molecule.

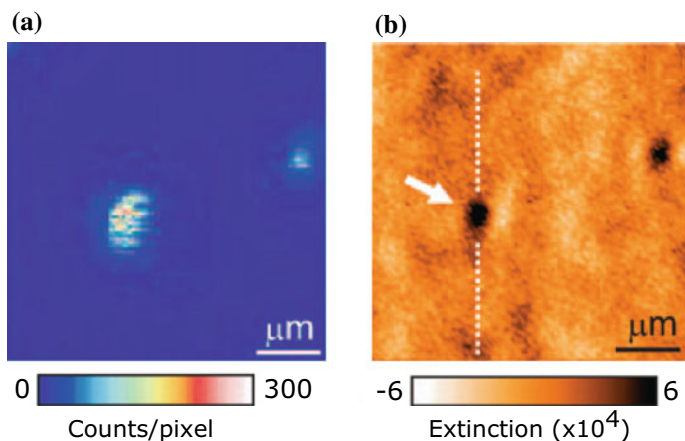


**Fig. 2.9** Imaging of single quantum dots through iSCAT. **a** A fluorescence image of two quantum dots on a substrate. **b** Transmission iSCAT image of the same region as **(a)** recorded in scanning mode, similarly revealing the interferometric extinction of the two nanocrystals identified in **(a)** [114]. Reproduced with permission from the American Chemical Society

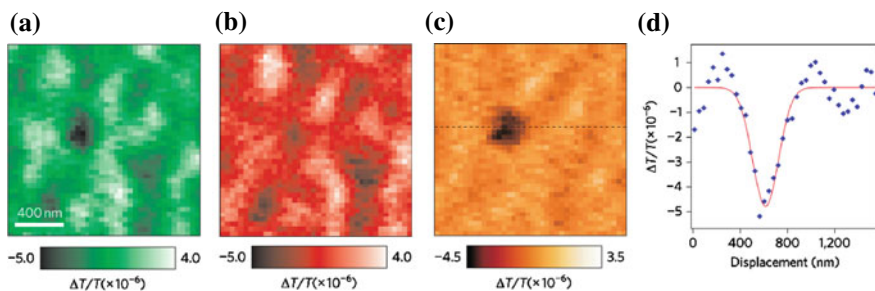


**Fig. 2.10** Imaging of a single TDI molecule through confocal-scanned transmission iSCAT. Shown are the extinction raster images of a single embedded dye molecule when illuminated **a** near resonance (633 nm) and **b** off resonance (671 nm). The difference between image **(a)** and **(b)**—shown in panel **(c)** clearly reveals the single molecule, and evidences wavelength-dependent detection of a molecule, a prerequisite for single-molecule absorption spectroscopy. **d** Intensity profile through the cross section marked in **(c)** [133]. Reproduced with permission from Nature Publishing Group

Here, a better suppression of laser noise and of the background was required. To address the first issue, commercial balanced detectors were used [143] since home-built referencing solutions, e.g. as was used in the previous experiment on quantum dots, usually suffer from small performance differences between the two detectors, resulting in unwanted signal fluctuations. To improve the background issue, we chose to immerse the molecules in index matching oil and measured in transmission. These measures pushed the sensitivity beyond  $1 \times 10^{-6}$  and led to the first successful direct detection of single-molecule absorption [143]. This work was progressed to the imaging of strongly quenched molecules and of molecules at different wavelengths [133]. By detecting a single molecule both on and off resonance, the way for single-molecule absorption spectroscopy was paved (see Fig. 2.10). We point out in passing that a transmission measurement of extinction is equivalent to an iSCAT measurement in reflection, which can be easily seen as a folded transmission experiment. A central feature of a reflection measurement is access to the traveling phase and thus to the axial position of the nano-object, which might complicate simple absorption spectroscopy.

Let us now connect the underlying physics of the results presented above with those discussed in Sect. 2.3.1. When considering a two-level system in a nonideal environment where the quantum transition is homogeneously broadened beyond the natural linewidth, the expression for the extinction cross section is generalized to  $\sigma = \frac{3\lambda^2}{2\pi} \times \frac{\gamma_{\text{rad}}}{\gamma_{\text{tot}}}$  where  $\gamma_{\text{rad}}$  is the radiative linewidth and  $\gamma_{\text{tot}} = \gamma_{\text{rad}} + \gamma_{\text{nr}} + \gamma_{\text{deph}}$  with  $\gamma_{\text{nr}}$  and  $\gamma_{\text{deph}}$  denoting the nonradiative and dephasing contributions to the linewidth, respectively. For nearly all emitters in the solid state, the quotient  $\gamma_{\text{rad}}/\gamma_{\text{tot}}$  amounts to about  $10^{-6} - 10^{-5}$  at room temperature. It is now important to note that for most quenched systems this strong reduction is dominated by  $\gamma_{\text{deph}}$ , i.e., quenching is not the main factor. Hence, it follows that the extinction cross section of a system that is quenched by as much as 1000 remains essentially the same. In other words, whether the system has a high quantum efficiency (given by  $\frac{\gamma_{\text{rad}}}{\gamma_{\text{rad}} + \gamma_{\text{nr}}}$ ) or not is not decisive

for extinction measurements. This is why quenched molecules can be detected in extinction but not in fluorescence.

Gold nanoparticles, quantum dots and dye molecules all have resonances, with their polarizability experiencing a maximum in a certain spectral range. While this enhances the extinction cross section, and thus the iSCAT signal, it is not nearly as decisive as the influence of the particle size. A consequence is that even a dielectric nanoparticle can yield a large interferometric signal given it is of sufficient size. In what follows, we show that all viruses and a vast range of proteins easily satisfy this criterion, prompting efforts in their detection.

### 2.4.1.3 Viruses

Viruses play a crucial role in biology, whether causing harmful diseases or performing an integral symbiotic function within living systems [157] or even serving as novel disease treatment vectors [158]. Detection of viruses, as with most other cell biological entities, has traditionally been performed in fluorescence. However, it turns out that viruses and virus-like particles such as X31 virus, H1N1, Zika, Ebola, and SV40, which could range from dimensions of about 20 nm to beyond 200 nm [159], can be easily detected via iSCAT. This has been demonstrated in environments such as microfluidic channels [160, 161], on synthetic lipid bilayers (see Fig. 2.11a) [115, 116], and on dielectric substrates [77, 83]. Simultaneous iSCAT and fluorescence tracking of a virus and a quantum dot on its surface made it possible to visualize not only the nanoscopic binding domains on the membrane but also the rocking and tumbling motion of single viruses (see Fig. 2.11a) [116]. Moreover, iSCAT has been used to uncover to nanometer precision the position and orientational configuration of bacteriophages interacting with a surface as well as to resolve, to a precision of 4200 basepairs, the kinetics of DNA ejection following stimulation [162]—shown in Fig. 2.11b. These activities have also motivated attempts to detect pure scattering of single viruses in conventional dark-field [139] and through light scattering from a nanofluidic channel [163].

The large iSCAT signal of most viruses opens the way to label-free high-speed, high-resolution and long-term imaging of single viruses and quantitative study of their interactions with cells and cellular environment [106]. iSCAT imaging of viral interactions is still in its infancy and is somewhat slowed down by the difficulty of integrating biosafe conditions into conventional optical laboratories, but it promises to provide invaluable insight about the secrets of viruses, which contain strong inherent inhomogeneities in their structure and function.

### 2.4.1.4 Proteins

Proteins are omnipresent in our body, taking on critical roles in essentially every step of our physiology. They are responsible for the function, structure, and regulation of our organs and tissue, as well as performing many of the functions of the cell. For

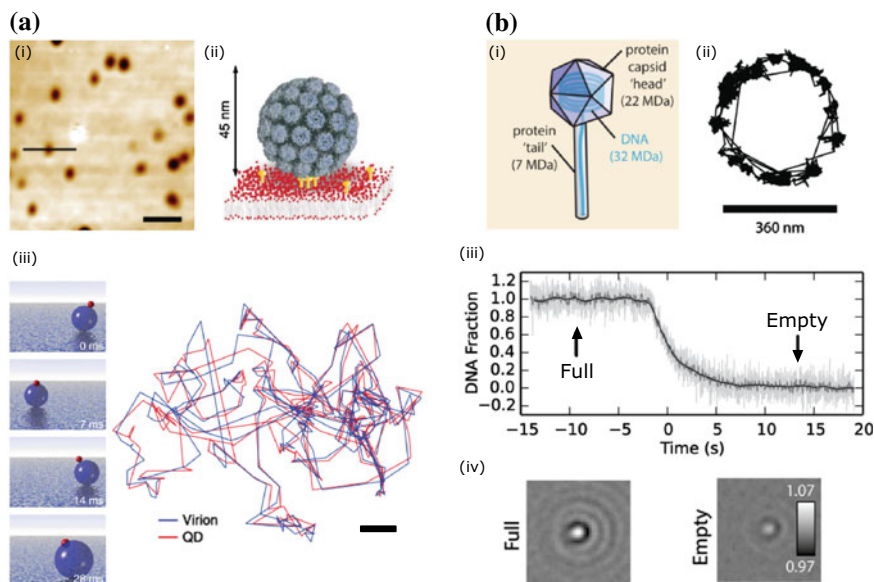


**Fig. 2.11** iSCAT microscopy on individual viruses. **a** iSCAT detection of individual 45 nm SV40 viruses: (i) immobilized on glass, imaged via a confocal-reflection modality. Scale bar denotes  $1\ \mu\text{m}$  and mean contrast of the viruses is 2% [115]. Reproduced with permission from the American Chemical Society. When bound to a synthetic membrane, shown schematically in (ii) it is possible to record the trajectory of a single virus. By simultaneous tracking of the virus and a quantum dot attached to its surface, comparisons of both trajectories reveal the mobility to be composed of a rocking and tumbling motion. Scale bar denotes 100 nm [116]. Reproduced with permission from Nature Publishing Group. **b** Dynamic measurements of bacteriophages: (i) schematic of bacteriophage anatomy, (ii) when bound by the tail to the substrate, rotational motion of the bacteriophages can be tracked. (iii) Monitoring of DNA ejection out of the capsid head from the calibrated iSCAT contrast as a function of time. (iv) Images show corresponding video frames of a single bacteriophage while full and empty, each showing a differing contrast [162]. Reproduced with permission from the American Chemical Society

these reasons, the study of single proteins presents an enormously instructive, but challenging, prospect.

Proteins range in molecular weight from a few to a several hundred kDa. The ubiquitous protein albumin, for example, has a molecular weight of 65 kDa. The size of proteins lie in the range of a few nanometers, and considering that the effective refractive index of biological matter does not vary much about a value of 1.5, the iSCAT signal of a typical protein can be more than 1000 times smaller than that of a typical virus. Nevertheless, the scattering cross section of a protein such as albumin turns out to be in the order  $2.5 \times 10^{-15}\ \text{cm}^{-2}$  at 280 nm, thus comparable to the absorption cross section of a dye molecule.

While detection of single dye molecules via iSCAT was performed in a focused laser beam, we had to adopt a wide-field imaging scheme for developing a practical biosensing platform. Here, we focused the incident laser beam in the back focal

plane of the microscope objective to achieve uniform illumination of an area with lateral extension in the order of 5–10  $\mu\text{m}$  and used CMOS cameras for imaging. Aside from the simultaneous study of many particles, an advantage of a camera as detector is that the total power recorded over all pixels can be conveniently used to register the incident power and thus account for its fluctuations. Moreover, recent camera technologies easily allow imaging at speeds of several tens of kHz up to MHz, which is far faster than scanning schemes, whether they use piezoelectric actuators [73, 115, 133] or acousto-optical deflectors [116, 120].

The first sensing experiments were reported in 2014 on single proteins as light as about 50 kDa [119], shown in Fig. 2.12a. A careful analysis of the obtained iSCAT contrast for several proteins of different size and mass as well as comparison with single-molecule fluorescence measurements demonstrated the potential of iSCAT for label-free detection of single proteins. This method has several decisive advantages over other biosensing solutions. First, the ability to count single proteins brings sensing to its absolute limit. Second, this happens over a large surface area as opposed to methods relying on plasmonic antennas [165] or optical microcavities [166] with very limited active area. Third imaging provides invaluable information about the spatial distribution and position of each protein, and finally, the essential setup is very simple. As in the great majority of biosensing platforms based on surface plasmons, mechanical oscillators, or microcavities, however, specificity has to be reached via surface functionalization.

The linearity of iSCAT contrast with protein mass allows classification of the detected proteins according to their size (see Fig. 2.12b). This feature has been recently used to demonstrate the application of iSCAT to quantitative mass spectrometry [108]. Moreover, this work nicely shows the ability of iSCAT to watch the dynamics of molecular processes, such as protein aggregation, cross-linking and oligomerization. Indeed, iSCAT has been successfully applied to a range of related investigations such as self-assembly of individual tubulin dimers to a growing microtubule [167], disassembly of a single microtubule [168], real-time monitoring of 28 nm viral capsid self-assembling around a viral RNA scaffold [169], and the growth, attachment, and retraction of bacterial pili [170].

Another recent application of label-free single-protein detection was showcased in the context of real-time investigation of cellular secretion [134, 164], illustrated in Fig. 2.12c. Secretion is the basis of intercellular communication and has been a subject of single-cell studies using different methods [171], however single-protein sensitivity was only possible with iSCAT. In a proof of principle experiment, immunoglobulin G (IgG) antibodies of mass 150 kDa (4 nm size) were detected in a spatiotemporally resolved fashion following secretion by Laz388 cells [134, 164].

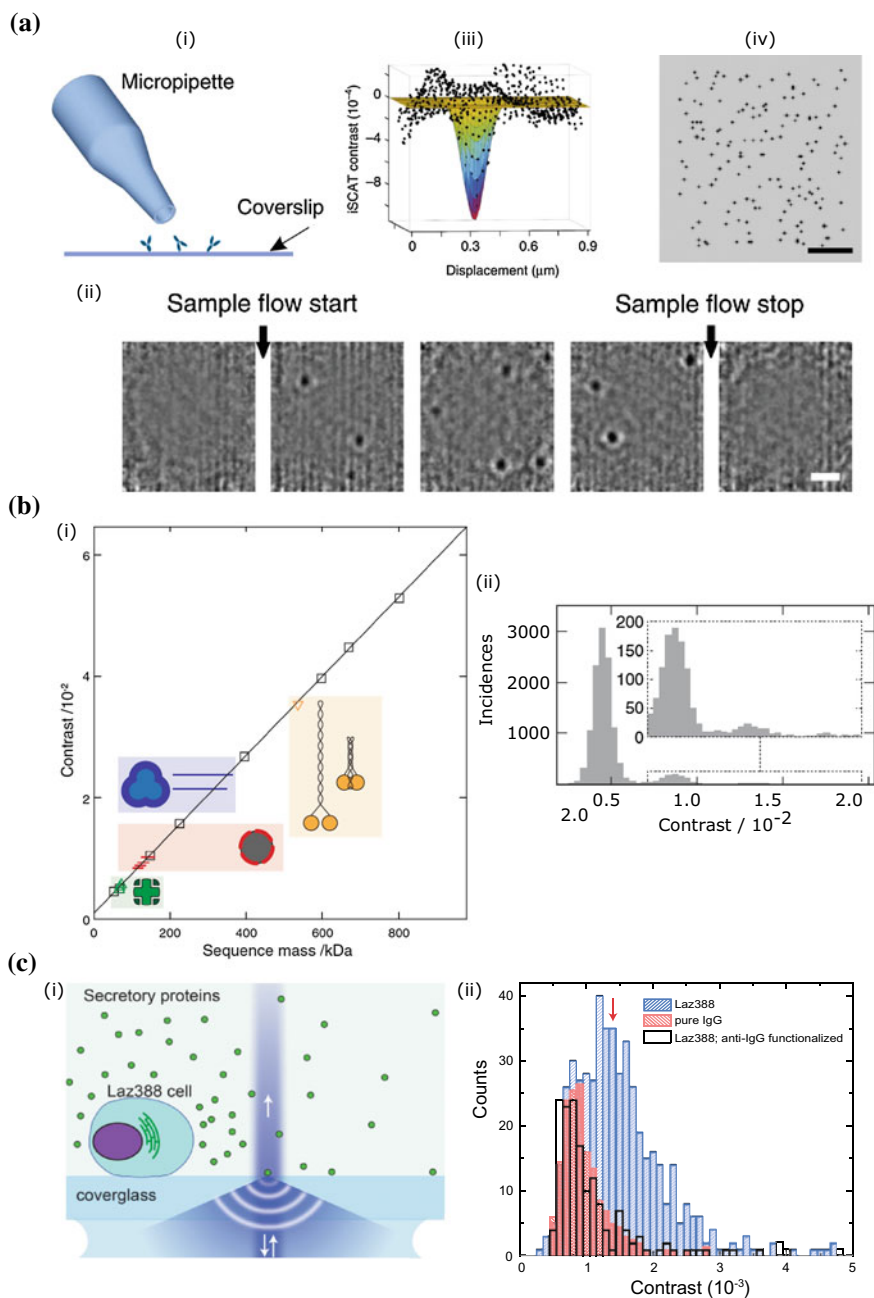


Fig. 2.12 (continued)

◀ **Fig. 2.12** Detection of single-protein extinction. **a** Schematic for the first demonstration of single-protein detection: (i) A solution of proteins is pipetted upon a functionalized coverslip. (ii) Background-corrected differential iSCAT images showing the coverslip as pipette flow begins and ends, depositing single proteins which appear as dark spots. (iii) A super-localizing fit to one protein PSF indicates how individual binding sites can be super-resolved (iv) [119]. Reproduced with permission from Nature Publishing Group. Mass calibration (**b**): The contrast of single and complexed proteins can be calibrated to their mass (i), with monomeric and oligomeric derivatives also resolvable by this technique (ii) [108]. Reproduced with permission from the American Association for the Advancement of Science. **c** Single-cell secretion dynamics resolved at single-protein sensitivity with iSCAT. (i) Schematic of the experimental arrangement wherein a secreting cell is positioned near to the iSCAT field of view. The contrast distribution of proteins secreted by the cell as they bind to an anti-IgG functionalized surface (blank) agrees with that expected from pure IgG (red). iSCAT also reveals an abundance of other secreted products (blue) [164]. Reproduced with permission from the American Chemical Society

This study paves the way for a wide range of future experiments e.g., the interaction of immune cells. iSCAT investigation of secretion has also been recently extended to plasmonic substrates, where the incident light is coupled to surface plasmons in a thin gold surface [88].

## 2.4.2 Dynamics in Nanobiology

High-speed, high-spatial precision and a long measurement duration in imaging are some of the key advantages of iSCAT that become particularly important when investigating processes such as diffusion and transport of viruses, proteins, lipids or other nanoscopic entities. In this section, we present a few case studies where iSCAT was used in this context.

### 2.4.2.1 Protein Tracking

In the previous section, we discussed the power of iSCAT in detecting unlabeled proteins. The precision and fast temporal imaging of iSCAT microscopy also lends itself to investigation of the *mobility* of single proteins such as myosin-5 motor protein on actin [120, 172] (see Fig. 2.13). In addition, the mobility of single microtubules can be investigated to high precision when forming a gliding assay upon kinesin [168]. Furthermore, the motion of unlabeled small proteins upon landing on a surface has been visualized using iSCAT [118].

### 2.4.2.2 Lipid Membranes

Lipid membranes are one of the most important substrates in biology, often composed of a bilayer of phospholipid molecules and integral and peripheral proteins

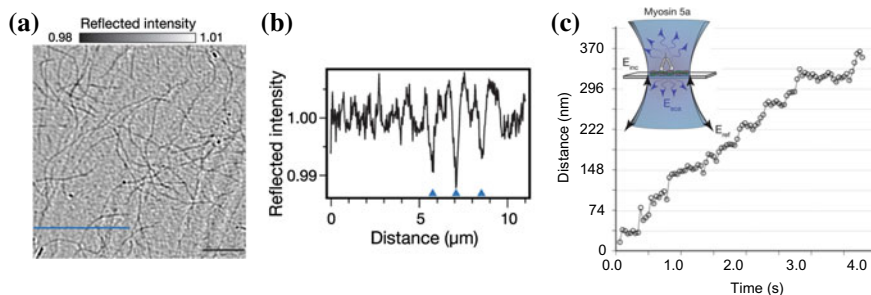


**Fig. 2.13** Single-protein tracking on an actin filament. **a** iSCAT image of unlabeled actin filaments adhered to a coverslip. Scale bar denotes  $5\ \mu\text{m}$ . **b** Signal intensity for the blue line marked in **(a)**. Blue arrow heads denote three actin filaments. **c** Motor protein myosin 5a walking velocity along a single actin filament when tracked by iSCAT. Frame rate is 25 Hz after temporal averaging. Inset: schematic of specimen detection [120]. Reproduced with permission from the American Chemical Society

of dynamic composition. The membrane functions as a selectively permeable barrier and a catalytic reaction site which gates cellular function and communication. Although the ultimate goal is the understanding of full cellular membranes, investigations into the mobility and statistical physics of diffusion within well-defined biophysical model systems are highly instructive and form an active area of research.

Previous efforts to investigate diffusion in membranes, stretching back to the 1970s and still active today, have depended upon fluorescence labeling, whether that be for ensemble measurements such as in fluorescence recovery after photobleaching (FRAP), fluorescence correlation spectroscopy (FCS) and its resolution-enhanced version STED-FCS or alternatively single-molecule tracking. The spatial and temporal resolution to which one can investigate diffusion using these strategies are throttled by the limitations within the photophysics of fluorescence, namely a finite and low yield of emitted photons as well as blinking and bleaching behavior.

After its early studies of viruses bound to supported lipid bilayers, iSCAT was extended to tracking the diffusion of lipids labeled by GNPs. For example, a CTxB-tagged 20 nm GNP probe was tethered to either DOPE lipids or GM1 gangliosides mixed at low concentration in DOPC membranes on glass substrates [136], illustrated in Fig. 2.14. The high resolution achieved (2 nm precision, 1000 frames per second) led to the observation of mixed mobility of lipid diffusion as well as identification of transient nanoscale confinements [118, 136]. The curious confinement modes were attributed to the molecular pinning and inter-leaflet coupling between lipid tail domains, explaining the observed transient immobilization on the millisecond time scale [173]. Quantitative iSCAT studies have also enabled clear discrimination of the varying mobility of a lipid diffusing between differently ordered phases within a membrane [174]. Furthermore, the extended duration over which measurements can be performed has inspired researchers to develop new statistical models to interpret the new generation of experimental results [175]. It has to be borne in mind, however, that quantitative comparison of diffusion performed by different methods remains a

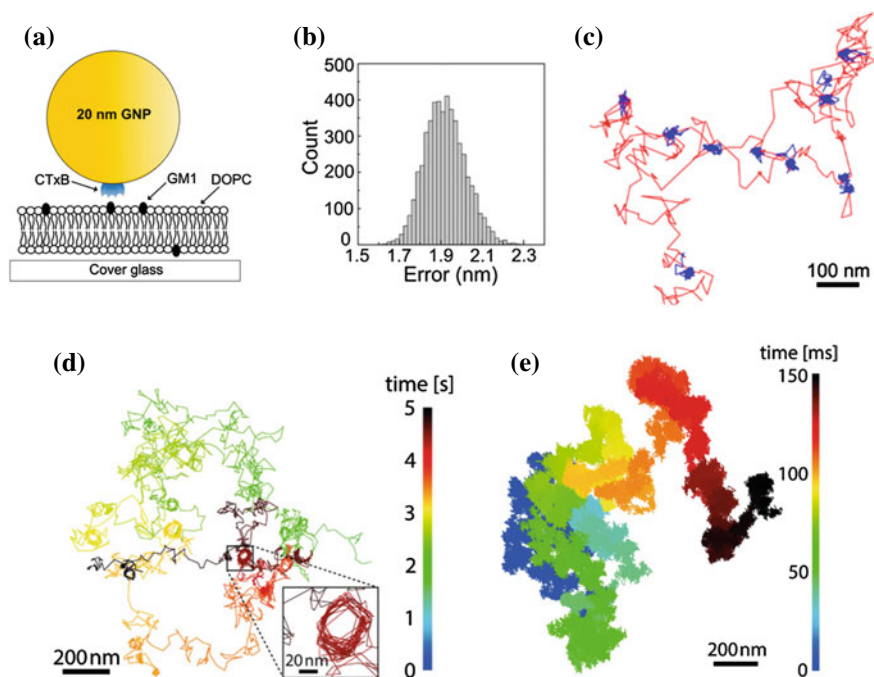


**Fig. 2.14** High spatiotemporal resolution of lipid diffusion in a bilayer membrane. **a** Schematic of a GNP tagging a GM1 lipid within a synthetic bilayer membrane. **b** Lateral localization of the GNP probe to nanometric precision. The diffusive trajectory of the mobile lipid (**c**) reveals regions of transient confinement (marked blue), features resolved by the nanometric precision and 1 kHz temporal resolution [136]. Reproduced with permission from the American Chemical Society. **d** Additionally, trajectories can reveal circular nanoconfinements (inset), trajectory duration 5 s. **e** Ultra-fast temporal resolution: the diffusive trajectory of a 20 nm GNP bound to a biotinylated DOPE lipid in a DOPC bilayer, recorded at 913,000 fps with duration 0.152 s [118]. Reproduced with permission from IOP Publishing

challenge since each labeling approach might introduce a certain systematic bias, and indeed, diffusion coefficients obtained from different techniques might vary [176].

We point out that aside from the nanometric precision to which the particle can be localized in space, iSCAT microscopy enables ultra-short exposure times, granting temporal resolutions that have thus far approached one million frames per second [118, 177], which for a 20 nm GNP gives a 10 nm localization precision. The sheer density of positional information of iSCAT trajectories permits robust statistical analysis of transient behavior contained within. Here, it is important to realize that a high localization precision resulting from long integration times are meaningless in particle tracking if the dynamics at hand are faster than the imaging speed so that the positional information becomes smeared.

As well as measuring the diffusive properties of membrane constituents, the sensitivity to which iSCAT can image small and faint microscopic entities can be used

in imaging the formation of lipid membranes in a similar *label-free* fashion. Here, it is helpful to note that a small unilamellar vesicle (SUV) has already a sufficiently large polarizability to be comfortably detected in iSCAT [117]. This high sensitivity can be exploited to observe, in real time, the docking and rupture of SUVs with a size down to 20 nm [118, 122] and coexisting dynamic phases within a supported membrane [123].

Whilst the planar bilayer membrane serves as a convenient model system, concerns over the perturbative influence of the substrate motivate efforts to investigate free-standing model membranes. One such system is the pore-spanning membrane [178], where a continuous lipid membrane spans an array of micron-sized pores, providing regions of supported and free-standing membranes, shown in Fig. 2.15. High-resolution iSCAT trajectories from GNP-tagged lipids revealed that nanoscale transient confinements were only observed on the supported regions, confirming suspicions as to the influence of the substrate raised in earlier work [178].

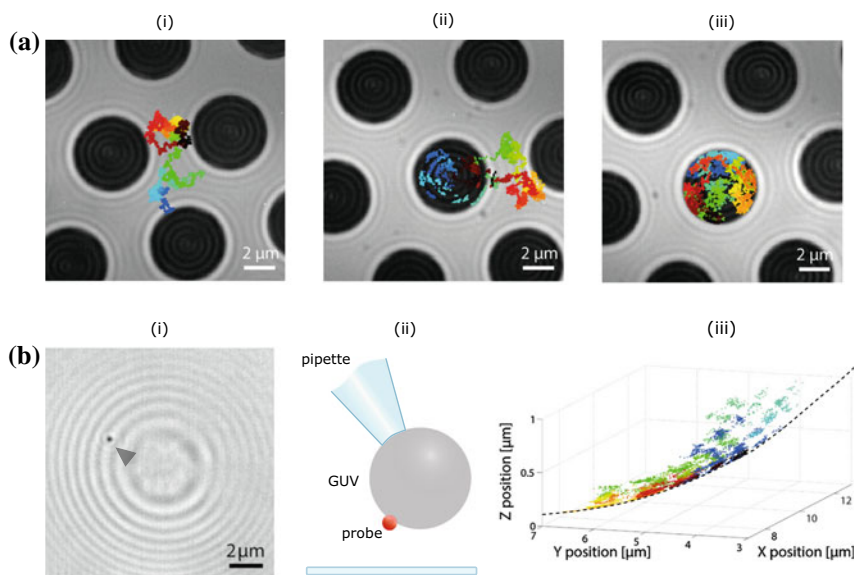


**Fig. 2.15** iSCAT microscopy of nonplanar model lipid systems. **a** Pore-spanning membrane wherein the synthetic bilayer covers a 5 μm hole-filled substrate, such that the membrane is supported (bright contrast) or free-standing (dark contrast). Shown are the trajectories for an GNP-tagged biotinylated DOPE lipid indicating different mobilities depending on whether the membrane is supported (i) or free-standing (iii), with a change in mobility evident upon region transition [178]. Reproduced with permission from the American Chemical Society. **b** Giant unilamellar vesicles (GUVs) provide a completely uniform, substrate-free membrane. (i) Wide-field reflection iSCAT image of a GUV, revealing a Newton ring-like pattern. (ii) A schematic of a GUV held by a pipette during iSCAT imaging, such as that shown in (i). (iii) A 10-s-long trajectory of the Tat virus-like particle which faithfully reproducing the spherical topology of the GUV [118]. Reproduced with permission from IOP Publishing

Another option for substrate-free membrane studies is to work with giant unilamellar vesicles (GUVs) with diameters in the range of tens of micrometers [179], which have been pursued as a platform for a minimal cell model [180]. Preliminary results have been reported on tracking of the three-dimensional diffusion of viral-mimetic particles on the GUV surface, where the particle could be localized to nanometer precision in all dimensions over an extended range [118], illustrated in Fig. 2.15b.

### 2.4.2.3 Imaging Cells and Associated Elements

Three-dimensional monitoring of molecules on the plasma membrane of live cells to high speed and precision stands as one of the most exciting challenges to unravel in cell biology [181, 182]. To date, nanoscale transient organization has precluded satisfactory or compelling investigation by fluorescence methodologies, which fall short in many respects, especially in capturing three-dimensional landscapes. While iSCAT is highly suited for addressing this issue, its ultrahigh sensitivity virtue is accompanied by the vice of a large speckle-like pattern originating from the cellular membrane and corpus, thus making cellular iSCAT particle tracking a challenge. Nevertheless, first attempts in tackling this issue have been successfully reported [106, 138, 183] (see Fig. 2.16). In particular, very fast detection allows one to reach nanometric-microsecond three-dimensional tracking of a transmembrane protein on the live HeLa cell, unraveling details such as heterogenous mobility of the protein, confinement into clathrin-like lattices and extended-duration directed diffusion along filopodia [138].

When imaging super-wavelength objects such as cells, cell nuclei or bacteria, one no longer speaks of scattering, but rather of reflection, absorption and transmission, as is common in elementary textbooks. As pointed out in the introductory section, interferometric microscopy has a long and rich history. In the past decade, however, iSCAT and its related techniques have ushered in a revival of interferometric imaging

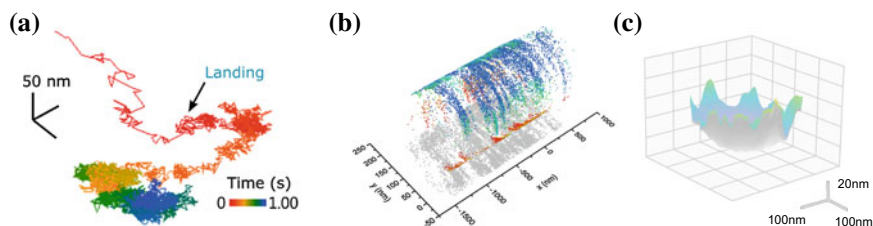


**Fig. 2.16** Imaging of cellular features with iSCAT. **a** 3D high-speed tracking of a vaccinia virus landing upon the surface of a live HeLa cell [106]. Reproduced with permission from American Chemical Society. **b** 3D diffusion of a GNP on a live neurite [183]. Reproduced with permission from Elsevier. **c** High-speed tracking of protein-labeled GNP diffusion within a pit on a live HeLa cell, which when interpolated renders a bowl-like surface [138]. Reproduced with permission from Nature Publishing Group

for cell biology applications, such as imaging microtubules [75, 76, 91, 184], actin [120], the actomyosin network [185], as well as organelles and micron or smaller sized vesicle containers which assist in the transport of material throughout the cell [186]. Echoing previous efforts from the holographic community [187, 188], interferometric efforts are now also focusing on identifying the small changes in the cell membrane, whereas previously the whole cell was profiled. Examples include the progression of ideas from holography to gradient light interference microscopy [105], recent efforts to profile membrane adhesion sites and topology in both wide-field [189] and confocal-scanning reflection interference microscopy [94] or wide-field iSCAT [190].

Similarly, there have been increasing efforts to harness interferometric imaging to investigate the mechanical properties of the cell membrane. Building upon initial efforts from quantitative phase imaging [191, 192], recent works have sought to turn attention to fast and nanometer-level dynamics that require high sensitivity to elucidate inherent fluctuations [193–196]. Results provide insight into the mechanical properties or changes in the membrane following the execution of action potentials and sub-nanometer-level twitching across the neuronal cell in response to stimulation.

Finally, it is interesting to note that some of the early efforts of the 1990s actually used iSCAT in transmission mode to track membrane proteins in living cells [197] although the underlying physics was not formulated, and thus, the virtues of iSCAT were not harnessed to reach the quality of trajectories that are accessible today.

#### 2.4.2.4 Other Emerging Applications

More recently, iSCAT imaging was also used to visualize excitation and relaxation of charge carriers within various semiconductor and organic crystals, following ultra-fast pumping [107]. The changes in local carrier density (refractive index) induced by the pump excitation mark the flow of energy in the material, which is visualized as local changes in contrast, with contrast sensitivity down to  $10^{-4}$ . The relaxation dynamics could thus be imaged through microscopy, and the role of grain boundaries and material anisotropy explored. In the wake of such efforts, we also anticipate great utility of this technique in the field of atomic physics.

## 2.5 Summary and Outlook

We began this chapter with a historical overview of different microscopy modalities where interference plays a central role. In particular, we emphasized that the physical mechanism behind conventional bright-field microscopy is extinction, which follows from formulating an interference problem between the illumination and the field that has interacted with the object. Methods such as phase contrast microscopy, differential interference microscopy, various versions of interference reflection microscopy and digital holography all share the same fundamental physics and only differ in the

way phases, path difference, and index modulations are introduced in the problem. The main focus of the book chapter has been to discuss the latest developments of interferometric scattering (iSCAT) microscopy upon the past decade and a half for detecting, sensing, imaging and tracking *nanoparticles* [73, 113–116]. Although the equation describing iSCAT uses very much the same interference expression known in conventional interferometric microscopy, its application to nanoparticles was indeed new and has led to a wealth of recent studies. These have often been presented under new acronyms inspired by variations of the illumination and detection schemes. In this work, we have aimed at unifying these efforts under a common theoretical and experimental roof and have attempted to present a concise discussion of some case studies and various implementations of iSCAT that are rapidly emerging.

While in its infancy, we believe that iSCAT microscopy stands as an exciting next-generation tool for uncovering the nanobiology of the cell membrane as well as advanced diagnostics and laboratory analytics applications. The sensitivity and performance of iSCAT is only limited by the signal-to-noise ratio, which in turn depends on factors such as the choice of detector and background fluctuations that result from specimen dynamics. Advances in detector technologies, image processing and machine learning, as well as optical techniques for imaging through scattering media, promise to pave the way to these goals. Thus, we are convinced that the limits of iSCAT will be continually pushed in the near future, exploring unlabeled proteins well under 20 kDa not only in a biosensor geometry but also in the living cell membrane. The simplicity of an iSCAT microscope lends itself to miniaturization into a compact instrument as well as integration into existing microscope stations such as a laser scanning confocal microscope, thus providing prospects of very widespread use.

**Acknowledgements** We are grateful to a large number of fantastic group members, former and present, who have contributed to the advances of iSCAT in our laboratories. We also thank the Alexander von Humboldt Foundation for their generous support in the context of a Humboldt Professorship (VS) and Postdoctoral Fellowship (RWT) as well the Max Planck Society for continuous support.

## References

1. M. Fernández-Suárez, A.Y. Ting, Fluorescent probes for super-resolution imaging in living cells. *Nat. Rev. Mol. Cell Biol.* **9**(12), 929–943 (2008)
2. E. Abbe, Beiträge zur Theorie des Mikroskops und der mikroskopischen Wahrnehmung. *Arch. Mikrosk. Anat.* **9**(1), 413–418 (1873)
3. J. Steinhardt, Intensity discrimination in the human eye: I. The relation of  $\Delta I/I$  to intensity. *J. Gen. Physiol.* **20**(2), 185–209 (1936)
4. L.C. Martin, B.K. Johnson, *Practical Microscopy* (Blackie & Son Limited, 1931)
5. J.J. Lister, On some properties in achromatic object-glasses applicable to the improvement of the microscope. *Philos. Trans. R. Soc. Lond.* **120**, 187–200 (1830)
6. S.H. Gage, Modern dark-field microscopy and the history of its development. *Trans. Am. Microsc. Soc.* **39**(2), 95–141 (1920)

7. H. Siedentopf, R. Zsigmondy, Über Sichtbarmachung und Größenbestimmung ultramikroskopischer Teilchen, mit besonderer Anwendung auf Goldrubingläser. *Ann. Phys.* **315**(1), 1–39 (1902)
8. F. Zernike, Diffraction theory of the knife-edge test and its improved form, the phase-contrast method. *Mon. Not. R. Astron. Soc.* **94**(5), 377–384 (1934)
9. F. Zernike, The concept of degree of coherence and its application to optical problems. *Physica* **5**(8), 785–795 (1938)
10. F. Zernike, How I discovered phase contrast. *Science* **121**(3141), 345–349 (1955)
11. F. Zernike, Phase contrast, a new method for the microscopic observation of transparent objects part I. *Physica* **9**(7), 686–698 (1942)
12. F. Zernike, Phase contrast, a new method for the microscopic observation of transparent objects part II. *Physica* **9**(10), 974–986 (1942)
13. G. Normarski, Dispositif Oculaire a Contraste De phase pour microscope. *J. De Phys. Et Le Radiu.* **11**(12), 9–10 (1950)
14. J. Jamin, Neuer interferential-refractor. *Ann. der Phys. und Chem.* **174**(6), 345–349 (1856)
15. J.L. Sirks, Over een interferentiemicroscop. *Handelingen van het vierde Nederlandisch Natuurgen. Geneskundig Congress* **4**, 92–98 (1893)
16. W.E. Kock, Nobel Prize for Physics: Gabor and Holography. *Science* **174**(4010), 674–675 (1971)
17. G.W. Ellis, Holomicrography: transformation of image during reconstruction a posteriori. *Science* **154**(3753), 1195–1197 (1966)
18. W. Krug, J. Rienitz, G. Schulz, *Contributions to Interference Microscopy* (Hilger & Watts, 1964)
19. M. Shribak, in *Handbook of Optics*, vol. 1, ed. by M. Bass (McGraw-Hill, 2006)
20. G.A. Dunn, Quantitative interference microscopy, in *New Techniques of Optical Microscopy and Microspectroscopy*, ed. by R.J. Cherry (CRC Press, 1991)
21. P. de Groot, Principles of interference microscopy for the measurement of surface topography. *Adv. Opt. Photonics* **7**(1), 1–65 (2015)
22. M. Renz, Fluorescence microscopy a historical and technical perspective. *Cytom. Part A* **83**(9), 767–779 (2013)
23. B.R. Masters, The development of fluorescence microscopy, in *Encyclopedia of Life Sciences (ELS)* (Wiley, 2010)
24. M. Minsky, Memoir on inventing the confocal scanning microscope. *Scanning* **10**(4), 128–138 (1988)
25. A.S.G. Curtis, The mechanism of adhesion of cells to glass. A study by interference reflection microscopy. *J. Cell Biol.* **20**(2), 199–215 (1964)
26. J.S. Ploem, Reflection-contrast microscopy as a tool for investigation of the attachment of living cells to a glass surface, in *Mononuclear Phagocytes in Immunity, Infection and Pathology*, ed. by R. van Furth (Blackwell Scientific, 1975)
27. M. Abercrombie, G.A. Dunn, Adhesions of fibroblasts to substratum during contact inhibition observed by interference reflection microscopy. *Exp. Cell Res.* **92**(1), 57–62 (1975)
28. C.S. Izzard, L.R. Lochner, Cell-to-substrate contacts in living fibroblasts: an interference reflexion study with an evaluation of the technique. *J. Cell Sci.* **21**, 129–159 (1976)
29. J.P. Heath, G.A. Dunn, Cell to substratum contacts of chick fibroblasts and their relation to the microfilament system. A correlated interference-reflexion and high-voltage electron-microscope study. *J. Cell Sci.* **29**(1), 197–212 (1978)
30. J. Wehland, M. Osborn, K. Weber, Cell-to-substratum contacts in living cells: a direct correlation between interference-reflexion and indirect-immunofluorescence microscopy using antibodies against actin and alpha-actinin. *J. Cell Sci.* **37**, 257–273 (1979)
31. M. Opas, V.I. Kalnins, Surface reflection interference microscopy: a new method for visualizing cytoskeletal components by light microscopy. *J. Microsc.* **133**(3), 291–306 (1984)
32. J. Bereiter-Hahn, C.H. Fox, B. Thorell, Quantitative reflection contrast microscopy of living cells. *J. Cell Biol.* **82**(3), 767–779 (1979)

33. A. Zilker, H. Engelhardt, E. Sackmann, Dynamic reflection interference contrast (RIC-) microscopy: a new method to study surface excitations of cells and to measure membrane bending elastic moduli. *J. Phys.* **48**(12), 2139–2151 (1987)
34. J. Rädler, E. Sackmann, Imaging optical thicknesses and separation distances of phospholipid vesicles at solid surfaces. *J. Phys. II* **3**(5), 727–748 (1993)
35. G. Wiegand, K.R. Neumaier, E. Sackmann, Microinterferometry: three-dimensional reconstruction of surface microtopography for thin-film and wetting studies by reflection interference contrast microscopy (RICM). *Appl. Opt.* **37**(29), 6892 (1998)
36. J. Dvorak et al., Invasion of erythrocytes by malaria merozoites. *Science* **187**(4178), 748–750 (1975)
37. R.D. Allen, N.S. Allen, J.L. Travis, Video-enhanced contrast, differential interference contrast (AVEC-DIC) microscopy: a new method capable of analyzing microtubule-related motility in the reticulopodial network of *Allogromia laticollaris*. *Cell Motil.* **1**(3), 291–302 (1981)
38. S. Inoué, Video image processing greatly enhances contrast, quality, and speed in polarization-based microscopy. *J. Cell Biol.* **89**(2), 346–356 (1981)
39. R.J. Walter, M.W. Berns, Computer-enhanced video microscopy: digitally processed microscope images can be produced in real time. *Proc. Natl. Acad. Sci. U.S.A.* **78**(11), 6927–6931 (1981)
40. R.D. Allen, N.S. Allen, Video-enhanced microscopy with a computer frame memory. *J. Microsc.* **129**(1), 3–17 (1983)
41. E.D. Salmon, P. Tran, High-resolution video-enhanced differential interference contrast light microscopy. *Methods Cell Biol.* **72**, 289–318 (2003)
42. S. Inoué, *Video Microscopy* (Springer, 1986)
43. S.T. Brady et al., Fast axonal transport in extruded axoplasm from squid giant axon. *Science* **218**(4577), 1129–1131 (1982)
44. R.D. Allen et al., New observations on cell architecture and dynamics by video-enhanced contrast optical microscopy. *Annu. Rev. Biophys. Chem.* **14**(1), 265–290 (1985)
45. B.J. Schnapp et al., Single microtubules from squid axoplasm support bidirectional movement of organelles. *Cell* **40**(2), 455–462 (1985)
46. D.G. Weiss, Visualization of the living cytoskeleton by video-enhanced microscopy and digital image processing. *J. Cell Sci. Suppl.* **5**, 1–15 (1986)
47. B. Herman, D.F. Albertini, A time-lapse video image intensification analysis of cytoplasmic organelle movements during endosome translocation. *J. Cell Biol.* **98**(2), 565–576 (1984)
48. M. De Brabander et al., Microtubule-dependent intracellular motility investigated with nanometer particle video ultramicroscopy (nanovid ultramicroscopy). *Ann. N. Y. Acad. Sci.* **466**, 666–668 (1986)
49. H. Geerts et al., Nanovid tracking: a new automatic method for the study of mobility in living cells based on colloidal gold and video microscopy. *Biophys. J.* **52**(5), 775–782 (1987)
50. B.J. Schnapp, J. Gelles, M.P. Sheetz, Nanometer-scale measurements using video light microscopy. *Cell Motil. Cytoskelet.* **10**, 47–53 (1988)
51. M. De Brabander et al., Dynamic behavior of the transferrin receptor followed in living epidermoid carcinoma (A431) cells with nanovid microscopy. *Cell Motil. Cytoskelet.* **9**(1), 30–47 (1988)
52. M.P. Sheetz et al., Nanometre-level analysis demonstrates that lipid flow does not drive membrane glycoprotein movements. *Nature* **340**(6231), 284–288 (1989)
53. H. Geerts, M. De Brabander, R. Nuydens, Nanovid microscopy. *Nature* **351**(6231), 765–766 (1991)
54. A. Kusumi et al., Paradigm shift of the plasma membrane concept from the two-dimensional continuum fluid to the partitioned fluid: high-speed single-molecule tracking of membrane molecules. *Annu. Rev. Biophys. Biomol. Struct.* **34**(1), 351–378 (2005)
55. A. Kusumi et al., Dynamic organizing principles of the plasma membrane that regulate signal transduction: commemorating the fortieth anniversary of singer and nicolson’s fluid-mosaic model. *Annu. Rev. Cell Dev. Biol.* **28**(1), 215–250 (2012)

56. D.R. Pettit, T.W. Peterson, Coherent detection of scattered light from submicron aerosols. *Aerosol Sci. Technol.* **2**(3), 351–368 (1982)
57. J.S. Batchelder, M.A. Taubenblatt, Interferometric detection of forward scattered light from small particles. *Appl. Phys. Lett.* **55**(3), 215–217 (1989)
58. D.W. Pohl, W. Denk, M. Lanz, Optical stethoscopy: Image recording with resolution  $\lambda/20$ . *Appl. Phys. Lett.* **44**(7), 651–653 (1984)
59. G. Binnig, C.F. Quate, Ch. Gerber, Atomic Force Microscope. *Phys. Rev. Lett.* **56**(9), 930–933 (1986)
60. W.E. Moerner, L. Kador, Optical detection and spectroscopy of single molecules in a solid. *Phys. Rev. Lett.* **62**(21), 2535–2538 (1989)
61. R.P. Feynman, There's plenty of room at the bottom. *Eng. Sci.* **23**(5), 22–36 (1960)
62. F. Zenhausern, M.P. O'Boyle, H.K. Wickramasinghe, Apertureless near-field optical microscope. *Appl. Phys. Lett.* **65**(13), 1623–1625 (1994)
63. V. Sandoghdar et al., Reflection scanning near-field optical microscopy with uncoated fiber tips: How good is the resolution really? *J. Appl. Phys.* **81**(6), 2499–2503 (1997)
64. R. Hillenbrand, B. Knoll, F. Keilmann, Pure optical contrast in scattering-type scanning near-field microscopy. *J. Microsc.* **202**(1), 77–83 (2001)
65. T. Taubner, R. Hillenbrand, F. Keilmann, Performance of visible and mid-infrared scattering-type near-field optical microscopes. *J. Microsc.* **210**(3), 311–314 (2003)
66. I. Amenabar et al., Structural analysis and mapping of individual protein complexes by infrared nanospectroscopy. *Nat. Commun.* **4**, 1–9 (2013)
67. T. Klar et al., Surface-plasmon resonances in single metallic nanoparticles. *Phys. Rev. Lett.* **80**(19), 4249–4252 (1998)
68. S. Schultz, D.R. Smith, J.J. Mock, D.A. Schultz, Single-target molecule detection with non-bleaching multicolor optical immunolabels. *Proc. Natl. Acad. Sci. U.S.A.* **97**(3), 996–1001 (2000)
69. C. Sönnichsen et al., Spectroscopy of single metallic nanoparticles using total internal reflection microscopy. *Appl. Phys. Lett.* **77**(19), 2949–2951 (2000)
70. M.Y. Sfeir et al., Probing electronic transitions in individual carbon nanotubes by Rayleigh scattering. *Science* **306**(5701), 1540–1543 (2004)
71. D. Boyer et al., Photothermal imaging of nanometer-sized metal particles among scatterers. *Science* **297**(5584), 1160–1163 (2002)
72. S. Berciaud et al., Photothermal heterodyne imaging of individual nonfluorescent nanoclusters and nanocrystals. *Phys. Rev. Lett.* **93**(25), 2–5 (2004)
73. K. Lindfors et al., Detection and spectroscopy of gold nanoparticles using supercontinuum white light confocal microscopy. *Phys. Rev. Lett.* **93**(3), 037401 (2004)
74. A. Arbouet et al., Direct measurement of the single-metal-cluster optical absorption. *Phys. Rev. Lett.* **93**(12), 127401 (2004)
75. S. Simmert et al., LED-based interference-reflection microscopy combined with optical tweezers for quantitative three-dimensional microtubule imaging. *Opt. Express* **26**(11), 14499 (2018)
76. M. Mahamdeh et al., Label-free high-speed wide-field imaging of single microtubules using interference reflection microscopy. *J. Microsc.* **272**(1), 60–66 (2018)
77. G.G. Daaboul et al., High-throughput detection and sizing of individual low-index nanoparticles and viruses for pathogen identification. *Nano Lett.* **10**(11), 4727–4731 (2010)
78. O. Avci et al., Interferometric Reflectance Imaging Sensor (IRIS)—A Platform Technology for Multiplexed Diagnostics and Digital Detection. *Sensors* **15**(7), 17649–17665 (2015)
79. A. Yurt et al., High-throughput size determination of nearly spherical gold nanoparticles, in *2011 XXXth URSI General Assembly and Scientific Symposium*, vol. 1 (2011), pp. 1–4
80. A. Matlock et al., Differential Phase Contrast and Digital Refocusing in a Computational Reflection Interferometric Microscope for Nanoparticle Imaging CTh4B.2 (2017)
81. S.M. Scherr et al., Real-time capture and visualization of individual viruses in complex media. *ACS Nano* **10**(2), 2827–2833 (2016)

82. G.G. Daaboul et al., Digital detection of exosomes by interferometric imaging. *Sci. Rep.* **6**, 1–10 (2016)
83. G.G. Daaboul et al., Enhanced light microscopy visualization of virus particles from Zika virus to filamentous ebola viruses. *PLoS ONE* **12**(6), 1–15 (2017)
84. D. Sevenler, O. Avci, M.S. Ünlü, Quantitative interferometric reflectance imaging for the detection and measurement of biological nanoparticles. *Biomed. Opt. Express* **8**(6), 2976 (2017)
85. D. Sevenler et al., Digital microarrays: single-molecule readout with interferometric detection of plasmonic nanorod labels. *ACS Nano* **12**(6), 5880–5887 (2018)
86. S. Wang et al., Label-free imaging, detection, and mass measurement of single viruses by surface plasmon resonance. *Proc. Natl. Acad. Sci. U.S.A.* **107**(37), 16028–16032 (2010)
87. H. Yu et al., Plasmonic imaging and detection of single DNA molecules. *ACS Nano* **8**(4), 3427–3433 (2014)
88. Y. Yang et al., Interferometric plasmonic imaging and detection of single exosomes. *Proc. Natl. Acad. Sci. U.S.A.* **115**(41), 10275–10280 (2018)
89. X. Shan et al., Imaging the electrocatalytic activity of single nanoparticles. *Nat. Nanotechnol.* **7**(10), 668–672 (2012)
90. M.D. Koch, A. Rohrbach, Label-free imaging and bending analysis of microtubules by ROCS microscopy and optical trapping. *Biophys. J.* **114**(1), 168–177 (2018)
91. M.E. Kandel et al., Label-free imaging of single microtubule dynamics using spatial light interference microscopy. *ACS Nano* **11**(1), 647–655 (2017)
92. J. Schilling et al., Absolute interfacial distance measurements by dual-wavelength reflection interference contrast microscopy. *Phys. Rev. E.* **69**(2), 1–9 (2004)
93. L. Limozin, K. Sengupta, Quantitative reflection interference contrast microscopy (RICM) in soft matter and cell adhesion. *ChemPhysChem* **10**(16), 2752–2768 (2009)
94. T. Matsuzaki et al., High contrast visualization of cell-hydrogel contact by advanced interferometric optical microscopy. *J. Phys. Chem. Lett.* **5**(1), 253–257 (2014)
95. T. Matsuzaki et al., Quantitative evaluation of cancer cell adhesion to self-assembled monolayer-patterned substrates by reflection interference contrast microscopy. *J. Phys. Chem. B.* **120**(7), 1221–1227 (2016)
96. P. Dillard et al., Nano-clustering of ligands on surrogate antigen presenting cells modulates T cell membrane adhesion and organization. *Interg. Biol.* **8**(3), 287–301 (2016)
97. M.J. DeJardin et al., Lamellipod reconstruction by three-dimensional reflection interference contrast nanoscopy (3D-RICN). *Nano Lett.* **18**(10), 6544–6550 (2016)
98. F. Jünger, P.V. Olshausen, A. Rohrbach, Fast, label-free super-resolution live-cell imaging using rotating coherent scattering (ROCS) microscopy. *Sci. Rep.* **6**, 1–11 (2016)
99. F. Jünger, A. Rohrbach, Strong cytoskeleton activity on millisecond timescales upon particle binding revealed by ROCS microscopy. *Cytoskeleton* **75**(9), (2018)
100. J.C. Contreras-Naranjo, V.M. Ugaz, A nanometre-scale resolution interference-based probe of interfacial phenomena between microscopic objects and surfaces. *Nat. Commun.* **4**(1), 1919 (2013)
101. L.D. Chiu et al., Use of a white light supercontinuum laser for confocal interference-reflection microscopy. *J. Microsc.* **246**(2), 153–159 (2012)
102. B. Redding et al., Full-field interferometric confocal microscopy using a VCSEL array. *Opt. Lett.* **39**(15), 4446 (2014)
103. I. Sencan et al., Ultrahigh-speed, phase-sensitive full-field interferometric confocal microscopy for quantitative microscale physiology. *Biomed. Opt. Express* **7**(11), 4674 (2016)
104. A.J. Schain, R.A. Hill, J. Grutzendler, Label-free in vivo imaging of myelinated axons in health and disease with spectral confocal reflectance microscopy. *Nat. Med.* **20**(4), 443–449 (2014)
105. T.H. Nguyen et al., Gradient light interference microscopy for 3D imaging of unlabeled specimens. *Nat. Commun.* **8**(1) (2017)
106. Y.F. Huang et al., Coherent brightfield microscopy provides the spatiotemporal resolution to study early stage viral infection in live cells. *ACS Nano* **11**(3), 2575–2585 (2017)

107. M. Delor et al., Imaging material functionality through 3D nanoscale tracking of energy flow. arXiv:1805.09982v3 (2019)
108. G. Young et al., Quantitative mass imaging of single biological macromolecules. *Science* **360**(6387), 423–427 (2018)
109. A.E. Siegman, *Lasers* (University Science Books, 1986)
110. X. Pang, T.D. Visser, E. Wolf, Phase anomaly and phase singularities of the field in the focal region of high-numerical aperture systems. *Opt. Commun.* **284**(24), 5517–5522 (2011)
111. C.F. Bohren, D.R. Huffman, *Absorption and Scattering of Light by Small Particles Absorption and Scattering of Light by Small Particles* (Wiley-VCH, 1998)
112. H.A. Haus, *Electromagnetic Noise and Quantum Optical Measurements* (Springer, 2000)
113. V. Jacobsen et al., Interferometric optical detection and tracking of very small gold nanoparticles at a water-glass interface. *Opt. Express* **14**(1), 405–14 (2006)
114. P. Kukura et al., Imaging a single quantum dot when it is dark. *Nano Lett.* **9**(3), 926–929 (2009)
115. H. Ewers et al., Label-free optical detection and tracking of single virions bound to their receptors in supported membrane bilayers. *Nano Lett.* **7**(8), 2263–2266 (2007)
116. P. Kukura et al., High-speed nanoscopic tracking of the position and orientation of a single virus. *Nat. Methods* **6**(12), 923–927 (2009)
117. M. Krishnan et al., Geometry-induced electrostatic trapping of nanometric objects in a fluid. *Nature* **467**(7316), 692–695 (2010)
118. S. Spindler et al., Visualization of lipids and proteins at high spatial and temporal resolution via interferometric scattering (iSCAT) microscopy. *J. Phys. D: Appl. Phys.* **49**(27), 274002 (2016)
119. M. Piliarik, V. Sandoghdar, Direct optical sensing of single unlabelled proteins and super-resolution imaging of their binding sites. *Nat. Commun.* **5**, 1–8 (2014)
120. J.O. Arroyo et al., Label-free, all-optical detection, imaging, and tracking of a single protein. *Nano Lett.* **14**(4), 2065–2070 (2014)
121. J.O. Arroyo, P. Kukura, Non-fluorescent schemes for single-molecule detection, imaging and spectroscopy. *Nat. Photonics* **10**(1), 11–17 (2016)
122. J. Andrecka et al., Direct observation and control of supported lipid bilayer formation with interferometric scattering microscopy. *ACS Nano* **7**(12), 10662–10670 (2013)
123. G. de Wit et al., Dynamic label-free imaging of lipid nanodomains. *Proc. Natl. Acad. Sci. U.S.A.* **112**(40), 12299–12303 (2015)
124. R. Loudon, *The Quantum Theory of Light* (Oxford University Press, 2000)
125. G. Zumofen et al., Perfect reflection of light by an oscillating dipole. *Phys. Rev. Lett.* **101**(18), 180404 (2008)
126. K.G. Lee et al., A planar dielectric antenna for directional single-photon emission and near-unity collection efficiency. *Nat. Photonics* **5**(3), 166–169 (2011)
127. W. Lukosz, Light emission by magnetic and electric dipoles close to a plane dielectric interface. III. Radiation patterns of dipoles with arbitrary orientation. *J. Opt. Soc. Am.* **69**(11), 1495–1503 (1979)
128. M. Liebel et al., Ultrasensitive label-free nanosensing and high-speed tracking of single proteins. *Nano Lett.* **17**(2), 1277–1281 (2017)
129. D. Cole et al., Label-free single-molecule imaging with numerical-aperture-shaped interferometric scattering microscopy. *ACS Photonics* **4**(2), 211–216 (2017)
130. O. Avci et al., Pupil function engineering for enhanced nanoparticle visibility in wide-field interferometric microscopy. *Optica* **4**(2), 247–254 (2017)
131. S. Faez et al., Coherent interaction of light and single molecules in a dielectric nanoguide. *Phys. Rev. Lett.* **113**(21), 213601 (2014)
132. S. Faez, Y. Lahini, S. Weidlich, R.F. Garmann, Fast, label-free tracking of single viruses and weakly scattering nanoparticles in a nanofluidic optical fiber. *ACS Nano* **9**(12), 12349–12357 (2015)
133. M. Celebrano et al., Single-molecule imaging by optical absorption. *Nat. Photonics* **5**(2), 95–98 (2011)

134. A. Gemeinhardt et al., Label-free imaging of single proteins secreted from living cells via iSCAT microscopy. *J. Vis. Exp.* (141), e58486 (2018)
135. G. Wrigge et al., Exploring the limits of single emitter detection in fluorescence and extinction. *Opt. Express* **16**(22), 17358 (2008)
136. C.L. Hsieh et al., Tracking single particles on supported lipid membranes: multimobility diffusion and nanoscopic confinement. *J. Phys. Chem. B.* **118**(6), 1545–1554 (2014)
137. C.Y. Cheng, C.L. Hsieh, Background estimation and correction for high-precision localization microscopy. *ACS Photonics* **4**(7), 1730–1739 (2017)
138. R.W. Taylor et al., Interferometric scattering microscopy reveals microsecond nanoscopic protein motion on a live cell membrane. *Nat. Photonics* **13**, 480–487 (2019)
139. A. Weigel, A. Sebesta, P. Kukura, Dark field microspectroscopy with single molecule fluorescence sensitivity. *ACS Photonics* **1**(9), 848–856 (2014)
140. H. Deschout et al., Precisely and accurately localizing single emitters in fluorescence microscopy. *Nat. Methods* **11**(3), 253–266 (2014)
141. O. Avci et al., Physical modeling of interference enhanced imaging and characterization of single nanoparticles. *Opt. Express* **24**(6), 6094 (2016)
142. R. Gholami Mahmoodabadi et al. Fast and precise 3D tracking of nanoparticles in interferometric scattering microscopy, In preparation
143. P. Kukura et al., Single-molecule sensitivity in optical absorption at room temperature. *J. Phys. Chem. Lett.* **1**(23), 3323–3327 (2010)
144. J.T. Trueb et al., Robust visualization and discrimination of nanoparticles by interferometric imaging. *IEEE J. Sel. Top. Quantum Electron* **23**(2), 394–403 (2017)
145. K. Holanová, M. Vala, M. Piliarik, Optical imaging and localization of prospective scattering labels smaller than a single protein. *Opt. Laser Technol.* **109**, 323–327 (2019)
146. T. Kalkbrenner et al., A single gold particle as a probe for apertureless scanning near-field optical microscopy. *J. Microsc.* **202**(1), 72–76 (2001)
147. L. Zhang et al., Interferometric detection of single gold nanoparticles calibrated against TEM size distributions. *Small* **11**(29), 3550–3555 (2015)
148. I.B. Lee et al., Interferometric scattering microscopy with polarization-selective dual detection scheme: capturing the orientational information of anisotropic nanometric objects. *ACS Photonics* **5**(3), 797–804 (2018)
149. P. Stoller, V. Jacobsen, V. Sandoghdar, Measurement of the complex dielectric constant of a single gold nanoparticle. *Opt. Lett.* **31**(16), 2474 (2006)
150. J.T. Kim, S. Spindler, V. Sandoghdar, Scanning-aperture trapping and manipulation of single charged nanoparticles. *Nat. Commun.* **5**(1), 3380 (2014)
151. S. Fringes, M. Skaug, A.W. Knoll, *In situ* contrast calibration to determine the height of individual diffusing nanoparticles in a tunable confinement. *J. Appl. Phys.* **119**(2), 024303 (2016)
152. Y. Tuna et al., Levitated plasmonic nanoantennas in an aqueous environment. *ACS Nano* **11**(8), 7674–7678 (2017)
153. R. Rigler, M. Orrit, T. Basche (eds.), *Single Molecule Spectroscopy* (Springer, Berlin, Heidelberg, 2001)
154. J. Hwang, M.M. Fejer, W.E. Moerner, Scanning interferometric microscopy for the detection of ultrasmall phase shifts in condensed matter. *Phys. Rev. A* **73**(2), 021802 (2006)
155. A. Gaiduk et al., Room-temperature detection of a single molecule’s absorption by photothermal contrast. *Science* **330**(6002), 353–356 (2010)
156. S. Chong, W. Min, X. Sunney Xie, Ground-state depletion microscopy: detection sensitivity of single-molecule optical absorption at room temperature. *J. Phys. Chem. Lett.* **1**(23), 3316–3322 (2010)
157. C.M. Robinson, J.K. Pfeiffer, Viruses and the microbiota. *Annu. Rev. Virol.* **1**(1), 55–69 (2014)
158. M. Mietzsch, M. Agbandje-McKenna, The good that viruses do. *Ann. Rev. Virol.* **4**(1), iii–v (2017)
159. R. Milo, R. Phillips, *Cell Biology by the Numbers* (Taylor & Francis Ltd., 2015)

160. F.V. Ignatovich, L. Novotny, Real-time and background-free detection of nanoscale particles. *Phys. Rev. Lett.* **96**(1), 013901 (2006)
161. A. Mitra et al., Nano-optofluidic detection of single viruses and nanoparticles. *ACS Nano* **4**(3), 1305–1312 (2010)
162. A.M. Goldfain et al., Dynamic measurements of the position, orientation, and DNA content of individual unlabeled bacteriophages. *J. Phys. Chem. B* **120**(26), 6130–6138 (2016)
163. S. Faez et al., Fast, label-free tracking of single viruses and weakly scattering nanoparticles in a nanofluidic optical fiber. *ACS Nano* **9**(12), 12349–12357 (2015)
164. M.P. McDonald et al., Visualizing single-cell secretion dynamics with single-protein sensitivity. *Nano Lett.* **18**(1), 513–519 (2018)
165. P. Zijlstra, P.M.R. Paulo, M. Orrit, Optical detection of single non-absorbing molecules using the surface plasmon resonance of a gold nanorod. *Nat. Nanotechnol.* **7**(6), 379–382 (2012)
166. F. Vollmer, S. Arnold, Whispering-gallery-mode biosensing: label-free detection down to single molecules. *Nat. Methods* **5**(7), 591–596 (2008)
167. K.J. Mickolajczyk et al., Direct observation of individual tubulin dimers binding to growing microtubules. *Proc. Natl. Acad. Sci. U.S.A.* **116**(15), 7314–7322 (2019)
168. J. Andrecka et al., Label-free imaging of microtubules with sub-nm precision using interferometric scattering microscopy. *Biophys. J.* **110**(1), 214–217 (2016)
169. R.F. Garmann, A.M. Goldfain, V.N. Manoharan, Measurements of the self-assembly kinetics of individual viral capsids around their RNA genome. *bioRxiv* 265330 (2018)
170. L. Talà et al., *Pseudomonas aeruginosa* orchestrates twitching motility by sequential control of type IV pili movements. *Nat. Microbiol.* **4**, 774–780 (2019)
171. J.R. Heath, A. Ribas, P.S. Michel, Single-cell analysis tools for drug discovery and development. *Nat. Rev. Drug Discov.* **15**(3), 204–216 (2016)
172. J. Andrecka et al., Structural dynamics of myosin 5 during processive motion revealed by interferometric scattering microscopy. *eLife* **4**, e05413 (2015)
173. K.M. Spillane et al., High-speed single-particle tracking of GM1 in model membranes reveals anomalous diffusion due to interleaflet coupling and molecular pinning. *Nano Lett.* **14**(9), 5390–5397 (2014)
174. H.-M. Wu, Y.-H. Lin, T.-C. Yen, C.-L. Hsieh, Nanoscopic substructures of raft-mimetic liquid-ordered membrane domains revealed by high-speed single-particle tracking. *Sci. Rep.* **6**(1), 20542 (2016)
175. P.J. Slator, N.J. Burroughs, A hidden Markov model for detecting confinement in single-particle tracking trajectories. *Biophys. J.* **115**(9), 1741–1754 (2018)
176. F. Reina et al., Complementary studies of lipid membrane dynamics using iSCAT and super-resolved fluorescence correlation spectroscopy. *J. Phys. D: Appl. Phys.* **51**(23), 235401 (2018)
177. Y.-H. Lin, W.-L. Chang, C.-L. Hsieh, Shot-noise limited localization of single 20 nm gold particles with nanometer spatial precision within microseconds. *Opt. Express* **22**(8), 9159–9170 (2014)
178. S. Spindler et al., High-speed microscopy of diffusion in pore-spanning lipid membranes. *Nano Lett.* **18**(8), 5262–5271 (2018)
179. H. Stein et al., Production of isolated giant unilamellar vesicles under high salt concentrations. *Front. Physiol.* **8**, 1–16 (2017)
180. P.L. Luisi, P. Walde, *Giant Vesicles* (Wiley, 2000)
181. J. Bernardino de la Serna et al., There is no simple model of the plasma membrane organization. *Front. Cell Dev. Biol.* **4**(106), 1–17 (2016)
182. E. Sezgin et al., The mystery of membrane organization: composition, regulation and roles of lipid rafts. *Nat. Rev. Mol. Cell Biol.* **18**(6), 361–374 (2017)
183. G. de Wit et al., Revealing compartmentalized diffusion in living cells with interferometric scattering microscopy. *Biophys. J.* **114**(12), 2945–2950 (2018)
184. B. Gutiérrez-Medina, S. M. Block, Visualizing individual microtubules by bright field microscopy. *Am. J. Phys.* **78**(11), 1152–1159 (2010)
185. D. Köster et al., Visualizing acto-myosin dynamics and vortices at a membrane surface using interferometric scattering microscopy. *bioRxiv* 199778v3 (2018)

186. Y.-F. Huang et al., Label-free, ultrahigh-speed, 3D observation of bidirectional and correlated intracellular cargo transport by coherent brightfield microscopy. *Nanoscale* **9**(19), 6567–6574 (2017)
187. W. Choi et al., Tomographic phase microscopy. *Nat. Methods* **4**(9), 717–719 (2007)
188. Z. Yaqoob et al., Single-shot full-field reflection phase microscopy. *Opt. Express* **19**(8), 7587 (2011)
189. K. Klein et al., Cell membrane topology analysis by RICM enables marker-free adhesion strength quantification. *Biointerphases* **8**(1), 1–13 (2013)
190. J.-S. Park et al., Label-free and live cell imaging by interferometric scattering microscopy. *Chem. Sci.* **9**, 2690–2697 (2018)
191. G. Popescu et al., Optical measurement of cell membrane tension. *Phys. Rev. Lett.* **97**(21), 1–4 (2006)
192. G. Popescu et al., Erythrocyte structure and dynamics quantified by Hilbert phase microscopy. *J. Biomed. Opt.* **10**(6), 060503 (2005)
193. C. Monzel, K. Sengupta, Measuring shape fluctuations in biological membranes. *J. Phys. D: Appl. Phys.* **49**(24), 243002–6 (2016)
194. A. Biswas, A. Alex, B. Sinha, Mapping cell membrane fluctuations reveals their active regulation and transient heterogeneities. *Biophys. J.* **113**(8), 1768–1781 (2017)
195. H. Yu et al., Tracking fast cellular membrane dynamics with sub-nm accuracy in the normal direction. *Nanoscale* **10**(11), 5133–5139 (2018)
196. Y. Yang et al., Imaging action potential in single mammalian neurons by tracking the accompanying sub-nanometer mechanical motion. *ACS Nano* **12**(5), 4186–4193 (2018)
197. A. Kusumi, Y. Sako, M. Yamamoto, Confined lateral diffusion of membrane receptors as studied by single particle tracking (nanovid microscopy). Effects of calcium-induced differentiation in cultured epithelial cells. *Biophys. J.* **65**(5), 2021–2040 (1993)

# Chapter 3

## Label-Free, Ultrahigh-Speed, Direct Imaging and Tracking of Bionanoparticles in Live Cells by Using Coherent Brightfield Microscopy



Chia-Lung Hsieh

**Abstract** Many important biological phenomena, ranging from cell signaling to viral infection, are accomplished by transportation of biological substances encapsulated in native nano-sized particles. Thermal fluctuation drives nanoparticles through cellular environments; this movement is facilitated by their small size. To understand how a specific cell function can be achieved through random collisions, it is useful to know the interactions between single particles and the local environment, as determined by measuring cell dynamics at high spatial and temporal resolutions. In this chapter, a simple yet powerful wide-field optical technique, coherent brightfield (COBRI) microscopy, is presented. COBRI microscopy detects linearly scattered light from a nanoparticle through imaging-based interferometry, which enables direct observation of small biological nanoparticles in live cells without labels. Proper image post-processing further improves the detection sensitivity of small particles by removing the scattering background of cell structures. COBRI microscopy can easily operate at a high speed due to its wide-field nature and stable, indefinite scattering signal. Using COBRI, the dynamics of single virus particles and cell vesicles in live cells can be successfully captured at a microsecond temporal resolution and nanometer spatial precision in three dimensions. The ultrahigh spatiotemporal resolution and shot-noise-limited sensitivity of COBRI microscopy provide an opportunity to study the biophysics and biochemistry of live cells at the nanoscale.

### 3.1 Introduction to Label-Free Imaging in Live Cells Through Linear Scattering

A biological cell is a highly dynamic system. Cell organelles and other subcellular structures constantly evolve and migrate to facilitate cell functions. Active transportation is an effective method for the redistribution of substance in live cells [1,

---

C.-L. Hsieh (✉)

Institute of Atomic and Molecular Sciences (IAMS), Academia Sinica, No. 1, Roosevelt Road, Section 4, Taipei 10617, Taiwan  
e-mail: [clh@gate.sinica.edu.tw](mailto:clh@gate.sinica.edu.tw)

© Springer Nature Switzerland AG 2019  
V. Astratov (ed.), *Label-Free Super-Resolution Microscopy*,  
Biological and Medical Physics, Biomedical Engineering,  
[https://doi.org/10.1007/978-3-030-21722-8\\_3](https://doi.org/10.1007/978-3-030-21722-8_3)

2]. In neuronal cells, active transport is especially critical for appropriate neuron activities [3, 4]. For active transportation, cargos are enclosed in small lipid vesicles or micelles, and their translocation is accomplished by motor proteins and cytoskeletons. The fundamental interaction between individual molecules underlies the regulatory mechanisms of intracellular transport, determining when and where the cargo is delivered [5, 6]. However, this sophisticated cell machinery developed through evolution is also utilized by viruses, which hijack the cell machinery by encapsulating their genomes in small particles with specific surface functionalities [7]. Thus, examining how viruses infect cells is not only useful in the battle against disease but also in understanding the cell machinery.

Through biochemical and molecular biology approaches, many proteins have been identified that play crucial roles in cell uptake and transportation [8]. However, these studies have tended to provide static results that lack spatial and temporal resolutions. Optical microscopy is a powerful tool that provides high spatiotemporal resolution. Through labeling with fluorescent proteins and dyes, cell dynamics—including intracellular transport and virus uptake—have been visualized in real time [9–11]. Using this technique, individual cell vesicles and virus particles can be seen under the microscope and their trajectories can be reconstructed by single-particle tracking (SPT) [11–13]. The main challenge in fluorescence-based optical observation is the limited photon budget that strictly restricts the observation time and data acquisition rate. Fluorescence-based SPT typically provides a spatial precision of 1–10 nm and a temporal resolution of a few to tens of milliseconds [14–16]. This spatiotemporal resolution has enabled many studies of interactions between particles and their local environment. However, probing molecular interactions at the nanometer scale requires higher spatiotemporal resolutions that fluorescence-based approaches struggle to provide.

For high-precision and high-speed measurements, a robust signal is required. Linear scattering meets these requirements—unlike fluorescence, which suffers from photobleaching, blinking and saturation, linear scattering from small particles is stable and indefinite, making it a promising contrast mechanism. Using scattering-based optical microscopy, including darkfield and brightfield microscopy, many high-speed and high-precision localization measurements have been reported that uncovered important biophysical and biochemical processes [17–20]. For a biological nanoparticle with a diameter of 100 nm in an aqueous solution, its scattering cross section in visible light is on the order of  $10^{-13}$  cm<sup>2</sup> (assuming a refractive index of 1.45), which is three orders of magnitude larger than the fluorescence cross section of an organic fluorophore. Therefore, intrinsic scattering from a bio-nanoparticle should be sufficient for direct observation and dynamic study. Indeed, endogenous biological nanoparticles (virus particles and extracellular vesicles) have been detected in cell-free *in vitro* environments by using several scattering-based imaging techniques, including darkfield [21–23], holographic, and other interferometric microscopies [24–28]. Among these imaging techniques, interferometric detection has the advantage of achieving shot-noise-limited sensitivity, independent of the detector noise [29].

Label-free imaging of endogenous bio-nanoparticle is complicated in live cells because of the scattering background of cell structures [30–34]. The smallest particle that can be detected and tracked in a live cell is often limited by imaging specificity, not by optical sensitivity. Having a strategy for distinguishing the signal from the background is therefore highly valuable. In addition, a cell is a three-dimensional (3D) object, and the dynamics of small particles are also 3D. Projection of 3D dynamics onto two-dimensional (2D) can cause misinterpretation. Thus, a label-free 3D imaging and tracking technique is highly desirable.

In this chapter, a simple, yet powerful imaging modality, namely coherent bright-field (COBRI) microscopy, is presented for sensitive and high-speed direct imaging of biological nanoparticles [31, 32]. By using a highly coherent light source (i.e., a laser) for illumination, COBRI microscopy facilitates rapid and sensitive imaging beyond what conventional brightfield microscopy can offer. Through interference, COBRI microscopy also enables tracking in 3D. Section 3.2 describes the concepts, technical details and characterization of COBRI microscopy. In Sect. 3.3, strategies of background estimation and correction for COBRI imaging in live cells are discussed. Section 3.4 presents two examples of COBRI imaging and tracking of single bio-nanoparticles in live cells. Specifically, Sect. 3.4.1 describes how the highly diffusive motion of single virus particles on a cell's surface is captured with nanometer spatial precision and microsecond temporal resolution; Sect. 3.4.2 describes how active transport of individual native cell vesicles inside a living cell is resolved with ultrahigh clarity. Finally, Sect. 3.5 concludes the chapter by discussing the sensitivity limit and possible applications of ultrasensitive and ultrahigh-speed label-free imaging.

## 3.2 COBRI Microscopy

COBRI microscopy essentially works by employing a brightfield microscope and a highly coherent laser light source [31]. The high temporal coherence maximizes imaging contrast and thus sensitivity. The high spatial coherence enables versatile beam shaping (e.g., focusing and structured illumination). Laser also provides sufficient illumination intensity at the sample for high-speed measurements. A schematic of COBRI microscopy is shown in Fig. 3.1. A laser beam is focused onto the sample through a condenser lens. The choice of the condenser lens determines the available spatial frequency bandwidth in illumination. For example, when using a low-numerical-aperture (low-NA) condenser (as plotted in Fig. 3.1), the illumination has a Gaussian-like profile of a few to tens of micrometers [31]. When using a high-NA condenser, a sharp submicrometer focus can be created at the sample [35]. Although stationary illumination is sufficient for the operation of COBRI microscopy, a rapid, 2D scan of the illumination often makes the measurement easier [31]. Such 2D beam scanning is achieved by using a 2-axis acousto-optic deflector (AOD) that typically scans at approximately 100 kHz. The beam scanning is synchronized with image acquisition, which ensures identical beam scanning is performed within each image

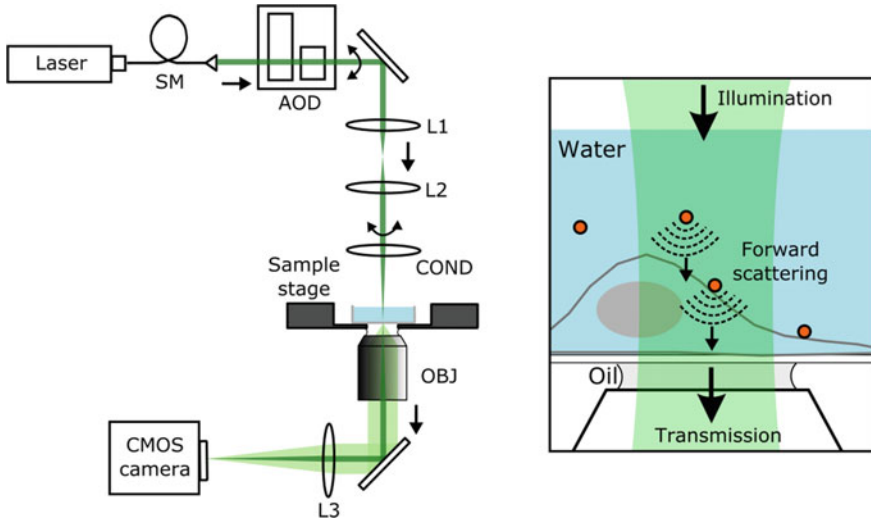


**Fig. 3.1** Schematics of COBRI microscopy. SM, single-mode fiber; AOD, acousto-optic deflector; L1–L3, lenses; COND, condenser; OBJ, objective. Adapted from [36], with permission from Elsevier

integration time. When choosing a high-NA condenser together with rapid beam scanning, an arbitrary illumination pattern can be created at the sample. Using rapid beam scanning, stable and uniform laser illumination is created at the sample for measurements at various image acquisition rates, from a few frames per second (fps) to 100,000 fps [31]. For measurements at higher acquisition rates (>100,000 fps), stationary illumination is preferred because beam scanning using an AOD is too slow.

Upon illumination, the sample (e.g., a nanoparticle or a biological cell) scatters and absorbs light. The transmitted light, containing the spatial information of the sample, is collected by a high-NA oil-immersion microscope objective. The magnified image is projected onto a camera through a tube lens. COBRI microscopy captures extinction images of the sample in transmission. For small particles, forward scattering light is collected, which interferes with the non-scattered transmitted light. Specifically, the recorded COBRI intensity is written as

$$I_{\text{det}} = |t|^2 + |s|^2 + 2|t||s| \cos \varphi \tag{3.1}$$

where  $t$  is the transmitted light field,  $s$  is the forward scattered field, and  $\varphi$  is the phase difference between the two fields. The first term represents the illumination intensity transmitted through the sample; the second term is the forward scattering intensity of the particle, and the third term is the interference between the two fields. For a small particle in a transparent medium (e.g., bio-nanoparticles in cellular environments), the scattering intensity is considerably weaker than the transmitted light, and thus the second term is negligible in the presence of the first term and the third term. COBRI microscopy detects the particle by using the third interference

term. In such interferometric detection, the scattering field of a nanoparticle and the non-scattered transmitted field are often referred to as the signal and reference, respectively. Notably, the phase difference  $\varphi$  between the scattering signal and the transmitted reference is a function of the axial position of the particle relative to the imaging microscope objective. This is because the phases of these two fields evolve differently throughout the microscope objective due to their distinct spatial modes [37]. In general,  $\varphi$  goes from 0 to  $\pi$  over the depth of focus of the imaging microscope objective, which is approximately  $1 \mu\text{m}$  for visible light and a high-NA objective. In other words,  $\varphi$  can be manipulated by controlling the axial position of the particle relative to the optical focus. In 2D imaging and tracking, the axial position of the nanoparticle is adjusted by a sample stage to ensure that its absolute contrast is maximized (as a bright spot when  $\varphi \cong 0$  and as a dark spot when  $\varphi \cong \pi$ ).

To quantify interference visibility, and thus COBRI sensitivity, the COBRI contrast of a particle is defined as the normalized intensity difference caused by the particle. It can be written as

$$\text{COBRI contrast} = \frac{I_{\text{det}} - |t|^2}{|t|^2}. \quad (3.2)$$

In this definition, zero COBRI contrast represents no detectable interference visibility, and thus no contrast is observed. To compare the sensitivity of COBRI and conventional brightfield microscopes, dielectric nanoparticles, metallic nanoparticles, and biological cells are imaged with increasing illumination spectral bandwidth ( $\Delta\lambda$ ), from  $\Delta\lambda = 0.05 \text{ nm}$  of a laser to  $\Delta\lambda > 350 \text{ nm}$  of a halogen lamp. As illustrated in Fig. 3.2, COBRI with laser illumination provides the highest contrast, typically two- to three-fold stronger than a conventional brightfield microscope. The stronger contrast of COBRI is mainly due to the higher temporal coherence, not the spatial coherence; the figure shows that narrow spectral filtering of a halogen lamp can provide contrast similar to that provided by laser illumination. However, although the interference visibility of a spectrally filtered low-coherence light source is comparable to that of a laser, the illumination intensity at the sample position of a low-coherence light source is limited and typically insufficient for high-speed measurements.

COBRI microscopy captures extinction image of the sample, and for small particles, extinction is a combined effect of absorption in the particle and scattering in all directions by the particle. It is interesting to note that the measured extinction (i.e., the COBRI contrast) depends only on the scattering amplitude in the forward direction, independent of its absorption [35]. This is because extinction by nanoparticle is nothing more than interference between incident and forward scattered light [38].

The height-dependent phase difference  $\varphi$  enables localization of a particle in the axial direction after appropriate calibration. Figure 3.3 displays how the COBRI contrast of a single vaccinia virus particle changes as a function of the axial position. In this calibration measurement, the virus particle is deposited on a coverglass and its height is adjusted by a sample stage. By calibrating the height-dependent COBRI

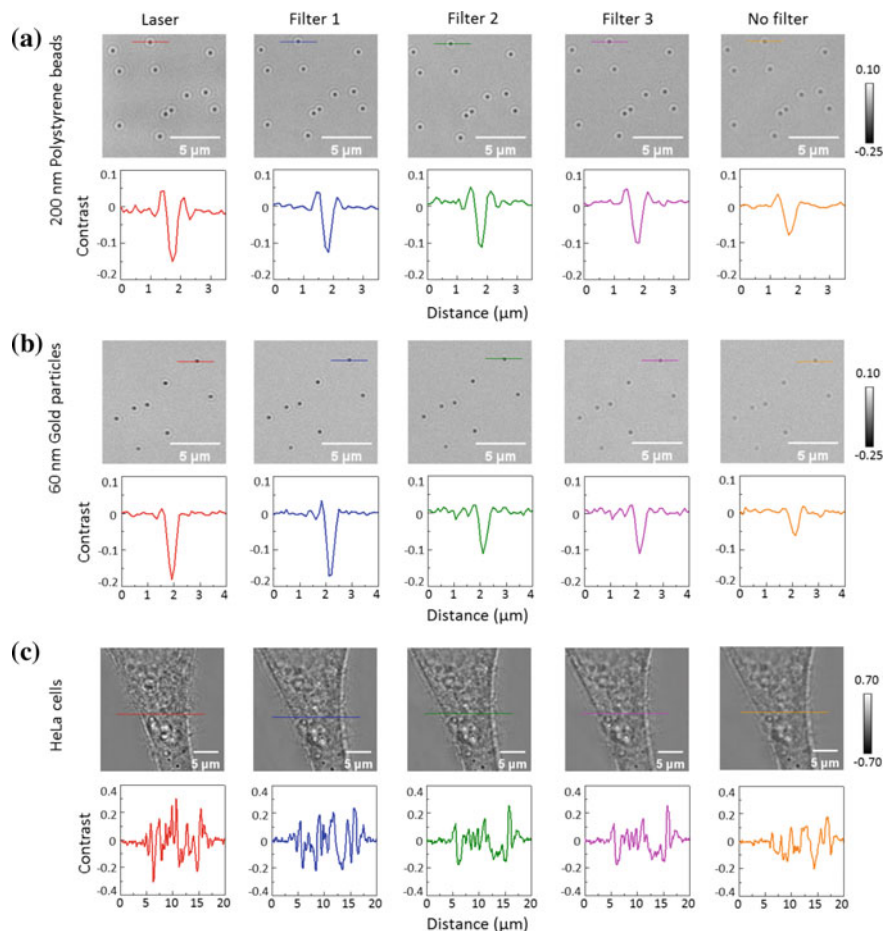


**Fig. 3.2** Comparison of COBRI imaging and conventional brightfield imaging of nanoparticles and living cells. The laser light source was a solid state laser at 532 nm and the white light source was a halogen lamp. Three bandpass filters were added separately to the white light source: filter 1 (527–537 nm), filter 2 (500–550 nm), and filter 3 (350–700 nm). These filters had similar central wavelengths but increasing bandwidths. Together with white light without a filter, five illumination conditions were prepared for comparison. **a** 200 nm polystyrene beads, **b** 60 nm gold particles, and **c** HeLa cells, all immersed in aqueous solution were imaged under the five illumination conditions. The contrast of the samples increased when the spectral bandwidth decreased, showing that imaging sensitivity is enhanced using light sources of higher temporal coherence. Reproduced from [31] with permission from the American Chemical Society

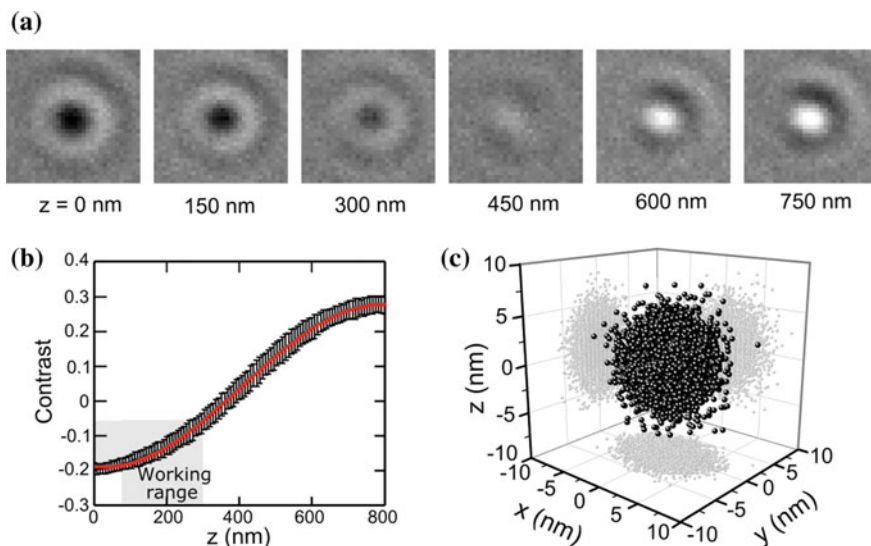


**Fig. 3.3** Height-dependent COBRI contrast of a vaccinia virus particle deposited on a coverglass. **a** COBRI contrast changes from dark to bright when the axial position of the virus relative to the microscope objective was varied. **b** Dependency of COBRI contrast to the axial position was well fitted by a sinusoidal function. **c** Localization precisions of 2.3, 1.7, and 2.3 nm in the  $x$ ,  $y$ , and  $z$  axes were estimated by measuring repeatedly the center position of an immobile virus particle. Reproduced from [31] with permission from the American Chemical Society

contrast of the particle, the axial position of the particle can be estimated from the measured contrast. The lateral position of the nanoparticle is determined by finding the center of the spot through image analysis (e.g., 2D Gaussian fitting). Thus, 3D localization from a 2D COBRI image can be accomplished. Taking a vaccinia virus particle as an example, COBRI microscopy can localize it with 1.7–2.3 nm precision in 3D [31].

COBRI microscopy is a wide-field interferometric transmission microscopy, which shares many common features with holographic microscopy and related techniques [39–41]. However, by placing the sample at the focal plane of the microscope objective, COBRI lacks the image reconstruction step which makes COBRI distinct from holographic microscopy. The concept of COBRI microscopy is similar to that of interferometric scattering (iSCAT) microscopy [42–44]. The similarities and differences between COBRI and iSCAT are discussed below [35]. The iSCAT microscopy can be considered the reflection counterpart of COBRI microscopy. In COBRI, forward scattering light is collected as signal and transmitted non-scattered light serves as the reference beam, whereas in iSCAT, the backscattering light is the signal and the partial reflection from an interface close to the sample (e.g., the supporting coverglass) serves as the reference beam. Both COBRI and iSCAT provide shot-noise-limited sensitivity through interferometric detection; that is, the sensitivity is determined by the number of detected signal photons. It is demonstrated that COBRI and iSCAT indeed have the same sensitivity given the identical illumination

intensity [35]. Different designs of the reference beam, however, lead to several distinctions between COBRI and iSCAT microscopy. First, COBRI and iSCAT have different axial dependencies of particle contrast. In COBRI, when the particle moves in the axial direction, its scattered field has a different phase evolution from the transmitted reference beam, leading to a full contrast inversion over the depth of field of the microscope objective (typically around  $1\ \mu\text{m}$  for high NA microscope objective, see Fig. 3.3a). In iSCAT, the reflection geometry makes the particle contrast more sensitive to its axial position relative to the substrate from which the reflected reference beam is created. A full modulation of iSCAT contrast of a particle occurs over a distance of  $1/4$  optical wavelength, and thus the iSCAT contrast inverts several times over the depth of field [45]. Contrast inversion interrupts continuous imaging and tracking of nanoparticle in the axial direction because the detection of nanoparticle fails when the contrast is zero. As a result, COBRI has a larger working range in the axial direction for continuous imaging and tracking, while iSCAT has a sharper axial dependency of the particle contrast. Second, COBRI imaging is nearly insensitive to the presence of semi-transparent interfaces in the sample because of its transmission geometry. On the contrary, iSCAT detects weak reflections from those interfaces easily, and this property has been exploited to image the flatness of live cell membranes at the nanoscale [34]. However, the sensitive interface detection of iSCAT could complicate the observation of small nanoparticles in live cells due to the highly dynamic and random reflection from the cell membranes. Third, a beamsplitter is inevitably needed in the reflection geometry of iSCAT, which not only increases the complexity of optical alignment but also complicates signal collection at a high efficiency [46]. On the other hand, COBRI does not need a beamsplitter, offering higher signal collection efficiency in principle. Finally, in transmission geometry, COBRI can easily be operated at low light intensity, typically 100-fold lower than the intensity at which iSCAT can be operated under identical image acquisition conditions. For example, COBRI works at an illumination intensity of  $0.01\ \text{kW}/\text{cm}^2$  with an image acquisition rate of 1000 fps, whereas iSCAT requires  $1\ \text{kW}/\text{cm}^2$  correspondingly. The low operational intensity of COBRI makes it useful for live cell imaging where the light dose is of a critical concern [47]. Increasing the illumination intensity in COBRI, and thus its detection sensitivity, is possible through pupil function engineering. By inserting a dot-shaped attenuator at the back focal plane of the microscope objective in the detection path, the illumination intensity of COBRI can reach up to  $150\ \text{kW}/\text{cm}^2$  at 1000 fps where single 10 nm gold nanoparticles are detected [35]. Therefore, COBRI microscopy potentially covers a wider range of illumination intensities, providing a large tunable range of sensitivity for different applications.

### 3.3 Scattering Background Estimation and Correction

Obtaining a high-quality micrograph where the object of interest (e.g., a nanoparticle) is clearly seen is the goal of microscope imaging. Scattering-based label-free imaging is complicated by the random scattering background because any imperfect

optical element along the beam path scatters light and contributes to the background. The general goal of background estimation and correction is to achieve faithful, artifact-free imaging of the signal without the presence of an undesired background. Background correction should not be mistaken for noise reduction or image restoration [48, 49]. Here, the background, in the most general definition, refers to light arriving at the detector that does not carry a signal of interest. The presence of a background complicates or even prevents signal detection. Depending on the application, the signal of interest varies, and so does the background. For example, in some applications, the cell structure and morphology are the signal targets, whereas in other applications, the signal targets are sub-cellular organelles. These different definitions of a signal lead to distinct strategies for estimating and removing the background. In this section, a few methods for background estimation and correction are overviewed, and their performance in live cell imaging is illustrated. In addition, a sophisticated background estimation method that can resolve the nanoscopic motion of a nanoparticle throughout the observation time is discussed [50]. These methods rely on the distinct spatial and temporal characteristics of a signal and background. COBRI and iSCAT share background correction strategies because they both employ scattering-based imaging interferometry.

The simplest measurement in microscopy is perhaps imaging spatially separated particles attached on a clean coverglass. At first glance, such a measurement appears to have no source of an undesired background. However, when the particles are extremely small and have a weak visibility of 0.01 or less, a spatially heterogeneous background due to imperfect, non-uniform illumination begins to complicate any measurement. The illumination background can be measured using several methods. One method is to capture the background before the particle appears on the coverglass—this method is especially useful in the application of “landing assays” [51–53]. If the particle is already attached to the coverglass before the measurement, a common method is to modulate the lateral position of the sample, during which a video is recorded. The static illumination background can be extracted from the moving signal in the video. This can be accomplished by calculating the temporal median background of the video. Alternatively, the signal modulated at a specific frequency can be reconstructed through Fourier analysis. This method of spatial modulation works well for estimating and removing the illumination background, but it does not correct the background caused by the sample (e.g., by roughness of the coverglass) because it moves together with the signal. In the most sensitive COBRI and iSCAT imaging, the scattering background caused by the roughness of the coverglass prevents direct visualization of a weak signal [52].

In many applications, a particle is in constant motion, and the task is to measure this motion. This provides an opportunity for convenient background correction. By recording a video containing the dynamic particle of interest, a static background can be extracted that represents the combined effect of illumination, coverglass roughness, and any other background contributions that are relatively static within the observation time. Correcting that background from the raw video gives a background-free video showing only the signal. This method is particularly powerful in applications of SPT where a particle of interest moves over the observation area. In

such cases, the temporal median image of the video is often a reasonable estimation of the static background [54].

Single virus particles and intracellular vesicles have been imaged and tracked in live cells using temporal median background correction and COBRI microscopy [31, 32]. Due to their small sizes, virus particles and cell vesicles move and diffuse constantly because of thermal fluctuation. By contrast, cell structures move and evolve slowly. When capturing a COBRI video at high speed ( $>5,000$  fps) for a few seconds, the median background conveniently represents the scattering background of large cell structures and other static background contributions (i.e., the non-uniform illumination). Many endogenous macromolecules in the cell membrane or inside the cell are expected to move rapidly. If these macromolecules provide sufficient optical contrast, they appear in the background-corrected images and make detection of the particle signal more difficult. Thus, for optimal performance, the imaging sensitivity should be sufficient for detecting the particle of interest but not unnecessarily high to ensure that other smaller entities remain indiscernible. The capability of temporal median background correction in removing cell background scattering has been evaluated experimentally [31]. A cell peripheral area was imaged using COBRI microscopy at 5000 fps for 1 s. A median background was calculated from the recorded video and this was used to normalize the raw video frame by frame. In the normalized video, no cell feature remained. Moreover, the temporal fluctuation of each pixel in the background-corrected video corresponded to the photon shot-noise fluctuation, indicating no additional cell background fluctuation. These findings show that temporal median background correction has favorable performance for removing cell scattering background in high-speed COBRI microscopy.

Distinguishing the signal from the background according to their different spatiotemporal characteristics is a powerful strategy in label-free imaging. Temporal median background correction is convenient, but it requires a highly static background and also a dynamic signal over the space. These requirements cannot be met in some applications, for example, when the motion of the signal is highly localized (close to the size of the signal) throughout the observation time. In such cases, some pixels are continuously occupied by the signal, and the median background estimation at those pixels is biased. In principle, superior background estimation can be made by accounting for the signal or background spatiotemporal characteristics, if they are available.

A more general method for background estimation was proposed and demonstrated [50]. Instead of examining the data pixel by pixel independently, as in the case of temporal median filtering, the new method exploits the information encoded in neighboring pixels. Specifically, it takes advantage of a priori knowledge of the shape of the signal. For small particles, their optical image is the point spread function (PSF) of the microscope, typically an airy disk. Specifically, the background estimation is optimized by minimizing the residual error of fitting the background-corrected image with a known PSF through an iterative process. This optimization process repeats itself until the estimation converges. Intuitively, because the signal spot moves over

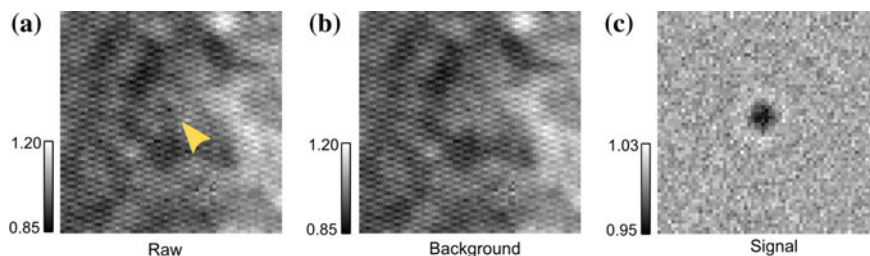


**Fig. 3.4** Background estimation and correction. **a** Raw image; the yellow arrow points to the position of the signal that is embedded in a heterogeneous background. **b** Static background image estimated from a series of raw images with a spatially moving signal. **c** Signal reconstructed by removing the background from the raw image. Note that the range of the color map of (c) is much smaller than that of (a) and (b). Reproduced from [50] with permission from the American Chemical Society

space, every pixel is occupied differently by the signal PSF throughout the video. Even when some pixels are continuously affected by the signal PSF (and thus have no opportunity to reveal their background values directly), their neighboring pixels are likely to be less influenced by the signal because of the moving nature of the signal. For these neighboring pixels, superior estimation of the background values is possible. The estimations of the neighboring pixels eventually help to determine the background value of the pixels that were originally inaccessible, because their intensities are correlated through the signal PSF. Figure 3.4 displays the result of background estimation and correction. The weak signal can barely be seen in the raw image where the signal-to-noise ratio is close to one. By estimating the background with the aforementioned method followed by background removal, the signal appears and its position can be accurately determined in the background-corrected images.

### 3.4 Label-Free, Ultrahigh-Speed Imaging and Tracking of a Single Bionanoparticle in Live Cells

In this section, two examples of ultrahigh-speed imaging and tracking of native bionanoparticles in live cells by using COBRI microscopy are presented. The first example captured the diffusive motion of a single virus particle on a cell plasma membrane with nanometer spatial precision in 3D at 100,000 fps [31]. Rapid local diffusion and highly transient nanoscopic confinements were disclosed in microsecond timescales. The second example measured the dynamics of single cellular vesicles in the cytoplasm of live cells [32]. Various types of motion were resolved at high spatiotemporal resolutions, including local diffusive motion, stepwise motion by motor proteins, as well as bidirectional and correlated motions. These two examples demonstrated the sensitivity of COBRI microscopy that enables it to conduct nanometer-precise track-

ing of native biological nanoparticles at ultrahigh speed. Moreover, they illustrated successful live-cell background removal for single particle dynamics on the cell surface and inside the cell.

### 3.4.1 Single Virus Dynamics on Cell Membrane

Using the 3D tracking capability of COBRI (Sect. 3.2) and cell background correction (Sect. 3.3), highly diffusive motion of a single vaccinia virus particle was revealed on a live HeLa cell membrane captured at an ultrahigh speed of 100,000 fps. The virus particles were locally delivered by a micropipette placed close to the cell under observation. The virus landing process was recorded continuously for a few seconds. The goal of the experiment was to resolve the early interaction between the virus particle and the cell plasma membrane receptors immediately after attachment.

Figure 3.5 displays the 1-s trajectory of the virus exploring the cell membrane right after attachment. The high spatial precision and high temporal resolution unveil the nanoscopic motion of the virus over microsecond timescales. The first surprise is that the virus particle was locally confined to an area of hundreds of nanometers close to the landing site. Moreover, within this confined area, the virus diffused lat-

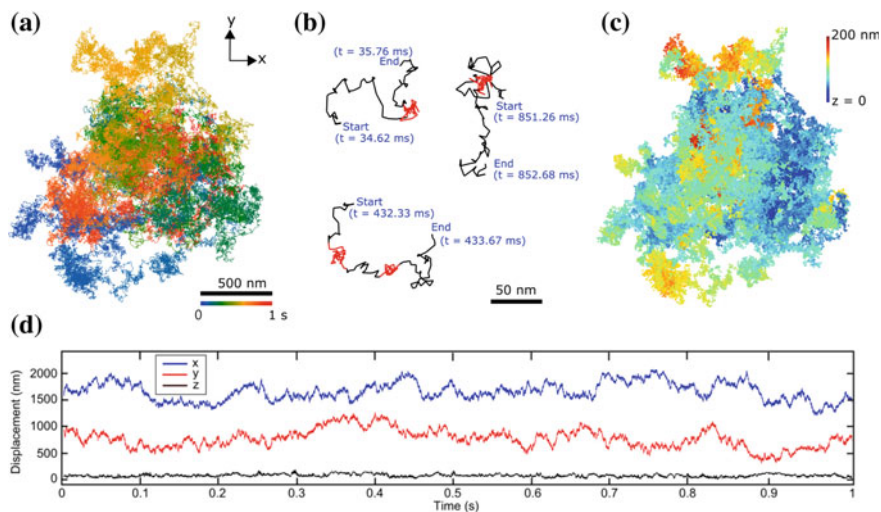


**Fig. 3.5** Ultrahigh-speed single virus tracking on the plasma membrane of live cells. **a** Diffusion trajectory of a vaccinia virus on the cell surface captured at 100,000 fps. **b** Sub-millisecond transient confinements of the virus particle at nanoscopic zones (highlighted in red). **c** 3D reconstruction of the virus diffusion trajectory. **d** 3D displacements as a function of time. The displacement in the  $z$  axis is much smaller than it is in  $x$  and  $y$  axes, showing that the virus particle adhered to the cell surface and explored the plasma membrane laterally. Reproduced from [31] with permission from the American Chemistry Society

erally on the plasma membrane with a very high diffusion coefficient ( $\sim 1 \mu\text{m}^2/\text{s}$ ), which is as high as its free diffusion in water. This observation indicates that the virus weakly adhered to the membrane and was free to explore the cell surface. Strikingly, from the trajectory, numerous zones of 10–20 nm were present where the virus was transiently confined for sub-milliseconds. The observed viral dynamics are hypothesized to reflect the interaction between the virus and the cell membrane molecules (e.g., glycosaminoglycan). The transient nano-confinements may be evidence of virus interplay with immobile membrane receptors. Notably, the trajectory was 3D, which indicates the 3D cell membrane morphology.

### ***3.4.2 Nanoscopic Dynamics of a Cell Vesicle During Active Transportation***

COBRI microscopy also makes it possible to visualize the intracellular dynamics of individual cell vesicles and organelles. With improved sensitivity and speed, a native fibroblast cell appears highly dynamic under COBRI microscopy. Many cell vesicles are locally confined and restricted to diffuse within small volumes created by cytoskeleton networks inside the cytosol. Rapid and directional transportations of cell vesicles are also occasionally observed. Through lipophilic dye labeling, most vesicles were found to be lipid-rich, presumably lipid droplets. Estimated from their COBRI contrast, most vesicles under observation were approximately 300 nm in diameter. The sensitivity of COBRI microscopy is sufficient for tracking single vesicles with nanometer spatial precision in 3D. By capturing vesicle motions at 30,000 fps, their nanoscopic motion is unveiled. Figure 3.6 shows typical transportation of a vesicle with clearly resolved stepwise motion by motor proteins. The bidirectional motion of the vesicle resulting from a tug-of-war between oppositely directed motor proteins attached to the same cargo can clearly be seen. Under ultrahigh-resolution observation, the transient pausing at the moment the vesicle switches directions is clearly resolved where an oscillating behavior over 10-nm is disclosed. In addition to the ultrahigh spatiotemporal resolution, label-free COBRI microscopy offers the opportunity to probe intracellular dynamics in their native condition.

## **3.5 Conclusions and Future Perspectives**

In this chapter, COBRI microscopy was shown to enable ultrahigh-speed imaging with a frame time of microseconds. The high sensitivity of COBRI facilitates nanometer-precise 3D tracking of endogenous biological nanoparticles with diameters as small as 100–200 nm. The cell scattering background can be selectively removed through proper background estimation and correction. The current strategy of background correction is favorable when tracking mobile nanoparticles in a rela-

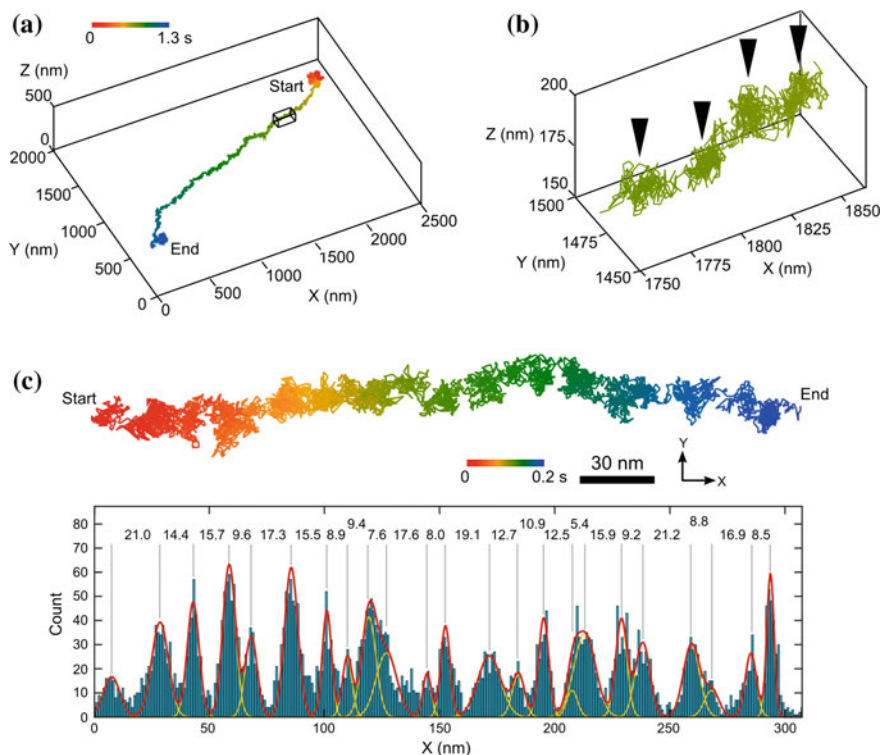


**Fig. 3.6** Directional intracellular transportation of a native cell vesicle captured using ultrahigh-speed COBRI microscopy. **a** Reconstructed 3D trajectory of the cell vesicle being translocated inside a live fibroblast cell recorded at 30,000 fps. **b** Close-up view of the trajectory in (a), revealing the discrete stepping motion of the vesicle. Four clusters of localizations caused by transient pausing between steps are indicated by black arrows. **c** Analysis of the stepwise motion of the cell vesicle, showing an average step size of 16 nm. Reproduced from [32] with permission of The Royal Society of Chemistry

tively stationary environment. Using COBRI microscopy and background correction, the rapid dynamics of virus particles and vesicles in live cells have been explored at unprecedented resolutions (nanometer spatial precision and microsecond temporal resolution). In these two experiments described in this chapter, simultaneous high speed and high localization precision made it possible to probe interactions of a nanoparticle with its local environment at the molecular (nanometer) scale. This capability cannot be matched easily by any other techniques.

COBRI microscopy is not a replacement for fluorescence microscopy—instead, simultaneous COBRI and fluorescence imaging can be a powerful combination, with COBRI supporting long-term, high-precision, high-speed measurements, and fluorescence imaging providing excellent imaging specificity through labeling. Indeed, COBRI imaging can easily be added to fluorescence microscopy by operating COBRI simultaneously with an appropriate laser wavelength. For tracking bionanoparticles,

fluorescence labeling and imaging can identify nanoparticles of interest, and then COBRI can be employed for long-term, high-resolution observation and tracking of the targeted particles. This approach makes optimal use of the fluorescence photon budget and thus prolongs the observation time. When combining COBRI with fluorescence superresolution microscopy [55], the nanoparticle trajectory can be superimposed on a super-resolved molecular map, providing direct visualization of the local interplay between the nanoparticle and molecules.

COBRI microscopy is more sensitive than conventional brightfield microscopy, but what is the ultimate detection limit? As outlined in Sect. 3.2, the sensitivity of COBRI is shot-noise limited, and thus the number of detected signal photons directly determines whether the target can be perceived. For extremely small nanoparticles, the scattering cross section is very small, and therefore it requires high illumination intensity and long signal integration time to detect them. Conceptually, given sufficient illumination intensity or signal integration time, arbitrarily small nanoparticles can be detected. In practice, illumination intensity is restricted by the damage threshold of the sample and optics, whereas the signal integration time is limited by the signal and background stability that is required for proper background correction. It is worth noting that detecting small signal under strong illumination is complicated by the saturation of photodetector—the full well capacity of the camera sets the maximal light intensity it can detect, determining the strongest illumination intensity of the sample in COBRI and other common-path interferometry. To further increase the illumination intensity without saturation of the camera, pupil function engineering has been employed to selectively attenuate the reference beam and leave the signal of nanoparticle nearly untouched [35, 52, 56–58]. This approach effectively enhances the contrast of the signal by matching the amplitude of the reference and the signal. Through pupil function engineering and image postprocessing, COBRI microscopy detects very small nanoparticles (as small as 10 nm gold nanoparticles) at 1000 fps [35]. By similar approaches of contrast enhancement, ultrahigh sensitivity is achieved by iSCAT microscopy where single protein macromolecules are detected without any labels at an effective image acquisition rate of a few hertz [51, 52, 59, 60].

With enhanced sensitivity, live cells are expected to be highly dynamic and heterogeneous under COBRI microscopy because cell molecules are in constant motion. The spatial resolution of COBRI is diffraction limited, which means that it cannot resolve individual molecules densely packed in live cells. Nevertheless, the spatially resolved fluctuation of the COBRI signal contains information regarding local molecule dynamics that may be revealed by correlation spectroscopy [61, 62]. The high temporal resolution of COBRI microscopy enables investigation of cell molecular dynamics in microsecond timescales. Further investigation could examine whether diffusion, self-assembly, transportation, or even new dynamics are resolvable in a label-free manner.

Light doses are a concern for live cell imaging because of photo-toxicity [47, 63]. To minimize the light dose, ultrahigh-speed COBRI image recording at 100,000 fps is only performed for a few seconds at an illumination intensity of  $1 \text{ kW/cm}^2$ . Otherwise, continuous observation and sample exploration are conducted with a separate

camera that captures identical COBRI images at a much lower speed (<1000 fps) that only requires an illumination intensity of <0.01 kW/cm<sup>2</sup>. Under these conditions, no photo-toxicity is observed.

COBRI microscopy is a simple and powerful imaging modality that provides high sensitivity and high temporal resolution. COBRI is useful for exploring new cell dynamics, including the uptake and release of cell vesicles, cell membrane dynamics, and intracellular or intranuclear dynamics. Research employing COBRI microscopy requires not only optical observation but also sophisticated data processing and analyses. This makes it an exciting multidisciplinary area combining optics, biophysics, chemistry, biology, and engineering.

## References

1. R.D. Vale, Intracellular transport using microtubule-based motors. *Annu. Rev. Cell Biol.* **3**(1), 347–378 (1987)
2. J. Suh, D. Wirtz, J. Hanes, Efficient active transport of gene nanocarriers to the cell nucleus. *Proc. Natl. Acad. Sci.* **100**(7), 3878–3882 (2003)
3. N. Hirokawa, S. Niwa, Y. Tanaka, Molecular motors in neurons: transport mechanisms and roles in brain function, development, and disease. *Neuron* **68**(4), 610–638 (2010)
4. B.W. Guzik, L.S.B. Goldstein, Microtubule-dependent transport in neurons: steps towards an understanding of regulation, function and dysfunction. *Curr. Opin. Cell Biol.* **16**(4), 443–450 (2004)
5. N. Segev, Coordination of intracellular transport steps by GTPases. *Semin. Cell Dev. Biol.* **22**(1), 33–38 (2011)
6. N. Hirokawa et al., Kinesin superfamily motor proteins and intracellular transport. *Nat. Rev. Mol. Cell Biol.* **10**, 682 (2009)
7. D. Mudhakar, H. Harashima, Learning from the viral journey: how to enter cells and how to overcome intracellular barriers to reach the nucleus. *AAPS J.* **11**(1), 65 (2009)
8. R.D. Vale, The molecular motor toolbox for intracellular transport. *Cell* **112**(4), 467–480 (2003)
9. D.J. Stephens, V.J. Allan, Light microscopy techniques for live cell imaging. *Science* **300**(5616), 82–86 (2003)
10. P.L. Leopold et al., Fluorescent virions: dynamic tracking of the pathway of adenoviral gene transfer vectors in living cells. *Hum. Gene Ther.* **9**(3), 367–378 (1998)
11. I. Wacker et al., Microtubule-dependent transport of secretory vesicles visualized in real time with a GFP-tagged secretory protein. *J. Cell Sci.* **110**(13), 1453–1463 (1997)
12. M. Lakadamyali et al., Visualizing infection of individual influenza viruses. *Proc. Natl. Acad. Sci. U.S.A.* **100**(16), 9280–9285 (2003)
13. K. Jaqaman et al., Robust single-particle tracking in live-cell time-lapse sequences. *Nat. Methods* **5**, 695 (2008)
14. N. Ruthardt, D.C. Lamb, C. Bräuchle, Single-particle tracking as a quantitative microscopy-based approach to unravel cell entry mechanisms of viruses and pharmaceutical nanoparticles. *Mol. Ther.* **19**(7), 1199–1211 (2011)
15. S. Manley, J.M. Gillette, J. Lippincott-Schwartz, Chapter 5 Single-particle tracking photoactivated localization microscopy for mapping single-molecule dynamics, in *Methods in Enzymology*, ed. by N.G. Walter (Academic Press, 2010), pp. 109–120
16. Z. Liu, Luke D. Lavis, E. Betzig, Imaging live-cell dynamics and structure at the single-molecule level. *Mol. Cell* **58**(4), 644–659 (2015)
17. C. Dietrich et al., Relationship of lipid rafts to transient confinement zones detected by single particle tracking. *Biophys. J.* **82**, 274–284 (2002)

18. H. Isojima et al., Direct observation of intermediate states during the stepping motion of kinesin-1. *Nat. Chem. Biol.* **12**, 290–297 (2016)
19. H. Ueno et al., Simple dark-field microscopy with nanometer spatial precision and microsecond temporal resolution. *Biophys. J.* **98**(9), 2014–2023 (2010)
20. J.L. Martin et al., Anatomy of F<sub>1</sub>-ATPase powered rotation. *Proc. Natl. Acad. Sci.* **111**(10), 3715–3720 (2014)
21. S. Faez et al., Fast, label-free tracking of single viruses and weakly scattering nanoparticles in a nanofluidic optical fiber. *ACS Nano* **9**(12), 12349–12357 (2015)
22. S. Enoki et al., Label-free single-particle imaging of the influenza virus by objective-type total internal reflection dark-field microscopy. *PLoS ONE* **7**(11), e49208 (2012)
23. B. Agnarsson et al., Evanescent light-scattering microscopy for label-free interfacial imaging: from single sub-100 nm vesicles to live cells. *ACS Nano* **9**(12), 11849–11862 (2015)
24. E. McLeod et al., High-throughput and label-free single nanoparticle sizing based on time-resolved on-chip microscopy. *ACS Nano* **9**(3), 3265–3273 (2015)
25. P. Kukura et al., High-speed nanoscopic tracking of the position and orientation of a single virus. *Nat. Methods* **6**, 923–927 (2009)
26. S.M. Scherr et al., Real-time capture and visualization of individual viruses in complex media. *ACS Nano* **10**(2), 2827–2833 (2016)
27. G.G. Daaboul et al., Digital detection of exosomes by interferometric imaging. *Sci. Rep.* **6**, 37246 (2016)
28. H.-M. Wu et al., Nanoscopic substructures of raft-mimetic liquid-ordered membrane domains revealed by high-speed single-particle tracking. *Sci. Rep.* **6**, 20542 (2016)
29. Y.-H. Lin, W.-L. Chang, C.-L. Hsieh, Shot-noise limited localization of single 20 nm gold particles with nanometer spatial precision within microseconds. *Opt. Express* **22**(8), 9159–9170 (2014)
30. Y. Yang et al., Label-free tracking of single organelle transportation in cells with nanometer precision using a plasmonic imaging technique. *Small* **11**(24), 2878–2884 (2015)
31. Y.-F. Huang et al., Coherent brightfield microscopy provides the spatiotemporal resolution to study early stage viral infection in live cells. *ACS Nano* **11**(3), 2575–2585 (2017)
32. Y.-F. Huang et al., Label-free, ultrahigh-speed, 3D observation of bidirectional and correlated intracellular cargo transport by coherent brightfield microscopy. *Nanoscale* **9**, 6567–6574 (2017)
33. C. Kural et al., Tracking melanosomes inside a cell to study molecular motors and their interaction. *Proc. Natl. Acad. Sci.* **104**(13), 5378–5382 (2007)
34. J.-S. Park et al., Label-free and live cell imaging by interferometric scattering microscopy. *Chem. Sci.* **9**(10), 2690–2697 (2018)
35. C.-Y. Cheng, Y.-H. Liao, C.-L. Hsieh, High-speed imaging and tracking of very small single nanoparticles by contrast enhanced microscopy. *Nanoscale*. **11**, 568–577 (2019)
36. C.-L. Hsieh, Label-free, ultrasensitive, ultrahigh-speed scattering-based interferometric imaging. *Opt. Commun.* **422**, 69–74 (2018)
37. J. Hwang, W.E. Moerner, Interferometry of a single nanoparticle using the Gouy phase of a focused laser beam. *Opt. Commun.* **280**(2), 487–491 (2007)
38. C.F. Bohren, D.R. Huffman, *Absorption and Scattering of Light by Small Particles* (Wiley-VCH, 2004)
39. M.K. Kim, Digital holographic microscopy, in *Digital Holographic Microscopy: Principles, Techniques, and Applications* (Springer, New York, 2011), pp. 149–190
40. V. Mico, Z. Zalevsky, J. García, Common-path phase-shifting digital holographic microscopy: a way to quantitative phase imaging and superresolution. *Opt. Commun.* **281**(17), 4273–4281 (2008)
41. J. Garcia-Sucerquia et al., Digital in-line holographic microscopy. *Appl. Opt.* **45**(5), 836–850 (2006)
42. J. Ortega-Arroyo, P. Kukura, Interferometric scattering microscopy (iSCAT): new frontiers in ultrafast and ultrasensitive optical microscopy. *Phys. Chem. Chem. Phys.* **14**(45), 15625–15636 (2012)

43. K. Lindfors et al., Detection and spectroscopy of gold nanoparticles using supercontinuum white light confocal microscopy. *Phys. Rev. Lett.* **93**(3), 037401 (2004)
44. V. Jacobsen et al., Interferometric optical detection and tracking of very small gold nanoparticles at a water-glass interface. *Opt. Express* **14**, 405–414 (2006)
45. M. Krishnan et al., Geometry-induced electrostatic trapping of nanometric objects in a fluid. *Nature* **467**(7316), 692–695 (2010)
46. J. Ortega Arroyo, D. Cole, P. Kukura, Interferometric scattering microscopy and its combination with single-molecule fluorescence imaging. *Nat. Protocols* **11**(4), 617–633 (2016)
47. P.P. Laissue et al., Assessing phototoxicity in live fluorescence imaging. *Nat. Methods* **14**, 657 (2017)
48. X. Huang et al., Fast, long-term, super-resolution imaging with Hessian structured illumination microscopy. *Nat. Biotechnol.* **36**, 451 (2018)
49. M. Weigert et al., Content-aware image restoration: pushing the limits of fluorescence microscopy. *Nat. Methods* **15**(12), 1090–1097 (2018)
50. C.-Y. Cheng, C.-L. Hsieh, Background estimation and correction for high-precision localization microscopy. *ACS Photonics* **4**(7), 1730–1739 (2017)
51. M. Piliarik, V. Sandoghdar, Direct optical sensing of single unlabelled proteins and super-resolution imaging of their binding sites. *Nat. Commun.* **5**, 4495 (2014)
52. D. Cole et al., Label-free single-molecule imaging with numerical-aperture-shaped interferometric scattering microscopy. *ACS Photonics* **4**(2), 211–216 (2017)
53. G. Young et al., Quantitative mass imaging of single biological macromolecules. *Science* **360**(6387), 423–427 (2018)
54. C.L. Hsieh et al., Tracking single particles on supported lipid membranes: multimobility diffusion and nanoscopic confinement. *J. Phys. Chem. B* **118**(6), 1545–1554 (2014)
55. B. Huang, M. Bates, X. Zhuang, Super-resolution fluorescence microscopy. *Annu. Rev. Biochem.* **78**(1), 993–1016 (2009)
56. O. Avci et al., Pupil function engineering for enhanced nanoparticle visibility in wide-field interferometric microscopy. *Optica* **4**(2), 247–254 (2017)
57. Q.D. Pham et al., Digital holographic microscope with low-frequency attenuation filter for position measurement of a nanoparticle. *Opt. Lett.* **37**(19), 4119–4121 (2012)
58. K. Goto, Y. Hayasaki, Three-dimensional motion detection of a 20-nm gold nanoparticle using twilight-field digital holography with coherence regulation. *Opt. Lett.* **40**(14), 3344–3347 (2015)
59. J. Ortega Arroyo et al., Label-free, all-optical detection, imaging, and tracking of a single protein. *Nano Lett.* **14**(4), 2065–2070 (2014)
60. M.P. McDonald et al., Visualizing single-cell secretion dynamics with single-protein sensitivity. *Nano Lett.* **18**(1), 513–519 (2018)
61. H. Liu, C. Dong, J. Ren, Tempo-spatially resolved scattering correlation spectroscopy under dark-field illumination and its application to investigate dynamic behaviors of gold nanoparticles in live cells. *J. Am. Chem. Soc.* **136**(7), 2775–2785 (2014)
62. R. Pecora, *Dynamic Light Scattering: Applications of Photon Correlation Spectroscopy* (Plenum Press, New York, 1985)
63. J.-Y. Tinevez et al., Chapter 15 A quantitative method for measuring phototoxicity of a live cell imaging microscope, in *Methods in Enzymology*, ed. by P.M. Conn (Academic Press, 2012), pp. 291–309

# Chapter 4

## Tomographic Diffractive Microscopy: Principles, Implementations, and Applications in Biology



Bertrand Simon and Olivier Haeberlé

**Abstract** Tomographic Diffractive Microscopy (TDM) is an advanced digital microscopic imaging technique, extending the capabilities of Digital Holographic Microscopy (DHM), which delivers 3D quantitative images of the index of refraction distribution within the observed sample. It is a two-step imaging approach based first on recording of multiple holograms under varying conditions of illumination, and second on applying sample-adapted numerical inversion procedures to reconstruct the 3-D image of the specimen under consideration. After a short recall of DHM principles, applications, and limitations, the principle of TDM is introduced, and then several of its practical implementations are described. We put emphasis on their respective advantages and limitations, through various examples of application for biological samples imaging. Perspectives, and challenges for this imaging modality, as well as some hints to address them, are finally presented in the conclusion.

### 4.1 Introduction

Its unique capabilities for imaging living specimens, in three dimensions, possibly over long periods make the optical microscope an invaluable tool for biological research. This has motivated, since its invention and its adoption as a scientific tool, the development of numerous techniques to improve the contrast and visibility of the observed sample, through, for example, oblique and Rheinberg illuminations, dark-field microscopy, phase contrast and differential interference contrast (DIC), Dodt gradient contrast, Hoffman modulation, or polarized microscopy [1]. All these

---

B. Simon (✉) · O. Haeberlé

Laboratoire Photonique et Nanosciences (LP2N - UMR 5298), Institut d'Optique Graduate School, Université de Bordeaux, CNRS, Bordeaux, France  
e-mail: [bertrand.simon@institutoptique.fr](mailto:bertrand.simon@institutoptique.fr)

O. Haeberlé

e-mail: [olivier.haeberle@uha.fr](mailto:olivier.haeberle@uha.fr)

Institut de Recherche en Informatique, Mathématiques, Automatique et Signal (IRIMAS - EA7499), Université de Haute-Alsace, Mulhouse, France

© Springer Nature Switzerland AG 2019

V. Astratov (ed.), *Label-Free Super-Resolution Microscopy*,  
Biological and Medical Physics, Biomedical Engineering,  
[https://doi.org/10.1007/978-3-030-21722-8\\_4](https://doi.org/10.1007/978-3-030-21722-8_4)

methods have found their preferred domain of application. But, while very powerful for phenomenon detection, or morphological measurements, they are all limited in the sense that interpretation of the observed contrast is difficult in terms of quantitative measurements of the optical properties.

Nowadays, fluorescence microscopy is often the reference method, because it allows for specific labeling of cellular structures, therefore cellular functions, with ever-increasing set of natural or especially chemically designed fluorescence labels. Being indeed a dark field technique, fluorescence microscopy has an extreme sensitivity, leading to single molecule detection and tracking, and in recent years, fluorescence microscopy has also evolved into fluorescence nanoscopy, with an unsurpassed resolution obtainable with modern techniques like STED microscopy or pointillism microscopies [1–5]. Conversely, fluorescence microscopy also has the ability to study at the cellular, and even subcellular scale, large samples such as organoids, and even entire model organisms as large as *Danio rerio* [6].

In some cases, fluorescence labeling may, however, induce unfavorable effects like photo-toxicity. Labeling itself may be difficult for some samples. Speed is also rather limited, especially for 3D imaging, because fluorescence signal is often weak (compared to transmission microscopy for example). In some cases, use of fluorescence is also to be avoided. For example, for long time-lapse studies, fluorophores are diluted in dividing cells, leading to vanishing signal over time, and for some studies on natural cell lines, use of genetically modified organisms is simply not possible.

These limitations explain that, in recent years, there has been a growing interest for developing new imaging techniques not requiring specific sample labeling, like second or third harmonic generation (SHG and THG) microscopy, Raman or Coherent Anti-Stokes Raman Scattering (CARS) microscopies [7–11]. These methods have proven their interest, CARS being, for example, very effective for lipid detection, but having as drawback that they require expensive instrumentation for signal generation/detection.

As possible alternate for efficient label-free microscopy, the coupling of fast-, high-sensitivity, and high-resolution electronic sensors with the exploding computational and memory capacities of modern computers has recently open new possibilities for revisiting conventional transmission optical microscopy.

## 4.2 Digital Holographic Microscopy

In conventional transmission microscopy (classical wide-field, dark-field, phase-contrast, Differential Interference Contrast, Hoffman modulation...), the image is formed by a complex interaction of the incoherent illuminating light with the specimen. The recorded image is an intensity-only image, which contrast is very efficient to detect structures, and therefore is for example very helpful for morphological evolution studies, but which does not easily deliver quantitative information on the optical characteristics of the observed specimen. In particular, refraction and absorp-

tion properties mix to form the final image, and for example, a darker, therefore apparently more absorbing zone, may in fact simply result from a localized destructive interference phenomenon. Similarly, phase contrast microscopy images [12, 13] are often affected by halo artifacts surrounding sharp structures of the observed sample.

Note that computer-based phase reconstruction techniques have been developed, encountering growing success, thanks to modern computers computational power. Techniques relying on solving the transport of intensity equation [14–18], DIC image reconstruction [19–23], and ptychography [24–29], have demonstrated their ability to reconstruct the phase of recorded field. They do however rely on some assumptions, which may limit their domain of application.

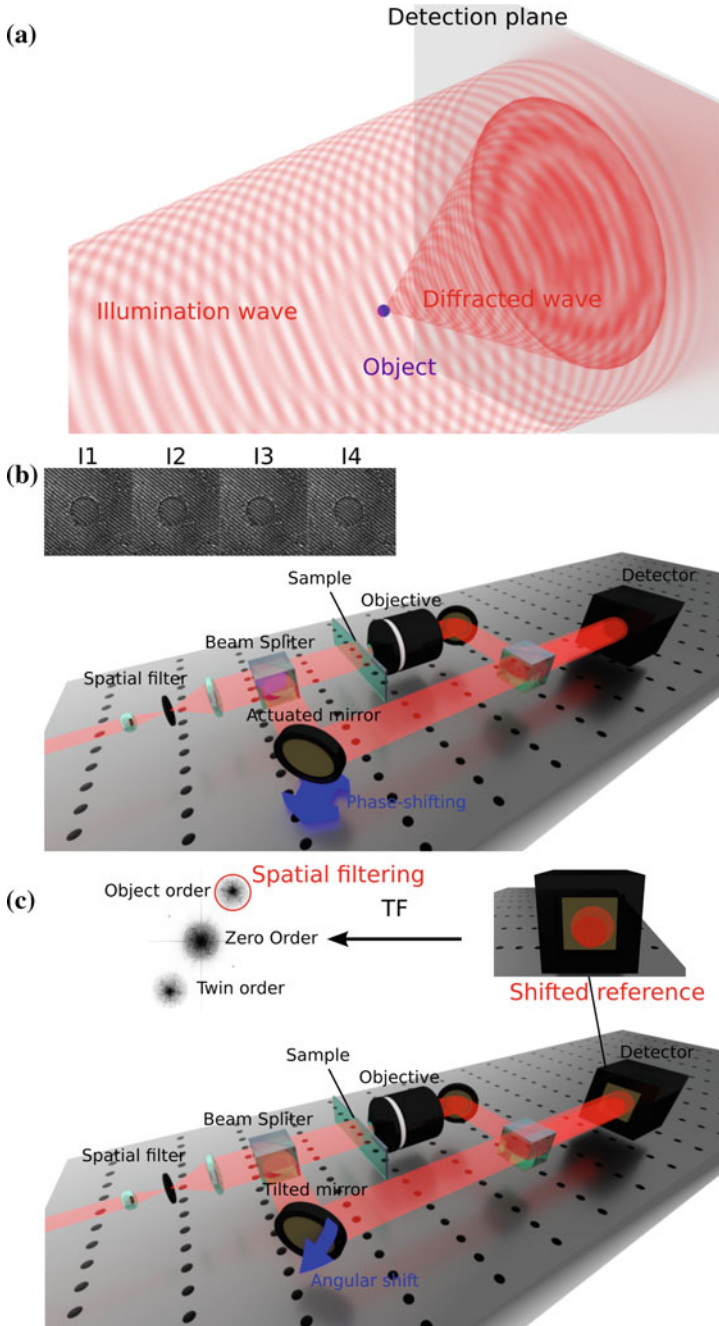
Use of coherent light illumination, combined with interferometric detection, permits on the contrary to directly record holograms [30], encoding amplitude and phase of the light interacting with the microscopic specimen [31], therefore delivering complete information about the diffraction phenomenon, but not relying on numerical reconstruction. Wavefront analyzers also permit to record the amplitude and phase of the diffracted light, without the need of an interferometer, and with short coherence illumination [32, 33]. Commercial implementations of this technique are growing [34]. These approaches, known under the name of Digital Holographic Microscopy or of Phase Microscopy, have in particular proven to be very sensitive to small sample changes, thanks to unsurpassed *precision* of interferometric measurements. Phase imaging is now used for many biological studies [35–67].

Figure 4.1 describes the principle of holographic imaging. Three configurations are often used in holographic microscopy: Gabor holography, phase-shifting holography, and off-axis holography.

The simplest is Gabor holography [43], or in-line holography, first proposed for electron microscopy, and adapted to digital optical holography [44]. A coherent wave illuminates the observed sample, and is partly diffracted by it (Fig. 4.1a). Interference fringes result from the coherent addition of the diffracted field and the illumination, modulating phase and amplitude of the diffracted wave. A direct demodulation is not possible, but numerical reconstruction of the phase and amplitude is feasible [45]. The main advantage of this technique is its robustness, the system being self-aligned, so very insensitive to perturbation, allowing work in harsh environment (see for example the system developed by the 4Deep company [34] for submarine applications).

In order to address the hologram demodulation problem, one can also use phase-shifting holography [46, 52]. In this configuration (Fig. 4.1b), a reference beam is used to create the holograms, and modulated in phase, usually using a piezoelectric-driven mirror, or an electro-optic modulator. Recording of series of holograms permits to solve the holographic equation and extract the amplitude and phase of the diffracted beam, separated from the reference beam and the non-diffracted component of the illuminating beam. The holograms are acquired sequentially, which may limit speed, but parallelization or use of several cameras is possible [49, 50].

Off-axis holography has also been applied to microscopy [31, 51]. In this technique, an inclined reference beam (Fig. 4.1c) directly modulates the interferogram.



**Fig. 4.1** Principle of holographic microscopy. **a** Gabor holography. **b** Phase-shifting holography. **c** Off-axis holography

Demodulation is easily performed in Fourier space, in which the different orders of diffraction are spatially separated. This technique has the advantage, compared to phase-shifting holography, that a single hologram is enough to extract amplitude and phase of the diffracted beam, but at the price of a reduced field of view, because of the demodulation constraints in Fourier space.

Note that combined approach can also be used [52]. For more details about digital holographic data acquisition and reconstruction, the interested reader will find extensive description in [53–58].

Indeed, DHM is a very powerful technique of investigation when considering integral measurements, by projections of the accumulated phase changes when light travels through the observed samples [59], rapid phase variations, for example, corresponding to samples fluctuations [60, 61], very weak sample phase changes, thanks to its high sensitivity, which can be linked to other physical quantities, for example, allowing for optical patch clamp measurements [62]. It is also able to acquire long time-lapse, without inducing photodamages to the sample, thanks to the low level of light necessary to acquire interferograms (compared to confocal fluorescence), which reveals useful for cell cycle, cell division, cell migration, drug influence or cell apoptosis studies, cell detection and identification [63–66].

However, its main drawback is probably its low *resolution* when reconstructing 3D images of transparent specimens, especially along the optical axis. This limitation is easily understood when remembering that only one illumination direction is used in holographic microscopy, translating into limited quantity of recorded information, so poor 3D image reconstructions [67]. Such a configuration indeed does not fulfill the classical requirement of transmission microscopy that a high numerical aperture condenser is to be used in conjunction with a high numerical aperture objective, satisfying Köhler illumination, in order to obtain high-resolution image. Indeed, it is not possible with coherent light to illuminate the sample under large numerical aperture, as in that case a focal spot would be produced, resulting from the interference of the various illuminations. So, DHM, strictly speaking, is in fact not an efficient 3D imaging technique for imaging transparent samples in transmission mode, and is sometimes referred to as being a 2.5D imaging method, i.e., imaging a 2D surface wrapped in a 3D volume.

In order to compensate for that limited resolution of DHM, phase tomography has been proposed. Rotating the sample, one can record a set of 2D phase maps from the sample observed under different angles, which are then converted into 3D index of refraction maps, using classical backprojection of the data (Radon transform). The observed sample itself can be easily rotated in the case of an optical fiber [68], while free-standing samples like pollens, diatoms, amoeba, can be embedded within a microcapillary, which is then rotated to perform phase tomography [69, 70].

However, this simplified approach neglects the effects of diffraction. So while perfectly adapted at macroscopic scale, when characteristic sample features approach wavelength dimension, as in microscopy, the image reconstruction quality is more and more limited, especially for high-contrast samples. This limits the quality of the reconstructed data in terms of quantitative index of refraction measurements, as

well as the final resolution [71, 72], and can even in some cases lead to misleading reconstructions [73].

In order to obtain the most accurate reconstructions, and as pointed out by pioneering work in the domain [74, 75], a diffractive approach is to be taken into account, whose basis is briefly recalled in the next section.

### 4.3 TDM with Illumination Rotation

In the previous part, digital holographic microscopy was briefly described, highlighting some of its strengths and limitations. In this section, the link between the three-dimensional distribution of the sample refractive index and the measurement of its diffracted field (in phase and amplitude) is recalled, within the scalar approximation for the sake of simplicity. The interested reader will complete this rapid introduction by the lecture of classical textbooks on electromagnetism or wave diffraction (for example [76, 77]), and/or by general introductory reviews of tomographic diffractive microscopy [78, 79], as well as the seminal papers of the domain [74, 75], and their extension to high-numerical aperture imaging [80] and take into account the vectorial nature of the illuminating electromagnetic field [81].

One considers an object characterized by its relative permittivity  $\varepsilon(\mathbf{r})$ , and illuminated by a scalar monochromatic incident plane wave, (wavelength  $\lambda = 2\pi c/\omega$ ) from a source  $S(\mathbf{r})$ . Helmholtz equation (omitting the  $\exp(-i\omega t)$  time dependence) is then written as

$$\Delta E(\mathbf{r}) + k_0^2 E(\mathbf{r}) = X(\mathbf{r})k_0^2 E(\mathbf{r}) + S(\mathbf{r}) \quad (4.1)$$

with  $k_0 = 2\pi/\lambda$ , and  $X = 1 - \varepsilon$  being the permittivity contrast. Introducing the Green function:

$$G(\mathbf{r}) = -\exp(ik_0\mathbf{r})/4\pi r, \quad (4.2)$$

one can write the integral equation for the total field as

$$E(\mathbf{r}) = E_{\text{inc}}(\mathbf{r}) + k_0^2 \int G(\mathbf{r} - \mathbf{r}') X(\mathbf{r}') E(\mathbf{r}') d\mathbf{r}' \quad (4.3)$$

In (4.3),  $E_{\text{inc}}$  depicts the field that would exist in the absence of the object. The integral in (4.3) is to be calculated onto the support  $\Omega$  of the object. In transmission microscopy, only considering the far-field, so for an observation point  $\mathbf{r}$  far from the object, one has  $\mathbf{r}^2/\lambda \ll r$ , with  $\mathbf{r}'$  in  $\Omega$ , so that the diffracted field simplifies as

$$E_d(\mathbf{r}) = -\frac{\exp(ik_0\mathbf{r})}{4\pi r} e(\mathbf{k}) \quad (4.4)$$

The scattered far-field amplitude is written as

$$e(\mathbf{k}) = k_0^2 \int \exp(-i\mathbf{k} \cdot \mathbf{r}') X(\mathbf{r}') E(\mathbf{r}') d\mathbf{r}' \tag{4.5}$$

Considering a plane wave with wavevector  $k_{inc}$  as incident field, the incident field is written as  $E_{inc}(\mathbf{r}) = A_{inc} \exp(ik_{inc} \cdot \mathbf{r})$ , and limiting the development to a weakly diffracting object, for which the first Born approximation holds, one can finally write

$$e(\mathbf{k}, \mathbf{k}_{inc}) = C \tilde{X}(\mathbf{k} - \mathbf{k}_{inc}) \tag{4.6}$$

In (4.6),  $C = 8\pi^3 A_{inc} k_0^2$ . Equation (4.6) provides a direct correspondence between the diffracted far-field amplitude and the Fourier coefficient of the relative permittivity of the object.

Energy conservation in the diffraction process implies that diffracted  $\mathbf{k}_{diff}$  vectors have same amplitude as  $\mathbf{k}_{inc}$ , and therefore depict the so-called Ewald sphere. Because of the limited numerical aperture of the detection objective, only a cap of the Ewald sphere can be captured.

Then from the elastic scattering condition, this set of diffracted  $\mathbf{k}_{diff}$  vectors transforms into object  $\mathbf{k}_o$  vectors, via a simple translation:

$$\mathbf{k}_o = \mathbf{k}_{diff} - \mathbf{k}_{inc} \tag{4.7}$$

Figure 4.2 describes the process of information acquisition in DHM (Fig. 4.2a), and for filling Fourier space to expand the Optical Transfer Function (OTF) in TDM with illumination rotation (Fig. 4.2b, c). From Fig. 4.2a, one understands that the lateral extension of the  $\mathbf{k}_o$  vector set in Fourier space will provide good lateral resolution in image space. In contrary, the narrow extension along the  $k_z$  axis translates into very poor resolution and optical sectioning along the corresponding optical axis [67].

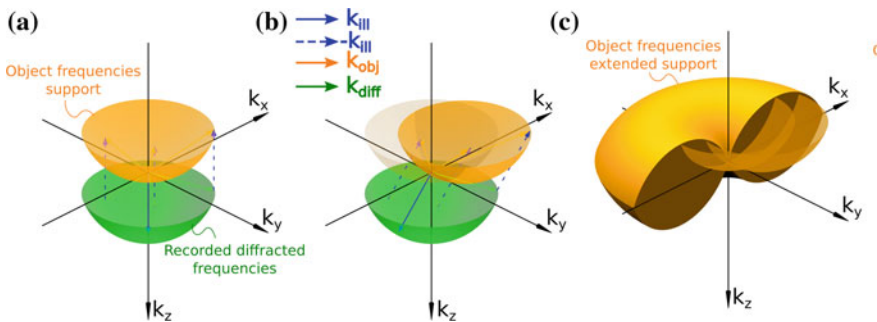


**Fig. 4.2** Principle of information acquisition in  $k$ -vector space for **a** Digital Holographic Microscopy with one illumination parallel to the optical axis, and **b, c** Tomographic Diffractive Microscopy with varying illumination angle

So, in order to improve image quality, one has to expand the  $k_0$  coverage. In TDM with illumination rotation, the illumination can be tilted (Fig. 4.2b). In that case, one can finally record a complementary subset of information (Fig. 4.2c).

For a large number of illuminations, a synthetic aperture approach delivers an enlarged frequency support. In that configuration, one recognizes the characteristic “doughnut” shape of transmission optical microscopy [82]. This extended frequency support explains the better resolution and optical sectioning capability of TDM, compared to DHM. One can theoretically double the lateral resolution [78, 81], experimentally reaching resolution in the 100 nm range [83].

Figure 4.3 illustrates this improved resolution, obtained on a carbon mesh, comparing images obtained in wide-field microscopy, laser-scanning confocal microscopy, and TDM, with a scanning-electron microscopy as a reference (from [83]), and imaging a diatom frustule, revealing inner porous structures (from [84]).

Another interesting feature of TDM is that it allows for clear distinction of refractive and absorptive subregions within the observed sample (Fig. 4.4), while conventional transmission microscopy mix these quantities into gray-level images. This unique feature has not yet been used for biological analysis, but may provide new insight for natural (as well as artificial) samples investigations [67, 83, 85, 86].

The technique is developed in several laboratories, and has been successfully used to study a wide variety of biological sample: neurons, red or white blood cells, hepatocyte cells, cancerous cells, cell–cell adhesion, chromosome, human hair, but also pollens, microalgae, or for pharmacological effects studies [84, 87–105]. Figure 4.5

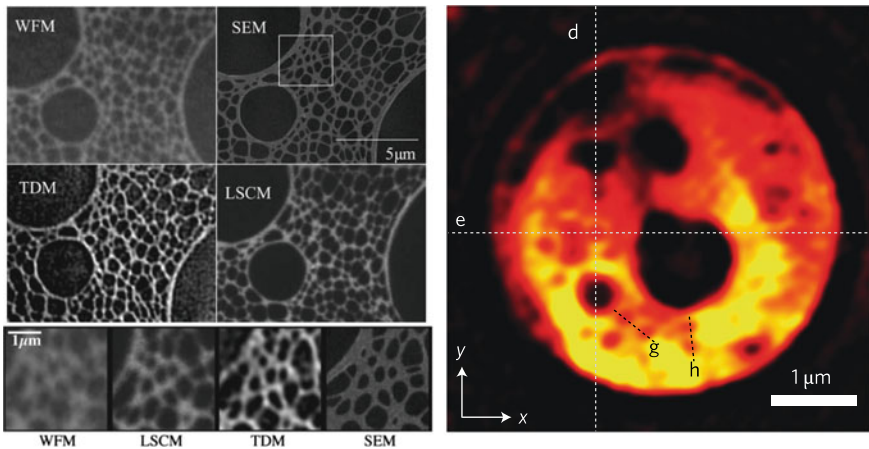


**Fig. 4.3** Left: Electron (SEM), wide-field (WFM), tomographic (TDM), and confocal fluorescence (LSCM) images of a lacey carbon membrane. Bottom, magnified view of the square region depicted on the SEM image (from [83], reproduced with permission from OSA The Optical Society). Right: Super-resolved phase images of nanoscopic porous cell frustule (diatoms) (from [84], reproduced with permission from Springer Nature). These images illustrate the TDM ability to reach a far-field resolution in the 100 nm range

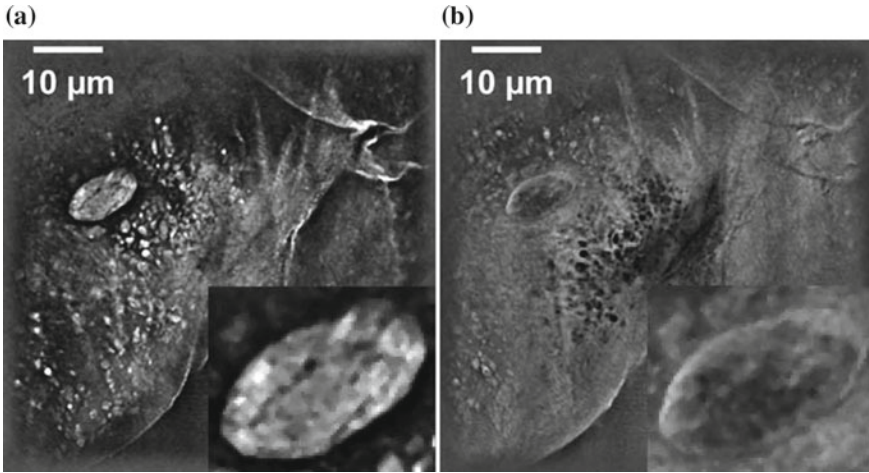


**Fig. 4.4** Epithelial cheek cells observed with tomographic diffractive microscopy. **a** Optical index and **b** absorption (uncalibrated gray levels) (from [86], reproduced with permission from Wiley-VCH). These images illustrate the ability of TDM to clearly distinguish refractive and absorptive regions at the sub cellular scale

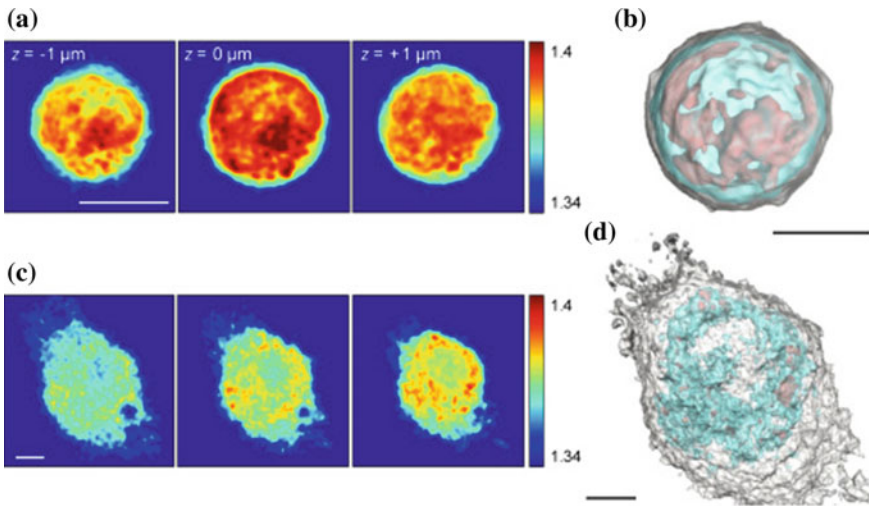


**Fig. 4.5** 3D visualization of WBCs. Cross-sectional slices of the RI distribution of **a** a lymphocyte and **c** a macrophage at various axial planes. Scale bar, 4  $\mu\text{m}$ . Rendered iso-surfaces of the RI map of **b** a lymphocyte and **d** a macrophage. For visualization purposes, the threshold iso-surfaces of the plasma membrane (white) and the internal structures (cyan, red) are set to 1.345, 1.375, and 1.39, respectively. Scale bar, 3  $\mu\text{m}$  (from [94], reproduced with permission from OSA The Optical Society). These images illustrate the ability to process images, only using RI as a criterion, efficiently segmenting membrane from internal structures without any specific labeling

depicts human white blood cells images with TDM, highlighting its ability to segment membrane from internal structures, without any specific labeling.

Commercial implementations of TDM with illumination rotation are now available. See the websites of *Nanolive* [106] and *Tomocube* [107] companies for various examples of applications on biological samples. The nanolive system has the advantage to offer a large accessible space over the sample, while the Tomocube allows for faster acquisitions at slightly higher resolutions.

## 4.4 Multiwavelength TDM

Tomographic Diffractive Microscopy with illumination rotation is now developed in several laboratories, and even commercially available, but requires specific illumination systems to perform numerical aperture synthesis of the condenser. This can be performed onto a standard microscope body [67, 83–85], but explains why specific setups are often preferred for laboratory prototyping, as well as for commercial implementations [106, 107]. This has then the drawback that TDM cannot be performed using a standard widefield or confocal fluorescence microscope, often already available in biological laboratories.

Figure 4.2a indicates that it is indeed possible to increase frequency coverage in Fourier space in a different way, by varying the illumination wavelength, which translates into varying the curvature radius of the cap of sphere, which is centered on the zero of frequencies. Figure 4.6a describes the obtained object frequency support for three illumination wavelengths. In a standard holographic configuration with illumination along the optical axis, both caps of sphere have, therefore, common summit at the frequency origin, but different extensions, in  $x$ - $y$ , as well as along

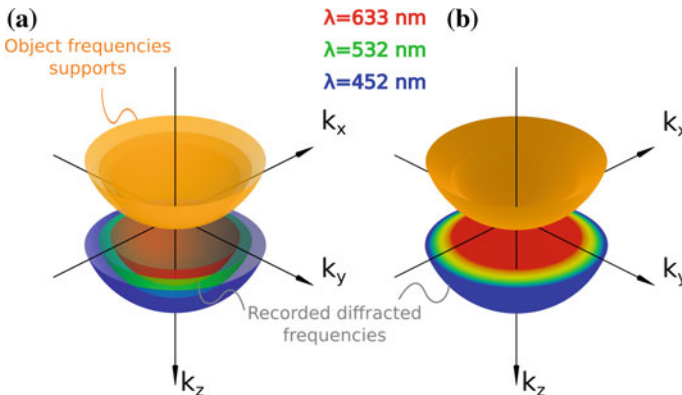


**Fig. 4.6** TDM with illumination wavelength variation: construction of the object frequency support, **a** for three wavelengths, **b** for a continuously varying wavelength

the  $z$ -axis. A continuous wavelength scanning could provide an extended and filled frequency support (Fig. 4.6b).

The main advantage of this wavelength variation approach is that a no-moving-part setup could be built, contrary to TDM with illumination rotation (or with sample rotation, see next section). The drawback of this approach is that it gives access to a more limited frequency support, compared to the previous one. The support being asymmetric, the same restrictions as before will apply with respect to the sample reconstruction, if a simple and direct Fourier inversion is used. A further possible limitation is also that wide spectrum (“white”) coherent light sources are still of limited availability, and complex. This explains that this approach, with standard holographic microscopy, has not gain much success (variants in reflection micro-holography have been developed [108–110]).

An elegant solution to this problem has been proposed with the introduction of white-light diffraction tomography [111–113], which can be considered as an extension of phase contrast microscopy, but with a controllable phase mask, instead of a static one. Figure 4.7a describes the principle of Spatial Light Interference

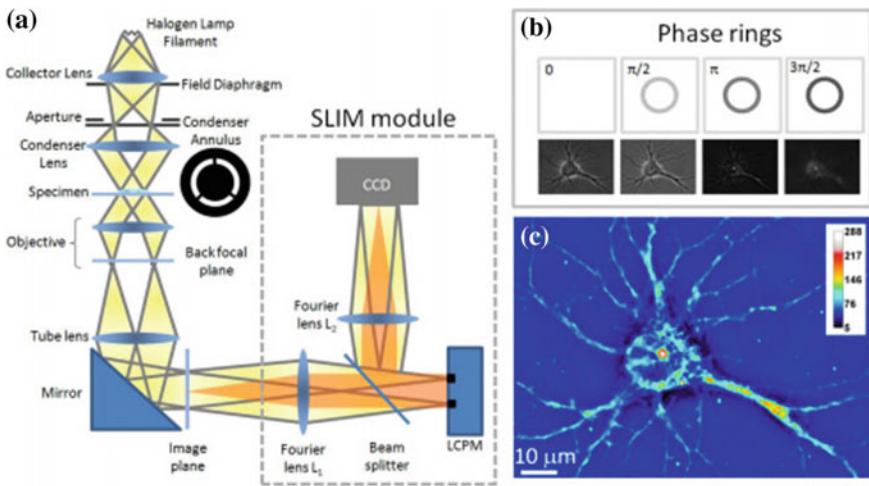


**Fig. 4.7** SLIM principle. **a** Schematic setup for SLIM. The SLIM module is attached to a commercial phase contrast microscope (Axio Observer Z1, Zeiss, in this case). The lamp filament is projected onto the condenser annulus. The annulus is located at the focal plane of the condenser, which collimates the light toward the sample. For conventional phase contrast microscopy, the phase objective contains a phase ring, which delays the unscattered light by a quarter wavelength and also attenuates it by a factor of 5. The image is delivered via the tube lens to the image plane, where the SLIM module processes it further. The Fourier lens L<sub>1</sub> relays the back-focal plane of the objective onto the surface of the liquid crystal phase modulator (LCPM, Boulder Nonlinear). By displaying different masks on the LCPM, the phase delay between the scattered and unscattered components is modulated accurately. Fourier lens L<sub>2</sub> reconstructs the final image at the CCD plane, which is conjugated with the image plane. **b** The phase rings and their corresponding images recorded by the CCD. **c** SLIM quantitative phase image of a hippocampal neuron (from [116], reproduced with permission from OSA The Optical Society)

Microscopy (SLIM) [114–117], which is at the basis of white-light diffraction tomography or Spatial Light Interference Tomography (SLIT). The optical train is based on a phase contrast microscopy, in which the observed sample is not illuminated using full condenser aperture, but through an annular aperture, so that only inclined rays illuminate the specimen.

In conventional phase contrast microscopy, those rays from the illumination, which have passed through the sample without being diffracted (but which are already phase retarded by passing through the sample), are focused in the back-focal plane of the objective, where an annular phase filter adds a supplemental (but fixed) phase shift. This phase shift is not added to the diffracted rays, which are not focused in the back-focal plane of the objective, or Fourier plane. In the image plane, interference between the diffracted and non-diffracted parts of the field creates a contrasted image between the background and the sample.

In the SLIM approach, an optical module is added, to relay the Fourier plane onto an active optical element: a spatial light modulator, which projects a controlled sequence of four phase masks, with  $0$ ,  $0.5\pi$ ,  $\pi$ , and  $1.5\pi$  delay (Fig. 4.7b). The final phase image (Fig. 4.7c) is computed from the four frames. Finally, scanning the observed sample in  $z$ , and properly processing of the data then allows for reconstruction of 3-D transparent samples in a tomographic mode.

This technique is also commercially distributed [118], with the advantage of being available as an add-on module, which can be fitted to a standard microscope body. The *PhiOptics* website describes applications of the SLIM and SLIT techniques.

Note also that a similar approach, but for DIC microscopy instead of phase contrast microscopy, has also been developed, under the GLIM acronym (Gradient Light Interference Microscopy), which allows for observation of larger, scattering samples at the tissue scale instead of the cellular scale [119].

## 4.5 TDM with Sample Rotation

Tomographic Diffractive Microscopy with illumination rotation has demonstrated its usefulness for many biological applications, and is even commercially available (see previous section). It however suffers from the so-called “missing cone” problem along the optical axis, leading to poor optical sectioning, if simple Fourier reconstructions, based on the Born or Rytov approximations, are used. Things are well improved if more elaborate reconstruction methods and/or a priori knowledge about the sample are used, to numerically fill the missing cone, leading to improved optical sectioning, but anyway, final images are characterized by a strong anisotropic resolution resulting from the shape of the OTF, which is much wider in  $x$ - $y$  directions than along the optical axis. Same limitation holds for white-light TDM, because of the peculiar shape of its OTF.

At macroscopic scale, it is common to perform tomography by rotating the sample or by rotating the source-sensor ensemble around the sample; so, trying to adapt the technique at microscopic scale is a natural approach [68–73], despite the strong

precision requirements. When neglecting diffraction, this permits easily to obtain isotropic resolution images. Indeed, in that case, the set of captured frequencies depicts a disk in Fourier space, which rotates around one of its diameter describing a filled sphere.

When taking into account diffraction, and especially at high numerical aperture, one cannot neglect the curvature of the set of captured frequencies. In that case, the final OTF differs in its shape, not being anymore a complete ball. Figure 4.8a describes the obtained object frequency support. Because of the initial cap of sphere curvature, a so-called “missing apple-core” (Fig. 4.8b) appears along the specimen rotation axis [120]. So, strictly speaking, this approach delivers quasi-isotropic resolution images, with a small but anyway noticeable remaining elongation along the sample rotation axis [120, 121]. A solution to completely fill the OTF is then to perform a second full rotation of the sample around another axis of rotation, perpendicular to the first one.

The main advantage of this technique is that a standard DHM can be used, as the interferometric acquisition system is static. The difficulty is, however, successfully performing high-precision sample rotations, compatible with interferometric measurements for TDM reconstructions, while a large number of acquisitions is necessary if one wants to appropriately fill Fourier space. To do so, samples can be embedded within a rotating microcapillary [121–123], which then serves a mechanical support for the rotation (Fig. 4.9). This approach simplifies sample manipulation, but may require some precautions in the image reconstruction process, as the microcapillary may act as a cylindrical lens, deforming the observed sample [124]. Because of the microcapillary dimensions, it also must be performed with longer working distance objectives, therefore having a lower numerical aperture, limiting the final achievable resolution. So, while this technique has been proven to work, sample manipulation is not easy, which has limited its adoption. Note however that in some cases, the

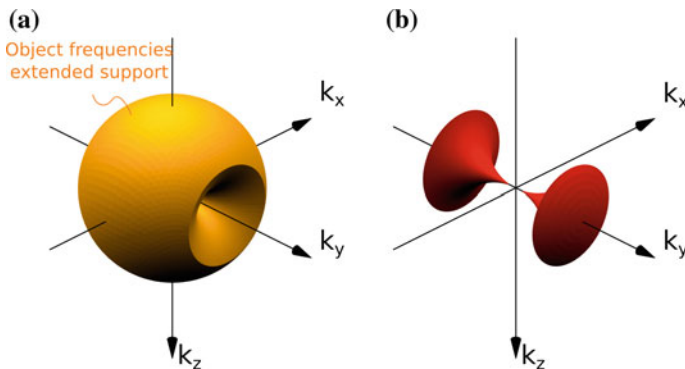


**Fig. 4.8** Object frequency support for TDM with specimen rotation. **a** Support obtained when rotating the holographic OTF (see Fig. 4.2a) around the  $y$ -axis. The curvature of the initial cap of sphere induces a so-called “missing apple-core” of unrecorded frequencies along that axis, depicted on **(b)**

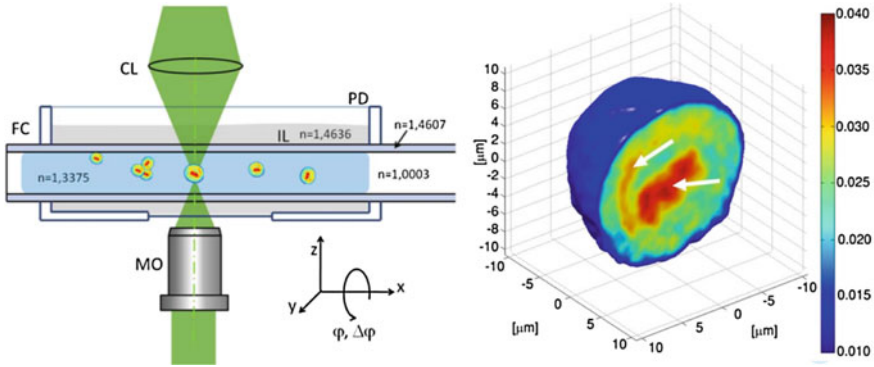


**Fig. 4.9** Principle of TDM with sample rotation (from [122], reproduced with permission from SPIE). Left: The rotary fiber holder setup: CL: condenser lens, PD: Petri dish, IL: immersion liquid, FC: fiber capillary, MO: Microscope objective,  $(x, y, z, \varphi)$ : movement directions of the fiber capillary,  $\Delta\varphi$ : rotation step for  $N$  projections, RH: rotary holder. Right: The refractive index distribution in a single U937 cell. Refractive index peak to valley value  $\Delta n = 0.030$

sample itself can be directly rotated, as, for example, when observing optical fibers or microtips [73, 125–129], but this does not generally apply for biological samples, for which softer manipulation approaches should be developed (it may work for peculiar samples like microfibers or hairs).

Manipulation of microscopic object by light [130–132] is an active research topic, and recently, optical tweezers [133–135] have indeed been successfully used to perform TDM observations. Conversely, it has been shown that the precise knowledge by TDM measurements of the sample 3D index of refraction distribution could be used to optimize trapping by optical tweezers of arbitrarily shaped microscopic samples [136]. In some cases, the sample presenting electric potential variations, use of externally applied field induces sample movement. Dielectrophoretic cell rotation [137], initially used to perform isotropic observations in confocal microscopy [138], has also been applied to tomographic investigations [139]. Recently, simple natural rotation of samples such as red blood cells when flowing through microfluidic channels [140–142] has been successfully used for tomographic observations. Similarly, translational motion of cells through a peculiarly focused beam has been used to perform tomographic reconstructions of the moving cells [143]. These approaches have the advantage that they use completely passive optical systems, with no optical scanning of the illumination beam nor controlled movements of the sample. Sample rotation has also been used with inline holographic microscopy to perform TDM with a simpler setup [144].

## 4.6 Combined Approaches

In TDM with illumination rotation, the lateral and axial resolutions are improved, and true 3D imaging is possible. However, from Fig. 4.2, one can deduce that the smaller extension of the OTF along the  $k_z$ -direction (along the optical axis) and the presence of the so-called “missing cone” of non-captured frequencies along same axis will translate into lower axial resolution than lateral one, and will limit sectioning capabilities for 3D samples.

In TDM with sample rotation (Fig. 4.8), an almost completely filled, spherical OTF is obtained, but a small set of missing frequencies does exist along the rotation axis, slightly degrading the resolution in this direction. Also, the diameter of the spherical OTF is smaller than the lateral extension of the OTF with illumination rotation. Furthermore, this approach requires a large number of sample rotations to properly fill the quasi-spherical OTF.

In order to combine both-of-best-worlds, and simultaneously obtain an improved and isotropic resolution in the final images, it has been proposed to associate illumination rotation and specimen rotation [145]. Such a combination would allow for merging several “doughnuts” from TDM with illumination rotation, requiring only a few sample rotations. Figure 4.10a–c shows the obtained OTF support for 1, 2, and 4 views, which already permits to obtain a quasi-spherical, extended OTF, which would translate into improved and isotropic resolution images without any specific direction being plagued by missing frequencies.

Comparing the extension of their respective OTFs gives a direct insight about imaging capabilities of various TDM configurations [146]. The lateral and axial extensions of the frequency support for holographic microscopy are given by

$$\Delta v_{x,y}^{\text{Holo}} = \frac{2n \sin \theta}{\lambda} \Delta v_z^{\text{Holo}} = \frac{n(1 - \cos \theta)}{\lambda} \quad (4.9)$$

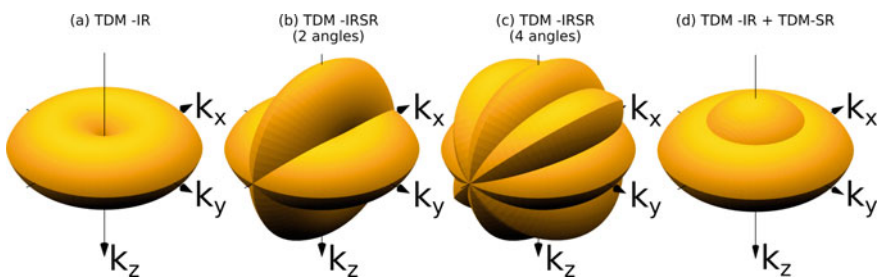


**Fig. 4.10** Combined tomography, with illumination and specimen rotation. **a–c** TDM with illumination rotation acquisitions for 1, 2 and 4 sample positions, respectively. **d** Resulting OTF from the combination of one TDM with illumination rotation acquisition and one TDM with sample rotation acquisition

TDM with illumination rotation (TDM-IR) permits to double the lateral frequency support, with improved axial resolution too:

$$\Delta v_{x,y}^{\text{TDM-IR}} = \frac{4n \sin \theta}{\lambda} \Delta v_z^{\text{TDM-IR}} = \frac{2n(1 - \cos \theta)}{\lambda} \quad (4.10)$$

When rotating the sample along one axis (TDM-SR), one gets:

$$\Delta v_{x,z}^{\text{TDM-SR}} = \frac{4n \sin(\theta/2)}{\lambda} \Delta v_y^{\text{TDM-SR}} = \frac{2n \sin \theta}{\lambda} \quad (4.11)$$

When rotating the sample along two orthogonal axes (TDM-dualSR), one gets

$$\Delta v_{x,z,z}^{\text{TDM-dualSR}} = \frac{4n \sin(\theta/2)}{\lambda} \quad (4.12)$$

And finally, when combining illumination rotation with sample rotation (TDM-IRSR), one obtains the highest isotropic OTF extension:

$$\Delta v_{x,y,z}^{\text{TDM-IRSR}} = \frac{4n \sin \theta}{\lambda} \quad (4.13)$$

A variant to fill the missing cone from TDM-IR would be to combine one TDM-IR acquisition with one TDM-SR acquisition, as both techniques present sets of uncaptured frequencies, but oriented along different axes ( $z$ -axis, or optical axis for TDM with illumination rotation, and sample rotation axis for TDM with sample rotation), which are perpendicular to each other (see Fig. 4.10d). Initially proposed in [145], this configuration was recently tested experimentally, using optical tweezers [147]. In that case, one obtains for the OTF extension:

$$\Delta v_{x,y}^{\text{TDM-IR+TDM-SR}} = \frac{4n \sin \theta}{\lambda} \quad \Delta v_z^{\text{TDM-IR+TDM-SR}} = \frac{4n \sin(\theta/2)}{\lambda} \quad (4.14)$$

However, the OTF extension is only an indication of the theoretical achievable resolution. In practice, results are slightly lower, but anyway, a lateral resolution of 130 nm was achieved at  $\lambda = 633$  nm in [83], and using shorter wavelength, 75 nm resolution was obtained at  $\lambda = 405$  nm in [84], in the case of TDM-IR. In the context of TDM-IRSR, a single acquisition achieved a resolution of 95 nm at  $\lambda = 475$  nm, but when merging several acquisitions, results were slightly degraded, indicating that the merging process was not optimal, but anyway, three-dimensional images with resolution below 200 nm in all directions could be obtained, a premiere for label-free, far-field optical microscopy [146].

Note also that experimental measurement of the resolution in coherent imaging presents specific challenges [148], especially in 3D [146, 149].

Figure 4.11 shows a *Betula pendula* pollen grain, obtained with TDM-IRSR, which delivers dual views of this triporate pollen grain, clearly segmenting the refrac-

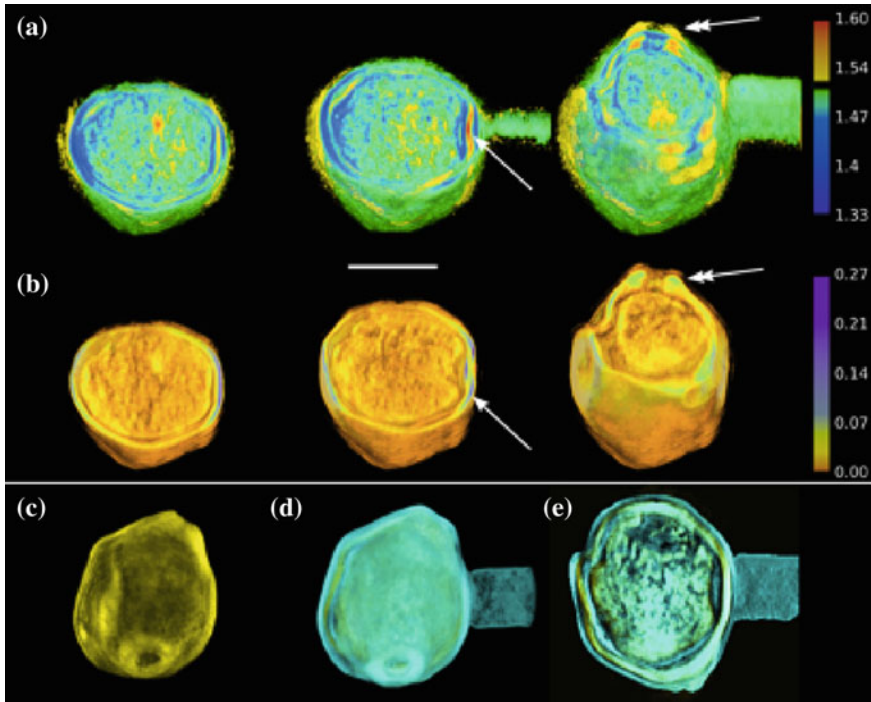


**Fig. 4.11** Betula pollen grain observed with tomographic diffractive microscopy, **a, b** volumetric cuts ( $x$ - $y$  views) through the 3D index of refraction image and the absorption image, respectively. Note the higher index of refraction of the pollen walls, especially near the pores (double-headed arrow), and the doubled outer wall (arrow). Scale bar: 10  $\mu$ m. See also Visualization 3, **c** outer view of the pollen: image of the absorption component, displayed in yellow, **d** outer view of the pollen: image of the complex index of refraction, with refractive component displayed in cyan. The photopolymer tip used to handle the sample is purely refractive, hence visible on the index component, but not on the absorption image, **e** ( $x$ - $y$ ) cut through the pollen. Note that the absorptive components are confined to the interior of the pollen: nucleus and intine, and absent from the exine (from [146], reproduced with permission from The Optical Society (OSA))

tion and absorption contributions into two separate images. Figure 4.11a depicts volumetric cuts in the  $z$  direction ( $x$ - $y$  views) through the index of refraction image. Figure 4.11b depicts same volumetric cuts through the absorption image. Note the inner structures of the pollen grain and its double-layer outer structure (marked by arrow), with chambers separating inner and outer walls (vestibulum), and protruding pores (double-headed arrow). The Refraction Index (RI) in this image has been calibrated from the known RIs of the immersion medium into which the pollen is immersed, and of the photopolymer tip, used here to handle and rotate the pollen grain [146].

The pollen walls are composed of highly refractive components, while the vestibulum is of lower RI and some regions within the nucleus exhibit high RI. Note that the absorptive components seem confined to the interior of the pollen. In conventional

optical transmission microscopy, gray-level images mix these quantities, which are here clearly distinguished.

Figure 4.11c, d shows 3D views of the absorption within the pollen (in yellow), and of the complex index of refraction (refraction and absorption, refraction being segmented in cyan), respectively. The photopolymer tip, used to handle and rotate the pollen, is clearly visible on Fig. 4.11d, but not on Fig. 4.11c. The absorption image (yellow) appears clearly being embedded within the refraction image (cyan), as shown on the cut through the pollen (Fig. 4.11e).

This interesting property of clearly separating absorption and refraction has, to the best of our knowledge, not yet been investigated for biological research, while refraction and absorption images indeed deliver complementary information [67, 83, 86, 146].

Note that other approaches are possible to obtain improved and isotropic resolution in TDM. A 4-Pi TDM setup, combining transmission and reflection acquisitions, has been proposed in [81]. A simplified variant has also been investigated [150], cleverly making use of the mirroring effect to achieve 4-Pi detection using only a single objective and a special object support. These two techniques have, however, not yet been experimentally implemented.

## 4.7 Conclusion and Perspectives

Tomographic diffractive microscopy is able to deliver high-resolution images of unlabeled samples, with various implementations, and attracts the interest of more and more end-users in various domains. It, however, still suffers from some limitations, which may contribute to slow-down its adoption.

Because it is not limited by low-level fluorescence signal, it has the potential to be a fast imaging technique. However, its sequential nature limits the final speed of acquisition, a single 3D images requiring tens to hundreds of holograms to be recorded. Also, its computational nature limits final 3D image delivery rate. This motivates developments to increase speed of data acquisition, as well as to fasten image computation and rendering [151–161]. Ultra-fast cameras can be used to accelerate acquisitions, fewer images can be taken to compute tomographic images when requirements in image quality and resolution are less severe, and modern Graphic Processing Unit (GPU) computation can greatly fasten image reconstruction. So, in practice, the present bottleneck is in fact the data transfer between fast camera and fast computer, which still limits imaging acquisition and rendering speed. But progresses in the domain are rapid, as well as in the domain of 3D display systems. We believe that by combining rapid acquisitions with fast transfer rates and fast GPU reconstructions, a real-time 3D display of the observed sample images would be possible [161], which could greatly facilitate adoption of tomographic imaging by nonspecialists.

Another active domain of research is about simplifying the data acquisition system, which, in its most common form, is based onto an interferometric setup, with

a reference arm and an object arm. To facilitate alignment, common-path tomography has been proposed [162–164]. Use of partially coherent interferometry can also be helpful, leveraging the illumination source requirements, and contributing to increase image quality (no speckle noise), but may require more stringent alignment and stability of the interferometer [165–167].

Wavefront analyzers, which allows for direct measurement of amplitude and phase, have also been used with success for tomographic investigations at the microscopic scale [168–171]. They present the advantage that they can be directly fitted to standard microscopes, adding a new imaging modality to existing setups, while specific TDM instruments often lack the possibility of doing multimodal imaging.

At the present time, fluorescence imaging is for example proposed to be added to commercial TDM systems, but not yet laser confocal fluorescence microscopy, and associated imaging modes like fluorescence life-time imaging (FLIM), or fluorescence recovery after photobleaching (FRAP), or modern superresolution methods like structured illumination microscopy (SIM), or stimulated emission depletion (STED) microscopy.

It is likely, that, offering complementary information, more imaging modalities will be added to TDM systems in the future, to enlarge the investigations it allows for. Among new approaches are multispectral or hyperspectral imaging [109, 172, 173], which could be especially interesting when considering absorbing samples, as absorption in natural sample is often very variable with wavelength. Polarization delivers specific information about birefringent samples, and can even be used to further improve resolution [174]. Extension of the technique in the infrared has also been considered, giving access to new characterizations [175]. TDM has also been considered to investigate turbid media [176], and it has also been shown that 3D differential interference contrast microscopy mode can be computed from synthetic aperture microscopy data [177].

A possible limitation for a wide adoption of TDM is its associated costs, because of the use of high numerical aperture objectives when high resolution is needed, the complex interferometric systems to be used to record the diffracted field, or the cost of wavefront analyzers. Several groups are therefore active in developing simplified, low-cost approaches, based on lensless imaging techniques [178–182]. Conversely, illumination angular scanning, usually performed using tip-tilt or galvanometric mirrors, or digital micromirror devices, can be replaced by an all-electronic, led-based illumination array [183, 184].

In this overview of TDM, we have introduced the most straightforward image reconstruction method, based on the first Born approximation, therefore allowing for very simple and fast image reconstructions based on Fourier inversions. This obviously limits the class of objects, which can be imaged, but a large literature has been devoted to develop inversion approaches going beyond this limitation, involving deconvolution, techniques to decrease the number of images to be taken, approaches taking into account large phase changes in thick samples, and/or absorption, as well as possible multiscattering [185–201].

Machine learning approaches have also recently attracted the interest of the community, to facilitate image reconstruction and/or go beyond classical inversion methods [202–205].

Note also that a close relationship does exist between conventional microscopy and TDM [78], and recently, a unified description of TDM has been proposed, to which the interested reader is referred [206] for more details. In particular, TDM in reflection mode, not developed here, also present some advantages compared to standard optical microscopy, even when only basic image reconstruction approaches are used [207, 208].

Finally, the interested reader will find in recent reviews and specials issues about quantitative phase imaging [209–212] latest developments, as well as applications of the technique into many domains. While many results apply for phase microscopy, which is in fact a simplified version of TDM, the domains of application highlighted in these contributions, will certainly also benefit from the better imaging capabilities of TDM.

## References

1. S.W. Hell, J. Wichmann, Breaking the diffraction resolution limit by stimulated emission: stimulated-emission-depletion fluorescence microscopy. *Opt. Lett.* **19**, 780–782 (1994)
2. E. Betzig et al., Imaging intracellular fluorescent proteins at nanometer resolution. *Science* **313**, 1642–1645 (2006)
3. M.J. Rust, M. Bates, X. Zhuang, Sub-diffraction-limit imaging by stochastic optical reconstruction microscopy (STORM). *Nat. Methods* **3**, 793–796 (2006)
4. S.T. Hess, T.P.K. Girirajan, M.D. Mason, Ultra-high resolution imaging by fluorescence photoactivation localization microscopy. *Biophys. J.* **91**, 4258–4272 (2006)
5. F. Balzarotti et al., Nanometer resolution imaging and tracking of fluorescent molecules with minimal photon fluxes. *Science* **355**, 606–612 (2017)
6. S.-L. Liu et al., Observing the cell in its native state: imaging subcellular dynamics in multicellular organisms. *Science* **360**, 284–297 (2018)
7. P.J. Campagnola, M.-D. Wei, A. Lewis, L.M. Loew, High-resolution nonlinear optical imaging of live cells by second harmonic generation. *Biophys. J.* **77**, 3341–3349 (1999)
8. L. Moreaux, O. Sandre, M. Blanchard-Desce, J. Mertz, Membrane imaging by simultaneous second-harmonic generation and two-photon microscopy. *Opt. Lett.* **25**, 320–322 (2000)
9. D. Oron et al., Depth-resolved structural imaging by third-harmonic generation microscopy. *J. Struct. Biol.* **147**, 3–11 (2004)
10. G. Turrell, J. Corset, *Raman Microscopy. Developments and Applications* (Academic Press, 1996)
11. X. Nan, J.X. Cheng, X.S. Xie, Vibrational imaging of lipid droplets in live fibroblast cells with coherent anti-stokes Raman scattering microscopy. *J. Lipid Res.* **44**, 2202–2208 (2003)
12. F. Zernike, Phase contrast, a new method for the microscopic observation of transparent objects. Part I *Physica* **9**, 686–698 (1942)
13. F. Zernike, Phase contrast, a new method for the microscopic observation of transparent objects. Part II *Physica* **9**, 974–986 (1942)
14. T.E. Gureyev, K.A. Nugent, Rapid quantitative phase imaging using the transport of intensity equation. *Opt. Commun.* **133**, 339–346 (1997)
15. A. Barty, K.A. Nugent, D. Paganin, A. Roberts, Quantitative optical phase microscopy. *Opt. Lett.* **23**, 817–819 (1998)

16. N. Jayshree, G. Keshava Datta, R.M. Vasu, Optical tomographic microscope for quantitative imaging of phase objects. *Appl. Opt.* **39**, 277–283 (2000)
17. M. Soto, E. Acosta, Improved phase imaging from intensity measurements in multiple planes. *Appl. Opt.* **46**, 7978–7981 (2007)
18. L. Waller, Y. Luo, S.Y. Yang, G. Barbastathis, Transport of intensity phase imaging in a volume holographic microscope. *Opt. Lett.* **35**, 2961–2963 (2010)
19. C. Preza, D.L. Snyder, J.A. Conchello, Theoretical development and experimental evaluation of imaging models for differential-interference-contrast microscopy. *J. Opt. Soc. Am. A* **16**, 2185–2199 (1999)
20. M. Shribak, S. Inoue, Orientation-independent differential interference contrast microscopy. *Appl. Opt.* **45**, 460–469 (2006)
21. B. Kouskousis et al., Quantitative phase and refractive index analysis of optical fibers using differential interference contrast microscopy. *Appl. Opt.* **47**, 5182–5189 (2008)
22. D. Fu et al., Quantitative DIC microscopy using an off-axis self-interference approach. *Opt. Lett.* **35**, 2370–2372 (2010)
23. S.S. Kou, L. Waller, G. Barbastathis, C.J.R. Sheppard, Transport-of-intensity approach to differential interference contrast (TI-DIC) microscopy for quantitative phase imaging. *Opt. Lett.* **35**, 447–449 (2010)
24. G. Zheng, R. Horstmeyer, C. Yang, Wide-field, high-resolution Fourier ptychographic microscopy. *Nat. Photonics* **7**, 739–745 (2013)
25. J. Marrison, L. Rätty, P. Marriott, P. O’Toole, Ptychography—a label free, high-contrast imaging technique for live cells using quantitative phase information. *Sci. Rep.* **3**, 2369 (2013)
26. X. Ou, R. Horstmeyer, G. Zheng, C. Yang, High numerical aperture Fourier ptychography: principle, implementation and characterization. *Opt. Express* **23**, 3472–3491 (2015)
27. R. Horstmeyer et al., Diffraction tomography with Fourier ptychography. *Optica* **3**, 827–835 (2016)
28. A. Maiden, D. Johnson, P. Li, Further improvements to the ptychographical iterative engine. *Optica* **4**, 736–745 (2017)
29. P. Ferrand, A. Baroni, M. Allain, V. Chamard, Quantitative imaging of anisotropic material properties with vectorial ptychography. *Opt. Lett.* **43**, 763–766 (2018)
30. U. Schnars, Direct phase determination in hologram interferometry with use of digitally recorded holograms. *J. Opt. Soc. Am. A* **11**, 2011–2015 (1994)
31. E. Cuche, P. Marquet, C. Depeursinge, Simultaneous amplitude-contrast and quantitative phase-contrast microscopy by numerical reconstruction of Fresnel off-axis holograms. *Appl. Opt.* **38**, 6994–7001 (1999)
32. P. Bon, G. Maucort, B. Wattellier, S. Monneret, Quadriwave lateral shearing interferometry for quantitative phase microscopy of living cells. *Opt. Express* **17**, 13080–13094 (2009)
33. R. Barankov, J.-C. Baritiaux, J. Mertz, High-resolution 3D phase imaging using a partitioned detection aperture: a wave-optic analysis. *J. Opt. Soc. Am. A* **32**, 2123–2135 (2015)
34. See for example of systems used for biological applications: <https://www.lynceetec.com>, <http://www.phiab.se>, <https://www.holmarc.com/dhm.php>, <http://advscientific.com/multimodal-holographic-microscope-q-phase/>, <http://www.ovizio.com/en/microscopes/QMod>, <http://4-deep.com>, <http://phasicscorp.com/cameras/sid4bio/>, <http://www.iprasense.com>
35. M.K. Kim, *Digital Holographic Microscopy: Principles, Techniques, and Applications*. *Springer Series in Optical Science*, vol. 162 (Springer, 2011)
36. G. Popescu, *Quantitative Phase Imaging of Cells and Tissues* (McGraw Hill, 2011)
37. K. Alm et al., *Digital Holography and Cell Studies, in Holography, Research and Technologies* (InTech, 2011)
38. P. Ferraro, A. Wax, Z. Zalevsky, *Coherent Light Microscopy: Imaging and Quantitative Phase Analysis* (Springer, 2011)
39. N.T. Shaked, Z. Zalevsky, L. Satterwhite (eds.), *Biomedical Optical Phase Microscopy and Nanoscopy* (Elsevier, 2012)

40. B. Kemper, Digital holographic microscopy: quantitative phase imaging and applications in live cell analysis, in *Handbook of Coherent-Domain Optical Methods*, ed. by V.V. Tuchin (Springer, 2013), pp. 215–257
41. B. Bhaduri et al., Diffraction phase microscopy: principles and applications in materials and life sciences. *Adv. Opt. Photonics* **6**, 57–119 (2014)
42. T. Tahara et al., Digital holography and its multidimensional imaging applications: a review. *Microscopy* **67**, 55–67 (2018)
43. D. Gabor, A new microscopic principle. *Nature* **161**, 777–778 (1948)
44. J. García-Sucerquia et al., Digital in-line holographic microscopy. *Appl. Opt.* **45**, 836–850 (2006)
45. J.R. Fienup, Phase retrieval algorithms: a comparison. *Appl. Opt.* **21**, 2758–2769 (1982)
46. I. Yamaguchi, T. Zhang, Phase-shifting digital holography. *Opt. Lett.* **22**, 1268–1270 (1997)
47. T. Zhang, I. Yamaguchi, Three-dimensional microscopy with phase-shifting digital holography. *Opt. Lett.* **23**, 1221–1223 (1998)
48. V. Mico, Z. Zalevsky, J. Garcia-Monreal, Common-path phase-shifting digital holographic microscopy: a way to quantitative phase imaging and superresolution. *Opt. Commun.* **281**, 4273–4281 (2008)
49. T. Tahara et al., Parallel phase-shifting digital holographic microscopy. *Biomed. Opt. Express* **1**, 610–616 (2010)
50. H. Jun-He et al., Two-step phase shifting differential-recording digital holographic microscopy. *Sci. Rep.* **7**, 1992 (2017)
51. R.A. Briones, L.O. Heflinger, R.F. Wuerker, Holographic microscopy. *Appl. Opt.* **17**, 944–950 (1978)
52. V. Micó, J. García, Z. Zalevsky, B. Javidi, Phase-shifting Gabor holography. *Opt. Lett.* **34**, 1492–1494 (2009)
53. U. Schnars, W. Jüptner, *Digital Holography: Digital Hologram Recording, Numerical Reconstruction, and Related Techniques* (Springer, 2005)
54. P. Picart, J.-C. Li, *Digital Holography* (Wiley, 2012)
55. W. Osten et al., Recent advances in digital holography [Invited]. *Appl. Opt.* **53**, G44–G63 (2014)
56. T.-C. Poon, J.-P. Liu, *Introduction to Modern Digital Holography* (Cambridge University Press, 2014)
57. G.T. Nehmetallah, R. Aylo, L. Williams, *Analog and Digital Holography with MATLAB* (SPIE Press, 2015)
58. P. Picart (ed.), *New Techniques in Digital Holography* (Wiley, 2015)
59. B. Rappaz et al., Measurement of the integral refractive index and dynamic cell morphometry of living cells with digital holographic microscopy. *Opt. Express* **13**, 9361–9373 (2005)
60. G. Popescu, T. Ikeda, R.R. Dasari, M.S. Feld, Diffraction phase microscopy for quantifying cell structure and dynamics. *Opt. Lett.* **31**, 775–777 (2005)
61. B. Rappaz et al., Spatial analysis of erythrocyte membrane fluctuations by digital holographic microscopy. *Blood Cells Mol. Dis.* **42**, 228–232 (2009)
62. P. Jourdain et al., Simultaneous optical recording in multiple cells by digital holographic microscopy of chloride current associated to activation of the ligand-gated chloride channel GABA<sub>A</sub> receptor. *PLoS ONE* **7**, e51041 (2012)
63. B. Rappaz et al., Noninvasive characterization of the fission yeast cell cycle by monitoring dry mass with digital holographic microscopy. *J. Biomed. Opt.* **14**, 034049 (2009)
64. A. El Mallahi, C. Minetti, F. Dubois, Automated three-dimensional detection and classification of living organisms using digital holographic microscopy with partial spatial coherent source: Application to the monitoring of drinking water resources. *Appl. Opt.* **52**, A68–A80 (2013)
65. M. Falck Miniotis, A. Mukwaya, A. Gjørloff Wingren, Digital holographic microscopy for non-invasive monitoring of cell cycle arrest in L929 cells. *PLoS ONE* **9**, e106546 (2014)
66. S. Aknoun et al., Living cell dry mass measurement using quantitative phase imaging with quadriwave lateral shearing interferometry: an accuracy and sensitivity discussion. *J. Biomed. Opt.* **20**, 126009 (2015)

67. M. Debailleul et al., Holographic microscopy and diffractive microtomography of transparent samples. *Meas. Sci. Technol.* **19**, 074009 (2008)
68. A. Barty, K.A. Nugent, A. Roberts, D. Paganin, Quantitative phase tomography. *Opt. Commun.* **175**, 329–336 (2000)
69. F. Charrière et al., Cell refractive index tomography by digital holographic microscopy. *Opt. Lett.* **31**, 178–180 (2006)
70. F. Charrière et al., Living specimen tomography by digital holographic microscopy: morphometry of testate amoeba. *Opt. Express* **14**, 7005–7013 (2006)
71. A.J. Devaney, A filtered backpropagation algorithm for diffraction tomography. *Ultrason. Imaging* **4**, 336–350 (1982)
72. T.C. Wedberg, J.J. Stamnes, W. Singer, Comparison of the filtered backpropagation and the filtered backprojection algorithms for quantitative tomography. *Appl. Opt.* **34**, 6575–6581 (1995)
73. W. Gorski, W. Osten, Tomographic imaging of photonic crystal fibers. *Opt. Lett.* **32**, 1977–1979 (2007)
74. E. Wolf, Three-dimensional structure determination of semi-transparent objects from holographic data. *Opt. Commun.* **1**, 153–156 (1969)
75. R. Dändliker, K. Weiss, Reconstruction of the three-dimensional refractive index from scattered waves. *Opt. Commun.* **1**, 323 (1970)
76. J.D. Jackson, *Classical Electrodynamics* (Wiley, 1999)
77. M. Born, E. Wolf, *Principles of Optics* (Cambridge University Press, 1999)
78. O. Haeberlé, K. Belkebir, H. Giovannini, A. Sentenac, Tomographic diffractive microscopy: basics, techniques and perspectives. *J. Mod. Opt.* **57**, 686–699 (2010)
79. D. Jin, R. Zhou, Z. Yaqoob, P.T.C. So, Tomographic phase microscopy: principles and applications in bioimaging [Invited]. *J. Opt. Soc. Am. B* **34**, B64–B77 (2017)
80. S.S. Kou, C.J.R. Sheppard, Image formation in holographic tomography: high-aperture imaging conditions. *Appl. Opt.* **48**, H168–H175 (2009)
81. V. Lauer, New approach to optical diffraction tomography yielding a vector equation of diffraction tomography and a novel tomographic microscope. *J. Microscopy* **205**, 165–176 (2002)
82. N. Streibl, Three-dimensional imaging by a microscope. *J. Opt. Soc. Am. A* **2**, 121–127 (1985)
83. M. Debailleul et al., High-resolution three-dimensional tomographic diffractive microscopy of transparent inorganic and biological samples. *Opt. Lett.* **34**, 79–81 (2009)
84. Y. Cotte et al., Marker-free phase nanoscopy. *Nat. Photonics* **7**, 113–117 (2013)
85. T.C. Wedberg, W.C. Wedberg, Tomographic reconstruction of the cross-sectional refractive index distribution in semi-transparent, birefringent fibres. *J. Microscopy* **177**, 53–67 (1995)
86. B. Simon et al., High-resolution tomographic diffractive microscopy of biological samples. *J. Biophotonics* **3**, 462–467 (2010)
87. W. Choi et al., Tomographic phase microscopy. *Nat. Methods* **4**, 717–719 (2007)
88. Y. Park et al., Refractive index maps and membrane dynamics of human red blood cells parasitized by *Plasmodium falciparum*. *Proc. Natl. Acad. Sci. U.S.A.* **105**, 13730–13735 (2008)
89. Y. Sung et al., Optical diffraction tomography for high resolution live cell imaging. *Opt. Express* **17**, 266–277 (2009)
90. Y. Sung et al., Stain-free quantification of chromosomes in live cells using regularized tomographic phase microscopy. *PLoS ONE* **7**, e49502 (2012)
91. J.W. Su et al., Digital holographic microtomography for high-resolution refractive index mapping of live cells. *J. Biophotonics* **6**, 416–424 (2013)
92. Y. Sung et al., Three-dimensional holographic refractive-index measurement of continuously flowing cells in a microfluidic channel. *Phys. Rev. Appl.* **1**, 014002 (2014)
93. K. Kim et al., High-resolution three-dimensional imaging of red blood cells parasitized by *Plasmodium falciparum* and in situ hemozoin crystals using optical diffraction tomography. *J. Biomed. Opt.* **19**, 011005 (2014)

94. J. Yoon et al., Label-free characterization of white blood cells by measuring 3D refractive index maps. *Biomed. Opt. Express* **6**, 3865–3875 (2015)
95. H. Park et al., Characterizations of individual mouse red blood cells parasitized by *Babesia microti* using 3-D holographic microscopy. *Sci. Rep.* **5**, 10827 (2015)
96. S. Lee et al., Measurements of morphology and refractive indexes on human downy hairs using three-dimensional quantitative phase imaging. *J. Biomed. Opt.* **20**, 111207 (2015)
97. K. Kim et al., Three-dimensional label-free imaging and quantification of lipid droplets in live hepatocytes. *Sci. Rep.* **6**, 36815 (2016)
98. K. Kim et al., Optical diffraction tomography techniques for the study of cell pathophysiology. *J. Biomed. Photon. Eng.* **2**, 020201 (2016)
99. Z. Lai et al., Facile preparation of full-color emissive carbon dots and their applications in imaging of the adhesion of erythrocytes to endothelial cells. *J. Mater. Chem. B* **5**, 5259–5264 (2017)
100. J. Gatfield et al., The selezipag active metabolite ACT-333679 displays strong anti-contractile and anti-remodeling effects, but low  $\beta$ -arrestin recruitment and desensitization potential. *J. Pharm. Exp. Ther.* *jpet*.116.239665 (2017)
101. S.Y. Lee et al., Refractive index tomograms and dynamic membrane fluctuations of red blood cells from patients with diabetes mellitus. *Sci. Rep.* **7**, 1039 (2017)
102. S.Y. Lee et al., The effects of ethanol on the morphological and biochemical properties of individual human red blood cells. *PLoS ONE* **10**, e0145327 (2015)
103. S. Chowdhury, W.J. Eldridge, A. Wax, J. Izatt, Refractive index tomography with structured illumination. *Optica* **4**, 537–545 (2017)
104. J. Jung et al., Label-free non-invasive quantitative measurement of lipid contents in individual microalgal cells using refractive index tomography. *Sci. Rep.* **8**, 6524 (2018)
105. G. Kim, S. Lee, S. Shin, Y. Park, Three-dimensional label-free imaging and analysis of *Pinus* pollen grains using optical diffraction tomography. *Sci. Rep.* **8**, 1782 (2018)
106. <http://nanolive.ch>
107. <http://www.tomocube.com>
108. J. Kühn et al., Submicrometer tomography of cells by multiple-wavelength digital holographic microscopy in reflection. *Opt. Lett.* **34**, 653–655 (2009)
109. L. Yu, Z. Chen, Digital holographic tomography based on spectral interferometry. *Opt. Lett.* **32**, 3005–3007 (2007)
110. L. Yu, M.K. Kim, Wavelength-scanning digital interference holography for tomographic three-dimensional imaging by use of the angular spectrum method. *Opt. Lett.* **30**, 2092–2094 (2005)
111. Z. Wang et al., Spatial light interference tomography (SLIT). *Opt. Express* **19**, 19907–19918 (2011)
112. T. Kim et al., White-light diffraction tomography of unlabelled live cells. *Nat. Photonics* **8**, 256–263 (2014)
113. M. Mir et al., Visualizing *escherichia coli* sub-cellular structure using sparse deconvolution spatial light interference tomography. *PLoS ONE* **7**, e38916 (2012)
114. H. Ding, G. Popescu, Instantaneous spatial light interference microscopy. *Opt. Express* **18**, 1569–1575 (2010)
115. Z. Wang, G. Popescu, Quantitative phase imaging with broadband fields. *Appl. Phys. Lett.* **96**, 051117 (2010)
116. Z. Wang et al., Spatial light interference microscopy (SLIM). *Opt. Express* **19**, 1016–1026 (2011)
117. T.H. Nguyen, G. Popescu, Spatial light interference microscopy (SLIM) using twisted-nematic liquid-crystal modulation. *Biomed. Opt. Express* **4**, 1571–1583 (2013)
118. <http://phioptics.com>
119. T.H. Nguyen et al., Gradient light interference microscopy for 3D imaging of unlabeled specimens. *Nat. Commun.* **8**, 210 (2017)
120. S. Vertu, J.-J. Delaunay, I. Yamada, O. Haeberlé, Diffraction microtomography with sample rotation: influence of a missing apple core in the recorded frequency space. *Centr. Eur. J. Phys.* **7**, 22–31 (2009)

121. Y.-C. Lin, C.-J. Cheng, Sectional imaging of spatially refractive index distribution using coaxial rotation digital holographic microtomography. *J. Opt.* **16**, 065401 (2014)
122. A. Kuś et al., Tomographic phase microscopy of living three-dimensional cell cultures. *J. Biomed. Opt.* **19**, 4600 (2014)
123. M. Kujawińska et al., Problems and solutions in 3-D analysis of phase biological objects by optical diffraction tomography. *Int. J. Optomechatron.* **8**, 357–372 (2014)
124. J. Kostencka, T. Kozacki, A. Kuś, M. Kujawińska, Accurate approach to capillary-supported optical diffraction tomography. *Opt. Express* **23**, 7908–7923 (2015)
125. N.M. Dragomir, X.M. Goh, A. Roberts, Three-dimensional refractive index reconstruction with quantitative phase tomography. *Microsc. Res. Tech.* **71**, 5–10 (2008)
126. Y. Jeon, C.-K. Hong, Rotation error correction by numerical focus adjustment in tomographic phase microscopy. *Opt. Eng.* **48**, 105801 (2009)
127. T. Kozacki, R. Krajewski, M. Kujawińska, Reconstruction of refractive-index distribution in off-axis digital holography optical diffraction tomographic system. *Opt. Express* **17**, 13758–13767 (2009)
128. J. Kostencka, T. Kozacki, M. Józwick, Holographic tomography with object rotation and two-directional off-axis illumination. *Opt. Express* **25**, 23920–23934 (2017)
129. J. Kostencka, T. Kozacki, M. Dudek, M. Kujawińska, Noise suppressed optical diffraction tomography with autofocus correction. *Opt. Express* **22**, 5731–5745 (2014)
130. V. Bingelyte, J. Leach, J. Courtial, M.J. Padgett, Optically controlled three-dimensional rotation of microscopic objects. *Appl. Phys. Lett.* **82**, 829–831 (2003)
131. M.K. Kreysing et al., The optical cell rotator. *Opt. Express* **16**, 16984–16992 (2008)
132. B. Caoa et al., Rotation of single live mammalian cells using dynamic holographic optical tweezers. *Opt. Lasers Eng.* **92**, 70–75 (2017)
133. M. Habaza, B. Gilboa, Y. Roichman, N.T. Shaked, Tomographic phase microscopy with 180° rotation of live cells in suspension by holographic optical tweezers. *Opt. Lett.* **40**, 1881–1884 (2015)
134. Y.-C. Lin et al., Optically driven full-angle sample rotation for tomographic imaging in digital holographic microscopy. *Opt. Lett.* **42**, 1321–1324 (2017)
135. K. Kim, J. Yoon, Y. Park, Simultaneous 3-D visualization and position tracking of optically trapped particles using optical diffraction tomography. *Optica* **2**, 343 (2015)
136. K. Kim, Y. Park, Tomographic active optical trapping of arbitrarily shaped objects by exploiting 3D refractive index maps. *Nat. Commun.* **8**, 15340 (2017)
137. J. Gimsa, P. Marszalek, U. Loewe, T.Y. Tsong, Dielectrophoresis and electrorotation of neurospora slime and murine myeloma cells. *Biophys. J.* **60**, 749–760 (1991)
138. B. Le Saux et al., Isotropic high-resolution three-dimensional confocal micro-rotation imaging for non-adherent living cells. *J. Microsc.* **233**, 404–416 (2009)
139. M. Habaza et al., Rapid 3D refractive-index imaging of live cells in suspension without labeling using dielectrophoretic cell rotation. *Adv. Sci.* **4**, 1600205 (2017)
140. F. Merola, et al., Tomographic flow cytometry by digital holography. *Light Sci. Appl.* **6**, e16241 (2017)
141. M. Massimiliano et al., Full angle tomographic phase microscopy of flowing quasi-spherical cells. *Lab Chip* **18**, 126–131 (2017)
142. F. Merola et al., Phase contrast tomography at lab on chip scale by digital holography. *Methods* **136**, 108–115 (2018)
143. N. Lue et al., Synthetic aperture tomographic phase microscopy for 3D imaging of live cells in translational motion. *Opt. Express* **16**, 16240–16246 (2008)
144. C. Remacha, B.S. Nickerson, H.J. Kreuzer, Tomography by point source digital holographic microscopy. *Appl. Opt.* **53**, 3520–3527 (2014)
145. S. Vertu, J. Flügge, J.-J. Delaunay, O. Haeberlé, Improved and isotropic resolution in tomographic diffractive microscopy combining sample and illumination rotation. *Centr. Eur. J. Phys.* **9**, 969–974 (2011)
146. B. Simon et al., Tomographic diffractive microscopy with isotropic resolution. *Optica* **4**, 460–463 (2017)

147. B. Vinoth et al., Integrated dual-tomography for refractive index analysis of free-floating single living cell with isotropic superresolution. *Sci. Rep.* **8**, 5943 (2018)
148. R. Horstmeyer et al., Standardizing the resolution claims for coherent microscopy. *Nat. Phot.* **10**, 68–71 (2016)
149. C. Park, S. Shin, Y. Park, Generalized quantification of three-dimensional resolution in optical diffraction tomography using the projection of maximal spatial bandwidths. [arXiv:1806.01067](https://arxiv.org/abs/1806.01067)
150. E. Mudry et al., Mirror-assisted tomographic diffractive microscopy with isotropic resolution. *Opt. Lett.* **35**, 1857–1859 (2010)
151. M. Kim et al., High-speed synthetic aperture microscopy for live cell imaging. *Opt. Lett.* **36**, 148–150 (2011)
152. C. Fang-Yen et al., Video-rate tomographic phase microscopy. *J. Biomed. Opt.* **16**, 011005 (2011)
153. J. Hahn et al., Video-rate compressive holographic microscopic tomography. *Opt. Express* **19**, 7289–7298 (2011)
154. K. Kim et al., Real-time visualization of 3-D dynamic microscopic objects using optical diffraction tomography. *Opt. Express* **21**, 32269–32278 (2013)
155. G. Dardikman, M. Habaza, L. Waller, N.T. Shaked, Video-rate processing in tomographic phase microscopy of biological cells using CUDA. *Opt. Express* **24**, 11839–11854 (2016)
156. K. Lee et al., Time-multiplexed structured illumination using a DMD for optical diffraction tomography. *Opt. Lett.* **42**, 999–1002 (2017)
157. D. Jin, R. Zhou, Z. Yaqoob, P.T.C. So, Dynamic spatial filtering using a digital micromirror device for high-speed optical diffraction tomography. *Opt. Express* **26**, 428–437 (2018)
158. J.A. Rodrigo, J.M. Soto, T. Alieva, Fast label-free microscopy technique for 3D dynamic quantitative imaging of living cells. *Biomed. Opt. Express* **8**, 5507–5517 (2017)
159. G. Dardikman et al., Optimal spatial bandwidth capacity in multiplexed off-axis holography for rapid quantitative phase reconstruction and visualization. *Opt. Express* **25**, 33400–33415 (2017)
160. R. Ling et al., High-throughput intensity diffraction tomography with a computational microscope. *Biomed. Opt. Express* **9**, 2130–2141 (2018)
161. J. Bailleul et al., Tomographic diffractive microscopy: towards high-resolution 3-D real-time data acquisition, image reconstruction and display of unlabeled samples. *Opt. Commun.* **422**, 28–37 (2018)
162. W.-C. Hsu et al., Tomographic diffractive microscopy of living cells based on a common-path configuration. *Opt. Lett.* **39**, 2210–2213 (2014)
163. Y. Kim et al., Common-path diffraction optical tomography for investigation of three-dimensional structures and dynamics of biological cells. *Opt. Express* **22**, 10398–10407 (2014)
164. Y. Kim et al., Profiling individual human red blood cells using common-path diffraction optical tomography. *Sci. Rep.* **4**, 6659 (2014)
165. J.M. Soto, J.A. Rodrigo, T. Alieva, Label-free quantitative 3D tomographic imaging for partially coherent light microscopy. *Opt. Express* **25**, 15699–15712 (2017)
166. J.M. Soto, J.A. Rodrigo, T. Alieva, Optical diffraction tomography with fully and partially coherent illumination in high numerical aperture label-free microscopy [Invited]. *Appl. Opt.* **57**, A205–A214 (2018)
167. J. Li et al., Three-dimensional tomographic microscopy technique with multi-frequency combination with partially coherent illuminations. *Biomed. Opt. Express* **9**, 2526–2542 (2018)
168. Y. Ruan et al., Tomographic diffractive microscopy with a wavefront sensor. *Opt. Lett.* **37**, 1631–1633 (2012)
169. K. Kim et al., Diffraction optical tomography using a quantitative phase imaging unit. *Opt. Lett.* **39**, 6935–6938 (2014)
170. I. Iglesias, Tomographic imaging of transparent biological samples using the pyramid phase microscope. *Biomed. Opt. Express* **7**, 3049–3055 (2016)
171. P. Bon, S. Aknoun, S. Monneret, B. Wattellier, Enhanced 3D spatial resolution in quantitative phase microscopy using spatially incoherent illumination. *Opt. Express* **22**, 8654–8671 (2014)

172. P. Hosseini et al., Scanning color optical tomography (SCOT). *Opt. Express* **23**, 19752–19762 (2015)
173. J. Jung, K. Kim, J. Yoon, Y. Park, Hyperspectral optical diffraction tomography. *Opt. Express* **24**, 2006–2012 (2016)
174. C. Godavarthi et al., Superresolution with full-polarized tomographic diffractive microscopy. *J. Opt. Soc. Am. A* **32**(2), 287–292 (2015)
175. L. Quaroni, M. Obst, M. Nowak, F. Zobi, Three-dimensional mid-infrared tomographic imaging of endogenous and exogenous molecules in a single intact cell with subcellular resolution. *Angew. Chem. Int. Ed. Engl.* **54**, 318–322 (2015)
176. Y. Choi et al., Synthetic aperture microscopy for high-resolution imaging through a turbid medium. *Opt. Lett.* **36**, 4263–4266 (2011)
177. M. Kim et al., 3D differential interference contrast microscopy using synthetic aperture imaging. *J. Biomed. Opt.* **17**, 026003 (2012)
178. S.O. Isikman, et al., Lens-free optical tomographic microscope with a large imaging volume on a chip. *PNAS* 1015638108 (2011)
179. S.O. Isikman, W. Bishara, A. Ozcan, Partially coherent lensfree tomographic microscopy [Invited]. *Appl. Opt.* **50**, H253–H264 (2011)
180. W. Luo, A. Greenbaum, Y. Zhang, A. Ozcan, Synthetic aperture-based on-chip microscopy. *Light Sci. Appl.* **4**, e261 (2015)
181. F. Momey et al., Lensfree diffractive tomography for the imaging of 3D cell cultures. *Biomed. Opt. Express* **7**, 949–962 (2016)
182. A. Berdeu et al., Comparative study of fully three-dimensional reconstruction algorithms for lens-free microscopy. *Appl. Opt.* **56**, 3939–3951 (2017)
183. C. Chao Zuo, et al., Lensless phase microscopy and diffraction tomography with multi-angle and multi-wavelength illuminations using a LED matrix. *Opt. Express* **23**, 14314–14328 (2015)
184. L. Tian, L. Waller, Quantitative differential phase contrast imaging in an LED array microscope. *Opt. Express* **23**, 11394–11403 (2015)
185. T. Kozacki, M. Kujawińska, P. Książewski, Investigation of limitations of optical diffraction tomography. *Opto-Electron. Rev.* **15**, 102–109 (2007)
186. B.D. Arhatari, F. De Carlo, A.G. Peele, Direct quantitative tomographic reconstruction for weakly absorbing homogeneous phase objects. *Rev. Sci. Instrum.* **78**, 053701 (2007)
187. S.J. LaRoque, E.Y. Sidky, X. Pan, Accurate image reconstruction from few-view and limited-angle data in diffraction tomography. *J. Opt. Soc. Am. A* **25**, 1772–1782 (2008)
188. G.R. Myers, D.M. Paganin, T.E. Gureyev, S.C. Mayo, Phase-contrast tomography of single-material objects from few projections. *Opt. Express* **16**, 908–919 (2008)
189. L. Rigon, A. Astolfo, F. Arfelli, R.H. Menk, Generalized diffraction enhanced imaging: application to tomography. *Eur. J. Radiol.* **68**, S3–S7 (2008)
190. Y. Sung, R.R. Dasari, Deterministic regularization of three-dimensional optical diffraction tomography. *J. Opt. Soc. Am. A* **28**, 1554–1561 (2011)
191. A.D. Yablon, Multifocus tomographic algorithm for measuring optically thick specimens. *Opt. Lett.* **38**, 4393–4396 (2013)
192. M.H. Jenkins, T.K. Gaylord, Three-dimensional quantitative phase imaging via tomographic deconvolution phase microscopy. *Appl. Opt.* **54**, 9213–9227 (2015)
193. J. Lim et al., Comparative study of iterative reconstruction algorithms for missing cone problems in optical diffraction tomography. *Opt. Express* **23**, 16933–16948 (2015)
194. L. Su, L. Ma, H. Wang, Improved regularization reconstruction from sparse angle data in optical diffraction tomography. *Appl. Opt.* **54**, 859–868 (2015)
195. J. Kostencka et al., Holographic tomography with scanning of illumination: space-domain reconstruction for spatially invariant accuracy. *Biomed. Opt. Express* **7**, 4086–4101 (2016)
196. M. Malek et al., Microtomography imaging of an isolated plant fiber: a digital holographic approach. *Appl. Opt.* **55**, A111–A121 (2016)
197. E. Soubies, T. Pham, M. Unser, Efficient inversion of multiple-scattering model for optical diffraction tomography. *Opt. Express* **25**, 21786–21800 (2017)

198. S. Tomioka et al., Weighted reconstruction of three-dimensional refractive index in interferometric tomography. *Appl. Opt.* **56**, 6755–6764 (2017)
199. M. Lee, S. Shin, Y. Park, Reconstructions of refractive index tomograms via a discrete algebraic reconstruction technique. *Opt. Express* **25**, 27415–27430 (2017)
200. J. Lim et al., Beyond Born-Rytov limit for super-resolution optical diffraction tomography. *Opt. Express* **25**, 30445–30458 (2017)
201. Y. Bao, T.K. Gaylord, Iterative optimization in tomographic deconvolution phase microscopy. *J. Opt. Soc. Am. A* **35**, 652–660 (2018)
202. U.S. Kamilov et al., Learning approach to optical tomography. *Optica* **2**, 517–522 (2015)
203. J. Yoon et al., Identification of non-activated lymphocytes using three-dimensional refractive index tomography and machine learning. *Sci. Rep.* **7**, 6654 (2017)
204. Y. Rivenson et al., Phase recovery and holographic image reconstruction using deep learning in neural networks. *Light Sci. Appl.* **7**, 17141 (2018)
205. H. Qiao et al., GPU-based deep convolutional neural network for tomographic phase microscopy with  $\ell_1$  fitting and regularization. *J. Biomed. Opt.* **23**, 066003 (2018)
206. A. Sentenac, J. Mertz, Unified description of three-dimensional optical diffraction microscopy: from transmission microscopy to optical coherence tomography: tutorial. *J. Opt. Soc. Am. A* **35**, 748–754 (2018)
207. M. Sarmis et al., High-resolution reflection tomographic diffractive microscopy. *J. Mod. Opt.* **57**, 740–745 (2010)
208. H. Liu et al., Tomographic diffractive microscopy and multiview profilometry with flexible aberration correction. *Appl. Opt.* **53**, 748–755 (2014)
209. K. Lee, Quantitative phase imaging techniques for the study of cell pathophysiology: from principles to applications. *Sensors* **13**, 4170–4191 (2013)
210. H. Majeed et al., Quantitative phase imaging for medical diagnosis. *J. Biophoton.* **10**, 177–205 (2017)
211. J. Nadeau, Y.K. Park, G. Popescu (eds.), Methods in quantitative phase imaging in life science. *Methods* **136**, 1–168 (2018)
212. N. Smith, B. Kemper, K. Fujita, S.-W. Chu, N. Pavillon, M. Booth (eds.), Trends in label-free imaging. *Opt. Commun.* **422**, 1–84 (2018)
213. The interested reader will find detailed introductions to these techniques on: <https://www.olympus-lifescience.com/en/microscope-resource/> or, <https://www.microscopyu.com>

# Chapter 5

## Near-Field Scanning Optical Microscope Combined with Digital Holography for Three-Dimensional Electromagnetic Field Reconstruction



Nancy Rahbany, Ignacio Izeddin, Valentina Krachmalnicoff,  
Rémi Carminati, Gilles Tessier and Yannick De Wilde

**Abstract** Near-field scanning optical microscopy (NSOM) has proven to be a very powerful imaging technique that allows overcoming the diffraction limit and obtaining information on a scale much smaller than what can be achieved by classical optical imaging techniques. This is achieved using nanosized probes that are placed in close proximity to the sample surface, and thus allow the detection of evanescent waves that contain important information about the properties of the sample on a sub-wavelength scale. In particular, some aperture-based probes use a nanometer-sized hole to locally illuminate the sample. The far-field radiation of such probes is essential to their imaging properties, but cannot be easily estimated since it highly depends on the environment with which it interacts. In this chapter, we tackle this problem by introducing a microscopy method based on full-field off-axis digital holography that allows us to study in details the three-dimensional electromagnetic field scattered by a NSOM probe in different environments. We start by describing the NSOM and holography techniques independently, and continue by highlighting the advantage of combining both methods. We present a comparative study of the reconstructed light from a NSOM tip located in free space or coupled to transparent and plasmonic media. While far-field methods, such as back-focal plane imaging, can be used to infer the directionality of angular radiation patterns, the advantage of our technique is that a single hologram contains information on both the amplitude and phase of the scattered light, allowing to reverse numerically the propagation of the electromagnetic field toward the source. We also present Finite-Difference Time-Domain (FDTD) simulations to model the radiation of the NSOM tip as a superposition of a magnetic and an electric dipole. We finally propose some promising applications that could be performed with this combined NSOM-holography technique.

---

N. Rahbany · I. Izeddin · V. Krachmalnicoff · R. Carminati · Y. De Wilde (✉)  
Institut Langevin, ESPCI Paris, CNRS, PSL University, 1 rue Jussieu, 75005 Paris, France  
e-mail: [yannick.dewilde@espci.fr](mailto:yannick.dewilde@espci.fr)

G. Tessier  
Sorbonne Université, CNRS, INSERM, Institut de La Vision, 17 Rue Moreau, 75012 Paris, France  
e-mail: [gilles.tessier@sorbonne-universite.fr](mailto:gilles.tessier@sorbonne-universite.fr)

© Springer Nature Switzerland AG 2019  
V. Astratov (ed.), *Label-Free Super-Resolution Microscopy*,  
Biological and Medical Physics, Biomedical Engineering,  
[https://doi.org/10.1007/978-3-030-21722-8\\_5](https://doi.org/10.1007/978-3-030-21722-8_5)

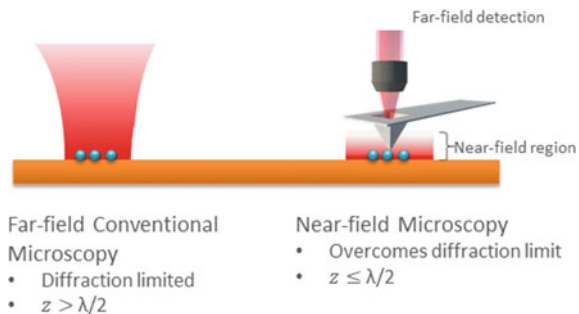
## 5.1 Introduction to Near-Field Scanning Optical Microscopy (NSOM)

*Near-field Scanning Optical Microscopy* (NSOM) is an important super-resolution imaging technique which is used to overcome the diffraction limit and study light-matter interaction at a subwavelength scale [1].

Since the high-frequency spatial components of the electromagnetic (EM) field are contained in the near field and decay exponentially with the distance from the sample, they are entirely lost when using far-field optical microscopy techniques. Therefore, the idea of near-field microscopy is to collect the information contained in the near field and make it measurable with traditional far-field detection tools. Scattering-type NSOM uses a scanning probe, which is typically a tip with a sub- $\lambda$  sized scatterer at its extremity, to measure the evanescent waves that are confined in the near field. The evanescent signal is scattered from the near field and is converted to a far-field propagating wave which is directed to a detector measuring its intensity. Then, the sample is scanned with respect to the tip to obtain a complete image of the scanned area point by point. Probing the near field allows to overcome the diffraction limit, which is why NSOM has proven to be a powerful “super-resolution” technique. The method allows one indeed to perform sub- $\lambda$  imaging, or to detect purely evanescent fields such as surface plasmon polaritons (SPPs). A schematic is shown in Fig. 5.1. The resolution of an image obtained by NSOM depends on three parameters: the distance between adjacent points in the scanned area, the size of the tip, and the distance between the tip and the sample. Evidently, the highest resolution is obtained for a small tip apex and a small tip-sample distance. Figure 5.2 shows an example of a NSOM image taken from [2], where the propagating SPPs generated by metallic grating couplers are clearly detected.

The history of the NSOM technique dates back to the beginning of the twentieth century, when E. Synge in collaboration with A. Einstein [3, 4] came up with two concepts that led to the two main NSOM families known today: the apertureless scattering NSOM, and the aperture NSOM. Experimentally, the first near-field optical microscope functioning in the visible range was developed in 1986 [1, 5].

**Fig. 5.1** Schematic of the advantages of NSOM compared to conventional far-field microscopy



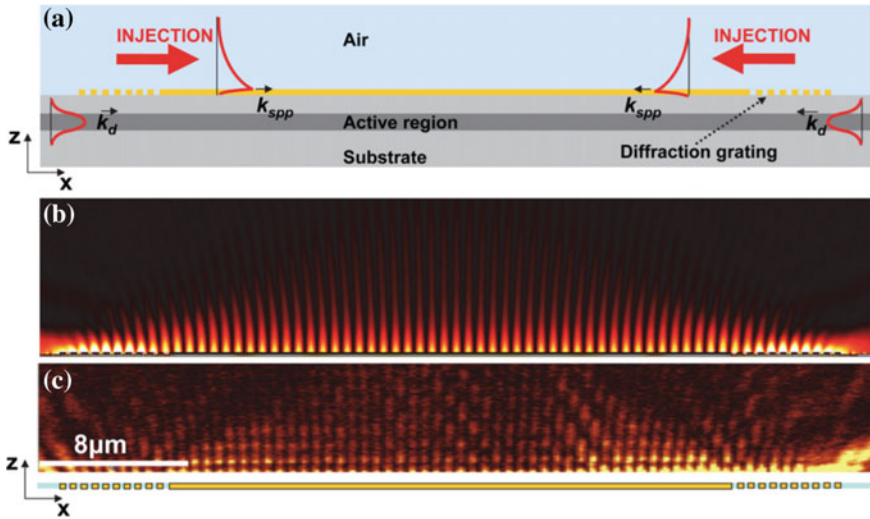


**Fig. 5.2** Scattering NSOM measurement: **a** Schematic side view of the metallic grating couplers device imaged here. Details about the structure can be found in [9]. The red curves schematically represent the mode profiles of waveguided SPP modes. **b** Color-plot of the calculated squared modulus of the electric field in the  $x$ - $z$  plane (SPP interference pattern). **c** NSOM measurement in the  $x$ - $z$  plane, i.e., NSOM signal as a function of the tip-to-surface distance at several  $x$ -positions on the sample. The measurement qualitatively agrees with the simulation in panel **b**. Figure taken from [2]

- Apertureless scattering NSOMs include a diffusing tip or a nanoparticle that scatters the near-field signal into the far field. In free space, such tips are usually modeled as effective electric dipoles, where the electric field component parallel to the tip axis is enhanced [6–8].
- Aperture NSOMs use tips fitted with a nano-aperture. This tip is sometimes made of metal, with a hole at its extremity, or most often a tapered metal-coated optical fiber (except for its end, where the aperture is located). Aperture NSOM tips can therefore be used in two different ways: as a collection aperture to detect the near-field signal, or as a nanoscale source of light through which the sample is illuminated locally. In the latter case, a precise knowledge of the characteristics of this nanosource is essential in order to quantitatively understand images obtained by scanning it above the sample. In particular, the shape and directionality (scattering diagram) of such sources are essential to the imaging properties of such systems, but are poorly known, either for NSOM tips in air, or in contact with a surface.

Aperture NSOM tips were first studied theoretically by Bethe [10] and were modeled as a subwavelength hole in a perfectly conducting plane screen. Its radiation in free space corresponded to that of a coherent superposition of a magnetic and an electric dipole [6, 11–13]. However, recent studies have shown that metal-coated hollow pyramidal probes behave solely as tangential magnetic dipoles when placed

in the vicinity of metallic nanoantennas [14]. Therefore, characterizing NSOM probes is not a straightforward and easy task. Their radiation patterns strongly depend on the type of probe as well as on the environment that they interact with. When such probes are placed close to the surface of a sample, the scattered field is highly affected by multiple reflections and interferences at the surface. This strong coupling between the probe and the surface makes it even more difficult to predict their EM radiation pattern in a given environment [15, 16].

In addition to its detection role, a NSOM tip can also be used to excite and launch surface plasmon polaritons on the surface of metallic films [17]. It is important to mention here that the excitation of surface plasmons can also be performed by other techniques such as exciting surface defects [6, 17], point-like dipoles [18], and tunneling electrons [19, 20], in addition to classical techniques such as prism or grating couplers. The far-field radiation pattern of leaky surface plasmons launched on metallic thin films by NSOM tips was previously studied using conventional back-focal plane imaging techniques [17, 21, 22]. In such techniques, the intensity of the EM field is accurately measured in the Fourier plane of an optical system [23, 24]. However, no information about the phase is obtained. In order to fully characterize the scattered EM field in three dimensions, both the intensity and the phase must be calculated. For this reason, we developed a combined NSOM-holography technique to accurately describe the radiation patterns of individual NSOM probes as a function of the local environment. The main advantage of our combined system is that it can directly deliver information about both the amplitude and the phase of the scattered light through the NSOM probe from a single recorded hologram. Then, following the procedure described in Sect. 5.2, we can reconstruct the full three-dimensional scattered field coupled to the environment [25]. It is important to mention that Digital Holographic Microscopy was previously combined with NSOM for the purpose of achieving super-resolution imaging through a disordered scattering medium that is illuminated by subwavelength tips that act as point-like sources [26].

## 5.2 Principles of Digital Holography

*Holography* is a technique that combines the processes of interference and diffraction to record and reconstruct the amplitude and phase of an electromagnetic field in three dimensions. It was discovered in 1948 by Denis Gabor [27, 28] who received a Nobel Prize in Physics for his work later in 1971. It wasn't until the development of the lasers in 1960 that holography took its place in the optics domain [29].

The advantage of holography over conventional photography techniques is that it contains information about the entire three-dimensional wavefield which is contained in interference patterns. These patterns arise when the wave scattered by the object, or *object wave*, is illuminated by a *reference wave*, creating a *hologram*. This hologram is then illuminated with the reference wave again to obtain the three-dimensional reconstructed image of the electromagnetic field scattered by the object [30–36].

The general holography method is depicted in Fig. 5.3. For recording a hologram (Fig. 5.3a, left image), light from the laser is split into a reference beam and an object beam that illuminates the object. Both beams are directed to a detector where they interfere creating a hologram. For the reconstruction process (Fig. 5.3a, right image) of photographic-plate holograms, the developed hologram is illuminated with the reference wave. This creates a *virtual image* of the three-dimensional reconstructed object at a distance  $d$ , which is the position where the object had been before. Nowadays, holography is almost exclusively conducted using cameras, and the latter reconstruction step is performed digitally.

Mathematically, the reference and object waves,  $E_R$  and  $E_O$ , are modeled by complex electric fields with amplitude  $A$  and phase  $\varphi$ :

$$E_R(x, y, z) = A_R(x, y, z)\exp(i\varphi_R(x, y, z)) \tag{5.1}$$

$$E_O(x, y, z) = A_O(x, y, z)\exp(i\varphi_O(x, y, z)) \tag{5.2}$$

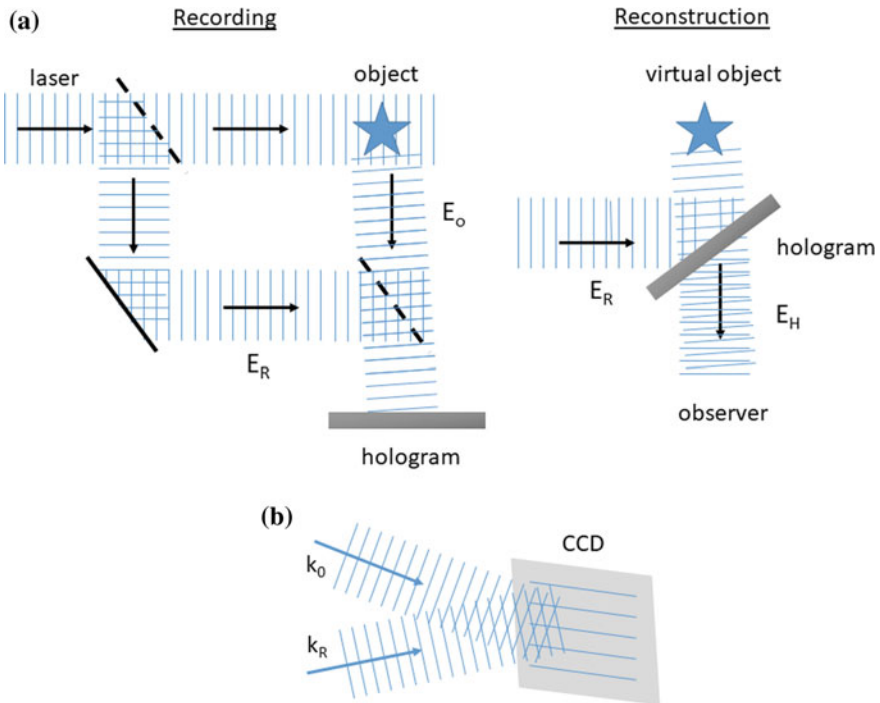


**Fig. 5.3** a Schematic of the holography method: hologram recording (left), and reconstruction (right). b Object and reference wavefronts incident on the detector plane shifted by a small angle, in a configuration known as *off-axis* holography

The recorded intensity at the detector plane ( $z = 0$ ) is expressed as the square of the two complex fields:

$$\begin{aligned}
 I(x, y, 0) &= |E_O(x, y, 0) + E_R(x, y, 0)|^2 \\
 &= (E_O(x, y, 0) + E_R(x, y, 0)) \cdot (E_O(x, y, 0) + E_R(x, y, 0))^* \\
 &= E_O(x, y, 0)E_O^*(x, y, 0) + E_R(x, y, 0)E_R^*(x, y, 0) \\
 &\quad + E_O(x, y, 0)E_R^*(x, y, 0) + E_R(x, y, 0)E_O^*(x, y, 0) \quad (5.3)
 \end{aligned}$$

The first term is the intensity of the scattered light from the object  $I_O(x, y, 0) = E_O(x, y, 0)E_O^*(x, y, 0)$ . The second term is the intensity of the reference wave  $I_R(x, y, 0) = E_R(x, y, 0)E_R^*(x, y, 0)$ . Unlike the last two terms, these terms contain no information about the phase, and are therefore useless for the reconstruction process.

The reconstruction procedure requires the illumination of the hologram with the reference wave. The resulting wave  $E_H$  of the virtual image is

$$\begin{aligned}
 E_H(x, y, z) &\propto E_R(x, y, z) \cdot I(x, y, 0) \\
 E_H(x, y, z) &\propto E_R(x, y, z) \cdot (I_R(x, y, 0) + I_O(x, y, 0)) \\
 &\quad + E_R(x, y, z) \cdot (E_O(x, y, 0) + E_R^*(x, y, 0)) \\
 &\quad + E_R(x, y, z) \cdot (E_R(x, y, 0) + E_O^*(x, y, 0)) \quad (5.4)
 \end{aligned}$$

The first term is the zeroth diffraction order and corresponds to the reference wave. The second term is the  $+1$  diffraction order and corresponds to the virtual image, or the wave diffracted by the object which we care about in this study. The third term is the  $-1$  diffraction order and corresponds to a conjugate object image, called the *real image*, positioned symmetrically with respect to the virtual image.

One wishes to be able to select only the  $+1$  order and suppress the other two. This is done experimentally by *off-axis* holography (Fig. 5.3b), where the reference beam is shifted by a small angle with respect to the object beam [34]. As a consequence, the three diffraction orders are separated, allowing the selection of the desired order easily. These operations are usually performed in the Fourier space, or wave vectors  $k$ -space.

A fast Fourier transform (FFT) algorithm is used to reconstruct the original field. The hologram first undergoes a Fourier transform into the frequency space where spatial filtering of the unwanted diffraction orders takes place. The obtained complex field is then propagated toward the source before it is finally transformed back to the spatial domain. This is done in 4 main steps as follows:

1. *A first Fourier Transform* to move to the frequency space:

$$\hat{E}_H(k_x, k_y, 0) = \text{FT}\{E_H(x, y, 0)\}$$

2. *Spatial Filtering* in  $k$ -space to select the  $+1$  order and eliminate the other two:

$$\hat{E}_H^{\text{SF}}(k_x, k_y, 0) = \text{SF} \left\{ \hat{E}_H(k_x, k_y, 0) \right\}$$

3. *Propagation* in k-space from  $z = 0$  to any plane  $z$ . This is done by multiplying the resulting complex field by a  $z$ -propagation function  $G(k_x, k_y, z) = \exp(ik_z z)$ :

$$\hat{E}_H^{\text{SF}}(k_x, k_y, z) = \hat{E}_H^{\text{SF}}(k_x, k_y, 0) \cdot G(k_x, k_y, z)$$

4. *Second Fourier Transform* to move back to the spatial domain:

$$E_O(x, y, z) = \text{FT}^{-1} \left\{ \hat{E}_H^{\text{SF}}(k_x, k_y, z) \right\}$$

An example of the above reconstruction procedure is presented in Fig. 5.4. Here, we use an aperture NSOM tip in contact with a sample made up of a 40 nm gold film on a glass substrate. A typical hologram recorded in the plane of the camera is shown in Fig. 5.4a. This hologram is the result of interference between the light scattered through the aperture probe and the reference beam. Because of our off-axis configuration, interference fringes can be clearly seen (Fig. 5.4a inset). The first step of the reconstruction (Fourier transform of the recorded real space hologram) is shown in Fig. 5.4b, where we can clearly see the three diffraction orders separated in k-space. The zeroth order is seen at the center, and the +1 and -1 diffraction orders are separated symmetrically on both sides, also because of the off-axis configuration. The +1 interference term needed to reconstruct the 3D image (highlighted by a red circle) is chosen and the two other terms are filtered out. We then propagate the filtered Fourier transform of the hologram in k-space by multiplying by the propagator  $G$ . Finally, an inverse Fourier transform is performed which allows us to calculate the complex electromagnetic field in any  $z$  plane from the plane of the camera up to the plane of the NSOM tip. Piling up all the images together gives us the 3D reconstructed EM field scattered from the probe, where both the amplitude and phase can be calculated from a single hologram. Examples of the reconstructed images of intensity scattered through the substrate are shown in Fig. 5.4c for  $z = 10 \mu\text{m}$  below the tip up to the contact position ( $z = 0 \mu\text{m}$ ).

### 5.3 Near-Field Scanning Optical Microscopy Combined with Digital Holography

In this section, we describe the results that we obtained with our integrated holography-NSOM technique, where we study the light scattered by nanosized probes in various environments. We observe that the aperture tip in free space scatters light mainly in the forward direction with a broad angular distribution. When it is placed in contact with a glass substrate, light is scattered exactly at an angle matching the critical angle of an air/glass interface. Finally, when the tip is placed

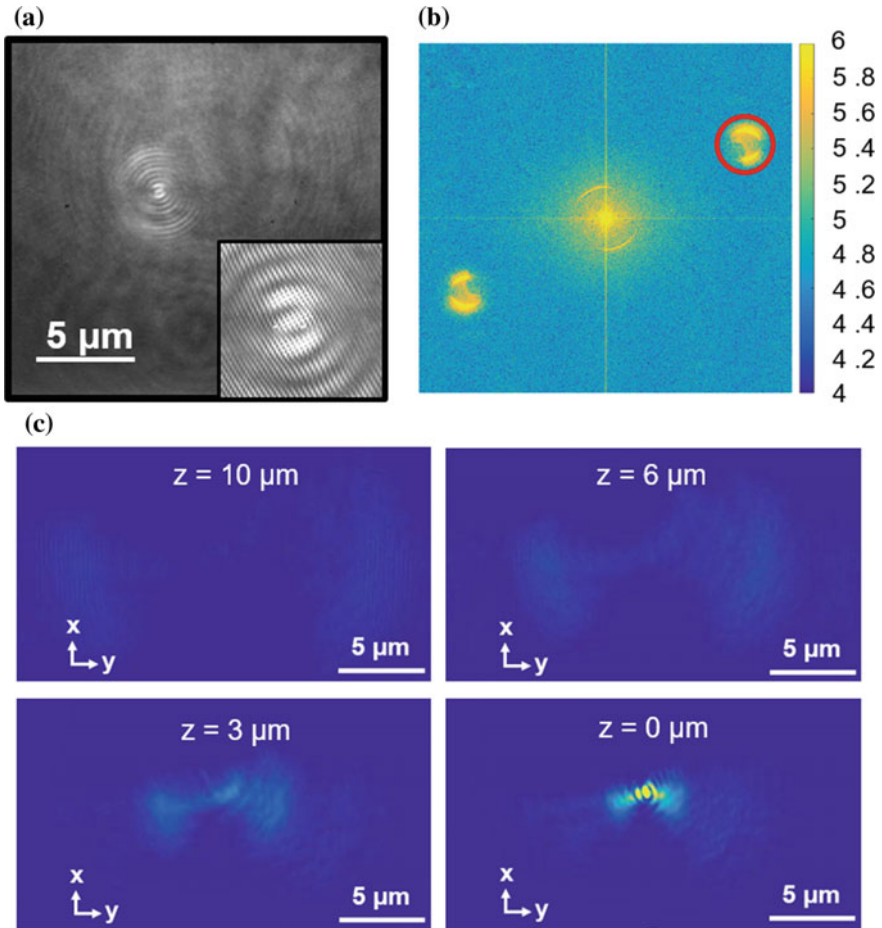


**Fig. 5.4** **a** Procedure for the reconstruction of the scattered EM field. **a** Recorded hologram resulting from the interference between the reference beam and the light scattered by a NSOM probe through a plasmonic metal layer. Inset: magnified image showing the interference fringes. **b** Fourier transform of the hologram showing the three diffraction orders in  $k$ -space: zeroth order of diffraction in the center,  $+1$  interference term (highlighted by the red circle, yields the virtual image after reconstruction) and the  $-1$  interference term (real image). **c** Images of the field scattered by the tip in planes perpendicular to the tip axis, at distances varying between  $z = 0$  and  $z = 10 \mu\text{m}$  from the tip

in contact with a plasmonic metallic sample, leaky surface plasmons are observed at a supercritical emission angle. We also perform Finite-Difference Time-Domain (FDTD) simulations that support a model of the NSOM tip as a superposition of electric and magnetic dipoles.

### 5.3.1 Experimental Setup

In Fig. 5.5, we show a schematic of our optical setup, which is made up of a Mach-Zehnder off-axis interferometer combined with a commercial NSOM (WITec GmbH alpha 300 s) [37] (figure taken from [38]). In our experiments, we use a single mode He-Ne laser (Research Electro Optics R-32413,  $\lambda = 633 \text{ nm}$ ,  $P = 35 \text{ mW}$ ) that is coupled to a 90-10 fiber splitter. This splits the incident light into a sample beam with 90% of the initial power and a reference beam with the remaining 10%. We then focus our sample beam through a  $20\times$ ,  $\text{NA} = 0.4$  objective at the apex of a  $150 \text{ nm}$   $\text{SiO}_2$  pyramidal aperture probe with an angle of  $\sim 70^\circ$ , coated with  $120 \text{ nm}$  of

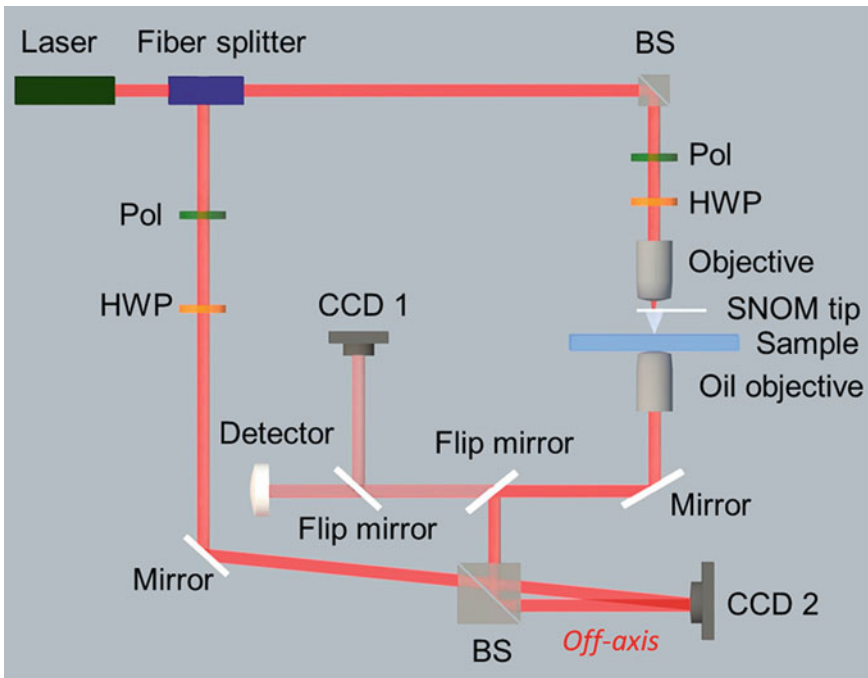


**Fig. 5.5** Schematic of the optical setup: an off-axis digital holographic microscope (DHM) is combined with a near-field scanning optical microscope (NSOM) using a metal-coated hollow pyramidal aperture tip. BS: beam splitter, Pol: polarizer, HWP: half-wave plate, CCD: charge coupled device camera. Figure taken from [38]

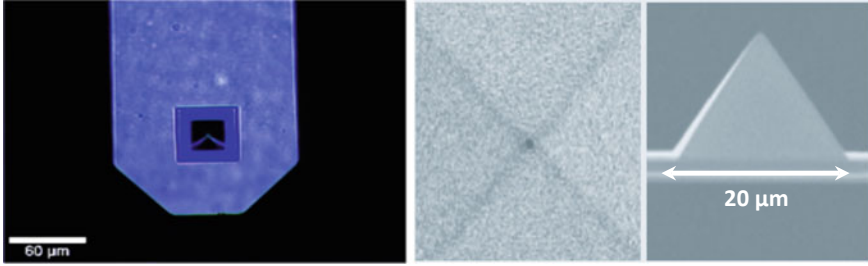


**Fig. 5.6** Optical and SEM images of the NSOM probe with an aperture size  $\sim 150$  nm. Images provided by the WITec company [39]

aluminum (Al). This tip is placed either in free space or in contact with the sample to be studied. A closer look at this type of probes is given in the optical and SEM images of Fig. 5.6 (provided by the WITec company [39]). To finely control the relative position of the sample and the tip, we place our sample on a piezoelectric three-axis translation stage. Then the light transmitted through the tip apex is collected with a  $100\times$ ,  $NA = 0.9$  objective when the tip is in free space, and a  $100\times$ ,  $NA = 1.4$  oil immersion objective in the presence of a sample.

It is then directed to a CMOS camera (Photon Focus MV-D1024  $\times$  10–160-CL, sensor resolution:  $1024 \times 1024$ ,  $8 \mu\text{m} \times 8 \mu\text{m}$  pixel matrix, 0.2 s exposure time). The reference beam is also sent with a few degree shift to the CMOS (off-axis configuration), where interference with the sample beam occurs. This detected hologram is all we need experimentally to be able to calculate the amplitude and phase of the scattered field and reconstruct the 3D pattern. Maximum contrast is attained by placing a polarizer and a half-wave plate in the path of both the sample and reference beams, ensuring that identical linear polarizations are being used. The reconstruction procedure is carried out numerically by a fast Fourier transform (FFT) algorithm following the procedure described in Sect. 5.2.

### 5.3.2 3D Reconstructed EM Field Through Different Media

With this method, we characterize the scattered radiation pattern of a hollow NSOM probe placed in free space, and coupled to two types of surfaces: a transparent glass sample made of a  $160 \mu\text{m}$  thick glass coverslip (VWR Micro Cover Glasses, No. 1), and a plasmonic sample made of a  $40 \text{ nm}$  gold film evaporated on an identical glass coverslip. The numerical analysis described in Fig. 5.4 relies on the method proposed by Cuche et al. [25, 34]. In our calculations, we approximate the nanoaperture as a point-like source, and thus account for the fast decay of the optical intensity as  $\rho^{-2}$ , where  $\rho$  is the distance to the tip in spherical coordinates. Therefore, all the intensity graphs are multiplied by  $\rho^2$  for clearer representation purposes.

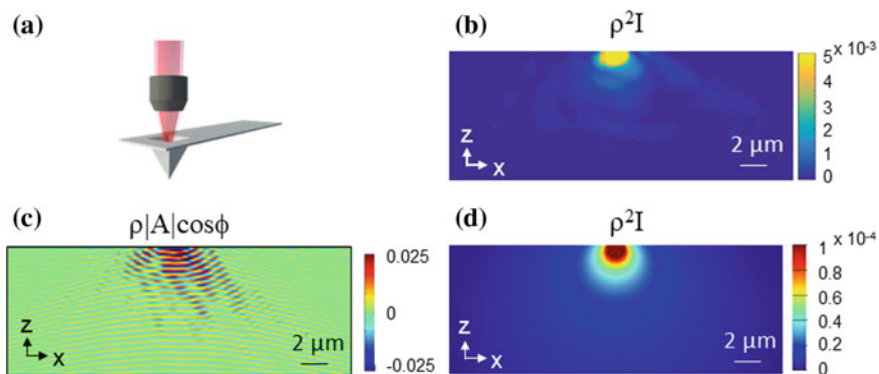


**Fig. 5.7** Reconstructed EM field scattered from the hollow metal-coated aperture probe placed in air (free space). **b** Intensity profile in the  $x$ - $z$  plane along the axis of the tip. For clarity, the intensity values are multiplied by  $\rho^2$ . **c** Complex EM field represented by the product  $\rho|A(x, y, z)|\cos(\phi(x, y, z))$ , where  $A(x, y, z)$  is the amplitude, and  $\phi(x, y, z)$  the phase. Wavefronts are clearly observed. **d** Corresponding FDTD simulated intensity multiplied by  $\rho^2$

We start by representing the reconstructed EM field for the probe placed in free space (Fig. 5.7a). A 2D cross-section is taken in the  $x$ - $z$  plane that is perpendicular to the sample surface ( $x$ - $y$ ), contains the axis of the linearly polarized illumination ( $x$ ), and is perpendicular to the axis of the cantilever ( $y$ ). We chose to calculate the intensity (Fig. 5.7b), as well as the amplitude  $|A(x, y, z)|$  multiplied by the cosine of the corresponding phase  $\cos \phi(x, y, z)$  (Fig. 5.7c) which allows us to easily observe the wavefronts of the propagating field. A map of the phase alone can also be reconstructed with our method [34]. From these results, we infer that a tip placed in free space, or in other words, without any coupling to an external environment, behaves as a Lambertian point source, scattering an EM field centered about  $\theta = 0^\circ$  with a broad angular distribution. In addition, Finite Difference Time-Domain (FDTD) simulations were performed to compare these experimental results to the theoretical description. Those simulations were done using the Lumerical Solutions software, where our metal-coated aperture probe is modeled as a superposition of lateral magnetic ( $M_y \propto H_y$ ) and electric dipoles ( $P_x \propto E_x$ ) of respective strengths 2 and 1, with  $x$  being the direction parallel to the incident light polarization direction. This model is adapted from the work of Obermüller and Karrai on the free space radiation of metal coated aperture tips [11]. In our simulations, we place a frequency-domain field monitor in the  $x$ - $z$  plane at the position of the NSOM tip, which allows us to calculate the complex EM intensity up to a distance of  $10 \mu\text{m}$  in the substrate. We place another monitor in the  $x$ - $y$  plane at a distance of  $10 \mu\text{m}$  below the sample surface, which determines using Fourier transform calculations, the projection of the scattered EM field into the far field. We use perfectly matched layer (PML) absorbing boundary conditions (32 PML layers) that are impedance-matched to the simulation region and its materials, and the value of the complex permittivity of gold is  $\epsilon_{\text{gold}} = -12.047 + 1.163i$  at 633 nm, taken from Olmon et al. [40]. It is important to note here

that the simulations give only a qualitative approximation of the EM field radiated from the probes. This is due to two main reasons. First, this model can only be used to accurately describe small radiation angles [41], and second, the subwavelength details of the geometry of the metal-coated hollow probe and its interaction with two plane metal/dielectric interfaces are not taken into account [42]. The latter interaction can become important when the tip is coupled to a plasmonic sample [18, 20]. We see from Fig. 5.7d that the simulation results are in good agreement with the experimental results. Note that this agreement is not achieved if the probe is modelled as an electric or magnetic dipole only, which confirms the fact that such hollow probes are best modelled as a superposition of perpendicular electric and magnetic dipoles.

Subsequently, we perform the same analysis for the tip placed in contact with the transparent glass sample (Fig. 5.8), and then with the plasmonic gold film sample (Fig. 5.9). For the glass sample, we observe that in addition to the forward scattering around  $\theta = 0^\circ$ , light emerges along two preferred directions that correspond exactly to the critical angle of the air–glass interface ( $|\theta_{c,\text{glass}}| = 41.8^\circ$  from Snell’s law). For the gold-coated sample, we observe that leaky surface plasmons are launched and emerge into the substrate at the resonance angles that satisfy the phase matching condition at the air–gold interface. This is calculated by the following conservation of momentum equation:

$$n_{\text{glass}} \frac{2\pi}{\lambda} \sin\theta_{c,\text{gold}} = \text{Re} \left\{ \frac{2\pi}{\lambda} \sqrt{\frac{\varepsilon_{\text{gold}}}{\varepsilon_{\text{gold}} + 1}} \right\} \quad (5.5)$$

where  $n_{\text{glass}}$  is the index of refraction of the glass substrate,  $\lambda$  is the incident excitation wavelength, and  $\varepsilon_{\text{gold}}$  is the complex permittivity of the gold film. Using the index of refraction of the glass coverslip provided by the manufacturer ( $n_{\text{glass}} = 1.525$ , from

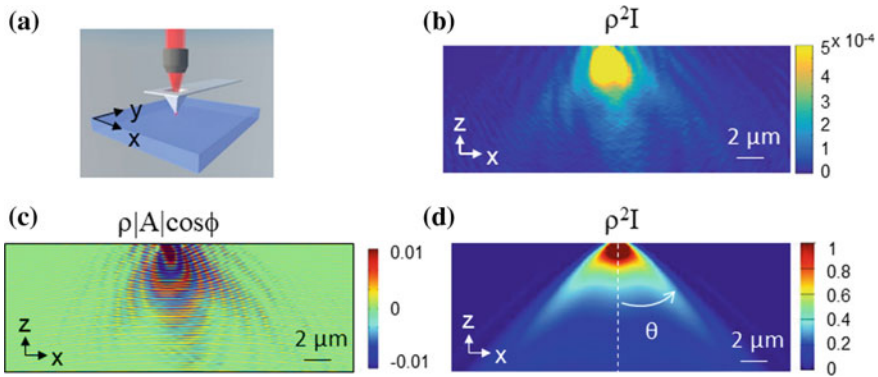


**Fig. 5.8** Reconstructed EM field scattered from the hollow metal-coated aperture probe placed in contact with the transparent glass substrate. **b** Intensity profile in the  $x$ – $z$  plane along the axis of the tip. For clarity, the intensity values are multiplied by  $\rho^2$ . **c** Complex EM field represented by the product  $\rho|A(x, y, z)|\cos(\phi(x, y, z))$ , where  $A(x, y, z)$  is the amplitude, and  $\phi(x, y, z)$  the phase. Wavefronts are clearly observed. **d** Corresponding FDTD simulated intensity multiplied by  $\rho^2$

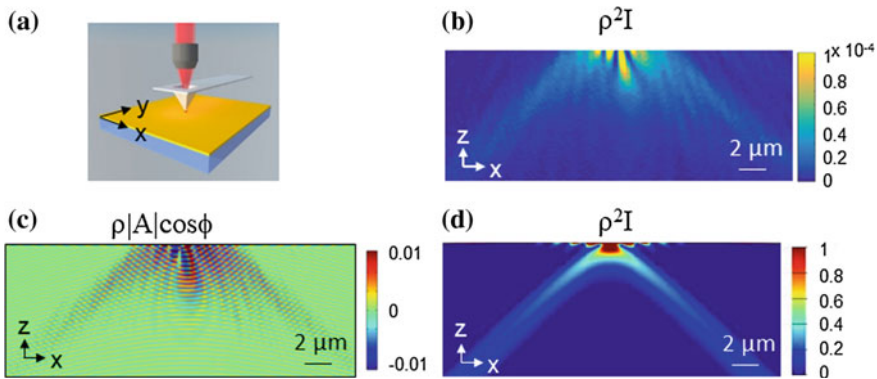


**Fig. 5.9** Reconstructed EM field scattered from the hollow metal-coated aperture probe placed in contact with the plasmonic sample made of a gold thin film on a glass substrate. **b** Intensity profile in the  $x$ - $z$  plane along the axis of the tip. For clarity, the intensity values are multiplied by  $\rho^2$ . **c** Complex EM field represented by the product  $\rho |A(x, y, z)| \cos(\phi(x, y, z))$ , where  $A(x, y, z)$  is the amplitude, and  $\phi(x, y, z)$  the phase. Wavefronts are clearly observed. **d** Corresponding FDTD simulated intensity multiplied by  $\rho^2$

VWR International [43]),  $\lambda = 633 \text{ nm}$ , and  $\varepsilon_{\text{gold}} = -12.047 + 1.163i$  (from Olmon et al. [40]), we find that  $|\theta_{\text{c, gold}}| = 43.3^\circ$ . We are able to detect such emission angles experimentally because of the use of an oil objective with a high numerical aperture. FDTD simulation results agree with the experimental results for both the transparent (Fig. 5.8d) and the plasmonic sample (Fig. 5.9d).

The directional emission of the leaky surface plasmons observed at the two resonance angles in the presence of the gold film clarifies the presence of the two narrow lobes seen in the Fourier transform image of the hologram (Fig. 5.4b). Because the probe is illuminated with linearly polarized light, surface plasmons are excited along a preferred direction which results in the two lobes observed both in  $k$ -space and in the reconstructed images in real space [17]. We also notice that due to the interference between the generated surface plasmons and the transmitted leaked radiation, fringes in the gold film are observed in both the experimental and simulation results (Fig. 5.9b, d) [26]. This behavior is also seen in the  $x$ - $y$  intensity images presented in Fig. 5.10 that show the two lobes of the surface plasmons excited by the incident linear illumination [6, 17]. These results highly resemble the results obtained by Drezet et al. [18] that are given in Fig. 5.10d.

### 5.3.3 Characterization of the Angular Scattering

From the results presented in the previous section, we can quantify the angular radiation patterns of the light scattered by the NSOM tip through different environments. In the graphs of Fig. 5.11, we plot the normalized intensity of the scattered light as a

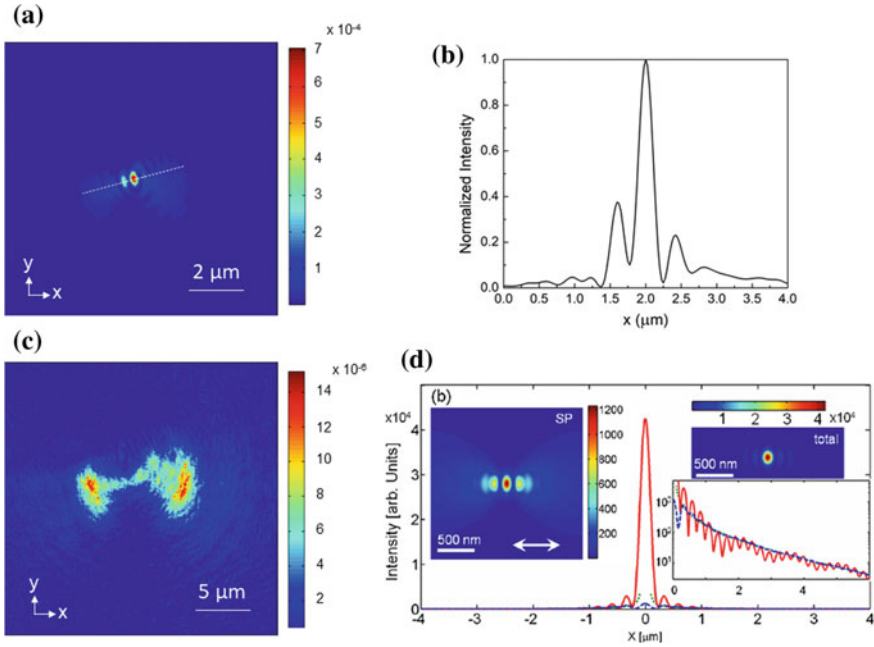


**Fig. 5.10** Reconstructed intensity of the scattered EM field calculated in the  $x$ - $y$  plane at **a** the surface of the metallic film sample, and at **c** a distance of  $5 \mu\text{m}$  inside the substrate. **b** Normalized intensity profile along the dashed line in **(a)**. **d** Figure taken from Drezet et al. [18] for comparison: Direct space images associated with a point-like dipole radiating through the metal film and recorded in the back-focal plane of the microscope ocular

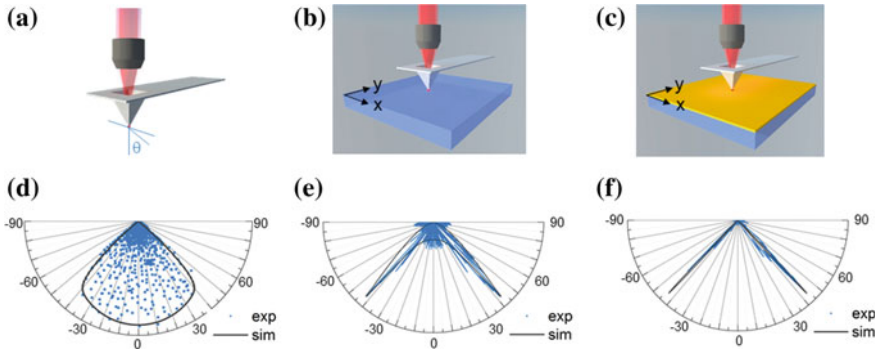


**Fig. 5.11** Angular radiation patterns of the scattered light from a NSM probe placed in **a** air, **b** in contact with a glass substrate, and **c** a gold thin film on a glass substrate. **d**, **e**, **f** Normalized intensity plotted in polar coordinates as a function of the angle of emission  $\theta$ . Emission peaks point to an angle  $\pm |\theta_{c,\text{glass}}| = 41.8^\circ$  in **(e)** and to  $\pm |\theta_{c,\text{gold}}| = 43.3^\circ$  in **(f)**

function of the emission angle in polar coordinates for the three cases studied previously: tip in free space (Fig. 5.11a), in contact with the glass substrate (Fig. 5.11b), and in contact with the gold film on a glass substrate (Fig. 5.11c). The plotted experimental data points (in blue) are in spherical coordinates and are selected in a way to obey two selection rules. First, they are chosen to lie in the  $x$ - $z$  plane of the NSOM tip perpendicular to the surface of the sample. Second, we made sure that each angle  $\theta$  has only one attributed intensity value. To this end, we select the data that lie only in a spherical shell of thickness  $\Delta\rho = 30$  nm centered on the aperture tip. The corresponding FDTD simulation results of the far-field radiation patterns of a superposition of a magnetic and electric dipole are plotted in black. Very good agreement is obtained in all the three cases. The angular radiation patterns confirm the observations presented in Sect. 5.3.2 (Figs. 5.7, 5.8 and 5.9). In fact, we observe that the intensity of the scattered light from the tip in free space decays exponentially around a maximum value centered at  $\theta = 0^\circ$  (Fig. 5.11d). We also quantitatively verify that for the tip placed in contact with the glass sample (Fig. 5.11e), most of the light is scattered exactly at the critical angle  $\pm|\theta_{c,\text{glass}}| = 41.8^\circ$  in addition to a broad distribution around  $\theta = 0^\circ$ . As for the plasmonic sample, we verify that the generated leaky plasmons are transmitted into the substrate at an angle of  $\pm|\theta_{c,\text{gold}}| = 43.3^\circ$ , which is higher than the critical angle of the medium. This highly directional scattering, narrower than in the previous cases, again reinforces our previous observation of the two lobes with a preferential direction caused by the surface plasmons. Surface plasmons are indeed highly selective in angle, both for their excitation and, as shown here, their leakage.

Next, we aim at comparing the behavior of the NSOM probe in the case where it is placed in the far-field region above the sample to the case where it is placed in contact with the sample in the near-field region. To do that, we place the tip at a distance of  $3\ \mu\text{m}$  above the sample surface, and repeat the same characterization procedure. The angular radiation pattern is plotted in Fig. 5.12. By comparing Fig. 5.12b to Fig. 5.11e, we notice the very high resemblance between the two plots, which allows us to conclude that the gold film has no effect on the transmitted light through the substrate when the incident light source is placed in the far field. This is because in this case, only small wavevectors are created by the tip, and therefore surface plasmons cannot be generated. The angular emission thus corresponds to that of a glass substrate, with maxima occurring at an angle of  $\pm 40.5^\circ$  (below  $\theta_{c,\text{glass}}$ ). We verified this result by performing the same experiment with the tip placed at a  $3\ \mu\text{m}$  height above a glass substrate, and the same exact emission angle was observed. In addition, due to the weak transmission of the gold film, the maximum intensity at  $\rho = 10\ \mu\text{m}$  is found to decrease by a factor of 2.5 when the tip is placed in the far field. These results agree with those obtained by Hecht et al. [17] using back-focal plane and real space imaging. The complex EM field represented by the product  $\rho A(x, y, z)\text{lc}\cos(\phi(x, y, z))$  is shown in Fig. 5.12c, where we can also clearly see that there are no leaky surface plasmons generated as opposed to the case where the tip is in contact with the film (Fig. 5.9c).

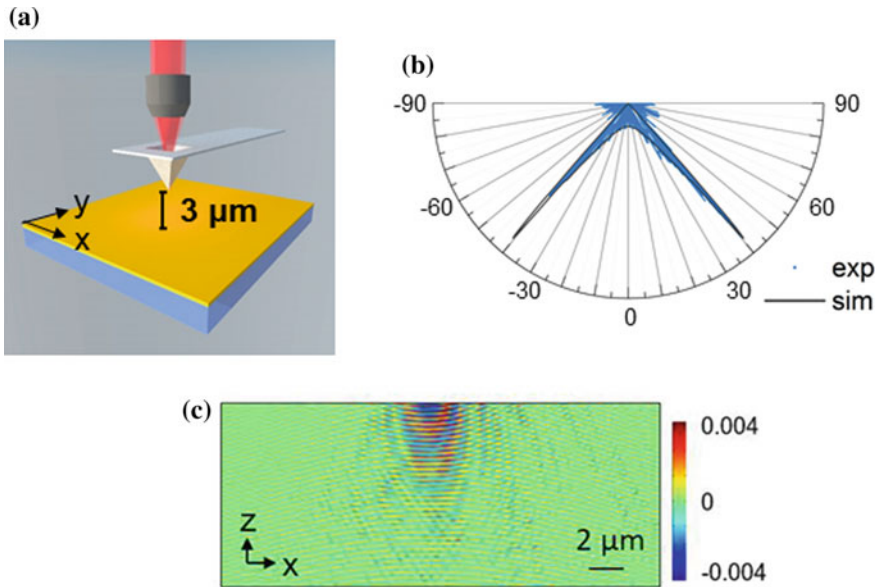


**Fig. 5.12** Angular radiation patterns of the scattered light from a NSOM probe placed **a** at  $3 \mu\text{m}$  above a gold thin film on a glass substrate. **b** Normalized intensity plotted in polar coordinates as a function of the angle of emission  $\theta$ . Emission peaks point to an angle  $\pm|\theta| = 40.5^\circ$ . **c** Corresponding complex EM field represented by the product  $\rho|A(x, y, z)|\cos(\phi(x, y, z))$ , where  $A(x, y, z)$  is the amplitude, and  $\phi(x, y, z)$  the phase

## 5.4 Possible Applications

### 5.4.1 Coupled Nanoantennas

Now that we are certain of the functionality of our near-field scanning optical microscope combined with digital holography, we can use it to fully characterize the scattered electromagnetic field from any nanostructure. Optical nanoantennas are interesting candidates due to their unique control of absorption and emission at the nanometer scale: high confinement, enhancement, and directivity of electromagnetic radiation at subwavelength dimensions. They have wide applications such as wavelength tuning, nano-trapping, nano-sensing, near-field imaging, photodetection, directional emission, etc. As discussed above, many techniques such as back-focal plane imaging were successfully used to describe the radiation pattern and scattering angles of different types of nanoantennas. However, we emphasize that the advantage of our technique is that both the amplitude and phase of the EM field scattered by an optical nanoantenna can be measured in one plane located in the far field, and then backpropagated to perform 3D reconstructions near the nano-antenna. Previous work using heterodyne holography were successfully done by the group of G. Tessier, where the simultaneous localization and selection of gold nanoparticles in

three dimensions was studied with near-diffraction resolution [44]. The full scattered three-dimensional electromagnetic field of plasmonic gold nanodisk chains fabricated by e-beam lithography was also measured using the same holography technique [25] using single-shot hologram acquisition associated to a reconstruction of the 3D scattering pattern of the antennas. Cross-sections of the reconstructed scattered field in different planes is shown in Fig. 5.13 (taken from the paper of Suck et al. [25]). Although the holographic images are diffraction limited, the shape of the

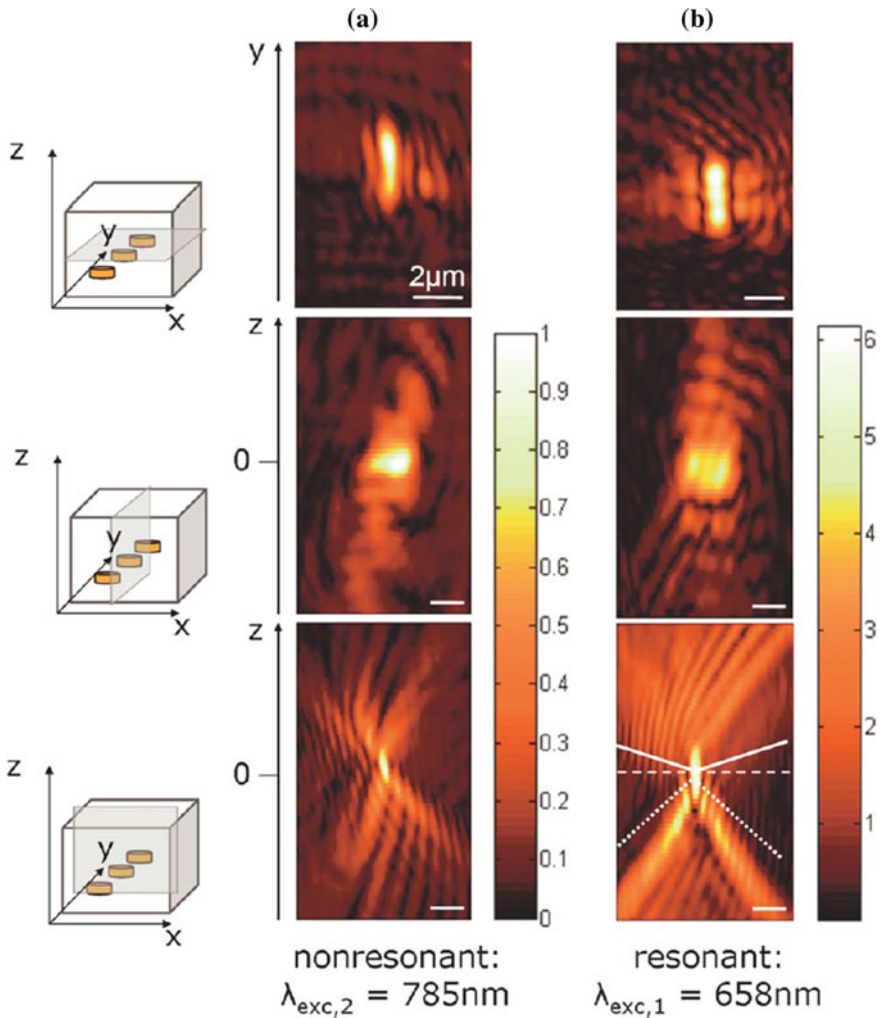


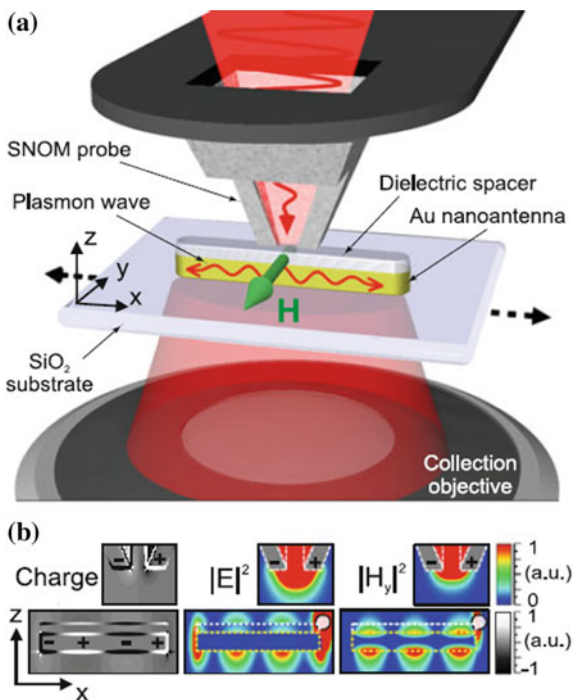
**Fig. 5.13** Scattered field reconstructed from a single hologram of a nanodisk chain at nonresonant ( $\lambda = 785\text{ nm}$ ) (a) and resonant ( $\lambda = 658\text{ nm}$ ) (b) wavelengths, for an illumination polarized along the long axis (y) of the nanoantenna system. Cross-sections along different planes centered on the antenna: x-y (top), y-z (middle), and x-z (bottom). Figure taken from [25]

disk chain is clearly identified, as well as electromagnetic hotspots that are created in the nanoantennas. In addition, strong directional scattering is observed (note the different scalebars in Fig. 5.13a, b, showing an approximately 6 times enhancement of the scattering near the resonant wavelength).

With the combined NSOM-holography setup described in the present chapter, such studies can be extended further to study the coupling between NSOM tips and different types of optical nanoantennas. The full 3D scattering pattern of a locally excited nanoantenna and the influence of the position of the excitation source should become accessible. As mentioned earlier, recent studies have shown that a metal-coated hollow pyramidal probe coupled to a nanoantenna behaves as a tangential magnetic dipole. A schematic of the mentioned results is shown in Fig. 5.14 and is taken from the paper of Denkova et al. [14]. Here, digital holography can be helpful to experimentally characterize this coupling behavior between nanosized probes and different types of nanoantennas using only a single hologram.

Another application would be to characterize the scattering behavior of NSOM probes with embedded nanoantennas at their extremities [23, 45]. Due to the presence of defects at the subwavelength scale [46], the optical response of such nanoantennas might strongly deviate from expectations, and will depend on the environment. This problem can be fully addressed and controlled by our technique as well.

**Fig. 5.14** **a** Schematic of a hollow-pyramid NSOM probe coupled to a plasmonic nanoantenna. **b** Simulations of the charge density, electric and magnetic field distributions. Figure taken from [14]



### 5.4.2 Brownian Nanoparticles as Stochastic Optical Probes

In much the same way as a scattering NSOM probe, nanoparticles can be used to scatter the local near field. In liquids, one can take advantage of the Brownian motion of nanoparticles in order to explore the volume of the sample: the movement of the probes is then stochastic, instead of deterministic as in classical NSOM experiments. Each of the particles can behave as a subwavelength probe and, as it moves in an illuminated region of the sample, scatter the local field toward the holographic microscope described above. The reconstruction of the scattering field allows the 3D super localization of the particle, i.e., the determination of its center of mass with an accuracy which is only limited by the signal-to-noise ratio of the detection [47]. This localization can be achieved with  $3 \times 3 \times 10 \text{ nm}^3$  accuracy, and the scattering intensity is directly proportional to the local optical field provided that the particles are monodisperse, and therefore have identical scattering cross sections. Figure 5.15 shows the 3D image of a focused laser beam obtained by accumulating 36000 localization events. As shown in [48], the acquisition time required to reach the desired volume coverage can be estimated, and a full super-resolved 3D image of the optical scene can be acquired with a resolution which is only limited by either the size of the particles (here, 100 nm) or the localization accuracy.

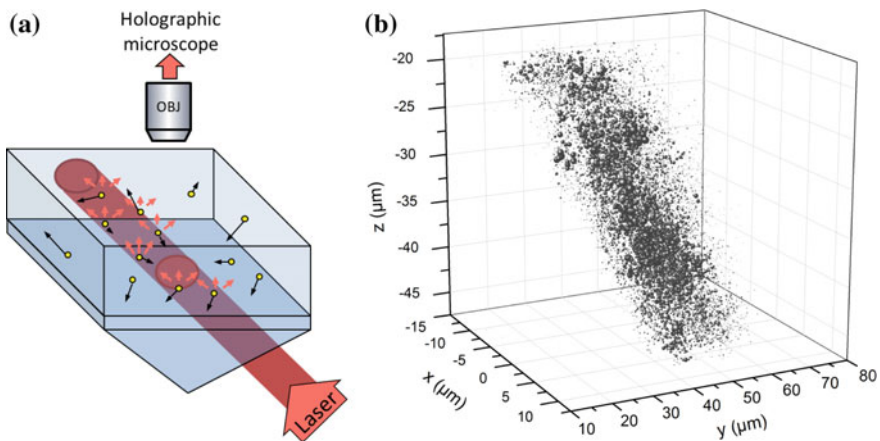


**Fig. 5.15** **a** Schematic description of an experiment using gold nanoparticles in Brownian motion in water as local probes. A  $\lambda = 660 \text{ nm}$  diode laser beam is focused in water. Light is scattered by  $r = 50 \text{ nm}$  gold nanoparticles toward a holographic microscope. Each particle is localized in 3D with a  $3 \times 3 \times 10 \text{ nm}^3$  accuracy in post-processing. **b** 3D position of 36000 localization events. The intensity  $I(x, y, z)$  recorded at each location is represented by the size of the spheres. The resolution of the image is limited only by the localization accuracy and the size of the particle, both well below the diffraction limit. Adapted from [47]

### 5.4.3 Scattering Through Disordered Media

It has been recently proposed that scattering media can be used to couple the information contained in the near-field wave vectors to the observable far-field with conventional optics [49]. The multiple elastic scattering that light experiences in such a medium exhibits time-reversal symmetry, a property that has been used in optics to achieve image transmission through opaque materials [50] or perfect absorption [51], among other phenomena.

Near-field scanning optical microscope combined with digital holography can be applied to probe the optical properties of such strongly scattering media using aperture tips. The nanosized tips act as point-like sources and are used to excite the input modes of strongly scattering media. The transmitted far-field signal is measured holographically and, as shown before, the complex field can be reconstructed at any point in space between the camera and the output of the scattering media. This allows us to accurately describe the amplitude and phase of the propagating electromagnetic field and compare its behavior through different scattering media. An example of holographic reconstruction of the 3D speckle formed after placing a NSOM tip acting as a temporally coherent nanolight source on a disordered scattering medium made of 100 nm diameter  $\text{TiO}_2$  nanoparticles is shown in Fig. 5.16. This reconstruction can be seen as the spatial point spread function corresponding to a local sub- $\lambda$  sized excitation of the disordered medium. By measuring a hologram when the NSOM tip is at every possible location over the disordered medium, the full spatial response of the medium (or its Green's function) can be determined. Conversely, this can subsequently be used as a superlens allowing super-resolution imaging in the visible spectrum. With such holographic characterization combined to point-like excitation of the disordered medium, it therefore becomes possible to get access to full-field subwavelength imaging of structures containing high spatial frequencies typically not propagating into the far-field. A proof of principle of the coupling of the near-field information to the far field by means of a disordered medium, and of its holographic detection has been achieved by Park et al. [49]. Figure 5.17, taken from the cited paper by Park et al., shows a schematic of the experimental concept

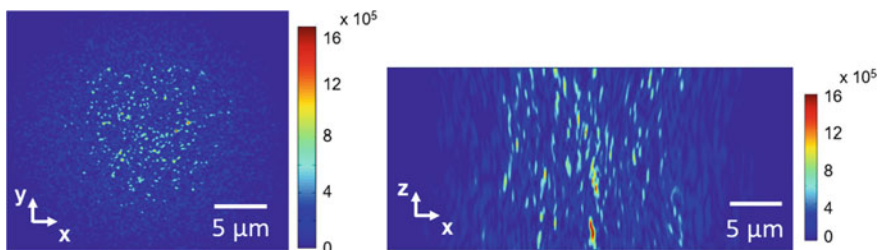


**Fig. 5.16** Intensity plots in the  $x$ - $y$  plane (left) and  $x$ - $z$  plane (right) of the reconstructed speckle generated by the scattered light from the NSOM tip through a disordered medium made up of 100 nm  $\text{TiO}_2$  nanoparticles

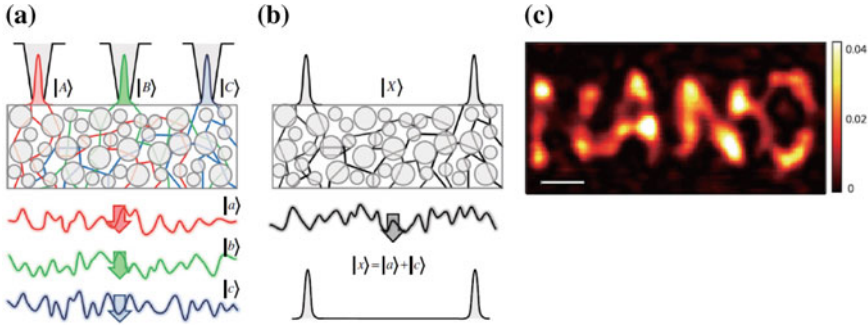


**Fig. 5.17** Schematic diagram of experimental concept. **a** Measurement of the transmission matrix with a point-like source generated by a near-field aperture as the input basis. The transmission matrix is composed of speckle fields propagating through the turbid medium from the near-field aperture. **b** Recovery of the original field on the turbid medium from the speckle field generated by an arbitrary sample based on the linear relation between the input and output modes. **c** Example of super-resolved image produced point by point with a NSOM aperture probe obtained by means of holographic measurements of the speckle field at various probe positions (Scale bar corresponds to 500 nm). Figures taken from [49]

where the transmitted far-field signal generated from a near-field aperture tip has been detected holographically at different locations on the sample, and the original field has been recovered.

## 5.5 Conclusion

In this chapter, we presented a full-field off-axis holography technique combined with a NSOM. This combination yields an accurate three-dimensional description of the scattered electromagnetic field from a subwavelength probe. This is possible because, from a single recorded hologram, we are able to obtain information not only about the intensity, but also about the phase of the scattered electromagnetic field in any plane away from the tip. We applied this method to fully characterize the light scattered by the metal-coated hollow pyramidal aperture tip of a NSOM placed in free space, and coupled to transparent and plasmonic media. We supported our experimental results with FDTD simulations that model such type of probes as a superposition of an electric and magnetic dipole. We can also conclude that the behavior of a NSOM probe is highly related to its coupling to the environment.

This experimental and numerical validation opens the way for a broad range of new applications taking advantage of both the subwavelength localization possibilities of NSOM and the amplitude and phase imaging capabilities of holography. The study of complex subwavelength systems such as nanoantennas and resonators as well as multiple scattering through disordered media should now be within reach.

## References

1. D.W. Pohl, W. Denk, M. Lanz, Optical stethoscopy: image recording with resolution  $\lambda/20$ . *Appl. Phys. Lett.* **44**(7), 651–653 (1984)
2. D. Costantini, L. Greusard, A. Bousseksou, R. Rungswang, T.P. Zhang, S. Callard, J. Decobert, F. Lelarge, G.-H. Duan, Y. De Wilde, R. Colombelli, In situ generation of surface plasmon polaritons using a near-infrared laser diode. *Nano Lett.* **12**(9), 4693–4697 (2012)
3. E.H. Synge, A suggested method for extending microscopic resolution into the ultra-microscopic region. *Lond. Edinb. Dublin Philos. Mag. J. Sci.* **6**(35), 356–362 (1928)
4. E.H. Synge, An application of piezo-electricity to microscopy. *Lond. Edinb. Dublin Philos. Mag. J. Sci.* **13**(83), 297–300 (1932)
5. U. Dürig, D.W. Pohl, F. Rohner, Near-field optical-scanning microscopy. *J. Appl. Phys.* **59**(10), 3318–3327 (1986)
6. L. Novotny, B. Hecht, *Principles of Nano-Optics* (Cambridge University Press, 2006)
7. E.J. Sánchez, L. Novotny, X.S. Xie, Near-field fluorescence microscopy based on two-photon excitation with metal tips. *Phys. Rev. Lett.* **82**(20), 4014 (1999)
8. J.-J. Greffet, R. Carminati, Image formation in near-field optics. *Prog. Surf. Sci.* **56**(3), 133–237 (1997)
9. D. Costantini, A. Bousseksou, M. Fevrier, B. Dagens, R. Colombelli, Loss and gain measurements of tensile-strained quantum well diode lasers for plasmonic devices at telecom wavelengths. *IEEE J. Quantum Electron.* **48**(1), 73–78 (2012)
10. H.A. Bethe, Theory of diffraction by small holes. *Phys. Rev.* **66**(7–8), 163 (1944)
11. C. Obermüller, K. Karrai, Far field characterization of diffracting circular apertures. *Appl. Phys. Lett.* **67**(23), 3408–3410 (1995)
12. C. Obermüller, K. Karrai, G. Kolb, G. Abstreiter, Transmitted radiation through a subwavelength-sized tapered optical fiber tip. *Ultramicroscopy* **61**(1), 171–177 (1995)
13. A. Drezet, J.C. Woehl, S. Huant, Diffraction by a small aperture in conical geometry: application to metal-coated tips used in near-field scanning optical microscopy. *Phys. Rev. E* **65**(4) (2002)
14. D. Denkova, N. Verellen, A.V. Silhanek, V.K. Valev, P.V. Dorpe, V.V. Moshchalkov, Mapping magnetic near-field distributions of plasmonic nanoantennas. *ACS Nano* **7**(4), 3168–3176 (2013)
15. A. Babuty, K. Joulain, P.-O. Chapuis, J.-J. Greffet, Y. De Wilde, Blackbody spectrum revisited in the near field. *Phys. Rev. Lett.* **110**(14), 146103 (2013)
16. K. Joulain, P. Ben-Abdallah, P.-O. Chapuis, Y. De Wilde, A. Babuty, C. Henkel, Strong tip-sample coupling in thermal radiation scanning tunneling microscopy. *J. Quant. Spectrosc. Radiat. Transf.* **136**(Supplement C), 1–15 (2014)
17. B. Hecht, H. Bielefeldt, L. Novotny, Y. Inouye, D.W. Pohl, Local excitation, scattering, and interference of surface plasmons. *Phys. Rev. Lett.* **77**(9), 1889–1892 (1996)
18. A. Drezet, C. Genet, Imaging surface plasmons: from leaky waves to far-field radiation. *Phys. Rev. Lett.* **110**(21), 213901 (2013)
19. P. Bharadwaj, A. Bouhelier, L. Novotny, Electrical excitation of surface plasmons. *Phys. Rev. Lett.* **106**(22) (2011)
20. R. Marty, C. Girard, A. Arbouet, G. Colas des Francs, Near-field coupling of a point-like dipolar source with a thin metallic film: implication for STM plasmon excitations. *Chem. Phys. Lett.* **532**, 100–105 (2012)
21. A. Drezet, A. Hohenau, D. Koller, A. Stepanov, H. Dittlacher, B. Steinberger, F.R. Aussenegg, A. Leitner, J.R. Krenn, Leakage radiation microscopy of surface plasmon polaritons. *Mater. Sci. Eng. B* **149**(3), 220–229 (2008)
22. M. Berthel, Q. Jiang, A. Pham, J. Bellessa, C. Genet, S. Huant, A. Drezet, Directional local density of states of classical and quantum propagating surface plasmons. *Phys. Rev. Appl.* **7**(1), 14021 (2017)
23. A.G. Curto, G. Volpe, T.H. Taminiau, M.P. Kreuzer, R. Quidant, N.F. van Hulst, Unidirectional emission of a quantum dot coupled to a nanoantenna. *Science* **329**(5994), 930–933 (2010)

24. M.A. Lieb, J.M. Zavislan, L. Novotny, Single-molecule orientations determined by direct emission pattern imaging. *JOSA B* **21**(6), 1210–1215 (2004)
25. S.Y. Suck, S. Collin, N. Bardou, Y. De Wilde, G. Tessier, Imaging the three-dimensional scattering pattern of plasmonic nanodisk chains by digital heterodyne holography. *Opt. Lett.* **36**(6), 849–851 (2011)
26. C. Park, J.-H. Park, C. Rodriguez, H. Yu, M. Kim, K. Jin, S. Han, J. Shin, S. H. Ko, K. T. Nam, Y.-H. Lee, Y.-H. Cho, Y. Park, Full-field subwavelength imaging using a scattering superlens. *Phys. Rev. Lett.* **113**(11) (2014)
27. D. Gabor, *A New Microscopic Principle* (Nature Publishing Group, 1948)
28. D. Gabor, Microscopy by reconstructed wave-fronts. *Proc. R. Soc. Lond. A* **197**(1051), 454–487 (1949)
29. E.N. Leith, J. Upatnieks, Reconstructed wavefronts and communication theory. *JOSA* **52**(10), 1123–1130 (1962)
30. U. Schnars, W.P. Jüptner, Digital recording and numerical reconstruction of holograms. *Meas. Sci. Technol.* **13**(9), R85 (2002)
31. J.W. Goodman, R.W. Lawrence, Digital image formation from electronically detected holograms. *Appl. Phys. Lett.* **11**(3), 77–79 (1967)
32. M.A. Kronrod, N.S. Merzlyakov, L.P. Yaroslavskii, Reconstruction of a hologram with a computer. *Sov. Phys. Tech. Phys.* **17**, 333 (1972)
33. U. Schnars, W. Jüptner, Direct recording of holograms by a CCD target and numerical reconstruction. *Appl. Opt.* **33**(2), 179–181 (1994)
34. E. Cuche, P. Marquet, C. Depeursinge, Spatial filtering for zero-order and twin-image elimination in digital off-axis holography. *Appl. Opt.* **39**(23), 4070–4075 (2000)
35. F. Le Clerc, L. Collot, M. Gross, Numerical heterodyne holography with two-dimensional photodetector arrays. *Opt. Lett.* **25**(10), 716–718 (2000)
36. M. Gross, M. Atlan, Digital holography with ultimate sensitivity. *Opt. Lett.* **32**(8), 909–911 (2007)
37. V. Parigi, E. Perros, G. Binard, C. Bourdillon, A. Maître, R. Carminati, V. Krachmalnicoff, Y.D. Wilde, Near-field to far-field characterization of speckle patterns generated by disordered nanomaterials. *Opt. Express* **24**(7), 7019–7027 (2016)
38. N. Rahbany, I. Izeddin, V. Krachmalnicoff, R. Carminati, G. Tessier, Y. De Wilde, One-shot measurement of the three-dimensional electromagnetic field scattered by a subwavelength aperture tip coupled to the environment. *ACS Photonics* **5**(4), 1539–1545 (2018)
39. [www.witec.de](http://www.witec.de), Witec GmbH
40. R.L. Olmon, B. Slovick, T.W. Johnson, D. Shelton, S.-H. Oh, G.D. Boreman, M.B. Raschke, Optical dielectric function of gold. *Phys. Rev. B* **86**(23), 235147 (2012)
41. A. Drezet, J.C. Woehl, S. Huant, Extension of Bethe’s diffraction model to conical geometry: application to near-field optics. *EPL Europhys. Lett.* **54**(6), 736 (2001)
42. A. Drezet, A. Cuche, S. Huant, Near-field microscopy with a single-photon point-like emitter: resolution versus the aperture tip? *Opt. Commun.* **284**(5), 1444–1450 (2011)
43. [www.vwr.com](http://www.vwr.com), VWR International—Chemicals and Laboratory Scientific Supplies
44. E. Absil, G. Tessier, M. Gross, M. Atlan, N. Warnasooriya, S. Suck, M. Coppey-Moisand, D. Fournier, Photothermal heterodyne holography of gold nanoparticles. *Opt. Express* **18**(2), 780–786 (2010)
45. Z. Xie, Y. Lefier, M.A. Suarez, M. Mivelle, R. Salut, J.-M. Merolla, T. Grosjean, Doubly resonant photonic antenna for single infrared quantum dot imaging at telecommunication wavelengths. *Nano Lett.* **17**(4), 2152–2158 (2017)
46. M. Thomas, J.J. Greffet, R. Carminati, J.R. Arias-Gonzalez, Single-molecule spontaneous emission close to absorbing nanostructures. *Appl. Phys. Lett.* **85**(17), 3863–3865 (2004)
47. A. Martinez-Marrades, J.-F. Rupprecht, M. Gross, G. Tessier, Stochastic 3D optical mapping by holographic localization of Brownian scatterers. *Opt. Express* **22**(23), 29191–29203 (2014)
48. J.-F. Rupprecht, A. Martinez-Marrades, Z. Zhang, R. Chngede, P. Kanchanawong, G. Tessier, Trade-offs between structural integrity and acquisition time in stochastic super-resolution microscopy techniques. *Opt. Express* **25**(19), 23146–23163 (2017)

49. C. Park, J.-H. Park, C. Rodriguez, H. Yu, M. Kim, K. Jin, S. Han, J. Shin, S.H. Ko, K.T. Nam, Y.-H. Lee, Y.-H. Cho, Y. Park, Full-field subwavelength imaging using a scattering superlens. *Phys. Rev. Lett.* **113**(11), 113901 (2014)
50. S.M. Popoff, G. Lerosey, M. Fink, A.C. Boccara, S. Gigan, Image transmission through an opaque material. *Nat. Commun.* **1**(6), 1–5 (2010)
51. W. Wan, Y. Chong, L. Ge, H. Noh, A.D. Stone, H. Cao, Time-reversed lasing and interferometric control of absorption. *Science* **331**(6019), 889–892 (2011)

# Chapter 6

## Absorption-Based Far-Field Label-Free Super-Resolution Microscopy



Chen Li and Ji-Xin Cheng

**Abstract** Materials absorption, which happens in all light–matter interactions, has been studied systematically and inspires various chemical-specific measurement methods for extensive non-fluorescent species. In this chapter, we review recent achievements of far-field label-free super-resolution microscopy (LFSRM) that deploys materials absorption to provide the contrast. In the linear absorption modalities, samples convert photon energy to heat efficiently, which turns the photothermal detection with single-molecule sensitivity into possible. The photothermal microscope breaks the diffraction limit of the excitation beam by probing the localized thermal lens effect using a shorter-wavelength beam. In the nonlinear absorption modalities, one pump beam profile could be engineered to doughnut shape and reduce the size of the nonlinear region, which helps achieve sub-diffraction resolution. Both mechanisms use the intrinsic vibrational or electronic absorption of molecules, through which different species are readily discriminated. Owing to the chemical specificity and high sensitivity, this label-free LFSRM provides unique advantages in various materials and in biomedical applications, including nanomaterial inspection and in vivo imaging of living cells and organisms.

### 6.1 Introduction to Absorption-Based Far-Field Label-Free Super-Resolution Microscopy

The development of biological and biomedical sciences in the twentieth century has expedited the growth of far-field microscopy, which enabled numerous intracellular studies with minimal invasion [1]. However, traditional far-field microscopy cannot focus light onto a spot that is smaller than the diffraction limit [2]. As a consequence,

---

C. Li

Department of Chemistry, Purdue University, West Lafayette, IN 47906, USA

J.-X. Cheng (✉)

Boston University Photonics Center, Boston, MA 02215, USA

e-mail: [jxcheng@bu.edu](mailto:jxcheng@bu.edu)

URL: <http://sites.bu.edu/cheng-group/>

© Springer Nature Switzerland AG 2019

V. Astratov (ed.), *Label-Free Super-Resolution Microscopy*,

Biological and Medical Physics, Biomedical Engineering,

[https://doi.org/10.1007/978-3-030-21722-8\\_6](https://doi.org/10.1007/978-3-030-21722-8_6)

objects that are closer or smaller than about half the wavelength cannot be discerned and those sub-cellular structures such as organelles can only be visualized down to this scale [3]. To break the diffraction limit, the last two decades have seen an emerging interest of developing fluorescence-based far-field super-resolution microscopy, or the so-called “far-field fluorescence nanoscopy”. Among them, photoactivated localization microscopy and stochastic optical reconstruction microscopy use the on/off blinking and switching behavior of fluorescent proteins to partially excite and localize the fluorophores with  $\sim 10$  nm precision [4–7]. Stimulated emission depletion microscopy [8–10], along with ground-state depletion (GSD) microscopy [11] and saturated structured illumination microscopy [12, 13] are based on nonlinear optical effects that reduce the point spread function (PSF) of the focused light by controlling the excitation beam geometry.

Although the power of far-field fluorescence nanoscopy approaches enabled many breakthrough and discoveries in cell biology and biomedical sciences, due to the necessity of employing fluorescent labeling, many important intracellular processes that could be perturbed by the fluorophores remain unexplored [14–18]. In addition, many intrinsic biomolecules and nanomaterials, such as hemes, nanotubes, and graphene, have strong absorption yet low quantum efficiency [19–21], which makes it hard to visualize these species using far-field fluorescence nanoscopy. Label-free super-resolution microscopy (LFSRM), which uses other inherent chemical or physical properties from the samples to provide the contrast, thus shows advantages over fluorescence-based approaches for *in vivo* imaging of cells and organisms and draws increasing interests in the recent years.

One way to provide contrast mechanism in the label-free imaging manner is to use the intrinsic molecular absorption that is prevalent from inorganic materials to biomolecules. Linear absorption has been well studied since the early twentieth century and inspired various widely used measurement methods, including infrared (IR) spectroscopy (vibrational state absorption) [22] and UV–Vis spectroscopy (electronic state absorption) [23]. On comparing with scattering or multiphoton processes, we found that the large cross-section of linear absorption allows researchers to push the sensitivity of absorption spectroscopy to single-molecule detection [24, 25]. The application of Fourier transform in the interferometric spectroscopy enables the extraction of absorption spectra with high spectral resolution from the measured interferogram [26–29]. The development of bright coherent sources, like synchrotron radiation or quantum cascade lasers [30, 31], along with the deployment of fast electronics or sensitive detectors [27, 32] has improved not only the signal-to-noise ratio to an extreme but also the spectral resolution and has reduced the data acquisition time. These advancements in linear absorption spectroscopy have all facilitated the deployment of spectroscopic imaging in chemistry, materials science, pharmaceuticals, and polymer sciences [33–36]. Meanwhile, the advancements in nonlinear optics have also seen the growth of nonlinear absorption-based spectroscopy, such as transient absorption spectroscopy and stimulated Raman scattering spectroscopy [15, 19, 37–41]. Transient absorption microscopy, being able to provide the time-resolved spectroscopic imaging of various ultra-fast processes, is deployed in the field of nanomaterials, semiconductors, catalysts, and so on [42–46]. Stimulated Raman scattering

microscopy, on the other hand, is rising as a popular tool in biology, biomedicine, and so on [47–49].

Although absorption-based spectroscopic imaging techniques have come a long way to pursue fast and sensitive measurement, the limited spatial resolution remains to be a problem for further applications that require sub-micron or nanoscale resolution. In particular, the most popular absorption-based spectroscopic imaging techniques, such as mid-IR microscopy, near-IR microscopy, and transient-absorption microscopy, all use long wavelength light source (0.8–10  $\mu\text{m}$ ) whose spatial resolution stay in the micrometer scale. To achieve higher resolution, many methods have been reported during the recent years. One way of improving the image resolution is to deconvolve the captured image with the PSF of the system through image processing [50, 51]. Albeit widely applied and ready to use, deconvolution method could not really break the diffraction limit in far-field imaging systems. Thus, other methods using near-field configuration to achieve absorption-based super-resolution imaging were proposed. In 2000s, scanning near-field microscopy was combined with IR spectroscopy to achieve 20 nm resolution [52]. Later, atomic force microscope tips were used to probe the thermal expansion of objects induced by the absorption of IR, which obtained IR absorption spectroscopy from samples smaller than 10 nm [53–56]. However, the low throughput and sample-probe contact of these near-field methods limited their applications in biomedical sciences.

To address this problem, ideas of absorption-based far-field LFSRM were proposed in recent years. The first category is featured as photothermal (PT) microscopy, which uses a probe beam to detect the subtle PT lens effect induced by the linear absorption of the excitation (pump) beam. The PT lens measurement was first conducted in 1965 in a single-beam apparatus which uses the same beam for both pump and detection [57]. The dual-beam apparatus was then exploited to further take advantage of the sensitivity of PT detection [58]. It was not until the twenty-first century when PT detection was realized to be an approach to break the diffraction limit of the pump beam. As an example, various mid-infrared PT microscopes achieve sub-micron IR spectroscopic imaging by confocally exciting the objects with a mid-IR beam and probing with another tightly focused visible or near-IR beam [59]. The improved spatial resolution ( $\sim 700$  nm) allows those methods to obtain the IR spectra from the sub-cellular structures of living organisms or tissue slices for the first time. Besides, recent attempts which deploy counter-propagation measures have pushed the resolution up to 300 nm to obtain the IR spectrum of single *Escherichia coli* and local cation heterogeneities in mixed cation perovskite [60]. The idea of detecting the nonlinear PT terms to further increase the spatial resolution has also been demonstrated [61].

The second category of absorption-based far-field LFSRM, instead of probing the linear absorption, uses an apparatus that is inspired by super-resolution GSD microscopy and measures the nonlinear absorption of incident beams [62]. In the saturated transient absorption, a doughnut-shaped saturation pump beam was applied to confine the transient absorption signal within the very center of the focal spot to achieve super-resolution pump-probe imaging. The same apparatus can be used in other nonlinear optical processes to detect the materials absorption with sub-

diffraction resolution. In one example, a doughnut-shaped decoherence beam was combined with the confocal pump and probe beams to confine the stimulated Raman gain within the center of the beams, which enables sub-diffraction Raman imaging [63].

In this review, we review the history and fundamental principles of both linear and nonlinear absorption-based LFSRM techniques, scrutinize the pros and cons of different modalities, and present the latest applications and possible future directions of the field.

## 6.2 Breaking the Diffraction Limit in IR Microscopy Through Photothermal Detection

### 6.2.1 *Laser-Induced Photothermal Lens Effect: The Origin of the Photothermal Contrast*

The PT lens effect was first reported and discussed by Gordon et al., whose analysis built the basis of later works in this field [57]. In that experiment, a liquid sample cell filled with various pure samples was placed in the beam path and heated by the absorption of the laser power to produce a thermal gradient in the vicinity of the incident beam, which resulted in long transients of intensity profiles of the transmitted beam. It is believed that such observations were induced by the lens effect arising from the refractive index change near the beam as a result of the thermal gradient. To further explain it, Gordon et al. built a model to quantitatively depict the refractive index gradient produced by the PT process as a function of the temperature coefficient of the refractive index ( $\partial n/\partial T$ ), through which the detected beam intensity profile could be used to retrieve the unknown quantities related to the sample, such as concentration and thermal constants. Since most liquids have a negative value of  $\partial n/\partial T$ , the thermal lens effect is usually divergent [58]. That very first experiment achieved measurement of absorptivity as low as  $10^{-4} \text{ cm}^{-1}$ , indicating a promising approach to probe weak absorptions indirectly with high sensitivity.

### 6.2.2 *Improvement of Detection Sensitivity of Photothermal Spectroscopy*

Soon after Gordon's experiment, many other works were reported to improve the physical model of the PT lens effect [64–68]. On the other hand, more efforts were dedicated to the enhancement of detection sensitivities of the PT measurements [69–71]. Stone designed an interferometry to better resolve the phase shift induced by the PT lens effect and achieved  $\sim 10^{-5} \text{ cm}^{-1}$  sensitivity [72]. Boccara et al. exploited an accurate position sensor and applied fast modulation to the pump beam to measure

the periodic distortion induced by the PT process and deduced the sample absorptivity with high sensitivity [73]. It is also suggested that heat dissipation from the hot spot, located at the center of the beam, to the surrounding medium will affect the detected PT lens profile. Therefore, liquids with lower heat conductivity tend to produce larger thermal gradient in smaller space, which leads to higher detection sensitivity [74]. Note that all those attempts deployed the single-beam apparatus in which only one laser was used to both excite and probe the PT lens effect. And the best sensitivity for absorptivity measurements reported was limited to  $\sim 10^{-6} \text{ cm}^{-1}$  [75].

The breakthrough was not realized until the deployment of the dual-beam apparatus along with the synchronous detection which achieved an ultimate sensitivity of less than  $10^{-11} \text{ cm}^{-1}$  for absorptivity determination [58]. Unlike its single-beam counterpart, the dual-beam setup uses a second laser to probe the PT lens effect induced by the sample absorption of the pump beam, as illustrated in Fig. 6.1. The probe beam can be either collinear [58] or perpendicular [76, 77] to the pump beam, resulting in similar performances.

Despite the addition of slight complexity of beam path alignment, the dual-beam apparatus has a major advantage over the single-beam apparatus on the improvement of sensitivity because it enables the use of a probe beam that has different wavelengths and beam path from those of the pump beam. First, the probe beam reacts only with the refractive index gradient produced by the PT lens effect, and the wavelength of probe beam can be chosen from low-absorption regions to maintain high probe power at the detector and hence achieves the ultimate signal-to-noise ratio (SNR) [74]. In addition, the pump beam wavelength is usually selected from spectral regions that are strongly absorbed by samples of interest to maximize the PT lens effect at

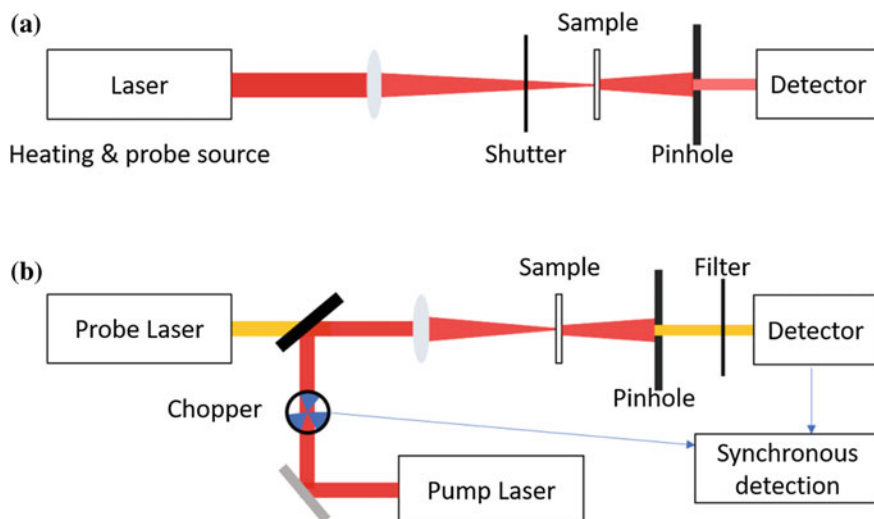


**Fig. 6.1** Comparison of two different experimental setups: **a** single-beam apparatus and **b** dual-beam apparatus with pump beam modulation and synchronous detection

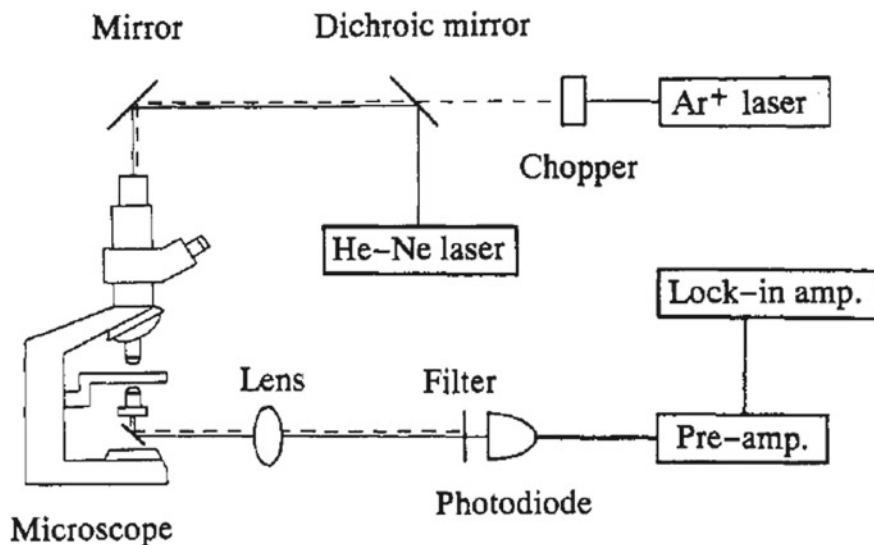


**Fig. 6.2** Schematic of the first PT microscopy setup. Reprinted from [83] with permission. Copyright 1993 American Chemistry Society

extremely low concentrations ( $<10^{-12}$  mol/L). Last but not the least, the dual-beam apparatus allows separate modulation of both the pump and probe beams, enabling lock-in detections which maximizes the SNR of a periodic process [78]. Single nanocluster and nanoparticle (1.4 nm diameter) imaging [79–81] as well as single-molecule detection [82] via PT imaging have all been reported in recent years. With such extraordinary improvement of sensitivity, the PT spectroscopy is applied in numerous studies in non-fluorescent analytes [80, 81] and further developed as one of the most used absorption-based label-free microscopy by Harada et al. in the early 1990s [83]. As shown in Fig. 6.2, the pump and probe beams are collinearly combined by a dichroic mirror and then sent to the sample through the same objective. Such coaxial configuration is adopted by most of the latest PT microscopes due to the ease of alignment. Details of super-resolution PT microscopy (PTM) techniques will be discussed next.

### 6.2.3 Beat the Diffraction Limit of the Pump Beam

Consider the Abbe diffraction limit calculated as  $d = \lambda/2NA$  of the smallest object that can be resolved by a diffraction-limited optical microscope. Either shorter wavelength ( $\lambda$ ) or larger numerical aperture (NA) will result in the improvement of the spatial resolution of microscopes. Since the spatial resolution of PTM is only determined by the probe beam instead of the pump beam, the dual-beam apparatus brings

in possibilities of beating the diffraction limit of the pump beam by manipulating the probe beam. Based on the preceding argument, super-resolution PTM imagings have been achieved mainly in three different ways.

The first method is to choose shorter wavelength laser source as the probe beam. This approach is the simplest way to realize sub-diffraction imaging and most used in vibrational spectromicroscopy such as the detection of mid-IR absorptions. The wavelength of mid-IR pump beam usually falls in the range of 2.5–10  $\mu\text{m}$  and most IR objectives have relatively small NA values ( $\leq 0.8$ ) given the fact that IR source cannot be used in water or immersion oil. Thus, the best spatial resolution of conventional absorption-based IR microscopes is still limited to  $\sim 3 \mu\text{m}$  even with the synchrotron-based diffraction-limited system [31]. Besides, since the IR region covers such a broad spectral window, the chromatic aberration will significantly degrade the image quality. However, with the deployment of a visible probe beam (785 nm), Zhang and colleagues achieved sub-micrometer ( $\sim 0.6 \mu\text{m}$ ) chemical imaging of living cells or microorganisms via confocal mid-IR PTM with a Cassegrain objective (0.65 NA) [59]. As the schematic shows in Fig. 6.3a, b, the probe focus is  $\sim 1/10$  of the size of the pump mid-IR beam such that objects outside the probe beam focus are not detected, resulting in the ninefold improvement of the spatial resolution shown in Fig. 6.3c. Since the mid-IR pump beam can fully exploit the rich chemical information encoded in intrinsic chemical bond vibrations, mid-IR PTM emerges as a promising LFSRM approach for biomedical and pharmaceutical applications [59, 84]. We will discuss the recent advances and applications of mid-IR PTM in the following sections.

The second approach is to separate the beam paths and deploy a high NA objective for the counter-propagating probe beam. As shown in Fig. 6.4, Li et al. reached an ultimate resolution of 300 nm using a 532 nm probe beam and a 0.9 NA objective in their counter-propagating mid-IR PT microscope [60]. The main advantage of this approach is that the visible probe beam can go through a refractive objective instead of low NA reflective objectives that are typically used for IR source. Since there are numerous high NA refractive objectives available for visible probe beams, this approach could potentially reach the spatial resolution on the scale of 100 nm. In addition, this approach is often combined with the first approach, which results in higher resolution than those coaxial PT microscopes. However, the counter-propagating configuration does increase the complexity for system alignment in order to overlay the pump and probe beams in the sample plane and maximize the PT signal. Another drawback is that this approach requires the epi-detection design in which the probe photon collection efficiency is lower than that of the transmission mode, resulting in slower data acquisition. Thus, there is a trade-off between spatial resolution and imaging frame rate in this approach.

Last but not the least, super-resolution PTM can be achieved by probing the nonlinear PT lens effect whose signal profile is much narrower than the linear PT signal [61, 85–90]. Zharov first demonstrated the nonlinear dependence of PT signal to the pump beam intensity when the laser energy reaches certain thresholds using nanoparticles, through which the detected nonlinear PT signal arises only from the nonlinear center of the samples [61].

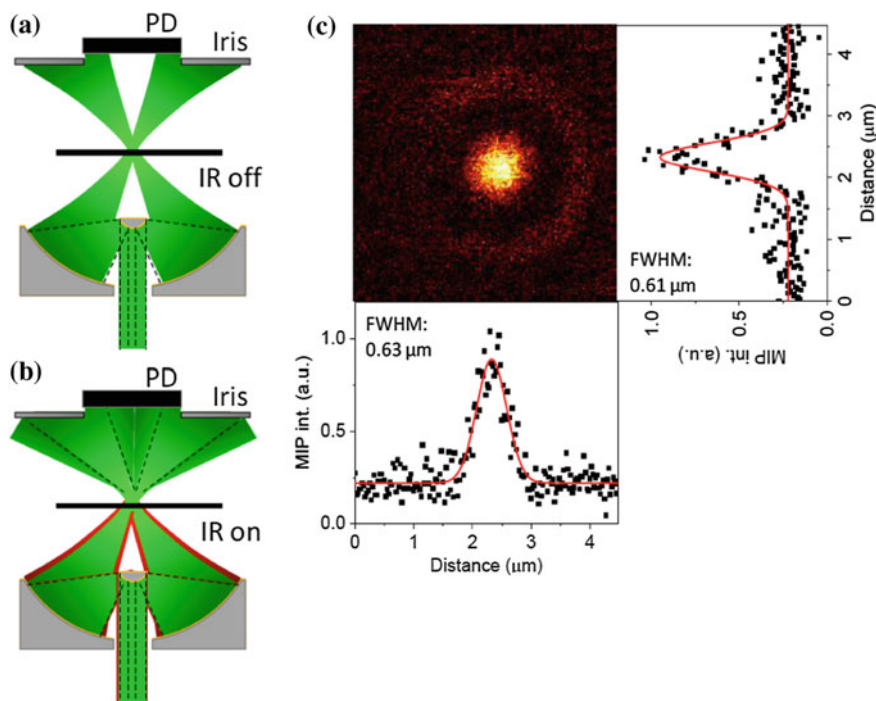


**Fig. 6.3** **a** Probe beam propagation through the sample via a dark-field objective without an infrared beam (not to scale, condenser omitted for simplicity). **b** The probe beam propagation is perturbed by the addition of the infrared pump beam due to infrared absorption and development of a thermal lens. **c** Mid-IR PT imaging of a 500 nm PMMA bead. The vertical and horizontal intensity profiles indicate the spatial resolution is  $\sim 0.6 \mu\text{m}$ . Adapted from [59] with permission. Copyright 2016 American Association for the Advancement of Science

As depicted in Fig. 6.5a, the nonlinear PT resonance intensity profile is much narrower ( $\sim 1/2$ ) than that of either the linear PT signal or the laser beams. Therefore, two adjacent nanoparticles whose distance is smaller than the diffraction limit of both the probe and pump beams are readily resolved by detecting the nonlinear PT signals, as shown in Fig. 6.5b. Experimental results also verified the anticipated improvement of the spatial resolution in nonlinear PTM, as shown in Fig. 6.5c, d. Based on the experimental results, the nonlinear PTM improved the lateral resolution from  $(260 \pm 20 \text{ nm})$  to  $(90 \pm 20 \text{ nm})$  with laser fluence level just above the threshold  $(0.7 \text{ J/cm}^2)$  in this case). Since the nonlinear configuration requires the use of a stronger beam intensity compared to linear PTM, the concern of laser-induced photodamage was inevitably raised. Nedosekin et al. estimated that the minimum laser fluence needed to achieve spatially selective signal amplification is 10–30% higher than the nonlinear threshold, while the photodamage typically occurs when the laser fluence is at 3–5 times higher than the nonlinear threshold [61]. The early nonlinear PT studies were mainly conducted using plasmonic nanoparticles since the enhancement of

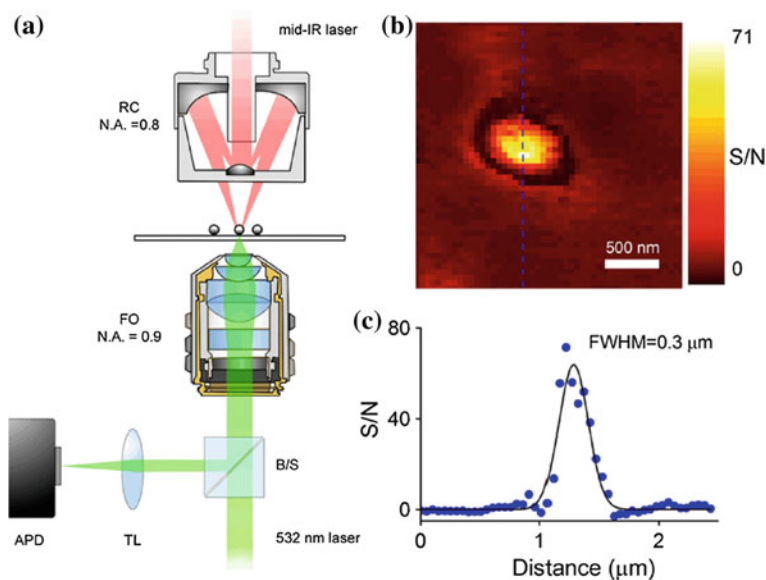


**Fig. 6.4** **a** Schematic diagram of the counter-propagating mid-IR PT microscopy. The mid-IR pump and visible probe beams are focused on the sample with separate objectives. APD: avalanche photodiode, RC = reflective Cassegrain, FO = focusing objective, B/S = beam splitter, and TL = tube lens. **b** Mid-IR PT imaging of a  $0.1 \mu\text{m}$  diameter polystyrene bead recorded with a step size of  $0.05 \mu\text{m}$ . **c** Line profile extracted from the image in panel **(b)** showing a full-width at half-maximum (FWHM) of  $0.3 \mu\text{m}$ . Adapted from [60] with permission. Copyright 2017 American Chemical Society

local electromagnetic field results in stronger nonlinear PT signal. Thanks to the recent development of high power laser sources with broader spectral coverage; this approach has also been demonstrated in liquid crystal [89], cells [91], and tissues [92].

It is noteworthy to mention that another approach uses time-resolved PT response to discriminate adjacent objects within the probe beam and diffraction limit was also realized [85, 91]. The principle behind such approach is that sub-diffraction objects exhibit different photo-induced thermal field dissipation rate. Therefore, by actively tuning the delay between pump and probe beams, time-resolved PT signal can be exploited to retrieve the actual shapes of different hot spots before the thermal fields expands to surroundings and prevent nano-objects from being resolved, as shown in Fig. 6.6a, b. This approach was demonstrated in nanoscale liposome imaging (Fig. 6.6c). Albeit sub-diffraction resolution is achieved, this method requires prior knowledge of physical or chemical parameters of samples to be studied in practical operations to optimize the time delays set between pump and probe beams. In addition, the sub-diffraction images require at least two independent measurements to compose, which prohibits high-speed PT imaging of nano-objects. Consequently, this approach is not widely used in this field.

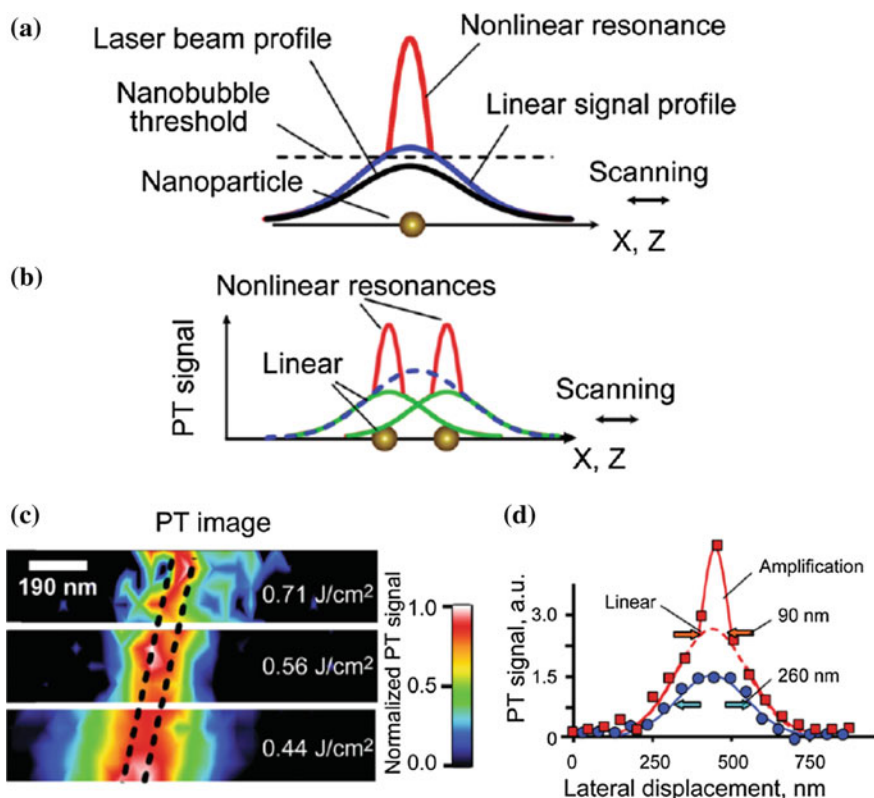


**Fig. 6.5** **a** Nonlinear PT amplification for a nano-object in the center of the laser beam. **b** Nonlinear sequential PT spatial resonances during laser scanning from two nano-objects separated by a distance smaller than the size of the diffraction-limited beam spot. The dashed line represents a sum of two linear (green solid lines) PT signals. **c** Super-resolution nonlinear PT imaging of a 75-nm single gold nanowire at different laser fluences. **d** Lateral resolution in linear and nonlinear modes of PT microscopy. Adapted from [61] with permission from Wiley-VCH Verlag GmbH & Co

### 6.2.4 Visible Beam Excited Photothermal Microscopy

We will discuss more technical details of PTM techniques using visible pump beams. Visible excited PTM was first demonstrated by Harada et al. in 1993 as an extremely sensitive method for non-fluorescent microscale particle analysis [83]. As illustrated in Fig. 6.7, a typical visible excited PT microscope setup consists of a modulated pump beam and a continuous wave or modulated probe beam which are combined at a dichroic mirror and sent to the objective collinearly. Both laser scan and sample scan configurations have been demonstrated [93, 94]. The probe beam is further modulated by the periodic PT effect and detected by either forward or backward mode. With the deployment of a lock-in amplifier, the PT signal modulated at high frequencies (typically 100 kHz–1 MHz) is demodulated with high SNR which enables superb

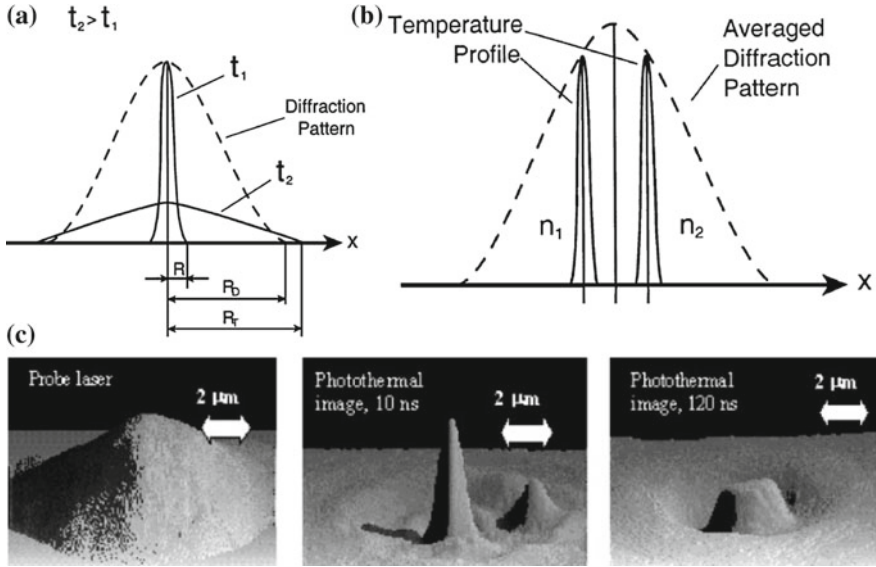


**Fig. 6.6** Thermal fields (solid curves) and diffraction pattern (dashed curves) around **a** a single nano-object, and **b** two adjacent nano-objects within the diffraction pattern. Adapted from [85], Copyright 2003 Optical Society of America. **c** Left: Probe laser diffraction pattern. Middle: Super-resolution PT imaging of two 90-nm liposomes with 10 ns time delay. Right: Hardly resolved PT imaging of the same liposomes with 120 ns delay time. Adapted from [91]. Copyright 2002 Wiley-Liss, Inc.

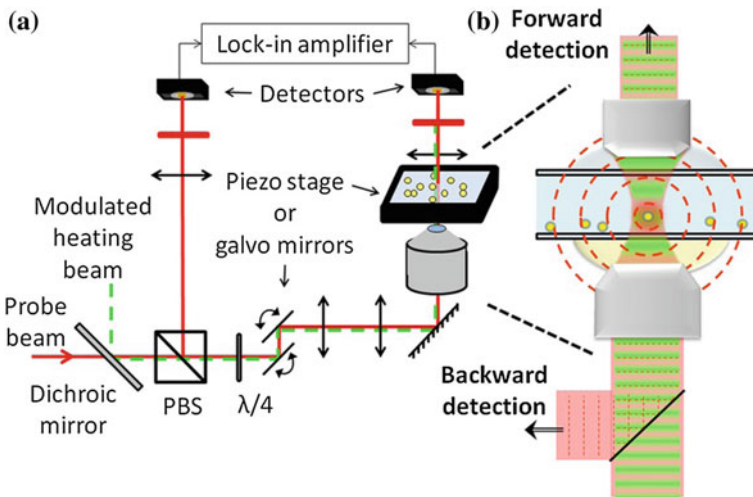


**Fig. 6.7** **a** Setup of a typical visible excited PTM with lock-in amplified detection (PBS: polarizing beam splitter;  $\lambda/4$ : quarter wave plate). **b** Detailed depiction of probe beam propagation in both forward and backward detection. Reprinted from [94] with permission. Copyright 2014 Royal Microscopical Society

sensitivity. The limit of detection of visible excited PTM was first determined to be at femtogram level [95]. This limit was soon pushed to single nanoparticle detection [81], statistically sub-molecule detection [96], and single-molecule imaging [82]. Note that the impact of solvents in sample cells on SNR has already been noticed and investigated. Since the PT signal is proportional to the refractive change rate as a function of the change in temperature ( $\partial n/\partial T$ ), this value determines the signal level and SNR when other parameters are the same. It was demonstrated experimentally that performing PT detections in glycerol results in five times improvement of the SNR than in water [74]. Furthermore, recent experiments indicated that critical Xeon medium will enhance the SNR by over 100 times compared to glycerol [97].

Visible excited PTM endows several advantages over other label-free microscopy techniques. First, for many molecules, electronic state absorption cross-sections are much larger ( $>10^9$  times) than vibrational state absorption or Raman scattering processes, resulting in extremely sensitive detection of various species [98]. For instance, heme proteins are known to have extremely fast internal conversion rate and short excited state lifetime ( $<50$  fs) of Soret band such that almost all absorbed photon energy is converted to heat [99, 100]. Therefore, PT effect provides ideal contrast for the detection of these molecules at fairly low concentrations (100  $\mu$ M hemoglobin solution) [98]. Besides, gold nanoparticles and nanorods are a group of nano-objects that often being studied using visible excited PTM since the plasmonic resonances at 550–800 nm increases local electromagnetic fields and enhances the PT signals allowing nanoparticles as small as 1.4 nm to be detected [80].

Another advantage is that optics are well-designed and readily operated for visible beams compared to mid-IR sources that require special materials for coatings and substrates. There are no specific sample preparation requirements for visible excited PTM compared to fluorescence microscopy or IR microscopy. Liquid sample cells or sandwiched glass slides are usually used for transparent samples at forward detection mode. Although some experiments were conducted in glycerol or other organic solvents in order to enhance the SNR, the practical steps are nothing more complicated than preparing samples suspended in water. For opaque samples, backward detection mode allows visible excited PT imaging of only the surface of the samples due to dramatic power attenuation as both pump and probe beams propagate deep into the samples. But the operation is relatively easy in this case. Such advantage significantly simplifies the customized development, broader applications, and routine maintenance of the PT microscopes.

Third, laser engineering has come a long way in developing visible laser sources with higher power, lower noise, and broader tunable range, which all benefits the overall performances of PTM with visible pump beams. At first, the pump and probe beams power in samples are limited to 2 and 0.1 mW, respectively [96]. The application of high-power lasers increases the power dissipated to samples to 10 times for each beam, which leads to 100 times PT signal and 10 times SNR, given the quadratic relation of laser power and signal level in PT process [74]. Before tunable lasers were implemented, PTM is excited by monochromatic visible pump beams including He–Ne laser, Ar–ion laser, and 532 nm diode laser, through which only one type of molecules can be determined at a time. Then, dual pump beams appa-

ratus was exploited to perform simultaneous multiwavelength PT imaging, enabling the detection of two different species in one measurement [101]. The deployment of diode laser pumped optical parametric oscillator finally enables full coverage of the visible to NIR spectral region in PTM, which significantly enhances the ability to differentiate complex samples using PT spectromicroscopy technique [102].

The concern of laser-induced photodamage, especially thermal damage, also exists in visible beam excited PTM. Unlike fluorescence-based techniques that are vulnerable to photobleaching, the photodamage in visible beam excited PTM mainly comes from local thermal damage. The pump lasers used in PTM are usually nanosecond lasers, while the heat dissipation rate in condensed matters falls in tens of nanoseconds to microsecond scale [103]. Therefore, potential damage from local heat accumulation must be considered when determining the appropriate sampling rate for PT experiments. Some hypothetical and experimental works investigating the damage threshold of various biological samples have been reported [61, 104]. However, the experimental results of cell damage thresholds show dramatic variations among different cell lines and pump beam wavelengths [105]. Thus, more systematic studies on the photodamage in visible excited PTM are in need to facilitate spreading.

### ***6.2.5 Mid-IR Excited Photothermal Microscopy***

Ever since the publication of Coblentz's high-quality IR spectral database in 1905 [106], advances in IR spectroscopy and spectromicroscopy including Fourier transform IR (FTIR) spectroscopy [26], FTIR imaging [27] attenuated total reflectance IR imaging [107], and focal plane arrays IR imaging [108] have all improved the measurement of IR absorption from the aspects of higher sensitivity and spatial resolution. However, the fundamental limit of IR diffraction ( $\sim 5 \mu\text{m}$ ) was not defeated by preceding approaches. Besides, the broad spectral window (typically 2–10  $\mu\text{m}$ ) invokes the problem of measurement accuracy since the wavelength-dependent light scattering could produce dramatic fluctuations in the IR signal intensity, which leads to huge baseline artifacts [109]. Furthermore, water shows strong absorption in the entire mid-IR region, which hinders the application of IR spectroscopic imaging to investigate biomolecules in living cells or organisms in aqueous environment. These problems were addressed collectively by the invention of mid-IR excited PTM. We will focus on the hardware and practical operation aspects of this technique in detail in this section.

Mid-IR excited PTM was demonstrated by Furstenberg et al. in 2012 [110], about 20 years later than the first demonstration of visible excited PTM. The pivotal difficulties of developing mid-IR based PTM are: (1) the lack of high-quality mid-IR laser sources; and (2) complications to integrate mid-IR pump beam with visible probe beam in the same optical system without introducing severe chromatic aberrations and mid-IR power losses.

The first problem was addressed by recent advances in mid-IR laser sources in the last two decades. In particular, modern quantum cascade laser (QCL) offers the ability to perform broadband wavelength scan with ultra-high spectral resolution ( $\sim 0.1 \text{ cm}^{-1}$ ) discretely [111–113], in which specific vibrational bands of interests are pinpointed at high speed while providing enough chemical information to determine the composition of samples through spectra analysis [30]. Therefore, the majority of mid-IR PT microscopes use QCL as IR pump beam [59, 84, 110]. Besides QCL, difference frequency generation (DFG) is another effective approach to produce tunable mid-IR sources as the pump beam of PT microscope [114–116]. The fundamental beams usually consist of a tunable beam and a monochromatic beam. Both beams are focused onto nonlinear crystals, such as periodically poled LiNbO<sub>3</sub>, to produce tunable nanosecond mid-IR pulses whose average power can reach up to 200 mW with less than  $10 \text{ cm}^{-1}$  linewidth, which is sufficient to induce strong PT effect in most absorption bands and measure liquid phase IR spectra. Despite the additional complexity of DFG, the produced mid-IR pump beam can be tuned to various wavelengths with better coverage of high wavenumber mid-IR regions, including the “cell silent region”, where most intrinsic biomolecules show no absorption, and deuterated molecules are often used to investigate cell metabolisms [116, 117]. Therefore, QCL and DFG collectively provide more options to the pump beam selection of mid-IR excited PTM and enable more important applications in biological studies.

The second problem found a solution by the deployment of reflective optics, including the Cassegrain objectives and off-axis parabolic mirrors, since these optics are immune to chromatic aberration across the whole spectral window. Like visible excited PTM, a typical mid-IR excited PT microscope deploys coaxial configuration, as illustrated in Fig. 6.8a, where the mid-IR pump beam and visible probe beam are combined at the dichroic mirror and collinearly sent to the Cassegrain objective [59]. To avoid mid-IR beam power losses, the reflective optics are usually coated with gold or silver, and the samples are sandwiched by ultra-broadband IR transparent materials such as CaF<sub>2</sub> or MgF<sub>2</sub>. Since the water vapor and some other trace organic vapors in air all absorb mid-IR, the beam path of the mid-IR pump beam is usually designed with minimum distance, to further maintain the pump beam power at the sample. In some cases, to diminish the power loss and push the detection limit, methods used in conventional mid-IR measurements, including purging dry nitrogen into the system to reduce water vapor and CO<sub>2</sub> absorption, are needed [118]. Note that the reflected mid-IR residue (power  $< 1 \text{ mW}$ ) from the dichroic mirror is collected by a mercury–cadmium–telluride (MCT) detector to record the IR power at each wavelength in real time. This power spectrum is used to normalize the PT signal acquired by the photodiode to produce the IR absorption spectra of samples.

There have been several reports aiming to improve the SNR in mid-IR excited PTM through various optimization approaches. For instance, Zhang et al. investigated the frequency dependence of the mid-IR PT signal, laser noise, and the system SNR (Fig. 6.8b) [59]. By considering the trade-off between the SNR and data acquisition speed, the pump beam modulation frequency was set at 100 kHz for optimal performance. As shown in Fig. 6.8c, a high-Q tunable resonant amplifier with a center frequency of 102.5 kHz was installed after the photodiode such that the modulated

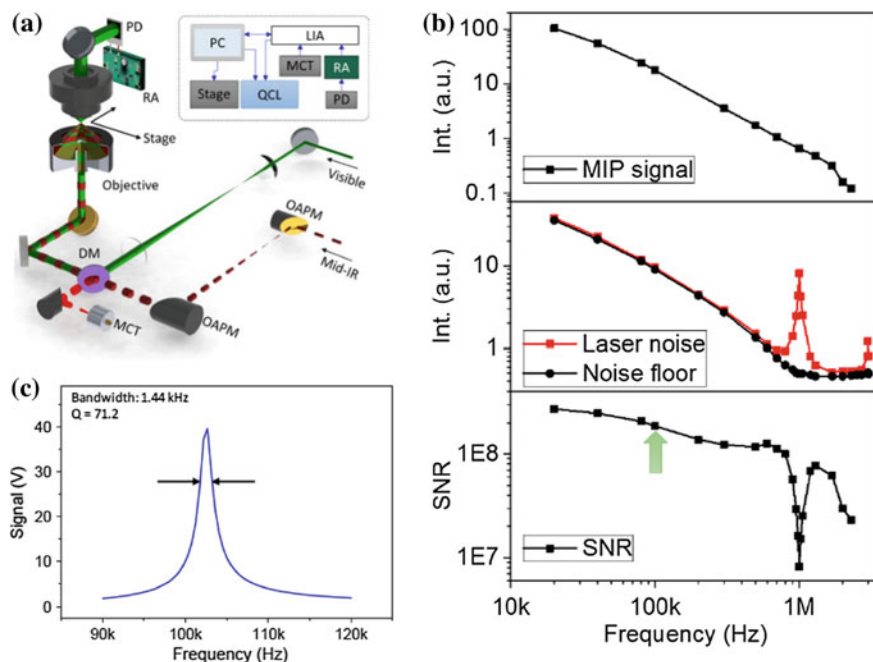


**Fig. 6.8** **a** Setup of a typical mid-IR excited PTM using a Cassegrain objective. **b** Comparison of the frequency dependence of the mid-IR photothermal signal, QCL laser noise, and SNR. **c** Frequency response of a high-Q tunable resonant amplifier. Adapted from [59] with permission. Copyright 2016 American Association for the Advancement of Science

PT signal is amplified by  $10^3$  times while non-resonant noises are suppressed. Apart from the denoise strategies in optimizing the pump beam modulation frequency and detection frequency, Totachawattana et al. proposed a method to reduce background noises and enhance the SNR by introducing high-frequency modulation (1.04 GHz) to the probe beam [118]. On comparing with the results obtained using continuous wave probe beam, they found that the ultra-fast modulation increased the ultimate SNR by nine times. Another strategy was attempted by a couple of reports, in which the excitation wavelength is tuned to a specific “silent spectral region” to minimize the background absorption and maximize the analyte absorption with the prior knowledge of the system to be measured [59, 116].

As discussed in Sect. 6.2.3, the highest spatial resolution that have been achieved in mid-IR PTM is  $0.3 \mu\text{m}$  using a highest NA air objective (NA 0.9) among all reported works [60]. In the most recent report on the resolution improvement of mid-IR excited PTM, Huffman et al. claimed that 202 nm resolution was achieved by roughly comparing the images obtained from the PTM and confocal microscope without quantitative evaluations [119]. Although it has been suggested to use water or immersion oil objectives to further increase the NA (to 1.3–1.5) to achieve better spatial resolution, the strong absorption of water and oil in the mid-IR region,

especially in the biologically informative amide I and C=O carboxyl bands [120], limited the broad interests of such strategy in practical applications since the mid-IR pump wavelength has to be tuned off resonance with these bands. The nonlinear PT effect has been observed in spectroscopy studies [89, 121], but super-resolution mid-IR excited PTM has not been enabled via nonlinear PT effects. With this field actively growing, those technical barriers that limit the pursuit of higher resolution will eventually be eliminated.

Similar to the case of visible excited PTM, the pump laser-induced photodamage is also considered in mid-IR excited PTM. Just like what have been discussed in the visible excited PTM in Sect. 6.2.4, the photodamage in mid-IR excited PTM is also induced by the thermal damage instead of direct photon excitation. However, the mid-IR photodamage threshold for most samples is much higher than that in the case of visible excitation since mid-IR photons only induce covalent bond vibrations which are more reversible processes compared to the electronic state excitation induced in visible excited PTM. To avoid accumulated heat causing damage to the sample, it is suggested to control the duty cycle of the mid-IR pump beam according to the heat dissipation rate of the sample and surroundings. Li et al. proposed a model to simulate the PT relaxation time as a function of object size for a series of polystyrene spheres in the air-glass surface [60]. Their results indicated that the accumulated heat will vanish in  $10^{-6}$  s, which is apparently faster than experimental observations in other reports [59, 116]. Therefore, such model needs further amendment to be more accurate in predicting the actual relaxation time in mid-IR excited PT processes. So far, most of the reported mid-IR PTM studies adopted  $\sim 10$   $\mu$ s as a single period of PT measurement. Note that some mediums with large heat capacity like water (4.18 J/kg K) will accelerate the heat dissipation, which helps reduce the photodamage from local overheating. Such phenomenon was found in the in vivo mid-IR PT imaging of cells and organisms [59].

### **6.2.6 Applications of Super-Resolution Photothermal Microscopy**

Owing to the superb sensitivity in the detection of non-fluorescent species, both the visible and mid-IR excited super-resolution photothermal microscopies (SR-PTMs) have found numerous applications in the detection of trace analytes in materials science and biomedical studies. As discussed in the preceding sections, compared to mid-IR excitation, visible excited SR-PTM is able to take advantage of plasmonic resonance of metallic analytes to achieve single-molecule detection limit, high spatial resolution ( $\sim 100$  nm), and provides electronic absorption information. Therefore, it has been widely applied in the label-free imaging of individual nanoparticles, nanoclusters, and nanocrystals [80, 122]. Note that the size dependence of the PT signal has been well studied, as shown in Fig. 6.9, which enables the discrimination among different-sized particles that are much smaller than the diffraction limits of

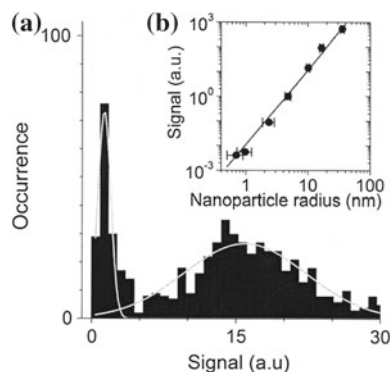


**Fig. 6.9** **a** Signal distribution obtained from a sample containing both 2 and 5 nm gold nanoparticles. **b** Size dependence of the signal, that is, absorption cross-section (circles) deduced from a series of histograms as presented in **(a)** and, in comparison to the Mie theory (solid line). Reprinted from [80] with permission. Copyright 2004 The American Physical Society

the PTM. For instance, gold nanoclusters as small as 1.4 nm can be differentiated from 5 nm nanoclusters referring to the differences of their PT signal intensities even though they look alike in the PT images due to the limited spatial resolution [80]. Such observation has been exploited in studying molecular binding dynamics, especially for non-fluorescent molecules, at the single-molecule/single-nanorod level since it allows the researchers to significantly reduce the volume of nanorods to mimic the actual protein receptor sizes and construct better dynamic models (Fig. 6.10) [123]. The size distribution of nanoparticles with varying volumes below the diffraction limit can also be retrieved readily according to the PT signal intensity [74, 79]. Gaiduk et al. further demonstrated single molecule detection at room temperature by fully exploiting the advantage of high sensitivity provided by visible excited SR-PTM [82]. Owing to the label-free nature, Bogart et al. introduced a technique to monitor in vivo cell uptake of dextran-coated iron oxide nanoparticles, which is considered as a useful cell tracker [124]. Kitagawa et al. successfully integrated visible excited PTM with the electrodynamic chromatography, which enables separation and label-free detection of trace amino acids simultaneously [125]. Other reports have demonstrated the application of the visible excited SR-PTM to study the thermal properties of materials such as diamond [126], single-layer thin films [127], nanoscale defects in materials [128], and PT detection sensitivity as a function of temperature increase [129].

Apart from plasmonic nanoparticles, visible excited SR-PTM has found broad applications in label-free imaging of certain intrinsic molecules in biological samples. The greatest challenge of imaging complex biological specimen using visible excited SR-PTM is that the low concentration of most biomolecules requires extremely high sensitivity without surface plasmon. One solution is to select those analytes with relatively large absorption cross-sections such that the PT signal is significantly stronger than background absorptions. For instance, cytochromes as a group of intrinsic intra-

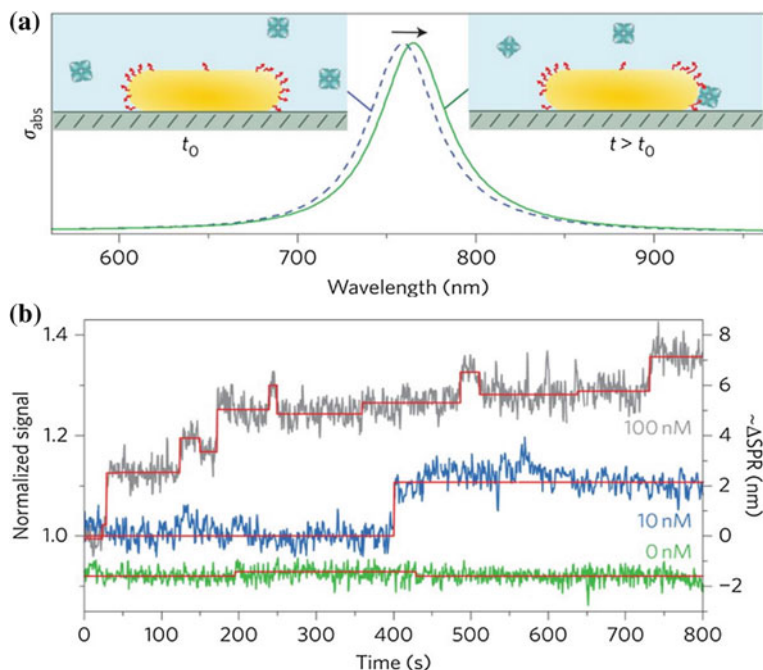


**Fig. 6.10** **a** A single gold nanorod functionalized with biotin is introduced into an environment with the protein of interest. Binding of the analyte molecules to the receptors induces a redshift of the longitudinal surface plasmon resonance (exaggerated in the illustration). This shift is monitored at a single frequency using photothermal microscopy. **b** Photothermal time trace showing single-molecule binding events. The normalized photothermal signal as a function of time for biotin-functionalized gold nanorods in the presence of a streptavidin–R-phycoerythrin conjugate. The photothermal signal was recorded on three different nanorods in the presence of different concentrations of the protein. The red lines are fits to the time traces using a step-finding algorithm. Adapted from [123] with permission. Copyright 2012 Macmillan Publishers Limited obtained

cellular proteins that have strong absorption in the visible region are often studied by visible excited SR-PTM [130]. The deployment of tunable pump lasers allows the collection of absorption spectroscopy simultaneously with PT imaging, which enabled identification, quantification, and differentiation of cytochromes *c* in mitochondria, live cells, and solutions [131]. The visible excited SR-PTM has also been demonstrated in tissue histology to image nuclei (hematoxylin), cell bodies (eosin), and melanin with H&E stained skin tissues [132]. However, the number of such intracellular analytes is limited and cannot be applied universally. The other solution is provided by the integration of radially segmented balanced (RSB) detection to the conventional PTM to enhance the modulated PT signal and suppress the noise arising from probe intensity fluctuations as well as electronic cross-talks (Fig. 6.11). As a result, the overall SNR of the SR-PTM with RSB detection is improved by  $\sim 2.3$  times [133, 134]. Such enhancement may not look dramatic but is sufficient to obtain decent label-free images of skin tissues [133], skeletal muscle mitochondria [135],

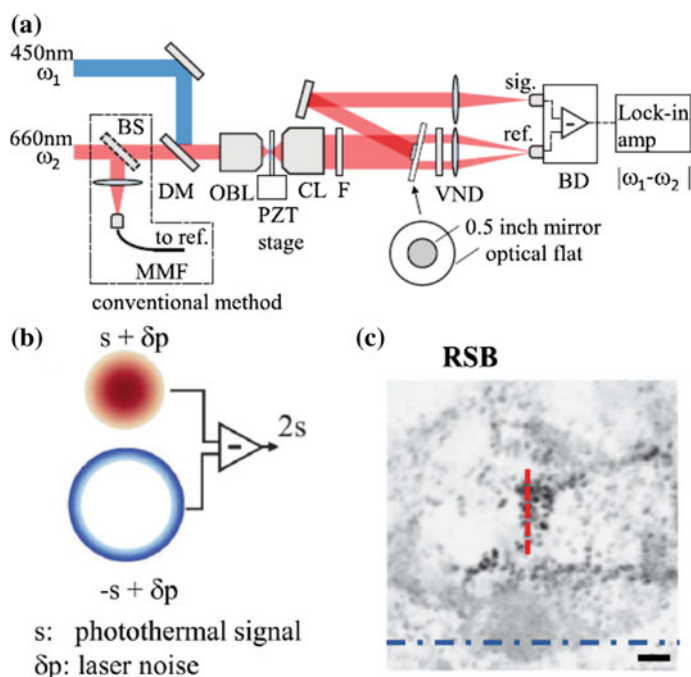


**Fig. 6.11** **a** Experimental setup of laser diode-based photothermal microscopy with radially segmented balanced detection. DM: dichroic mirror; BS: beam splitter; OBL: objective lens; CL: condenser lens; F: band pass filter; VND: variable neutral-density filter; BD: balanced photodetector; MMF: multimode fiber. **b** Conceptual scheme of the radially segmented balanced detection for improving signal intensity  $s$  and reducing intensity noise of the probe beam  $\delta p$ . **c** PTM image of a slice of mouse melanoma observed by RSB detection. Adapted from [133] with permission. Copyright 2015 Optical Society of America

3-D imaging of non-fluorescent tissues [136], and tumor tissues [137], to provide molecular spectroscopy information to assist disease diagnosis in clinics.

Although mid-IR excited SR-PTM cannot achieve the same spatial resolution as visible excited configurations due to the limitations of optics, the informative IR spectrum strengthens the chemical selectivity for organic molecules in particular, and the detection sensitivity could achieve micromolar in solutions. Compared to visible absorption spectroscopy, mid-IR spectroscopy endows narrower characteristic peaks which is of value in molecule differentiations, and broader spectral coverage that allows detection of all kinds of covalent bond vibrations. Thus, mid-IR excited SR-PTM has been actively used in label-free imaging of complex systems such as live cells [59, 116], microorganisms [60], tissue slices [118, 138], polymer composites [110, 139], pharmaceutical formulations [84], mixed cation perovskites [140], graphene oxide detection [141], trace gas detection [142], and so on. One of the most important applications is the demonstration of label-free multicolor imaging of intracellular distribution of lipid droplets and drug molecules through mid-IR

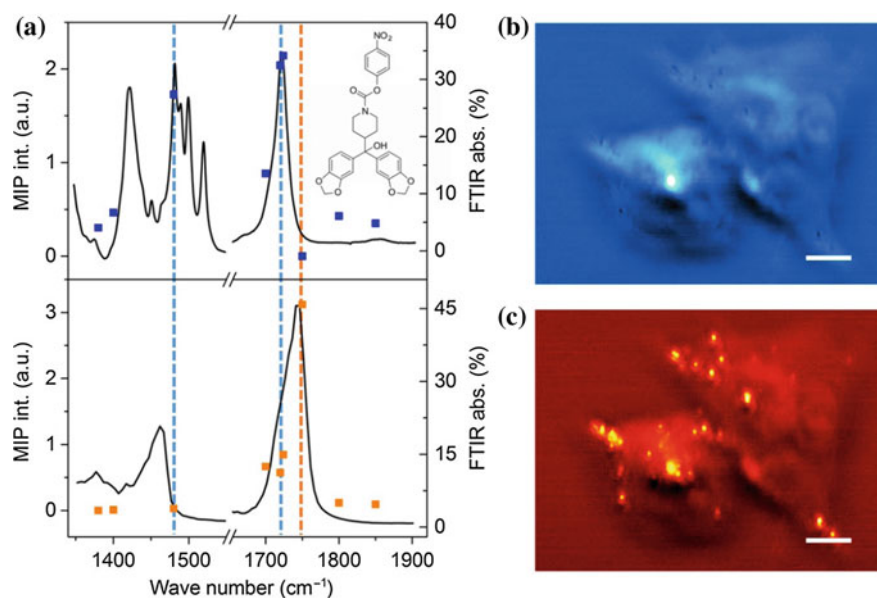


**Fig. 6.12** Multispectral mid-IR PT imaging of cellular drug uptake. **a** Infrared spectra of the lipid inhibitor JZL184 (top, line) and olive oil (bottom, line). Squares indicate the multivariate curve resolution results for drug and lipid content. Dashed lines indicate the characteristic peaks for drug (blue) and lipid (orange) content. Inset shows the molecular structure of the drug. **b** and **c** Multivariate curve resolution output of multispectral mid-IR PT imaging of JZL184-treated MIA PaCa-2 cells for drug (**b**) and lipid (**c**) content. Scale bars, 20  $\mu\text{m}$ . Reprinted from [59] with permission. Copyright 2016 American Association for the Advancement of Science

excited SR-PTM since it proves such technique to be a promising imaging platform in the field of cell biology and biomedical studies (Fig. 6.12) [59]. By combining the advantages of conventional IR hyperspectral imaging and submicrometer spatial resolution of confocal optical microscopy, the mid-IR excited SR-PTM for sure will become a powerful analytical approach in scientific researches. Furthermore, the demonstration of fiber-based [143] mid-IR excited PTM increases the portability of the system. Also, the backward detection apparatus (Fig. 6.13) will simplify the sample preparation process and appeal to users from the industry specifically [84]. In short, this field is actively growing since the first report about mid-IR excited SR-PTM in 2012. There will be more technical breakthroughs in the near future.

### 6.3 Super-Resolution Transient Absorption Microscopy

Owing to the advancement of laser techniques and fast electronics since the 1980s, the field of nonlinear optical microscopy has come a long way in developing imaging techniques with higher resolution, lower detection limit, and higher frame rate with

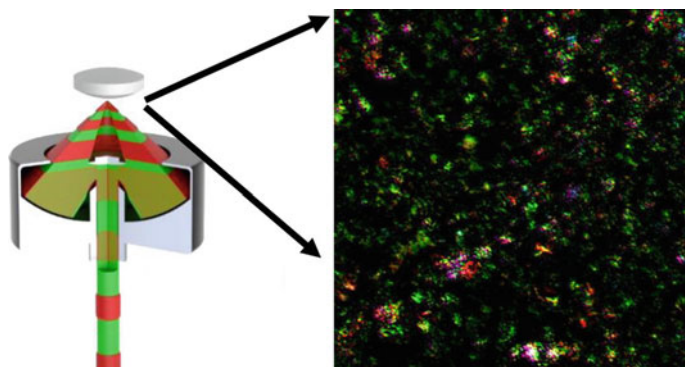


**Fig. 6.13** Backward detected mid-IR excited SR-PTM is able to quantify the size distribution and chemical compositions of active pharmaceutical ingredients as well as excipients in pharmaceutical tablets through direct imaging. Reprinted from [84] with permission. Copyright 2017 American Chemical Society

decent chemical selectivity, to attract broader interests in other research areas. Based on the fundamental principles, those nonlinear optical spectromicroscopy approaches can be classified into three main categories, including parametric generation (e.g. second harmonic generation [144], third harmonic generation [145], coherent anti-Stokes Raman scattering [14], etc.), pump-probe (e.g. transient absorption (TA) [46]), and nonlinear dissipation (e.g. two-photon excited fluorescence [146], stimulated Raman scattering (SRS) [15], etc.).

In this section, we focus on the principle and technical details of two novel approaches to perform nonlinear absorption-based LFSRM, saturated TA and SRS microscopy, both of which were realized through nonlinear absorption and implementing the mechanism of reversible saturable optical linear fluorescence transitions (RESOLFT) microscopy in recent years and expected to find interesting applications in biological and materials science.

### 6.3.1 *Transient Absorption Microscopy*

TA spectroscopy, also known as pump-probe spectroscopy or time-resolved spectroscopy, has been widely used to elucidate fundamental ultra-fast processes (picoseconds and sub-picoseconds) in chemistry, biology, and condensed matters [19, 46, 147, 148]. In a typical TA experiment, a pump beam is applied to reduce the population of ground states and induce intensity fluctuations of the transmitted probe beam, which is detected as the TA signal. The contrast types that contribute to the TA signals include three main components, including ground-state bleach, stimulated emission, and excited-state absorption (Fig. 6.14) [148]. In ground-state bleach process, an intense pump beam is usually used to deplete molecules in the

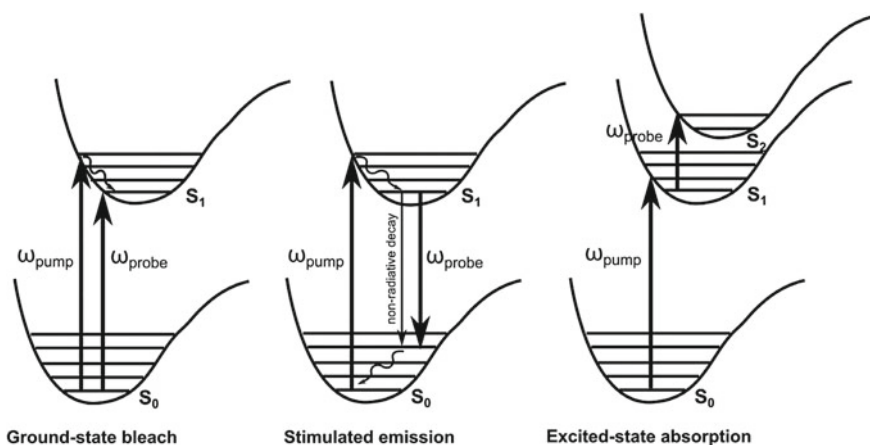


**Fig. 6.14** Contributions to TA spectrum: ground-state bleach, stimulated emission, and excited-state absorption. Reprinted from [148] with permission. Copyright 2015 by Wiley-VCH Verlag GmbH & Co. KGaA, Weinheim

ground state such that the absorption of probe beam is suppressed and increases the transmitted probe intensity. While in the case of stimulated emission, the pump beam first excites molecules to excited states and then, the slightly delayed probe beam induces stimulated emission to produce more photons in the probe frequency which increases the probe beam intensity. As for excited-state absorption, the excited molecules keep absorbing probe beam photons and are excited to higher states, which results in the decreased transmitted probe beam intensity. Note that the contributions to TA signals are not limited to the above-mentioned processes, but this review will not include other mechanisms. As a nonlinear optical approach, one advantage of TA microscopy over linear absorption-based microscopy is the removal of off-focal signal. Furthermore, since TA involves nonlinear response from samples, it offers the opportunity to achieve super-resolution by breaking the diffraction limit in conventional confocal microscopy. We will discuss the two recently demonstrated LFSRM approaches in the following sections.

### 6.3.2 Spatially Controlled Saturated Transient Absorption

The idea of spatially controlled saturated transient absorption (SCSTA) originates from the GSD microscopy first proposed by Hell et al. [149], in which a doughnut-shaped depletion beam and a regularly focused probe beam are overlaid at the sample to reduce the PSF, which represents the smallest spot that can be spatially resolved (Fig. 6.15) [150]. In typical GSD microscopy, fluorophores located at the outer ring will be excited to the  $T_1$  triplet state and have a much longer lifetime ( $\sim 10^{-2}$  s level) than normal  $S_0 \rightarrow S_1$  relaxation ( $10^{-9}$  to  $10^{-7}$  s level). Thus, after the depletion beam

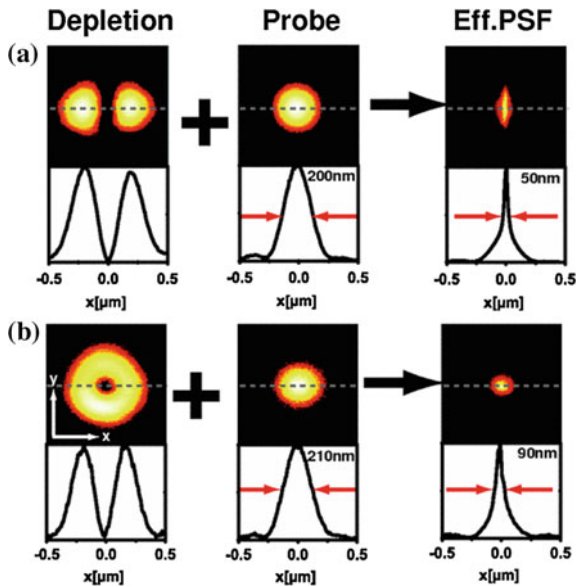


**Fig. 6.15** Creating effective PSFs of sub-diffraction extent in a single-point scanning GSD microscope. **a** Squeezing the spot just along the  $x$ -axis and **b** along all directions in the focal plane. The depletion spot (Depletion) overlaid with the regularly focused probe spot (Probe) produces the effective PSF (Eff. PSF). The probe spot probes the fluorescence right after the depletion spot has pumped the dye into the triplet state. Focal plane cross-section of the PSF (upper panel) and profiles along the  $x$ -axis [dashed line in upper panels] showing FWHM values (lower panels). Wavelengths for depletion and probing: 532 nm; fluorescence wavelength: 560 nm. Reprinted from [150] with permission. Copy right 2007 American Physical Society

bleaches the surrounding fluorophores, the delayed probe beam can only measure the molecular absorption from the very center of the overlaid beams, whose diameter is predicted to be capable of achieving 10–20 nm [149].

Wang et al. introduced such idea to SCSTA experiments by GSD of the electron–charge carrier in graphene-like materials (Fig. 6.16) [62]. The saturable absorption properties of graphene-like structures have been well studied [151–153]. In particular, the charge carrier dynamics in epitaxial graphene has been investigated by TA microscopy [42]. It was observed that the carrier–phonon interactions in graphene-like structures occur in the timescale of 100 fs to a few picoseconds. Therefore, by tuning the temporal delay between pump and probe pulses to sub-picosecond scale, the transient absorption signal is able to be detected. To actively suppress the off-focal signal, an intense doughnut-shaped depletion pulse is temporally inserted between the pump and probe pulses. As a consequence, the transient absorption signal (shown as the probe beam intensity loss) is generated only from the very center of the overlaid beams similar to GSD microscopy. The doughnut-shaped depletion beam is often tailored by spatial light modulator or spatial phase modulator. According to the experimental results shown in Fig. 6.16d–f, the PSF in SCSTA (FWHM

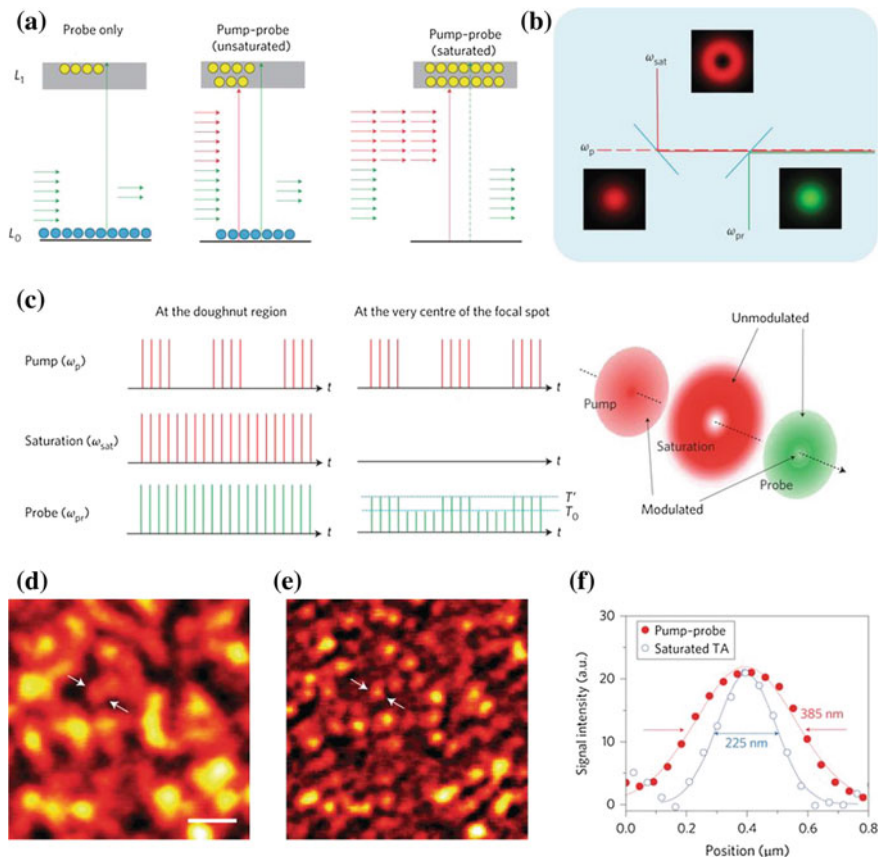


**Fig. 6.16** Principle of saturated transient absorption microscopy. **a** Illustration of the saturation effect in a two-level electronic transition. Pump and probe photons are indicated by red and green arrows, respectively. **b** Simple layout of the setup. The dashed line indicates that the pump beam is modulated. **c** The pulse train of pump, saturation, and probe beams at the focused doughnut-shaped region (left panel) and at the very center of the focal spot (middle panel). The modulation transfer from pump to probe only occurs at the center where the saturation field intensity is close to zero (right panel). Sub-diffraction-limited imaging of graphite nanoplates obtained from **d** conventional pump-probe microscopy and **e** SCSTA microscopy. **f** Intensity profiles along the lines indicated by arrows in **(d, e)**. Scale bar: 1  $\mu\text{m}$ . Adapted from [62] with permission. Copyright 2013 Macmillan Publishers Limited

is 225 nm) is 42% of that in the conventional pump-probe microscopy (FWHM is 385 nm).

One of the major concerns of such approach is the issue of photodamage since the molecules are repeatedly excited/depleted by the pump/depletion beam in the raster scanning mode. As Bretschneider et al. discussed in their report on GSD microscopy, care must be taken when determining the pixel dwell time since molecules excited to the triplet state must relax to ground state before beam moves on [150]. In SCSTA experiments, Wang et al. also investigated the photodamage threshold of the intense depletion beam and recovery of TA signals after repeated excitations using graphene nanoplate as a model. The photodamage was observed when power density exceeds  $\sim 2.4 \text{ MW cm}^{-2}$ , while the TA signal recovery rate could reach 100% below that threshold. This approach can be applied to other materials that have saturable absorption properties, such as single-walled carbon nanotubes [154–156], iron oxides [157], or zinc oxides [158].

### 6.3.3 *Super-Resolution Stimulated Raman Microscopy*

Inspired by the success of other super-resolution nonlinear optical microscopy [62, 79], Gong et al. proposed to combine the advantages of stimulated emission depletion (STED) microscopy and SRS microscopy by developing the super-resolution saturated SRS microscopy in a theoretical study [159]. They proposed to split the Stokes beam into two components, one of which is modulated as an intense doughnut-shape by a phase plate and the other one remains a normal Gaussian beam. By recombining the two Stokes components, an effective Stokes beam with narrower PSF is created at the focus. However, according to their simulated results, the power density required for the intense Stokes saturation beam is as high as a few  $\text{TW cm}^{-2}$ , which is almost impossible to reach in most laboratory conditions.

The super-resolution SRS microscopy was realized in 2015 by Silva et al. using a triple-beam configuration [63]. Instead of splitting the Stokes beam to create a doughnut-shape Stokes, Silva et al. deploy another beam as the decoherence beam whose wavelength is close to that of Stokes beam and destroy the vibrational coherence at the ring of the doughnut-shape. According to some preliminary super-resolution SRS imaging results, the spatial resolution was improved by a factor of  $\sim 1.7$ . As measured in the experiment, the power density of the decoherence beam required to induce the saturation SRS is  $\sim 10 \text{ W cm}^{-2}$ , which is close to the average power used in previously reported SRS experiments [15, 38, 160]. Note that this approach uses the same idea as STED microscopy. Thus, an ultimate resolution of  $\sim 50 \text{ nm}$  is expected as such technique can be actively developed in the future. Along with the ability of SRS microscopy providing the informative vibrational spectroscopy of various biomolecules and inorganic materials, super-resolution SRS microscopy will find broad applications in biological and materials sciences.

## 6.4 Conclusion and Outlook

The functions of biomolecules, biosystems, and nanomaterials are inextricably linked with the structures and chemical compositions. Absorption-based LFSRM, with superior detection limit and spatial resolution, is growing as a significant tool to enhance the understanding of biology and materials sciences. In this review, we have introduced both linear and nonlinear absorption-based LFSRM techniques that provide excellent sensitivity, fast imaging speed, as well as informative spectroscopic information. We have highlighted how the recent advancements in mid-IR excited PTM have successfully defeated the diffraction limit of mid-IR beam. As a relatively new field, it is to be expected that absorption-based LFSRM approaches will be further improved by ongoing developments in laser engineering, optical and electronic technology.

## References

1. J.B. Pawley, in *Handbook of Biological Confocal Microscopy*, ed. by J.B. Pawley (Springer US, Boston, MA, 2006), pp. 20–42
2. E. Abbe, Beiträge zur Theorie des Mikroskops und der mikroskopischen Wahrnehmung. *Archiv für mikroskopische Anatomie* **9**, 413–418 (1873)
3. S.W. Hell, Microscopy and its focal switch. *Nat. Methods* **6**, 24–32 (2009)
4. R.M. Dickson, A.B. Cubitt, R.Y. Tsien, W.J.N. Moerner, On/off blinking and switching behaviour of single molecules of green fluorescent protein. *Nature* **388**, 355–358 (1997)
5. E. Betzig, G.H. Patterson, R. Sougrat, O.W. Lindwasser, S. Olenych, J.S. Bonifacino, M.W. Davidson, J. Lippincott-Schwartz, H.F.J.S. Hess, Imaging intracellular fluorescent proteins at nanometer resolution. *Science* **313**, 1642–1645 (2006)
6. M.J. Rust, M. Bates, X. Zhuang, Sub-diffraction-limit imaging by stochastic optical reconstruction microscopy (STORM). *Nat. Methods* **3**, 793–795 (2006)
7. B. Huang, W. Wang, M. Bates, X.J.S. Zhuang, Three-dimensional super-resolution imaging by stochastic optical reconstruction microscopy. *Science* **319**, 810–813 (2008)
8. S.W. Hell, J.J.O.L. Wichmann, Breaking the diffraction resolution limit by stimulated emission: stimulated-emission-depletion fluorescence microscopy. *Opt. Lett.* **19**, 780–782 (1994)
9. K.I. Willig, B. Harke, R. Medda, S.W. Hell, STED microscopy with continuous wave beams. *Nat. Methods* **4**, 915–918 (2007)
10. K.I. Willig, S.O. Rizzoli, V. Westphal, R. Jahn, S.W. Hell, STED microscopy reveals that synaptotagmin remains clustered after synaptic vesicle exocytosis. *Nature* **440**, 935–939 (2006)
11. S.W. Hell, M.J.A.P.B. Kroug, Ground-state-depletion fluorescence microscopy: a concept for breaking the diffraction resolution limit. *Appl. Phys. B* **60**, 495–497 (1995)
12. M.G. Gustafsson, Surpassing the lateral resolution limit by a factor of two using structured illumination microscopy. *J. Microsc.* **198**, 82–87 (2000)
13. M.G. Gustafsson, Nonlinear structured-illumination microscopy: wide-field fluorescence imaging with theoretically unlimited resolution. *Proc. Natl. Acad. Sci. U.S.A.* **102**, 13081–13086 (2005)
14. J.-X. Cheng, X.S. Xie, Coherent anti-Stokes Raman scattering microscopy: instrumentation, theory, and applications. *J. Phys. Chem. B* **108**, 827–840 (2004)
15. C.W. Freudiger, W. Min, B.G. Saar, S. Lu, G.R. Holtom, C. He, J.C. Tsai, J.X. Kang, X.S.J.S. Xie, Label-free biomedical imaging with high sensitivity by stimulated Raman scattering microscopy. *Science* **322**, 1857–1861 (2008)

16. T.T. Le, I.M. Langohr, M.J. Locker, M. Sturek, J.-X. Cheng, Label-free molecular imaging of atherosclerotic lesions using multimodal nonlinear optical microscopy. *J. Biomed. Opt.* **12**, 054007 (2007)
17. N. Olivier et al., Cell lineage reconstruction of early zebrafish embryos using label-free nonlinear microscopy. *Science* **329**, 967–971 (2010)
18. J.-X. Cheng, X.S. Xie, Vibrational spectroscopic imaging of living systems: an emerging platform for biology and medicine. *Science* **350**, 1054–1063 (2015)
19. A.J. Chen, X. Yuan, J. Li, P. Dong, I. Hamza, J.-X. Cheng, Label-free imaging of heme dynamics in living organisms by transient absorption microscopy. *Anal. Chem.* **90**, 3395–3401 (2018)
20. L. Tong, Y. Liu, B.D. Dolash, Y. Jung, M.N. Slipchenko, D.E. Bergstrom, J.-X. Cheng, Label-free imaging of semiconducting and metallic carbon nanotubes in cells and mice using transient absorption microscopy. *Nat. Nanotechnol.* **7**, 56–61 (2011)
21. K.-C. Huang, J. McCall, P. Wang, C.-S. Liao, G. Eakins, J.-X. Cheng, C. Yang, High-speed spectroscopic transient absorption imaging of defects in graphene. *Nano Lett.* **18**, 1489–1497 (2018)
22. B. Schrader, *Infrared and Raman Spectroscopy: Methods and Applications* (Wiley, Weinheim, 2008)
23. H. Förster, UV/VIS spectroscopy, in *Characterization I*, ed. by H.G. Karge, J. Weitkamp (Springer, Berlin, Heidelberg, 2004), pp. 337–426
24. W.E. Moerner, M.J.S. Orrit, Illuminating single molecules in condensed matter. *Science* **283**, 1670–1676 (1999)
25. M. Celebrano, P. Kukura, A. Renn, V. Sandoghdar, Single-molecule imaging by optical absorption. *Nat. Photonics* **5**, 95–98 (2011)
26. P.R.J.S. Griffiths, Fourier transform infrared spectrometry. *Science* **222**, 297 (1983)
27. E.N. Lewis, P.J. Treado, R.C. Reeder, G.M. Story, A.E. Dowrey, C. Marcott, I.W. Levin, Fourier transform spectroscopic imaging using an infrared focal-plane array detector. *Anal. Chem.* **67**, 3377–3381 (1995)
28. R.A. Dluhy, R. Mendelsohn, Emerging techniques in biophysical FT-IR. *Anal. Chem.* **60**, 269A–278A (1988)
29. A. Thorne, High resolution Fourier transform spectrometry in the visible and ultraviolet regions. *J. Anal. At. Spectrom.* **13**, 407–411 (1998)
30. M.R. Kole, R.K. Reddy, M.V. Schulmerich, M.K. Gelber, R. Bhargava, Discrete frequency infrared microspectroscopy and imaging with a tunable quantum cascade laser. *Anal. Chem.* **84**, 10366–10372 (2012)
31. M.J. Nasse, M.J. Walsh, E.C. Mattson, R. Reininger, A. Kajdacsy-Balla, V. Macias, R. Bhargava, C.J. Hirschmugl, High-resolution Fourier-transform infrared chemical imaging with multiple synchrotron beams. *Nat. Methods* **8**, 413–416 (2011)
32. H. Chih-Cheng, W. Chung-Yu, J. Far-Wen, S. Tai-Ping, Focal-plane-arrays and CMOS readout techniques of infrared imaging systems. *IEEE Trans. Circuits Syst. Video Technol.* **7**, 594–605 (1997)
33. W. Haiss, N.T.K. Thanh, J. Aveyard, D.G. Fernig, Determination of size and concentration of gold nanoparticles from UV-Vis spectra. *Anal. Chem.* **79**, 4215–4221 (2007)
34. S. Wartewig, R.H.H. Neubert, Pharmaceutical applications of mid-IR and Raman spectroscopy. *Adv. Drug Deliv. Rev.* **57**, 1144–1170 (2005)
35. K.A. Bunding Lee, S.C. Johnson, Comparison of mid-IR with NIR in polymer analysis. *Appl. Spectrosc. Rev.* **28**, 231–284 (1993)
36. B. Stuart, *Infrared Spectroscopy* (Kirk-Othmer Encyclopedia of Chemical Technology, 2015)
37. Y. Jung, M.N. Slipchenko, C.H. Liu, A.E. Ribbe, Z. Zhong, C. Yang, J.-X. Cheng, Fast detection of the metallic state of individual single-walled carbon nanotubes using a transient-absorption optical microscope. *Phys. Rev. Lett.* **105**, 217401 (2010)
38. J. Li, W. Zhang, T.-F. Chung, M.N. Slipchenko, Y.P. Chen, J.-X. Cheng, C. Yang, Highly sensitive transient absorption imaging of graphene and graphene oxide in living cells and circulating blood. *Sci. Rep.* **5**, 12394 (2015)

39. C.-S. Liao, M.N. Slipchenko, P. Wang, J. Li, S.-Y. Lee, R.A. Oglesbee, J.-X. Cheng, Microsecond scale vibrational spectroscopic imaging by multiplex stimulated Raman scattering microscopy. *Light Sci. Appl.* **4**, e265 (2015)
40. X. Chen, C. Zhang, P. Lin, K.-C. Huang, J. Liang, J. Tian, J.-X. Cheng, Volumetric chemical imaging by stimulated Raman projection microscopy and tomography. *Nat. Commun.* **8**, 15117 (2017)
41. H. Lin, C.-S. Liao, P. Wang, N. Kong, J.-X. Cheng, Spectroscopic stimulated Raman scattering imaging of highly dynamic specimens through matrix completion. *Light Sci. Appl.* **7**, 17179 (2018)
42. L. Huang, G. V. Hartland, L. Q. Chu, Luxmi, R.M. Feenstra, C. Lian, K. Tahy, H. Xing, *Nano Lett.* **10**, 1308–1313 (2010)
43. Z. Guo, Y. Wan, M. Yang, J. Snaider, K. Zhu, L. Huang, Long-range hot-carrier transport in hybrid perovskites visualized by ultrafast microscopy. *Science* **356**, 59–62 (2017)
44. L. Yuan, T.-F. Chung, A. Kuc, Y. Wan, Y. Xu, Y.P. Chen, T. Heine, L. Huang, Photocarrier generation from interlayer charge-transfer transitions in WS<sub>2</sub>-graphene heterostructures. *Sci. Adv.* **4**, e1700324 (2018)
45. T. Yoshihara, R. Katoh, A. Furube, Y. Tamaki, M. Murai, K. Hara, S. Murata, H. Arakawa, M. Tachiya, Identification of reactive species in photoexcited nanocrystalline TiO<sub>2</sub> films by wide-wavelength-range (400–2500 nm) transient absorption spectroscopy. *J. Phys. Chem. B* **108**, 3817–3823 (2004)
46. H. Ohkita et al., Charge carrier formation in polythiophene/fullerene blend films studied by transient absorption spectroscopy. *J. Am. Chem. Soc.* **130**, 3030–3042 (2008)
47. H.J. Lee et al., Assessing cholesterol storage in live cells and *C. elegans* by stimulated Raman scattering imaging of phenyl-diyne cholesterol. *Sci. Rep.* **5**, 7930 (2015)
48. J. Li, S. Condello, J. Thomes-Pepin, X. Ma, Y. Xia, T.D. Hurley, D. Matei, J.-X. Cheng, Lipid desaturation is a metabolic marker and therapeutic target of ovarian cancer stem cells. *Cell Stem Cell* **20**, 303–314.e305 (2017)
49. C. Zhang et al., Stimulated Raman scattering flow cytometry for label-free single-particle analysis. *Optica* **4**, 103–109 (2017)
50. S.W. Hell, Toward fluorescence nanoscopy. *Nat. Biotechnol.* **21**, 1347–1355 (2003)
51. T.A. Klar, S. Jakobs, M. Dyba, A. Egner, S.W. Hell, Fluorescence microscopy with diffraction resolution barrier broken by stimulated emission. *Proc. Natl. Acad. Sci. U.S.A.* **97**, 8206–8210 (2000)
52. B. Knoll, F. Keilmann, Near-field probing of vibrational absorption for chemical microscopy. *Nature* **399**, 134–137 (1999)
53. A. Dazzi, R. Prazeres, F. Glotin, J.M. Ortega, Local infrared microspectroscopy with sub-wavelength spatial resolution with an atomic force microscope tip used as a photothermal sensor. *Opt. Lett.* **30**, 2388–2390 (2005)
54. F. Lu, M. Jin, M.A. Belkin, Tip-enhanced infrared nanospectroscopy via molecular expansion force detection. *Nat. Photonics* **8**, 307–312 (2014)
55. A. Dazzi, C.B. Prater, AFM-IR: technology and applications in nanoscale infrared spectroscopy and chemical imaging. *Chem. Rev.* **117**, 5146–5173 (2017)
56. I. Amenabar, S. Poly, M. Goikoetxea, W. Nuansing, P. Lasch, R. Hillenbrand, Hyperspectral infrared nanoimaging of organic samples based on Fourier transform infrared nanospectroscopy. *Nat. Commun.* **8**, 14402 (2017)
57. J.P. Gordon, R.C.C. Leite, R.S. Moore, S.P.S. Porto, J.R. Whinnery, Long-transient effects in lasers with inserted liquid samples. *J. Appl. Phys.* **36**, 3–8 (1965)
58. M.E. Long, R.L. Swofford, A.C. Albrecht, Thermal lens technique: a new method of absorption spectroscopy. *Science* **191**, 183–185 (1976)
59. D. Zhang, C. Li, C. Zhang, M.N. Slipchenko, G. Eakins, J.-X. Cheng, Depth-resolved mid-infrared photothermal imaging of living cells and organisms with submicrometer spatial resolution. *Sci. Adv.* **2**, e1600521 (2016)
60. Z. Li, K. Aleshire, M. Kuno, G.V. Hartland, Super-resolution far-field infrared imaging by photothermal heterodyne imaging. *J. Phys. Chem. B* **121**, 8838–8846 (2017)

61. D.A. Nedosekin, E.I. Galanzha, E. Dervishi, A.S. Biris, V.P. Zharov, Super-resolution non-linear photothermal microscopy. *Small* **10**, 135–142 (2013)
62. P. Wang, M.N. Slipchenko, J. Mitchell, C. Yang, E.O. Potma, X. Xu, J.X. Cheng, Far-field imaging of non-fluorescent species with sub-diffraction resolution. *Nat. Photonics* **7**, 449–453 (2013)
63. W.R. Silva, C.T. Graefe, R.R. Frontiera, Toward label-free super-resolution microscopy. *ACS Photonics* **3**, 79–86 (2015)
64. R.C.C. Leite, S.P.S. Porto, T.C. Damen, The thermal lens effect as a power-limiting device. *Appl. Phys. Lett.* **10**, 100–101 (1967)
65. R.L. Carman, P.L. Kelley, Time dependence in the thermal blooming of laser beams. *Appl. Phys. Lett.* **12**, 241–243 (1968)
66. F. Dabby, R. Boyko, C. Shank, J. Whinnery, Short time-constant thermal self-defocusing of laser beams. *IEEE J. Quantum Electron.* **5**, 516–520 (1969)
67. J.N. Hayes, Thermal blooming of laser beams in fluids. *Appl. Opt.* **11**, 455–461 (1972)
68. H. Kleiman, R.W. O’Neil, Thermal blooming of pulsed laser radiation. *Appl. Phys. Lett.* **23**, 43–44 (1973)
69. R.C.C. Leite, R.S. Moore, J.R. Whinnery, Low absorption measurements by means of the thermal lens effect using an He-Ne laser. *Appl. Phys. Lett.* **5**, 141–143 (1964)
70. D. Solimini, Loss measurement of organic materials at 6328 Å. *J. Appl. Phys.* **37**, 3314–3315 (1966)
71. D. Solimini, Accuracy and sensitivity of the thermal lens method for measuring absorption. *Appl. Opt.* **5**, 1931–1939 (1966)
72. J. Stone, Measurements of the absorption of light in low-loss liquids. *J. Opt. Soc. Am.* **62**, 327–333 (1972)
73. A.C. Boccara, D. Fournier, J. Badoz, Thermo-optical spectroscopy: detection by the “mirage effect”. *Appl. Phys. Lett.* **36**, 130–132 (1980)
74. A. Gaiduk, P.V. Ruijgrok, M. Yorulmaz, M. Orrit, Detection limits in photothermal microscopy. *Chem. Sci.* **1**, 343–350 (2010)
75. C. Hu, J.R. Whinnery, New thermo-optical measurement method and a comparison with other methods. *Appl. Opt.* **12**, 72–79 (1973)
76. J.C. Murphy, L.C. Aamodt, Photothermal spectroscopy using optical beam probing: mirage effect. *J. Appl. Phys.* **51**, 4580–4588 (1980)
77. L.C. Aamodt, J.C. Murphy, photothermal measurements using a localized excitation source. *J. Appl. Phys.* **52**, 4903–4914 (1981)
78. A.C. Boccara, D. Fournier, W. Jackson, N.M. Amer, Sensitive photothermal deflection technique for measuring absorption in optically thin media. *Opt. Lett.* **5**, 377–379 (1980)
79. D. Boyer, P. Tamarat, A. Maali, B. Lounis, M. Orrit, Photothermal imaging of nanometer-sized metal particles among scatterers. *Science* **297**, 1160–1163 (2002)
80. S. Berciaud, L. Cognet, G.A. Blab, B. Lounis, Photothermal heterodyne imaging of individual nonfluorescent nanoclusters and nanocrystals. *Phys. Rev. Lett.* **93**, 257402 (2004)
81. S. Berciaud, D. Lasne, G.A. Blab, L. Cognet, B. Lounis, Photothermal heterodyne imaging of individual metallic nanoparticles: theory versus experiment. *Phys. Rev. B* **73**, 045424 (2006)
82. A. Gaiduk, M. Yorulmaz, P.V. Ruijgrok, M. Orrit, Room-temperature detection of a single molecule’s absorption by photothermal contrast. *Science* **330**, 353–356 (2010)
83. M. Harada, K. Iwamoto, T. Kitamori, T. Sawada, Photothermal microscopy with excitation and probe beams coaxial under the microscope and its application to microparticle analysis. *Anal. Chem.* **65**, 2938–2940 (1993)
84. C. Li, D. Zhang, M.N. Slipchenko, J.-X. Cheng, Mid-infrared photothermal imaging of active pharmaceutical ingredients at submicrometer spatial resolution. *Anal. Chem.* **89**, 4863–4867 (2017)
85. V.P. Zharov, Far-field photothermal microscopy beyond the diffraction limit. *Opt. Lett.* **28**, 1314–1316 (2003)
86. J. He, J. Miyazaki, N. Wang, H. Tsurui, T. Kobayashi, Biological imaging with nonlinear photothermal microscopy using a compact supercontinuum fiber laser source. *Opt. Express* **23**, 9762–9771 (2015)

87. J. He, J. Miyazaki, N. Wang, H. Tsurui, T. Kobayashi, Label-free imaging of melanoma with nonlinear photothermal microscopy. *Opt. Lett.* **40**, 1141–1144 (2015)
88. K. Nakata, H. Tsurui, T. Kobayashi, Further resolution enhancement of high-sensitivity laser scanning photothermal microscopy applied to mouse endogenous. *J. Appl. Phys.* **120**, 214901 (2016)
89. A. Mertiri, H. Altug, M.K. Hong, P. Mehta, J. Mertz, L.D. Ziegler, S. Erramilli, Nonlinear midinfrared photothermal spectroscopy using Zharov splitting and quantum cascade lasers. *ACS Photonics* **1**, 696–702 (2014)
90. V.P. Zharov, Ultrasharp nonlinear photothermal and photoacoustic resonances and holes beyond the spectral limit. *Nat. Photonics* **5**, 110–116 (2011)
91. D.O. Lapotko, T.Y.R. Romanovskaya, A. Shnip, V.P. Zharov, Photothermal time-resolved imaging of living cells. *Lasers Surg. Med.* **31**, 53–63 (2002)
92. J. Miyazaki, T. Kobayashi, Photothermal microscopy for high sensitivity and high resolution absorption contrast imaging of biological tissues. *Photonics* **4**(2), 32 (2017)
93. S. Arunkarthick, M.M. Bijeesh, G.K. Varier, M. Kowshik, P. Nandakumar, Laser scanning photothermal microscopy: fast detection and imaging of gold nanoparticles. *J. Microsc.* **256**, 111–116 (2014)
94. P. Vermeulen, L. Cognet, B. Lounis, Photothermal microscopy: optical detection of small absorbers in scattering environments. *J. Microsc.* **254**, 115–121 (2014)
95. M. Harada, M. Shibata, T. Kitamori, T. Sawada, Application of coaxial beam photothermal microscopy to the analysis of a single biological cell in water. *Anal. Chim. Acta* **299**, 343–347 (1995)
96. M. Tokeshi, M. Uchida, A. Hibara, T. Sawada, T. Kitamori, Determination of subyoctomole amounts of nonfluorescent molecules using a thermal lens microscope: subsingle-molecule determination. *Anal. Chem.* **73**, 2112–2116 (2001)
97. T.X. Ding, L. Hou, H.V.D. Meer, A.P. Alivisatos, M. Orrit, Hundreds-fold sensitivity enhancement of photothermal microscopy in near-critical Xenon. *J. Phys. Chem. Lett.* **7**, 2524–2529 (2016)
98. S. Lu, W. Min, S. Chong, G.R. Holtom, X.S. Xie, Label-free imaging of heme proteins with two-photon excited photothermal lens microscopy. *Appl. Phys. Lett.* **96**, 113701 (2010)
99. P.M. Champion, G.J. Perreault, Observation and quantitation of light emission from cytochrome c using Soret band laser excitation. *J. Chem. Phys.* **75**, 490–491 (1981)
100. R. Jimenez, F.E. Romesberg, Excited state dynamics and heterogeneity of folded and unfolded states of cytochrome c. *J. Chem. Phys. B* **106**, 9172–9180 (2002)
101. J. Miyazaki, H. Tsurui, K. Kawasumi, T. Kobayashi, Simultaneous dual-wavelength imaging of nonfluorescent tissues with 3D subdiffraction photothermal microscopy. *Opt. Express* **23**, 3647–3656 (2015)
102. V.P. Zharov, D.O. Lapotko, Photothermal imaging of nanoparticles and cells. *IEEE J. Sel. Top. Quantum Electron.* **11**, 733–751 (2005)
103. S.E. Braslavsky, G.E. Heibel, Time-resolved photothermal and photoacoustic methods applied to photoinduced processes in solution. *Chem. Rev.* **92**, 1381–1410 (1992)
104. D.O. Lapotko, V.P. Zharov, Spectral evaluation of laser-induced cell damage with photothermal microscopy. *Lasers Surg. Med.* **36**, 22–30 (2005)
105. D. Lasne, G.A. Blab, S. Berciaud, M. Heine, L. Groc, D. Choquet, L. Cognet, B. Lounis, Single nanoparticle photothermal tracking (SNaPT) of 5-nm gold beads in live cells. *Biophys. J.* **91**, 4598–4604 (2006)
106. W.W. Coblenz, *Investigations of Infra-red Spectra* (Carnegie Institution of Washington, Washington, D.C., 1905), p. 3 v (35, 65, 97)
107. K.L.A. Chan, S.G. Kazarian, A. Mavraki, D.R. Williams, Fourier transform infrared imaging of human hair with a high spatial resolution without the use of a synchrotron. *Appl. Spectrosc.* **59**, 149–155 (2005)
108. P. Heraud, S. Caine, G. Sanson, R. Gleadow, B.R. Wood, D. McNaughton, Focal plane array infrared imaging: a new way to analyse leaf tissue. *New Phytol.* **173**, 216–225 (2006)
109. J. Chalmers, P. Griffiths, *Handbook of Vibrational Spectroscopy, 5 volumes set* (Wiley, 2002)

110. R. Furstenberg, C.A. Kendziora, M.R. Papantonakis, V. Nguyen, R. McGill, Chemical imaging using infrared photothermal microspectroscopy, in *Next-Generation Spectroscopic Technologies V* (International Society for Optics and Photonics, Baltimore, MD, 2012), p. 837411
111. A. Tredicucci, C. Gmachl, F. Capasso, D.L. Sivco, A.L. Hutchinson, A.Y. Cho, A multiwavelength semiconductor laser. *Nature* **396**, 350–353 (1998)
112. C. Gmachl, D.L. Sivco, R. Colombelli, F. Capasso, A.Y. Cho, Ultra-broadband semiconductor laser. *Nature* **415**, 883–887 (2002)
113. Y. Yao, A.J. Hoffman, C.F. Gmachl, Mid-infrared quantum cascade lasers. *Nat. Photonics* **6**, 432–439 (2012)
114. F. Rotermund, V. Petrov, F. Noack, Difference-frequency generation of intense femtosecond pulses in the mid-IR (4–12  $\mu\text{m}$ ) using  $\text{HgGa}_2\text{S}_4$  and  $\text{AgGaS}_2$ . *Opt. Commun.* **185**, 177–183 (2000)
115. C. Erny, K. Moutzouris, J. Biegert, D. Khlke, F. Adler, A. Leitenstorfer, U. Keller, Mid-infrared difference-frequency generation of ultrashort pulses tunable between 3.2 and 4.8  $\mu\text{m}$  from a compact fiber source. *Opt. Lett.* **32**, 1138–1140 (2007)
116. Y. Bai, D. Zhang, C. Li, C. Liu, J.-X. Cheng, Bond-selective imaging of cells by mid-infrared photothermal microscopy in high wavenumber region. *J. Phys. Chem. B* **121**, 10249–10255 (2017)
117. L. Wei, Y. Yu, Y. Shen, M.C. Wang, W. Min, Vibrational imaging of newly synthesized proteins in live cells by stimulated Raman scattering microscopy. *Proc. Natl. Acad. Sci. U.S.A.* **110**, 11226 (2013)
118. A. Totachawattana, S. Erramilli, M.Y. Sander, Optimization of mid-IR photothermal imaging for tissue analysis, in *SPIE Optical Engineering + Applications* (SPIE, 2015), p. 7
119. T.J. Huffman, R. Furstenberg, C.A. Kendziora, R.A. McGill, Infrared spectroscopy below the diffraction limit using an optical probe, in *SPIE Commercial + Scientific Sensing and Imaging* (SPIE, 2018), p. 6
120. D. Bashford, M. Karplus, pKa's of ionizable groups in proteins: atomic detail from a continuum electrostatic model. *Biochemistry* **29**, 10219–10225 (1990)
121. A. Totachawattana, M.K. Hong, S. Erramilli, M.Y. Sander, Multiple bifurcations with signal enhancement in nonlinear mid-infrared thermal lens spectroscopy. *Analyst* **142**, 1882–1890 (2017)
122. M. Yorulmaz, S. Nizzero, A. Hoggard, L.-Y. Wang, Y.-Y. Cai, M.-N. Su, W.-S. Chang, S. Link, Single-particle absorption spectroscopy by photothermal contrast. *Nano Lett.* **15**, 3041 (2015)
123. P. Zijlstra, P.M.R. Paulo, M. Orrit, Optical detection of single non-absorbing molecules using the surface plasmon resonance of a gold nanorod. *Nat. Nanotechnol.* **7**, 379–382 (2012)
124. L.K. Bogart, A. Taylor, Y. Cesbron, P. Murray, R. Lvy, Photothermal microscopy of the core of dextran-coated iron oxide nanoparticles during cell uptake. *ACS Nano* **6**, 5961–5971 (2012)
125. F. Kitagawa, Y. Akimoto, K. Otsuka, Label-free detection of amino acids using gold nanoparticles in electrokinetic chromatography–thermal lens microscopy. *J. Chromatogr. A* **1216**, 2943–2946 (2009)
126. J. Hartmann, P. Voigt, M. Reichling, Measuring local thermal conductivity in polycrystalline diamond with a high resolution photothermal microscope. *J. Appl. Phys.* **81**, 2966–2972 (1997)
127. M. Reichling, E. Welsch, A. Duparre, E. Matthias, Laterally and depth resolved photothermal absorption measurements on  $\text{ZrO}_2$  and  $\text{MgF}_2$  single-layer films, in *Optical Systems Design '92* (SPIE, 1993), p. 11
128. A. During, M. Commandr, C. Fossati, B. Bertussi, J.-Y. Natoli, J.-L. Rullier, H. Bercegol, P. Bouchut, Integrated photothermal microscope and laser damage test facility for in-situ investigation of nanodefekt induced damage. *Opt. Express* **11**, 2497–2501 (2003)
129. R. Chatterjee, I.M. Pavlovets, K. Aleshire, M. Kuno, Single semiconductor nanostructure extinction spectroscopy. *J. Phys. Chem. C* **122**, 16443–16463 (2018)

130. V.P. Zharov, E.I. Galanzha, V.V. Tuchin, Photothermal imaging of moving cells in lymph and blood flow in vivo, in *Biomedical Optics 2004* (SPIE, 2004), p. 11
131. A.V. Brusnichkin, D.A. Nedosekin, E.I. Galanzha, Y.A. Vladimirov, E.F. Shevtsova, M.A. Proskurnin, V.P. Zharov, Ultrasensitive label-free photothermal imaging, spectral identification, and quantification of cytochrome c in mitochondria, live cells, and solutions. *J. Biophotonics* **3**, 791–806 (2010)
132. D.A. Nedosekin, E.V. Shashkov, E.I. Galanzha, L. Hennings, V.P. Zharov, Photothermal multispectral image cytometry for quantitative histology of nanoparticles and micrometastasis in intact, stained and selectively burned tissues. *Cytometry Part A* **77A**, 1049–1058 (2010)
133. J. Miyazaki, H. Tsurui, K. Kawasumi, T. Kobayashi, Sensitivity enhancement of photothermal microscopy with radially segmented balanced detection. *Opt. Lett.* **40**, 479–482 (2015)
134. J. Miyazaki, Y. Toumon, Experimental evaluation of temperature increase and associated detection sensitivity in shot noise-limited photothermal microscopy. *Opt. Commun.* **430**, 170–175 (2019)
135. T. Tomimatsu, J. Miyazaki, Y. Kano, T. Kobayashi, Photothermal imaging of skeletal muscle mitochondria. *Biomed. Opt. Express* **8**, 2965–2975 (2017)
136. J. Miyazaki, H. Tsurui, T. Kobayashi, Reduction of distortion in photothermal microscopy and its application to the high-resolution three-dimensional imaging of nonfluorescent tissues. *Biomed. Opt. Express* **6**, 3217–3224 (2015)
137. J. He, N. Wang, H. Tsurui, M. Kato, M. Iida, T. Kobayashi, Noninvasive, label-free, three-dimensional imaging of melanoma with confocal photothermal microscopy: differentiate malignant melanoma from benign tumor tissue. *Sci. Rep.* **6**, 30209 (2016)
138. A. Totachawattana, M.S. Regan, N.Y.R. Agar, S. Erramilli, M.Y. Sander, Label-free mid-Infrared photothermal spectroscopy and imaging of neurological tissue, in *Conference on Lasers and Electro-optics* (Optical Society of America, San Jose, California, 2017), p. ATu4A.3
139. A. Totachawattana, D. Huang, L. Li, K.A. Brown, S. Erramilli, M.Y. Sander, Robust mid-infrared photothermal imaging system for characterization of thin films at high spatial resolution, in *Conference on Lasers and Electro-optics* (Optical Society of America, San Jose, California, 2017), p. JW2A.47
140. R. Chatterjee, I.M. Pavlovetc, K. Aleshire, G.V. Hartland, M. Kuno, Subdiffraction infrared imaging of mixed cation perovskites: probing local cation heterogeneities. *ACS Energy Lett.* **3**, 469–475 (2018)
141. J.J. Bae et al., Sensitive photo-thermal response of graphene oxide for mid-infrared detection. *Nanoscale* **7**, 15695–15700 (2015)
142. J.W. Thomas, A. Polak, G.M. Bonner, S. Enderle, M.H. Dunn, D.J.M. Stothard, Optical parametric oscillator-based trace detection of gases in the mid-infrared region using phase-fluctuation optical heterodyne spectroscopy, in *SPIE Defense + Security* (SPIE, 2018), p. 9
143. Z. Li, Z. Wang, F. Yang, W. Jin, W. Ren, Mid-infrared fiber-optic photothermal interferometry. *Opt. Lett.* **42**, 3718–3721 (2017)
144. R.C. Miller, Optical second harmonic generation in piezoelectric crystals. *Appl. Phys. Lett.* **5**, 17–19 (1964)
145. K. Wang, C. Xu, Tunable high-energy soliton pulse generation from a large-mode-area fiber and its application to third harmonic generation microscopy. *Appl. Phys. Lett.* **99**, 071112 (2011)
146. W. Denk, J.H. Strickler, W.W. Webb, Two-photon laser scanning fluorescence microscopy. *Science* **248**, 73–76 (1990)
147. C.Y. Dong, P.T. So, T. French, E. Gratton, Fluorescence lifetime imaging by asynchronous pump-probe microscopy. *Biophys. J.* **69**, 2234–2242 (1995)
148. D.Y. Davydova, A. Cadena, D. Akimov, B. Dietzek, Transient absorption microscopy: advances in chemical imaging of photoinduced dynamics. *Laser Photonics Rev.* **10**, 62–81 (2015)
149. S.W. Hell, M. Kroug, Ground-state-depletion fluorescence microscopy: a concept for breaking the diffraction resolution limit. *Appl. Phys. B* **60**, 495–497 (1995)

150. S. Bretschneider, C. Eggeling, S.W. Hell, Breaking the diffraction barrier in fluorescence microscopy by optical shelving. *Phys. Rev. Lett.* **98**, 218103 (2007)
151. Q. Bao, H. Zhang, Y. Wang, Z. Ni, Y. Yan, Z.X. Shen, K.P. Loh, D.Y. Tang, Atomic-layer graphene as a saturable absorber for ultrafast pulsed lasers. *Adv. Funct. Mater.* **19**, 3077–3083 (2009)
152. Z. Sun, T. Hasan, F. Torrisi, D. Popa, G. Privitera, F. Wang, F. Bonaccorso, D.M. Basko, A.C. Ferrari, Graphene mode-locked ultrafast laser. *ACS Nano* **4**, 803–810 (2010)
153. F.T. Vasko, Saturation of interband absorption in graphene. *Phys. Rev. B* **82**, 245422 (2010)
154. A.G. Rozhin, Y. Sakakibara, H. Kataura, S. Matsuzaki, K. Ishida, Y. Achiba, M. Tokumoto, Anisotropic saturable absorption of single-wall carbon nanotubes aligned in polyvinyl alcohol. *Chem. Phys. Lett.* **405**, 288–293 (2005)
155. P. Avouris, M. Freitag, V. Perebeinos, Carbon-nanotube photonics and optoelectronics. *Nat. Photonics* **2**, 341–350 (2008)
156. I.H. Baek et al., Single-walled carbon nanotube saturable absorber assisted high-power mode-locking of a Ti:sapphire laser. *Opt. Express* **19**, 7833–7838 (2011)
157. C.P. Singh, K.S. Bindra, G.M. Bhalerao, S.M. Oak, Investigation of optical limiting in iron oxide nanoparticles. *Opt. Express* **16**, 8440–8450 (2008)
158. L. Irimpan, V.P.N. Nampoory, P. Radhakrishnan, Spectral and nonlinear optical characteristics of nanocomposites of ZnO–CdS. *J. Appl. Phys.* **103**, 094914 (2008)
159. L. Gong, H. Wang, Breaking the diffraction limit by saturation in stimulated-Raman-scattering microscopy: a theoretical study. *Phys. Rev. A* **90**, 013818 (2014)
160. B. Liu, H.J. Lee, D. Zhang, C.-S. Liao, N. Ji, Y. Xia, J.-X. Cheng, Label-free spectroscopic detection of membrane potential using stimulated Raman scattering. *Appl. Phys. Lett.* **106** (2015)

# Chapter 7

## Label-Free Pump–Probe Nanoscopy



Paolo Bianchini, Giulia Zanini and Alberto Diaspro

**Abstract** In the last few decades fluorescence microscopy has been the most widely used microscopy technique and much effort has been put into the development of advanced super-resolution fluorescence microscopy techniques to circumvent the diffraction limit. Despite their well-established benefits, these techniques have to rely on the photo-physical properties of fluorescent molecules to obtain the desired contrast and spatial resolution. The labeling procedure may cause unwanted alterations in the sample. With the advent of ultrashort-pulsed laser sources, it became possible to better explore novel non-fluorescent-based contrast mechanisms that rely solely on intrinsic properties of the molecules of interest and which led to the development of label-free microscopy approaches. In this chapter, the imaging capabilities of absorption-based pump–probe microscopy are presented. This technique explores the ultrafast dynamic properties of the sample with high spatial and temporal resolution, as well as high sensitivity and chemical specificity. Two pulses, a pump and a probe, with a proper spatial and temporal overlap are used. The pump is absorbed, inducing a measurable change in the sample carrier population, which is then monitored by a delayed probe pulse. The development of new label-free approaches also represents a key challenge for the exploration of super-resolution approaches in non-fluorescence-based methods.

### 7.1 Nonlinear Optical Interactions

Familiar optical phenomena, like reflection, refraction, and absorption, which allow us to see the colors or to focus the light by a lens, are a consequence of the interaction of light with matter. They can be explained taking into account the wave-like nature of light and assigning a set of optical parameters to the material. In normal conditions these parameters are constant (linear optics), while under strong illumination they become functions of the light intensity (nonlinear optics).

---

P. Bianchini (✉) · G. Zanini · A. Diaspro  
Istituto Italiano di Tecnologia, via Morego 30, 16163 Genoa, Italy  
e-mail: [paolo.bianchini@iit.it](mailto:paolo.bianchini@iit.it)

© Springer Nature Switzerland AG 2019  
V. Astratov (ed.), *Label-Free Super-Resolution Microscopy*,  
Biological and Medical Physics, Biomedical Engineering,  
[https://doi.org/10.1007/978-3-030-21722-8\\_7](https://doi.org/10.1007/978-3-030-21722-8_7)

The macroscopic electric polarizability  $\mathbf{P}(t)$  of the material is the main parameter that characterizes the interaction, and it can be expanded in powers of the incident light electric field  $\mathbf{E}(t)$  as [1]

$$\mathbf{P}(t) = \varepsilon_0(\chi^{(1)} \cdot \mathbf{E}(t) + \chi^{(2)} \cdot \mathbf{E}^2(t) + \chi^{(3)} \cdot \mathbf{E}^3(t) + \dots), \quad (7.1)$$

where  $\varepsilon_0$  is the electric permittivity of free space and  $\chi^{(n)}$  is the  $n$ th-order susceptibility tensor. With weak incident fields the linear term ( $n = 1$ ) is dominant and governs interactions like absorption, reflection, refraction, and scattering. Nonlinear terms ( $n > 1$ ) start to appear with stronger fields, comparable with the typical atomic electric field ( $\sim 10^{11}$  V/m) [1], and they mainly govern *nonlinear frequency conversion*, *nonlinear variation of the refractive index*, and *nonlinear absorption* processes. Most of the nonlinear phenomena used in optical microscopy involve the second- and the third-order susceptibilities,  $\chi^{(2)}$  and  $\chi^{(3)}$ , respectively.  $\chi^{(2)}$  vanishes in centrosymmetric media with inversion symmetry, and is responsible for second harmonic generation (SHG) [2], sum/difference frequency generation (SFG/DFG), and optical parametric oscillation processes.  $\chi^{(3)}$  is present in any media (liquid, gases, amorphous solids, and crystals with inversion symmetry) and is responsible for third harmonic generation (THG), four wave mixing (FWM), nonlinear absorption, and coherent Raman scattering (CRS) processes. The nonlinear coefficients are many orders of magnitude smaller than the linear one, which means that nonlinear optical effects require high incident powers to become relevant. Thanks to the advent of lasers in the 1960s and the further development of ultrashort (pico/femtosecond) pulsed laser sources working mainly in the near-infrared (NIR) part of the spectrum; it was possible to achieve a local irradiance, which is strong enough to access nonlinear interactions without damaging the sample under investigation. Their exploitation in microscopy allowed the overcoming of most of the limitations given by the conventional linear microscopy techniques: (i) providing access to novel contrast mechanisms and to a wider range of functional, structural, and chemical information of the specimen, without any need for external (fluorescent) labeling, (ii) a confinement of the interaction volume, with consequent optical sectioning capabilities and photo-bleaching reduction, and (iii) improved penetration depth due to the use of longer wavelengths, particularly interesting when imaging thick samples [3–6].

### 7.1.1 Nonlinear Absorption

Nonlinear absorption refers to the change in the transmission properties of a material as a function of the incident intensity, and it is governed by the imaginary part of  $\chi^{(3)}$ . Nonlinear absorption properties are often studied using two distinct ultrashort pulsed incident beams, commonly called *pump* and *probe*, and by looking at the *probe difference transmission signal* in the presence as well as absence of the pump. Quantitative information can be achieved by varying the pump wavelength, the probe

wavelength, and the delay time between the two pulses. The pump intensity needs to be kept at a higher intensity with respect to the probe one, because it needs to induce a measurable change in the carrier population, while the probe should simply monitor this perturbation, without any additional effects. In this way, the pump–probe signal will exhibit a “weak” nonlinearity, and its intensity will vary proportionally to the product of pump and probe intensities,  $I_{\text{pu}}$  and  $I_{\text{pr}}$ , respectively, and to the analyte concentration  $c$  [7, 8]

$$\Delta T \propto c I_{\text{pu}} I_{\text{pr}}. \quad (7.2)$$

The overall quadratic dependence on the incident intensity marks the nonlinearity, while the linear concentration dependence permits quantification.

The main nonlinear absorption mechanisms are sketched and illustrated in Fig. 7.1.

**Two-photon absorption (TPA)** (Fig. 7.1a). TPA involves the *simultaneous* absorption of two photons (of equal or different energy) via an intermediate virtual state (v.s.) to match the (usual) one-photon transition between ground and excited state. The “simultaneity” is achieved within a time window in the order of  $10^{-16}$  s [3, 9], which is in the scale of molecular energy fluctuations. Using two different fields at frequencies  $\omega_{\text{pu}}$  and  $\omega_{\text{pr}}$ , the transition is approximately resonant at  $\omega_{\text{pu}} + \omega_{\text{pr}}$  and, in the case of negligible TPA by the single field, the loss in transmission of the probe beam is proportional to their intensity product  $I_{\text{pu}} I_{\text{pr}}$  [10]. Usually, the one-photon transition is achieved via the absorption of an UV–Vis photon, which means that longer wavelengths (smaller energies) toward the NIR part of the spectrum need to be used to induce TPA. This phenomenon was originally predicted by Maria Göppert-Mayer in 1931 in her doctoral dissertation [11].

**Excited state absorption (ESA)** (Fig. 7.1b). ESA involves the absorption of a probe photon  $\omega_{\text{pr}}$  by the first excited state, previously populated by a pump photon

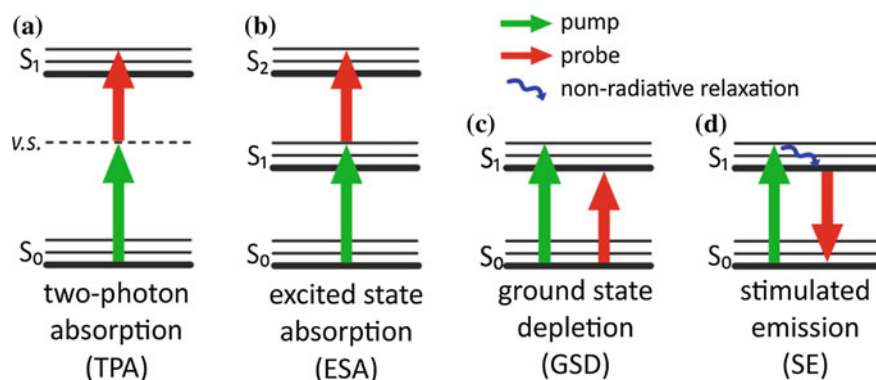


**Fig. 7.1** Transition diagrams of the main nonlinear absorption processes that can be studied with pump–probe methods: **a** two-photon absorption (TPA), **b** excited state absorption (ESA), **c** ground-state depletion (GSD), and **d** stimulated emission (SE). Electronic states are drawn in thick solid lines, vibrational states in thin solid lines, and virtual states in dashed lines

$\omega_{\text{pu}}$ . As in TPA, ESA will lead to a decrease in the probe transmission, whose change  $\Delta T$  can be described by the equation [12, 13]

$$\Delta T = - \int \frac{N_0 \sigma_{\text{pu}} [\sigma'_{\text{pr}} - \sigma_{\text{pr}}] I_{\text{pu}} I_{\text{pr}} \exp(-\Delta t / \tau)}{\hbar \omega_{\text{pu}}} dz, \quad (7.3)$$

where  $N_0$  is the molecular concentration of the ground state,  $\sigma_{\text{pr}}$  and  $\sigma'_{\text{pr}}$  are the linear absorption cross-sections of the ground and excited states for the probe beam, respectively,  $\Delta t$  is the time delay between pump and probe pulses, and  $\tau$  is the lifetime of the excited state. Only at  $\Delta t = 0$  does  $\Delta T$  have the maximum value, while with increasing  $\Delta t$ ,  $\Delta T$  exponentially decreases according to the lifetime  $\tau$  of the excited state.

**Ground state depletion (GSD)** (Fig. 7.1c). The absorption of an intense pump beam highly populates the excited state while depleting the ground state, and consequently the absorption coefficient decreases. A probe beam in resonance with the absorption transition will thus exhibit a transmission increase, given by the formula [12]

$$\Delta T = - \int \frac{N_0 \sigma_{\text{pu}} \sigma_{\text{pr}} I_{\text{pu}} I_{\text{pr}} \exp(-\Delta t / \tau)}{\hbar \omega_{\text{pu}}} dz, \quad (7.4)$$

where all the parameters were previously introduced for (1.3). Even in this case the strongest signal is achieved when  $\Delta t = 0$ , while an exponential decrease is achieved by delaying the probe pulse from the pump pulse, reflecting the characteristic relaxation time  $\tau$  of the excited state.

**Stimulated emission (SE)** (Fig. 7.1d). As another consequence of the highly populated excited state due to pump absorption, a probe beam in resonance with the relaxation transition will stimulate the excited state to emit at its same frequency. The probe will thus undergo a transmission increase described by an equation similar to (1.4) [12], with the only difference that in this case the probe wavelength is chosen away from the absorption peak.

## 7.2 Pump–Probe Microscopy

Among nonlinear optical approaches, pump–probe methods were first introduced in *time-resolved spectroscopy* [14–16] to resolve and monitor chemical and atomic ultrafast processes, which occur on a picosecond (or lower) timescale, much faster than the typical bandwidth of conventional detectors and electronics. Using the interaction of two ultrashort pulses and monitoring how this interaction changes as a function of the delay between pulses, the temporal resolution becomes dependent not on the detector speed but on the temporal size of the pulses. In addition, *transient absorption* pump–probe methods provide non-fluorescent-based contrast from

highly absorbing chromophores by detecting probe absorption changes induced by *nonlinear absorption* processes (presented in Chap. 1). Absorption-based measurements are advantageous because they permit the investigation of non-emissive and dark states, broadening the range of available targets. Moreover, compared to scattering techniques, they are less dependent on the particle size and they can be used to study smaller structures [12, 17]. The implementation of these absorption-based methods in a nonlinear microscopy platform with a proper detection scheme [3–6] completes the temporal and spectral information of the ultrafast phenomena with the spatial localization at the microscopic scale.

### 7.2.1 Pump–Probe Microscope Design

The typical pump–probe microscope is based on a nonlinear laser-scanning microscope where two ultrashort pulsed laser beams with a proper spatial and temporal overlap are used in order to achieve highly sensitive nonlinear imaging and, moreover, to follow ultrafast processes with sub-picosecond temporal resolution. An example of this setup is shown in Fig. 7.2a.

The two pump and probe beams may be generated by two different pulsed laser sources synchronized with each other in order to have precise control over the timing of the two pulse trains. More typically, the two beams come from the same laser source, usually from a mode-locked Ti:sapphire, tuneable in the red and NIR part of the spectrum, with a pulse repetition frequency around 70–90 MHz and a pulse width between 50 and 10 ps. The single laser output can be split into two beams, and one of them frequency doubled in a barium borate (BBO) nonlinear crystal in order to obtain a different wavelength in the visible range, at exactly half the initial value. Another approach consists of using the Ti:sapphire output to synchronously pump an optical parametric oscillator (OPO), which is a coherent light source based on optical gain from parametric amplification in a nonlinear crystal. OPOs are more versatile because their synchronized outputs can be tuned over a wide wavelength range, reaching wavelengths that cannot be provided by conventional lasers. Compared to the direct frequency doubling which always provides two wavelengths, one half of the other, the OPO allows for different pump–probe wavelength combinations, with the possibility of working only in the NIR region. The intensity of the beams may be controlled through variable neutral density filters or through a combination of half-wave plates and linear polarizers.

The two beams are spatially combined with a dichroic mirror (DM), sent to a scanning unit (SU) made by a pair of galvanometric mirrors, and collinearly focused onto the sample (S) by a high numerical aperture objective (O). Three-dimensional imaging can be achieved through an axial piezo-stage with nanometer resolution. Owing to chromatic aberrations, pump and probe foci at the sample plane may differ (see Fig. 7.2b). Adding two relay lenses with regulating distance in one of the two optical paths may help in adjusting the input divergence of one beam in the objective to match the other focus. Alternatively, the focusing of the probe may be optimized,

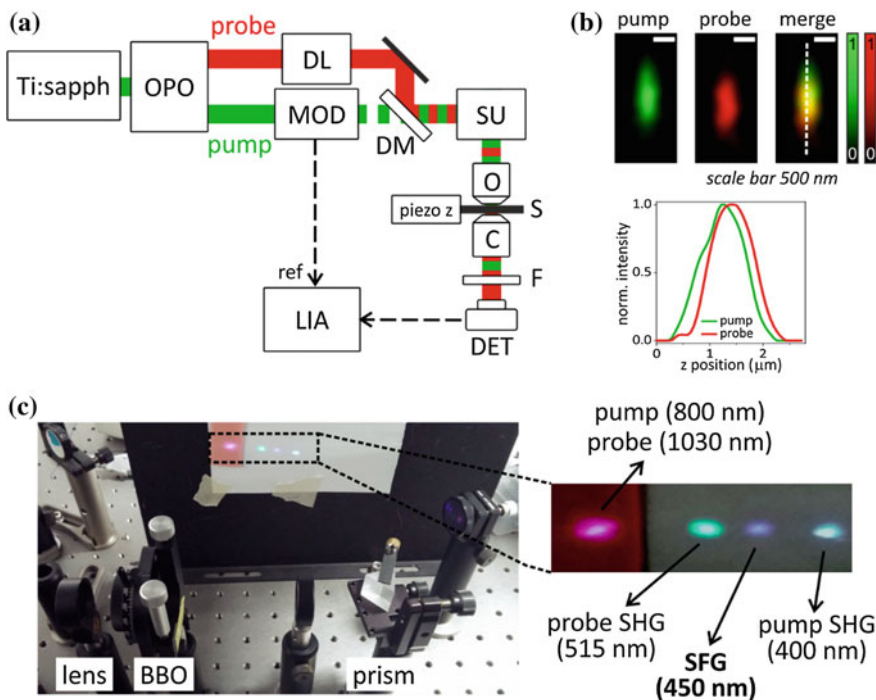


**Fig. 7.2** **a** An example of a two-beam laser-scanning pump–probe microscopy setup with transmission detection. OPO: optical parametric oscillator, MOD: intensity modulator, DL: delay line, DM: dichroic mirror, SU: scanning unit, O: objective, S: sample, C: condenser, F: filter, DET: detector, LIA: lock-in amplifier, ref: reference. **b** Pump and probe beams point spread functions (PSFs) obtained in reflection imaging 150-nm gold beads. Chromatic aberration is revealed by the displacement of the foci positions, as shown in the axial profiles along the dashed line. **c** Optical components inserted into the pump–probe setup for the temporal alignment of pump and probe pulses through SFG on a nonlinear BBO crystal. A lens is used to focus pump and probe beams onto the BBO crystal, while a prism is used to chromatically separate the outputs and project them onto a screen. The transmitted NIR input beams (in this case 800 and 1030 nm) are made visible using a NIR card and they appear like a red spot. Three new beams appear as output. The violet and green spots represent the frequency-doubled inputs at exactly half the input wavelengths (400 and 515 nm, respectively). The blue spot at 450 nm represents the SFG generated by the simultaneous interaction of the two pump and probe pulses with the BBO

while providing the pump with a uniform excitation volume larger than the locally probed area [18].

The temporal delay between pump and probe pulses is finely adjusted through a delay line (DL), usually made by a mechanical translational stage and placed in one of the two optical paths. The precision and range of the delay line need to be chosen in accordance to the timescale of the process of interest. The temporal resolution of the final system is determined by the pump and probe pulse widths, and by the spatial resolution of the delay line. To find the position of the delay line for which the pulses are precisely overlapped, after the DM the beams can be focused

onto a BBO crystal to detect the sum frequency generation (SFG) signal when the pulses arrive on the crystal at the same time (Fig. 7.2c). The same principle can be exploited using an autocorrelator. In order to optimize the temporal alignment at the sample, the scattering signal coming from a stimulated Raman scattering (SRS) pump–probe process [19] can be collected and maximized by moving the delay line. By being a scattering process, this interaction can be considered instantaneous, and the symmetric signal response as a function of the pump–probe delay gives a measure of the system temporal resolution.

The pump–probe signal is recorded as the change in transmission (or in reflection)  $\Delta T$  of the probe beam due to the pump absorption. Transmission experiments are most appropriate when dealing with highly transparent samples, while reflection detection is preferable with highly scattering specimens and in deep tissue imaging. The probe beam is chromatically separated from the pump beam using appropriate filters (F) in front of the detector, which is usually a photodiode.

Since the beam intensity variations  $\Delta T$  are usually very small, of the order of <1% of the total signal  $T$  [20], a higher detection sensitivity is required to extract the pump–probe signal from the background. This can be achieved introducing a *high-frequency modulation scheme*, where the pump intensity is modulated at a high frequency (typically >1 MHz [7]) and the detected probe is demodulated by a lock-in amplifier (LIA) to extract its modulation amplitude at the same frequency. These high-frequency intensity modulations cannot be achieved with mechanical choppers, instead acousto- or electro-optic modulators (AOM, EOM) need to be used in the pump optical path. With this approach, the low-frequency  $1/f$  laser intensity noise is circumvented and shot-noise limited detection sensitivity is achieved. In this limit, the noise equals the square root of the detected signal, and detection sensitivities down to  $\Delta T/T = 10^{-7}$  were reported, much higher than the typical  $10^{-4}$  value obtained with kHz modulation [8, 18].

The pump–probe detection scheme is sketched in Fig. 7.3a. Pump and probe pulse trains before (left) and after (right) the interaction with the sample are presented. The reference pump modulation is drawn as a dashed square wave, and the inset shows the temporal alignment between the pulses. The input probe intensity level is defined by a horizontal dashed line.  $\Delta T$  is the variation in the probe intensity with respect to the input value, and its amplitude is extracted by the lock-in amplifier. The different types of pump–probe interaction presented in Sect. 7.1.1 will generate different output signals, equivalent to gain or loss in the probe intensity, as will be fully explained in Sect. 7.2.2. In Fig. 7.3b an experimental example is shown, where single-layer graphene (SLG) is imaged with the pump–probe technique without (left) and with (right) the lock-in demodulation. Pump and probe beams are tuned to 800 and 1030 nm, respectively. Without the lock-in amplifier, a transmission image (TD) is obtained. Switching the lock-in amplifier on, the small modulated fraction of the transmitted probe beam can be extracted with high signal-to-noise ratio (SNR), and a pump–probe image (PP) is obtained, showing high contrast and a high level of sample details. For example, according to the line profiles shown, the central area exhibits the highest signal in the TD image, while it results in being completely dark in the PP image, confirming the presence of a hole in SLG sample.

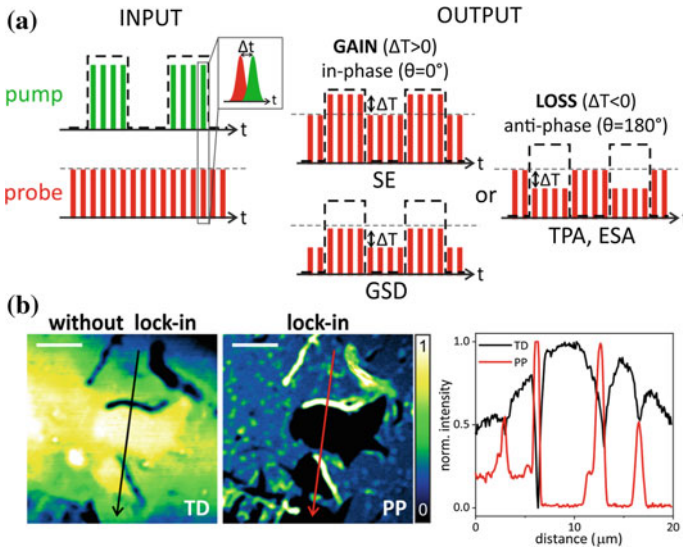


**Fig. 7.3** **a** Representation of pump and probe pulse trains before (left) and after (right) the pump–probe interaction with the sample. The pump beam is modulated and the reference modulation is shown as a dashed square wave. The input probe intensity level is shown as a dashed horizontal line.  $\Delta T$  is the variation of the probe intensity with respect to the input value, and its amplitude is extracted by the lock-in amplifier as pump–probe signal. Gain and loss processes generate pump–probe signals with opposite sign and phase. **b** Single-layer graphene imaged with the high-frequency modulation pump–probe scheme. The transmitted probe is detected without (left) and with (right) the demodulation of the lock-in amplifier. Without the lock-in, a transmission image is obtained (TD). Switching the lock-in on, the small modulated fraction of the transmitted probe beam can be extracted and a pump–probe image can be obtained (PP). Scale bar 5  $\mu\text{m}$ . Intensity line profiles across the central hole are also shown

The implementation of the setup on a typical nonlinear microscopy platform allows the collection of other nonlinear signals, such as two-photon excited fluorescence (TPEF), second harmonic generation (SHG), or coherent Raman scattering (CRS), obtaining a multi-modal nonlinear platform [4, 5].

The dual-wavelength laser-scanning pump–probe setup is the most commonly used pump–probe microscopy, but other variations have also been proposed [8]. Single-wavelength pump–probe microscopy can be achieved by discriminating the probe in polarization or by a dual-frequency modulation, where both pump and probe beams are modulated at different frequencies and the pump–probe signal is detected at the sum/difference frequencies. Moreover, an ultrafast optical wide-field microscope was proposed [21], based on a 2D smart pixel array detector capable of acquiring images with high sensitivity, femtosecond time resolution, and sub-micrometer spatial resolution.

## 7.2.2 Pump–Probe Signal Information

The pump–probe signal  $\Delta T$  is extracted from the total signal with a lock-in amplifier and its amplitude  $R = |\Delta T|$  can be retrieved, which is linearly dependent on the applied powers and on the analyte concentration, as introduced in (1.2). With a more advanced two-phase lock-in amplifier, the *phase difference*  $\theta$  of the demodulated signal with respect to the reference pump modulation can also be recovered. Two outputs,  $X = R \cos \theta$  (in-phase component) and  $Y = R \sin \theta$  (quadrature component), are obtained which represent the signal as a vector relative to the lock-in reference oscillator. The modulus can be retrieved as  $R = \sqrt{X^2 + Y^2}$  and the phase as  $\tan \theta = Y/X$ .

Depending on the type of nonlinear absorption interaction, one of the two situations may occur, as sketched in Fig. 7.3a. The probe beam can experience a *gain* in its transmission (or reflection), equivalent to an in-phase pump–probe signal with *amplitude*  $> 0$ ,  $\theta = 0^\circ$ ,  $X = R$ ,  $Y = 0$ ). This is the case of ground-state depletion (GSD) and stimulated emission (SE) interactions. The probe beam can alternatively experience a *loss*, equivalent to an anti-phase pump–probe signal with *amplitude*  $< 0$ ,  $\theta = 180^\circ$ ,  $X = -R$ ,  $Y = 0$ . This is the case in two-photon absorption (TPA) and excited state absorption (ESA) interactions. This means that the type of interaction can be distinguished by looking at the phase of the signal or at the sign of the X component.

Varying the delay between pump and probe pulses ( $\Delta t$  in Fig. 7.3a), the pump–probe signal intensity will vary according to the excited state relaxation dynamics of the involved species. The obtained time-resolved spectra will feature a maximum pump–probe signal when pump and probe pulses are overlapped, and an exponential decrease with increasing delay. The extrapolation of a single- or multiple-decay constant increases the molecular specificity of the technique, and may help in the discrimination of different sample components. The time traces can be analyzed in the *time domain*, performing multi-exponential fitting to derive the characteristic decay constants. Alternatively, time-resolved spectra can be analyzed in the *frequency domain* with the phasor analysis introduced for fluorescence lifetime imaging [22], which provides an intuitive graphical view of the lifetimes without any a priori assumption. It was proven that the application of the phasor analysis with pump–probe imaging provides a robust method for efficiently distinguishing pigments in biological and in art samples [23], avoiding the fitting procedure which typically requires high SNRs for a reliable separation of the different components. Moreover, TPA and ESA processes, which cannot be distinguished with the phase information, can be easily distinguished by looking at their temporal behavior. TPA is an instantaneous process exhibiting a symmetric cross-correlation trace, while ESA shows an instantaneous rise followed by a decay reflecting the characteristic lifetime of the excited state [8].

### 7.2.3 *State-of-the-Art of Pump–Probe Microscopy*

The first pump–probe microscope was realized by Dong et al. in the 1990s to measure the fluorescence lifetime through SE detection [24, 25]. Their approach relied on the use of two ultrafast pulsed lasers characterized by slightly different repetition rates and a consequent variable delay between their pulses. In this way, the probe pulse, tuned to induce stimulated emission in the fluorophore, was repeatedly sampling the excited population at different delays, providing dynamic information with superior spatial and temporal resolution without any amplitude modulation and delay line. In 2007, the Warren group proposed the first pump–probe microscope based on a high-frequency modulation scheme to detect melanins in cells and differentiate them by looking at the phase as well as at the temporal evolution of the pump–probe signal [26, 27]. Since then, transient absorption microscopy has started to be explored more in different research fields, from *material* to *biological* to *art* sciences.

Because of its non-fluorescent-based contrast, single-particle sensitivity, and high temporal resolution, pump–probe microscopy is extensively used in imaging and characterizing the carrier dynamics of metallic and semiconducting nanostructures for studying their optoelectronic properties [17, 28–39]. Pump–probe techniques have acquired importance also in mapping weakly or non-fluorescent nanostructures (like single-walled carbon nanotubes, nanodiamonds, gold nanoparticles, etc.) used as biorthogonal labels and for biomedical applications inside living cells and tissues [40–44].

Among nanomaterials, recently graphene has started to be intensively studied for the development of novel electronic and optoelectronic devices [45]. Owing to its particular linear electronic band structure, graphene shows a wavelength-independent, broadband optical absorption ( $\sim 2.3\%$  per layer [46]) in the NIR part of the spectrum [47], together with a large third-order susceptibility  $\chi^{(3)}$  [48]. This makes pump–probe microscopy an ideal technique for studying its carrier dynamics and for performing imaging, mainly using NIR wavelengths [49–62]. The carrier dynamics were extensively explored for different graphene structures, like in few-layer epitaxial graphene [49], single- and multi-layer exfoliated graphene [50, 55], graphene suspensions [56, 58], and graphene oxide [59]. Few experiments were performed on single-layer graphene (SLG) [50, 57]. For all these graphene-based structures, the relaxation dynamics results are characterized by two timescales. The faster one falls in the range of 70–120 fs and it is attributed to carrier thermalization by electron–electron interactions. The slower one is in the range of 0.4–1.7 ps; it is associated with carrier cooling via electron–phonon interactions and its value is inversely proportional to the crystal disorder [45]. In Fig. 7.4a an example of time-resolved spectrum of multi-layer graphene flakes is presented, fitted with a double exponential decay. The fast component is sub-resolved due to the limited temporal resolution of the system. The slow component falls in the range found in the literature. Images of a graphene flake at different delays are also shown.

In 2010, Huang et al. [60] first obtained pump–probe microscopy imaging of multi-layer epitaxial graphene grown on a silicon substrate, and showed the linear

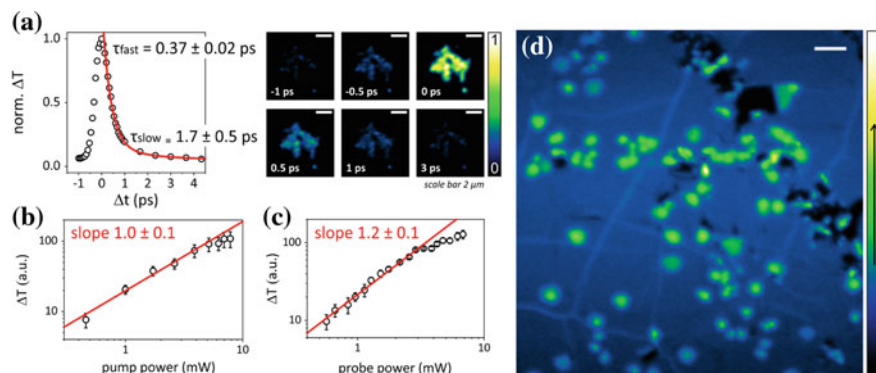


**Fig. 7.4** **a** Time-resolved spectrum of multi-layer graphene flakes obtained recording the pump–probe signal modulus ( $R$ ) at different pump–probe delays ( $\Delta t$ ). A double exponential fit is performed on the data and it retrieves a fast sub-resolved time constant and a slow time constant in the range found in the literature for graphene relaxation dynamics. Images at different time delays are also shown. **b–c** Log–log plots of  $R$  as a function of the applied pump (**b**) and probe (**c**) powers for multi-layer graphene flakes. Linear fits at low powers are also shown, confirming the linear behavior of the signal (1.2). Saturation occurs at higher powers. **d** Large field-of-view pump–probe image of single-layer graphene (SLG). Scale bar  $5 \mu\text{m}$

dependence of the pump–probe signal intensity on the pump power and on the number of layers, as expected from the theory (see (1.2)). The linearity of the pump–probe signal with respect to the applied pump and probe powers is presented in Fig. 7.4b, c for multi-layer graphene flakes. The linear behavior is fulfilled at low powers, while at higher powers the signal saturates, as predicted by the state-filling effect of the higher electronic states [63–65]. After that first publication, many other works reported the use of pump–probe microscopy for rapid and highly sensitive imaging of multi- and single-layer graphene, achieving the mapping of the local excited state dynamics, the characterization of nano-defects toward a real-time non-destructive approach for manufacturing applications, and the real-time quantitative imaging of graphene oxide in vitro and in circulating blood [51–54, 61, 62]. In Fig. 7.4d, an example of a large field-of-view pump–probe image of single-layer graphene (SLG) is shown. SLG covers the majority of the field-of-view, exhibiting a uniform signal. Brighter multi-layer defects and darker cracks are also present in the structure. Pump and probe wavelengths were tuned to 800 and 1020 nm, respectively, and their pulses were kept temporally aligned for maximum signal generation.

Transient absorption microscopy also has started to be used in biological research for imaging highly absorbing intrinsic chromophores. SE microscopy was employed to visualize chromoproteins and hemoglobin, to map transdermal drug distribution [66], and for fluorescence lifetime imaging of selected fluorophore [67, 68], taking advantage of signal and SNR enhancement [69]. Eumelanin and pheomelanin were studied and differentiated using their strong nonlinear absorption signals [26], and this contrast was implemented for skin cancer diagnosis, both ex vivo and in vivo [70, 71]. Hemoglobin was imaged in microvasculature [13] and in red blood cells

flow [72, 73], and its excited state lifetime turned out to be a useful indicator of the oxygenation level [13].

Apart from biological pigments studies, pump–probe microscopy is also used in identifying historical art pigments and/or pigment mixtures, to study their 3D-layer structure and their method of application [74, 75].

### 7.3 Breaking the Diffraction Limit in Pump–Probe Microscopy

Diffraction is the basis of image formation in an optical microscope, and the cause of its limited resolving power. The image of a point source through an objective lens does not look like an infinitely small point in the image plane, but instead, a constructive and destructive interference produces a characteristic diffraction pattern which consists of a central bright spot (Airy disk) surrounded by concentric rings (Airy pattern). The German physicist Abbe defined the *fundamental resolution limit* of a microscope as [76]

$$d = \frac{\lambda}{2NA}, \quad (7.5)$$

where  $\lambda$  is the wavelength of the light and  $NA$  is the numerical aperture of the objective, defined as  $NA = n \sin \alpha$ , where  $n$  is the refractive index of the medium between lens and sample, and  $\alpha$  is half the acceptance angle of the objective lens. This states that a specific detail in the sample can be resolved when the numerical aperture of the objective is large enough to capture the zeroth-order diffraction pattern (central Airy disk) that is produced. This means that, even under optimized imaging conditions, a resolution better than 200 nm cannot be achieved with conventional microscopy techniques that exploit visible light. Looking also at the point source image in the axial direction, the typical elongated intensity distribution called the point spread function (PSF) exhibits an axial resolution even worse than the lateral one, given by the formula [77]:

$$d_z = \frac{2\lambda n}{NA^2}. \quad (7.6)$$

In *nonlinear microscopy*, resolution is expected to be worse due to the use of longer illumination wavelengths in the NIR range, even if this effect is slightly compensated by a higher background signal suppression and by the spatial confinement of the multi-photon interaction, leading to slightly better resolution values [6]. The spatial resolution is proportional to the illumination point spread function (IPSF) elevated to the number of involved photons, getting a considerably reduced excitation volume compared with that for one-photon imaging at the same NIR wavelength [3].

In particular, in pump–probe microscopy the spatial resolution is related to the product of the IPSFs of the pump and probe beams. With the condition of the pump and probe processes involving one-photon transition, a resolution improvement of  $\sqrt{2}$  is expected compared to the resolution achieved by linear optical microscopy at the same wavelengths [24, 28]. This improvement is comparable to the one obtained in confocal fluorescence microscopy [78].

The improvement of the spatial resolution of optical microscopes has been a central challenge in the last few decades, and a lot of effort has been put to circumvent this limitation. Exploiting interference by two opposing high aperture lenses [79–82] or by structured illumination patterns [83], an isotropic two-fold resolution improvement down to 100 nm was demonstrated in fluorescence microscopy. A step forward toward the real circumvention of the diffraction barrier was achieved with the exploitation of *nonlinearities* in order to prevent the simultaneous signaling of adjacent identical target molecules.

In fluorescence microscopy, two families of super-resolution techniques, based on the switching between *ON* (bright) and *OFF* (dark) molecular states, were introduced in the 1990s.

The first family is based on *stochastic switching and read-out* [84, 85], where single molecules are stochastically switched on in a sparse ensemble and localized with a precision given by the inverse of the square root of the number of detected photons (here the nonlinearity). Techniques like stochastic optical reconstruction microscopy (STORM) and photo-activatable localization microscopy (PALM) use the stochastic approach and achieved resolution of <20 nm [86].

The second super-resolution family is based on *targeted switching and read-out*, and on the general RESOLFT (reversible saturable optical fluorescence transition) concept [87]. In this approach, the diffraction-limited excitation volume that actually fluoresces is engineered by superimposing a second beam, for example, a doughnut-shaped one that switches off the molecules at the periphery, leaving in the on state only the ones at the very center. The central region can be made arbitrarily small by saturating—that is the nonlinearity—the off transition. One of the main realizations of this technique is stimulated emission depletion (STED) [88–90], which uses the stimulated emission transition to quench the fluorescent molecules. In cellular imaging, a resolution down to 20 nm was demonstrated [91].

### 7.3.1 The Generalized RESOLFT Concept

The RESOLFT concept is very general, and it can be applied to any saturable transition; that is fluorescence is not mandatory. In fact, the RESOLFT principle consists of switching the target molecules between an *ON* state, which gives a detectable signal, and an *OFF* state, which is optically dark. In order to prevent the simultaneous signaling of adjacent identical target molecules, the volume that actually gives a detectable signal is manipulated. First, the *OFF*  $\rightarrow$  *ON* transition is achieved in a diffraction-limited focal spot. Second, the *ON*  $\rightarrow$  *OFF* transition (called *depletion*)

is realized using a beam with a spatially controlled intensity distribution featuring a “zero” (doughnut shape). In this way, the signal of interest is switched off at the periphery of the focal spot, and it can be detected only from an arbitrarily small volume at the very center of the depletion beam by saturating the depletion transition. By collinearly scanning the beams, super-resolved images can be directly acquired. The signal suppression due to the depletion beam depends exponentially on the depletion intensity [92], and this *nonlinear* behavior is essential for breaking the diffraction barrier. The obtained resolution  $d$  is inversely proportional to the intensity of the depletion beam and is given by the formula [87, 92, 93]:

$$d = \frac{\lambda}{2NA\sqrt{1 + a\frac{I_{\max}}{I_0}}}, \quad (7.7)$$

where  $\lambda$  is the detected wavelength,  $NA$  is the objective numerical aperture,  $a > 0$  is a parameter that takes into consideration the shape of the “zero” of the depletion beam,  $I_{\max}$  is the depletion beam intensity at the crest of the doughnut, and  $I_0$  is the saturation intensity, a characteristic parameter of the depletion transition, which scales inversely with the lifetime of the two states [94]. When the depletion is brought to saturation ( $I_{\max} \gg I_0$ ), a narrow spatial confinement is achieved. Moreover, it can be noticed that, in principle, the resolution can be continuously and infinitely increased by increasing the saturation level, but the effective resolution enhancement is limited by the SNR.

As stated before, any saturable optical process between molecular states, not necessarily involving fluorescent transitions, is a potential candidate for breaking the diffraction limit in optical microscopy, thus opening the possibility to use these approaches in *label-free microscopy*.

The RESOLFT concept was theoretically and experimentally proposed for nonlinear vibrational imaging [95–99] and nonlinear absorption imaging [54, 100–102] after identifying proper competing transitions to be saturated with an additional doughnut-shaped beam.

### 7.3.2 Saturated Pump–Probe Nanoscopy

The exploitation of the generalized RESOLFT concept to achieve sub-diffraction imaging capabilities in label-free optical microscopy was recently proposed and demonstrated with the pump–probe microscopy approach.

Silien et al. [101, 102] theoretically proposed a vibrational depletion pump–probe scheme for IR absorption microscopy, where a resolution improvement down to  $\lambda/10$  could be achieved by saturating the vibrational mode of interest with a vortex-shaped beam.

Wang et al. [100] exploited a spatially controlled absorption saturation in order to achieve sub-diffraction pump–probe imaging of graphene-based samples. A similar

approach was proposed by Bianchini et al. [54]. This absorption–saturation approach is based on the collinear superimposition, in a conventional two-beam pump–probe configuration (presented in Sect. 7.2.1), of a high-intensity non-modulated doughnut-shaped pump beam, whose purpose is to transiently saturate the absorption at the periphery of the focal spot. The saturation prevents the absorption of the probe beam, which will be transmitted without any modulation, while the probe intensity variation induced by the absorption of the modulated pump will be detected only from the very center of the focal spot. The interaction of the three pulses and the detection signal at the center and at the periphery of the focal spot are presented in Fig. 7.5a. The saturated pump–probe nanoscopy setup is presented in Fig. 7.5b. The saturation pump beam can be picked before the pump intensity modulator (MOD) using a beam splitter (BS). The doughnut shape can be generated applying a  $0-2\pi$  phase mask (PM) through a vortex phase plate (VPP) [54] or a spatial light modulator (SLM) [100]. The lateral and axial profiles of a typical doughnut-shaped beam are shown in Fig. 7.5c. Saturation pulses need to be temporally aligned with the pump and probe ones using a delay line (DL). Alternatively, as proposed in [100], the pump beam alignment can be adjusted through a delay line instead of the saturation

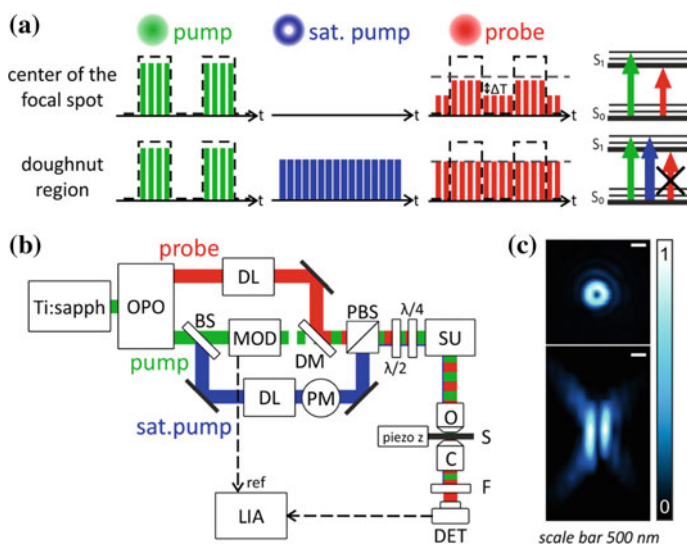


**Fig. 7.5** **a** Saturated pump–probe pulse sequence. At the center of the focal spot, the signal detection is like the one presented in Fig. 7.3a for a GSD process. At the doughnut region, the non-modulated saturation pump beam saturates the absorption leaving the probe beam unmodified, and no modulation at the reference pump frequency is detected. **b** The saturated pump–probe nanoscopy setup as presented in [54]. The saturation pump beam is picked before the modulator (MOD) with a beam splitter (BS), sent to a delay line (DL) for temporally overlapping the pulses, and then to a phase mask (PM) to create the doughnut shape. The saturation beam is then collinearly combined with the other two beams with a polarizing beam splitter (PBS). The polarization of the saturation beam is controlled by a pair of  $\lambda/2$  and  $\lambda/4$  wave plates. **c** Experimental lateral and axial PSFs of the doughnut-shaped saturation beam

one. The SFG technique presented in Sect. 7.2.1 can also be applied to achieve the temporal overlap of the saturation pump pulses with the probe ones. In order to assure optimal performances, the circular polarization of the doughnut beam [103] needs to be maintained at the focal plane using a pair of half- and quarter-wave plates ( $\lambda/2$  and  $\lambda/4$ , respectively). The saturation beam can be collinearly combined with the pump beam with a beam combiner before the dichroic mirror of the probe beam (as proposed in [100]), or it can be combined directly with both beams using a polarizing beam splitter (PBS, as proposed in [54] and sketched in Fig. 7.5b).

Wang et al. [100] demonstrated this technique to image graphite nanoplatelets, which are strong absorber and saturable materials. The suppression of the pump–probe signal results is exponentially dependent on the saturation pump power ( $I_{\text{sat}}$ ), a behavior that is at the basis for achieving a reduction of the detection volume below the diffraction limit (see Sect. 7.3.1). By fitting the depletion curve to the function [100]

$$\frac{\Delta T}{T} = \frac{1}{1 + \frac{I_{\text{sat}}}{I_0}} \quad (7.8)$$

values of 0.43 and 0.28 MW cm<sup>-2</sup> were derived for the characteristic saturation power  $I_0$  for graphite and graphene nanoplatelets, respectively. By setting the saturation power to 2.0 MW cm<sup>-2</sup> and its temporal delay to 0.4 ps, sub-diffraction imaging of graphite nanoplatelets was achieved and features of 225 nm ( $\sim \lambda/3.0NA$ ) were probed with an 830 nm probe beam. Bianchini et al. [54] reached a resolution of the order of  $\sim \lambda/10$  in transient absorption imaging of SLG using wavelengths longer than 1000 nm (Fig. 7.6c).

In Fig. 7.6a the experimental depletion curve of multi-layer graphene flakes is presented. Data is fitted with (1.8) and a saturation intensity of 0.6 MW cm<sup>-2</sup> is obtained. In Fig. 7.6b, c two examples of conventional (PP) and saturated (SPP) pump–probe images of SLG foldings are shown, where the superimposition of the doughnut-shaped saturation beam allows for a remarkable increase in spatial resolution. The saturation beam was kept at around 20 mW, and no sample damage was observed during the acquisition. Experiments were performed using the setup presented in [54].

### 7.3.3 Other Super-Resolution Approaches in Pump–Probe Microscopy

Some other approaches have been applied in label-free pump–probe microscopy for achieving super-resolution imaging capabilities.

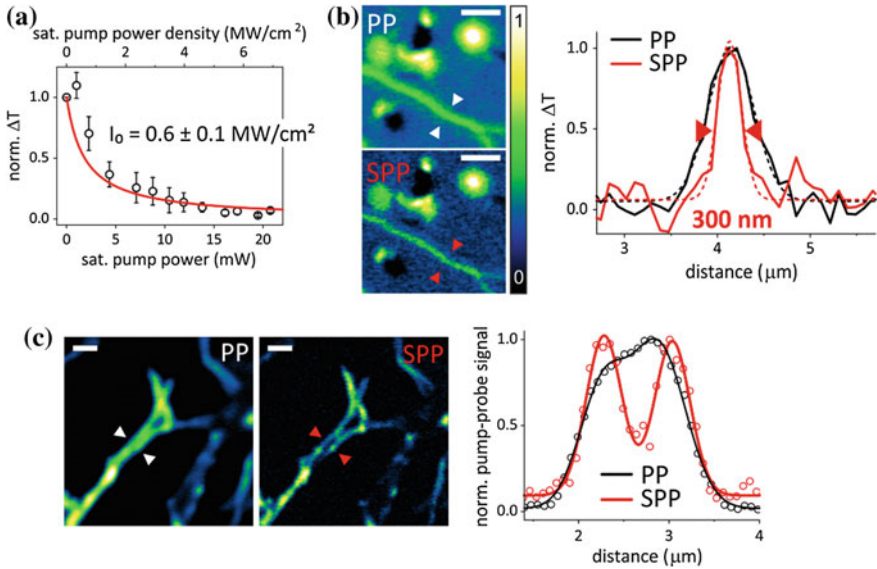


**Fig. 7.6** **a** Depletion curve of graphene flakes fitted with (1.8). **b–c** Conventional (PP) and saturated (SPP) pump-probe images of SLG foldings acquired with the setup presented in [54] and with pump and probe beams tuned to 800 and 1020 nm, respectively. Scale bar 2  $\mu\text{m}$ . Line profiles taken across the arrows are also compared, showing a remarkably improved resolution in the SPP case

Massaro et al. [104] developed a structured pump-probe microscope (SPPM) based on a spatially modulated pump field and a focused diffraction-limited probe field, and they used it to characterize the free carrier dynamics of silicon nanowires with 114 nm sub-diffraction resolution.

Another alternative solution for contrast and resolution enhancement is based on an image subtraction approach. The method consists of subtracting two images that are consecutively taken with Gaussian and doughnut-shaped excitation beams with an appropriate normalizing coefficient. The class of implementation that relies on this method is known as switching laser mode (SLAM) or fluorescence emission difference (FED) [105, 106]. Interestingly, one of the main issues with these methods is over-subtraction, which limits their use for dense molecular structures. A solution, that is, intensity weighted subtraction (IWS), has recently been proposed by Korobchevskaya et al. [107]. They calculate the subtraction coefficient pixel-by-pixel by taking into account the original image intensity distributions. A similar concept applied to the imaging of CdSe semiconductor nanobelts demonstrates a resolution of about  $\sim\lambda/3.0NA$  [108]. These approaches do not rely on saturation phenomena, but they lead to a comparably good resolution enhancement, and can be applied to any absorber not exhibiting saturable transitions.

## 7.4 Summary and Future Perspectives

Among nonlinear optical approaches, pump–probe methods allow the resolving and monitoring of chemical and atomic ultrafast processes, which occur on a picosecond (or lower) timescale; no other mediators are required, for example, fluorescence. Such ability is of interest in the microscopy field. The standard optical microscope often uses fluorescence, and it relies on the photo-physical properties of fluorescent molecules to obtain the desired contrast and spatial resolution. A label-free approach is highly desirable since the labeling procedure can be invasive, and fluorescence can degrade and photo-bleach. The direct imaging of the molecules of interest using pump–probe methods allows gathering insights about molecular organization and interaction, while it does not exclude the simultaneous use of the fluorescence. It is worth noting that when the absorption process is saturable, super-resolution can also be achieved following the general RESOLFT concept.

Among nanomaterials, recently graphene has started to be intensively studied for the development of novel electronic and optoelectronic devices. Owing to its particular linear electronic band structure, graphene shows a wavelength-independent, broadband optical absorption in the NIR, together with a large third-order susceptibility  $\chi^{(3)}$ . This characteristic makes pump–probe spectroscopy and microscopy ideal techniques to explore carrier dynamics in all its different graphene forms, for example, few-layer epitaxial graphene, single- and multi-layer exfoliated graphene, graphene suspensions, and graphene oxide. Interestingly, since its absorption property in the NIR is saturable and allows super-resolution imaging, it is opening a new envisaging way to study it. Nevertheless, since transient saturable absorption is not a unique property of graphene, many other materials could be studied using absorption-based super-resolution imaging approaches.

**Acknowledgments** The authors thank Kseniya Korobchevskaya, Colin Sheppard, Amira El Merhie, Silvia Dante, Antonio Esau Del Rio Castillo, Camilla Coletti (Fondazione Istituto Italiano di Tecnologia, Genova, Italy), and Fumihiko Dake (Nikon Corporation, Yokohama, Japan) for the scientific discussion; Eileen Sheppard for proofreading the chapter and the Nikon Imaging Center at the Fondazione Istituto Italiano di Tecnologia for help with light microscopy. This work was partially funded by the European Community's Seventh Framework Programme (FP7/20012-2015) under grant agreement no. 280804 in the LANIR project framework.

## References

1. R.W. Boyd, *Nonlinear Optics* (2003)
2. P. Bianchini, A. Diaspro, Three-dimensional (3D) backward and forward second harmonic generation (SHG) microscopy of biological tissues. *J. Biophotonics* **1**(6), 443–450 (2008)
3. W.R. Zipfel, R.M. Williams, W.W. Webb, Nonlinear magic: multiphoton microscopy in the biosciences. *Nat. Biotechnol.* **21**(11), 1369–77 (2003)
4. H. Chen, H. Wang, M.N. Slipchenko, Y. Jung, Y. Shi, J. Zhu, K.K. Buhman, J.-X. Cheng, A multimodal platform for nonlinear optical microscopy and microspectroscopy. *Opt. Express* **17**(3), 1282–1290 (2009)

5. T. Meyer, M. Schmitt, B. Dietzek, J. Popp, Accumulating advantages, reducing limitations: multimodal nonlinear imaging in biomedical sciences—the synergy of multiple contrast mechanisms. *J. Biophotonics* **6**(11–12), 887–904 (2013)
6. A. Diaspro, P. Bianchini, G. Vicidomini, M. Faretta, P. Ramoino, C. Usai, Multi-photon excitation microscopy. *Biomed. Eng. Online* **5**(1), 36 (2006)
7. L. Wei, W. Min, Pump-probe optical microscopy for imaging nonfluorescent chromophores. *Anal. Bioanal. Chem.* **403**(8), 2197–2202 (2012)
8. M.C. Fischer, J.W. Wilson, F.E. Robles, W.S. Warren, Invited review article: pump-probe microscopy. *Rev. Sci. Instrum.* **87**(3) (2016)
9. A. Diaspro, G. Chirico, M. Collini, Two-photon fluorescence excitation and related techniques in biological microscopy. *Q. Rev. Biophys.* **38**(2), 97–166 (2005)
10. R.L. Sutherland, *Handbook of Nonlinear Optics*, vol. 36(3) (1997)
11. M. Göppert-Mayer, M. Göppert-Mayer, Über elementarakte mit zwei quantensprüngen [Elementary processes with two quantum transitions]. *Ann. Phys.* (1931)
12. P.-T. Dong, J.-X. Cheng, Pump-probe microscopy: theory, instrumentation, and applications. *Spectroscopy* **32**(4), 2–11 (2017)
13. D. Fu, T.E. Matthews, T. Ye, I.R. Piletic, W.S. Warren, Label-free in vivo optical imaging of microvasculature and oxygenation level. *J. Biomed. Opt.* **13**(4), 040503 (2008)
14. G. Porter, Flash photolysis and spectroscopy. A new method for the study of free radical reactions. *Proc. R. Soc. A Math. Phys. Eng. Sci.* **200**(1061), 284–300 (1950)
15. G. Porter, M.R. Topp, Nanosecond flash photolysis and the absorption spectra of excited singlet states. *Nature* **220**(5173), 1228–1229 (1968)
16. G. Porter, M.R. Topp, Nanosecond flash photolysis. *Proc. R. Soc. A Math. Phys. Eng. Sci.* **315**(1521), 163–184 (1970)
17. G.V. Hartland, Ultrafast studies of single semiconductor and metal nanostructures through transient absorption microscopy. *Chem. Sci.* **1**(3), 303–309 (2010)
18. T. Virgili, G. Grancini, E. Molotokaite, I. Suarez-Lopez, S.K. Rajendran, A. Liscio, V. Palermo, G. Lanzani, D. Polli, G. Cerullo, Confocal ultrafast pump-probe spectroscopy: a new technique to explore nanoscale composites. *Nanoscale* **4**(7), 2219 (2012)
19. J.X. Cheng, X.S. Xie, *Coherent Raman Scattering Microscopy* (2013)
20. A. Beeby, Pump-probe laser spectroscopy, in *An Introduction to Laser Spectroscopy* (Springer US, 2002), pp. 105–137
21. M. Seo, S. Boubanga-Tombet, J. Yoo, Z. Ku, A.V. Gin, S.T. Picraux, S.R.J. Brueck, A.J. Taylor, R.P. Prasankumar, Ultrafast optical wide field microscopy. *Opt. Express* **21**(7), 8763 (2013)
22. M.A. Digman, V.R. Caiolfa, M. Zamai, E. Gratton, The phasor approach to fluorescence lifetime imaging analysis. *Biophys. J.* (2008)
23. F.E. Robles, J.W. Wilson, M.C. Fischer, W.S. Warren, Adapting phasor analysis for nonlinear pump-probe microscopy. *Opt. Express* **20**(15), 858908 (2013)
24. C.Y. Dong, P.T. So, T. French, E. Gratton, Fluorescence lifetime imaging by asynchronous pump-probe microscopy. *Biophys. J.* **69**(6), 2234–2242 (1995)
25. C. Buehler, C.Y. Dong, P.T.C. So, T. French, E. Gratton, Time-resolved polarization imaging by pump-probe (Stimulated Emission) fluorescence microscopy. *Biophys. J.* **79**(July), 536–549 (2000)
26. D. Fu, T. Ye, T.E. Matthews, G. Yurtsever, W.S. Warren, Two-color, two-photon, and excited-state absorption microscopy. *J. Biomed. Opt.* **12**(5), 054004 (2007)
27. D. Fu, T. Ye, T.E. Matthews, G. Yurtsever, L. Hong, J. D. Simon, W.S. Warren, Two-color excited-state absorption imaging of melanins, in *Photonic Therapeutics and Diagnostics III*, ed. by N. Kollias, B. Choi, H. Zeng, R.S. Malek, B.J. Wong, J.F.R. Ilgner, K.W. Gregory, G.J. Tearney, H. Hirschberg, S.J. Madsen, vol. 6424 (International Society for Optics and Photonics, 2007), p. 642402
28. D. Davydova, A. de la Cadena, D. Akimov, B. Dietzek, Transient absorption microscopy: Advances in chemical imaging of photoinduced dynamics. *Laser Photonics Rev.* **10**(1), 62–81 (2016)

29. Z. Guo, N. Zhou, O.F. Williams, J. Hu, W. You, A.M. Moran, Imaging carrier diffusion in perovskites with a diffractive optic-based transient absorption microscope. *J. Phys. Chem. C* **122**(19), 10650–10656 (2018)
30. Y. Jung, M.N. Slipchenko, C.H. Liu, A.E. Ribbe, Z. Zhong, C. Yang, J.-X.X. Cheng, Fast detection of the metallic state of individual single-walled carbon nanotubes using a transient-absorption optical microscope. *Phys. Rev. Lett.* **105**(21), 1–4 (2010)
31. Y. Wan, Z. Guo, T. Zhu, S. Yan, J. Johnson, L. Huang, Cooperative singlet and triplet exciton transport in tetracene crystals visualized by ultrafast microscopy. *Nat. Chem.* **7**(10), 785–792 (2015)
32. M.M. Gabriel, J.R. Kirschbrown, J.D. Christesen, C.W. Pinion, D.F. Zigler, E.M. Grumstrup, B.P. Mehl, E.E.M. Cating, J.F. Cahoon, J.M. Papanikolas, Direct imaging of free carrier and trap carrier motion in silicon nanowires by spatially-separated femtosecond pump-probe microscopy. *Nano Lett.* **13**(3), 1336–1340 (2013)
33. S.S. Lo, T.A. Major, N. Petchsang, L. Huang, M.K. Kuno, G.V. Hartland, Charge carrier trapping and acoustic phonon modes in single CdTe nanowires. *ACS Nano* **6**(6), 5274–5282 (2012)
34. C.Y. Wong, S.B. Penwell, B.L. Cotts, R. Noriega, H. Wu, N.S. Ginsberg, Revealing exciton dynamics in a small-molecule organic semiconducting film with subdomain transient absorption microscopy. *J. Phys. Chem. C* **117**(42), 22111–22122 (2013)
35. D. Davydova, A. De La Cadena, S. Demmler, J. Rothhardt, J. Limpert, T. Pascher, D. Akimov, B. Dietzek, Ultrafast transient absorption microscopy: study of excited state dynamics in PtOEP crystals. *Chem. Phys.* **464**, 69–77 (2016)
36. S. Chong, W. Min, X.S. Xie, Ground-state depletion microscopy: detection sensitivity of single-molecule optical absorption at room temperature. *J. Phys. Chem. Lett.* **1**(23), 3316–3322 (2010)
37. Q. Cui, F. Ceballos, N. Kumar, H. Zhao, Transient absorption microscopy of monolayer and bulk WSe<sub>2</sub>. *ACS Nano* **8**(3), 2970–2976 (2014)
38. Z. Guo, J.S.S. Manser, Y. Wan, P.V.V. Kamat, L. Huang, Spatial and temporal imaging of long-range charge transport in perovskite thin films by ultrafast microscopy. *Nat. Commun.* **6**(1), 1–8 (2015)
39. Z. Guo, Y. Wan, M. Yang, J. Snaider, K. Zhu, L. Huang, Long-range hot-carrier transport in hybrid perovskites visualized by ultrafast microscopy. *Science* (80–). **356**(6333), 59–62 (2017)
40. L. Tong, Y. Liu, B.D. Dolash, Y. Jung, M.N. Slipchenko, D.E. Bergstrom, J.-X. Cheng, Label-free imaging of semiconducting and metallic carbon nanotubes in cells and mice using transient absorption microscopy. *Nat. Nanotechnol.* **7**(1), 56–61 (2012)
41. T. Chen, F. Lu, A.M. Streets, P. Fei, J. Quan, Y. Huang, Optical imaging of non-fluorescent nanodiamonds in live cells using transient absorption microscopy. *Nanoscale* **5**(11), 4701–4705 (2013)
42. T. Chen, S. Chen, J. Zhou, D. Liang, X. Chen, Y. Huang, Transient absorption microscopy of gold nanorods as spectrally orthogonal labels in live cells. *Nanoscale* **6**(18), 10536–10539 (2014)
43. L. Zhang, S. Shen, Z. Liu, M. Ji, Label-free, quantitative imaging of MoS<sub>2</sub>-nanosheets in live cells with simultaneous stimulated Raman scattering and transient absorption microscopy. *Adv. Biosyst.* **1**(4), 1700013 (2017)
44. J. Liu, J.M.K. Irudayaraj, Non-fluorescent quantification of single mRNA with transient absorption microscopy. *Nanoscale* **8**(46), 19242–19248 (2016)
45. E. Malic, A. Knorr, *Graphene and Carbon Nanotubes: Ultrafast Relaxation Dynamics and Optics* (Wiley-VCH Verlag GmbH & Co, KGaA, 2013)
46. R.R. Nair, P. Blake, A.N. Grigorenko, K.S. Novoselov, T.J. Booth, T. Stauber, N.M.R. Peres, A.K. Geim, Fine structure constant defines visual transparency of graphene. *Science* (80–). **320**(5881), 1308 (2008)
47. K.F. Mak, J. Shan, T.F. Heinz, Seeing many-body effects in single- and few-layer graphene: observation of two-dimensional saddle-point excitons. *Phys. Rev. Lett.* (2011)

48. E. Hendry, P.J. Hale, J. Moger, A.K. Savchenko, S.A. Mikhailov, Coherent nonlinear optical response of graphene. *Phys. Rev. Lett.* **105**(9), 1–4 (2010)
49. J.M. Dawlaty, S. Shivaraman, M. Chandrashekar, F. Rana, M.G. Spencer, Measurement of ultrafast carrier dynamics in epitaxial graphene. *Appl. Phys. Lett.* **92**(4), (2008)
50. M. Breusing, S. Kuehn, T. Winzer, E. Malić, F. Milde, N. Severin, J.P. Rabe, C. Ropers, A. Knorr, T. Elsaesser, Ultrafast nonequilibrium carrier dynamics in a single graphene layer. *Phys. Rev. B Condens. Matter Mater. Phys.* **83**(15), 1–4 (2011)
51. J. Li, W. Zhang, T. Chung, M.N. Slipchenko, Y.P. Chen, J.-X. Cheng, C. Yang, Highly sensitive transient absorption imaging of graphene and graphene oxide in living cells and circulating blood. *Sci. Rep.* **5**(February), 12394 (2015)
52. H. Patel, R.W. Havener, L. Brown, Y. Liang, L. Yang, J. Park, M.W. Graham, Tunable optical excitations in twisted bilayer graphene form strongly bound excitons. *Nano Lett.* **15**(9), 5932–5937 (2015)
53. K.-C.C. Huang, J. McCall, P. Wang, C.-S.S. Liao, G. Eakins, J.-X.X. Cheng, C. Yang, High-speed spectroscopic transient absorption imaging of defects in graphene. *Nano Lett.* **18**(2), 1489–1497 (2018)
54. P. Bianchini, K. Korobchevskaya, G. Zanini, A. Diaspro, Pump-probe nanoscopy by means of transient absorption saturation, in *2018 20th International Conference on Transparent Optical Networks (ICTON)* (IEEE, 2018), pp. 1–4
55. R.W. Newson, J. Dean, B. Schmidt, H.M. van Driel, Ultrafast carrier kinetics in exfoliated graphene and thin graphite films. *Opt. Express* **17**(4), 2326 (2009)
56. P.J. Hale, S.M. Hornett, J. Moger, D.W. Horsell, E. Hendry, Hot phonon decay in supported and suspended exfoliated graphene. *Phys. Rev. B Condens. Matter Mater. Phys.* **83**(12), 4–7 (2011)
57. D. Brida, A. Tomadin, C. Manzoni, Y.J. Kim, A. Lombardo, S. Milana, R.R. Nair, K.S. Novoselov, A.C. Ferrari, G. Cerullo, M. Polini, Ultrafast collinear scattering and carrier multiplication in graphene. *Nat. Commun.* **4**(May), 1–9 (1AD)
58. S. Kumar, M. Anija, N. Kamaraju, K.S. Vasu, K.S. Subrahmanyam, A.K. Sood, C.N.R. Rao, Femtosecond carrier dynamics and saturable absorption in graphene suspensions. *Appl. Phys. Lett.* **95**(19), 2007–2010 (2009)
59. J. Shang, L. Ma, J. Li, W. Ai, T. Yu, G.G. Gurzadyan, Femtosecond pump-probe spectroscopy of graphene oxide in water. *J. Phys. D. Appl. Phys.* **47**(9) (2014)
60. L. Huang, G.V. Hartland, L.Q. Chu, Luxmi, R.M. Feenstra, C. Lian, K. Tahy, H. Xing, Ultrafast transient absorption microscopy studies of carrier dynamics in epitaxial graphene. *Nano Lett.* **10**(4), 1308–1313 (2010)
61. B. Gao, G. Hartland, T. Fang, M. Kelly, D. Jena, H. Xing, L. Huang, Studies of intrinsic hot phonon dynamics in suspended graphene by transient absorption microscopy. *Nano Lett.* **11**(8), 3184–3189 (2011)
62. G. Grancini, N. Martino, M. Bianchi, L.G. Rizzi, V. Russo, A. Li Bassi, C.S. Casari, A. Petrozza, R. Sordan, G. Lanzani, Ultrafast spectroscopic imaging of exfoliated graphene. *Phys. Status Solidi Basic Res.* **249**(12), 2497–2499 (2012)
63. Q. Bao, H. Zhang, Z. Ni, Y. Wang, L. Polavarapu, Z. Shen, Q.H. Xu, D. Tang, K.P. Loh, Monolayer graphene as a saturable absorber in a mode-locked laser. *Nano Res.* **4**(3), 297–307 (2011)
64. V.I. Klimov, Spectral and dynamical properties of multiexcitons in semiconductor nanocrystals. *Annu. Rev. Phys. Chem.* **58**(1), 635–673 (2007)
65. F.T. Vasko, Saturation of interband absorption in graphene. *Phys. Rev. B Condens. Matter Mater. Phys.* **82**(24), 1–6 (2010)
66. W. Min, S. Lu, S. Chong, R. Roy, G.R. Holtom, X.S. Xie, X. Sunney Xie, Imaging chromophores with undetectable fluorescence by stimulated emission microscopy. *Nature* **461**(7267), 1105–1109 (2009)
67. P.-Y. Lin, S.-S. Lee, C.-S. Chang, F.-J. Kao, Long working distance fluorescence lifetime imaging with stimulated emission and electronic time delay. *Opt. Express* **20**(10), 11445 (2012)

68. F. Dake, Y. Taki, Time-domain fluorescence lifetime imaging by nonlinear fluorescence microscopy constructed of a pump-probe setup with two-wavelength laser pulses. *Appl. Opt.* **57**(4), 757 (2018)
69. F. Dake, H. Yazawa, Experimental assessment of fluorescence microscopy signal enhancement by stimulated emission. *Opt. Rev.* **24**(5), 642–646 (2017)
70. T.E. Matthews, I.R. Piletic, M.A. Selim, M.J. Simpson, W.S. Warren, Pump-probe imaging differentiates melanoma from melanocytic nevi. *Sci. Transl. Med.* **3**(71) (2011)
71. J.W. Wilson, S. Degan, M.A. Selim, J.Y. Zhang, W.S. Warren, In vivo pump-probe microscopy of melanoma and pigmented lesions, vol. 8226 (2012), p. 822602
72. T. Chen, Y. Huang, Label-free transient absorption microscopy for red blood cell flow velocity measurement in vivo. *Anal. Chem.* **89**(19), 10120–10123 (2017)
73. A.J. Chen, X. Yuan, J. Li, P. Dong, I. Hamza, J.-X. Cheng, Label-free imaging of heme dynamics in living organisms by transient absorption microscopy. *Anal. Chem.* *acs.analchem.7b05046* (2018)
74. T.E. Villafana, J.K. Delaney, W.S. Warren, M.C. Fischer, High-resolution, three-dimensional imaging of pigments and support in paper and textiles. *J. Cult. Herit.* **20**, 583–588 (2016)
75. P. Samineni, A. de Cruz, T.E. Villafaña, W.S. Warren, M.C. Fischer, Pump-probe imaging of historical pigments used in paintings. *Opt. Lett.* **37**(8), 1310–1312 (2012)
76. E. Abbe, Beiträge zur Theorie des Mikroskops und der mikroskopischen Wahrnehmung. *Arch. für Mikroskopische Anat.* **9**(1), 413–418 (1873)
77. D.B. Murphy M.W. Davidson, *Fundamentals of Light Microscopy and Electronic Imaging*, 2nd edn. (2012)
78. C.J.R. Sheppard, A. Choudhury, Image formation in the scanning microscope. *Opt. Acta Int. J. Opt.* **24**(10), 1051–1073 (1977)
79. S. Hell, E.H.K. Stelzer, Properties of a 4Pi confocal fluorescence microscope. *J. Opt. Soc. Am. A* (1992)
80. S. Hell, E.H.K. Stelzer, Fundamental improvement of resolution with a 4Pi-confocal fluorescence microscope using two-photon excitation. *Opt. Commun.* (1992)
81. Gustafsson, Agard, Sedat, I5 M: 3D widefield light microscopy with better than 100 nm axial resolution. *J. Microsc.* **195**(1), 10–16 (1999)
82. M.G.L. Gustafsson, D.A. Agard, J.W. Sedat, Sevenfold improvement of axial resolution in 3D wide-field microscopy using two objective lenses, in *Three-Dimensional Microscopy: Image Acquisition and Processing II*, vol. 2412, ed. by T. Wilson, C.J. Cogswell (International Society for Optics and Photonics, 1995), pp. 147–156
83. M.G.L. Gustafsson, Surpassing the lateral resolution limit by a factor of two using structured illumination microscopy. *J. Microsc.* **198**(Pt 2), 82–7 (2000)
84. E. Betzig, J.K. Trautman, T.D. Harris, J.S. Weiner, R.L. Kostelak, Breaking the diffraction barrier: optical microscopy on a nanometric scale. *Science* (80–). **251**(5000), 1468–1470 (1991)
85. W.E. Moerner, L. Kador, Optical detection and spectroscopy of single molecules in a solid. *Phys. Rev. Lett.* (1989)
86. E. Betzig, G.H. Patterson, R. Sougrat, O.W. Lindwasser, S. Olenych, J.S. Bonifacino, M.W. Davidson, J. Lippincott-Schwartz, H.F. Hess, Imaging intracellular fluorescent proteins at nanometer resolution. *Science* (2006)
87. S.W. Hell, Fluorescence nanoscopy: breaking the diffraction barrier by the RESOLFT concept, in *Nanobiotechnology* (2005)
88. S.W. Hell, J. Wichmann, Breaking the diffraction resolution limit by stimulated emission: stimulated emission depletion microscopy. *Opt. Lett.* (1994)
89. P. Bianchini, C. Peres, M. Oneto, S. Galiani, G. Vicidomini, A. Diaspro, STED nanoscopy: a glimpse into the future. *Cell Tissue Res.* **360**(1), 143–150 (2015)
90. G. Vicidomini, P. Bianchini, A. Diaspro, STED super-resolved microscopy. *Nat. Methods* **15**(3), 173–182 (2018)
91. F. Göttfert, C.A. Wurm, V. Mueller, S. Berning, V.C. Cordes, A. Honigmann, S.W. Hell, Coaligned dual-channel STED nanoscopy and molecular diffusion analysis at 20 nm resolution. *Biophys. J.* (2013)

92. B. Harke, J. Keller, C.K. Ullal, V. Westphal, A. Schönle, S.W. Hell, Resolution scaling in STED microscopy. *Opt. Express* **16**(6), 4154 (2008)
93. S.W. Hell, Microscopy and its focal switch. *Nat. Methods* **6**(1), 24–32 (2009)
94. S.W. Hell, Toward fluorescence nanoscopy. *Nat. Biotechnol.* **21**(11), 1347–55 (2003)
95. W. Liu, H. Niu, Diffraction barrier breakthrough in coherent anti-stokes Raman scattering microscopy by additional probe-beam-induced phonon depletion. *Phys. Rev. A At. Mol. Opt. Phys.* **83**(2), 1–5 (2011)
96. C. Cleff, P. Groß, C. Fallnich, H.L. Offerhaus, J.L. Herek, K. Kruse, W.P. Beeker, C.J. Lee, K.J. Boller, Stimulated-emission pumping enabling sub-diffraction-limited spatial resolution in coherent anti-Stokes Raman scattering microscopy. *Phys. Rev. A At. Mol. Opt. Phys.* **87**(3), 1–9 (2013)
97. C. Cleff, P. Groß, C. Fallnich, H.L. Offerhaus, J.L. Herek, K. Kruse, W.P. Beeker, C.J. Lee, K.-J. Boller, Ground-state depletion for subdiffraction-limited spatial resolution in coherent anti-Stokes Raman scattering microscopy. *Phys. Rev. A* **86**(2), 023825 (2012)
98. W.R. Silva, C.T. Graefe, R.R. Frontiera, Toward label-free super-resolution microscopy. *ACS Photonics* **3**(1), 79–86 (2016)
99. D. Kim, D.S. Choi, J. Kwon, S.-H. Shim, H. Rhee, M. Cho, Selective suppression of stimulated Raman scattering with another competing stimulated Raman scattering. *J. Phys. Chem. Lett.*, 6118–6123 (2017)
100. P. Wang, M.N. Slipchenko, J. Mitchell, C. Yang, E.O. Potma, X. Xu, J.-X.X. Cheng, Far-field imaging of non-fluorescent species with subdiffraction resolution. *Nat. Photonics* **7**(6), 449–453 (2013)
101. C. Silien, N. Liu, N. Hendaoui, S.A.M. Tofail, A. Peremans, A framework for far-field infrared absorption microscopy beyond the diffraction limit. *Opt. Express* **20**(28), 29694–704 (2012)
102. I. Pita, N. Hendaoui, N. Liu, M. Kumbham, S.A.M. Tofail, A. Peremans, C. Silien, High resolution imaging with differential infrared absorption micro-spectroscopy. *Opt. Express* **21**(22), 25632 (2013)
103. S. Galiani, B. Harke, G. Vicidomini, G. Lignani, F. Benfenati, A. Diaspro, P. Bianchini, Strategies to maximize the performance of a STED microscope. *Opt. Express* **20**(7), 7362 (2012)
104. E.S. Massaro, A.H. Hill, E.M. Grumstrup, Super-resolution structured pump-probe microscopy. *ACS Photonics* **3**(4), 501–506 (2016)
105. H. Dehez, M. Piché, Y. De Koninck, Resolution and contrast enhancement in laser scanning microscopy using dark beam imaging. *Opt. Express* **21**(13), 15912 (2013)
106. S. You, C. Kuang, Z. Rong, X. Liu, Eliminating deformations in fluorescence emission difference microscopy. *Opt. Express* **22**(21), 26375 (2014)
107. K. Korobchevskaya, C. Peres, Z. Li, A. Antipov, C.J.R. Sheppard, A. Diaspro, P. Bianchini, Intensity weighted subtraction microscopy approach for image contrast and resolution enhancement. *Sci. Rep.* **6**(April), 25816 (2016)
108. N. Liu, M. Kumbham, I. Pita, Y. Guo, P. Bianchini, A. Diaspro, S.A.M. Tofail, A. Peremans, C. Silien, Far-field subdiffraction imaging of semiconductors using nonlinear transient absorption differential microscopy. *ACS Photonics* **3**(3), 478–485 (2016)

# Chapter 8

## Super-Resolution Imaging in Raman Microscopy



Katsumasa Fujita

**Abstract** Raman microscopy provides microscopic images of the sample with chemical information as the contrast. Since Raman microscopy uses light–material interactions associated with vibrational excitation of molecules, the spatial resolution of the microscope is limited to the half of the wavelength used to induce the Raman effect. In this chapter, we introduce various attempts for breaking the limit of the spatial resolution in Raman microscopy. Many of those techniques take similar approaches as super-resolution fluorescence microscopy, where the control of excitation and emission of fluorescence is the key to break the limit. Since there are many different types of Raman microscopy, such as spontaneous Raman scattering, coherent anti-Stokes Raman scattering, stimulated Raman scattering, and so on, various approaches are proposed for spatio-temporal manipulation of the Raman effect in micro- and nanometer scale. In this chapter, we categorize the approaches to realize super-resolution Raman imaging based on their strategies for breaking the limit and introduce the principles and the theoretical and experimental demonstrations of the techniques.

### 8.1 Introduction

Microscopic observation has been one of the key processes in many scientific experiments. Among the different types of technique for observing micro- and nanometer scale objects, optical microscopy has been utilized as a versatile technique that can be used to observe many different kinds of samples under various conditions. However, the spatial resolution of optical microscopy has been limited to about half the wavelength of light, which is often referred as the diffraction limit. The wave nature of light prevents itself from being focused onto a size smaller than the half of the wavelength. This fact has been used to explain the limitation of resolving power in many different types of optical microscopes.

---

K. Fujita (✉)

Department of Applied Physics, Osaka University, 2-1 Yamadaoka, Suita, Osaka 565-0871, Japan  
e-mail: [fujita@ap.eng.osaka-u.ac.jp](mailto:fujita@ap.eng.osaka-u.ac.jp)

© Springer Nature Switzerland AG 2019  
V. Astratov (ed.), *Label-Free Super-Resolution Microscopy*,  
Biological and Medical Physics, Biomedical Engineering,  
[https://doi.org/10.1007/978-3-030-21722-8\\_8](https://doi.org/10.1007/978-3-030-21722-8_8)

Recent developments in optical microscopy have paved various ways toward breaking the limit of the spatial resolution and visualizing structures or distributions of materials smaller than the half of the wavelength. The techniques, such as super-resolution microscopy, use light–material interactions to overcome the diffraction limit. Since the diffraction limit originated from the property of light propagation in the optical system, the deviation from the conventional framework of optical imaging can be achieved by taking the light–material interaction into account for image formation.

In particular, super-resolution microscopy has been developed intensively for fluorescence imaging [1]. The control of fluorescence emission property allows several different approaches to break the diffraction barrier. For example, stimulated emission depletion (STED) microscopy uses stimulated emission of fluorescence to reduce the volume of fluorescence emission after excitation, which obtains super-resolution images by scanning the detection volume over the sample [2]. Another super-resolution technique, known as single-molecule localization microscopy, manipulates the fluorescence emission or light absorption property to avoid simultaneous observation of two or more fluorescent molecules located within the diffraction limit [3–5]. Other super-resolution imaging techniques also use the relationship between fluorescence excitation and emission to realize the spatial resolution beyond the resolution limit determined by the wavelength [6, 7].

The approaches mentioned above can also be adopted to realize super-resolution imaging in Raman microscopy. Control of Raman scattering properties of the sample is not as easy as that with fluorescence molecules. However, understanding of the optical processes in Raman scattering allows us to manipulate the imaging property of optical systems. Actually, there are various approaches to induce Raman effect, such as coherent anti-Stokes Raman scattering, stimulated Raman scattering, and surface-enhanced Raman scattering, offering different strategies to break the diffraction limit. It has been well known that the use of the enhancement of Raman scattering at the apex of metallic probe for super-resolution imaging can realize the spatial resolution at nanometer scale [8–10]. The technique is known as tip-enhanced Raman scattering (TERS) microscopy and has found its applications in the material industry. Although TERS is a powerful technique for super-resolution Raman imaging, this chapter focuses on the super-resolution technique that detects signal light at far-fields where the property of imaging optics and the spatial and temporal control of Raman scattering take important roles in image formation. In this chapter, we categorize super-resolution techniques based on the strategies for breaking the diffraction limit and describe the implementation of each technique that achieves super-resolution imaging in Raman microscopy.

## 8.2 Point Spread Function (PSF) Engineering

Among the many different types of Raman microscopy, laser scanning is a typical approach to produce a Raman scattering image of a sample. In laser scanning tech-

niques, light from a laser source is focused onto a sample by using an objective lens. The Raman effect induced by the laser light is detected in different ways depending on the process of signal generation, such as spontaneous Raman scattering, coherent anti-Stokes Raman scattering (CARS), and stimulated Raman scattering (SRS). The spatial resolution is theoretically determined by two factors. One of the factors is the area of Raman effect induced in the sample, and the other is the imaging property of detection optics. In addition, the imaging property depends on whether the Raman effect is induced in incoherent or coherent processes and how the Raman effect is detected. In this section, we mainly discuss the size of the area where the Raman effect is induced in the sample, since, in the techniques proposed so far, the imaging property of the detection optical has a smaller contribution in the spatial resolution than that of the excitation laser spot for Raman excitation.

In the following parts of this section, we describe several techniques that improve the spatial resolution in Raman microscopy by reducing the area of Raman effect. The techniques can be further categorized into nonlinear or linear techniques.

### 8.2.1 Nonlinear Techniques

In CARS and SRS microscopy, the Raman effect is induced by products of laser intensities of pump and Stokes beams [11–14]. The signal is proportional to  $I_p I_p I_s$  and  $I_p I_s$  for CARS and SRS microscopy, where  $I_p$  and  $I_s$  are the intensities of pump and Stokes beams, respectively. Owing to the nonlinear relation between the light intensity and the Raman effect, the Raman effect can be induced in a volume smaller than the laser focus, as shown in Fig. 8.1. The actual imaging property is rather complicated since CARS and SRS microscopy detect coherent light of which propagation is significantly affected by the distribution of refractive index in the sample. As well discussed, CARS signal propagates in the directions that satisfy the phase-matching condition, which affects the imaging property in practical conditions [15]. SRS microscopy does not have such a requirement; however, the image formation

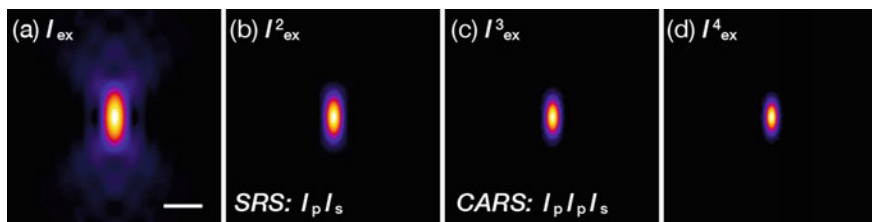


**Fig. 8.1** **a** Intensity distribution around a laser focus calculated for 800 nm light focused by an objective lens with an NA of 0.95. The scale bar shows 1  $\mu\text{m}$ . Distribution of signal generated to **b** square, **c** cube, and **d** fourth power of laser intensity shown in **(a)**. The distribution of **(b)** and **(c)** are equivalent to the distribution of signal generation for SRS and CARS microscopy assuming that the pump and Stokes beams have the same wavelength for simplicity

is affected by the refractive index distribution of the sample. Owing to this coherent imaging property in CARS and SRS microscopy, it is difficult to determine a point spread function (PSF) that can be convoluted with a sample distribution to calculate the resultant images, as typically done for the incoherent image formation in fluorescence imaging. However, as an image of a point object, the CARS/SRS excitation distribution shown in Fig. 8.1 is typically used as the PSF of CARS/SRS microscopy.

Although the spatial resolution of CARS/SRS microscopy suppresses the classical diffraction limit, the practical spatial resolution is still low since these techniques use near-infrared (NIR) light. The spatial resolution realized by the nonlinear interaction is equivalent to or even lower than that in conventional microscopy using visible light.

In laser scanning CARS microscopy, Raghunathan described a method to reduce the Raman excitation volume by using the multiplicative interaction of phase shaped pump and Stokes beams [16]. In typical CARS microscopy, both pump and Stokes beams have a Gaussian profile. In the proposed technique, the profile of Stokes beam is modified to have a more complicated phase distribution in order to control the spatial distribution of CARS effect. The technique was demonstrated by Kim et al. with the observation of polystyrene beads, where a spatial resolution of 130 nm was confirmed (Fig. 8.2) [17]. In their technique, Toraldo-style pupil filter was introduced to modulate the intensity distribution of the Stokes laser spot so that the center

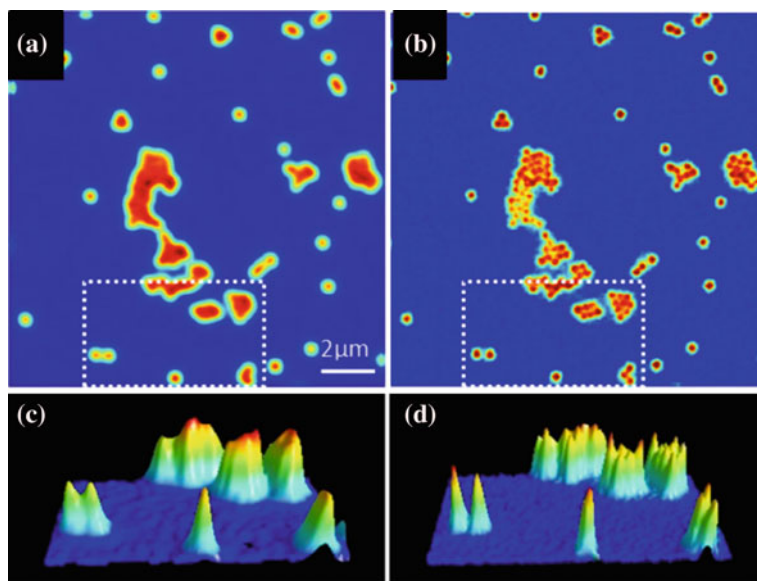


**Fig. 8.2** CARS images **a** without and **b** with the multiplicative focus field engineering. The images were reconstructed by using the Raman signal at  $1000\text{ cm}^{-1}$  of polystyrene beads with a diameter of 300 nm. 728 nm pump and 1785 nm Stokes beams are used for generation of CARS signal. The 3D-rendered images within the dotted rectangles in **(a)** and **(b)** are shown in **(c)** and **(d)**, respectively. Reproduced from [17] with permission from The Optical Society

peak of the laser spot becomes sharper in return for a significant increase of side lobes. However, in their CARS microscopy, the side lobes are not visible in resultant CARS images, thanks to the multiplicative interaction of pump and Stokes beams to generate CARS signal. Although the technique can provide a sharper main peak in the image of a point object, the bandwidth for transferring spatial frequency is still the same as CARS microscopy uses the Gaussian beams. The technique enhances the efficiency of transferring components with relatively high spatial frequencies and does not provide the expansion of the theoretical bandwidth. However, the technique is effective since laser scanning microscopy using a Gaussian spot typically has the low-pass characteristic, where the practical resolution is strongly affected by the noise in the detected signal. The enhancement of the transfer efficiency of high spatial frequency components effectively brings up the fine sample structures above the noise level and makes them visible in the resultant image.

In order to achieve the resolving power beyond the bandwidth that is determined by the Raman excitation volume, the strategies used for super-resolution fluorescence microscopy are also available. In laser scanning fluorescence microscopy, the area of fluorescence detection in a sample is reduced by using a highly nonlinear interaction between laser intensity and fluorescence emission.

Introducing saturation in optical effect is one of the ways to introduce high-order nonlinear relations between light intensity and the Raman effect. As shown in Fig. 8.1, higher-order nonlinear responses can be localized within a volume smaller than that of a laser spot and improve the spatial resolution in laser scanning microscopy. This approach is originally demonstrated for fluorescence imaging [18, 19] and also for plasmonic scattering [20]. Since coherent Raman effects can also be saturated due to the saturation of the population at vibrational excitation, the use of optical effect can also be utilized to improve the spatial resolution of CARS microscopy further. Yonemaru et al. used the harmonic demodulation technique to extract the higher-order nonlinear CARS signal (Fig. 8.3) and demonstrated super-resolution imaging of diamond nanoparticles [21]. This technique improves the spectral resolution in CARS spectroscopy. This is because the saturation is seen prominently when the difference between the frequencies of pump and Stokes beams matches with the vibrational frequency of molecules to be excited. For the same reason, it is also possible to reduce the effect of non-resonant background that gives image contrasts unrelated to vibrational excitation in CARS imaging. This technique was also demonstrated for improving the spatial resolution in SRS microscopy [22].

Another strategy is to use a laser beam for controlling the Raman effect, which is similar to the technique used in STED microscopy [2]. In STED microscopy for fluorescence imaging, a fluorescent sample is excited by a Gaussian laser spot. In addition, in order to reduce the detection volume, another laser beam, called a STED beam, is irradiated to the sample collinearly to the excitation beam. The STED beam is in the shape of a donut and induces stimulated emission from the sample, which depletes the fluorescence signal by spontaneous emission. Since the efficiency of stimulated emission is saturated with a strong STED beam, the area of stimulated emission becomes larger, while the spontaneous emission remains at the center of excitation spot due to zero intensity of the STED beam. Therefore, the

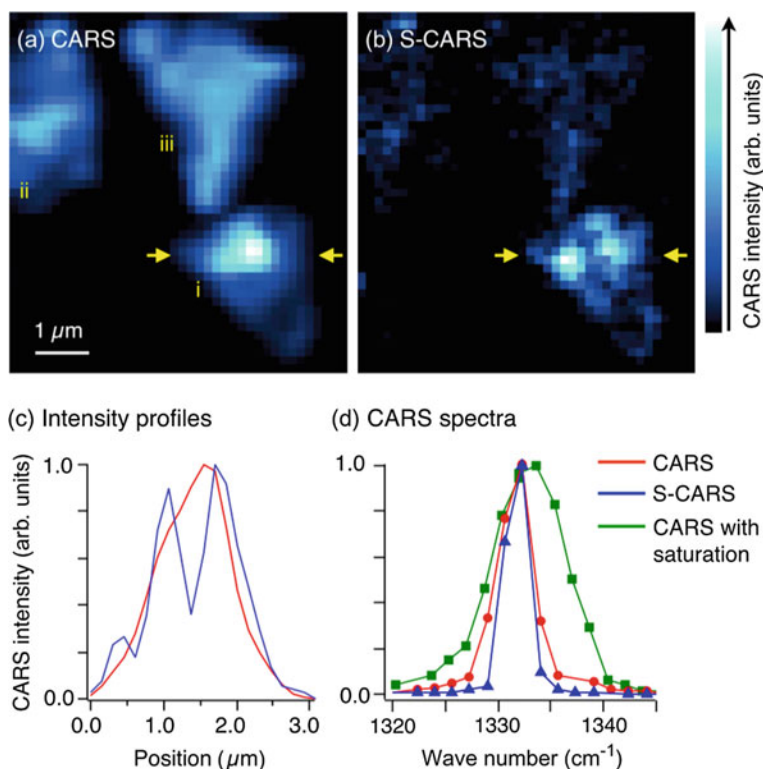


**Fig. 8.3** CARS images of diamond particles observed by using **a** non-saturated and **b** saturated CARS signals. The images were reconstructed by using  $1333\text{ cm}^{-1}$  peak of a diamond crystal. The intensity profiles between the two arrowheads are shown in (c). The CARS spectra of a diamond nanoparticle produced by (red) non-saturated CARS, saturated CARS (blue) with and (green) without extracting nonlinear components are shown in (d). Reprinted with permission from Yonemaru et al., *Phys. Rev. Applied* **4**(1), 014010 (2015). Copyright 2015 by the American Physical Society

signal detection volume becomes significantly smaller than that of the excitation to improve the spatial resolution beyond the diffraction limit (Fig. 8.4).

In order to realize the strategy used in STED microscopy into CARS imaging, Beeker et al. proposed the use of mid-infrared light as the suppression beam, which depletes CARS signal through pre-population at the vibrational state of interest, and theoretically demonstrated the resolution improvement in CARS microscopy [23]. As another approach for STED-like CARS microscopy, Choi et al. demonstrated the introduction of another Stokes beam with a shape of a donut [24]. The highly intense donut-shaped Stokes beam depletes pump photon to be used for CARS with the Gaussian shape Stokes beam, resulting in the resection of the effective CARS volume at the center of the laser spot. In addition to theoretical prediction, the experimental demonstration of suppressing CARS signal by using the second Stokes beam have been reported by using benzene as a sample.

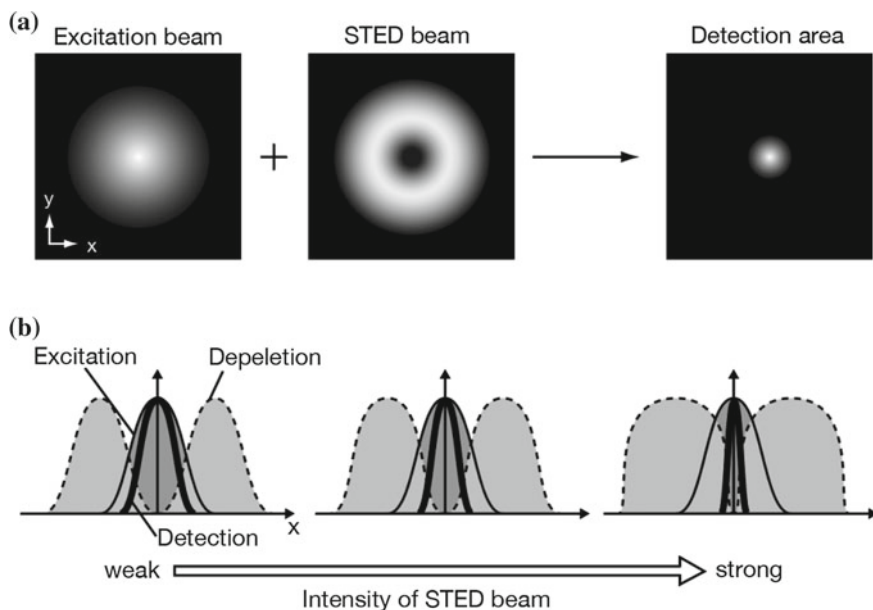


**Fig. 8.4** **a** Reduction of the detection area in STED microscopy. **b** Resolution improvement by saturation of depletion efficiency

The strategy of STED microscopy has also been applied to SRS microscopy. Gong et al. report a theoretical study of using saturation in stimulated Raman scattering for breaking the diffraction limit in SRS microscopy [25]. In addition to pump and Stokes beams with Gaussian shape, another Stokes beam with a donut shape is irradiated onto a sample in order to saturate the SRS process. The donut-shaped Stokes beam takes a role of STED beam, and the signal generated by the Gaussian beams is limited in a volume smaller than the diffraction limit. Another proposal for super-resolution SRS microscopy is using a decoherence beam [26]. Additional irradiation of intense laser beam can destroy vibrational coherence induced by pump and Stokes beams for SRS. This can be used to deplete SRS signal for super-resolution imaging with a similar mechanism as STED microscopy. Silva proposed the use of the decoherence beam in femtosecond SRS microscopy and demonstrated the resolution improvement by one-dimensional (1D) SRS imaging of an edge of a diamond plate [27]. With the decoherence laser, the edge of the diamond plate is sharply imaged (Fig. 8.5).

Suppression of spontaneous resonant Raman scattering is also possible by laser irradiation. Rieger et al. proposed the use of UV light to electrically excite a sample before inducing Raman scattering [27]. Since the irradiation of UV light excitation can reduce the population of molecules at the ground state, resonant Raman scattering from the ground state can be suppressed. Therefore, using a donut-shaped UV spot irradiated around the laser focus for Raman excitation can improve the spatial resolution in confocal imaging by using resonant Raman scattering.

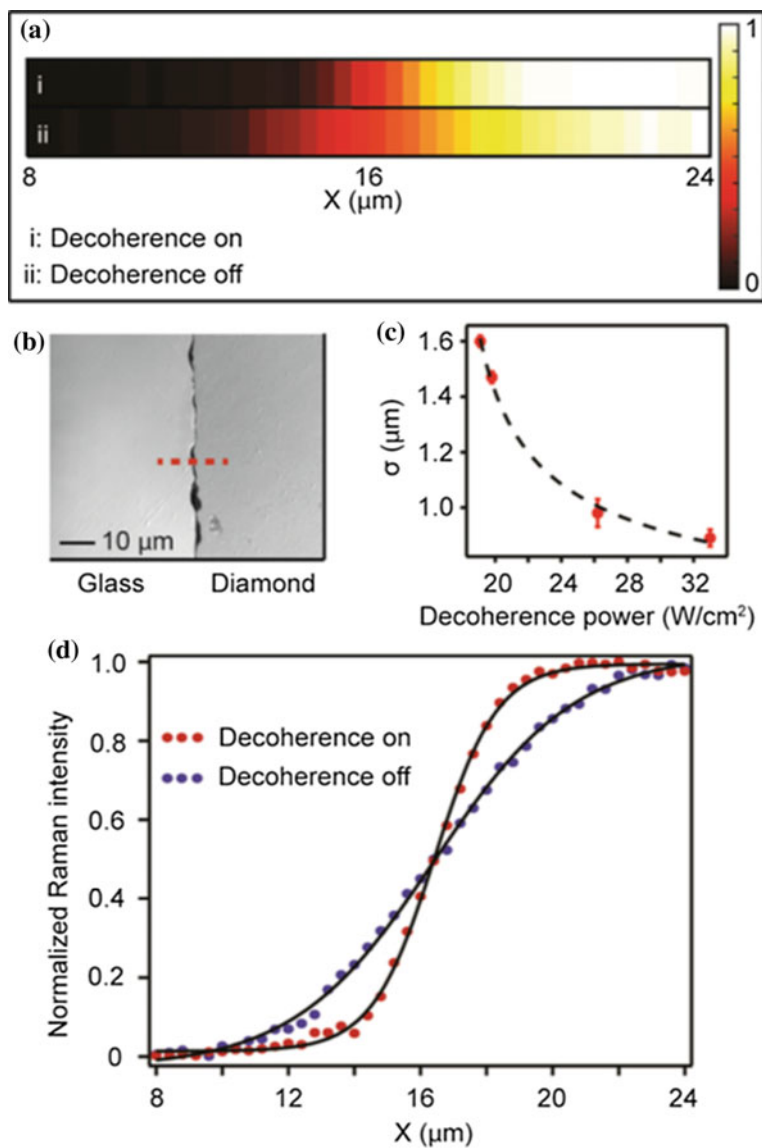


**Fig. 8.5** **a** SRS signal distribution across an edge of the diamond plate with and without decoherence beam. **b** Bright field image of the diamond plate. **c** Variation in the spatial resolution with different decoherence powers. **d** Line images of the diamond edge with and without decoherence beam. 800 nm pulsed laser light was used for pump and decoherence beams and focused by an objective lens with an NA of 0.4. Reprinted with permission from ACS Photonics 3(1), 79–86 (2016). Copyright 2016 American Chemical Society

Rieger et al. experimentally demonstrated the signal depletion by UV irradiation at tris(bipyridine)ruthenium(ii). They also theoretically explained the Raman suppression effect by using rate equations and density matrix calculations [27, 28].

As introduced above, using the STED technique and higher-order nonlinearities in material–light interaction can improve the spatial resolution beyond the diffraction limit. However, these techniques often require a high intensity of laser light in order to induce the higher-order nonlinearity and deleting Raman signal. In practice, this is a significant limitation of the technique for being applied to organic and biological samples. However, the techniques can be useful for imaging sample with a relatively higher damaging threshold such as inorganic materials, which still can claim a benefit of super-resolution imaging since Raman microscopy can provide material information and analysis in addition to their spatial resolutions without labeling.

### 8.2.2 *Linear Techniques*

There are also a few demonstrations for improvement of the spatial resolution of Raman microscopy without inducing nonlinear effects in Raman scattering. One simple approach is using a solid immersion lens in order to increase the numerical aperture for sample illumination and signal detection [29]. It is also possible to use the 4pi configuration to increase the axial resolution, which has also been developed for fluorescence microscopy [30]. Tormo et al. demonstrated the use of two objective lenses to irradiate a sample by two coherent laser spots. The interference fringe along the optical axis gives narrower excitation PSF in the axial direction. Separation of thin layers of PMMA, TiO<sub>2</sub>, and ARP of thicknesses 43, 23, and 65 nm, respectively, has been demonstrated [31].

Image scanning microscopy (ISM) is also a technique to improve the spatial resolution in linear imaging. The technique was first described by Sheppard in 1988 as super-resolution technique for confocal microscopy using a pinhole placed at off-axis positions [32]. Later, Müller et al. introduced this technique as ISM in laser scanning fluorescence microscopy by using a 2D detector [33]. This approach can be used for spontaneous Raman microscopy since it shares the same imaging property with fluorescence microscopy. Roeder et al. successfully implemented the ISM approach using a fiber bundle as a 2D detector coupled with a spectrometer [34]. The spatially segmented detection of Raman spectra improves the spatial resolution in confocal Raman imaging without sacrificing the signal amount as shown in Fig. 8.6. ISM has different implementations, such as pixel reassignment [35], instant SIM [36], and rescan [37, 38], which can also be combined with different types of Raman microscopy.

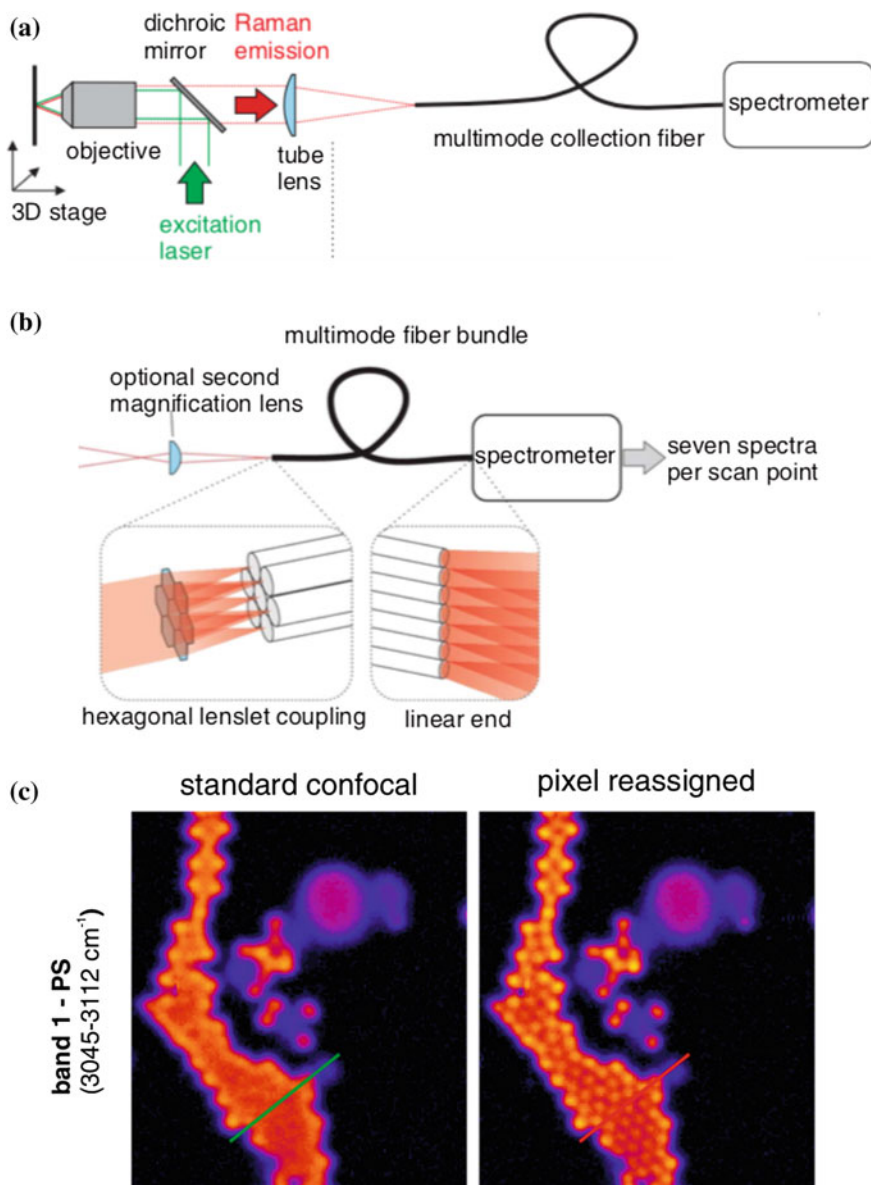


**Fig. 8.6** **a** Optical system of a confocal Raman microscope using fiber coupling to deliver Raman signal to a spectrophotometer. **b** Implementation of ISM in a fiber-coupled confocal Raman microscope by using a bundled fiber. **c** Raman images of polystyrene beads reconstructed by Raman signal at  $3045\text{--}3011\text{ cm}^{-1}$  with and without pixel reassignment. Reproduced from [34] with permission from The Optical Society

### 8.3 Structure Illumination Microscopy

Structure illumination microscopy (SIM) uses patterned illumination in order to shift the spatial frequency of the sample structure to lower frequency [7]. As a result, the information of structures with sub-diffraction-limited size can be transferred to the imaging optics, and post-processing of the obtained images provides images with a spatial resolution twice higher than that of conventional wide-field microscopy. For fluorescence microscopy, SIM can be realized by modifying the illumination optics using a conventional wide-field microscopy. Therefore, similar strategies have been proposed for improving the spatial resolution in various types of Raman microscopy.

Typical SIM requires the use of a 2D detector to record images under structured illumination. Therefore, optical imaging systems that image monochrome signal light can be easily combined with SIM. Since in typical CARS microscopy, the signal is given with a wavelength determined by the wavelengths of pump and Stokes beams, the structured illumination technique can be implemented in a wide-field CARS microscopy [39]. Hajek et al. proposed the introduction of structured illumination into a wide-field CARS microscope [40] and theoretically described that the structured illumination can improve the spatial resolution about three times compared to that with wide-field CARS microscopy using uniform illumination. CARS-SIM using 2D has also been proposed [41]. Although CARS microscopy is a coherent imaging technique, the signal is given as a product of pump and Stokes beams. This nonlinear process in signal generation can shift the spatial frequency of sample structured to lower frequency, allowing the wide-field imaging optics to resolve the sub-diffraction limit structures, which is different from SIM using linear coherent signals [42]. The cut-off frequency of CARS-SIM can be equivalent to a typical spot-scanning CARS microscopy. The wide-field configuration can have a higher contrast in imaging fine structures due to the illumination pattern that only contains the high spatial frequency. However, the wide-field CARS configuration requires high intensity to produce CARS process in the entire region of view area, and therefore the practical implementation of CARS-SIM is limited by available laser sources.

SIM can be combined easily with wide-field Raman microscopy using a narrow-band filter for spectral separation. The structured illumination is produced by an interference of two parallel beams similar to typical fluorescence SIM. The narrow-band filter transmits Raman scattering light of interest to produce a Raman image on a 2D detector. Chen et al. demonstrated the resolution improvement by using surface-enhanced Raman scattering to observe the distribution of SERS nanoparticles on glass substrate and in a living cell with a lateral resolution of 109 nm.

The structured illumination technique can be combined with line illumination Raman microscopy to obtain the benefits of both high spatial resolution and analytical capability [43]. In line illumination Raman microscopy, a sample is irradiated by a lined-shaped focus with which Raman scattering under the illumination line is detected simultaneously by using a 2D sensor [44, 45]. The scanning of line illuminated in the perpendicular direction produces hyper spectral Raman images of the sample. The line illumination microscope has the same imaging property as wide-

field imaging along the direction parallel to the illumination line. The SIM strategy can be applied to improve the resolution along the illumination line. The interference of two line-shaped foci produces structured line illumination for the resolution improvement. Watanabe et al. demonstrated the improvement in the spatial resolution observed in polymer, carbon, and biological samples (Fig. 8.7). The structured line illumination technique is beneficial in both spatial resolution improvement and spectral detection. However, the spatial frequency of the structured illumination cannot be as high as wide-field SIM due to the trade-off between the width of illumination line and the period of the structure.

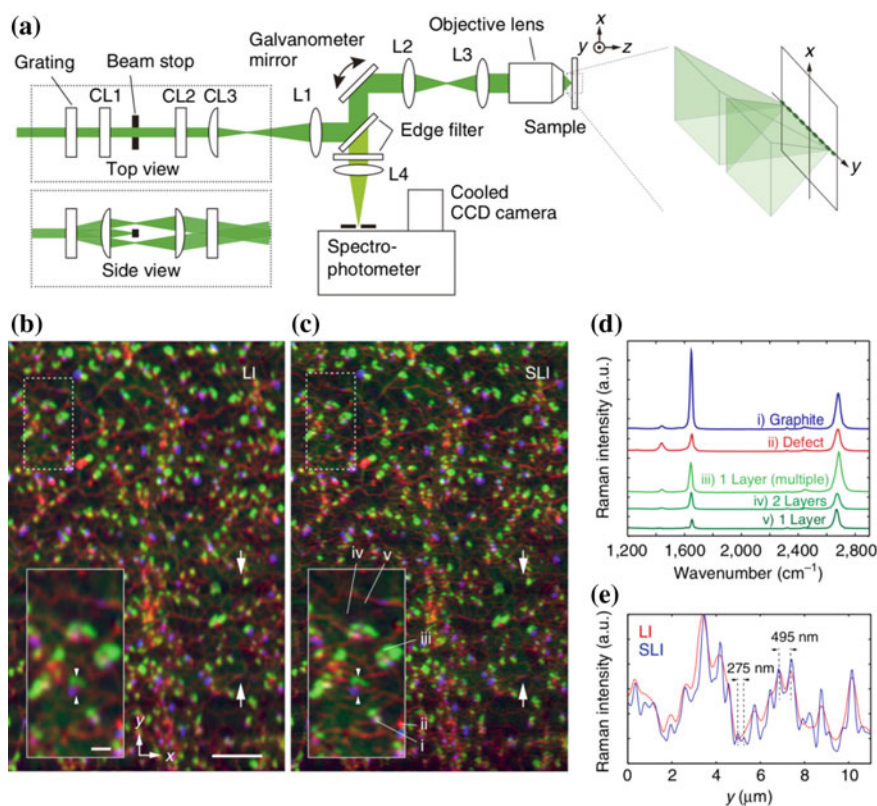


**Fig. 8.7** a Optical system of structured line illumination Raman microscopy. Raman images of a CVD graphene sheet observed by b line- and c structured-line illumination. The inset images are enlarged views of the dotted rectangles. d Spatial separation of Raman spectra showing different carbon compositions. e Intensity profiles of D band between the arrowheads shown in (b) and (c). Reprinted from [43] (Licensed under CC BY 4.0)

## 8.4 Localization Microscopy

In conventional wide-field fluorescence microscopy, fluorescence molecules or probes in a sample are irradiated simultaneously and imaged through an objective lens onto a 2D detector, such as a CCD camera. In such conditions, the images of each molecule are blurred due to the wave nature of light and the images of adjacent molecules are overlapped and cannot be separated in the resultant fluorescence image of the sample, as shown in Fig. 8.8a.

On the other hand, localization microscopy observes single fluorescent molecules separately, and accurately determines the position of the molecules individually [3–5]. As a result, the distribution of fluorescent molecules is obtained with a high-precision accuracy, which is beyond the resolution limit of the imaging system. As shown in Fig. 8.8b, if it can be assumed that a single molecule is imaged in isolation from others, the position of the molecule can be determined as the center of the image and the accuracy of the localization is given by  $\sigma/\sqrt{N}$ , where  $\sigma$  is a standard deviation of position detection, which is equivalent to the size of the PSF, and  $N$  is the number of detected fluorescence photons. In order to realize this image formation, the fluorescence emission from each molecule needs to be temporally separated, which can be done by using photoswitchable or spontaneously blinking fluorescent molecules.

Since the temporal separation of individual signal source is key to realize super-resolution imaging in localization microscopy, introducing the switching or temporal blinking capability in Raman signal allows us to apply the same strategy for super-resolution Raman imaging. In SERS spectroscopy, it is well known that the enhancement factor is very sensitive to the chemical or physical conditions around the sample, which brings large fluctuations or blinking in SERS signal. This fluctuations/blinking of SERS signal can be used to localize the position of hot spot with the

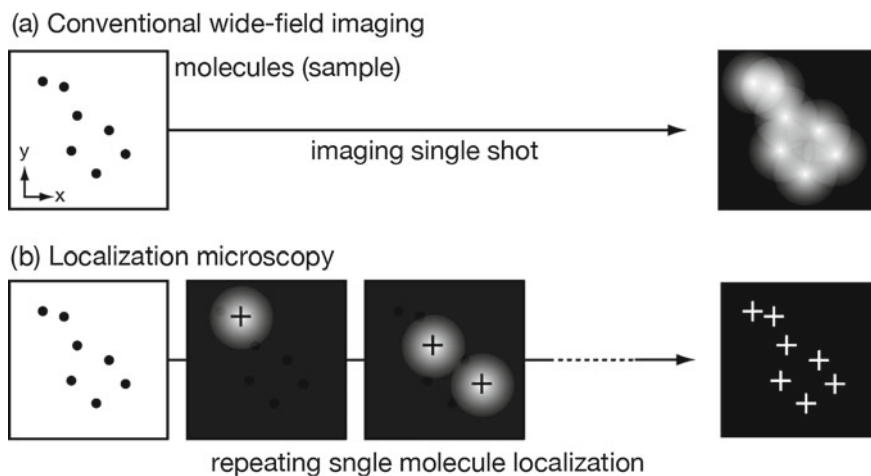


**Fig. 8.8** Image formation in **a** conventional wide-field and **b** localization microscopy

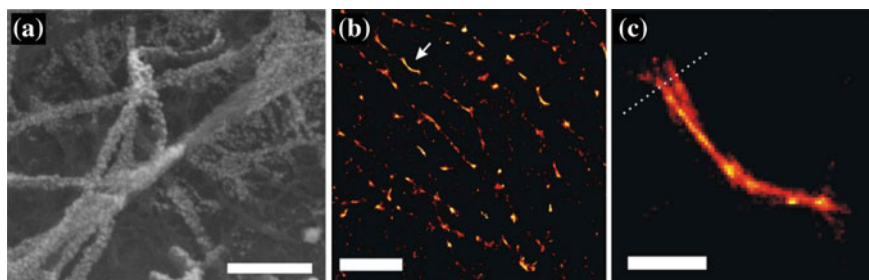


**Fig. 8.9** **a** SEM image of a part of a cardiomyocyte with evaporation of silver of thickness 3 nm. **b** Image reconstructed by stochastic emission of SERS from the hot spots produced by the evaporated silver. **c** Enlarged view of the fibrillar structure indicated by an arrow in **(b)**. Reprinted from [46] (Licensed under CC BY-NC-ND 3.0)

accuracy beyond the diffraction limit and provide us super-resolution images using Raman scattering as image contrast.

Ayas et al. placed a sample on SERS substrate that provides uniform distribution of hot spot by Ag nanoislands with a high density and obtained a series of image with fluctuating SERS signals [46]. The stochastic reconstruction of the images provided the SERS images of self-assembled peptide network. They also demonstrated that the evaporation of silver onto cardiomyocytes allows super resolution imaging of fibrillated lamellipodia with a spatial resolution of 20 nm (Fig. 8.9). However, there is a significant issue in SERS localization microscopy; molecules located at the hot spots can be imaged, and the resultant image does not provide the actual distribution of the molecules. To tackle this issue, the use of a spatial light modulator or an optical diffuser are proposed to manipulate the position of hot spots on a nanohole array by changing the phase of incident light [47, 48]. By using the localization image with different excitation phases, they successfully obtained the super resolution SERS images without the gaps given by non-continuous hot spots. Although the techniques are limited for observation of surface of a sample, it would be useful to applications that require label-free and analytical imaging of sample materials.

In the above implementation of localization microscopy into SERS imaging, SERS signal was separated by an optical filter. Since the SERS images were formed by the wide-field imaging, no spectral information was provided. However, compared to a typical wide-field Raman imaging mentioned earlier, it is easier to realize spectral detection in localization microscopy using SERS. Since SERS images from individual hot spots are spatially separated, it is possible to have a space on a 2D detector for spectral detection. Olson et al. inserted a transmission grating in the imaging system and obtained super-resolution images of bacteria with spectra in the fingerprint region (Fig. 8.10) [49]. By using the obtained SERS spectra, they have successfully classified different bacteria in the sample.

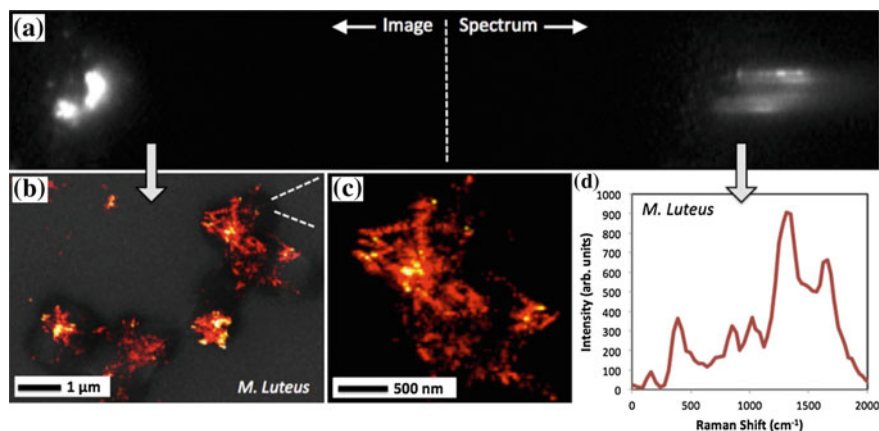


**Fig. 8.10** **a** An image frame recorded by a 2D detector showing the diffracted and non-diffracted SERS signal used for super resolution imaging and spectrum detection, respectively. **b** Super resolution SERS image reconstructed by localization of SERS spots obtained from *M. Luteus*. **c** Enlarged view of the part indicated by the dotted lines in **(b)**. **d** SERS spectrum simultaneously recorded with SERS images for super-resolution imaging. Reprinted from [49] (Licensed under CC BY 4.0)

The fluctuation and blinking effects are also useful in imaging a distribution of SERS hot spots [50]. Weber and Willets observed the SERS blinking of Rhodamine 6G adsorbed on aggregates of silver colloid located at the position of the hot spot by the localization technique [51].

## 8.5 Conclusions

In this chapter, we introduced the strategies for breaking the diffraction limit in Raman imaging. As described earlier, the strategies for super-resolution fluorescence imaging, which control the emission capability of fluorescence probes, are also applicable to Raman imaging. However, the spatial and temporal control of Raman scattering efficiency is more difficult compared to fluorescence probes. Many of the above techniques have not been examined in practical applications. The small cross-section of Raman scattering also makes it difficult to realize super-resolution Raman imaging under practical conditions since, as also seen in super resolution fluorescence imaging, the information on finer structures is usually carried by weak signals that have to be extracted from large background signals. Therefore, the shot noise in the Raman scattering signal fundamentally limits the spatial resolution of the practical conditions, and we need a breakthrough in the improvement of Raman scattering or detection efficiencies in order to bring the super-resolution Raman imaging into practical applications.

## References

1. B. Huang, M. Bates, X. Zhuang, Super-resolution fluorescence microscopy. *Annu. Rev. Biochem.* **78**(1), 993–1016 (2009)
2. S.W. Hell, J. Wichmann, Breaking the diffraction resolution limit by stimulated emission: stimulated-emission-depletion fluorescence microscopy. *Opt. Lett.* **19**(11), 780–782 (1994)
3. E. Betzig et al., Imaging intracellular fluorescent proteins at nanometer resolution. *Science* **313**(5793), 1642–1645 (2006)
4. S.T. Hess, T.P.K. Girirajan, M.D. Mason, Ultra-high resolution imaging by fluorescence photoactivation localization microscopy. *Biophys. J.* **91**(11), 4258–4272 (2006)
5. M.J. Rust, M. Bates, X. Zhuang, Sub-diffraction-limit imaging by stochastic optical reconstruction microscopy (STORM). *Nat. Methods* **3**(10), 793–796 (2006)
6. R. Heintzmann, C. Cremer, Laterally modulated excitation microscopy: improvement of resolution by using a diffraction grating, in *Optical Biopsies and Microscopic Techniques III* (SPIE—The International Society for Optical Engineering, 1999), pp. 185–196
7. M.G. Gustafsson, Surpassing the lateral resolution limit by a factor of two using structured illumination microscopy. *J. Microsc.* **198**(2), 82–87 (2000)
8. N. Hayazawa et al., Metallized tip amplification of near-field Raman scattering. *Opt. Commun.* **183**(1–4), 333–336 (2000)
9. S. Kawata et al., Nano-Raman scattering microscopy: resolution and enhancement. *Chem. Rev.* **117**(7), 4983–5001 (2017)
10. P. Verma, Tip-enhanced Raman spectroscopy: technique and recent advances. *Chem. Rev.* **117**(9), 6447–6466 (2017)
11. A. Zumbusch, G.R. Holtom, X.S. Xie, Three-dimensional vibrational imaging by coherent anti-Stokes Raman scattering. *Phys. Rev. Lett.* **82**(20), 4142–4145 (1999)
12. C.W. Freudiger et al., Label-free biomedical imaging with high sensitivity by stimulated Raman scattering microscopy. *Science* **322**(5909), 1857–1861 (2008)
13. Y. Ozeki et al., Analysis and experimental assessment of the sensitivity of stimulated Raman scattering microscopy. *Opt. Express* **17**(5), 3651–3658 (2009)
14. P. Nandakumar, A. Kovalev, A. Volkmer, Vibrational imaging based on stimulated Raman scattering microscopy. *New J. Phys.* **11**, 033026 (2009)
15. M. Hashimoto, T. Araki, Three-dimensional transfer functions of coherent anti-Stokes Raman scattering microscopy. *J. Opt. Soc. Am. A* **18**(4), 771–776 (2001)
16. V. Raghunathan, E.O. Potma, Multiplicative and subtractive focal volume engineering in coherent Raman microscopy. *J. Opt. Soc. Am. A* **27**(11), 2365–2374 (2010)
17. H. Kim, G.W. Bryant, S.J. Stranick, Superresolution four-wave mixing microscopy. *Opt. Express* **20**(6), 6042–6051 (2012)
18. K. Fujita et al., High-resolution confocal microscopy by saturated excitation of fluorescence. *Phys. Rev. Lett.* **99**(22), 228105 (2007)
19. S. Kawano et al., Determination of the expanded optical transfer function in saturated excitation imaging and high harmonic demodulation. *Appl. Phys. Express* **4**(4), 042401 (2011)
20. S.-W. Chu et al., Measurement of a saturated emission of optical radiation from gold nanoparticles: application to an ultrahigh resolution microscope. *Phys. Rev. Lett.* **112**(1), 017402 (2014)
21. Y. Yonemaru et al., Super-, spatial-, and spectral-resolution in vibrational imaging via saturated coherent anti-stokes Raman scattering. *Phys. Rev. Appl.* **4**(1), 014010 (2015)
22. L. Gong et al., Saturated stimulated-Raman-scattering microscopy for far-field superresolution vibrational imaging. *Phys. Rev. Appl.* **11**(3), 034041 (2019)
23. W.P. Beeker et al., A route to sub-diffraction-limited CARS microscopy. *Opt. Express* **17**(25), 22632–22638 (2009)
24. D.S. Choi et al., Selective suppression of CARS signal with three-beam competing stimulated Raman scattering processes. *Phys. Chem. Phys.* **20**(25), 17156–17170 (2018)
25. L. Gong, H. Wang, Breaking the diffraction limit by saturation in stimulated-Raman-scattering microscopy: a theoretical study. *Phys. Rev. A* **90**(1), 013818–10 (2014)

26. W.R. Silva, C.T. Graefe, R.R. Frontiera, Toward label-free super-resolution microscopy. *ACS Photonics* **3**(1), 79–86 (2016)
27. S. Rieger et al., Suppression of resonance Raman scattering via ground state depletion towards sub-diffraction-limited label-free microscopy. *Opt. Express* **24**(18), 20745–20754 (2016)
28. S. Rieger et al., Density matrix study of ground state depletion towards sub-diffraction-limited spontaneous Raman scattering spectroscopy. *J. Chem. Phys.* **148**(20), 204110–204116 (2018)
29. E. Ostertag et al., Extension of solid immersion lens technology to super-resolution Raman microscopy. *Nanospectroscopy* **1**(1), 1–11 (2014)
30. S. Hell, E.H.K. Stelzer, Properties of a 4Pi confocal fluorescence microscope. *J. Opt. Soc. Am. A* **9**(12), 2159–2166 (1992)
31. A.D. Tormo et al., Superresolution  $4\pi$  Raman microscopy. *Opt. Lett.* **42**(21), 4410–4414 (2017)
32. C. Sheppard, Super-resolution in confocal imaging. *Optik* **80**(2), 53–54 (1988)
33. C.B. Müller, J. Enderlein, Image scanning microscopy. *Phys. Rev. Lett.* **104**(19), 198101 (2010)
34. C. Roeder, M. Ritsch-Marte, A. Jesacher, High-resolution confocal Raman microscopy using pixel reassignment. *Opt. Lett.* **41**(16), 3825–3828 (2016)
35. C.J.R. Sheppard, S.B. Mehta, R. Heintzmann, Superresolution by image scanning microscopy using pixel reassignment. *Opt. Lett.* **38**(15), 2889 (2013)
36. A.G. York et al., Instant super-resolution imaging in live cells and embryos via analog image processing. *Nat. Methods* **10**(11), 1122–1126 (2013)
37. G.M.R. De Luca et al., Re-scan confocal microscopy: scanning twice for better resolution. *Biomed. Opt. Express* **4**(11), 2644–2656 (2013)
38. S. Roth et al., Optical photon reassignment microscopy (OPRA). *Opt. Nanoscopy* **2**, 5 (2013)
39. C. Heinrich, S. Bernet, M. Ritsch-Marte, Wide-field coherent anti-Stokes Raman scattering microscopy. *Appl. Phys. Lett.* **84**(5), 816–818 (2004)
40. K.M. Hajek et al., A method for achieving super-resolved widefield CARS microscopy. *Opt. Express* **18**(18), 19263–19272 (2010)
41. J.H. Park et al., A method for super-resolved CARS microscopy with structured illumination in two dimensions. *Opt. Express* **22**(8), 9854 (2014)
42. K. Wicker, R. Heintzmann, Resolving a misconception about structured illumination. *Nat. Photonics* **8**(5), 342–344 (2014)
43. K. Watanabe et al., Structured line illumination Raman microscopy. *Nat. Commun.* **6**, 10095 (2015)
44. K. Hamada et al., Raman microscopy for dynamic molecular imaging of living cells. *J. Biomed. Opt.* **13**(4), 044027 (2008)
45. A.F. Palonpon et al., Raman and SERS microscopy for molecular imaging of live cells. *Nat. Protoc.* **8**(4), 677–692 (2013)
46. S. Ayas et al., Label-free nanometer-resolution imaging of biological architectures through surface enhanced Raman scattering. *Sci. Rep.* **3**, 2624 (2013)
47. C.T. Ertsgaard et al., Dynamic placement of plasmonic hotspots for super-resolution surface-enhanced Raman scattering. *ACS Nano* **8**(10), 10941–10946 (2014)
48. A.P. Olson et al., Super-resolution chemical imaging with plasmonic substrates. *ACS Photonics* **3**(3), 329–336 (2016)
49. A.P. Olson et al., Chemically imaging bacteria with super-resolution SERS on ultra-thin silver substrates. *Sci. Rep.* **7**, 9135 (2017)
50. S.M. Stranahan, K.A. Willets, Super-resolution optical imaging of single-molecule SERS hot spots. *Nano Lett.* **10**(9), 3777–3784 (2010)
51. M.L. Weber, K.A. Willets, Correlated super-resolution optical and structural studies of surface-enhanced Raman scattering hot spots in silver colloid aggregates. *J. Phys. Chem. Lett.* **2**(14), 1766–1770 (2011)

# Chapter 9

## Usage of Silicon for Label-Free Super-Resolved Imaging



**Hadar Pinhas, Yossef Danan, Amihai Meiri, Omer Wagner, Asaf Shahmoon, Tali Ilovitsh, Yehonatan Ramon, Dror Malka, Meir Danino, Moshe Sinvani and Zeev Zalevsky**

**Abstract** In this chapter, we present a summary of research that uses silicon to enhance the imaging resolution and to push it toward the region of nanoscopy. The silicon has a nonlinear effect called the plasma dispersion effect (PDE), which can be used instead of the fluorescent dye in order to realize a stimulated emission depletion (STED) like microscopic imaging configuration. The silicon can be encapsulated into nanoparticles while the encapsulation may be biocompatible and yield the first step toward label-free bioimaging. The encapsulation may even be metallic to enhance the obtainable effect and to yield resolution enhancement at lower requirements from the pump beam. The silicon can even be used directly as a wafer but then the super-resolving imaging is mainly aimed at failure analysis of micro-electronic circuitry. When the silicon is encapsulated with metallic layer or when it is in the form of a wafer, while being illuminated with a pump beam (in visible wavelength being absorbed by the silicon) it modifies the imaging point spread function (PSF) of the probe beam (a near infra-red wavelength) into a doughnut-like shape, through the utilization of the PDE. This modified PSF has spatial components smaller than the diffraction limit, and by scanning the sample with it, super resolution can be achieved.

---

H. Pinhas · Y. Danan · A. Meiri · O. Wagner · A. Shahmoon · T. Ilovitsh · Y. Ramon · D. Malka · M. Danino · M. Sinvani · Z. Zalevsky (✉)  
Faculty of Engineering, Bar-Ilan University, 52900 Ramat-Gan, Israel  
e-mail: [Zeev.zalevsky@biu.ac.il](mailto:Zeev.zalevsky@biu.ac.il)

H. Pinhas · Y. Danan · A. Meiri · O. Wagner · A. Shahmoon · T. Ilovitsh · Y. Ramon · Z. Zalevsky  
The Bar-Ilan Institute of Nanotechnology & Advanced Materials, Bar Ilan University, 5290002  
Ramat-Gan, Israel

D. Malka  
Faculty of Engineering, Holon Institute of Technology, 5810201 Holon, Israel

## 9.1 Introduction

Imaging with optics, and specifically optical microscopy, has many advantages since it allows to perform non-destructive imaging of samples via low cost and portable means being much simpler than scanning electron microscopes (SEM), focused ion beam microscopes and so on. However, the use of optical means also has limitations. Mainly, the law of diffraction limits the imaging resolution to be half the optical wavelength, which for visible light is about 250 nm. Since the size of a typical biological cell is about 10  $\mu\text{m}$ , this resolution is not sufficient to allow observing internal cellular structures or understanding key biological processes and procedures. In the last two decades, various approaches have been used to break the law of diffraction and allow optically perform imaging with much better resolution. Those approaches include: confocal microscopy [1], multi-photon microscopy [2], structured illumination microscopy [3] and total internal reflection fluorescence microscopy [4]. These methods provide lateral resolutions in the 100 nm scale.

Another category includes methods that are based on labeling the sample with specific fluorophores. Sub-wavelength information can be obtained using a priori knowledge of the imaging parameters and the excitation pattern. Such techniques include near-field scanning optical microscopy [5], which uses an ultra-sharp tip that scans the inspected sample and collects sub-wavelength data point-by-point [6]. Instead of a physical tip, other approaches as stimulated emission depletion (STED) microscopy [7] and nonlinear (saturated) structured illumination microscopy (SSIM) [8], use excitation pattern to realize scanning sub-wavelength light structure. The super-resolution image is obtained because the scan is performed by PSF with higher spatial frequencies instead of ordinary Gaussian PSF, and also due to the nonlinear response of the fluorophore. The above-mentioned approaches indeed improve the resolution to be much below the optical wavelength and help to reach lateral resolution of 20–50 nm, but it also depends on the physical/chemical properties of the fluorophore which has the disadvantages such as autofluorescence of live cells, the phototoxicity against living organisms and photobleaching [9–13]. Another research direction includes use of gold nanoparticles (GNPs) as biomarkers in a variety of applications such as medical diagnostic [14], drug delivery [15], therapeutic [16, 17] and cellular imaging [18]. The main interest in these nanoparticles is because of the localized surface plasmonic resonance (LSPR), which results in high optical cross-sections at the plasmonic resonance wavelength. The resonance wavelength depends on the properties of the nanoparticles, such as its shape and refractive index, as well as the characteristics of its environment. The commonly used GNPs include spheres and rods. The spheres have one LSPR peak, while the gold nanorods (GNRs) have two peaks because of LSPR in its transverse and longitudinal dimensions. The LSPR wavelength will become longer at larger aspect ratio [19, 20].

In this chapter, we discuss the research we have performed in the field of optical super-resolution method based on the PDE of silicon that is either coated with gold and encapsulated into nanoparticles or used as a silicon wafer as part of the micro-

electronics industry. Note that the silicon nanostructures have a growing interest [21–23] and are fabrication-feasible.

Our final aim is to create a non-fluorescent label-free nanoscope that will be extremely applicable to the field of imaging, either biomedical or in failure analysis. In the case of biomedical imaging, the concept involves the illumination of objects tagged with high concentrated silicon-coated GNRs. The method uses two lasers for illumination; a high-intensity pump beam and a probe beam that is spatially aligned with the pump beam. The high-intensity pump beam generates electrons and holes pairs in the silicon shell and thus yields a change in the refractive index of the silicon shell, via the PDE. Owing to the PDE, the real part of the refractive index reduces, while the imaginary part grows. As a result, the silicon shell becomes more metallic. Since the laser illumination profile has a Gaussian shape, the refractive index change will be more dominant near the Gaussian peak. As a result, the LSPR of the coated GNRs will shift due to modification of the effective radius and aspect ratio of the structure. The probe beam (which is in the near infra-red wavelength) is fixed to the plasmonic resonance of this nanostructure without applying the pump illumination. The pump beam shifts the LSPR in accordance to the spatial location inside the Gaussian beam. The refractive index change caused by the pump is transformed into a change in the profile of the PSF and this modified PSF has a doughnut-like shape that contains higher spatial frequencies (i.e. sub-wavelength spatial features) compared to a regular Gaussian PSF. Scanning a sample with this elaborated PSF can reconstruct higher spatial frequencies within the inspected sample and obtain a sub-wavelength super-resolution image.

In the case of silicon wafers for failure analysis application, the optical configuration is the same but no metallic coating is used. In the case of wafers, one of the main advantages is the capability to perform a super-resolved imaging deep into the wafer and not only on its surface by using temporally pulsed pump illumination.

## 9.2 Theoretical Background

The PDE is a nonlinear effect yielding modification in the refractive index of nanoparticle made of silicon as a result of the change in the free carrier concentration. This alteration in the real part of the refractive index  $\Delta n$  and the absorption coefficient  $\Delta\alpha$  is given by [24]:

$$\Delta n = \frac{-e^2\lambda_0^2}{8\pi^2c^2\varepsilon_0n} \left( \frac{\Delta N_e}{m_e^*} + \frac{\Delta N_h}{m_h^*} \right) \quad (9.1)$$

$$\Delta\alpha = \frac{e^3\lambda_0^2}{4\pi^2c^3\varepsilon_0n} \left( \frac{\Delta N_e}{\mu_e m_e^{*2}} + \frac{\Delta N_h}{\mu_h m_h^{*2}} \right) \quad (9.2)$$

where  $e$  is the charge of an electron,  $\lambda_0$  is the free space wavelength of the probe beam,  $c$  is the speed of light,  $\varepsilon_0$  is the vacuum permittivity and  $n$  is the refractive

index. We denote the modifications of the electrons and holes carrier concentration generated due to the pump illumination by  $\Delta N_e$  and  $\Delta N_h$ , respectively.  $\mu_e$  and  $\mu_h$  are the mobility of the electrons and holes, respectively.  $m_e^*$  and  $m_h^*$  are the effective electron and hole masses, respectively. The change in the free carrier concentration is equal to:

$$\Delta N_e = \Delta N_h = \frac{\eta \cdot P}{h \cdot \nu} \quad (9.3)$$

where  $\eta$  is the quantum efficiency,  $P$  is the intensity of the illuminating pump beam and  $h\nu$  is the energy of each photon ( $h$  is the Planck's constant and  $\nu$  is its optical frequency).

Discrete dipole approximation (DDA) is a method to calculate the optical coefficients of the coated GNP. In this approach the nanoobject is divided into an array of  $N$  dipoles ( $j = 1 \dots N$ ), and the Maxwell's equations are solved by finding the dipole moment [25]. DDSCAT 7.3 [26] is the version of the software that we used in our calculations.

We express the electric field at each dipole as a sum of the incident field and the fields radiated by the other dipoles:

$$E_j = E_{inc,j} - \sum_{k \neq j} A_{jk} \cdot P_k \quad (9.4)$$

where  $E_{inc,j}$  is the incident field,  $A_{jk}$  is an interaction matrix between the  $j$  and  $k$  dipoles and  $P_k$  is the  $k$  dipole moment. Each interaction matrix  $A_{jk}$  is a  $3 \times 3$  tensor:

$$A_{jk} = \frac{\exp(ikr_{jk})}{r_{jk}} \cdot \left[ k^2 (\hat{r}_{jk} \hat{r}_{jk} - 1_3) + \frac{ikr_{jk} - 1}{r_{jk}^2} (3\hat{r}_{jk} \hat{r}_{jk} - 1_3) \right], \quad j \neq k \quad (9.5)$$

where  $r_{jk}$  is the distance between the dipoles  $j$  and  $k$ ,  $k = \frac{\omega}{c}$  is the wave vector,  $\hat{r}_{jk}$  is a vector with unit length in the direction of the vector  $r_j - r_k$  and  $1_3$  is the identity matrix [25]. The matrix equation is solved in order to find the dipole moment:

$$A \cdot P = E_{inc,j} \quad (9.6)$$

After calculating the dipole moment, we can estimate the absorption and the scattering cross-section according to:

$$Q_{ext} = \frac{4\pi k}{|E_0|^2} \sum_{j=1}^N \text{Im}(E_{inc,j}^* \cdot P_j) \quad (9.7)$$

$$Q_{\text{abs}} = \frac{4\pi k}{|E_0|^2} \sum_{j=1}^N \left\{ \text{Im} \left[ P_j \cdot (\alpha_j^{-1})^* P_j \right] - \frac{2}{3} k^3 |P_j|^2 \right\} \quad (9.8)$$

The scattering cross-section is equal to:  $Q_{\text{sca}} = Q_{\text{ext}} - Q_{\text{abs}}$  with  $\text{Im}$  being the imaginary part taking operation.

To properly run the software, the size of the object is characterized by the “effective radius”  $R_{\text{eff}}$ , being defined as:

$$R_{\text{eff}} \equiv \left( \frac{3V}{4\pi} \right)^{\frac{1}{3}} \quad (9.9)$$

where  $V$  is the actual volume of the nanoparticle. In our simulations, in order to achieve accurate solution, we chose the inter dipole separation to be around 1 nm.

In our investigation, we used nanoparticles involving both semi-conducting part (silicon) as well as gold core. The change in the refractive index, as explained in the PDE, was observed only in the semi-conducting part of the nanostructure, while the reference and the pump beams did not cause any change in the refractive index of the gold core. The pump beam illumination occurs at a wavelength that is not in the LSPR wavelength, and thus despite its high intensity it hardly affects the refractive index of the gold core due to nonlinear effects (such as two-photon absorption [27]). The reference beam occurs in the LSPR frequency but it has low intensity and therefore it causes nonlinear effects.

### 9.3 Usage of Silicon-Coated Nanostructures

The nanostructure used in the proposed method, including gold nanocores coated with silicon, is illustrated in Fig. 9.1 [28]. Two diffraction-limited focused laser beams are used: pump beam at 532 nm wavelength and probe beam at 750 nm. Figure 9.2 illustrates a single nanostructure that we investigate in this section. The nanostructure core consists of GNR with semi-major axis of 43–53 nm, semi-minor axis of 18–26 nm and silicon coating of 5–8 nm.

Owing to the PDE, the silicon coating changes its refractive index. Since the change is in accordance with the spatial profile of the focused laser pump beam, we obtain the strongest change in the spatial position of the Gaussian peak. This change in the refractive index causes shift of the LSPR of the nanostructure. Since the wavelength of the probe is calibrated to the LSPR without the pump, the reflected probe light from the specimen will be attenuated mostly in the Gaussian tip having a Gaussian distribution that has a doughnut shape, that is, a dip in the middle. Thus, the generated doughnut shape probe beam, which now scans the specimen, has spatial components smaller than the diffraction limit due to the dip, and thus super-resolved sensing of the sample can be obtained.

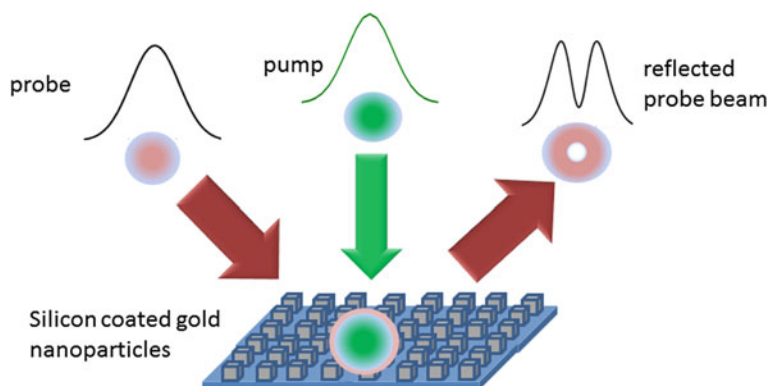


**Fig. 9.1** Schematic illustration of the system using silicon-coated nanostructures. The nanostructure is illuminated with two laser beams: 532 nm pump beam and a 750 nm probe beam

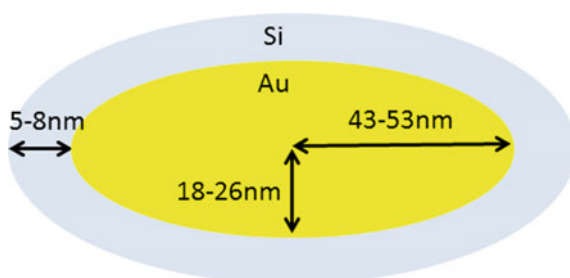


**Fig. 9.2** Illustration of the gold core silicon shell of a single nanostructure. The core consists of GNR with semi-major axis of 43–53 nm, semi-minor axis of 18–26 nm and silicon coating of 5–8 nm. Reproduced from [28]

Earlier literature reports demonstrate an approach to achieve optical control of the LSPR spectral location, including showing of LSPR blue shift up to 170 nm for a rectangular dimer antenna embedded in ITO [29], generation of linear antennas at THz frequencies [30] via photogeneration done by illuminating a thin GaAs layer and so on. All those approaches have investigated much bigger nanostructures that can be used in the proposed method.

Note that the recombination of the electrons and holes starts after tens of nanoseconds and causes a heating to the nanostructure. This heating can damage the biological sample, so a nanosecond pulsed laser should be used. The pump beam should also be at a suitable wavelength in the absorbance region of silicon (we used 532 nm in our simulations).

Our simulations used 10 ns pulsed Gaussian pump beam with varied peak intensities. As explained earlier, the resulting scattering coefficients change due to the pump beam was determined using DDSCAT 7.3 [26] software and the DDA approach was

used to calculate the change in the refractive index at each local point, in the nanostructure mesh, caused due to the PDE in the silicon coating.

In our simulations, we performed the testing at different intensities of the pump to examine how different spatial locations along the Gaussian pump beam affect the optical coefficients and thereafter the illumination PSF. All the simulations were performed for various aspect ratios (A.R) and effective radii ( $R_{\text{eff}}$ ) of the nanoparticle.

Some of the simulations are presented in Fig. 9.3, where we can see the spectra of GNRs coated with 5–8 nm silicon with overall effective radii ( $R_{\text{eff}}$ ) of 30 and 40 nm, and aspect ratio (A.R) of 1.62, 1.87 and 2, while the computations were performed at three different illumination pump intensities of:  $0 \text{ W/cm}^2$ ,  $0.5 \text{ MW/cm}^2$  and  $1 \text{ MW/cm}^2$  at temporal pulsed duration of 10 ns.

Following the PDE, an increase of the pump intensity makes the silicon shell more metallic; as a result, the overall effective radius of the nanoparticle increases and the aspect ratio decreases. This results in a blue shift of up to 120 nm to the LSPR. We can observe in Fig. 9.3a–c the increasing aspect ratio resulting in a red shift, with an increase in the absorption cross-section accompanied by a decrease in the scattering

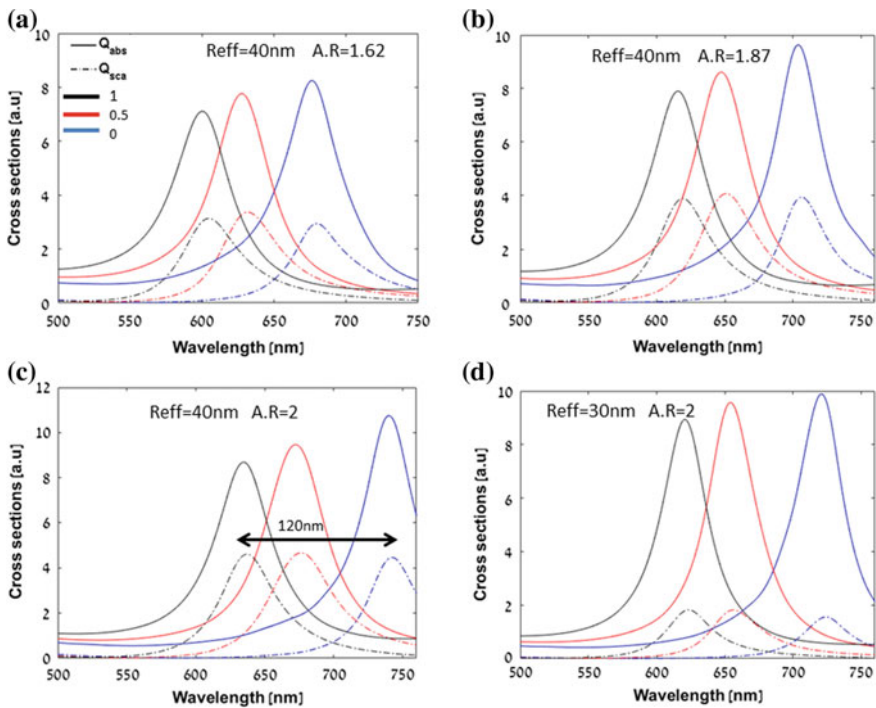


**Fig. 9.3** Calculated spectra of  $Q_{\text{sca}}$  (dashed line),  $Q_{\text{abs}}$  (line) for silicon-coated GNRs with different aspect ratio and effective spectra of  $Q_{\text{sca}}$  (dashed line),  $Q_{\text{abs}}$  (line) for silicon-coated GNRs with different aspect ratio and effective radius at three pump intensities:  $0 \text{ W/cm}^2$ ,  $0.5 \text{ MW/cm}^2$  and  $1 \text{ MW/cm}^2$  at 10 ns of temporal duration; In **a–c** an effective radius of 40 nm and aspect ratio of 1.62, 1.87 and 2, respectively are used and in **d** an effective radius of 30 nm and aspect ratio of 2 are used. Reproduced from [28]

cross-section. Figure 9.3c–d shows the increase in the scattering cross-section, and the decrease in the absorption cross-section when the volume of the nanoparticle increases.

In the simulations that we show in this section, the probe wavelength of 750 nm at the peak of the pump illumination was chosen because of the nanoparticle maximal shift of the LSPR. This shift is relative to the marginal nanoparticles located at the intensity of the tails of the illuminating Gaussian beam.

In order to demonstrate the feasibility of the proposed nanostructure to super-resolution, additional simulations were performed using DDSCAT, at 10 ns temporal pulsed pump duration and peak intensity of 1 MW/cm<sup>2</sup>. This pump illuminates an array of nanostructures. Figure 9.4a presents the three-dimensional profile of the pump beam and in Fig. 9.4b we can see the cross-section obtained at the center of the pump beam. The calculated scattering coefficients were multiplied with the probe Gaussian illumination beam at each of its spatial locations on the mesh of the inspected nanostructures. The result includes beam profile which has a central dip being generated due to the pump beam, while the dip is a reduction of about 50% in comparison to the maximal intensity of the reflected light (as can be seen in Fig. 9.4c, d).

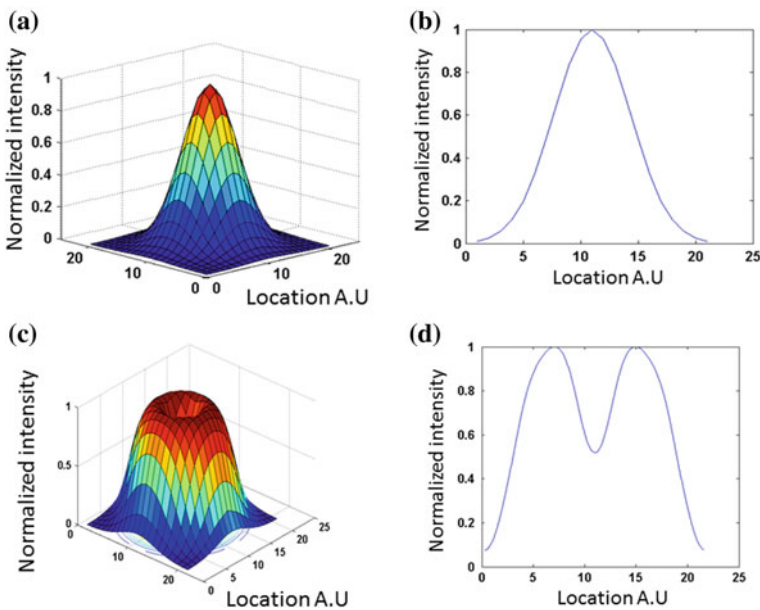


**Fig. 9.4** Normalized intensity of the pump and reflected light of GNR array with dimensions  $70 \times 30 \times 30$  nm and silicon shell of 8 at 750 nm wavelength of the probe light and 532 nm pump wavelength: **a** three-dimensional profile and **b** cross-section at the beam center of the pump light. **c** Three-dimensional profile and **d** cross-section at the beam center of the reflected light. Reproduced from [28]

In order to test the super-resolving capabilities of the proposed method, a resolution target containing three bars, as illustrated in Fig. 9.5a, was used. The size of the each bar was set to match the dimensions of the modified PSF. As mentioned earlier, the inspected sample was illuminated with a pump beam at wavelength of  $\lambda = 750$  nm and, as a result, the shape of the PSF was modified. This is presented in Fig. 9.5b. The sample was convolved with this PSF. The resulting low-resolution image, in which the three resolution bars are not seen, is presented in Fig. 9.5c.

The reconstruction of the super-resolved image is done by deconvolution of the captured image with the known shape of the PSF of the imaging system using the Richardson-Lucy algorithm. The obtained outcome is then followed by another deconvolution with the known shape of the coated GNRs PSF. This yields the super-resolved image, as presented in Fig. 9.5d. In this image, the three bars are clearly visible. For comparison purposes, the same reconstruction approach was applied with a Gaussian PSF shape with dimensions that are similar to that of the coated GNRs PSF, as presented in Fig. 9.5e. Now, the three bars are not visible.

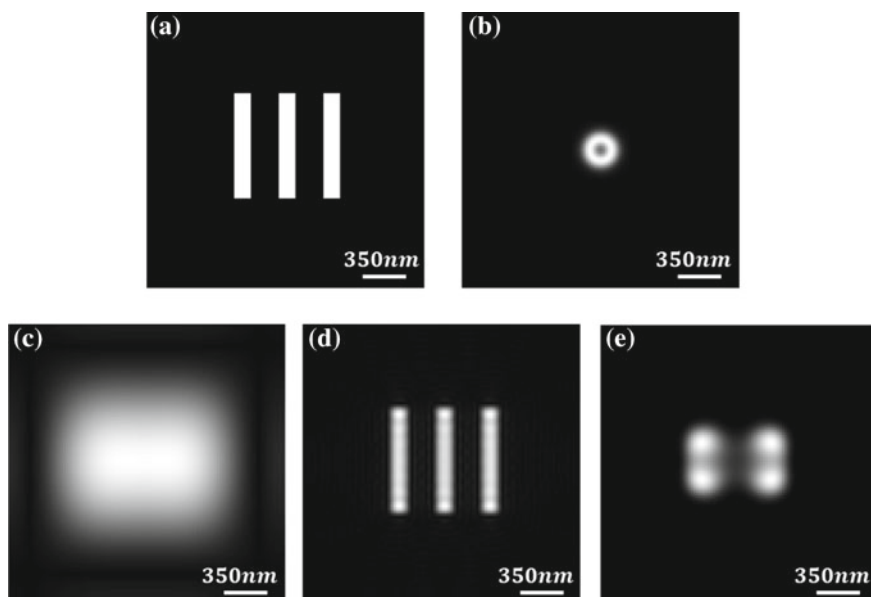


**Fig. 9.5** Simulation images of the **a** resolution target, **b** the modified shape of the PSF, **c** low-resolution image and **d** the deconvolved image. **e** The sample analysis carried out with a Gaussian PSF shape. Reproduced from [28]

## 9.4 Enhancement of the Effect

In this section we show how the effect described in the previous section can be enhanced by properly designing the shape of the silicon-based nanostructures [31]. The idea is to use metallic structures that are encapsulating the silicon, having edges that can enhance the electrical field density.

### a. Method

We performed our simulations on two basic configurations: a block configuration and a dimer configuration, as presented in Fig. 9.6.

The tested resonance excitation wavelength was within the range of 300–800 nm with steps of 2 nm at the critical area around the peak region and 10 nm outside this region. The dipoles were positioned at a distance of 1 nm apart in order to obtain accurate results with reasonable computational complexity. The polarization state of the incident beam coincided with the long axis of the nanoparticle while the beam arrived from an axial direction being perpendicular to this axis. The light source is located closer to the silver nanoparticle. The nanorod dimensions were 30 nm × 10 nm × 10 nm.

In addition to the extinction cross-section spectra, we have also calculated the enhancement of the electric field for the peak wavelength at two different locations (see Fig. 9.6). For a two-block structure the first point<sup>1</sup> is in the middle of the structure and the second<sup>2</sup> is  $H/2$  above the first, with  $H$  being the thickness of the block.

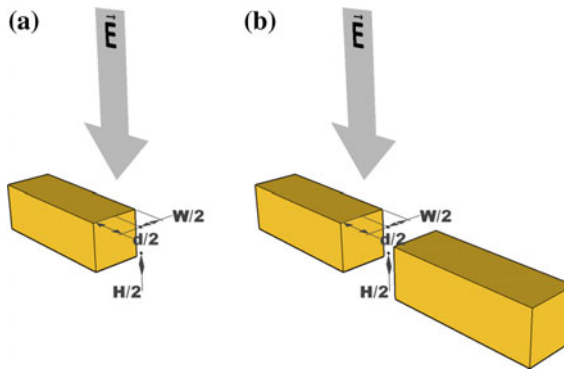


**Fig. 9.6** Simulated configurations. **a** A single block. **b** Dimer configuration. Each block consists of either a single nanoparticle or two attached nanoparticles with shape of a nanorod or a prism. The two measurement points for the electric field enhancement are also indicated. The distances  $W$ ,  $H$ ,  $d$  are the width of the nanorod or base of the prism, thickness of the block and distance between nanorods, respectively. The distance between nanorods in the case of nanorods was chosen as 4 nm and for prisms as 10 nm. Reproduced from [31]

<sup>1</sup>This point is referenced as the middle point in the rest of the text. The plain that crosses that point and is perpendicular to the light propagation direction is referred to as the middle plain.

<sup>2</sup>Denoted edge point.

An average of the electrical field was computed within a square with 1 nm vertex centered at the indicated locations in order to perform the calculations of the field's enhancement factor (the intensity enhancement is the fourth power of the electric field norm enhancement). The results were obtained for four pump intensities of:  $6.2 \times 10^{-3}$  [mW/ $\mu\text{m}^2$ ], 0.62 [mW/ $\mu\text{m}^2$ ], 6.2 [mW/ $\mu\text{m}^2$ ], 37.33 [mW/ $\mu\text{m}^2$ ] where the first two intensities are related to the nonconducting silicon nanoparticle and the last two are related to a conducting silicon nanoparticle. In the case of highest intensity, the concentration of free charge carriers in the silicon part is close to that of silver nanoparticle.

## b. Results

The structure examined in Fig. 9.7a consists of a single silver nanorod block on top of a silicon nanorod. When the intensity of the illumination pump is high the shape gradually changes from a silver nanorod on top of an insulator to two metal nanorods attached to each other. This leads to a decrease in aspect ratio and causes a blue shift to the extinction resonance (see in Fig. 9.7b). From Fig. 9.7c where typical electric field distribution is shown, the change in the intensity of the pump results in the change in the field's magnitude. Since the sharper the feature, the higher is the enhancement factor, the highest enhancement is obtained in the corners of the nanorod. For conducting silicon nanorod the structure looks as one larger nanorod and for non-conducting case, the structure is sharper with higher enhancement than in the conducting case of Fig. 9.7d. For further understanding, the enhancement was calculated along one of the vertical vertices of the nanorods and Fig. 9.7e shows the tag. Indeed, for the low pump intensity (sharper structure) there is a comparable enhancement between the two corners of the silver nanorods ( $z = 10$  and  $z = 0$ ) while for high pump intensity there is a metal to metal transition at  $z = 0$  and two enhancement factors (there is only one corner enhancement at  $z = 0$ ).

Another tested structure was a single-layer nanorod dimer composed of silicon and silver nanorods being positioned along the long axis of the nanorods (Fig. 9.8a). Here, if the pump intensity is increased, the silicon nanorod becomes metallic and the extinction resonance (Fig. 9.8b) has a red shift due to the essentially higher aspect ratio and longer nanorod.

In the case of weakly conduction (pump intensity of 0.62 [mw/ $\mu\text{m}^2$ ]) two close resonance peaks are generated and are matched with the two different metal-like nanoparticle. The resonator formed by the two nanoparticles in the conducting case enlarges the middle point enhancement in comparison to the enhancement of the edge. On the other hand, in the case of non-conducting, this situation is inverted. The electric field distribution of the non-conducting case and the highly conducting cases are seen in Fig. 9.8c and d, respectively. When the pump intensity is increased the electrical field moves more and more from surrounding only the silver nanoparticle to be surrounded also around the silicon nanoparticle while high electric field enhancement is obtained between the two particles.

Figure 9.9a and b shows the spectral response of the two-layer nanorod dimer, which is similar to the single two-layer nanorod structure and it is opposite to that of the single-layer nanorod dimer.

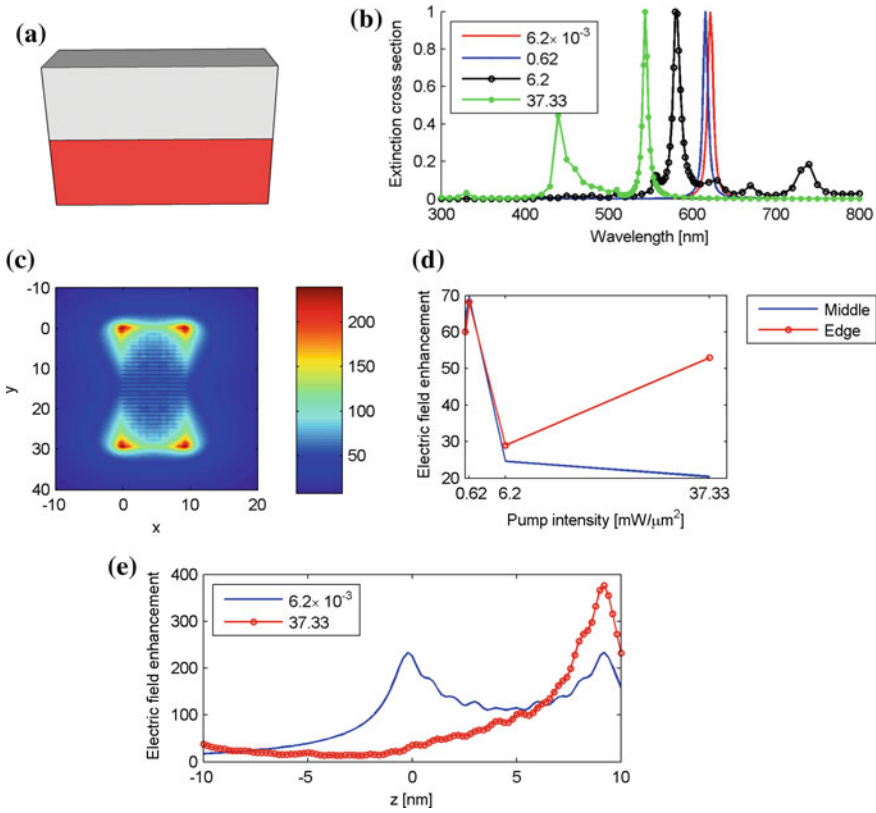


**Fig. 9.7** Two-layer structure: a silver nanorod on top of a silicon nanorod. **a** Structure. **b** Extinction cross-section spectrum for different pump intensities. The extinction cross-section is normalized with respect to the maximum cross-section for each case. **c** The norm of the electric field on top of the silver nanorod (middle plane of the structure) for pump intensity of  $6.2 \times 10^{-3}$ . **d** The electric field enhancement in the middle point and edge point as a function of pump intensity. **e** The electric field enhancement along a vertical vertex of the structure. The silicon nanorod is between  $z = -10$  nm and  $z = 0$  and the silver nanorod is between  $z = 0$  and  $z = 10$  nm. Reproduced from [31]

On comparing the results for the middle and edge planes, in Fig. 9.9c, we can see that the conducting silicon nanorod has sharper edge plane features and in the non-conducting case, a high refractive index of the silicon nanorod causes a higher electric field. For low pumping intensity the enhancement is the largest, while the sharper features of the non-conducting case are combined with the high refractive index of the silicon. In this structure the enhancement for the highest pump intensity is always high (except for the enhancement in the middle plane) in comparison to that of the single-layer nanorod dimer due to the two metal-like nanoparticles resonator; while in the case of single-layer, each part of the structure is thin and has sharper features.

A drawing of prism dimer structure is shown in Fig. 9.10a, while its enhancement

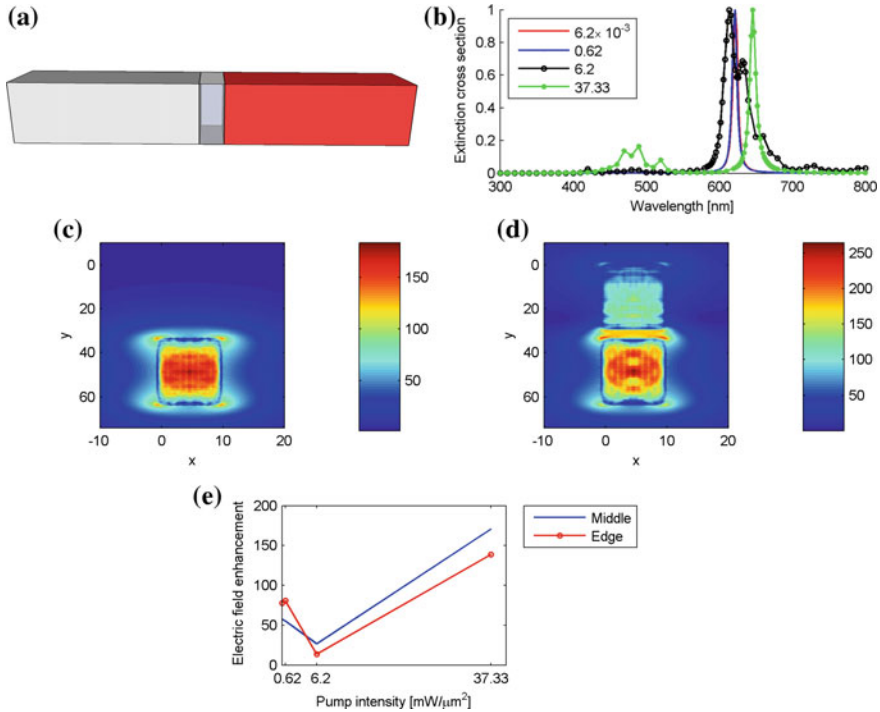


**Fig. 9.8** One-layer nanorod dimer. **a** The structure is composed of a silicon nanorod (red) and a silver nanorod (gray). **b** Extinction cross-section spectrum for different pump intensities. The extinction cross-section is normalized with respect to the maximum cross-section for each case. **c** and **d** The norm of the electric field in the middle plane of the structure for pump intensities of  $10^{25}$  and  $6 \times 10^{28}$ , respectively. **e** The electric field enhancement in the middle point and edge point as a function of the pump intensity. Reproduced from [31]

versus the pump intensity is seen in Fig. 9.10b and c. From these results, we may observe larger enhancement in the middle point due to the constant resonance and sharp prism edge. The longer gap between the blocks (10 nm as opposed to 4 nm before) produces significantly lower enhancements.

### 9.5 Feasibility Experimental Results

An array of silicon-coated GNR was fabricated on top of silicon oxide by spin coating of an SOI (silicon on insulator) wafer using poly-methyl-methacrylate A2 (an e-beam lithography resist), which resulted in GNR dimensions of  $80 \times 50 \times 10$  nm and 5–10 nm silicon coating. The sample was coated with PMMA and then baked for 2 min on a hot plate at 180 °C.

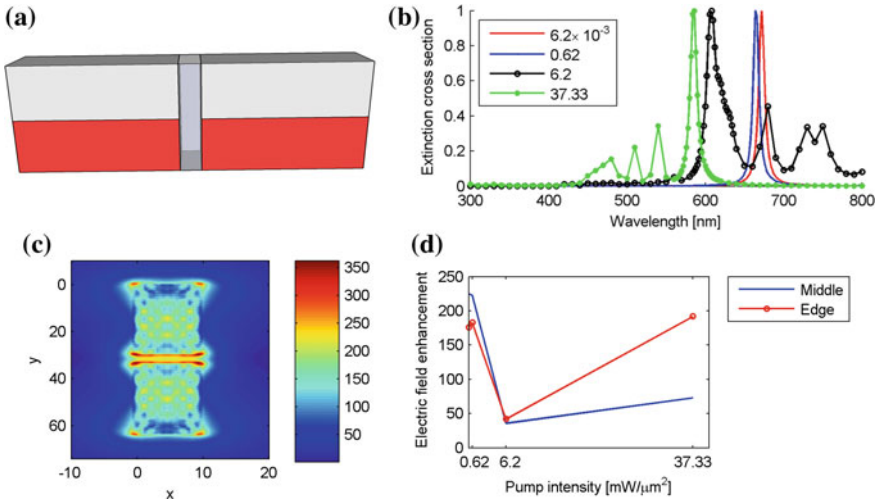


**Fig. 9.9** Two-layer nanorod dimer. **a** The structure is composed of two blocks, each with a silver nanorod (gray) on top of a silicon nanorod (red). The distance between blocks is 4 nm. **b** Extinction cross-section spectrum for different pump intensities. The extinction cross-section is normalized with respect to the maximum cross-section for each case. **c** Norm of the electric in the middle plane (between the silicon and silver nanorods) for pump intensity of  $10^{27}$ . **d** The electric field enhancement in the middle and edge points as a function of pump intensity. Reproduced from [31]

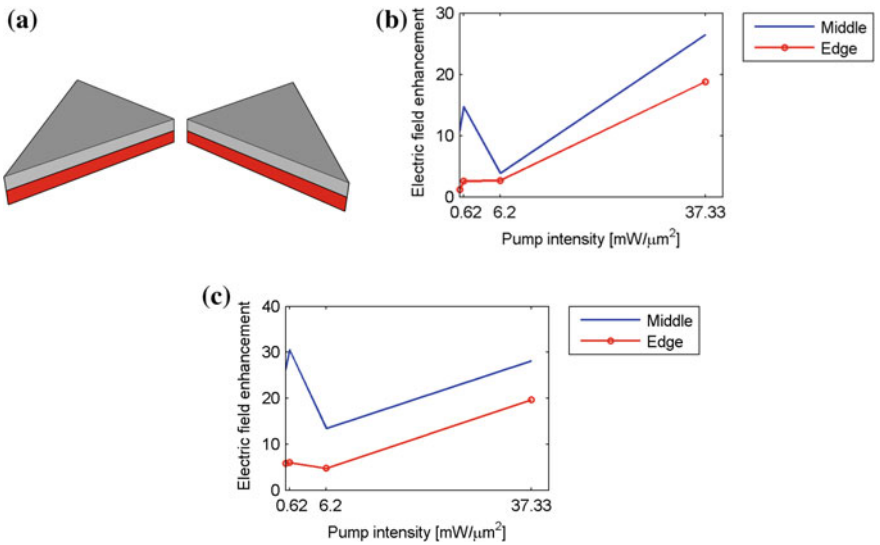


**Fig. 9.10** A prism dimer. **a** The structure consists of two blocks of a silver prism on top of a silicon prism with a gap of 10 nm between them. Both prisms have a thickness of 10 nm and a width of 60 nm. The enhancement in the gap was calculated for the structure with a prism base of **b** 30 nm and **c** 60 nm. Reproduced from [31]

CRESTEC CABLE-9000C, a high-resolution electron-beam lithography system, was used to expose the PMMA layer to different irradiation doses and right after the sample was developed for 50 seconds by MIBK (methyl-isobutyl-ketone) and rinsed with IPA.

Following this, the sample was dispositioned with 10 nm Au and 3 nm chrome. For the resist liftoff, the sample was immersed in acetone at 100 kHz ultrasonic bath for 3 h. The fabrication process ended up with deposition of more 10 nm silicon using BESTEC 2'' DC magnetron sputtering process. The SEM image of the generated sample as well as the cross-section TEM images of the coated GNRs can be seen in Fig. 9.11.

The next important step is adjusting this approach to microscopy. To do this, we should scan the sample with pump and probe beams. However, several considerations should be remembered. The illumination should not focus on the gap between the

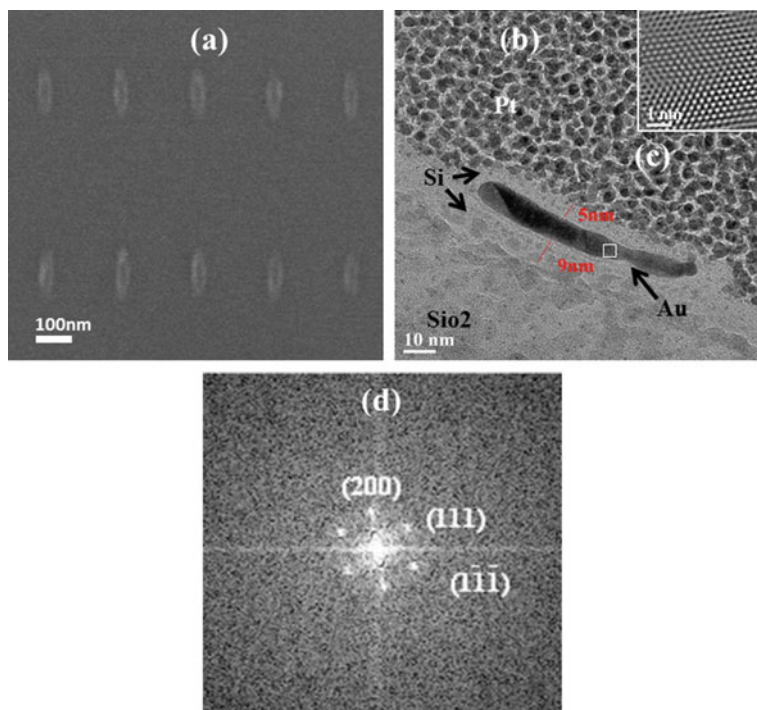


**Fig. 9.11** Images of the fabricated nanostructure with dimensions of  $80 \times 50 \times 10$  nm GNR core and 5–10 nm silicon coating. **a** SEM image of the GNRs before the deposition of the silicon. **b** TEM image of the coated GNRs. The GNR and the silicon coating are clearly seen. Inset **c** shows the magnified image of the area marked by the white square. In order to prove the presence of Au: **d** computed Fourier transform taken from the outlined area in **(b)**, showing reflections in accordance with the inter-planer spacing of Au. The layer above the silicon is platinum, intended to protect the structure from being damaged during the preparation of our specimen for the TEM inspection. Reproduced from [31]

two nanostructures since there the described doughnut-like shaping of the PSF will not occur similar to the Gaussian PSF. Thus, the gap between the two nanostructures should be smaller than the size of the PSF. Another issue is how the biosample is placed on top of the nanostructure. To make sure that the probe's beam will penetrate into the samples and reach the nanostructure, its chosen wavelength should be long enough (e.g. near IR) to have sufficient penetration depth.

## 9.6 Silicon Wafers Imaging

As in the silicon nanostructures concepts described in the earlier sections, the same approach can be applied on silicon wafers for failure analysis application [32]. As explained before, an IR laser beam in silicon can be shaped by changing the silicon complex refractive index locally via another laser beam absorbed in the silicon which acts as a pump. This change is induced by the change in the free charge carriers (FCC) density in the silicon due to the absorbed pump beam.

As mentioned earlier, spatial frequencies higher than the ordinary diffraction-limited Gaussian shape PSF frequencies are induced. Moreover, it is important to note that the proposed mechanism is nonlinear because the absorption coefficient for the probe is proportional to the power of the pump; therefore the total absorption of the probe is exponentially related to the absorption coefficient according to the Beer–Lambert law. Thus, the intensity of the probe is exponentially dependent on the intensity of the pump. The result of this technique is the improvement in the PSF of the IR beam.

Here we propose to perform the shaping of the IR beam's PSF in two modes: First is to induce a hole at its center. This is generated by applying a narrower Gaussian pump beam at its center [32], as seen in Fig. 9.12a. For this mode the PSF has a shape requiring post-processing (decoding) in order to reconstruct the super-resolved image.

The second mode is to apply a pump beam having a doughnut-like shape which will yield a central narrow part in the IR beam to pass through, and the rest of the beam will be blocked (see Fig. 9.12b). Then, no post-processing is required and the sample is scanned with a narrower probe PSF having Gaussian-like shape. Owing to the absorption mechanism in both modes, we generate higher spatial frequencies in the PSF of the probe, which leads to the extraction of the nanometric features of the sample.

In previous works [33–36] we presented the development of an all-optical silicon slab temporal data modulator applied on an IR laser probe beam, while the modulation is generated via a second pulsed green laser pump beam. The pump laser generated

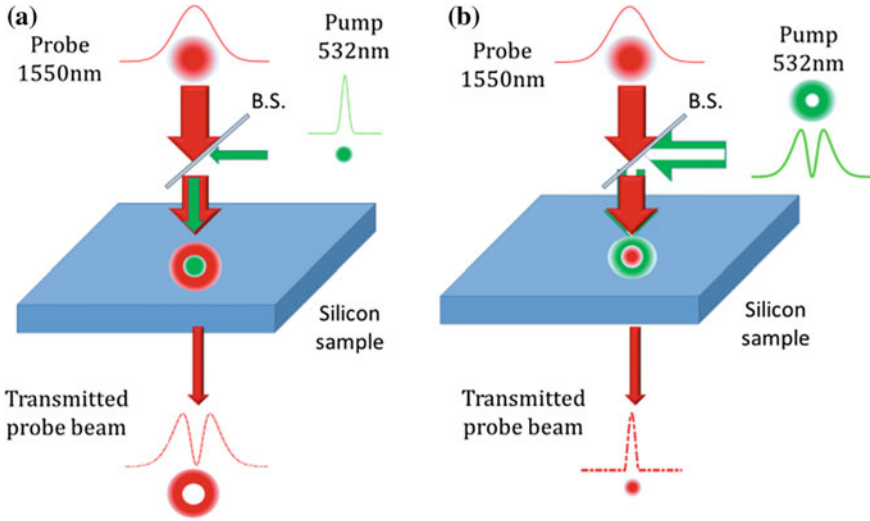


**Fig. 9.12** Illustrations of the principle of the proposed two beam shaping methods. **a** A narrow pump Gaussian beam at 532 nm, creates a hole in the middle of a wider IR beam. **b** Donut shape 532 nm pump beam blocks the periphery of the IR beam Gaussian and transmits a narrow beam in its center only. Reproduced from [32]

absorption in the silicon, and following that the generated FCC produced blockage of the IR probe beam due to the PDE.

This fundamental ability to perform temporal and spatial shaping of the probe beam by the pump beam is the basis for the adaptation of the proposed concept for super-resolved imaging in silicon wafers as described in this section.

**a. Experimental results**

The experimental setup is illustrated in Fig. 9.13, where a silicon slab is illuminated by two pulsed diffraction-limited Gaussian laser beams with a pump beam at wavelength of 532 nm and a probe beam at 1550 nm.

The 532 nm pump beam is being absorbed in the silicon which generates blocking of the center of the 1550 nm probe beam since the absorbed pump generates FCC causing temporary change in the complex refractive index of the silicon due to PDE and creation of the central hole in the probe beam.

The sample we use in our experiments is an intrinsic c-Si slab with resistivity  $\rho > 1000 \Omega \text{ cm}$ , 470  $\mu\text{m}$  thickness and an area of  $20 \times 20 \text{ mm}^2$ . The sample was optically polished on both sides in parallel and without coating. Since the silicon has high refraction index of 3.5, it acts as a low Finesse Fabry-Pérot (FP) resonator with spectral transmission (peak to valley) varying by factor of  $\sim 2\text{--}3$  for the probe laser [34].

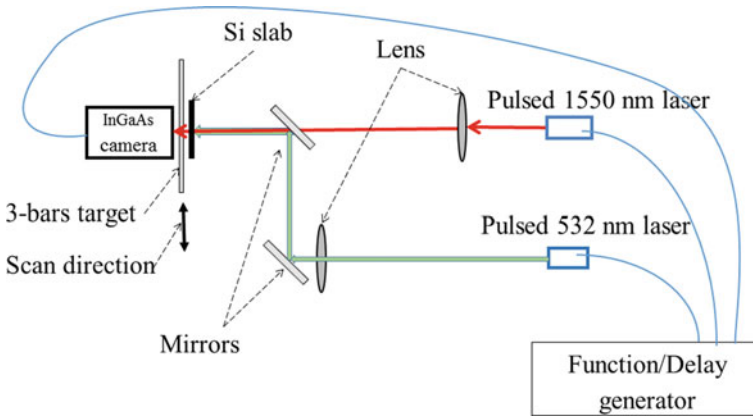


**Fig. 9.13** The experimental setup. Reproduced from [32]

In the first experiment a probe laser with  $\sim 50$  ps pulse width with jitter  $< 25$  ps and beam diameter ( $1/e^2$ ) of  $1200 \mu\text{m}$  was used. The pump laser had 17 ns pulse width with jitter  $< 4$  ns and the beam was focused to a diameter of  $\sim 30 \mu\text{m}$  on the silicon. The experiment was done where the probe and the pump lasers were focused on the silicon surface collinearly and pulsed simultaneously at a repetition rate of 10 pulses per second.

The images of the transmitted probe laser beam were taken by InGaAs lens-less camera. In Fig. 9.14 we present the obtained experimental results while in Fig. 9.14a we show the transmitted probe beam without the pump, and in Fig. 9.14b the probe with the pump beam being applied at its center. One may clearly see the generation of a beautiful dip in the center of the Gaussian probe beam.

In Fig. 9.15 we further show additional experimental results, where super-resolved imaging of resolution target containing three bars with a period of  $500 \mu\text{m}$  is demonstrated. The sample was scanned by the probe IR laser beam that was focused on the surface of the silicon with a very low NA (one diffraction limit unit is  $600 \mu\text{m}$ ). The results of the unshaped beam are shown in Fig. 9.15a, and of the shaped beam in Fig. 9.15b.

Since we know the PSF of the beam, we performed its deconvolution by realizing a standard Wiener filter algorithm via MATLAB software. The obtained results are colored in blue and the raw data in red. We can clearly see that the unshaped probe beam produces an unresolved pattern of the three bars, while the shaped beam of Fig. 9.15b yields a clear reconstruction of the desired three bars.

In Fig. 9.16 we demonstrate the obtained resolution enhancement in the PSF as seen in space domain versus its Fourier domain computed by performing a Fourier transform to the PSF response of the shaped beam (red trace) in comparison with the unshaped (blue trace) probe beam.

The fact that the dip in the probe beam is not reaching zero in its center affects the sharpness of the three-bar scan pattern. The shaped probe beam of Fig. 9.14b

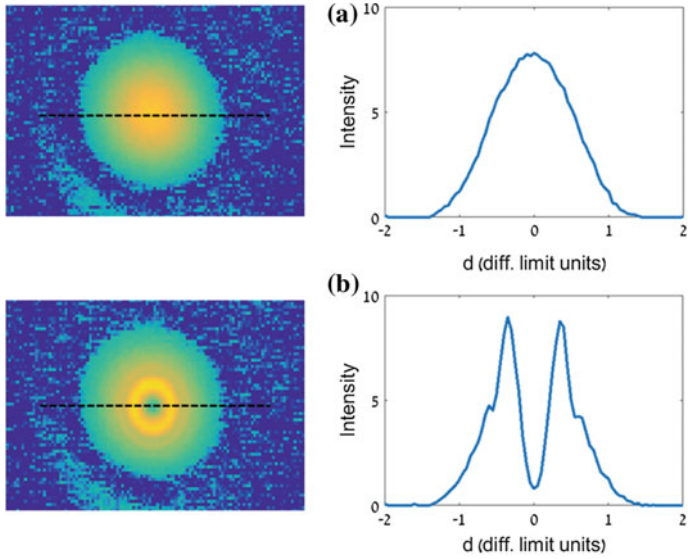


**Fig. 9.14** The dip in the IR probe Gaussian beam induced by the green pump beam. **a** The image of the transmitted Gaussian probe beam with its profile. **b** The probe beam shaped by the pump beam superimposed on it to create a dip in its center (see visualization 1 video that shows lateral and temporal behavior between probe and pump beams). One diffraction limit unit is 600  $\mu\text{m}$ . Reproduced from [32]

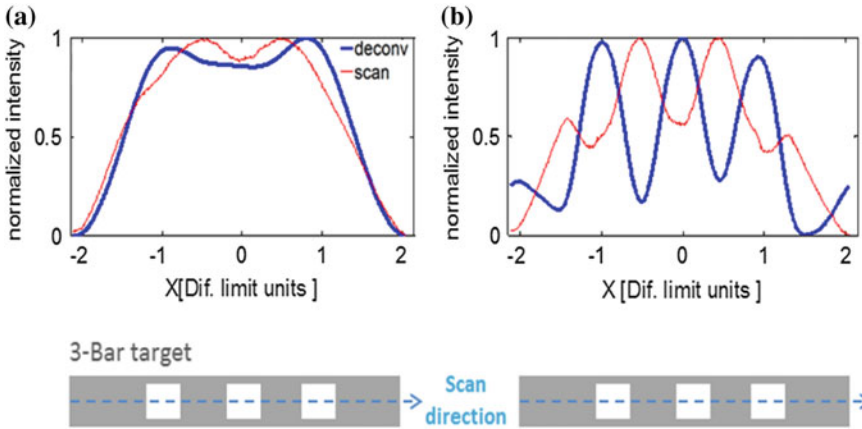


**Fig. 9.15** Probe Gaussian IR laser beam at the diffraction limit scan across a three-bars target (with a period of 500  $\mu\text{m}$ ) in two cases: **a** without the pump beam, which shows unresolved target. The second case, **b** is a scan of the target with the pump beam, with the dip in it, shows super-resolution where the target is well resolved. The red lines are the direct scan results and the blue lines are the direct scan results deconvoluted with the probe beam. Reproduced from [32]

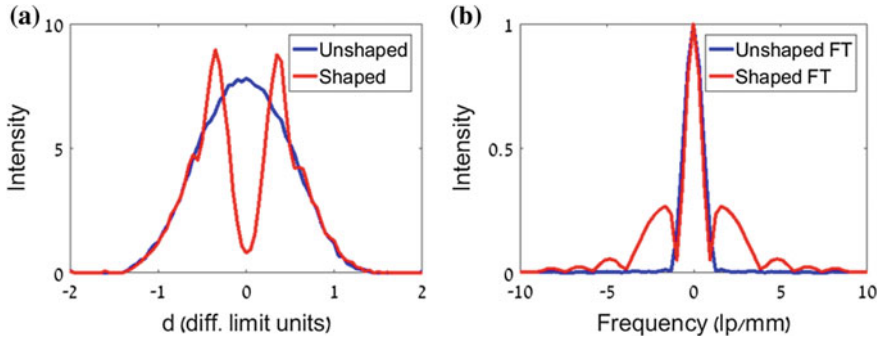


**Fig. 9.16** The spectral response enhancement of the shaped probe beam in comparison with the unshaped beam. Reproduced from [32]

was taken by the lens-less camera, but when a zoom lens is mounted on the camera and it is being focused on the front surface of the silicon (at the point where the two beams are focused on), a full dip is obtained in the probe (see Fig. 9.17a where the experimental results of the dips depth are shown for pump beam pulses with energies of 0.2, 0.5, 1.25, 2.5 and 5  $\mu\text{J}$ , respectively). This is obtained for pulse energy of 2.5  $\mu\text{J}$ . The dips depth as a function of the pump beam intensity is seen in Fig. 9.17b.

The fit line that we present in Fig. 9.17b is based on the Fabry–Perot (F-P)-based equation, which includes the PDE:

$$\frac{I_{\text{out}}}{I_{\text{in}}} = \frac{(1 - R)^2 e^{-(\Delta\alpha)d}}{(1 - R e^{-(\Delta\alpha)d})^2 + 4R \cdot e^{-(\Delta\alpha)d} \cdot \sin^2\left(\frac{2\pi(n \cdot L + \Delta n \cdot d)}{\lambda}\right)} \tag{9.10}$$

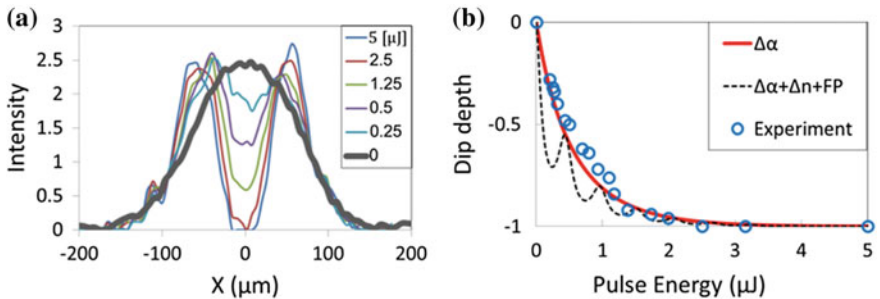


**Fig. 9.17** The dip depth as a function of pump pulse energy. **a** The profiles of the probe beam—without pump (black Gaussian) and with different five pump pulse intensities (the color traces). **b** The dip depth as a function of the pump laser pulse energy—experimental (the blue circles), calculations via the PDE + FP (dashed black line), and calculation of FCC absorption only (red line). Reproduced from [32]

where  $R$  is the reflectivity of F-P planes from both sides of the slab;  $\Delta\alpha$  and  $n$  are the silicon absorption coefficient and refractive index, respectively. The wavelength of the probe is designated with  $\lambda$  and  $d$  is the absorption depth + diffusion length.  $L$  is the silicon sample thickness.  $\Delta\alpha$  and  $\Delta n$  are defined in (9.1) and (9.2).

**b. Discussions**

There is some uncertainty regarding the size of the FCC volume induced by the pump beam because of the FCC diffusion [37–39]. For the temporal duration of the pump beam that we use, which was 17 ns, we assume diffusion of  $\sim 10 \mu\text{m}$  for the FCC into the silicon. This value includes  $1.3 \mu\text{m}$  for the penetration depth of the 532 nm pump photons, and  $8 \mu\text{m}$  diffusion depth that was calculated for diffusion coefficient of  $36 \text{ cm}^2/\text{s}$  for electrons in silicon during the 17 ns of the pump pulse. We assume high quantum efficiency such that each photon that penetrates into the silicon creates an  $e-h$  pair. The  $e-h$  pair recombination time is  $>100 \text{ ns}$  [34, 36] and it does not affect the FCC concentration during the pump pulse duration.

The maximum fluence used was  $0.2 \text{ J}/\text{cm}^2$ , which is lower by a factor of  $\sim 10$  than the damage threshold for silicon [40]. Under the above assumptions, the fluence intensity for the pump beam creates FCC density of  $\sim 10^{20} \text{ cm}^{-3}$ .

An interesting effect one can observe here is the defocusing. From Figs. 9.14b and 9.17a, it can be seen that the rim of the dip in the shaped beam is brighter than the pick of the original probe Gaussian beam. This is not expected for a subtraction of two Gaussians, as shown in Fig. 9.18, especially in Fig. 9.18b.

We attribute this effect to the defocusing [41–43] caused by the beam of the probe due to negative change in the refraction index of the silicon because of the applied pump.

The shape of the dip is controlled by the shape of the pump beam. Since PDE is a nonlinear effect the block of the probe beam is significantly stronger at the center rather than on its periphery. But, the low concentration of the FCC obtained in the

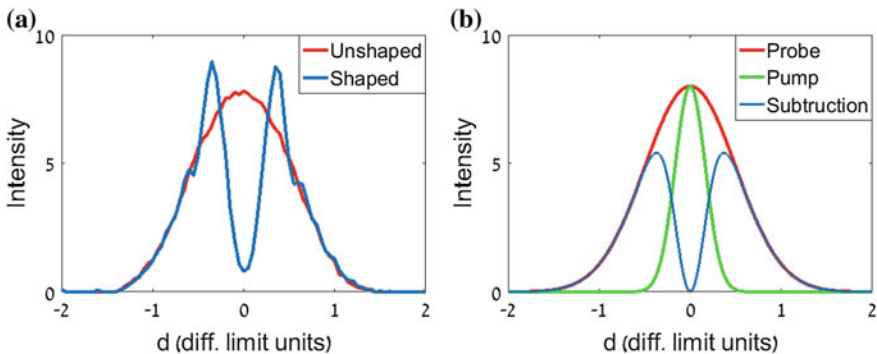


**Fig. 9.18** Defocusing observed in the experiment compared to simple subtraction of a narrow Gaussian from a wider one. **a** The probe beam in the experiment, without the pump beam (red line) and with the pump beam (blue line). **b** Mathematical subtraction (blue line) of pump (green line) Gaussian from probe (red) Gaussian. Reproduced from [32]

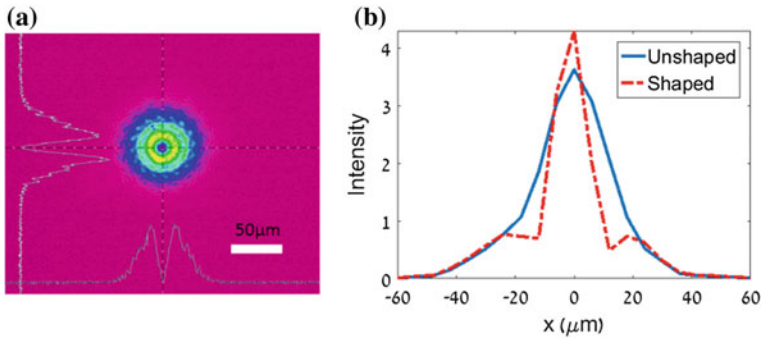


**Fig. 9.19** “Silicon Photonics STED”: preliminary experiment. **a** The donut shape pump beam. **b** The probe beam with (red dashed) and without (blue line) the donut pump on it. Reproduced from [32]

periphery of the PSF still slightly reduces the silicon index of refraction and causes defocusing of the probe beam.

In Fig. 9.19 we show additional experimental results in which we perform shaping of the IR beam PSF by a doughnut pump beam while the doughnut shape of the pump beam was generated by spiral phase plate (Vortex plate). This plate was inserted at the output of the pump laser.

The dip is not reaching zero and thus we tried to increase the fluence of the pump pulse by performing with better focus. However, as explained earlier, due to the diffusion of the FCC towards the center of the doughnut at the pump pulse duration (17 ns), the IR shaped beam was blurred. This problem can be overcome by the use of a picosecond pump laser.

Actually, it is an interesting future extension in which the temporal width of the pump pulse may control the diffusion range of the FCC towards the center of the hole in the doughnut which can result in setting its diameter, leading even to further enhancement of the super-resolving factor.

## 9.7 Conclusions

In this chapter we have presented the usage of silicon with its PDE nonlinearity in order to realize label-free super-resolved microscope or even a nanoscope. The silicon can be encapsulated into a metallic nanoparticle while the shape of the metallic nanoparticle can even enhance the nonlinearity used for the super resolution concept.

We believe that this concept can be used for the realization of a non-fluorescent nanoscope which will be extremely applicable to the field of biomedical imaging and as such it may have in the future an important role in understanding cellular trafficking pathways, identifying receptor expression and providing valuable insights into cellular processes.

Another approach presented here used silicon wafers where the PDE nonlinearity was applied in order to perform failure analysis of integrated circuits also for device located deeper below the surface of the wafer.

In all the approaches the optical configuration included optical pump beam and a probe beam while the object is scanned and the nonlinearity of the PDE generates optical point spread function having higher spatial frequencies (PSF shaping) which encode the high-resolution spatial data into the low-resolution imager. The operation principle resembles the approach used in STED microscopy, but no fluorescence dye is required in the proposed approaches.

## References

1. S. Hell, E. Stelzer, Fundamental improvement of resolution with a 4Pi-confocal fluorescence microscope using two-photon excitation. *Opt. Commun.* **93**, 277–282 (1992)
2. W.R. Zipfel, R.M. Williams, W.W. Webb, Nonlinear magic: multiphoton microscopy in the biosciences. *Nat. Biotechnol.* **21**(11), 1369–1377 (2003)
3. M.G. Gustafsson, Surpassing the lateral resolution limit by a factor of two using structured illumination microscopy. *J. Microsc.* **198**(Pt 2), 82–87 (2000)
4. D. Toomre, D.J. Manstein, Lighting up the cell surface with evanescent wave microscopy. *Trends Cell Biol.* **11**(7), 298–303 (2001)
5. R.C. Dunn, Near-field scanning optical microscopy. *Chem. Rev.* **99**(10), 2891–2928 (1999). <https://doi.org/10.1021/cr980130e>
6. E.J. Betzig et al., Breaking the diffraction barrier: optical microscopy on a nanometric scale. *Science* (80-) **251**(5000), 1468–1470 (1991)
7. S.W. Hell, J. Wichmann, Breaking the diffraction resolution limit by stimulated emission: stimulated-emission-depletion fluorescence microscopy. *Opt. Lett.* **19**(11), 780–782 (1994)
8. M.G.L. Gustafsson, Nonlinear structured-illumination microscopy: wide-field fluorescence imaging with theoretically unlimited resolution. *Proc. Natl. Acad. Sci. U.S.A.* **102**(37), 13081–13086 (2005)
9. J.R. Mansfield et al., Autofluorescence removal, multiplexing, and automated analysis methods for in-vivo fluorescence imaging. *J. Biomed. Opt.* **10**(4), 41207 (2014). [<https://doi.org/10.1117/1.2032458>]
10. R.A. Hoebe et al., Controlled light-exposure microscopy reduces photobleaching and phototoxicity in fluorescence live-cell imaging. *Nat. Biotechnol.* **25**(2), 249–253 (2007). <https://doi.org/10.1038/nbt1278>
11. J.N. Henderson et al., Structural basis for reversible photobleaching of a green fluorescent protein homologue. *Proc. Natl. Acad. Sci. U.S.A.* **104**(16), 6672–6677 (2007). <https://doi.org/10.1073/pnas.0700059104>
12. T. Bernas et al., Minimizing photobleaching during confocal microscopy of fluorescent probes bound to chromatin: role of anoxia and photon flux. *J. Microsc.* **215**(Pt 3), 281–296 (2004). <https://doi.org/10.1111/j.0022-2720.2004.01377.x>
13. P. Carpentier et al., Structural basis for the phototoxicity of the fluorescent protein KillerRed. *FEBS Lett.* **583**(17), 2839–2842. Federation of European Biochemical Societies (2009). <https://doi.org/10.1016/j.febslet.2009.07.041>
14. D. Fixler, Z. Zalevsky, In Vivo Tumor Detection Using Polarization and Wavelength Reflection Characteristics of Gold Nanorods (2013)
15. P.L. Truong, B.W. Kim, S.J. Sim, Rational aspect ratio and suitable antibody coverage of gold nanorod for ultra-sensitive detection of a cancer biomarker. *Lab Chip* **12**(6), 1102–1109 (2012). <https://doi.org/10.1039/c2lc20588b>

16. Q. Zhan et al., A study of mesoporous silica-encapsulated gold nanorods as enhanced light scattering probes for cancer cell imaging. *Nanotechnology* **21**(5), 055704 (2010). <https://doi.org/10.1088/0957-4484/21/5/055704>
17. R. Ankri et al., Intercoupling surface plasmon resonance and diffusion reflection measurements for real-time cancer detection. *J. Biophotonics* **6**(2), 188–196 (2013). <https://doi.org/10.1002/jbio.201200016>
18. T. Ilovitsh et al., Cellular imaging using temporally flickering nanoparticles. *Sci. Rep.* **5**, Macmillan Publishers Limited. All rights reserved (2015)
19. T. Ilovitsh et al., Cellular superresolved imaging of multiple markers using temporally flickering nanoparticles. *Sci. Rep.* **5**, 10965. Nature Publishing Group (2015). <https://doi.org/10.1038/srep10965>
20. Y. Danan et al., Decoupling and tuning the light absorption and scattering resonances in metallic composite nanostructures. *Opt. Express* **23**(22), 29089 (2015). <https://doi.org/10.1364/OE.23.029089>
21. Y.H. Fu et al., Directional visible light scattering by silicon nanoparticles. *Nat. Commun.* **4**, 1527. Nature Publishing Group, a division of Macmillan Publishers Limited. All Rights Reserved (2013). <https://doi.org/10.1038/ncomms2538>
22. S. Amoruso et al., Generation of silicon nanoparticles via femtosecond laser ablation in vacuum. *Appl. Phys. Lett.* **84**(22), 4502–4504 (2004). <https://doi.org/10.1063/1.1757014>
23. J.-H. Park et al., Biodegradable luminescent porous silicon nanoparticles for in vivo applications. *Nat. Mater.* **8**(April), 331–336 (2009). <https://doi.org/10.1038/nmat2398>
24. R. Soref, B. Bennett, Electrooptical effects in silicon. *IEEE J. Quantum Electron.* **23**(1), 123–129 (1987). <https://doi.org/10.1109/JQE.1987.1073206>
25. B.T. Draine, P.J. Flatau, Discrete-dipole approximation for scattering calculations. *J. Opt. Soc. Am. A* **11**(4), 1491 (1994). <https://doi.org/10.1364/JOSAA.11.001491>
26. B.T. Draine, P.J. Flatau, User guide for the discrete dipole approximation code DDSCAT 7.3. *Comput. Phys. Galaxy Astrophys. Mesoscale Nanoscale Phys. Opt.* **102** (2013)
27. K. Imura, T. Nagahara, H. Okamoto, Photoluminescence from gold nanoplates induced by near-field two-photon absorption. *Appl. Phys. Lett.* **88**(2), 1–3 (2006). <https://doi.org/10.1063/1.2161568>
28. Y. Danan, T. Ilovitsh, Y. Ramon, D. Malka, D. Liu, Z. Zalevsky, Silicon coated gold nanoparticles nanoscopy. *J. Nanophotonics* **10**(3), 036015-036015 (2016)
29. M. Abb et al., All-optical control of a single plasmonic nanoantenna-ITO hybrid. *Nano Lett.* **11**(6), 2457–2463 (2011). <https://doi.org/10.1021/nl200901w>
30. G. Georgiou et al., Photo-generated THz antennas. *Sci. Rep.* **4**, 3584 (2014). <https://doi.org/10.1038/srep03584>
31. A. Meiri, A. Shahmoon, Z. Zalevsky, Optically reconfigurable structures based on surface enhanced Raman scattering in nanorods. *Microelectron. Eng.* **111**, 251–255 (2013)
32. H. Pinhas, O. Wagner, Y. Danan, M. Danino, Z. Zalevsky, M. Sinvani, Plasma dispersion effect based super-resolved imaging in silicon. *Opt. Exp.* **26**, 25370–25380 (2018)
33. H. Pinhas, L. Bidani, O. Baharav, M. Sinvani, M. Danino, Z. Zalevsky, All optical modulator based on silicon resonator, in *SPIE*, vol. 9609 (2015), pp. 96090L–96090L–7
34. H. Pinhas, Y. Danan, M. Sinvani, M. Danino, Z. Zalevsky, Experimental characterization towards an in-fibre integrated silicon slab based all-optical modulator. *J. Eur. Opt. Soc. Publ.* **13**(1), 3 (2017)
35. R. Aharoni, M. Sinvani, O. Baharav, M. Azoulay, Z. Zalevsky, experimental characterization of photonic fiber-integrated modulator. *Open Opt. J.* **5**(1), 40–45 (2011)
36. R. Aharoni, O. Baharav, L. Bidani, M. Sinvani, D. Elbaz, Z. Zalevsky, All-optical silicon simplified passive modulation. *J. Eur. Opt. Soc. Rapid Publ.* **7**(12029) (2012)
37. M.S. Tyagi, R. Van Overstraeten, Minority carrier recombination in heavily-doped silicon. *Solid-State Electron.* **26**(6), 577–597 (1983)
38. D. Alamo, R.M. Swanson, Modelling of minority-carriers transport in heavily doped silicon emitters. *Solid-State Electron.* **30** (1987)

39. C. Canali, C. Jacoboni, F. Nava, G. Ottaviani, A. Alberigi-Quaranta, Electron drift velocity in silicon. *Phys. Rev. B* **12**(6), 2265–2284 (1975)
40. X. Wang, Z.H. Shen, J. Lu, X.W. Ni, Laser-induced damage threshold of silicon in millisecond, nanosecond, and picosecond regimes. *J. Appl. Phys.* **108**(3), 33103 (2010)
41. C. Jun, H.-J. Eichler, Laser beam defocusing at 1.06  $\mu\text{m}$  by carrier excitation in silicon. *Appl. Phys. B* **45**, 121–124 (1988)
42. T. Auguste, P. Monot, L.-A. Lompré, G. Mainfray, C. Manus, Defocusing effects of a picosecond terawatt laser pulse in an underdense plasma. *Opt. Commun.* **89**, 145–148 (1992)
43. V.V. Kononenko, E.V. Zavedeev, V.M. Gololobov, The effect of light-induced plasma on propagation of intense fs laser radiation in c-Si. *Appl. Phys. A* **122** (2016)

# Chapter 10

## Super-Resolution Imaging Based on Nonlinear Plasmonic Scattering



Tushar C. Jagadale and Shi-Wei Chu

**Abstract** During the last two decades, the resolution limit was well overcome by manipulating nonlinearity of fluorescence emission, including on/off switching and saturation, enabling resolution below 100 nm. However, fluorescence suffers from intrinsic photo-bleaching, which aggravates with repeated excitation for on/off switching or strong incident power for achieving saturation. Therefore, it is more than desirable to develop super-resolution imaging modality based on an alternative contrast agent without bleaching, such as scattering. An attractive candidate is scattering from surface plasmon resonance (SPR) nanostructures, whose scattering intensity is particularly strong, and can be spectrally tuned by structure. In this chapter, we review recent finding of nonlinear scattering, including saturation, reverse saturation, and all-optical switching, in an isolated plasmonic nanostructure. These nonlinear behaviours have been successfully applied to imaging, bringing spatial resolution down to nearly  $\lambda/10$ , which is enough to resolve surface plasmon polariton in nanoscale optoelectronic devices without labelling. Potential applications range from bio-medical imaging and functional plasmonic nanostructures. Our results are expected to be a stimulating example in finding more exotic contrast agency for improving optical resolution.

---

T. C. Jagadale · S.-W. Chu (✉)  
Department of Physics, National Taiwan University, No.1, Sec. 4, Roosevelt Rd., Taipei 10617,  
Taiwan (R.O.C.)  
e-mail: [swchu@phys.ntu.edu.tw](mailto:swchu@phys.ntu.edu.tw)

T. C. Jagadale  
Technical Physics Division, Bhabha Atomic Research Centre, Mumbai 400085, India

S.-W. Chu  
Molecular Imaging Centre, National Taiwan University, No.1, Sec. 4, Roosevelt Rd., Taipei  
10617, Taiwan (R.O.C.)

## 10.1 Introduction

### 10.1.1 *Why Label-Free Super-Resolution Light Microscopy?*

Light microscopes facilitate the magnified imaging of bio-specimen based on the principle that the rays from the specimen converge onto a corresponding single point at the image plane. However, beyond a critical magnification wherein size of structures becomes comparable to the wavelength of light, diffraction takes in and the structures cannot be well resolved. This is known as diffraction limit in light microscopy, which had been explained theoretically by Airy [1] (1835) and subsequently formulated by Ernst Abbe in 1873 [2] and Rayleigh in 1896 [3]. It states, in a loose sense, that it is impossible to resolve two structures that are closer to each other than half of an excitation wavelength in lateral plane ( $x, y$ ) and even further apart in the longitudinal plane ( $z$ ).

To overcome the resolution limit, non-optical imaging approaches such as electron microscopy and scanning probe microscopy [4, 5] have been developed to offer nano-scale resolution. However, compared to light microscopy, electron microscopy does not allow in vivo bio-imaging, and scanning probe microscopy is limited to surface observations. In addition, the mature fluorescence labelling in light microscopy provides precise molecular imaging with high contrast. Currently, the majority of research in life sciences is done using light microscopy since light is transparent to cells and provides non-invasive in vivo imaging into tissues, but with only sub-micrometre resolution [6]. Therefore, it has been a historically long pursuit to develop resolution enhancing techniques of light microscopy.

In the era of Abbe and Rayleigh, resolution is defined under the geometry of wide-field microscopy, in which the entire specimen is exposed to light, and the image can be viewed directly from an objective. The best wide-field microscope could reach the resolution of  $\sim 250$  nm laterally and  $\sim 800$  nm axially [7]. To extend the classical diffraction limit, Marvin Minsky in 1957 patented the concept of confocal microscopy [8], in which the sample is scanned with a focussed beam and a pinhole is used to block the out-of-focus light, improving lateral resolution by a factor of  $\sqrt{2}$ . In addition, confocal microscopy exhibits optical sectioning capability, so the axial contrast is greatly improved.

Another optical sectioning technique, multi-photon microscopy [9, 10], which is based on simultaneous absorption of two or more photons at longer wavelength (thus less scattering), significantly increases penetration depth in thick samples. The intrinsic nonlinearity sharpens the focal excitation volume and leads to a corresponding reduction of point spread function (PSF) width by a factor of  $\sqrt{2}$  for two-photon and  $\sqrt{3}$  for three-photon microscopy. Nevertheless, due to long excitation wavelengths, the lateral resolution is not as good as confocal microscopy. Presently, the main application of multi-photon microscopy is for deep-tissue imaging up to 1 mm, with sub-micrometre spatial resolution.

One major evolution in optical sectioning technique recently is the invention of selective plane illumination microscopy (SPIM), or more generally light sheet

microscopy. It features an imaging modality in which a sample is illuminated from the side perpendicular to the observation optic axis, by a beam engineered into a wide and relatively thin sheet. SPIM offers an axial resolution better than confocal ( $2\times$ ), wide-field ( $2.5\times$ ), and two-photon microscopy ( $3\times$ ), while the lateral resolution is the same as wide-field [11].

All these far-field approaches such as laser scanning confocal, multi-photon microscopy, SPIM, and so on have enhanced spatial resolution along lateral or axial axes, but are still considered as diffraction limited. Generally speaking, super-resolution microscopy techniques are defined as those capable of resolving structures beyond the classical diffraction limit and can be mainly divided into two categories, that is near-field and far-field. The examples of the former are near-field scanning optical microscopy (NSOM) and total internal reflection fluorescence microscopy (TIRFM). NSOM [12] uses fibre optic probe to funnel light to the nano-dimensions. This is accomplished by focussing the excitation laser through an aperture having a much smaller diameter than the excitation wavelength. This results in the formation of evanescent waves on the other side of the aperture. NSOM achieves a resolution of 20 nm in lateral and about 5 nm in axial, but suffers by the limitations such as zero working distance, small field depth, long scan times, and so on. On the other hand, TIRFM uses evanescent waves to excite fluorophores in a very small volume of the specimen immediately adjacent to the glass-medium interface. These evanescent waves are generated only when the incident light is totally internally reflected at the glass-medium interface. The evanescent EM field decays exponentially from the interface, and thus limits axial imaging depth to about 100 nm, that is improving the axial sectioning beyond diffraction [13].

For far-field super-resolution microscopy, Gustafsson [14] had explained the following three assumptions that limit light microscope resolution: (i) light for imaging is collected by a single objective; (ii) the excitation light is uniform throughout the sample; and (iii) fluorescence takes place through normal, linear absorption and emission of a single photon. The resolution limit can be challenged if somehow these assumptions are wisely tackled either by using multiple objectives, non-uniform illumination, or nonlinear absorption and emission. Below we introduce different techniques that are explored in the last two decades towards advancement of super-resolution microscopy based on the three limiting assumptions.

- (a) Objectives modifications: In the early 1990s, Stefan Hell proposed that by two opposing objectives, the collection aperture angle could be significantly improved, up to maximally  $4\pi$ , and thus could enhance axial resolution. The technique is called  $4\pi$  microscopy [15], wherein two face-to-face objectives, above and below the sample, were used. Both objectives illuminate and collect the emission from the same focal plane of the sample. The image is reconstructed by superposition of signals collected from both excitation and emission optical paths. This method achieves four times better axial resolution than CLFM. Later, Gustafsson developed image interference microscopy ( $I^2M$ ) [16], which used incoherent light source and also, two objectives for illumination and emission, wherein constructive interference between the excitation and emission light

paths decided the FWHM of illumination and detection PSF that gave 4–7-fold increase in axial resolution.

- (b) Non-uniform illumination: In 2000, Gustafsson [17] demonstrated that by illuminating the sample with patterned excitation light, called Moiré pattern, lateral resolution could be enhanced by two times, that is about 100 nm. This is called structured illumination microscopy (SIM).
- (c) Nonlinear absorption and emission: In the late 1990s, Hell [18] developed the methods to control the behaviours of fluorophores wherein all fluorophores are switched off except the centremost fluorophores within the diffraction-limited illumination volume of a laser scanning microscope, resulting in development of stimulated emission depletion (STED) microscopy with typical lateral resolution as high as 30–50 nm (can reach 6 nm with nano-diamond). During the same period, William Moerner demonstrated [19] that how certain mutants of green fluorescent protein showed remarkable ‘blinking’ behaviour in their individual fluorescence emission. After several rounds of blinking, these molecules would go into stable dark state, and could be recovered by a short burst of UV light. This idea had fascinated Betzig [20] to develop super-resolution microscope based on blinking fluorophores and principle of localisation. The demonstration of controlled on/off switching of fluorescent proteins had led to the discovery of PALM with a resolution as high as 10 nm. It is important to note that all these far-field super-resolution imaging techniques are all based on fluorescence as a contrast mode.

In any fluorescence microscope, the high energy photon (from lamp or laser) excites fluorophores in the specimen and the excited fluorophore subsequently emits its own lower energy photon. The high-contrast imaging is achieved by using spectral filtering of fluorescence from the excitation light. Imaging protein expression, localisation, and activity in living cells is possible with the development of genetically encoded fluorescent proteins [21, 22]. The high specificity of fluorescence light microscopy facilitates the collection of spatial and functional information about bio-structures using labelled molecules. In this way, the majority of light microscopy applications in life sciences today use fluorescence as a dominating contrast mode.

However, the widely used fluorescence microscopy has certain shortcomings that hinder further growth of the field. Some of these are: (1) Photo-bleaching: the fluorescent molecule on excitation over a period of time accumulates electrons in its excited state that often leads to a chemical damage of fluorophore, resulting in loss of fluorescence, that is photo-bleaching. Photo-bleaching severely limits the time over which a sample can be observed under microscope. (2) Photo-toxicity: this effect often occurs as fluorescent molecules under intense illumination, which have a tendency to generate reactive chemical species. Live cells are susceptible to them, resulting in cell mortality. (3) Low photo-stability: for super-resolution imaging based on on/off switching, typical fluorescent labels are not strong enough to undergo the switching cycle for multiple times, thus limiting the length of total acquisition time. (4) Auto-fluorescence: This reduces contrast by forming an image background that even the best excitation/emission filters could not completely get rid of. These shortcomings

in fluorescence microscopy arise mainly due to the basic requirement of labelling. Therefore, it is more than desirable to develop super-resolution label-free imaging modality based on an alternative contrast agent, such as scattering [23–26].

### ***10.1.2 Plasmonic Nanostructures for Super-Resolution Microscopy***

It is well known that plasmonic nanostructures provide extraordinarily strong scattering, thus ideal for the aim of scattering-based super-resolution imaging [27, 28]. A plasmon is a quantum of collective oscillation of free electrons. It is a quasiparticle observed at the interface of materials with real negative (such as metals or doped semiconductors) and real positive (such as dielectrics or air) dielectric constants. The concentration of electrons is tightly confined to the regions near the nanostructure surface that leads to enhancement in EM fields. The intensity of the enhanced EM fields can exceed  $10^4$ – $10^9$  of the incident light intensity [27]. Interestingly, these regions of enhanced fields are confined to volumes much smaller than the diffraction limit of light. Moreover, plasmonic nanoparticles offer high photo-stability, with near infinite photon budgets, yielding both high localisation precision and long observation times. Note that plasmonic nanostructure produces strong Rayleigh scattering at its plasmon resonance and allows single nanoparticles (NPs) to be easily imaged in an optical microscope. For instance, Rayleigh scattering by an 80 nm gold nanoparticle at surface plasmon resonance (SPR) is about five orders of magnitude higher than emission from a traditional fluorophore, and thus allows higher localisation precision [27, 28]. These properties make plasmonic NPs an attractive alternate in optical super-resolution imaging applications. In addition, it is facilitating to avail the tunability of the surface plasmon resonance (SPR), which is extremely sensitive to the size, shape, and composition of the NPs, as well as its local environment [23]. It is convenient that various facile synthesis routes of plasmonic NPs are well reported in the literature, including methods for its surface modifications towards higher biocompatibility and low toxicity [29]. Below we briefly review recent literatures on the combination of plasmonics for super-resolution imaging, based on the same three super-resolution approaches that we mentioned in the last section.

- (a) Objectives modifications (or super-lens): Plasmonic nanostructures can be explored in the realisation of super-lens and hyper-lens to detect high spatial frequency information from the sample to improve the overall spatial resolution. Zhang et al. demonstrated this using a thin slab of silver as a super-lens to image 60 nm features in a sample [30]. After passing through the super-lens, the high spatial frequency components again evanescently decay, which requires that the imaging lens must be placed in the near-field of the plasmonic super-lens in order to project the image into the far-field. As a super-lens only

enhances evanescent waves across the lens, the goal of a hyper-lens is to project the evanescent waves into the far-field by converting them into propagating waves. A plasmonic hyper-lens [31] consists of alternating layers of a metal and dielectric to form an anisotropic plasmonic material, which has the unique property of propagating high spatial frequencies. These lenses offer the possibility of imaging sub-diffraction-limited objects in real time. However, no exclusive reports on multiple objectives were found for super-resolution imaging.

- (b) Non-uniform illumination/collection: The tailoring of excitation light is achieved by the strong coupling between light and plasmonic materials. The concentration of light to small volume localised at the plasmonic surface is possible. This small region of strongly enhanced EM fields at the plasmonic surface is called as hot spot. The hot spots effectively serve as nanometre-sized excitation sources for any molecule that enters within this small excitation volume. As these hot spots are spatially localised to regions 1–10 nm in size, so, the molecules separated by distances smaller than the diffraction limit can be selectively excited, enabling super-resolution imaging of molecules that would otherwise overlap in a traditional far-field technique [32].

Similar to localised SPR hot spots, surface plasmon polaritons (SPP) standing wave interference patterns were also proved as near-field excitation sources. Using waves with different phases to shift the interference patterns and illuminate different regions of the sample allows reconstruction of a super-resolved image. A particularly interesting application of SPPs to super-resolution imaging is that radiation travelling as an SPP has a wavelength smaller than the original excitation light. This sets up the possibility to use SPPs as both small volume excitation sources as well as coupling agents for projecting high spatial frequencies into the far-field via interference [33].

SPP interferences can improve the resolution in conventional SIM by creating structured illumination patterns with higher spatial frequencies than typical excitation grid patterns. However, in 2010, Lui and co-workers proposed that surface plasmons could form interference patterns for illumination with much higher spatial frequencies, based on the fact that SPPs have larger wave-vectors than free space light. A silver film with periodic slits spaced by  $7.6\ \mu\text{m}$  is used to launch SPPs in opposing directions that form a standing wave, which interfere to double the spatial frequency of the surface plasmon. Liu and co-workers in 2014 [34] has experimentally demonstrated PSIM, which offered an advantage that the resolution is not strictly limited by the numerical aperture of an objective lens but rather by the emission wavelength, SPP wavelength, and interference pattern. But the major limitation of above two methods is the post-processing of images to get final super-resolved image.

Another strategy is to adopt non-uniform collection, such as dark-field microscopy, to resolve individual plasmonic NP within a diffraction-limited spot. Huang et al. devised a technique called photo-stable optical nanoscopy (PHOTON) [35], which relied on deconvolution of overlapping LSPR spectra

from silver nanoparticles of varying sizes. An LSPR spectrum is taken for a single diffraction-limited spot, which has multiple scatterers and the spectral deconvolution of the spot extracts the peak wavelengths of each NP within it. The corresponding diffraction-limited images are acquired at each peak wavelength, which are then fit into two-dimensional Gaussian to localise the emitter associated with each peak wavelength. This process is repeated multiple times to yield a super-resolution image. These results show very good agreement with TEM images.

- (c) Nonlinear absorption and emission (Saturation of emission and all-optical switching): It is well known that fluorescence exhibits saturation at high excitation intensity. In 2007, Fujita et al. [36] developed a super-resolution technique, saturation excitation microscopy (SAX), which is based on extraction of saturated emission. Since saturation starts from the centre of focus, such extraction provides resolution enhancement. In 2013–2014, we found that scattering signals from individual plasmonic nanostructures show strong nonlinearity, and applied SAX to significantly enhance spatial resolution. More details will be given in the following sections.

STED nanoscopy is a well-known strategy for super-resolution imaging based on optically switching on/off fluorophores. In traditional STED, higher STED laser powers lead to higher spatial resolution, but at the expense of dye photostability. Sivan et al. [37] proposed that using plasmonic NPs could address both of these issues. First, a plasmonic NP's light-concentrating ability from the far-field to small near-field volumes could lower the power needed from the STED beam to achieve a particular resolution. Second, if the triplet-state emission wavelength of the fluorophore overlapped with the LSPR spectrum of the NP, the dye stability would be increased due to an increased triplet-state decay rate. Thus, plasmonic-enhanced STED can work both at the lower STED beam power threshold with increased fluorophore photo-stability, but it is still based on fluorescence switching.

In 2016, all-optical switching of pure plasmonic scattering was found in our lab [26]. A simple two-colour method for modulating the scattering intensity from 80 nm gold nanoparticles with a plasmon resonance near 590 nm is used. In that work, a scanning confocal geometry was used to measure backscattering of a 543 nm laser from a gold nanoparticle. Our team developed a modified plasmonic-based STED approach called SUSI, that is suppression of scattering imaging, that can provide  $\lambda/9$  resolution.

In the following, we focus the discussion on super-resolution based on nonlinear absorption and emission. We will start by introducing fluorescence-based SAX and STED microscopy in Sect. 10.2, and then address the discovery of nonlinear emission from plasmonic nanoparticles in Sect. 10.3. The combination of nonlinear plasmonics and super-resolution techniques will be given in Sect. 10.4, along with a brief summary in Sect. 10.5.

## 10.2 Principle of Super-Resolution Based on Nonlinear Absorption and Emission

As mentioned in the previous section, super-resolution can be achieved by nonlinear absorption or emission. Below we specifically review the principle of two techniques, SAX and STED. The former relies on saturation of emission, and resolution is enhanced by extracting the saturated part by temporal modulation and demodulation. The latter is based on all-optical switching and saturation of stimulated emission, which can enhance spatial resolution by adding a spatial modulation pattern to deplete the emission around the centre of focus.

### 10.2.1 Saturation of Emission + Temporal Modulation: SAX

It is well known that fluorescence emission intensity saturates at high excitation power [24]. When a sample is illuminated by a focussed laser light, the saturated excitation dominates in the centre of focus spot due to Gaussian nature of illumination beam. Therefore, the extraction of nonlinear signals allows detecting emission signals from only a small fraction within the emission detection volume, resulting in the spatial resolution enhancement. This is the underlying concept of SAX.

The key of SAX super-resolution is the extraction of nonlinear signals from the mixture of linear and nonlinear signals within the excitation spot. One clever idea invented by Fujita et al. [36] is to adopt temporal modulation of the excitation followed by harmonic demodulation of the emission signal, as shown in Fig. 10.1. Figure 10.1a shows a focussed laser beam in  $x$ - $z$  plane, in which the intensity is higher at the centre. Assume that the intensity at the centre is just enough to induce saturation of emission; then in the edge of the focus, the emission should be linear. By separating the linear and nonlinear part, resolution shall be improved, and the trick to achieve this in SAX is to add temporal sinusoidal modulation in the excitation laser and to separate the nonlinear parts in frequency domain.

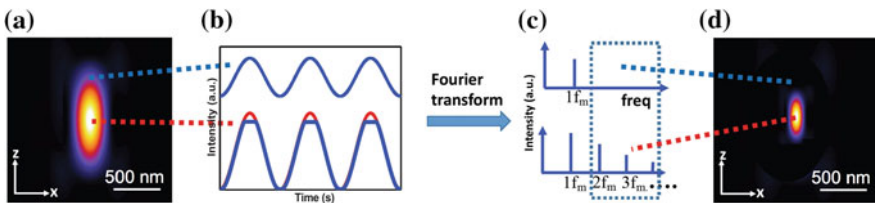


**Fig. 10.1** Demonstration of principle of resolution enhancement in SAX microscopy. **a** A PSF in  $x$ - $z$  direction with tight focussing, showing a typical elongated profile in  $z$ . **b** Excitation spot linear at periphery with single sinusoidal frequency, nonlinear at centre with frequency components; **c** represents the Fourier transforms

More specifically, since there is no nonlinearity in the edge (the blue dotted line), the emission should follow the sinusoidal modulation, as shown in the top curve of Fig. 10.1b. On the other hand, in the centre of focus, the excitation intensity is strong enough to induce saturation, so the corresponding emission in the bottom curve of Fig. 10.1b shows saturated modulation. By taking Fourier transform of the temporal curves, Fig. 10.1c shows their frequency components. Apparently, with linear response (the bottom one), only 1<sup>st</sup> component is observed, but in the nonlinear part, higher harmonics are found. Therefore, by taking the higher harmonics, the resulting PSF can be effectively reduced, leading to resolution enhancement, as shown in Fig. 10.1d. Subsequent laser scanning is necessary to form an image.

The high background elimination property of SAX allows us to observe deep finer structures in a thick sample with high spatial resolution and imaging contrast. However, the requirement of the high excitation intensity does limit the achievable spatial resolution because of photo-bleaching effects and the resultant decrease in signal-to-noise ratio in emission detection [38].

### 10.2.2 All-Optical Switching + Spatial Modulation + Saturation: STED

Figure 10.2a shows the principle of STED microscopy, in which two lasers are used, including an excitation beam (shown in blue colour) and a STED beam at longer wavelength (shown in red colour). One key element of resolution enhancement by STED is the capability of optically switching off spontaneous fluorescence emission (shown in green colour) via stimulated emission. The other key is to spatially modify the STED beam profile into a donut, which has zero intensity at the centre, so that the spontaneous emission is allowed at the centre only, as shown in Fig. 10.2b.

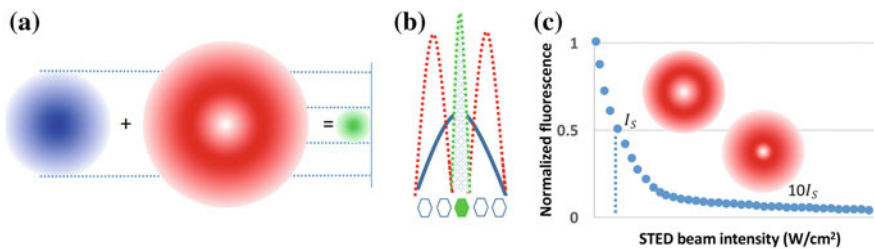


**Fig. 10.2** Demonstration of STED microscopy principle: **a** excitation spot in blue, STED spot in red, and resulting fluorescence emission in green. **b** Cross-sectional intensity profile of **(a)**, showing that the fluorescent molecules (green circles in the bottom) are switched off by the STED beam (red lines), leaving only a narrow region in the centre to emit fluorescence (green lines). **c** Owing to limited number and lifetime of fluorescent molecules, saturation of STED leads to higher resolution at higher intensity

Nevertheless, it is important to realise that the donut hole is produced by interference of light waves, and thus cannot reduce below the diffraction limit. By increasing the intensity of STED beam, the saturation of stimulated emission enables further localisation of spontaneous emission, as shown in Fig. 10.2c, thus providing diffraction-unlimited resolution. The lateral resolution is defined as  $\Delta r = \frac{\lambda}{\text{NA}\sqrt{1+(I/I_S)}}$ , where  $\lambda$  is the wavelength, NA is the numerical aperture,  $I$  is the excitation intensity, and  $I_S$  is the saturation intensity. The last term can be derived by spontaneous emission lifetime and absorption cross-section of the fluorescent molecule.

The stimulated emission and STED beam can be filtered out by using wavelength filter and only the spontaneous emission from the centre area of excitation spot is detected. On scanning the excitation and STED beams together on the sample and measuring the spontaneous emission intensity, the distribution of fluorescent probes in the sample can be imaged with an increased spatial resolution. In each excitation cycle, fluorophores absorb the photons and get promoted to excited state and within nanoseconds of lifetime, it undergoes spontaneous emission. The STED beam should be enough intense to achieve stimulated emission than spontaneous emission. But this increase in intensity of STED beam leads to the problems of photo-bleaching and photo-damage.

There are several variants of STED that reduce beam intensity requirement [39]. For example, RESOLFT (reversible saturable optical fluorescence transitions) technique adopts switchable fluorescent probe which has much longer lifetime compared to that of electronic transition [40]. Another technique is named as GSD (ground state depletion), also invented by Stefan Hell, who use long lifetime triplet states of fluorescent molecules to reduce saturation intensity  $I_S$  [41].

## 10.3 Discovery of Nonlinear Plasmonic Scattering

In the preceding section, super-resolution is based on nonlinearity of fluorescence emission. However, as mentioned earlier, fluorescence-based techniques suffer with problems of photo-bleaching, photo-toxicity, auto-fluorescence, and so on. Thereby, it is highly desirable to develop super-resolution techniques with an alternative contrast agent. Now, in this section, we introduce our recent discovery of nonlinear scattering by plasmonic nanostructures.

### 10.3.1 Nonlinear Scattering of Au Nanospheres

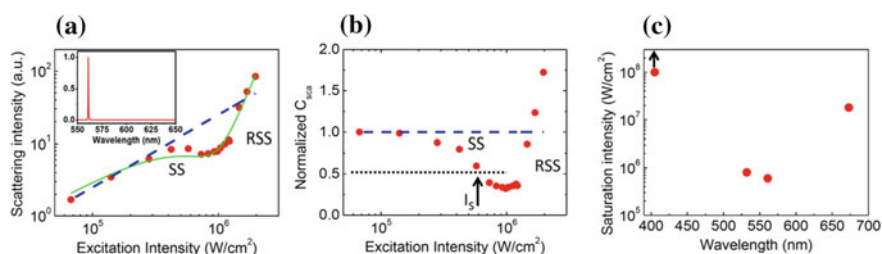
In plasmonic materials, saturable and reverse saturable absorption (SA and RSA) are one of the most studied nonlinearities, and it has proved its applicability in optical switching, optical limiting, all-optical processing, and so on. However, convention-

ally z-scan technique is used to study these absorption nonlinearities, so only ensemble behaviours are observed. Recently, our group proposed to use xy-scan in a laser scanning microscope to study optical properties of a single plasmonic nanostructure [24], leading to the novel discovery of saturable and reverse saturable scattering, as shown below.

Figure 10.3a presents scattering intensity versus excitation intensity on a single gold nanosphere with 80 nm diameter. The excitation wavelength is 561 nm, which is located near the plasmonic resonance peak of the nanosphere. At low intensity ( $<2 \times 10^5$  W/cm<sup>2</sup>), the intensity dependence is linear. With increasing excitation intensity, scattering deviates from linear trend showing saturation of scattering (SS). Further increase in excitation intensity ( $>10^6$  W/cm<sup>2</sup>) induce a sudden rise of the scattering intensity, exceeding the linear trend, and we call this as reverse saturation of scattering (RSS). The inset shows the backward spectrum from a single gold nanosphere (GNS), to rule out the possibility of other emissions such as two-photon luminescence.

Note that in Fig. 10.3a, the slope in the RSS region is much larger than that of the linear region, indicating the existence of large high-order nonlinearity. It is well known that resolution can be enhanced with high-order nonlinearity. We will show it in Sect. 10.4.

These results are depicted in terms of normalised scattering cross-section  $C_{sca}$  (representing the scattering ability of GNS) in Fig. 10.3b. At low intensity,  $C_{sca}$  is constant, that is linear response. In the SS and RSS regions,  $C_{sca}$  reduces and increases, respectively, that is transmission is enhanced and reduced, respectively. This is similar to SA and RSA, suggesting similar underlying physical mechanism. Additional verification is done by fitting the curve in Fig. 10.3a using a typical nonlinear equation,  $I_{sca} = \alpha I + \beta I^2 + \gamma I^3$ , where  $\alpha$  is linear and  $\beta, \gamma$  are nonlinear scattering coefficients and a good match between the values of  $\beta/\alpha$  and  $\gamma/\alpha$  with the same values derived from absorption-based experiment was noted.



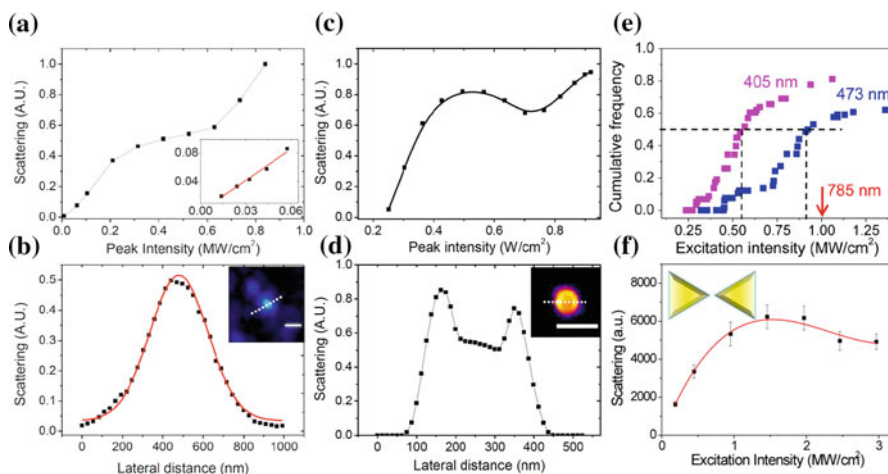
**Fig. 10.3** **a** Scattering intensity dependency from a single gold nanosphere under 561 nm excitation, showing clear saturation of scattering (SS) and reverse saturation of scattering (RSS) behaviours. The inset presents the emission spectrum, manifesting that only scattering signal is observed. **b** Normalised scattering cross-section, which is unity at low intensity, reduces at SS region, and increases above unity at RSS region. **c** Saturation intensity  $I_S$  with different excitation wavelengths. Reproduced from [24] with permission from American Chemical Society

Figure 10.3c shows that as the excitation wavelength is closer to plasmonic resonance peak, the required intensity for saturation is smaller, suggesting that the saturable scattering is dominated by surface plasmon resonance of GNS.

### 10.3.2 Nonlinear Scattering in Various Plasmonic Structures

In addition to gold nanospheres, we found that the nonlinear scattering is ubiquitous in various plasmonics materials and structures [23]. Here we give some examples of gold nanorods (GNR), silver nanosphere (SNS), and gold bowtie antenna. These studies not only help to extend the applicable wavelength ranges but also clarifies the mechanism of nonlinear scattering.

The GNR used in our study has 60 nm length and 10 nm width, resulting in a strong resonance peak at  $\sim 800$  nm that are preferred for deep-tissue imaging applications. By using a 785 nm excitation, which is close to the peak, Fig. 10.4a shows a clear nonlinear behaviour in GNRs. The threshold of saturation in scattering locates at about  $3 \times 10^5$  W/cm<sup>2</sup>, while the onset of reverse saturation in scattering occurs at  $7 \times 10^5$  W/cm<sup>2</sup>. Inset in Fig. 10.4a shows that scattering signal is linearly proportional to the excitation at lower excitation intensities. Figure 10.4b presents the PSF of a single GNR at excitation intensity that is adequate to induce saturation, but not reverse saturation, manifesting that nonlinear effect starts at the centre of focus under



**Fig. 10.4** **a** Scattering intensity at different 785 nm excitation intensities of a GNR; **b** PSF profile at  $5.2 \times 10^5$  W/cm<sup>2</sup> demonstrating saturation in a single GNR; **c** scattering intensity of a single 80 nm SNS at different 473 nm excitation intensities; **d** PSF profiles at  $7.8 \times 10^5$  W/cm<sup>2</sup> demonstrating saturation in a single SNS; **e** statistical threshold intensities for nonlinear scattering of SNS with different excitation wavelengths; **f** demonstration of nonlinear scattering in gold nanoantenna. Reproduced from [23] with permission from American Chemical Society

a laser-scanning microscope, that is  $xy$ -scan. Therefore, if the nonlinear response can be separated from linear response, the effective PSF would be reduced, leading to enhancement of spatial resolution, as demonstrated in Sect. 10.4.

For SNS, its diameter is 80 nm, leading to two resonance peaks at 400 and 490 nm. Figure 10.4c shows a clear nonlinear behaviour of a single 80 nm SNS using 473 nm excitation of wavelength, which is located inside the broad 490 nm resonance. Similar to the response of gold nanostructures, both saturation and reverse saturation are observed. Saturation in scattering is observed within the excitation range of  $5 \times 10^5$ – $7 \times 10^5$  W/cm<sup>2</sup>, and higher intensity induces reverse saturation. Once again, the nonlinear response can be visualised in the laser scanning PSF, that is  $xy$ -scan, as given in Fig. 10.4d. Here deep saturation is observed, resulting in an unusual PSF profile.

Based on Mie theory calculation, in the 80 nm SNS, absorption dominates at the 400 nm resonance peak, while scattering is the main component of the 490 nm resonance. It thus provides an interesting opportunity to clarify the mechanism of nonlinear scattering. Figure 10.4e shows the comparison of threshold laser intensities for nonlinear scattering using 405, 473, and 785 nm lasers. More than 100 nanoparticles are analysed, and the percentages of nanoparticles that start to show nonlinear scattering at certain excitation intensity is presented in the vertical axis. A dashed horizontal line marks the threshold intensity when 50% of the SNSs show nonlinear scattering, and apparently 405 nm gives lower threshold intensity. That is, nonlinear scattering is more probable to occur with the 405 nm laser, manifesting that SPR absorption is dominant. On the other hand, for the 785 nm laser, which is far from the SPR absorption of SNSs, no nonlinear scattering is observed at all. Since the consequence of absorption is temperature rise, the major mechanism behind the nonlinear scattering should be photo-thermal effect.

One particular interesting application of plasmonics is the hot spot created by sharp structures or neighbouring nanoparticles. Figure 10.4f presents the scattering intensity dependence of a gold bowtie antenna, which is composed of two triangular gold nanostructures, whose edge length is 150 nm, and the gap between them is 10 nm. It is interesting to see that saturation of scattering is again observed in the antenna, manifesting that nonlinear plasmonic scattering is universal with different materials and structures.

### 10.3.3 All-Optical Switch on a Plasmonic (Au) Nanospheres

In the preceding section, we have shown that saturation of plasmonic scattering is ubiquitous, and have found that deep saturation, that is scattering reduces as excitation intensity increases, is obtained when excitation wavelength is close to the plasmonic absorption peak. Here we show that the deep saturation affects not only the excitation wavelength, but also other wavelengths inside the plasmonic band, thus enabling all-optical switch of plasmonic scattering for the first time [26].

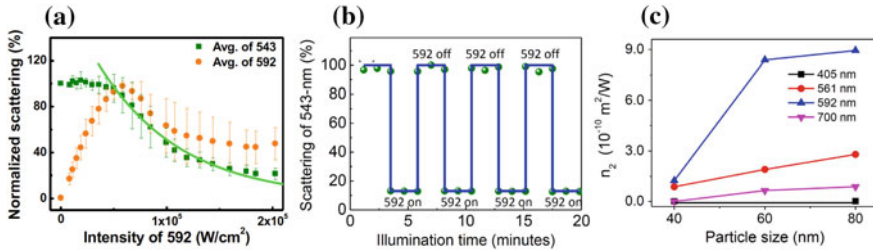


**Fig. 10.5** Demonstration of all-optical switch based on GNS: **a** Scattering intensity of probe beam ( $\lambda = 543$  nm) by single GNS as a function of control beam ( $\lambda = 592$  nm) intensity; **b** reversible switching of scattering at control beam intensity  $2 \times 10^5$  W/cm<sup>2</sup> without bleaching; **c** nonlinear index distribution with different GNS sizes and wavelengths. Reproduced from [26] with permission from Springer Nature

To demonstrate the all-optical switch capability, two lasers (543 and 592 nm) are focussed on a single 80 nm GNS, whose resonance wavelength is centred at 590 nm, and broad enough to cover the 543 nm. Figure 10.5a presents the scattering intensities of these two wavelengths, where the 543 nm ‘probe’ beam is fixed at low intensity (30 W/cm<sup>2</sup>) and the 592 nm ‘control’ beam gradually increases its intensity. The orange dots in Fig. 10.5a are the scattering intensity of the 592 nm beam, showing very deep saturation as we expected. The green dots represent the scattering intensity of the 543 nm beam. At low 592 nm control beam intensity, the 543 nm probe beam scattering remains constant.

The most intriguing finding is that when the intensity of 592 nm beam increases into the nonlinear regime, the scattering at 543 nm begins to decrease. Remarkably, when the excitation intensity at 592 nm reaches  $2 \times 10^5$  W/cm<sup>2</sup>, more than 80% of the scattering at 543 nm is suppressed, demonstrating the all-optical switching behaviour. The corresponding average power is less than 100  $\mu$ W, and the energy absorbed by the nanoparticle is less than the requirement to write a bit in a DVD. The repeatability and long-term stability of the all-optical switch is demonstrated in Fig. 10.5b.

It is well known that nonlinear index can be derived from the power dependency, and the results are given in Fig. 10.5c. If the mechanism is based on photo-thermal effect, as we concluded in the last section, the nonlinear index should be very sensitive to both particle sizes and excitation wavelengths. This is what we observed in Fig. 10.5c. Apparently, when the excitation wavelength is closer to the peak of SPR band, where the absorption is greatly enhanced, the nonlinear index is larger. Note that when wavelength is around the peak of SPR, the nonlinearity can be as high as  $8.8 \times 10^{-10}$  m<sup>2</sup>/W, which is the largest nonlinear index ever reported in GNS. The photo-thermal nonlinearity is much larger than possible contribution from hot electron effects.

On the other hand, the nonlinear index grows higher with large particles. Since the absorption cross-section increases with the volume of nanoparticle, while heat

dissipation is proportional to the surface area of the particle, it is reasonable to expect higher temperature for larger particles at equilibrium.

Although we focus on super-resolution imaging in this article, we would like to mention that one potential application of the plasmonic all-optical switch is towards realisation of high-density photonic circuits. Our novel plasmonic all-optical switch has a mode volume less than  $0.001 \mu\text{m}^3$ . The modulation depth of this ultra-small switch reaches 80%, and the switching behaviour is active within the broad band of plasmonic resonance. Our work could open the possibility to realise high-density integrated photonic nanocircuits in the future.

Now, based on our recent discovery of plasmonic nonlinear scattering, let us continue the journey to explore how one can utilise the property of nonlinear emission due to plasmonic nanoparticles to achieve super-resolution imaging.

## 10.4 Super-Resolution Based on Nonlinear Scattering

In the previous section, we have unravelled three novel nonlinearities in plasmonic scattering, that is saturation, reverse saturation, and all-optical switching. Here we are going to present three methods to enhance spatial resolution based on these nonlinearities. The first one is to use the high-order nonlinearity of reverse saturation, which causes significant reduction of PSF directly under a laser scanning microscope. The second one is the combination of saturable scattering and SAX, where the latter extracts nonlinear components of the former, and thus enhances spatial resolution. The third method is to adopt all-optical switching of scattering into a STED-like setup, to “turn off” scattering around the centre of a PSF, leading to resolution enhancement.

### 10.4.1 Super Resolution Based on Reverse Saturation of Scattering

Figure 10.6 presents a very interesting shape change of PSF from a single 80 nm GNS, as the excitation intensity gradually increases. At low excitation intensity in Fig. 10.6a, that is the linear response region, the PSF fits well to a Gaussian profile, as we expected. As excitation intensity exceeds  $10^5 \text{ W/cm}^2$  in Fig. 10.6b, flattening at the centre of PSF is observed, manifesting that saturation of scattering starts from the region with largest intensity. Figure 10.6c is the situation of deep saturation, where scattering intensity reduces with increase of excitation intensity. This unusual phenomenon creates an unexpected donut-like PSF, whose side lobes exhibit width of only 40 nm ( $\lambda/13$ ).

When the excitation intensity further increases to above  $10^6 \text{ W/cm}^2$ , the scattering signal at the centre of PSF rises, showing an onset of reverse saturation, while

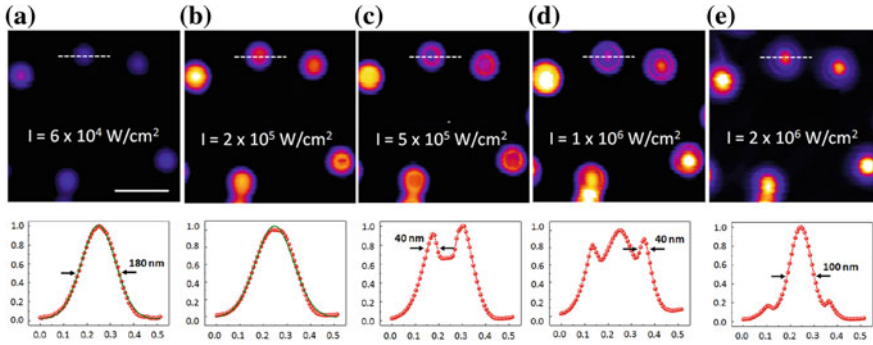


**Fig. 10.6** PSF variation with increasing excitation intensity from left to right. Top column shows the backscattering images, with excitation intensity marked in the centre, and lower column gives signal profile of a selected GNS. Reproduced from [24] with permission from American Chemical Society

the donut-like side lobes still remain, as shown in Fig. 10.6d. As mentioned in Sect. 10.3.1, higher-order nonlinearities exist in the reverse saturation region, whose slope of power dependency is much larger than one. The high-order nonlinearity leads to significant reduction of PSF below 100 nm in width, as demonstrated in Fig. 10.6e. This mechanism is applicable to super-resolution imaging in plasmonic structures by any conventional laser scanning microscope, without the need of system modification.

#### 10.4.2 *Super-Resolution Based on Combination of Saturation of Plasmonic Scattering and SAX*

The second method is to apply SAX to extract nonlinear components in saturation of plasmonic scattering. In Fig. 10.6b of the last section, we have shown that saturation starts from a small region in the centre of PSF. Therefore, if the saturated part can be separated from the linear part, spatial resolution can be enhanced. As introduced in Sect. 10.2.1, SAX uses temporal modulation of excitation beam, and Fourier analysis to extract harmonics of modulation frequencies, which corresponds to high-order nonlinearities, thus enhancing spatial resolution. However, earlier demonstration of SAX is based on fluorescence nonlinearity. Here we show not only that SAX helps to improve resolution based on nonlinearities of plasmonic scattering but that plasmonic SAX provides much higher resolution than fluorescence SAX, due to larger high-order nonlinearity in plasmonic scattering.

Figure 10.7a shows the result of harmonic frequency extraction of SAX. The modulation frequency is 10 kHz ( $f_m$ ), and two harmonics at double ( $2f_m$ ) and triple ( $3f_m$ ) frequencies are detected with a lock-in amplifier. By comparing with Fig. 10.3a and Fig. 10.6b, where nonlinear response starts around the intensity of  $2 \times 10^5$  W/cm<sup>2</sup>, it

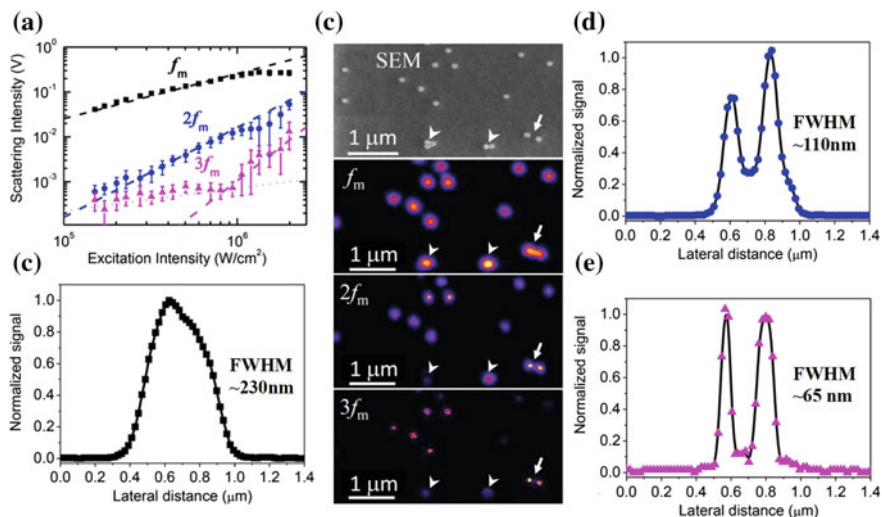


**Fig. 10.7** Demonstration on super-resolution based on saturable scattering combined with SAX: **a** Emergence of harmonics ( $f_m$ ,  $2f_m$ ,  $3f_m$ ) with increasing excitation intensity; **b** reference SEM image at top; super-resolved SAX images at below; **c–e** line profiles of the two white arrow marked GNSs corresponds to  $1f_m$ ,  $2f_m$ , and  $3f_m$ , respectively. Reproduced from [25] with permission from American Physical Society

is reasonable that harmonic components start to emerge at the same intensity range. It is important to notice that the slopes of the  $2f_m$  and  $3f_m$  components are much larger than the linear one ( $f_m$ ). This is the fundamental mechanism of resolution enhancement with SAX and nonlinear response.

By combining the demodulated frequency signals from a lock-in amplifier and a laser-scanning microscope, images of plasmonic nanostructures formed on a pixel-by-pixel basis. Figure 10.7b presents the images of  $1f_m$ ,  $2f_m$ , and  $3f_m$ , respectively, together with a scanning electron microscope image for comparison. The arrow in Fig. 10.7b indicates two nanoparticles that are not distinguishable in the  $1f_m$  image, whose resolution is equivalent to diffraction limit. Intriguingly, these two nanoparticles are well resolved in  $2f_m$  and  $3f_m$  images. The corresponding  $1f_m$ ,  $2f_m$ , and  $3f_m$  signal profiles are plotted in Fig. 10.7c–e, respectively, manifesting significant resolution enhancement. The FWHM of PSF is marked in each panel. With  $3f_m$  demodulation, resolution enhances to 65 nm, which is equivalent to  $\lambda/8$  (excitation wavelength is 561 nm in this case).

There are a few points for discussion. First, the resolution enhancement capability of plasmonic SAX is better than fluorescence SAX. From [36], in fluorescence SAX,  $nf_m$  provides at most  $\sqrt{n}$ -fold resolution enhancement. Nevertheless, plasmonic SAX apparently exceeds this limitation, possibly due to the unusual nonlinear response, as shown in Figs. 10.3a and 10.5a. It gives us a hint that SAX resolution may be unlimited if proper nonlinear response is discovered.

Second, different from incoherent fluorescent molecules, plasmonic structures exhibit coherent coupling when two or more metallic nanoparticles are adjacent to each other. As we can see in Fig. 10.7b, the arrowheads mark particles that aggregate together, which change the resonant wavelength. Therefore, although these aggregates still exhibit strong scattering intensity in the  $1f_m$  image, their  $2f_m$  and  $3f_m$  signals are relatively weaker compared to uncoupled nanoparticles. That is, SAX may be used to detect plasmonic coupling beyond diffraction limit.

Third, most of the current super-resolution techniques are not able to enhance resolution in tissues. For example, wide-field-based localisation techniques do not provide optical sectioning capability; thus lacking axial contrast. STED and SIM require spatial beam engineering, and thus are susceptible to beam distortion due to scattering/aberration. On the contrary, SAX relies on temporal modulation that is less affected when penetrating into tissues, and therefore should be the best candidate for deep-tissue resolution enhancement. This has been realized recently with plasmonic SAX, which provides three-fold resolution enhancement by  $3f_m$  signals throughout the whole working distance of an objective, that is 200  $\mu\text{m}$ , providing inspirational possibility towards deep-tissue super-resolution imaging [42].

### 10.4.3 Super-Resolution Based on Optical Suppression of Scattering Imaging (SUSI)

In Sect. 10.2.2, we have explained how STED improves spatial resolution via all-optical switch of fluorescence emission and a donut STED beam. In Sect. 10.3.3, we presented optically switchable scattering from plasmonic nanoparticles. Here we combine the two concepts to achieve super-resolution imaging based on suppression of scattering imaging (SUSI), as demonstrated in Fig. 10.8. Similar to the condition in Fig. 10.5, two lasers at 543 and 592 nm are aligned together.

In Fig. 10.8a, the top row shows a laser scanning image based on a single solid 543 nm beam (see inset), and the bottom row gives the PSF intensity profile for the nanoparticles in the centre of imaging area, with FWHM of 180 nm. Apparently, the resolution is inadequate to resolve whether there are two particles.

In Fig. 10.8b, the inset shows that a 592 nm beam is converted into a donut shape by a vortex phase plate, and the central hole is overlapped with the solid 543 nm excitation, similar to STED implementation. As mentioned in Fig. 10.5, when the 592 nm laser intensity increases to  $10^6 \text{ W/cm}^2$  (about 100  $\mu\text{W}$  in power), scattering of 543 nm is significantly suppressed, leading to remarkable enhancement of spatial resolution in Fig. 10.8b. Quantitatively, the averaged FWHM of a single particle is  $120 \pm 4 \text{ nm}$  at this intensity, agreeing well with theoretical prediction, and it is now possible to distinguish two particles in the centre of the image.

To further enhance spatial resolution, deconvolution is adopted in Fig. 10.8c, which achieves resolution of 60 nm (i.e.  $\lambda/9$ ). It is important to notice that not only the central region exhibits enhanced resolution but all nanoparticles in the imaging

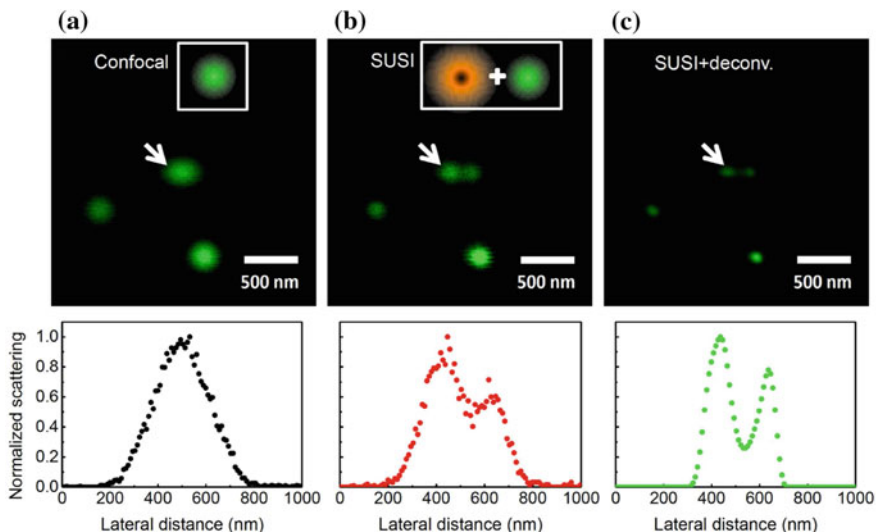


**Fig. 10.8** Demonstration of SUSI of 543 nm scattering, where the upper row shows laser-scanned images, and the bottom row are intensity profiles corresponding to the arrowed particle in the centre. **a** Confocal laser scanning microscopic image with only 543 nm excitation. **b** Combination of a donut-shaped 592 nm suppression beam and the same solid 543 nm excitation, that is SUSI, resolution of the 543 nm scattering image is obviously improved by all-optical switching of scattering. **c** Deconvolution helps to further enhance spatial resolution. Reproduced from [26] with permission from Springer Nature

area shows reduced FWHM, manifesting that the switchable scattering effect is universal to all plasmonic particles.

### 10.5 Summary

When considering imaging technologies, there are several important factors, including contrast, resolution, penetration depth, imaging speed, and so on. Among them, contrast should be the most important factor, since it determines the image visibility. In the last century, that is twentieth century, the most significant developments in the field of microscopy are mostly related to contrast; for instance, phase contrast, differential interference contrast, fluorescence labelling, and so on. The last one has been widely used in biology. With mature labelling methods, in the first two decades of the twenty-first century, the most significant development in microscopy is the emergence of super-resolution techniques, most of which rely on nonlinearity (switch on/off, blinking, or saturation) of fluorescence.

In this chapter, we introduce novel nonlinearity of scattering from plasmonic nanoparticles, and demonstrate that resolution enhancement is achieved with various nonlinearities, including reverse saturation, saturation plus SAX, and all-optical

switchable scattering plus STED-like setup. These nonlinear plasmonic scattering have been successfully applied to live cell imaging. Although strictly speaking, the metallic-nanoparticle-based imaging should not be considered as a label-free approach in biological samples, it does provide 'label-free' imaging for plasmonic nanocircuits with unprecedented resolution. In addition, since the nonlinear scattering is based on photo-thermal effect, it is possible to extend similar approaches into dielectric materials or even individual cell sub-organelles, to realise 'label-free' scattering super-resolution imaging in cells and tissues.

## References

1. G.B. Airy, On the diffraction of an object-glass with circular aperture. *Trans. Camb. Philos. Soc.* **5**(3), 283–291 (1835)
2. E. Abbe, Beiträge zur theorie des mikroskops und der mikroskopischen wahrnehmung. *Archiv für mikroskopische Anatomie* **9**(1), 413–418 (1873)
3. L. Rayleigh, On the theory of optical images with special reference to microscopy. *Philos. Mag.* **42**(255), 167–195 (1896)
4. G. Binnig, C.F. Qate, C. Gerber, Atomic force microscope. *Phys. Rev. Lett.* **56**(9), 930–933 (1986)
5. E. Ruska, The development of the electron microscope and of electron microscopy. *Angew. Chemie.* **26**(7), 595–706 (1987)
6. S.W. Hell, Far-field optical nanoscopy. *Science* **316**(5828), 1153–1158 (2007)
7. A. Stemmer, M. Beck, R. Foilka, Widefield fluorescence microscopy with extended resolution. *Histochem. Cell Biol.* **130**, 807–817 (2008)
8. M. Minsky, Microscopy apparatus. US patent 3013467 (1961)
9. W. Denk, J. Stricker, W. Webb, Two photon laser scanning fluorescence microscopy. *Science* **248**(4951), 73–76 (1990)
10. W.R. Zipfel, R.M. Williams, W.W. Web, Nonlinear magic: multiphoton microscopy in the biosciences. *Nat. Biotechnol.* **21**(11), 1369–1377 (2003)
11. C.J. Engelbrecht, E.H.K. Stelzer, Resolution enhancement in a light-sheet-based microscope (SPIM). *Opt. Lett.* **31**(10), 1477–1479 (2006)
12. R.C. Dunn, Near field scanning optical microscopy. *Chem. Rev.* **99**(10), 2891–2928 (1999)
13. G.I. Mashanov, D. Tacon, A.E. Knight, M. Peckham, J.E. Molloy, Visualizing single molecules inside living cells using total internal reflection fluorescence. *Methods* **29**(2), 142–152 (2003)
14. M.G.L. Gustafsson, Extended resolution fluorescence microscopy. *Curr. Opin. Struct. Biol.* **9**(5), 627–634 (1999)
15. S.W. Hell, E.H.K. Stelzer, Properties of a 4PI confocal fluorescence microscope. *J. Opt. Soc. Am. A* **9**(12), 2159–2166 (1992)
16. M.G.L. Gustafsson, D.A. Agard, J.W. Sedat, Sevenfold improvement of axial resolution in 3D widefield microscopy using two objective lenses. *Proc. SPIE* **2412**, 147–156 (1995)
17. M.G.L. Gustafsson, Surpassing the lateral resolution limit by a factor of two using structured illumination microscopy. *J. Microsc.* **198**(2), 82–87 (2000)
18. S.W. Hell, J. Wichmann, Breaking the diffraction resolution limit by stimulated-emission—stimulated-emission-depletion fluorescence microscopy. *Opt. Lett.* **19**(11), 780–782 (1994)
19. R.M. Dickson, A.B. Cubitt, R.Y. Tsien, W.E. Moerner, On/off blinking and switching behaviour of single molecules of green fluorescent protein. *Nature* **388**(6640), 355–358 (1997)
20. E. Betzig, G.H. Patterson, R. Sougrat, O.W. Lindwasser, S. Olenych, J.S. Bonifacino, M.W. Davidson, J. Lippincott-Schwartz, H.F. Hess, Imaging intracellular fluorescent proteins at nanometer resolution. *Science* **313**(5793), 1642–1645 (2006)

21. A.H. Coons, H.J. Creech, R.N. Jones, E. Berliner, The demonstration of pneumococcal antigen in tissues by the use of fluorescent antibody. *J. Immunol.* **45**(3), 159–170 (1942)
22. D.C. Prasher, V.K. Eckenrode, W.W. Ward, F.G. Prendergast, M.J. Cormier, Primary structure of the *Aequorea-victoria* green-fluorescent protein. *Gene* **111**(2), 229–233 (1992)
23. Y.T. Chen, P.H. Lee, P.T. Shen, J. Launer, R. Oketani, K.Y. Li, Y.T. Huang, K. Masui, S. Shoji, K. Fujita, S.W. Chu, Study of nonlinear plasmonic scattering in metallic nanoparticles. *ACS Photonics* **3**(8), 1432–1439 (2016)
24. S.W. Chu, H.Y. Wu, Y.T. Huang, T.Y. Su, H. Lee, Y. Yonemaru, M. Yamanaka, R. Oketani, S. Kawata, S. Shoji, K. Fujita, Saturation and reverse saturation of scattering in a single plasmonic nanoparticle. *ACS Photonics* **1**(1), 32–37 (2014)
25. S.W. Chu, T.Y. Su, R. Oketani, Y.T. Huang, H.Y. Wu, Y. Yonemaru, M. Yamanaka, H. Lee, G.Y. Zhuo, M.Y. Lee, S. Kawata, K. Fujita, Measurement of a saturated emission of optical radiation from gold nanoparticles: application to an ultrahigh resolution microscope. *Phys. Rev. Lett.* **112** (1), 017402–017404 (2014)
26. H.Y. Wu, Y.T. Huang, P.T. Shen, H. Lee, R. Oketani, Y. Yonemaru, M. Yamanaka, S. Shoji, K.H. Lin, C.W. Chang, S. Kawata, K. Fujita, S.W. Chu, Ultrasmall all-optical plasmonic switch and its application to super-resolution imaging. *Sci. Rep.* **6**, 24293 (2016)
27. K.A. Willets, A.J. Wilson, V. Sunderesan, P.B. Joshi, Super-resolution imaging and plasmonics. *Chem. Rev.* **117**(11), 7538–7582 (2017)
28. M. Kauranen, A.V. Zayats, Nonlinear plasmonics. *Nat. Photonics* **6**(11), 737–748 (2012)
29. P. Zhao, N. Li, D. Astruc, State of the art in gold nanoparticle synthesis. *Coord. Chem. Rev.* **257**(3–4), 638–665 (2013)
30. N. Fang, H. Lee, C. Sun, X. Zhang, Sub-diffraction-limited optical imaging with a silver superlens. *Science* **308**(5721), 534–537 (2005)
31. Z. Liu, H. Lee, Y. Xiong, C. Sun, X. Zhang, Far-field optical hyperlens magnifying sub-diffraction-limited objects. *Science* **315**(5819), 1686–1686 (2007)
32. H. Wang, C.S. Levin, N.J. Halas, Nanosphere arrays with controlled sub-10-nm gaps as surface-enhanced Raman spectroscopy substrates. *J. Am. Chem. Soc.* **127**(43), 14992–14993 (2005)
33. I.I. Smolyaninov, Y.J. Hung, C.C. Davis, Super-resolution optics using short-wavelength surface plasmon polaritons. *J. Mod. Opt.* **53**(16–17), 2337–2347 (2006)
34. F. Wei, Z. Liu, Plasmonic structured illumination microscopy. *Nano Lett.* **10**(7), 2531–2536 (2010)
35. T. Huang, X.X. Nancy, Multicolored nanometre-resolution mapping of single protein-ligand binding complexes using far-field photo-stable optical nanoscopy (PHOTON). *Nanoscale* **3**(9), 3567–3572 (2011)
36. K. Fujita, M. Kobayashi, S. Kawano, M. Yamanaka, S. Kawata, High-resolution confocal microscopy by saturated excitation of fluorescence. *Phys. Rev. Lett.* **99**(22), 228105 (2007)
37. Y. Sivan, Y. Sonnefraud, S. Keña-Cohen, J.B. Pendry, S.A. Maier, Nanoparticle-assisted stimulated-emission-depletion nanoscopy. *ACS Nano* **6**(6), 5291–5296 (2012)
38. M. Yamanaka, N.I. Smith, K. Fujita, Introduction to super-resolution microscopy. *Microscopy* **63**(3), 177–192 (2014)
39. H. Blom, J. Widengren, Stimulated emission depletion microscopy. *Chem. Rev.* **117**(11), 7377–7427 (2017)
40. M. Hofmann, C. Eggeling, S. Jakobs, S.W. Hell, Breaking the diffraction barrier in fluorescence microscopy at low light intensities by using reversibly photoswitchable proteins. *Proc. Natl. Acad. Sci. U. S. A.* **102**(49), 17565–17569 (2005)
41. S.W. Hell, M. Kroug, Ground-state-depletion fluorescence microscopy: a concept for breaking the diffraction resolution limit. *Appl. Phys. B* **60**(5), 495–497 (1995)
42. G. Deka, K. Nishida, K. Mochizuki, H.-X. Ding, K. Fujita, S.W. Chu, Resolution enhancement in deep-tissue nanoparticle imaging based on plasmonic saturated excitation microscopy. *APL Photonics* **3**(3), 031301 (2018)

# Chapter 11

## Label-Free Super-Resolution Microscopy by Nonlinear Photo-modulated Reflectivity



Omer Tzang, Dror Hershkovitz and Ori Cheshnovsky

**Abstract** Nonlinear photo-modulated reflectivity (NPMR) for far-field, label-free, super-resolution (SR) microscopy is based on the nonlinear changes in the reflectance of materials, induced by an ultra-short pump pulse. In NPMR, a modulated train of pump pulse is focused on the sample that photo-excites temperature and/or charge-carriers changes, spatially distributed inside the diffraction-limited spot. A spatially overlapping, delayed, and unmodulated train of probe pulse monitors the resulting nonlinear reflectance changes by the detection of the high harmonics in the probe reflectance. The resulting point spread function (PSF) of the combined pump and probe is narrower than the diffraction-limited PSF, and the improvement in resolution scales like  $\sqrt{n}$ , where  $n$  is the nonlinearity order. NPMR is suitable to characterize semiconductors and metals in vacuum, ambient and liquid, semi-transparent and opaque systems. In order to detect weak high-order nonlinearities at the harmonics of the modulation frequencies, pure sine modulation is required. We have succeeded in modulating our pump source with harmonic impurity down to  $10^{-4}$ . Examples of resolution enhancement include nanostructured silicon, plasmonic gold surfaces, and vanadium dioxide ( $\text{VO}_2$ ) upon photo-induction of its characteristic insulator-to-metal transition. To further reduce the PSF and improve the resolution, it is possible to couple NPMR to other resolution-enhancement approaches, such as spatial modulation and apodization of the pump beam. Additionally, under specific conditions, the method can be simplified to use a single-laser pulse. Finally, we show that the nonlinear response to photo-excitation can be coupled to other SR modalities, such as Raman scattering and nonlinear photo-acoustic signals.

---

O. Tzang · D. Hershkovitz · O. Cheshnovsky (✉)  
School of Chemistry, The Raymond and Beverly Sackler, Faculty of Exact Sciences, Tel Aviv University, Tel Aviv 6997801, Israel  
e-mail: [orich@post.tau.ac.il](mailto:orich@post.tau.ac.il)

© Springer Nature Switzerland AG 2019  
V. Astratov (ed.), *Label-Free Super-Resolution Microscopy*,  
Biological and Medical Physics, Biomedical Engineering,  
[https://doi.org/10.1007/978-3-030-21722-8\\_11](https://doi.org/10.1007/978-3-030-21722-8_11)

261

## 11.1 Introduction

The widely spread technology of microscopy can offer tremendous amount of information about the structural, electronic, optical, and chemical properties of materials, as well as a means to manipulate and trigger processes in materials and devices. Regrettably, in its conventional implementation, the spatial resolution of probing and manipulating materials is limited to about  $\lambda/2$ , due to the wave-like nature of light. The quest to understand structure, dynamics, and function at the nanoscale has inspired new ultra-high-resolution imaging techniques. In particular, optical microscopy has succeeded in surpassing the Abbé resolution limit ( $\sim 0.5\lambda$ ), either by near-field techniques [1] or by far-field super-resolution (SR) techniques, such as stimulated emission depletion (STED) [2, 3], photo-activated localization microscopy (PALM), stochastic optical reconstruction microscopy (STORM) [4, 5], saturated absorption (SAX) [6], structured illumination [7], SR optical fluctuation imaging (SOFI) [8], and quantum emitters microscopy [9].

These fluorescence-based techniques are very useful when functional groups can be reliably and selectively labeled. However, in many instances, such as optoelectronic devices or untreated biological tissues, far-field, label-free microscopy is desirable. Near-field scanning optical microscopy (NSOM) indeed serves such purpose by coupling light to nanostructures that are specifically designed to manipulate, enhance, and/or extract optical signals down to sizes in the order of 20 nm. Despite its diverse and sophisticated methods, such as absorption of light or tip-enhanced Raman scattering, its usability is limited to a range of few tens of nanometers from the surface.

Recently, far-field methods, free of fluorescent labeling, were introduced and many of them are reviewed in this book. We name here a couple of approaches which are not mentioned in the book. Wang and co-workers used ground-state depletion of the charge carriers in graphene-like structures in transmission mode [10]. Photo-acoustics microscopy has been recently developed to demonstrate label-free super-resolution [11]. In this chapter, we will present our methodology for far-field label-free SR that is based on the nonlinear response of the reflectance to photo-excitation.

### *11.1.1 Pump and Probe with Large Difference in Wavelengths for SR*

Implicit to our approach for SR is the use of pump–probe (P&P) configuration, where the two beams coincide and are focused with diffraction-limited point spread function (PSF) on the same spot of the sample. In the simple, linear case we assume that the change in the probe intensity, as a consequence of the interaction of the sample with the exciting pump, is linear with the exciting pump and the probe. A basic assumption in our method is that the instantaneous temperature or charge-carriers' distributions mimic the three-dimensional energy absorption profile of the pump. For instance,

the  $\text{PSF}_{\text{pp}}$  of the linear light-induced thermo-reflectance (TR) is the product of the individual PSFs of the pump,  $\text{PSF}_{\text{pump}}$ , and that of the probe,  $\text{PSF}_{\text{probe}}$ .

$$\text{PSF}_{\text{pp}} = \text{PSF}_{\text{pump}} \times \text{PSF}_{\text{probe}} \quad (11.1)$$

By itself, the P&P configuration bears considerable improvement in resolution over the single-beam PSF. In this respect, stimulated Raman scattering and coherent anti-Stokes Raman scattering microscopies are SR techniques. In the case when the P&P has similar wavelengths, the improvement amounts to  $\sim\sqrt{2}$ . However, when the interrogated property of the sample by the pump is in the mid-IR, while the probe monitors the deposited energy at visible wavelengths, the effective resolution surpasses the mid-IR PSF by almost an order of magnitude. The distinct fingerprints of the mid-IR spectral feature add chemical recognition in this modality, while the pump wavelength can be selected in much shorter wavelengths. This approach to achieve IR SR has been demonstrated recently using photo-thermal technique. Ji-Xin Cheng and co-workers [12] reported on label-free three-dimensional chemical imaging of live cells and organisms. Hartland and co-workers [13] reported on SR in polystyrene beads, thin polymer films, and single *Escherichia coli* bacterial cells.

## 11.2 Nonlinear Photo-modulated Reflectivity

### 11.2.1 Photo-Induced Reflectivity Changes

Upon ultra-fast photo-excitation, materials undergo fast dynamics of energy transfer between various degrees of freedom. Charge-carrier excitation (10–100 fs) is followed by carrier–carrier and carrier–phonon scattering/thermalization processes (10 fs–10 ps) [14, 15]. Eventually, on a timescale of a few picoseconds, the thermal transport can be treated classically. The instantaneous diffraction-limited photo-excited spatial profile diffuses quickly and blurs in time (see Fig. 11.1). The above dynamics induce spatial and temporal changes in the reflectivity. Photo-induced reflectance originates from numerous physical effects [16], mostly from changes in carrier concentration and in temperature. Light-induced thermo-reflectance (or time-domain thermo-reflectance), which records changes of reflectance upon photo-excitation, is extensively used to measure the thermal properties of materials using linear models [17–19]. We are concerned with the nonlinear components of photo-modulated reflectivity, in respect to photo-excitation, which allow the dramatic narrowing of the effective PSF.

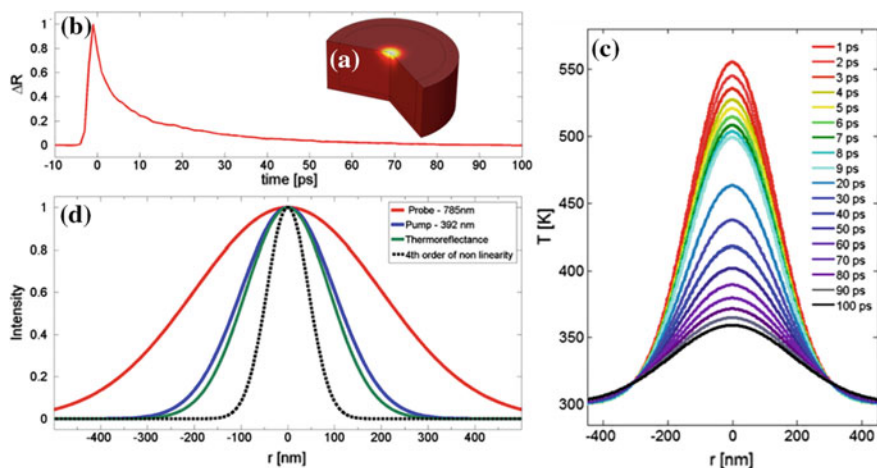


**Fig. 11.1** Key elements in NPMR. **a** Simulation of optical absorption and temperature distribution in a silicon wafer at pump–probe delay of 1 ps. Pump fluence is  $\sim 70 \text{ mJ/cm}^2$ . **b** Experimental dependence of thermo-reflectance in silicon on the pump–probe delay. **c** Simulation of time-dependent temperature profile in silicon following photo-excitation. **d** PSF simulation. Red—probe pulse at 785 nm. Blue—pump at 392 nm. Green—Thermo-reflectance at delay  $t = 1 \text{ ps}$ . In this case, the PSF conforms to the product of the pump and probe beam PSFs. Black—PSF resulting from fourth-order nonlinearities in thermo-reflectance. Reproduced with permission from [22]. Copyright 2015 American Chemical Society

It is beyond the scope of this review to discuss the mechanisms related to sample excitation and energy dissipation, leading to the above-mentioned nonlinearity. These effects can stem from changes in the light absorption during the interaction of the sample with the pump light such as multiphoton excitations. They can also originate from subsequent dynamical processes, such as Auger carriers annihilation [20, 21].

### 11.2.2 The Principles of Nonlinear Photo-Modulated Reflectivity

Nonlinear photo-modulated reflectivity (NPMR) is based on the nonlinear changes of the reflectance, induced by photo-excitation of material by an ultra-short pump pulse [22, 23]. In measuring NPMR, a train of ultra-short pump pulse, sine intensity-modulated (at  $\omega_m$ ), is focused on the sample. This train of pulses photo-excites temperature and/or charge-carriers changes, spatially distributed inside the diffraction-limited spot. A spatially overlapping, delayed, and unmodulated train of probe pulse monitors the nonlinear reflectance changes. NPMR is measured by recording the high harmonics in the reflectance of the unmodulated probe laser, induced by the pump sine modulation. The idea is illustrated in Fig. 11.2.

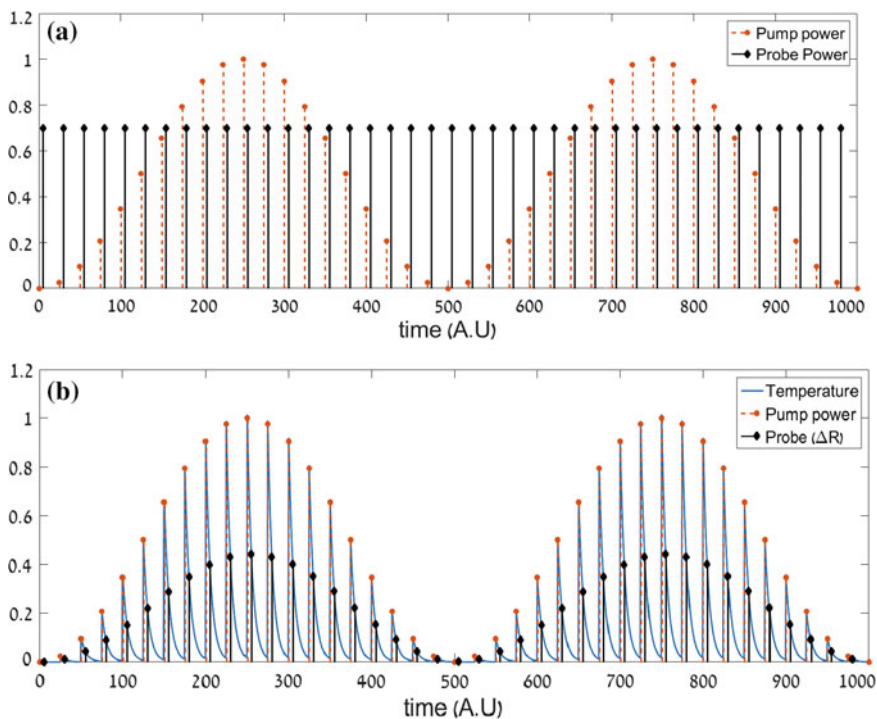


**Fig. 11.2** The basic principles of NPMR. **a** A train of intensity-modulated (at  $\omega_m$ ) pump pulse is focused on a sample. The overlapping focused probe pulses, with constant intensity, are delayed by a few picoseconds. **b** In the illustration, the pump pulses increase the sample temperature, giving rise to changes in the probe reflectivity (blue line). The black dots represent the probed changes in reflectivity. By analyzing the change in reflectivity with a lock-in amplifier, the harmonics content of the probe can be extracted

In order to extract the nonlinear components of reflection due to photo-modulation (at  $\omega_m$ ), we demodulate the reflection intensity at the corresponding harmonic frequencies ( $\omega_m, 2\omega_m, 3\omega_m \dots$ ) in a lock-in amplifier. The  $n$ th harmonics components of the reflectivity scale with the  $n$ th power of the excitation. Accordingly, the related effective  $\text{PSF}_{\text{pp}}$  comprises the product of  $\text{PSF}_{\text{probe}}$  and that of the pump laser to the power of the nonlinearity order  $n$ ,  $\text{PSF}_{\text{pump}}^n$ . The width of the  $\text{PSF}_{\text{pp}}$  scales down by  $\sqrt{n}$  for Gaussian-focused beams. By scanning over the sample and measuring the NPMR, spatial resolution is enhanced beyond the diffraction limit. This methodology was first demonstrated on Si nanostructures, and provided spatial resolution down to 85 nm [23].

SAX is a fluorescence-dependent SR technique, closely related to NPMR [6]. There, high-order harmonics of the fluorescence, induced by saturating the modulated excitation, are detected. Recently, a similar microscopy method, relying on

the nonlinear emission response of plasmonic nanoparticle labels, has been reported (see Chap. 8 by Shi-Wei Chu in this book). Note also that in laser-induced ablation, the nonlinear response of matter was used to achieve SR ablation with a diffraction-limited focused beam [24].

### 11.2.3 Timescales of the Experiment

Several timescales are relevant to the optimization of NPMR:

- A short pump pulse, in the femtosecond to picosecond range, is desirable so that the photo-excited spatial distribution of physical properties will not diffuse and blur the initial instantaneous profile [22].
- The delay between the pump and the probe should be optimized according to the monitored physical property. For example, to monitor the change in temperature, the desired delay should be about 1–2 ps to allow the transfer of energy to phonon degrees of freedom. With longer delays, heat diffusion will quickly induce spatial smearing and decay of intensity. On the other hand, a short pump–probe delay allows monitoring of charge–carrier excitation that may take 100 fs.
- Each P&P interaction lasts a few picoseconds, and within this timeframe, the temperature of the sample can reach up to a few hundreds of degrees. It is desirable that the next pair of P&P pulses in the train will reach the system after its complete electronic and thermal relaxation. Within this constraint, a high repetition rate laser is desired for high signal-to-noise ratio (SNR) and speed. The 12.5 ns pulse spacing in a ps/fs laser, with repetition rate of 80 MHz, is adequate to minimize the steady-state heating of a thermally conducting sample ( $\sim 7$  K), and also allows high-frequency ( $\sim 1.1$  MHz) modulation of the pulse train.

### 11.2.4 The Relation Between High Harmonics Detection and SR

The origin of resolution enhancement can be rationalized by representing the nonlinear change in reflectivity,  $\Delta R$ , as a Taylor series of the pump intensity  $I_{\text{pu}}$ :

$$\begin{aligned} \frac{\Delta R}{R}(\alpha, I_{\text{pu}}, \tau, \lambda_{\text{pr}}) &= a_1(\alpha, \tau, \lambda_{\text{pr}})I_{\text{pu}} + a_2(\alpha, \tau, \lambda_{\text{pr}})I_{\text{pu}}^2 \\ &+ a_3(\alpha, \tau, \lambda_{\text{pr}})I_{\text{pu}}^3 + \dots \end{aligned} \quad (11.2)$$

where  $\alpha$  denotes the material monitored,  $\lambda_{\text{pr}}$  denotes the wavelength of the probe (e.g. the coefficient of thermo-reflectance is wavelength-dependent), and  $\tau$  is the delay between the pump and the probe ultra-short pulses. The excitation of the sample

exhibits complex dynamics which determine the various coefficients of  $\Delta R$ . We assume that in the short times (ps-scale), the instantaneous distribution of charge carriers or phonons mimics the 3D absorption profile of the pump, and induces accordingly changes in reflectivity. When the train of the pump pulses is a amplitude-modulated pump in the form of a pure sine with modulation frequency  $\omega_m$ .

$$I_{\text{pu}}(t) = I_0 * 0.5(1 + e^{i\omega_m t}), \quad (11.3)$$

then the envelope of  $\Delta R$  will also follow a periodic function. Using this in (11.2) yields:

$$\begin{aligned} \frac{\Delta R}{R} \approx & a_1 I_0 * 0.5(1 + e^{i\omega_m t}) + a_2 [I_0 * 0.5(1 + e^{i\omega_m t})]^2 \\ & + a_3 [I_0 * 0.5(1 + e^{i\omega_m t})]^3 + \dots \end{aligned} \quad (11.4)$$

In practice, the nonlinear coefficients are much smaller than the TR signals and they decrease with increasing nonlinearity order  $a_1 \gg a_2 \gg a_3 \dots$ . Thus, it can be shown, by expanding 11.4, that by detecting the modulation harmonics ( $2\omega, 3\omega, \dots$ ), the nonlinear response, proportional to  $I_{\text{pu}}^n$ , is measured. Effectively, the nonlinear spatial intensity profile  $I_{\text{pu}}^n(x, y)$  is a Gaussian in the power of ( $n = 2, 3 \dots$ ). Accordingly, the  $\text{PSF}_{\text{pp}}$  of the  $n$ th harmonic demodulated signal scales down like  $\sqrt[n]{n}$  and is given by:

$$\text{PSF}_{\text{pp}} = (\text{PSF}_{\text{pump}})^n \times \text{PSF}_{\text{probe}} \quad (11.5)$$

### 11.2.5 The Need for Pure Sinusoidal Excitation

The existence of high harmonics  $\omega_m$  in the modulated pump beam can introduce nonlinearities directly into the photo-modulated (PM) reflection, masking the intrinsic high-harmonic response. Consequently, we have developed a methodology to obtain pure sinusoidal photo-modulation with minimal nonlinearities in the modulation. It is based on using an arbitrary wave generator (AWG) to drive the control voltage input of an acousto-optical modulator (AOM). With this approach we reduce high-order harmonic distortion to  $<0.05\%$  in high AOM diffraction efficiency regime. See details in the Appendix.



## 11.4 Examples of NPMR

### 11.4.1 Silicon on Sapphire

We first demonstrated SR using NPMR on fabricated silicon nanostructures. In silicon nanostructures, the major material in semiconductor industry, linear photo-modulated reflection has been studied extensively. Silicon, as any other reflective or scattering surface, contains nonlinear components in its reflectivity [25–27].

Experiments were performed on 100 nm thick silicon layers patterned on sapphire (Fig. 11.4b). At a pump fluence of  $\sim 100$  mJ/cm<sup>2</sup>, NPMR is discernible. The instantaneous temperature of silicon, immediately after the pump pulse, is  $\sim 700$  K, but it quickly cools down and the steady-state temperature elevation amounts to  $\sim 7$  K. Figure 11.4 depicts line scans orthogonal to 125 nm silicon stripes with variable spacing. The resolution enhancement with increasing harmonics is clearly discernible.

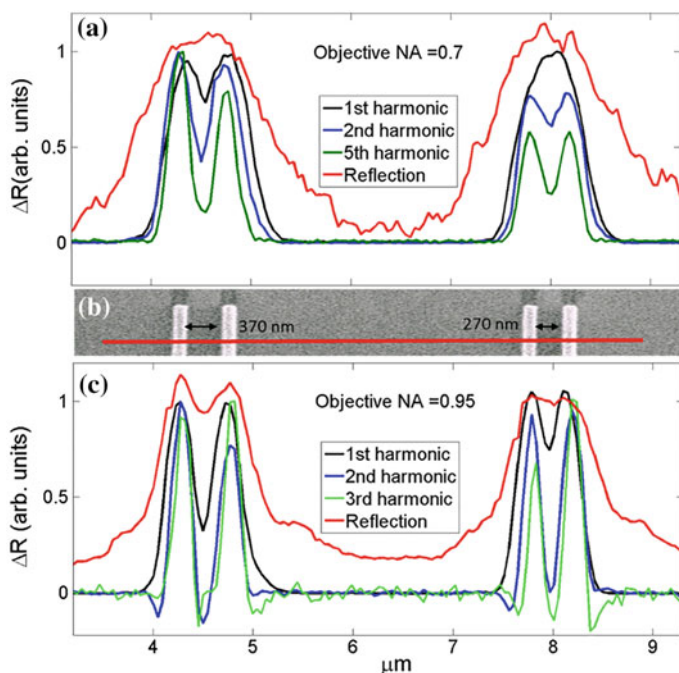


**Fig. 11.4** SR line imaging of silicon nanostructures on sapphire, silicon double lines, 125 nm wide, with gaps of 370 and 270 nm, respectively. **a** Scan with a 0.7 NA objective using the total probe reflection (red), the first (black), second (blue), and fifth (green) harmonics of  $\omega_m$ . **b** SEM image of the scanned sample. **c** Imaging with a 0.95 NA objective using first, second, and third harmonics. Resolution enhancement is consistent with the increase of the NA and the harmonic order. Reproduced with permission from [22]. Copyright 2015 American Chemical Society

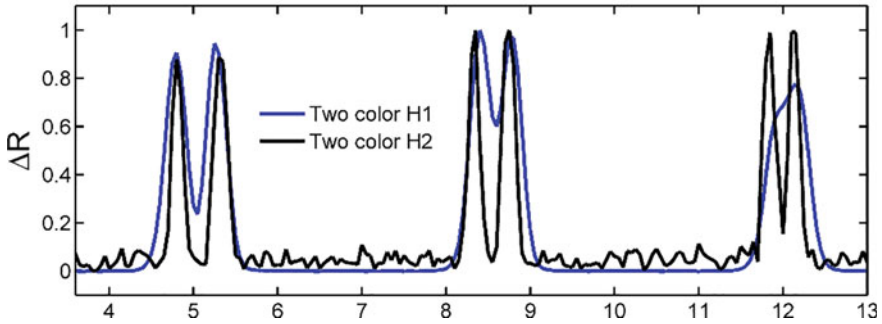


**Fig. 11.5** NMPR of a sample consisting of Au double lines, 125 nm wide; gaps of 370, 270, and 180 nm, respectively. NMPR line imaging using first (blue) and second (black) harmonics. Reproduced with permission from [23], OSA

Based on the SEM images of the patterned strips, the deconvoluted PSF of the fifth harmonic, performed with 0.7 NA objective lens, corresponds to  $140 \pm 10$  nm FWHM. Using a 0.95 NA objective, the resolution with the third harmonics corresponds to  $105 \pm 10$  nm. The resolution enhancement is  $>2\times$  ( $4\times$ ) of the pump (probe), respectively, and is consistent with the simulated resolution. As in SAX, the resolution improvement here is theoretically limited only by the SNR.

### 11.4.2 Gold on Sapphire

We tested the resolution of a sample consisting of a set of 100 nm thick, 125 nm wide pairs of gold stripes fabricated on sapphire substrate [23]. Here, due to superior pure harmonic modulation, using the optimized AOM, the resolution achieved was 95 nm, somewhat better than that achieved on the silicon samples. Similar results were obtained for gold structure on ITO-coated glass substrate (Fig. 11.5).

### 11.4.3 Vanadium Oxide on Silicon

A special case in which photo-excitation induces a phase transition of vanadium oxide ( $\text{VO}_2$ ) is presented here. In the case of abrupt photo-induced changes, the differential nonlinear response occurs only in the vicinity of the critical light intensity, while much below or above this intensity, linear or nonlinear response is distorted.

At  $T_c = 340$  K,  $\text{VO}_2$  undergoes a first-order structural phase transition (monoclinic to rutile) coinciding with an insulator-to-metal transition [28, 29]. Recently, the phase transition induced by ultra-fast photo-excitation has also been studied [30–32]. Above a critical pump fluence,  $\text{VO}_2$  undergoes a transition into a metallic state, accompanied by a large change in reflectivity within  $\sim 100$  fs. Within picosecond

timescale, electronic energy is transferred to lattice via electron–phonon coupling, and the volume of the thermally-induced phase transition expands. Cooling processes follow, and the reverse transition into the insulator state occurs in hundreds of picoseconds.

These photo-thermal properties can be used to realize SR. By fine-tuning the pump-laser fluence to be slightly above the phase transition threshold, only the intense center of the pump beam will induce the phase transition, invoking the narrowing of the PSF via NPMR.

The experiments were performed on a patterned granular film of  $\text{VO}_2$  (~100 nm thick), on a silicon substrate. The samples comprised ~150 nm wide lines of polycrystalline nanoparticles, in which the phase transition may occur at somewhat different temperatures or laser fluences depending on nanoparticle size [33]. The samples were scanned at varying pump fluences to characterize the onset of the photo-induced phase transition. In order to achieve SR, we have tuned the pump energy slightly above the onset of the phase transition on individual  $\text{VO}_2$  nanoparticles (Fig. 11.6). Note the highly nonlinear response of reflectance change to pump pulse energy. The best resolution (PSF of 165 nm) is achieved at pump energies slightly above the onset of the monoclinic-to-rutile phase transition (peak power  $6.6 \text{ mJ/cm}^2$ ). At lower ( $3.2 \text{ mJ/cm}^2$ ) and higher ( $20 \text{ mJ/cm}^2$ ) energies, the particles appear larger (PSF of ~280 nm FWHM).

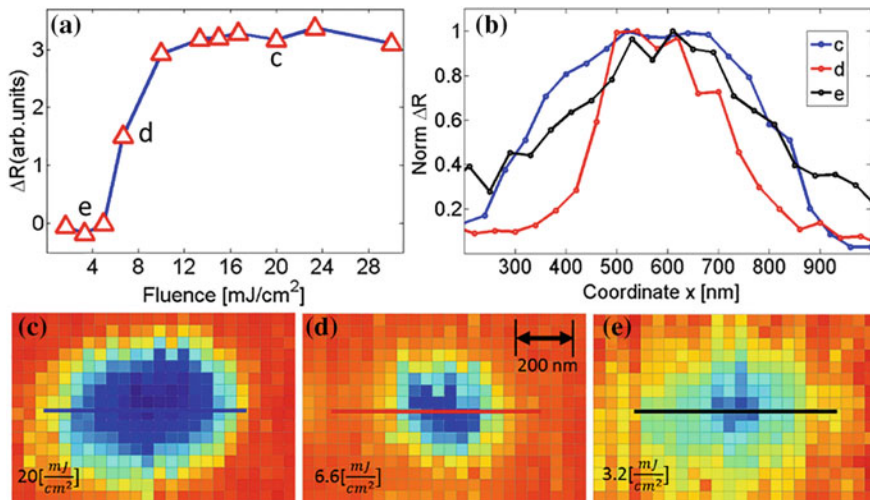


**Fig. 11.6** NPMR characterization of a single  $\text{VO}_2$  particle. A  $270 \times 200 \text{ nm}$   $\text{VO}_2$  particle (size verified by SEM) was scanned over a series of pump fluences. All at 1 ps pump–probe delay, and using 0.7 NA objective. **a** NPMR of the  $\text{VO}_2$  particle as a function of the pump energy. **b** Normalized cross-sections along x-axis of the scans (**c**, **d**, **e**) depicted in the bottom images. **c** Scan above phase transition ( $20 \text{ mJ/cm}^2$ ). **d** Scan at phase transition ( $6.6 \text{ mJ/cm}^2$ ). **e** Scan below phase transition ( $3.2 \text{ mJ/cm}^2$ ). (Reproduced with permission from [22]. Copyright 2015 American Chemical Society)

Figure 11.7 depicts a NPMR scan of several VO<sub>2</sub> nanoparticles (pump = 8 mJ/cm<sup>2</sup>) along with the corresponding SEM images. Note that two particles separated by 70 nm could be resolved. After deconvolution the PSF was found to be between 160 and 190 ± 10 nm (FWHM), about half the diffraction limit of the pump. The range of PSFs values reflects the variability of the nanoparticles in respect to phase transition as a function of size.

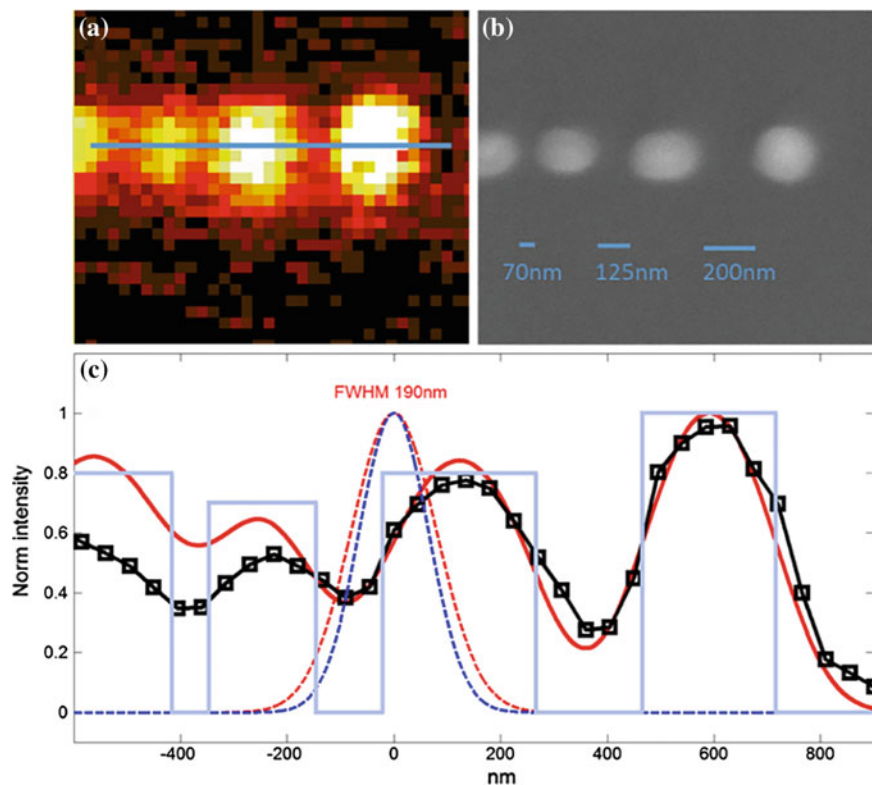


**Fig. 11.7** **a** VO<sub>2</sub> NPMR area scan. **b** SEM images of the same area. **c** Experimental results compared to simulation: the sample was modeled (blue rectangles) as step function with longitudinal dimensions taken from the SEM image and heights proportional to the width in the SEM image to account for the higher reflection signal in wider particles. Black—cross-section of the scan along the line in **a** the best fit to the experimental data is the red curve—convolution of the best PSF (red dotted Gaussian, FWHM of 190 ± 5 nm) and the sample model. On the left side of the figure, the 70 nm gap is discernible, and corresponds to a PSF of 160 nm FWHM (blue dotted Gaussian). Reproduced with permission from [22]. Copyright 2015 American Chemical Society

## 11.5 Modality Variations to Improve and Simplify NPMR

The use of NPMR to achieve SR converges as the nonlinearity order  $\sqrt{n}$ , while the signal of high orders decays exponentially. Therefore, it is useful to seek for additional effects that provide improvement in resolution and sensitivity, on top of NPMR. Here we present two such approaches.

### 11.5.1 Spatial Modulation

Spatial overlap modulation (SPOM) technique improves three-dimensional sectioning by suppressing out-of-focus signals, as the pump and probe spatial overlap is temporally modulated while scanning. In the focal region the modulation depth of the spatial overlap peaks, and decays fast toward the out-of-focus regions [34]. In SPOM nonlinear optical microscopy (SPOM-NOM), the spatial overlap between two color pulses is temporally modulated by means of beam pointing modulation or wavefront modulation, and nonlinear optical processes excited by a combination of two color pulses are monitored. This technique was used for imaging with enhanced spatial resolution in modalities such as sum frequency imaging [35] or stimulated Raman scattering [34]. However, the PSF of SPOM,  $\text{PSF}_{\text{SPOM}}$ , suffers from negative lobes, since it practically represents the second derivative of the image, and generates artifacts in the image.

The combination of NPMR with SPOM results in improved resolution and major reduction of the negative lobes. The effective PSF of this combined modality amounts to the product of  $\text{PSF}_{\text{pump}}^n$  and  $\text{PSF}_{\text{SPOM}}$ , and the negative lobes of  $\text{PSF}_{\text{SPOM}}$  overlap with low values of  $\text{PSF}_{\text{pump}}^n$ . In the experiments, the probe beam was spatially modulated at  $\omega_{\text{SPAT}}$  using a galvanometer-mounted mirror (see Fig. 11.3), while the intensity of the spatially fixed pump beam was modulated at  $\omega_m$  using the AOM. The demodulated signal at frequency  $\omega_{\text{ref}} = n\omega_m + 2\omega_{\text{SPAT}}$  provides the integrated response of SPOM (second order) and NPMR. Figure 11.8a depicts a simulation of the method using a pump beam at 392 nm and a probe beam at 785 nm, as in the experiments. The simulated improvement in resolution, and the decrease of the negative lobes of SPOM, is clearly demonstrated.

The experiments were performed on 100 nm thick silicon layers patterned on sapphire. Figure 11.8b depicts a scan of a single silicon 125 nm wide stripe in different modalities. The results are in good correspondence to our simulations. The introduction of SPOM improved the resolution of the second harmonics NPMR by ~15%, down to  $85 \pm 5$  nm, consistent with the simulation. Theoretically, the incorporation of SPOM is equivalent to additional 1–2 higher harmonics in NPMR, yet with about tenfold higher signal levels. Indeed, the typical negative lobes of SPOM are significantly reduced due to the narrow PSF of NPMR.

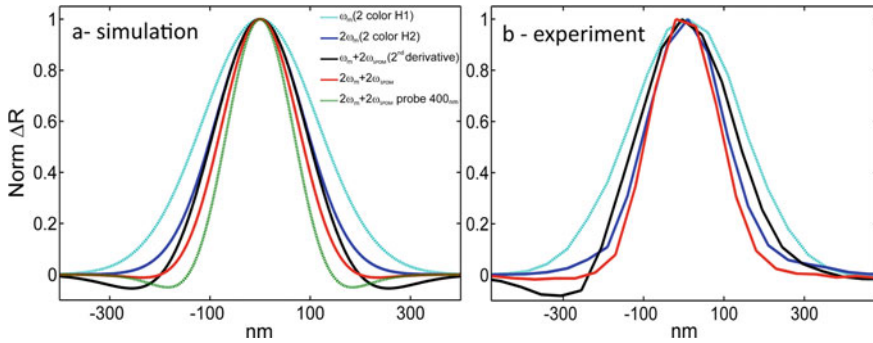


**Fig. 11.8** NPMR and SPOM, simulation vs. experiment. **a** Simulation of line scan using different imaging modalities: NPMR first modulation harmonic (turquoise), NPMR second harmonic (blue), second SPOM derivative (black), and second SPOM derivative with second NPMR harmonic (red). The green curve depicts the SPOM second derivative with the NPMR second harmonic using a probe at 400 nm for improved resolution (down to 75 nm). **b** Experimental results. Two color line scans of silicon on sapphire samples using the various modalities (same color codes as in the simulations). Reproduced with permission from [23], OSA

### 11.5.2 Pump and Probe with a Single Laser

A simpler version of NPMR, which requires only a single laser beam, eliminates the need for relative temporal and spatial adjustment of the pump and probe beams [23]. In this modality, the train of laser pulses is intensity modulated, and its reflectance is measured at high modulation harmonics with a lock-in amplifier. The photo-modulated reflectivity of a single pulse can be described as follows: The pump pulse excites the sample and probes it at the same time, which is equivalent to zero P&P delay. The measured change in reflectivity,  $\Delta R$ , due to a single pulse depends on the physical dynamics of the system, the pulse intensity, and the pulse length, and can be described as:

$$\Delta R = \int_{t=0}^{T_p} I_{\text{pump}}(t) * \Delta R_{\text{material}}(t, I_{\text{pump}}) dt / \int_{t=0}^{T_p} I_{\text{pump}}(t) dt \quad (11.6)$$

where  $\Delta R_{\text{material}}(t, I_{\text{pump}})$  represents the evolving reflectivity change at time  $t$ , which keep changing throughout the pulse duration up to its end at  $T_p$ . Effectively, the measured  $\Delta R$  is a weighted average, containing different level of excited charge carriers or phonons. The lack of optimized delay between the pump and the probe beams, and the pump wavelength that may not be optimal for probing the reflectance change, reduces the signal of this modality substantially, and it is highly dependent on the timescales of photo-excited charge carriers in the materials. However, the simplicity of the system (no delay line) may be attractive to some applications.

We tested the single-color scheme and compared it with the two-color method on a set of 100 nm thick, 125 nm wide pairs of gold stripes fabricated on sapphire substrate. We inferred that the reflectivity changes due to electron excitation in Au

are fast enough (approximately 100 fs [36, 37]) to be detected by a single pulse at a duration of 2 ps. On the other hand, in silicon, the carrier excitation which leads to changes in reflectance is slower ( $\sim 700$  fs) and we could not probe efficiently NMPR with a single 2 ps pulse. The results of two-color and single-color PM reflectivity on Au pattern are depicted in Fig. 11.9. Note that the resolution of the gold samples scan at the second harmonics of both single and P&P schemes is equal, and amount to  $95 \pm 5$  nm.

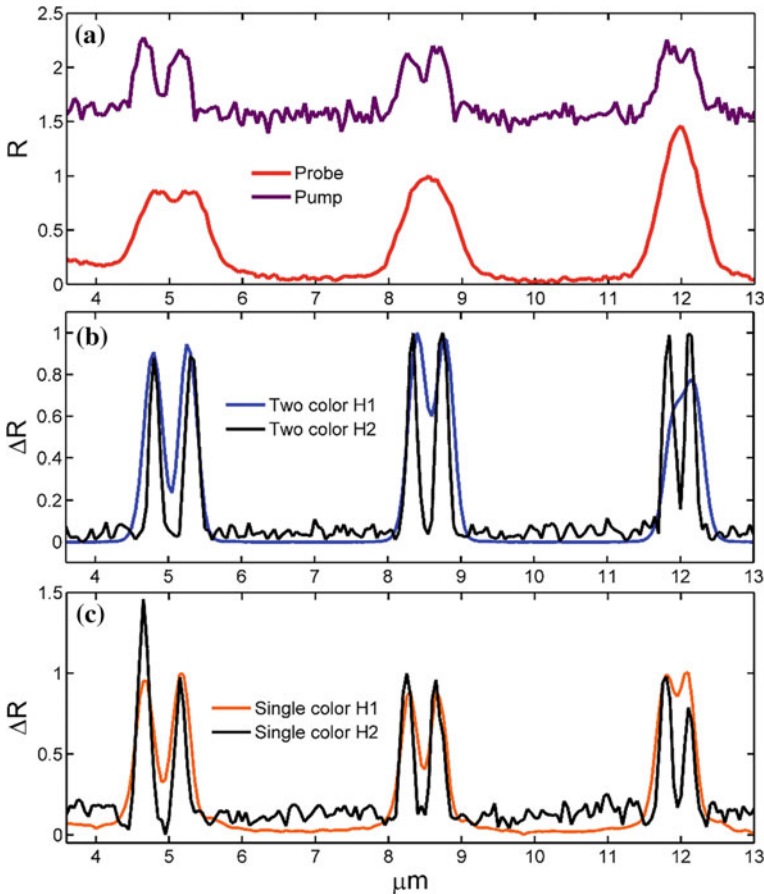


**Fig. 11.9** Super-resolution photo-modulated reflectivity using single color or two colors. The sample consists of Au double lines, 125 nm wide, with gaps of 370, 270, and 180 nm, respectively. **a** Line imaging of probe reflection (red) and pump reflection (purple). **b** Two-color photo-modulated reflectivity line imaging using first (blue) and second (black) harmonics. **c** Single-color photo-modulated reflectivity using first (orange) and second (black) harmonics. Note the resolution enhancement ( $95 \pm 5$  nm) at  $2\omega_1$  in both two- and single-color modalities. Reproduced with permission from [23], OSA

### 11.5.3 Resolution Improvement via Beam Apodization

So far, our discussion was limited to the case of a Gaussian diffraction-limited spot. However, by using a phase and/or amplitude filter in the beam path, a smaller spot at the focal plane is achievable. The disturbing existence of annular tails in the PSF, often associated with such filters, is less pronounced in higher orders of the  $\text{PSF}_{\text{pump}}$ , and are practically nulled in the overlap with the probe beam.

The use of spatial filters to achieve SR was investigated and used to improve the resolution in a confocal setup [38–40]. We followed the prediction of Lerman and Levi [41] on annular amplitude mask to test the improvement in resolution. We fabricated a circular gold mask (16 mm diameter) on glass. The mask was mounted in the beam path, to minimize far-field diffraction fringes. The mask position was fine-tuned while monitoring the focused beam image on camera to obtain a symmetric donut shape intensity profile. In Fig. 11.10 we compared two scans, with and without the mask in the beam path. In both scans we tested SR by measuring the second-order NPMR, using a single color, linearly polarized, 400 nm laser and a 0.95 NA air objective. The combination of the objective and the 16 mm mask provided apodization ratio of  $\frac{NA_{\text{min}}}{NA_{\text{max}}} = 0.60$ . SR test sample used consisted of gold nano-bars (125 nm wide) pairs on ITO, with varying spacing of 270, 160, 160 and 110 nm.

Deconvolution of the scan data with the object shape, taken from the SEM imaging, produced resolution of 155 and 130 nm for the clear and the apodized beams,

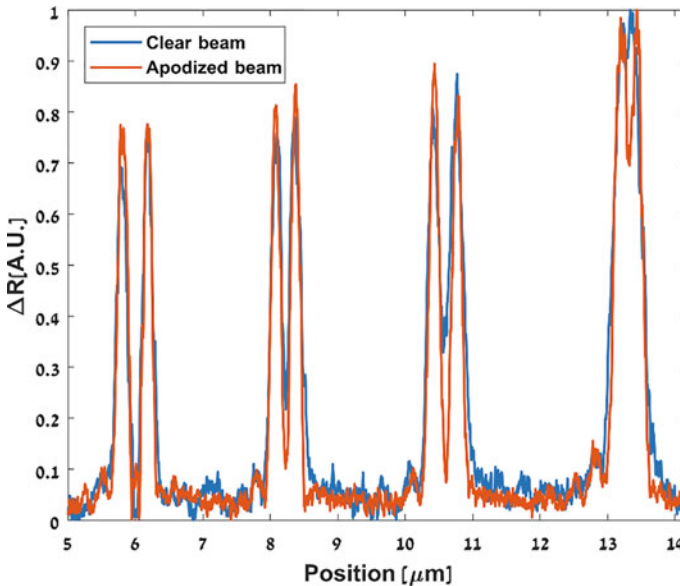


**Fig. 11.10** Line scan of gold nano bars pairs with varying spacing of 270, 160, 160 and 110 nm (left to right), using clear beam (blue) and apodized beam (brown)

respectively. This represents reduction of  $\sim 16\%$  in the  $\text{PSF}_{\text{pp}}$  width, which is in close agreement with the theoretical prediction.

## 11.6 Using Nonlinear Response in Other Label-Free Microscopy Modalities

### 11.6.1 *Temperature-Dependent Raman Scattering for SR*

Raman microscopy, in which specific spectral features discriminate between distinct materials, provides a label-free counterpart to fluorescence microscopy. Tip enhancement methods [42], combining scanning probe microscopy, such as STM [43] or AFM [44] and Raman spectroscopy, provide rich information with nanometric resolution on the studied system. However, the use of tip-enhanced Raman microscopy is limited to the surface. Katsumasa Fujita introduces in this book the combination of structured illumination and micro-Raman microscopy to achieve far-field Raman-based SR. We present the use of nonlinear response to achieve SR by monitoring photo-modulated Raman scattering [45].

As in NPMR, an ultra-short laser pulse (pump) is focused on the sample, and induces (within  $\sim 1$  ps) a diffraction-limited temperature profile. The integral intensity of the Raman peaks, as well as the peak frequency (energy) and shape, changes with the local temperature. An overlapping probe laser records specific spectral regions of interest (ROI) in the Raman spectrum. Our SR approach relies on measuring the changes in the Raman spectra, induced by the pump beam.

Simulations showed improvement of two to three times in resolution over the diffraction limit. Experimental validation of the concept by monitoring the changes in the total intensity of the Raman peaks shows mild resolution enhancement ( $\sqrt{2}$ ).

The experimental setup is illustrated in Fig. 11.11. As in NPMR, the pump (392 nm) and probe (785 nm) beams, with a controlled delay, are merged using a dichroic mirror and enter the Raman microscope. Scattered light is removed by a notch filter and the Raman spectra are detected by a spectrograph coupled to a CCD camera. The sample is scanned by an  $x$ - $y$  stage with 10 nm resolution. The difference in Raman signal is taken at 0.1 Hz square wave modulation of the delay in the probe beam.

Calibration measurements of the Raman spectra of silicon in the temperature range of 300–900 K were performed using a heating plate and a continuous wave 532 nm laser source (Fig. 11.12). On heating, the Stokes Raman peak shifts to lower vibrational energies, broaden and decrease its total intensity. The spectral “hot” ROI for detection in the simulation is marked. In our simulations, we modeled these spectral changes using an analytical model for the temperature dependence of the Raman peak [46], while scanning different sample geometries (point, line, and surface) formed images according to the intensity inside the spectral ROI. We assumed

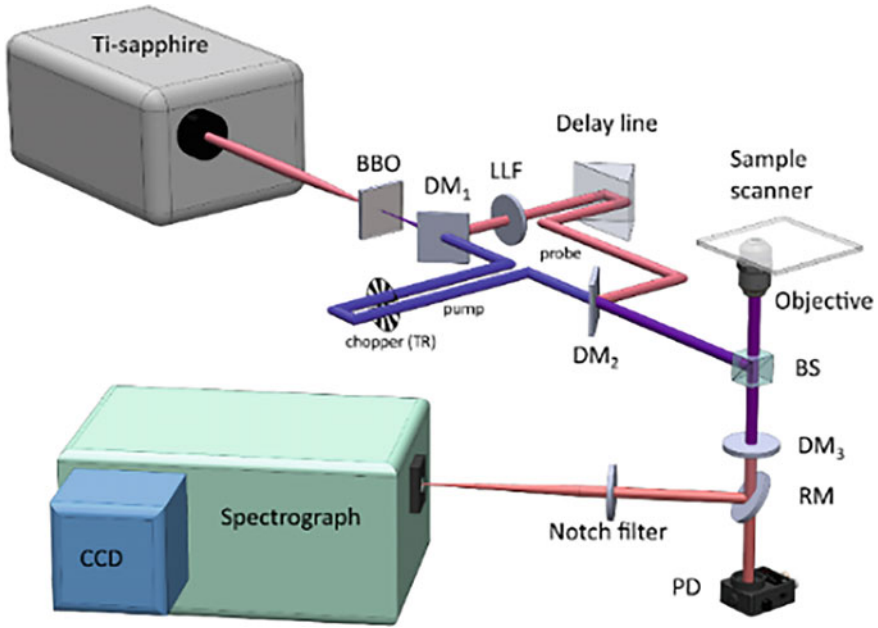


**Fig. 11.11** Optical setup for Raman-based SR. In a P&P configuration, a 785 nm probe pulse and 392 nm pump are temporally synchronized and spatially overlapped into a scanning microscope, and focused on the sample by a high NA air objective. Detection modalities include both Raman scattering spectral detection and NPMR. RM: removable mirror. DM: dichroic mirror. BS—beam splitter. PD—photodiode. LLF—laser line filter. Reproduced with permission from [45], OSA

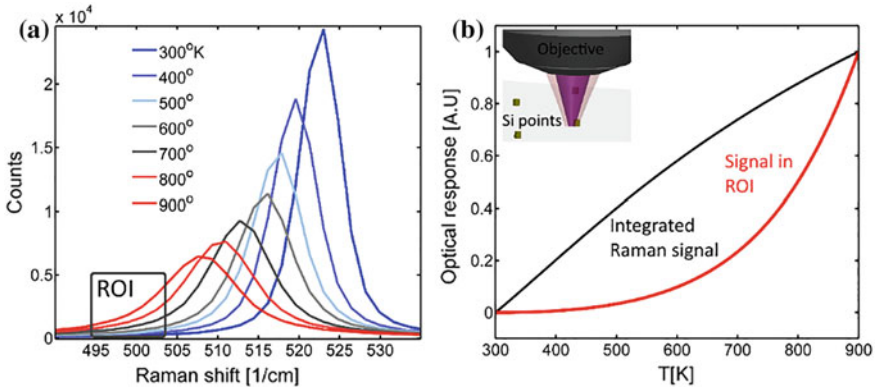


**Fig. 11.12** Response of a silicon Raman emitter to temperature. **a** Calibration measurements. Experimental temperature dependence of silicon Raman spectra using a temperature stabilized heating plate. **b** The integrated Raman signal for a point emitter as a function of temperature. Black—integrated changes in Stokes signal. Red—integrated Stokes signal in the ROI (defined in 12a). Note the nonlinear response. Top left inset—focused beams and Si point targets on sapphire substrate. Reproduced with permission from [45], OSA

that the probe laser is monitoring a surface that has reached full thermalization as imprinted by the focused pump laser. These conditions are practically achieved in a P&P delay up to about 5 ps.

The simulated intensity changes of the Raman peaks with temperature in selected spectral ROIs (Fig. 11.12b) show that while the integrated intensity of the whole Raman peak changes almost linearly (black curve), the Raman intensity in a specific spectral ROI (gray rectangle, Fig. 11.11a) is equivalent to introducing a fourth-order nonlinearity versus temperature (red curve). This dependence is vital for achieving SR.

The experiments consisted of line scans orthogonal to a 125 nm wide silicon stripe on a sapphire substrate (SOS). The scans depicted in Fig. 11.13a and c show enhanced resolution, improving from FWHM of  $650 \pm 50$  nm in the Raman Stokes scanning to  $440 \pm 50$  nm FWHM in the difference Stokes scanning. Figure 11.13b depicts the simulations on the differences in the integrated Stokes signal, with good correspondence to our experiments.

In our experiments, we could not monitor the “hot” ROI spectral changes due to very low signal levels. The realization of this method with nonlinear Raman modalities such as SRS [47] could provide higher sensitivity and could enable video rate SR imaging with high SNR.

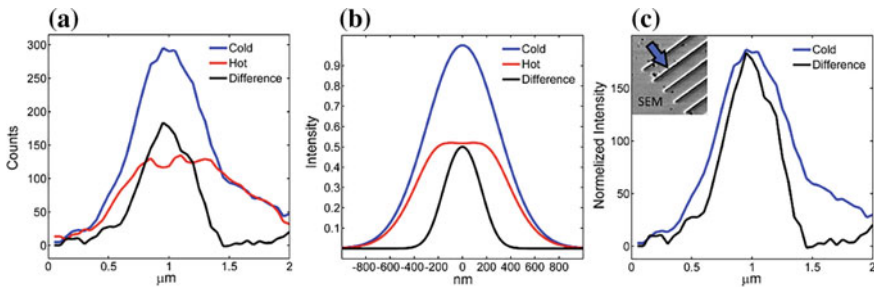


**Fig. 11.13** Resolution enhancement in photo-modulated Raman microscopy. **a** Experimental Raman scan of a single SOS strip. Blue—cold Raman scan (negative pump probe delay of  $-5$  ps). Red—hot Raman scan (pump probe delay of  $+5$  ps). Black—the difference signal,  $I_{\Delta\text{Raman}}$ . **b** Simulation: scan of a line Raman emitter. The difference signal,  $I_{\Delta\text{Raman}}$  (black), cold Stokes (blue), and the hot Stokes (red) scan profiles. **c** Black—difference Raman signal of single SOS stripe (Cold–Hot). Blue—rescaled cold Raman scan. The curve is rescaled to the height of the black (photo-modulated) curve to highlight the differences in widths (resolution). Top left inset: SEM image of the scanned SOS sample. Reproduced with permission from [45], OSA

### 11.6.2 Nonlinear Photo-acoustic Feedback Signal for Focusing Through Scattering Media

Motivated by the potential for high-resolution imaging deep inside biological tissues using wavefront shaping for controlling light propagation across scattering media, Tzang et al. used a lock-in detection scheme for measuring nonlinear photo-acoustic (PA) signals [48]. The goal was to use the nonlinear contributions for focusing tighter and potentially higher resolution imaging.

PA imaging is a hybrid modality that achieves optical contrast based on the PA effect by which absorption induces a transient thermo-elastic expansion and an associated acoustic emission [49]. PA reveals label-free optical contrast correlated to chemical composition by exciting the sample with different optical wavelengths, and it is considered a promising method for deep tissue biomedical imaging. In most PA modalities, the SNR of small, deeply buried, targets inside tissue is weak, and

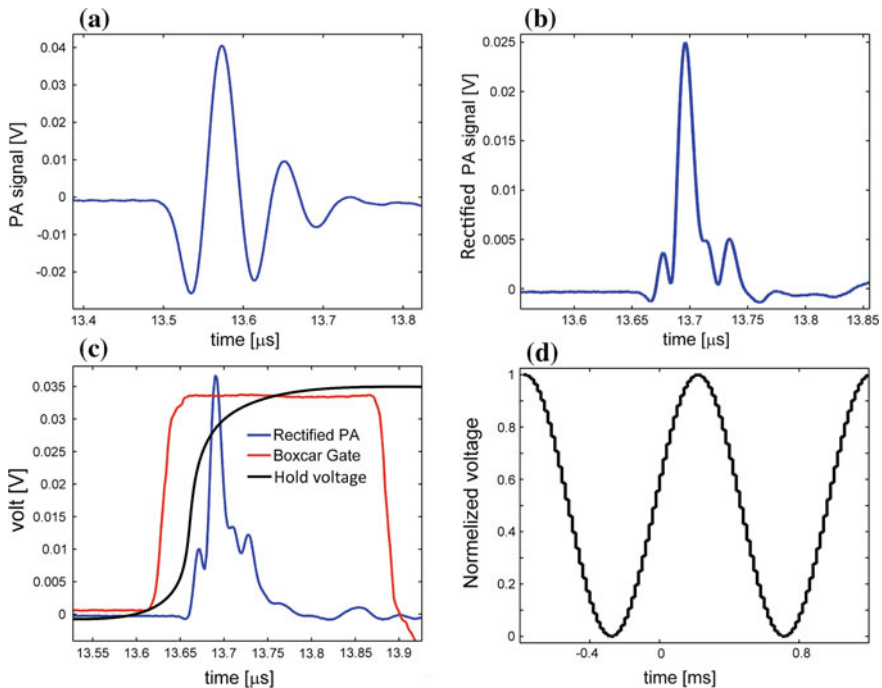


**Fig. 11.14** Analog signal processing for nonlinear PA. **a** Typical PA signal using a 15 MHz transducer. **b** Rectified PA signal. **c** Single-pulse sample and hold circuit, implemented by a boxcar integrator. The gate (red) shows the specific time window in which the PA signal (blue) is sampled. The integrated voltage (black) is held until the next pulse. **d** Schematic averaged output of the sample and hold circuit. Each pulse has now a discrete value and the modulation sidebands are enhanced with respect to the pulse train. Reproduced with permission from [48], OSA

its measurement is challenging. Nonlinear PA signal is even weaker but carries the potential for achieving enhanced resolution in microscopy [50] as well as improved feedback for noninvasive focusing through scattering media.

To increase the SNR in PA detection, and extract nonlinear PA signals, a modulation and lock-in detection scheme is used as feedback for adaptive focusing through scattering media [51]. Lock-in detection of PA signals, excited by optical pulses, requires several signal processing preparation steps in order to extract the modulation envelope. Figure 11.14 depicts the analog detection scheme that converts a modulated pulse train to a step-modulated signal. This step signal, containing the amplitude of the original PA signal, is fed into a lock-in amplifier. The demodulated PA amplitude is transferred to the computer to feed the optimization algorithm.

The photo-modulation is performed using an AOM (AA optoelectronic, MTS110) driven by an arbitrary function generator, as in the NPMR experiments, and nonlinear PA signals are detected by recording the high harmonics of the modulation. Note that in Fig. 11.15 the nonlinear feedback allows tighter focusing by narrowing down the effective detection area and generates fewer and brighter speckles.

The flexible detection of linear and/or  $n$ th-order nonlinearity as well as dual/multi-harmonic could be combined in a dynamic adaptive feedback algorithm. Compared to other nonlinear PA detection schemes such as dual pulse extraction of the Grueneisen parameter [52], and extraction of nonlinear coefficients by modulated pulse series [50], the analog method can deal better with high repetition rate lasers, noisier signals, and high data acquisition rate, and holds promise for effective detection of PA nonlinearities.

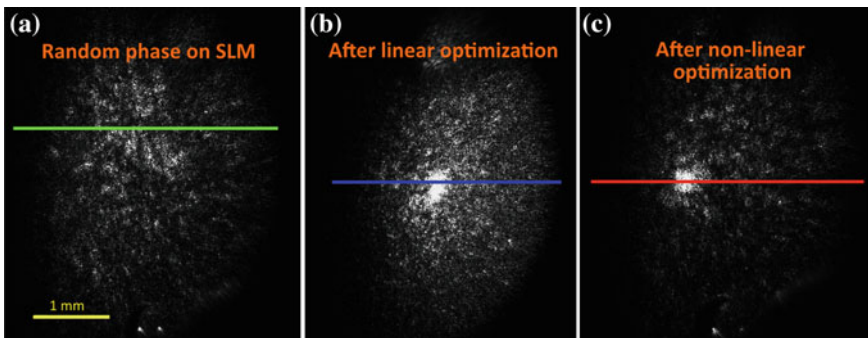


**Fig. 11.15** Results of focusing through scattering media using the lock-in amplifier and analog detection scheme. **a** Image of scattered light on a black tape sample with random wavefront. **b** Focusing on black tape using the linear PA feedback. **c** Focusing by nonlinear, second modulation harmonic, feedback from the lock-in amplifier. Repetition rate was 19 kHz, and optimized AOM sinusoidal modulation at 1.1 kHz. Reproduced with permission from [48], OSA

## 11.7 Conclusions

We have presented the essentials of nonlinear photo-modulated reflectivity (NPMR) for far-field, label-free, super-resolution (SR) microscopy. Unlike some other label-free SR techniques, no sample treatment or preparation is required here. NPMR is suitable to characterize semiconductors and metals in vacuum, ambient, and liquid, semi-transparent and opaque systems.

The improvement in resolution using NPMR scales like  $\sqrt{n}$ , where  $n$  is the nonlinearity order. While the intensities of high nonlinearity orders decrease exponentially, the incremental improvement in resolution slows down with the nonlinearity order. Therefore, in order to enhance resolution, it is desirable to combine NPMR with other resolution enhancement modalities, as demonstrated by us using SPOM.

A major challenge in any SR technique is the declining sensitivity as the examined objects decrease in size. One way to overcome this problem is to seek for resonance sensitivities in NPMR, by tuning the pump/probe wavelengths to a plasmonic resonant wavelength. We foresee an intense enhancement in label-free SR with such an approach.

## Appendix: Pure Sinusoidal Photo-Modulation Using an Acousto-optic Modulator

We have emphasized in Sect. 11.2.3 the need for pure sinusoidal light-intensity modulation in NPMR. This is a desirable requirement in numerous scientific and engineering applications. Here, we introduce our approach to achieve such a goal, using acousto-optical modulators.

The methodology, presented here, for clean sine photo-modulation is based on using an arbitrary wave generator (AWG) to drive the control voltage input of a single AOM [53]. This voltage input controls the amplitude of the RF driver, which determines the diffraction efficiency of the AOM. The diffracted intensity is not linear with input voltage. Thus, one looks for an arbitrary waveform (WF) to generate the required light intensity, having a pure sinusoidal time dependence at the modulation frequency  $f_m$ , while utilizing the full diffraction range of the AOM (90%).

The WF optimization consists of a two major stages. First, utilizing the static response (fixed control voltage) of the AOM to estimate the required WF. Second, using a feedback loop to optimize the WF to the dynamic frequency response of the AOM.

In the first stage, the modulator is driven by a set of static control voltages. The light output intensity at each voltage value is measured with a linear photo detector. The data are interpolated to a smooth function and are used to calculate the initial

WF. At modulation frequencies higher than 1000 Hz, the dynamic response of the AOM differs from the static response. Consequently, after the first stage, the harmonic content in our setup amounts to 1–2% and corrections to the initial fitting are needed.

In the second stage, that reduces the distortion by about additional two orders of magnitude, we use an iterative proportional–integral–derivative (PID) control. As in the first stage, the WF is synthesized by  $N$  discrete points defining a single cycle which is repeated at  $f_m$ . We assume that the errors at a definite time of the light intensity are solely determined by a corresponding point in the WF. At each PID cycle, we compare the normalized light intensity of a single modulation cycle with a pure sine function, and the errors are fed to the PID algorithm to generate a “new” corrected WF, as is shown in Fig. 11.16.

Results from our PID optimization at  $f_m = 1.13$  MHz (implemented using C# under Microsoft Visual Studio 2015 development environment) are presented in Fig. 11.17. The power spectra of the diffracted light intensity before PID optimization contained  $\sim 2\%$  distortion (Fig. 11.17a) and dropped down after PID optimization (Fig. 11.17c), by about two orders of magnitude. The low content of high harmonics stays stable for several hours. The optimized diffracted light intensity spans 98% of the full diffraction range of the AOM.

In a third stage, to further optimize and reduce the amplitude of the  $n$ th harmonics in the diffracted light intensity, we iteratively fine-tune the  $n$ th harmonic component of the PID-optimized WF in amplitude or/and phase. At each iteration, the WF

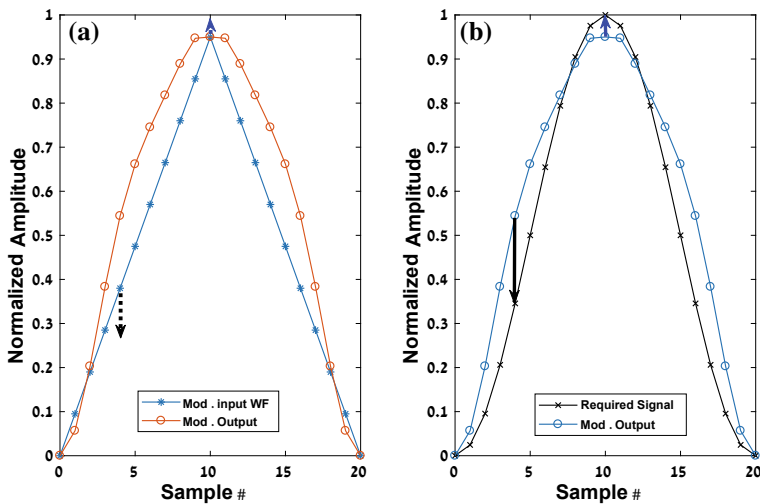


**Fig. 11.16** Optimization steps for pure sinusoidal modulation. **a** An example for the modulator input WF (blue) and the resulting modulated light intensity output (orange) during optimization. **b** Comparison of resulting light intensity with the required sinusoidal waveform. The difference between the two curves implicates that the modulators’ input has to be decreased (black arrow) or increased (blue arrow) to reduce the error between required signal and modulator output. The PID algorithm converges to a minimal error solution

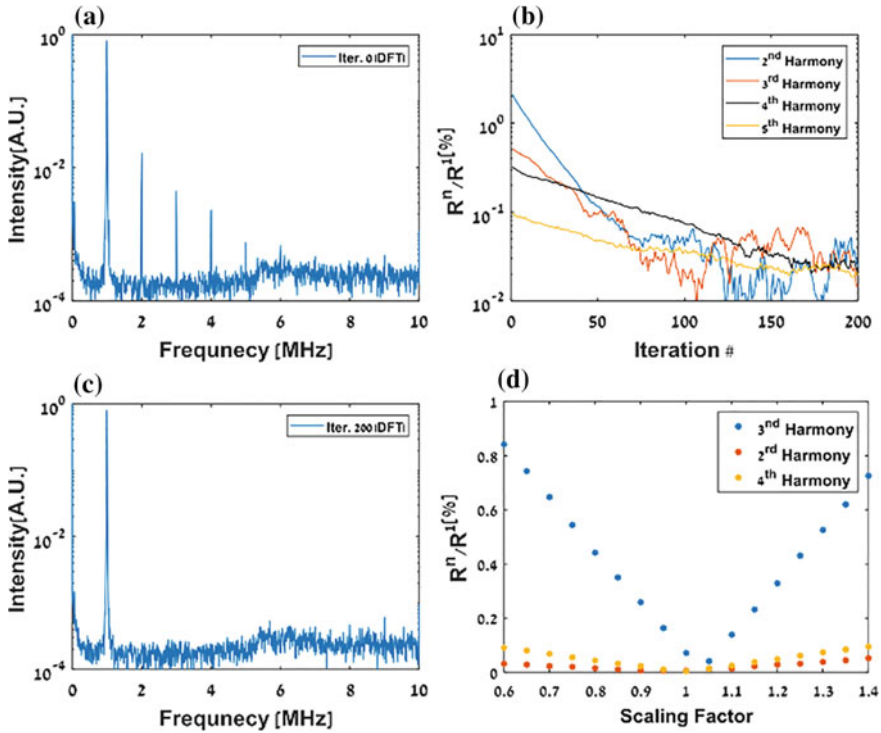


**Fig. 11.17** Optimization of pure sinusoidal modulation at  $f_m = 1.13$  MHz. **a** Power spectrum of light intensity for the initial WF. The second harmonic amplitude is 2% of the fundamental harmonic. **b** Normalized amplitude of the second–fifth harmonic (blue, orange, black, and yellow plots), with respect to fundamental harmonic, over the course of the PID optimization process. **c** Spectrum of the light intensity at the end of the PID algorithm. The second–seventh harmonics power is  $<0.05\%$  of the fundamental harmonic. **d** Analysis and fine-tuning of the harmonic content in WF after PID optimization. The effect of amplitude scaling of the third harmonic is shown here: The value “1” in the x-axis denotes the original amplitude at the end of the PID optimization. The second–fourth harmonics of  $f_m$  (orange, blue, and yellow) are normalized to the fundamental waveform amplitude

was Fourier transformed, the amplitude or the phase was slightly tuned, and a new time-domain WF was calculated and fed to the AOM (Fig. 11.17d). This computer-controlled tuning process results in further reduction of harmonic content by a factor of 2–3, to about 0.02%. An example for amplitude tuning of the third harmonic in WF is shown in Fig. 11.17d. This fine-tuning process can be repeated for other harmonics to get simultaneous reduction in overall distortion, usually taking about 4–6 min.

## References

1. A. Lewis et al., Near-field optics: from subwavelength illumination to nanometric shadowing. *Nat. Biotechnol.* **21**, 1378–1386 (2003); R.J. Hermann, M.J. Gordon, Nanoscale optical microscopy and spectroscopy using near-field probes. *Annu. Rev. Chem. Biomol. Eng.* **9**(1), 365–387 (2018)
2. T.A. Klar et al., Fluorescence microscopy with diffraction resolution limit broken by stimulated emission. *Proc. Natl. Acad. Sci. U.S.A.* **97**, 8206–8210 (2001)
3. T.A. Klar et al., Breaking Abbe's diffraction resolution limit in fluorescence microscopy with stimulated emission depletion beams of various shapes. *Phys. Rev. E* **64**, 066613 (2001)
4. R. Henriques et al., PALM and STORM: unlocking live-cell super-resolution. *Biopolymers* **95**, 322–331 (2011)
5. M.K. Rust et al., Sub-diffraction-limit imaging by stochastic optical reconstruction microscopy (STORM). *Nat. Methods* **3**, 793–795 (2006)
6. K. Fujita et al., High-resolution confocal microscopy by saturated excitation of fluorescence. *Phys. Rev. Lett.* **99**, 228105 (2007)
7. M.G.J. Gustafsson, Surpassing the lateral resolution limit by a factor of two using structured illumination microscopy. *J. Microsc.* **198**, 82–87 (2000)
8. T. Dertinger et al., Fast, background-free, 3D super-resolution optical fluctuation imaging (SOFI). *Proc. Natl. Acad. Sci.* **106**, 22287–22292 (2009)
9. O. Schwartz et al., Superresolution microscopy with quantum emitters. *Nano Lett.* **13**, 5832–5836 (2013)
10. P. Wang et al., Far-field imaging of non-fluorescent species with subdiffraction resolution. *Nat. Photonics* **7**, 449–453 (2013)
11. J. Yao et al., Photoimprint photoacoustic microscopy for three-dimensional label-free sub-diffraction imaging. *Phys. Rev. Lett.* **112**, 014302 (2014)
12. D. Zhang et al., Depth-resolved mid-infrared photothermal imaging of living cells and organism with sub-micron spatial resolution. *Sci. Adv.* **2**(9), NM4C.1 (2017)
13. Z. Li et al., Super-resolution far-field infrared imaging by photothermal heterodyne imaging. *J. Phys. Chem. B* **37**, 8838–8846 (2017)
14. E. Mazur, Spectroscopy and dynamics of collective excitations, in *Solids*, ed. by D.B. Bartolo, S. Kyrkos (Springer, Boston, MA, 1997), pp. 417–470
15. S.K. Sundaram, E. Mazur, Inducing and probing non-thermal transitions in semiconductors using femtosecond laser pulses. *Nat. Mater.* **1**, 217–224 (2002)
16. J. Bogdanowicz, *Fundamental Study of Photomodulated Optical Reflectance towards Non-Destructive Carrier Profiling in Silicon* (Springer, Berlin Heidelberg, 2012)
17. D.G. Cahill, Analysis of heat flow in layered structures for time-domain thermoreflectance. *Rev. Sci. Instrum.* **75**, 5119–5122 (2004)
18. D.G. Cahill et al., Nanoscale thermal transport. *J. Appl. Phys.* **93**, 793 (2003)
19. D.G. Cahill et al., Nanoscale thermal transport. II. 2003–2012. *Appl. Phys. Rev.* **1**, 011305 (2014)
20. A. Kar et al., Probing ultrafast carrier dynamics in silicon nanowires. *IEEE J. Sel. Top. Quantum Electron.* **17**, 889–895 (2011)
21. P. Hopkins et al., Excitation rate dependence of Auger recombination in silicon. *J. Appl. Phys.* **107**, 053713 (2010)
22. O. Tzang et al., Super-resolution in label-free photomodulated reflectivity. *Nano Lett.* **15**, 1362–1367 (2015)
23. O. Tzang, O. Cheshnovsky, New modes in label-free super resolution based on photo-modulated reflectivity. *Opt. Express* **23**, 20926–20932 (2015)
24. H.M. Phillips et al., Direct laser ablation of sub-100 nm line structures into polyimide. *Appl. Phys. A* **54**, 158–165 (1992)

25. R.E. Wagner, A. Mandelis, Nonlinear photothermal modulated optical reflectance and photocurrent phenomena in crystalline semiconductors. *Semicond. Sci. Technol.* **11**, 289–299 (1996)
26. R.E. Wagner, A. Mandelis, Nonlinear photothermal modulated optical reflectance and photocurrent phenomena in crystalline semiconductors. *Semicond. Sci. Technol.* **11**, 300–307 (1996)
27. Q. Lin et al., Nonlinear optical phenomena in silicon waveguides: modeling and applications. *Opt. Express* **15**, 16604–16644 (2007)
28. F.J. Morin, Oxides which show a metal-to-insulator transition at the neel temperature. *Phys. Rev. Lett.* **3**, 34–36 (1959)
29. D.N. Basov et al., Electrodynamics of correlated electron materials. *Rev. Mod. Phys.* **83**, 471–541 (2011)
30. A. Pashkin et al., Ultrafast insulator-metal phase transition in VO<sub>2</sub> studied by multiterahertz spectroscopy. *Phys. Rev. B* **83**, 195120 (2011)
31. C. Kübler et al., Coherent structural dynamics and electronic correlations during an ultrafast insulator-to-metal phase transition in VO<sub>2</sub>. *Phys. Rev. Lett.* **99**, 116401 (2007)
32. S. Wall et al., Tracking the evolution of electronic and structural properties of VO<sub>2</sub> during the ultrafast photoinduced insulator-metal transition. *Phys. Rev. B* **87**, 115126 (2013)
33. R. Lopez et al., Size effects in the structural phase transition of VO<sub>2</sub> nanoparticles. *Phys. Rev. B* **65**, 224113 (2002)
34. K. Isobe et al., Background-free deep imaging by spatial overlap modulation nonlinear optical microscopy. *Biomed. Opt. Express* **3**, 1594–1608 (2012)
35. K. Isobe et al., Implementation of spatial overlap modulation nonlinear optical microscopy using an electro-optic deflector. *Biomed. Opt. Express* **4**, 1937–1945 (2013)
36. R.W. Boyd et al., The third-order nonlinear optical susceptibility of gold. *Opt. Commun.* **326**, 74–79 (2014)
37. A. Marini et al., Ultrafast nonlinear dynamics of surface plasmon polaritons in gold s due to the intrinsic nonlinearity of metals. *New J. Phys.* **15**, 013033 (2013)
38. M.A.A. Neil et al., Optimized pupil-plane filters for confocal microscope point-spread function engineering. *Opt. Lett.* **25**, 245–247 (2000)
39. Hongxin Luo, Changhe Zhou, Comparison of superresolution effects with annular phase and amplitude filters. *Appl. Opt.* **43**, 6242–6247 (2004)
40. Yogesh G. Patel et al., Optimization of pupil design for point-scanning and line-scanning confocal microscopy. *Biomed. Opt. Express* **2**, 2231–2242 (2011)
41. G.M. Lerman, U. Levy, Effect of radial polarization and apodization on spot size under tight focusing conditions. *Opt. Express* **16**, 4567–4581 (2008)
42. L. Novotny, S.J. Stranick, Near-field optical microscopy and spectroscopy with pointed probes. *Annu. Rev. Phys. Chem.* **57**, 303–331 (2006)
43. B. Pettinger et al., Nanoscale probing of adsorbed species by tip-enhanced raman spectroscopy. *Phys. Rev. Lett.* **92**, 8–11 (2004)
44. A. Hartschuh et al., High-resolution near-field Raman microscopy of single-walled carbon nanotubes. *Phys. Rev. Lett.* **90**, 7–10 (2003)
45. O. Tzang et al., Super resolution methodology based on temperature dependent Raman scattering. *Opt. Express* **23**, 17929–17940 (2015)
46. M. Balkanski et al., Anharmonic effects in light scattering due to optical phonons in silicon. *Phys. Rev. B* **28**, 1928–1934 (1983)
47. C.W. Freudiger et al., Label-free biomedical imaging with high sensitivity by stimulated Raman scattering microscopy. *Science* **322**, 1857–1861 (2008)
48. O. Tzang, R. Piestun Lock-in detection of photoacoustic feedback signal for focusing through scattering media using wave-front shaping. *Opt. Express* **24**, 28122–28130 (2016)
49. M. Xu, M.L.V. Wang, Photoacoustic imaging in biomedicine. *Rev. Sci. Instrum.* **77**, 041101 (2006)
50. A. Danielli et al., Label-free photoacoustic nanoscopy. *J. Biomed. Opt.* **19**, 086006 (2014)

51. D.B. Conkey et al., Genetic algorithm optimization for focusing through turbid media in noisy environments. *Opt. Express* **20**, 4840–4849 (2012)
52. P. Lai et al., Photoacoustically guided wavefront shaping for enhanced optical focusing in scattering media. *Nat. Photonics* **9**, 126–132 (2015)
53. O. Tzang et al., Pure sinusoidal photo-modulation using an acousto-optic modulator. *Rev. Sci. Instr.* **89**, 123102 (2018)

# Chapter 12

## Nonlinear Label-Free Super-Resolution Microscopy Using Structured Illumination



Mikko J. Huttunen and Antti Kiviniemi

**Abstract** Optical microscopy is a standard tool to study biological objects. Diffraction limits the achievable lateral resolution of an optical microscope to around 200 nm restricting its applicability. However, recent advances in optical super-resolution techniques have shown that the diffraction does not impose a fundamental limit to resolution and can be circumvented. These super-resolution techniques can provide resolution approaching the nanometer scale and are enabling studies of biological objects with unprecedented capabilities. However, most of the super-resolution techniques are based on using fluorescent dyes, complicating their use in medical research and applications. Therefore, a need exists for label-free super-resolution techniques, which could be especially valuable for clinical applications. To answer this need, several such techniques have been recently developed. In this chapter, we introduce the reader to some of these techniques, discuss their applications, and of the possible future directions. In order to limit the scope of this vastly expanding topic, we focus on techniques based on structured illumination and intrinsic nonlinear responses of materials.

### 12.1 Introduction

Optical and electron microscopies are de facto tools for studying biological objects. Electron microscopy provides superior resolution [1], but requires more complicated instrumentation and sample preparation restricting its applicability [2]. Optical microscopy, on the other hand, provides coarser resolution, but is related with simpler sample preparation, capability for three-dimensional (3D) imaging and can be easily used to study living objects [3]. These advantages have made optical microscopy an indispensable tool for biological and medical research.

---

M. J. Huttunen (✉) · A. Kiviniemi  
Faculty of Engineering and Natural Sciences, Tampere University, Tampere, Finland  
e-mail: [mikko.huttunen@tuni.fi](mailto:mikko.huttunen@tuni.fi)

A. Kiviniemi  
e-mail: [antti.kiviniemi@tuni.fi](mailto:antti.kiviniemi@tuni.fi)

© Springer Nature Switzerland AG 2019  
V. Astratov (ed.), *Label-Free Super-Resolution Microscopy*,  
Biological and Medical Physics, Biomedical Engineering,  
[https://doi.org/10.1007/978-3-030-21722-8\\_12](https://doi.org/10.1007/978-3-030-21722-8_12)

Diffraction of light and the Abbe's law limit the practical achievable lateral resolution of an optical microscope to around 200 nm, while the axial resolution is often even coarser ( $\sim 600$  nm) [4, 5]. This resolving power limits the possibilities to study biological objects, which all exhibit molecular-scale features. For example, crucial building blocks of biological matter, such as DNA, RNA, and proteins, are all only a few nanometers in size. The Abbe's limit for optical resolution is not, however, a fundamental limit. As a consequence, several super-resolution techniques have been developed during the past two decades providing resolution greatly beyond the diffraction limit [6–11]. The vast majority of these super-resolution techniques are based on fluorescent probes, and often even require specific photo-switchable dyes [10]. For example, photo-activated localization microscopy (PALM) is based on photoactivatable dyes [11]. On the other hand, structured illumination microscopy (SIM) provides around 100 nm lateral resolution without requiring any specific dyes [7, 12].

Despite the fact that fluorescent dyes are widely used in optical microscopy, their use is not without problems. The labeling procedure maybe time consuming, some of the dyes are expensive and all exhibit photobleaching making long-term investigations difficult. Dyes may also disturb the studied system compromising the interpretation of results. Therefore, there is a need for the development of label-free super-resolution techniques, which are not hindered by the aforementioned problems and could be more suitable for clinical research and applications.

Several diffraction-limited label-free techniques have been already developed and are mostly based on autofluorescence of molecules or coherent scattering of light from the studied object and include holographic approaches and speckle imaging [13–15]. In addition, label-free imaging is possible by utilizing intrinsic nonlinear optical responses of objects, which also provide entirely new contrast mechanisms for microscopy [16, 17]. However, the development of label-free super-resolution techniques has proved challenging, since most of the realized super-resolution schemes are based on specific properties of fluorescent dyes. Perhaps due to this reason, many of the proposed and demonstrated label-free super-resolution techniques are based on the SIM scheme [18–23].

In this chapter, we discuss and review the recent progress on label-free super-resolution microscopy. In particular, we focus on techniques making use of the intrinsic nonlinear responses of objects, and which are based on the SIM scheme. The chapter is organized as follows. First, we introduce the reader to the theory behind conventional and laser-scanning SIM, and explain how the lateral resolution is increased using these techniques. Second, we provide a short tutorial on nonlinear optical microscopy, with the emphasis on the most commonly utilized nonlinear optical processes and in their practical implementation. Third, we review recent advances in nonlinear label-free super-resolution microscopy and discuss their applications. We end the chapter by highlighting some of the current challenges and discussing of the possible future directions in nonlinear label-free super-resolution microscopy.

## 12.2 Structured Illumination Microscopy

In conventional SIM based on incoherent illumination, the intensity modulation of the incident beam can be used to extend the range of spatial frequencies collected from the object and thus increase the achievable lateral resolution [7, 12]. This is based on the fact that an incoherent imaging system is approximately a linear translation-invariant (LTI) system in terms of the emitted and detected intensity distributions. This allows us to write the image formation process as a convolution

$$I_{\text{det}}(\mathbf{r}) = \text{PSF}(\mathbf{r}) * I_{\text{em}}(\mathbf{r}), \quad (12.1)$$

where  $I_{\text{det}}$  and  $I_{\text{em}}$  are, respectively, the detected and emitted intensity distributions and PSF is the point-spread function of the system. The emitted intensity  $I_{\text{em}}$  is given by the following equations:

$$I_{\text{em}}(\mathbf{r}) = S^{(1)}(\mathbf{r})I_{\text{inc}}(\mathbf{r}), \quad (12.2a)$$

$$I_{\text{em}}(\mathbf{r}) = S^{(2)}(\mathbf{r})I_{\text{inc}}(\mathbf{r})I_{\text{inc}}(\mathbf{r}), \quad (12.2b)$$

$$I_{\text{em}}(\mathbf{r}) = S^{(3)}(\mathbf{r})I_{\text{inc}}(\mathbf{r})I_{\text{inc}}(\mathbf{r})I_{\text{inc}}(\mathbf{r}), \quad (12.2c)$$

$$I_{\text{em}}(\mathbf{r}) = f(S^{(n)}, I_{\text{inc}}), \quad (12.2d)$$

where  $S^{(n)}$  is the  $n$ th order response function of the object and  $I_{\text{inc}}$  is the intensity distribution of the incident beam. In fluorescence microscopy, the dependence between the emitted and incident intensities is often linear motivating the use of (12.2a). However, this is not generally true, since nonlinear effects, such as two-photon fluorescence (2PEF), three-photon fluorescence (3PEF), multiphoton absorption or saturable behavior of the fluorescent molecules can make the dependence nonlinear [8, 24, 25]. In these cases, (12.2b)–(12.2d) should be used, respectively.

The convolution of (12.1) is written more conveniently in the spatial frequency domain as a point-wise multiplication

$$\hat{I}_{\text{det}}(\mathbf{k}) = \text{OTF}(\mathbf{k})\hat{I}_{\text{em}}(\mathbf{k}), \quad (12.3)$$

where the optical transfer function (OTF) is the Fourier transform (FT) of the PSF. The FT and its inverse transform are defined as

$$\hat{I}(\mathbf{k}) = \iint_{-\infty}^{\infty} I(\mathbf{r})e^{i\mathbf{k}\cdot\mathbf{r}} d\mathbf{r}, \quad (12.4)$$

$$I(\mathbf{r}) = \frac{1}{4\pi^2} \iint_{-\infty}^{\infty} \hat{I}(\mathbf{k})e^{-i\mathbf{k}\cdot\mathbf{r}} d\mathbf{k}. \quad (12.5)$$

It is convenient to define the lateral resolution using the highest spatial frequency component  $k'_{\text{max}}$  passing the system [26]. The smallest feature size resolved using the system is defined as

$$d = \frac{\lambda'}{2\text{NA}} = \frac{1}{2k'_{\max}}, \quad (12.6)$$

where  $\lambda'$  is the wavelength of the emitted light and NA is the numerical aperture of the imaging objective lens. Looking at (12.6), we see that the OTF restricts the achievable resolution. However, this resolution can be improved if we spatially modulate the incident beam  $I_{\text{inc}}$  given as

$$I_{\text{inc}}(\mathbf{r}) = 1 + 2 \cos(\mathbf{k}_{\text{mod}} \cdot \mathbf{r} + \phi), \quad (12.7)$$

where  $\mathbf{k}_{\text{mod}}$  is the spatial modulation frequency restricted by the NA of the illumination lens and  $\phi$  is an arbitrary phase factor. By looking at (12.2a) in spatial frequency domain we see that the modulation results in emitted intensity distribution given by

$$\hat{I}_{\text{em}}(\mathbf{k}) = \hat{S}(\mathbf{k}) + \hat{S}(\mathbf{k} - \mathbf{k}_{\text{mod}})e^{-i\phi} + \hat{S}(\mathbf{k} + \mathbf{k}_{\text{mod}})e^{i\phi}, \quad (12.8)$$

which contains higher spatial frequencies (in the direction of  $\mathbf{k}_{\text{mod}}$ ) from the object. Now, the detected field given by (12.3) can be written as a sum of three terms

$$\hat{I}_{\text{det}}(\mathbf{k}) = \text{OTF}(\mathbf{k})[\hat{S}(\mathbf{k}) + \hat{S}(\mathbf{k} - \mathbf{k}_{\text{mod}})e^{-i\phi} + \hat{S}(\mathbf{k} + \mathbf{k}_{\text{mod}})e^{i\phi}]. \quad (12.9)$$

Looking at (12.9), we see that the recorded image contains now spatial frequencies of the sample higher than  $k'_{\max}$ . In other words, spatially modulated incident beam shifts high spatial frequencies of the sample to the passband of the system's OTF. Therefore, if these three different contributions can be properly separated, the effective resolution of the system can be increased (see Fig. 12.1a–c). For the case of linear light-matter interactions [see (12.2a)], the lateral resolution can be increased up to twofold and has been demonstrated to result in lateral resolution of around 100 nm [7, 12].

Even better resolution improvement can be achieved if nonlinear effects in the imaging process are utilized [see (12.2b)–(12.2d), and also Sects. 12.4 and 12.5 below]. For the case of 2PEF (12.2b), the spatially modulated incident beam results in the following emitted intensity distribution [27]:

$$\begin{aligned} \hat{I}_{\text{em}}(\mathbf{k}) = & 3\hat{S}^{(2)}(\mathbf{k}) \\ & + 2\hat{S}^{(2)}(\mathbf{k} - \mathbf{k}_{\text{mod}})e^{-i\phi} + 2\hat{S}^{(2)}(\mathbf{k} + \mathbf{k}_{\text{mod}})e^{i\phi} \\ & + \hat{S}^{(2)}(\mathbf{k} - 2\mathbf{k}_{\text{mod}})e^{-2i\phi} + \hat{S}^{(2)}(\mathbf{k} + 2\mathbf{k}_{\text{mod}})e^{2i\phi}. \end{aligned} \quad (12.10)$$

Inserting (12.10) into (12.3), we see that in this case even higher spatial frequency components of the sample are shifted to the passband of the OTF. Similar equations can be written also for higher order processes, such as for 3PEF, or for material responses with saturable behavior [8, 28]. Demonstrations utilizing the saturable behavior of fluorescent molecules have shown resolutions even down to around 50 nm [8, 25].

The details of the procedure for extending the spatial frequency support in all possible directions are already well explained, for example, in [7, 23, 29], and due to this reason, we only outline the basic principles here. In short, we make use of the fact that for the case of linear SIM the FT of the recorded image  $\hat{I}_{\text{det}}$  is a linear superposition of three terms [see (12.9)], which all have a different dependence on  $\phi$ . Therefore, by performing three or more measurements while varying  $\phi$ , the resulting system of linear equations can be easily solved for [30]. For the case of nonlinear SIM, the FT of the recorded image  $\hat{I}_{\text{det}}$  is composed of more than three terms [see (12.10)], and therefore more than three measurements are required.

Once the terms have been separated, they are reassembled in the spatial frequency domain. Since even the ideal form of the OTF of an incoherent system is conical, the separated spatial frequency images are biased. This bias can be mitigated by filtering, where Wiener filtering is most commonly used [12, 31]. This step is essential for reconstructing a good quality super-resolution image, since the spatial frequency images are both biased by the shape of the OTF and contain noise. The above mentioned filtering technique requires a priori knowledge of the OTF, but such knowledge is not strictly necessary since approaches based on blind deconvolution have also been demonstrated [32, 33].

After correcting for the bias (and noise), the images are reassembled by shifting them to their correct locations. The images can be conveniently moved by taking use of the shifting property of the FT and thus multiplying the respective real space images by cosine waves resulting in shift in the spatial frequency domain. After the correct locations have been found, the overlapping pixels are combined with their weighted averages. Once these steps have been completed, the lateral resolution of the reassembled image has been improved in one direction (see Fig. 12.1b). A uniform resolution improvement is achieved by repeating the above steps while modulating

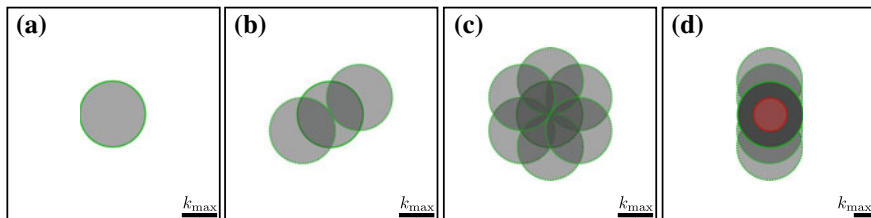


**Fig. 12.1** **a** OTF of the imaging system restricts the achievable resolution. **b** Higher spatial frequencies can be collected by modulating the incident beam. In this case, the FT of the recorded image contains several terms. By separating and shifting these terms in the Fourier domain, the OTF can be extended resulting in improved resolution (in one direction). **c** A uniformly extended OTF can be constructed by modulating the incident beam in many directions. **d** In 2PEF-SIM the excitation of the sample occurs at longer wavelengths resulting in less extended excitation OTF (red circle). By modulating the incident beam, the FT of the recorded image contains more terms than when using linear SIM, resulting in larger resolution improvement. However, due to the longer excitation wavelengths, in practice the best achievable resolution in multiphoton SIM is only similar to conventional linear SIM ( $\sim 100$  nm)

$\mathbf{k}_{\text{mod}}$  to several directions. In practice, three different directions ( $0^\circ$ ,  $60^\circ$  and  $120^\circ$ ) are enough to provide a close-to-uniform resolution improvement (see Fig. 12.1c). Finally, we note that several open-source software implementations for the above mentioned SIM reconstruction procedure already exist [34–36].

### 12.3 Laser-Scanning SIM Implementations

Spatial modulation of the incident beam for SIM (see 12.7) can be achieved in several ways, such as by imaging a diffraction grating into the sample plane (see Fig. 12.2a), or by using a point-scanning laser system (see Fig. 12.2b). In this section, we will focus on the latter scheme and pay special attention to nonlinear laser-scanning modalities, which will be discussed in more detail in the upcoming sections.

Nonlinear laser-scanning systems have at least two inherent advantages when compared to systems based on wide-field illumination. First, the nonlinear signal originates only from the focal point, which in fact provides intrinsic capability for optical sectioning and thus for three-dimensional imaging. Second, peak intensities at the focal point can reach much higher values than what would be easily achieved by using wide-field illumination. This latter fact is especially important in nonlinear microscopy.

A laser-scanning SIM system commonly consists of a mirror-based beam scanner, relay lens system, a microscope objective, and a camera (see Fig. 12.2b). In the typical form of SIM, a sinusoidal pattern consisting of one spatial frequency component is illuminated on the sample. In a laser-scanning SIM, this can be accomplished simply by modulating the light intensity while the scan is performed (see Fig. 12.3). Modulation can be achieved by an electro-optic modulator (EOM) [38], acousto-optic modulator (AOM) [27, 37] or by performing a “jump scan” [37]. A “jump scan” is performed by scanning the sample area with constant optical power while skipping one or more lines for every scanned line. Rotation of the scanning pattern

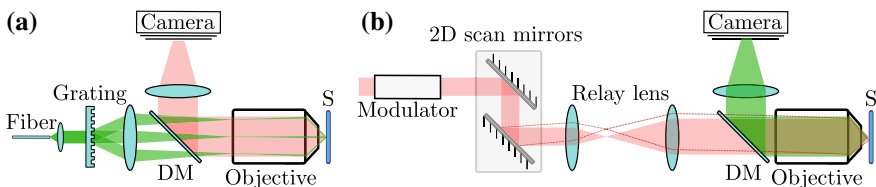


**Fig. 12.2** **a** In conventional wide-field SIM the modulated illumination pattern is produced by imaging a diffraction grating to the sample plane. The modulation of the illumination is controlled by rotating and translating the grating, while the sample (S) is imaged using a dichroic mirror (DM) to a camera. **b** In laser-scanning SIM, the incident beam is focused to the sample plane and scanned using, for example, galvanometric mirrors and a relay lens system. The spatially modulated illumination pattern is achieved by temporally modulating the intensity of the scanning beam using, for example, an acousto-optic modulator [37]

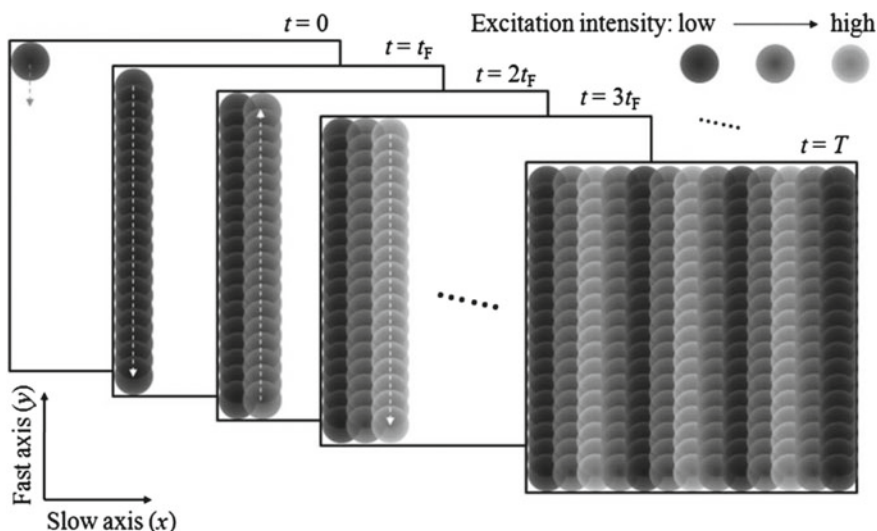


**Fig. 12.3** Generation process of structured illumination with a point-scanning geometry at  $t = 0$ ,  $t_F$ ,  $2t_F$ ,  $3t_F$ , and  $T$ .  $t_F$  is the fast-axis scan time.  $T$  is the frame time. Each gray circle represents an excitation spot, where different levels of gray indicate varying excitation intensities. The dashed arrows show the scanning directions in a zig-zag manner. Adapted with permission from [27]

is also a relatively simple and fast operation in laser-scanning systems. Especially with EOM and AOM implementations, the beam-scanning pattern does not require modification since the needed modulation patterns can be created using solely the modulator. We note that in addition to point-scanning SIM systems, line-scanning SIM systems have also been demonstrated [39]. These systems are a compromise between wide-field and point-scanning systems. The main advantage of such systems is that they can provide faster imaging capabilities than point-scanning systems.

Laser-scanning SIM techniques are easily adapted to confocal laser-scanning microscopes by removing the detection pinhole and replacing the detector with a camera. Additionally, a modulator can be inserted after the laser output. Without the modulator, this configuration has been used in other SIM-like super-resolution techniques such as in image-scanning microscopy (ISM) [40], in virtual k-space modulation optical microscopy (VIKMOM), and in optical pixel-reassignment microscopy (OPRA) [41, 42]. This configuration has also been utilized in the commercially available Airyscan (Zeiss). The availability and widespread use of confocal laser-scanning microscopes makes them viable commercially. Many of the developed techniques, such as ISM and VIKMOM, focus on the post-processing of image data are taken from the confocal aperture plane. In this respect, OPRA seems advantageous since no signal post processing is required due to the fact that the signal manipulation is performed optically.

## 12.4 Nonlinear Optical Processes

In nonlinear optical processes several fields interact with matter, creating new field components oscillating at new frequencies [16, 17]. Perhaps the most studied nonlinear process is called second harmonic generation (SHG), during which two fields at the fundamental frequency  $\omega$  are converted into a new field oscillating at doubled frequency  $2\omega$ . In an analogous process of third harmonic generation (THG), three incident fields at the fundamental frequency  $\omega$  are converted into a new field with a tripled frequency  $3\omega$ . Coherent anti-Stokes Raman scattering (CARS) is another widely used third-order nonlinear process where three incident fields with different frequencies give rise to a new field component [43]. Schematic energy diagrams for the above processes are shown in Fig. 12.4. These and other nonlinear processes intrinsically occur in the imaged object and can thus be used for label-free imaging [44–48].

The above mentioned nonlinear processes (SHG, THG, and CARS) are parametric processes and leave the quantum state of the studied object unchanged [17]. Thus no net energy (such as heat) is accumulated into the object during these processes (see Fig. 12.4), making them very suitable for studying living objects. In nonparametric processes a small portion of the incident energy is transferred to the object thus changing its quantum state. Examples of non-parametric processes include 2PEF and 3PEF (see Fig. 12.4a, b), which are also widely used nonlinear imaging modalities [49, 50]. Compared to conventional fluorescence, the advantages of 2PEF and 3PEF are that the fundamental beam is not markedly absorbed or scattered by the studied media. Therefore, these modalities can provide considerably deeper penetration depths ( $\sim 1.3\text{--}1.6$  mm) than conventional fluorescence microscopy [51, 52]. These modalities are also minimally invasive since multiphoton absorption occurs only at the focal point, and does not affect the surrounding volume of the object.

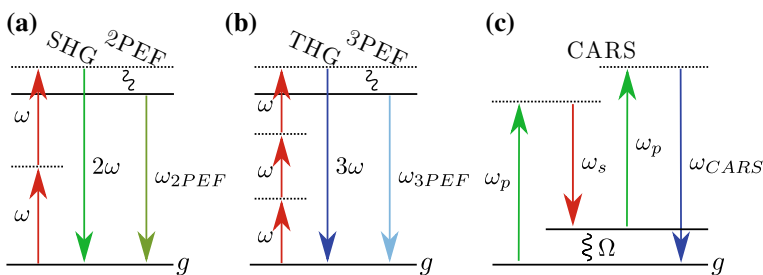


**Fig. 12.4** Energy-level diagrams of the nonlinear processes of interest. **a** During the process of SHG, two incident photons at frequency  $\omega$  are combined into a single photon oscillating at  $2\omega$ . In 2PEF, part of the excitation energy is transferred to the object resulting in the emission occurring at frequency  $\omega_{2PEF} < 2\omega$ . **b** In third-order processes of THG and 3PEF, three incident photons interact with the object giving rise to the signal photons oscillating at  $3\omega$  and  $\omega_{3PEF}$ . **c** In a typical CARS configuration, The pump ( $\omega_p$ ) and the Stokes ( $\omega_s$ ) beams give rise to the signal (anti-Stokes) beam ( $\omega_{CARS}$ ). The vibrational resonance frequency ( $\Omega$ ) is also shown

Since many molecules in biological structures show intrinsic fluorescence, i.e., are autofluorescent, 2PEF and 3PEF processes can be also used to study and visualize such molecules in label-free manner.

In the early days of multiphoton microscopy, it was believed that the resolution could be also improved due to the nonlinear nature of the interaction. However, the lateral resolution improvement while using conventional laser-scanning microscope was soon found to be only moderate [53], since the increased resolution is almost counterbalanced by the fact that the excitation occurs at longer wavelengths. For example, typical lateral resolutions in SHG and THG microscopy ( $NA = 0.9$ ,  $\lambda = 1230$  nm) are often around 400–500 nm whereas the axial resolution is around  $1\ \mu\text{m}$  [54]. While the relative axial resolution can be slightly improved when compared to linear modalities, the main advantage of using multiphoton modalities have not been the achievable resolution. However, this fact might be about to change, since several nonlinear super-resolution techniques, with many of them based on the SIM approach, have been recently proposed and demonstrated [18–23, 55]. These nonlinear super-resolution techniques are the topic of the next section.

## 12.5 Super-Resolution Using Nonlinear Processes and Structured Illumination

In this section, we discuss the recent developments in nonlinear super-resolution techniques. Some of the discussed techniques (mainly based on 2PEF and 3PEF) have not yet been used for label-free imaging as such, but the techniques have demonstrated their potential by using fluorescent probes. We emphasize that these techniques could be used also in label-free manner if they would make use of the autofluorescence of molecules. First, we will discuss super-resolution techniques based on incoherent processes, such as 2PEF and 3PEF. Second, we will discuss techniques based on coherent processes, such as SHG, THG and CARS.

### 12.5.1 *Super-Resolution Using Incoherent Nonlinear Processes*

A while after the conventional SIM was demonstrated for the first time, the approach was also applied to 2PEF and 3PEF microscopy [28, 56]. Implementation of these modalities were not trivial since the decrease in the achievable axial resolution of the conventional wide-field technique was seen as a major drawback [57]. A viable solution to improve the axial resolution and to enable optical sectioning was to utilize a technique known as temporal focusing, where ultrashort pulses are made to temporally overlap only at the focal plane of the microscope [58–60]. In other words, the incident ultrashort pulse is dispersed using a diffraction grating into different

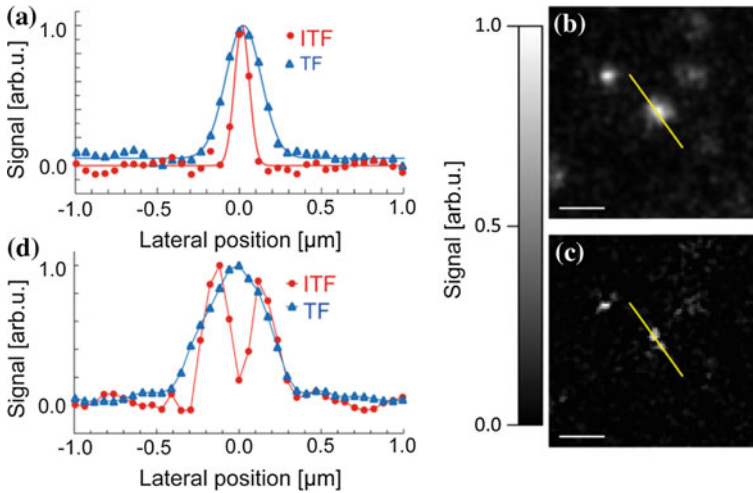


**Fig. 12.5** **a** Signal distributions of a fluorescent bead along the lateral direction, acquired using 3PEF temporal focusing (3PEF-TF) and 3PEF interferometric temporal focusing (3PEF-ITF) microscopies. **b** and **c** Cross-sectional images of 100 nm fluorescent beads acquired using **(b)** 3PEF-TF and **(c)** 3PEF-ITF microscopies, respectively. **d** Signal distributions along the yellow solid lines shown in panels **(b)** and **(c)**. Scale bars in **b** and **c** both correspond to 1  $\mu\text{m}$ . Adapted with permission from [28]

spectral components, which are then used to illuminate the object at slightly different incident angles. This way the high peak intensities, which are necessary for the occurrence of nonlinear interactions, are present only at the focal plane where the spectral components constructively add up to reform the ultrashort pulse. After the pulse passes the focal plane, the spectral components are again dispersed, due to which no nonlinear signal is generated. A recent and impressive demonstration of 3PEF-SIM combined with temporal focusing providing a lateral resolution of  $\sim 106$  nm is shown in Fig. 12.5.

As discussed earlier (Sect. 12.3), laser-scanning SIM is also possible through spatiotemporal modulation [37]. This approach seems very beneficial especially when combined with nonlinear imaging modalities. First, a good axial resolution can be easily achieved, without implementing the temporal focusing scheme. Therefore, laser-scanning SIM can facilitate 3D imaging with both good lateral and axial resolution. Second, high peak intensities are only needed at the focal point, and therefore less powerful and complicated laser systems are needed to illuminate the sample. A good example of the recent progress is seen in Fig. 12.6, where a twofold resolution improvement using a laser-scanning 2PEF-SIM is demonstrated.

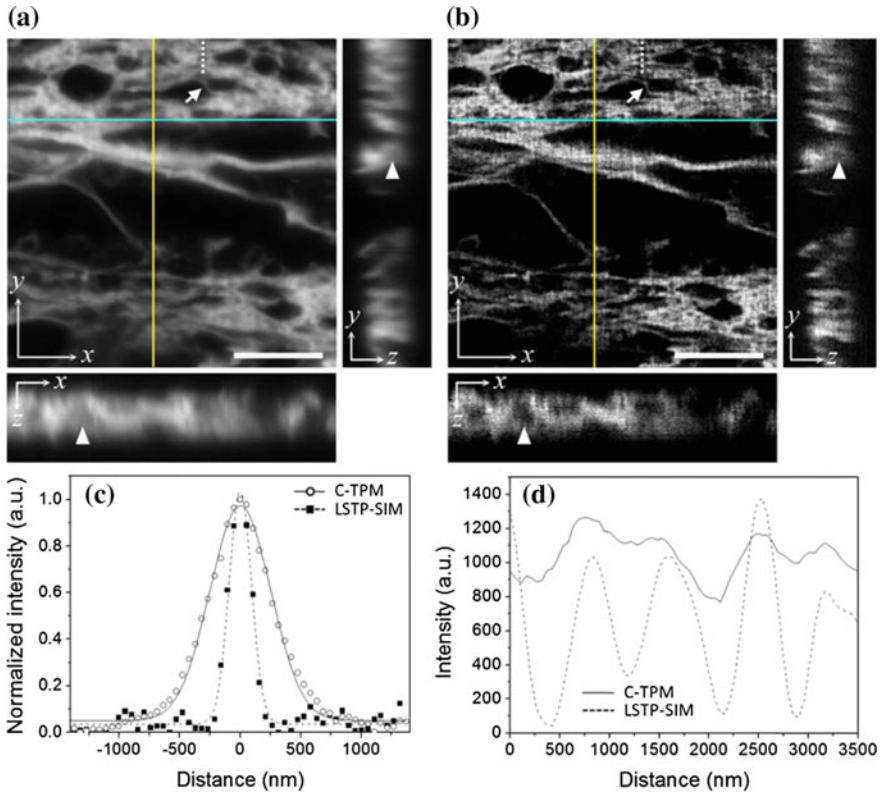


**Fig. 12.6** 3D imaging of an H&E-stained mouse collagenous tissue with thickness of  $6\mu\text{m}$ . **a** Camera-based 2PEF (C-TPM) and **b** laser-scanning 2PEF-SIM (LSTP-SIM) image sets of collagen fibers in the tissue, including  $xy$ -,  $xz$ -, and  $yz$ -sections. The  $xz$ - and  $zy$ -sections are at the positions indicated by blue (horizontal) and yellow (vertical) lines, respectively. The axial resolution of the LSTP-SIM is shown to be enhanced in contrast to that of C-TPM (arrowheads in the  $xz$ - and  $yz$ -sections); **c** the C-TPM and LSTP-SIM intensity profiles across a collagen fiber [arrows in **a** and **b**]; **d** the C-TPM and LSTP-SIM intensity profiles along the dashed lines in **(a)** and **(b)**. Scale bars are  $10\mu\text{m}$ . Adapted with permission from [27]

### 12.5.2 Super-Resolution Using Coherent Nonlinear Processes

During the last decade, several super-resolution schemes based on coherent nonlinear processes, such as SHG, THG, or CARS, have been proposed. Some have been based on approaches similar to STED microscopy [18, 20], while others have utilized the SIM scheme [19, 21, 23]. Here, we restrict our discussion on the later works.

Several of the proposed techniques have been based on a wide-field CARS configuration [61]. Conceptually, it is straightforward to generalize the SIM scheme to wide-field CARS microscopy. However, due to the coherence of the CARS process,

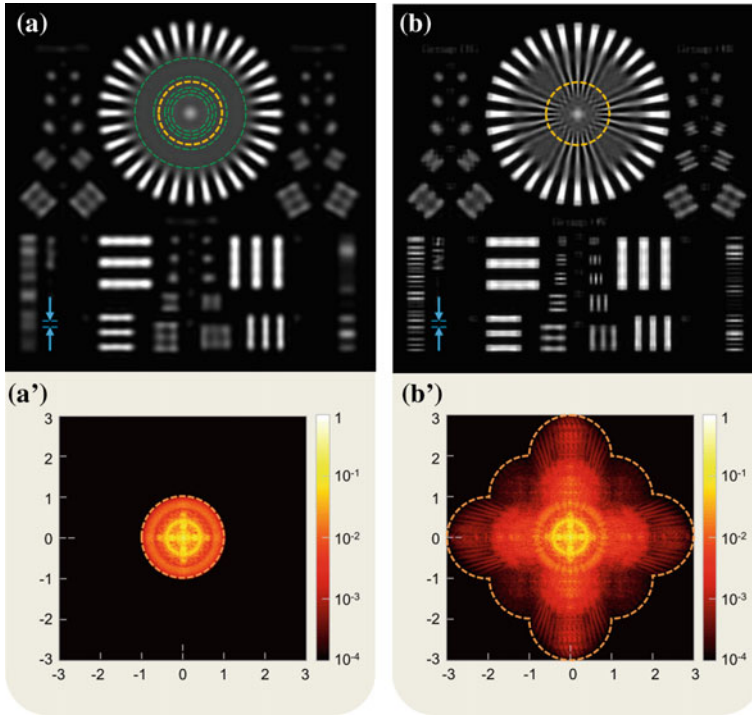


**Fig. 12.7** Simulated coherent images (top) and the associated spatial frequency spectra (bottom) for (a, a') the conventional wide-field CARS and (b, b') the super-resolution SIM CARS. The dashed circle (yellow) on the area of the sector star target is drawn to indicate the location on which the radial bars have a cycle period equal to the diffraction limit (311 nm). The radial bars at the circumferences of the five circles with increasing radii (green lines), have cycle periods of 0.58, 0.70, 0.81, 1.16, and 1.74 times the diffraction limit, respectively, which are equal to those of the line bar elements 10, 12, 14, 20, and 30. The image spectra (logarithmic scale) are displayed in false color with their horizontal and vertical axes normalized with the intensity cut-off frequency (the inverse of diffraction-limited resolution). Adapted with permission from [21]

phase-matching considerations do complicate the implementation as has been noted in [19, 21]. A numerical demonstration of the potential capabilities and the expected threefold enhancement of the resolution is shown in Fig. 12.7.

For SHG and THG modalities, only a few works proposing capability for super-resolution yet exist [22, 23, 55]. The work presented in [23] proposes how the SIM scheme could be generalized to nonlinear processes, such as to SHG and THG, by performing holographic detection [55, 62]. By considering an incident fundamental beam at  $\lambda = 1064$  nm and objectives with  $NA = 1.4$ , lateral resolution of 118 nm (77 nm) were predicted for SHG (THG) modality, corresponding to fourfold and sixfold increases in resolution, respectively (see Fig. 12.8).

An impressive experimental demonstration of combined super-resolution SHG and 2PEF microscopy has been described in [22]. The approach is based on spatial

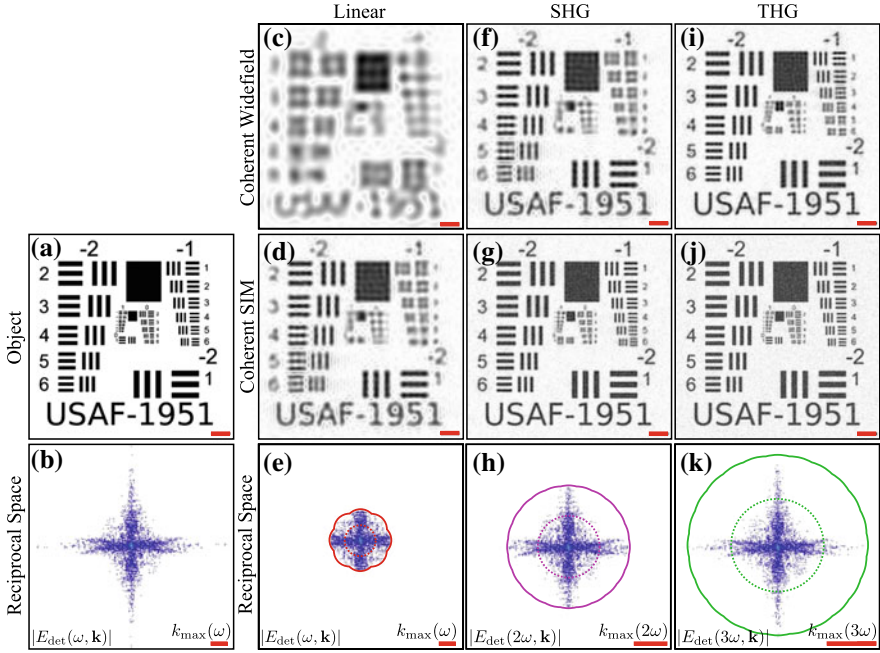


**Fig. 12.8** Simulated lateral resolution improvement using coherent SIM schemes [23]. The simulations were performed assuming a  $\text{SNR} = 500$ . **a** Original object with feature sizes below (50 nm) and **b** the FT of the object. The object is poorly resolved using only **c** conventional coherent wide-field microscopy, but **d** coherent SIM does provide somewhat better resolution because **e** the extent of the total CTF is doubled. The image features become also sharper with **f** wide-field SHG or **i** wide-field THG, but are significantly better resolved by the **g** SHG-SIM and **j** THG-SIM. The improvement using the SIM schemes occurs because each SIM extends the total CTF by almost a factor of **e** two, **h** four and **k** six, respectively (solid lines). Note that  $k_{\max}$  is doubled (tripled) for SHG (THG) (see dotted circles). The red scale bars are  $1\ \mu\text{m}$

frequency modulated imaging (SPIFI), which can in a way be understood as a form of line-scanning SIM. Interestingly, the image formation in SPIFI is achieved by illuminating the sample with structured illumination corresponding only to a single spatial frequency  $k_x(t)$  at a given time interval  $t$  while recording the detected signal  $\hat{I}_{\text{det}}(k_x)$  as a function of  $k_x$  using a fast detector. Then, by spatially modulating the illumination beam over the entire passband of the system ( $-k'_{\max} < k_x(t) < k'_{\max}$ ), the full  $\hat{I}_{\text{det}}(k_x)$  distribution can be recorded. This process is perhaps better understood by looking at (12.2b) in the spatial frequency domain. Since the illumination at a given time  $t$  contains only a single  $k_x(t)$  component, incident beam is to a good approximation a delta function  $\hat{I}_{\text{inc}}(k_x) \approx I_0 \delta(k_x)$ . In this case, the convolutions between the two incident beam terms and the sample distribution  $\hat{S}_{\text{em}}^{(2)}(\mathbf{k})$  are greatly simplified resulting in emitted beam distribution  $\hat{I}_{\text{em}}(k_x) \approx \hat{S}_{\text{em}}^{(2)}(\mathbf{k})(I_0 \delta(k_x))^2$ . Therefore, the measurement of the time-varying signal using the fast detector corresponds to the measurement of  $\hat{I}_{\text{det}}(k_x) = \text{OTF}(k_x) \hat{I}_{\text{em}}(k_x)$ . In other words, a single line of the

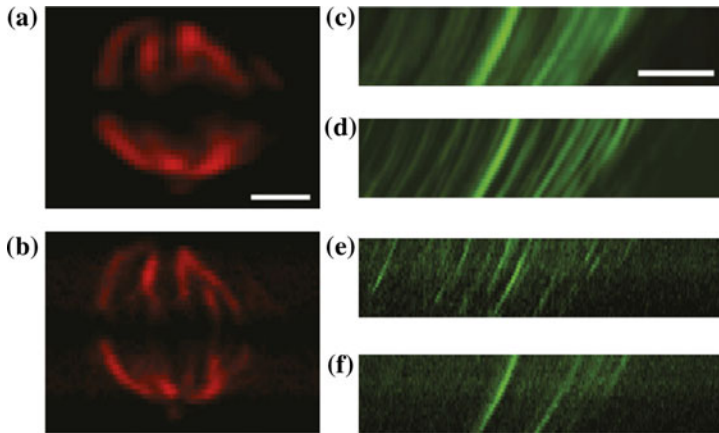


**Fig. 12.9** 2PEF and SHG images collected from biological media with MP-SPIFI. First-order (a) and second-order (b) MP-SPIFI images of 2PEF from a mitotic HeLa cell immunostained with primary antibodies against alpha tubulin and secondary antibodies tagged with Alexa 546. Scale bar is 3  $\mu\text{m}$ . c–f First- through fourth-order images of SHG from fixed, 16- $\mu\text{m}$ -thick rabbit tendon. Scale bars are 10  $\mu\text{m}$ . All images were collected at 0.8 NA with laser pulses centered at 1065 nm. 2PEF was collected in the epidirection and SHG was collected in the forward-scattered direction. Both datasets were captured at 31.6 Hz. The HeLa image is the average of 41 images for a total collection time of 58.4 s, whereas the images of rabbit tendon are averages formed from 1000 images for a total collection time of 665 s. Adapted from [22]

detected image  $I_{\text{det}}(x)$  can be formed by taking the inverse FT of the  $\hat{I}_{\text{det}}(k_x)$ , which is the measured signal. Finally, a two-dimensional image  $I_{\text{det}}(\mathbf{r})$  can be formed by moving the sample line by line in  $y$ -direction and repeating the data acquisition process for each line. A clear advantage of this imaging scheme is, that no laser-scanning equipment is needed simplifying the implementation of the technique. Unfortunately, scanning a two-dimensional object with SPIFI is still a time-consuming task, and the improved resolution was only demonstrated in one direction (see Fig. 12.9).

We end this section by stating that several techniques for label-free super-resolution have already been proposed and developed. Many of the experimentally realized techniques can already achieve around 100 nm lateral resolution while some of the proposed techniques promise to deliver even better resolution. Therefore, it can be envisaged that the achievable resolution will continue to improve in the future. This trend will certainly enable the emergence of new interesting applications for label-free imaging, and can be also very relevant in terms of the existing applications of nonlinear microscopy, which are the topic of the next section.

## 12.6 Current Applications of Nonlinear Microscopy

We start this section by reminding the reader of the advantages of performing multiphoton microscopy [16, 49]. After that, we will briefly review the current applications of multiphoton microscopy which could all benefit from super-resolution techniques. First, compared to conventional fluorescence microscopy, multiphoton modalities enable to study objects deeper inside intact tissues. This is due to the fact, that longer excitation wavelengths can be used, which do not scatter as strongly from tissues [63, 64]. For example, *in vivo* 3PEF imaging of subcortical structures within intact mouse brain have been recently demonstrated reporting very impressive imaging depths of over 1 mm [52]. Second, multiphoton modalities provide intrinsic optical sectioning, which in fact makes it straightforward to perform three-dimensional imaging [16]. Third, when carefully performed, the use of multiphoton excitation leads to smaller phototoxicity and bleaching effects, because the excitation occurs at longer wavelengths where single-photon fluorescence is negligible. The efficient excitation of fluorophores via multiphoton processes occurs only at the focal point [49].

When biological tissues are imaged using multiphoton modalities, it is important to understand the molecular origins for the contrast. In the case of label-free imaging techniques, the sources for contrast become more limited because external fluorescent molecules cannot be utilized. Fortunately, biological tissues contain many intrinsic fluorophores which can be used in 2PEF and 3PEF microscopies [49]. By far, the two most often utilized fluorophores are reduced nicotinamide adenine dinucleotide phosphates [NAD(P)H] and flavin adenine dinucleotides (FAD). In particular, assessment of the ratio of the relative amounts of NADH and FAD molecules, also known as the redox ratio, has been found to be very useful for monitoring metabolic activity of cells, which is known to be an important factor in carcinogenesis [65, 66]. An excellent source for further reading on intrinsic fluorophores and their use in multiphoton microscopy is found in [49].

In addition to 2PEF and 3PEF, also other nonlinear processes can be utilized for label-free contrast. Since the pioneering studies, SHG and THG microscopies have evolved into highly useful tools to study biological samples [44–46, 67]. For example, SHG microscopy can provide useful information of tissue morphology for diagnostic applications [68, 69], while THG microscopy can be used to study the organization of lipid molecules [70–72].

The detected nonlinear signal, and thus the contrast, originates in SHG microscopy mostly from *ordered* molecular structures, such as from fibrous collagen, elastin, myosin and actin proteins, and from microtubules [73]. The fact that SHG microscopy is particularly sensitive to the order of SHG-active molecules, and not just to their concentration, is because coherent second-order nonlinear processes are strongly affected by symmetry issues [17]. As a consequence, SHG imaging can be used to provide additional structural information of objects. This has been found to be very useful, for example, for performing collagen scoring in fibrotic tissues [68], in

discrimination of different types of collagens [74], in wound healing studies and in cancer research [69, 75–78].

In addition to using linearly polarized excitation beams and polarization-sensitive detection, also circularly polarized light can be used to provide information of the objects. A few recent works have studied if nonlinear optical activity (NOA) effects could provide additional, or more sensitive, morphological information of imaged objects [79–84]. In particular, NOA effects are related to the small-scale chirality and anisotropy of the studied objects and could, therefore, provide three-dimensional structural information. In principle, it is possible to link such information even down to protein-level structures of the object, however, it is not yet clear how sensitively the measured NOA effects could truly depend on such small-scale changes. Nevertheless, since changes in the protein-level structure are related to many diseases and disorders, such modalities could turn out to be highly useful in biomedical or diagnostic applications.

Another powerful and truly label-free nonlinear imaging modality is based on THG. Compared to SHG imaging, in THG microscopy the excitation of objects can be performed at longer wavelengths. Due to this advantage, THG modality has been used for imaging neurons, white-matter and blood cells deep inside live murine brain tissues [85]. THG microscopy has also found applications in lipid research, since lipid molecules act as efficient sources of THG [71, 72, 86]. For example, lipid bodies in liver tissues and cells have been studied using THG microscopy [70].

Besides THG, also other third-order processes can be utilized in imaging. In particular, CARS microscopy has shown its usefulness as a label-free technique which can also provide chemical contrast [43, 61]. Applications of CARS microscopy include lipid composition studies of lipid droplets and investigations of the progression of atherosclerosis in arterial tissues [87, 88]. An illustrative application example is shown in Fig. 12.10, where combined SHG, 2PEF and CARS microscopy has been performed to study atherosclerotic lesions of a rabbit model.

As is evident from the overall discussion above, label-free nonlinear microscopy modalities have already found many interesting and relevant biomedical applications. These existing applications could undoubtedly benefit from the improved capabilities that nonlinear super-resolution techniques could offer. In addition, new applications are bound to emerge once label-free super-resolution techniques establish themselves as a more mature technology. Finally, we need to mention that in addition to the aforementioned biomedical applications, nonlinear label-free microscopy has also been found very useful to investigate artificial metamaterials [90, 91], or one- and two-dimensional materials, such as carbon nanotubes or graphene [92–96]. Such applications could also greatly benefit from the improved resolution.

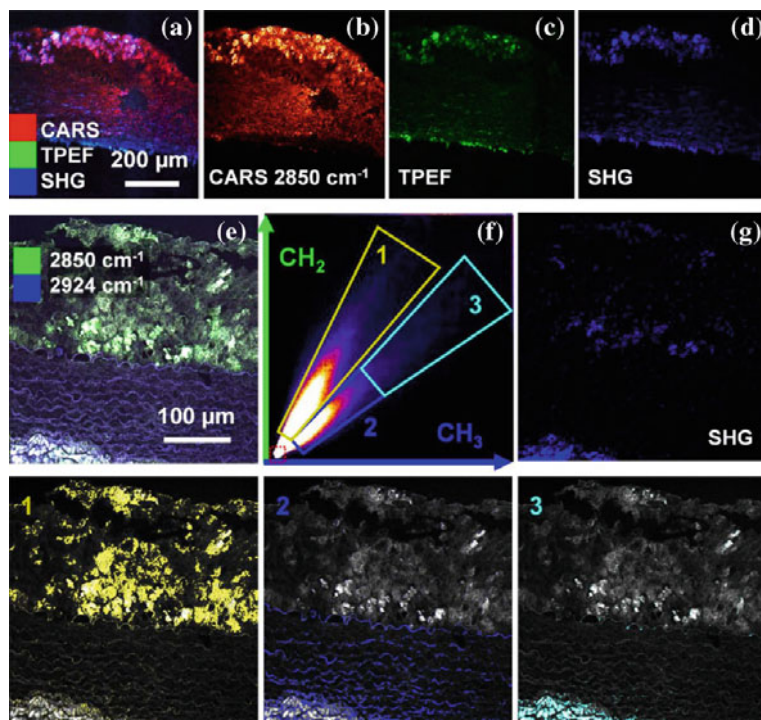


**Fig. 12.10** Analysis of the composition of an atherosclerotic lesion of a rabbit model for atherosclerosis by multimodal nonlinear imaging combining CARS at  $2850\text{ cm}^{-1}$ , SHG, and two-photon fluorescence (TPEF) (a–d), which can be significantly improved by multispectral high-resolution CARS (e–g). CARS at  $2850\text{ cm}^{-1}$  allows detection of high-concentrated lipids (b) and visualization of the morphology but cannot discern low-concentrated lipids from protein. Fluorescent lipids and elastin are visualized by TPEF (c), while SHG detects cholesterol crystals and collagen (d) colocalized with elastin. CARS at  $\text{CH}_3$  (blue) and  $\text{CH}_2$  (green), panel e, allows discerning protein from lipid contributions. The frequency scatter plot (f) shows distinct segments of protein and lipid pixels. Backprojection localizes the lipid component within the plaque (1), the low-intensity protein component within the tunica media (2), and the high-intensity protein within the tunica externa (3), which allows identification of the SHG-active component in panel g in the tunica externa as collagen, while the SHG-active marker within the plaque is assigned to crystalline cholesterol. Reprinted with permission from [89]. Copyright (2018) American Chemical Society

## 12.7 Future Directions and Challenges

Two important aspects and main advantages of optical microscopy has so far not been much discussed in this Chapter. These are the optical sectioning capability and the potential for long imaging depths. Multiphoton microscopy, in particular, can be used to image objects at very deep imaging depths now well beyond 1 mm, providing an almost order of magnitude improvement to conventional linear microscopy techniques [51, 52]. This improvement is due to the fact that the absorption and

scattering of light is considerably decreased when longer wavelengths are used to excite objects. However, combining super-resolution techniques with good imaging depths have turned out to be very challenging. Only in a very recent work a spatial resolution of 106 nm at imaging depth of around 100  $\mu\text{m}$  using 3PEF has been demonstrated [28]. The demonstrated technique is called interferometric temporal focusing (ITF) microscopy, and combines SIM microscopy with the temporal focusing scheme. Despite the impressive progress, additional work is necessary to further improve the imaging depths of multiphoton microscopies.

A promising route to image objects even deeper is to perform multiphoton endoscopy, which can provide over 1 cm imaging depths facilitating, for example, studies of intact animals [97–102]. Multiphoton endoscopes are minimally invasive and could thus be suitable for clinical applications, such as for label-free in situ histopathology diagnosis. In order to facilitate excitation of objects using short femtosecond pulses, gradient-index (GRIN) lenses are often used in multiphoton endoscopes due to their minimal pulse dispersion [97, 98]. Despite the advantages of multiphoton endoscopes a major drawback is their somewhat limited lateral and axial resolutions, which commonly are around 1  $\mu\text{m}$  and 6  $\mu\text{m}$ , respectively [99, 101]. This is mostly due to moderate NAs ( $\sim 0.8$ ) of available GRIN lenses. In addition, it seems very challenging to implement a diffraction-limited GRIN lens-based imaging system, in practice degrading the practical resolution further from the ideal one [97]. Therefore, major advances in the existing technology and capabilities seem entirely feasible in the near future. In addition, interesting possibilities might arise by developing super-resolution endoscopy [103].

Another upcoming trend is the implementation of multimodal multiphoton systems [89, 104–107]. The motivation for multimodal multiphoton imaging is the possibility to gather more detailed information of the object under study, as is seen in Fig. 12.10, demonstrating combined SHG, 2PEF, and CARS imaging of atherosclerotic lesions. In addition, modification of a multiphoton system into a multimodal one is often relatively straightforward, and can in some cases be achieved just by adding a few strategically placed dichroic mirrors, filters and detectors to the detection arms. This is especially the case for CARS microscopes, where several laser beams at different wavelengths are already used.

For future applications, there is also a need to develop automated image analysis, for example, to classify between healthy and cancerous ovarian tissues [78, 108]. Machine learning, convolutional neural networks, and deep learning are especially seen as key technologies, which can be used to transform massive amounts of data, easily recorded using a modern optical microscope, into as-it-is useful information. These technologies could be especially valuable in clinical in situ applications benefiting from real-time image analysis, such as detection of residual disease at the time of surgery. Because the amount (and quality) of data plays a key role in these machine learning approaches, we expect that multimodal imaging is becoming more and more important in the future.

## 12.8 Conclusion

We conclude this chapter by stating that label-free super-resolution multiphoton microscopy is a vibrant and timely research topic. Label-free techniques are minimally invasive and require very little sample preparation. Therefore, compared to conventional fluorescent microscopy modalities, nonlinear label-free techniques could be especially suitable for applications in clinical environments. Several label-free super-resolution techniques based on SIM approach have already been proposed and demonstrated. Although none of the existing works have yet experimentally demonstrated resolution better than 100 nm, we are confident that this landmark will be soon reached. Once that landmark has been achieved, label-free SIM microscopy becomes more competitive in its capabilities with conventional SIM, after which novel imaging applications benefiting of label-free modalities will surely follow.

The recent technological development of suitable laser sources and detectors has been impressive, and has driven the prices of commercial products down facilitating the progress in the field. Especially for SIM-based super-resolution approaches, the recent progress in sensitive CMOS camera technology is noteworthy and is motivating the users to move away from traditional electron-multiplying CCD cameras. In overall, we can envision a bright future for nonlinear label-free super-resolution microscopy, which will provide new possibilities both for basic research in biology and medicine as well as for biomedical applications.

**Acknowledgements** This work was supported by the Academy of Finland (Grant No. 308596).

## References

1. R. Erni, M.D. Rossell, C. Kisielowski, U. Dahmen, Atomic-resolution imaging with a sub-50-pm electron probe. *Phys. Rev. Lett.* **102**(9), 96101 (2009)
2. A.H. Zewail, 4D ultrafast electron diffraction, crystallography, and microscopy. *Annu. Rev. Phys. Chem.* **57**(1), 65–103 (2006)
3. B.R. Masters, P. So, *Handbook of Biomedical Nonlinear Optical Microscopy* (Oxford University Press, 2008)
4. E. Abbe, Beiträge zur Theorie des Mikroskops und der mikroskopischen Wahrnehmung. *Arch. für Mikroskopische Anat.* **9**(1), 413–418 (1873)
5. H.L.F. Helmholtz, H. Fripp, On the limits of the optical capacity of the microscope. *J. Microsc.* **16**(1), 15–39 (1876)
6. S.W. Hell, J. Wichmann, Stimulated-emission-depletion fluorescence microscopy. *Opt. Lett.* **19**(11), 780–782 (1994)
7. R. Heintzmann, C.G. Cremer, Laterally modulated excitation microscopy: improvement of resolution by using a diffraction grating. *Proc. SPIE* **3568**, 185–197 (1999)
8. M.G.L. Gustafsson, Nonlinear structured-illumination microscopy: wide-field fluorescence imaging with theoretically unlimited resolution. *Proc. Natl. Acad. Sci.* **102**(37), 13081–13086 (2005)
9. M.J. Rust, M. Bates, X. Zhuang, Sub-diffraction-limit imaging by stochastic optical reconstruction microscopy (STORM). *Nat. Methods* **3**(10), 793–795 (2006)
10. S.W. Hell, Far-field optical nanoscopy. *Science* **316**(101), 1153–1158 (2007)

11. E. Betzig, G.H. Patterson, R. Sougrat, O.W. Lindwasser, S. Olenych, J.S. Bonifacino, M.W. Davidson, J. Lippincott-Schwartz, H.F. Hess, Imaging intracellular fluorescent proteins at nanometer resolution. *Science* **313**(5793), 1642–1645 (2006)
12. M.G.L. Gustafsson, Surpassing the lateral resolution limit by a factor of two using structured illumination microscopy. *J. Microsc.* **198**(2), 82–87 (2000)
13. A.K. Dunn, H. Bolay, M.A. Moskowitz, D.A. Boas, Dynamic imaging of cerebral blood flow using laser speckle. *J. Cereb. Blood Flow Metab.* **21**(3), 195–201 (2001)
14. P. Marquet, B. Rappaz, P.J. Magistretti, E. Cuche, Y. Emery, T. Colomb, C. Depeursinge, Digital holographic microscopy: a noninvasive contrast imaging technique allowing quantitative visualization of living cells with subwavelength axial accuracy. *Opt. Lett.* **30**(5), 468–470 (2005)
15. F. Jünger, P.V. Olshausen, A. Rohrbach, Fast, label-free super-resolution live-cell imaging using rotating coherent scattering (ROCS) microscopy. *Sci. Rep.* **6**, 30393 (2016)
16. W. Denk, J. Strickler, W. Webb, Two-photon laser scanning fluorescence microscopy. *Science* **248**(4951), 73–76 (1990)
17. R.W. Boyd, *Nonlinear Optics* (Academic Press, San Diego, 2003)
18. W.P. Beeker, P. Gross, C.J. Lee, C. Cleff, H.L. Offerhaus, C. Fallnich, J.L. Herek, K.-J. Boller, A route to sub-diffraction-limited CARS microscopy. *Opt. Express* **17**(25), 22632–22638 (2009)
19. K.M. Hajek, B. Littleton, D. Turk, T.J. McIntyre, H. Rubinsztein-Dunlop, A method for achieving super-resolved widefield CARS microscopy. *Opt. Express* **18**(18), 19263–19272 (2010)
20. H. Kim, G.W. Bryant, S.J. Stranick, Superresolution four-wave mixing microscopy. *Opt. Express* **20**(6), 6042–6051 (2012)
21. J.H. Park, S.-W. Lee, E.S. Lee, J.Y. Lee, A method for super-resolved CARS microscopy with structured illumination in two dimensions. *Opt. Express* **22**(8), 9854–9870 (2014)
22. J.J. Field, K.W. Wernsing, S.R. Domingue, A.M.A. Motz, K.F. DeLuca, J.G. DeLuca, D. Kuciauskas, D.H. Levi, J.A. Squier, R.A. Bartels, Super-resolved multimodal multiphoton microscopy with spatial frequency-modulated imaging. *Proc. Natl. Acad. Sci.* **113**(24), 6605–6610 (2015)
23. M.J. Huttunen, A. Abbas, J. Upham, R.W. Boyd, Label-free super-resolution with coherent nonlinear structured-illumination microscopy. *J. Opt.* **19**(8), 085504 (2017)
24. R. Heintzmann, T.M. Jovin, C. Cremer, Saturated patterned excitation microscopy: a concept for optical resolution improvement. *J. Opt. Soc. Am. A* **19**(8), 1599–1609 (2002)
25. E.H. Rego, L. Shao, J.J. Macklin, L. Winoto, G.A. Johansson, N. Kamps-Hughes, M.W. Davidson, M.G.L. Gustafsson, Nonlinear structured-illumination microscopy with a photoswitchable protein reveals cellular structures at 50-nm resolution. *Proc. Natl. Acad. Sci.* **109**(3), E135–E143 (2012)
26. S. Van Aert, D. Van Dyck, A.J. den Dekker, Resolution of coherent and incoherent imaging systems reconsidered—classical criteria and a statistical alternative. *Opt. Express* **14**(9), 3830–3839 (2006)
27. C.-H. Yeh, S.-Y. Chen, Resolution enhancement of two-photon microscopy via intensity-modulated laser scanning structured illumination. *Appl. Opt.* **54**(9), 2309–2317 (2015)
28. K. Toda, K. Isobe, K. Namiki, H. Kawano, A. Miyawaki, K. Midorikawa, Interferometric temporal focusing microscopy using three-photon excitation fluorescence. *Biomed. Opt. Express* **20**(4), 237–239 (2018)
29. R. Heintzmann, T. Huser, Super-resolution structured illumination microscopy. *Chem. Rev.* **117**(23), 13890–13908 (2017)
30. M.A.A. Neil, R. Juškaitis, T. Wilson, Method of obtaining optical sectioning by using structured light in a conventional microscope. *Opt. Lett.* **22**(24), 1905–1907 (1997)
31. M. Ingaramo, A.G. York, P. Wawrzusin, O. Milberg, A. Hong, R. Weigert, H. Shroff, G.H. Patterson, Two-photon excitation improves multifocal structured illumination microscopy in thick scattering tissue. *Proc. Natl. Acad. Sci.* **111**(14), 5254–5259 (2014)

32. E. Mudry, K. Belkebir, J. Girard, J. Savatier, E. Le Moal, C. Nicoletti, M. Allain, A. Sentenac, Structured illumination microscopy using unknown speckle patterns. *Nat. Photonics* **6**, 312–315 (2012)
33. A. Jost, E. Tolstik, P. Feldmann, K. Wicker, A. Sentenac, R. Heintzmann, Optical sectioning and high resolution in single-slice structured illumination microscopy by thick slice blind-SIM reconstruction. *PLoS One* **10**(7), 1–10 (2015)
34. G.M. Hagen, P. Křížek, T. Lukeš, M. Ovesný, K. Fliegel, SIMToolbox: a MATLAB toolbox for structured illumination fluorescence microscopy. *Bioinformatics* **32**(2), 318–320 (2015)
35. G. Ball, J. Demmerle, R. Kaufmann, I. Davis, I.M. Dobbie, L. Schermelleh, SIMcheck: a toolbox for successful super-resolution structured illumination microscopy. *Sci. Rep.* **5**, 15915 (2015)
36. M. Müller, V. Mönkemöller, S. Hennig, W. Hübner, T. Huser, Open-source image reconstruction of super-resolution structured illumination microscopy data in ImageJ. *Nat. Commun.* **7**, 10980 (2016)
37. J. Lu, W. Min, J.-A. Conchello, X.S. Xie, J.W. Lichtman, J.-A. Conchello, X.S. Xie, J.W. Lichtman, Super-resolution laser scanning microscopy through spatiotemporal modulation. *Nano Lett.* **9**(11), 3883–3889 (2009)
38. B.E. Urban, J. Yi, S. Chen, B. Dong, Y. Zhu, S.H. Devries, V. Backman, H.F. Zhang, Super-resolution two-photon microscopy via scanning patterned illumination. *Phys. Rev. E* **91**(4), 042703 (2015)
39. O. Mandula, M. Kielhorn, K. Wicker, G. Krampert, I. Kleppe, R. Heintzmann, Line scan-structured illumination microscopy super-resolution imaging in thick fluorescent samples. *Opt. Express* **20**(22), 24167–24174 (2012)
40. C.B. Müller, J. Enderlein, Image scanning microscopy. *Phys. Rev. Lett.* **104**(19), 198101 (2010)
41. S. Roth, C.J.R. Sheppard, K. Wicker, R. Heintzmann, Optical photon reassignment microscopy (OPRA). *Opt. Nanoscopy* **2**(1), 5 (2013)
42. C. Kuang, Y. Ma, R. Zhou, G. Zheng, Y. Fang, Y. Xu, X. Liu, P.T. So, Virtual k-space modulation optical microscopy. *Phys. Rev. Lett.* **117**(2), 028102 (2016)
43. C.L. Evans, E.O. Potma, M. Puoris'haag, D. Cote, C.P. Lin, X.S. Xie, Chemical imaging of tissue in vivo with video-rate coherent anti-Stokes Raman scattering microscopy. *Proc. Natl. Acad. Sci.* **102**(46), 16807–16812 (2005)
44. J.N. Gannaway, C.J.R. Sheppard, Second-harmonic imaging in the scanning optical microscope. *Opt. Quantum Electron.* **10**(5), 435–439 (1978)
45. D. Yelin, Y. Silberberg, Laser scanning third-harmonic-generation microscopy in biology. *Opt. Express* **5**(8), 169–175 (1999)
46. J.A. Squier, K.R. Wilson, Third harmonic generation microscopy. *Opt. Express* **3**(9), 315–324 (1998)
47. C.L. Evans, X.S. Xie, Coherent anti-Stokes Raman scattering microscopy: chemical imaging for biology and medicine. *Annu. Rev. Anal. Chem.* **1**, 883–909 (2008)
48. C. Macias-Romero, M.E.P. Didier, P. Jourdain, P. Marquet, P. Magistretti, O.B. Tarun, V. Zubkovs, A. Radenovic, S. Roke, High throughput second harmonic imaging for label-free biological applications. *Opt. Express* **22**(25), 31102–31112 (2014)
49. W.R. Zipfel, R.M. Williams, W.W. Webb, Nonlinear magic: multiphoton microscopy in the biosciences. *Nat. Biotechnol.* **21**(11), 1369–1377 (2003)
50. F. Helmchen, W. Denk, Deep tissue two-photon microscopy. *Nat. Methods* **2**(12), 932–940 (2005)
51. D. Kobat, N.G. Horton, C. Xu, In vivo two-photon microscopy to 1.6-mm depth in mouse cortex. *J. Biomed. Opt.* **16**(10), 106014 (2011)
52. N.G. Horton, K. Wang, D. Kobat, C.G. Clark, F.W. Wise, C.B. Schaffer, C. Xu, In vivo three-photon microscopy of subcortical structures within an intact mouse brain. *Nat. Photonics* **7**(3), 205 (2013)
53. J. Squier, M. Müller, High resolution nonlinear microscopy: a review of sources and methods for achieving optimal imaging. *Rev. Sci. Instrum.* **72**(7), 2855–2867 (2001)

54. C.K. Sun, S.W. Chu, S.Y. Chen, T.H. Tsai, T.M. Liu, C.Y. Lin, H.J. Tsai, Higher harmonic generation microscopy for developmental biology. *J. Struct. Biol.* **147**(1), 19–30 (2004)
55. O. Masihzadeh, P. Schlup, R.A. Bartels, Enhanced spatial resolution in third-harmonic microscopy through polarization switching. *Opt. Lett.* **34**(8), 1240–1242 (2009)
56. K. Isobe, T. Takeda, K. Mochizuki, Q. Song, A. Suda, F. Kannari, H. Kawano, A. Kumagai, A. Miyawaki, K. Midorikawa, Enhancement of lateral resolution and optical sectioning capability of two-photon fluorescence microscopy by combining temporal-focusing with structured illumination. *Biomed. Opt. Express* **4**(11), 2396–2410 (2013)
57. D. Fittinghoff, P. Wiseman, J. Squier, Widefield multiphoton and temporally decorrelated multifocal multiphoton microscopy. *Opt. Express* **7**(8), 273–279 (2000)
58. G. Zhu, J. Van Howe, M. Durst, W. Zipfel, C. Xu, W. Denk, K.R. Delaney, A. Gelperin, D. Kleinfeld, B.W. Strawbridge, D.W. Tank, R. Yuste, Simultaneous spatial and temporal focusing of femtosecond pulses. *Opt. Express* **13**(6), 2153–2159 (2005)
59. E. Tal, D. Oron, Y. Silberberg, Improved depth resolution in video-rate line-scanning multiphoton microscopy using temporal focusing. *Opt. Lett.* **30**(13), 1686–1688 (2005)
60. K. Toda, K. Isobe, K. Namiki, H. Kawano, A. Miyawaki, K. Midorikawa, Temporal focusing microscopy using three-photon excitation fluorescence with a 92-fs Yb-fiber chirped pulse amplifier. *Biomed. Opt. Express* **8**(6), 2796–2806 (2017)
61. C. Heinrich, S. Bernet, M. Ritsch-Marte, Wide-field coherent anti-Stokes Raman scattering microscopy. *Appl. Phys. Lett.* **84**(5), 816–818 (2004)
62. Y. Pu, M. Centurion, D. Psaltis, Harmonic holography: a new holographic principle. *Appl. Opt.* **47**(4), A103–A110 (2008)
63. D. Kobat, M.E. Durst, N. Nishimura, A.W. Wong, C.B. Schaffer, C. Xu, Deep tissue multiphoton microscopy using longer wavelength excitation. *Opt. Express* **17**(16), 13354–13364 (2009)
64. V. Andresen, S. Alexander, W.-M. Heupel, M. Hirschberg, R.M. Hoffman, P. Friedl, Infrared multiphoton microscopy: subcellular-resolved deep tissue imaging. *Curr. Opin. Biotechnol.* **20**(1), 54–62 (2009)
65. S. Huang, A.A. Heikal, W.W. Webb, Two-photon fluorescence spectroscopy and microscopy of NAD(P)H and flavoprotein. *Biophys. J.* **82**(5), 2811–2825 (2002)
66. M.C. Skala, K.M. Riching, A. Gendron-Fitzpatrick, J. Eickhoff, K.W. Eliceiri, J.G. White, N. Ramanujam, In vivo multiphoton microscopy of NADH and FAD redox states, fluorescence lifetimes, and cellular morphology in precancerous epithelia. *Proc. Natl. Acad. Sci.* **104**(49), 19494–19499 (2007)
67. E.E. Hoover, J.A. Squier, Advances in multiphoton microscopy technology. *Nat. Photonics* **7**(2), 93 (2013)
68. M. Strupler, A.-M. Pena, M. Hernest, P.-L. Tharaux, J.-L. Martin, E. Beaurepaire, M.-C. Schanne-Klein, Second harmonic imaging and scoring of collagen in fibrotic tissues. *Opt. Express* **15**(7), 4054–4065 (2007)
69. X. Chen, O. Nadiarynk, S. Plotnikov, P.J. Campagnola, Second harmonic generation microscopy for quantitative analysis of collagen fibrillar structure. *Nat. Protoc.* **7**(4), 654–669 (2012)
70. D. Débarre, W. Supatto, A.-M. Pena, A. Fabre, T. Tordjmann, L. Combettes, M.-C. Schanne-Klein, E. Beaurepaire, Imaging lipid bodies in cells and tissues using third-harmonic generation microscopy. *Nat. Methods* **3**(1), 47–53 (2006)
71. N. Olivier, M.A. Luengo-Oroz, L. Duloquin, E. Faure, T. Savy, I. Veilleux, X. Solinas, D. Débarre, P. Bourguin, A. Santos, N. Peyriéras, E. Beaurepaire, Cell lineage reconstruction of early zebrafish embryos using label-free nonlinear microscopy. *Science* **329**(5994), 967–971 (2010)
72. G. Bautista, S.G. Pfisterer, M.J. Huttunen, S. Ranjan, K. Kanerva, E. Ikonen, M. Kauranen, Polarized THG microscopy identifies compositionally different lipid droplets in mammalian cells. *Biophys. J.* **107**(10), 2230–2236 (2014)
73. D.A. Dombeck, K.A. Kasischke, H.D. Vishwasrao, M. Ingelsson, B.T. Hyman, W.W. Webb, Uniform polarity microtubule assemblies imaged in native brain tissue by second-harmonic generation microscopy. *Proc. Natl. Acad. Sci.* **100**(12), 7081–7086 (2003)

74. P.-J. Su, W.-L. Chen, T.-H. Li, C.-K. Chou, T.-H. Chen, Y.-Y. Ho, C.-H. Huang, S.-J. Chang, Y.-Y. Huang, H.-S. Lee, C.-Y. Dong, The discrimination of type I and type II collagen and the label-free imaging of engineered cartilage tissue. *Biomaterials* **31**(36), 9415–9421 (2010)
75. R. Cicchi, D. Kapsokalyvas, V. De Giorgi, V. Maio, A. Van Wiechen, D. Massi, T. Lotti, F.S. Pavone, Scoring of collagen organization in healthy and diseased human dermis by multiphoton microscopy. *J. Biophotonics* **3**(1–2), 34–43 (2010)
76. S. Zhuo, J. Yan, G. Chen, J. Chen, Y. Liu, J. Lu, X. Zhu, X. Jiang, S. Xie, Label-free monitoring of colonic cancer progression using multiphoton microscopy. *Biomed. Opt. Express* **2**(3), 615–619 (2011)
77. X. Wu, G. Chen, J. Lu, W. Zhu, J. Qiu, J. Chen, S. Xie, S. Zhuo, J. Yan, Label-free detection of breast masses using multiphoton microscopy. *PLoS One* **8**(6), e65933 (2013)
78. M.J. Huttunen, A. Hassan, C.W. McCloskey, S. Fasih, J. Upham, B.C. Vanderhyden, R.W. Boyd, S. Murugkar, Automated classification of multiphoton microscopy images of ovarian tissue using deep learning. *J. Biomed. Opt.* **23**(6), 066002 (2018)
79. L.M. Hupert, G.J. Simpson, Chirality in Nonlinear Optics. *Annu. Rev. Phys. Chem.* **60**(1), 345–365 (2009)
80. X. Chen, C. Raggio, P.J. Campagnola, Second-harmonic generation circular dichroism studies of osteogenesis imperfecta. *Opt. Lett.* **37**(18), 3837–3839 (2012)
81. H. Lee, M.J. Huttunen, K.-J. Hsu, M. Partanen, G.-Y. Zhuo, M. Kauranen, S.-W. Chu, Chiral imaging of collagen by second-harmonic generation circular dichroism. *Biomed. Opt. Express* **4**(6), 909–916 (2013)
82. G.Y. Zhuo, H. Lee, K.J. Hsu, M.J. Huttunen, M. Kauranen, Y.Y. Lin, S.-W. Chu, Three-dimensional structural imaging of starch granules by second-harmonic generation circular dichroism. *J. Microsc.* **253**(3), 183–190 (2014)
83. M.J. Huttunen, M. Partanen, G. Bautista, S.-W. Chu, M. Kauranen, Nonlinear optical activity effects in complex anisotropic three-dimensional media. *Opt. Mater. Express* **5**(1), 11–21 (2015)
84. M.Y. Chen, M.J. Huttunen, C.W. Kan, G.Deka, Y.Y. Lin, Y.C. W., M.J. Wu, H.L. Liu, S.-W. Chu, Resonant nonlinear microscopy reveals changes in molecular level chirality in native biological tissues. *Opt. Commun.* **422**, 56–63 (2018)
85. S. Witte, A. Negrean, J.C. Lodder, C.P.J. De Kock, G.T. Silva, H.D. Mansvelder, M.L. Groot, Label-free live brain imaging and targeted patching with third-harmonic generation microscopy. *Proc. Natl. Acad. Sci.* **108**(15), 5970–5975 (2011)
86. G. de Wit, J.S.H. Danial, P. Kukura, M.I. Wallace, Dynamic label-free imaging of lipid nanodomains. *Proc. Natl. Acad. Sci.* **112**(40), 12299–12303 (2015)
87. T.T. Le, I.M. Langohr, M.J. Locker, M. Sturek, J.-X. Cheng, Label-free molecular imaging of atherosclerotic lesions using multimodal nonlinear optical microscopy. *J. Biomed. Opt.* **12**(5), 54007 (2007)
88. H.A. Rinia, K.N.J. Burger, M. Bonn, M. Müller, Quantitative label-free imaging of lipid composition and packing of individual cellular lipid droplets using multiplex CARS microscopy. *Biophys. J.* **95**(10), 4908–4914 (2008)
89. T. Meyer, M. Chemnitz, M. Baumgartl, T. Gottschall, T. Pascher, C. Matthäus, B.F. Romeike, B.R. Brehm, J. Limpert, A. Tünnermann, M. Schmitt, B. Dietzek, J. Popp, Expanding multimodal microscopy by high spectral resolution coherent anti-stokes Raman scattering imaging for clinical disease diagnostics. *Anal. Chem.* **85**(14), 6703–6715 (2013)
90. G. Bautista, M.J. Huttunen, J. Mäkitalo, J.M. Kontio, J. Simonen, M. Kauranen, Second-harmonic generation imaging of metal nano-objects with cylindrical vector beams. *Nano Lett.* **12**(6), 3207–3212 (2012)
91. M. Kauranen, A.V. Zayats, Nonlinear plasmonics. *Nat. Photonics* **6**, 737–748 (2012)
92. H. Kim, T. Sheps, P.G. Collins, E.O. Potma, Nonlinear optical imaging of individual carbon nanotubes with four-wave-mixing microscopy. *Nano Lett.* **9**(8), 2991–2995 (2009)
93. A. Saynatjoki, L. Karvonen, J. Riikonen, W. Kim, S. Mehravar, R.A. Norwood, N. Peyghambarian, H. Lipsanen, K. Kieu, Rapid large-area multiphoton microscopy for characterization of graphene. *ACS Nano* **7**(10), 8441–8446 (2013)

94. M.J. Huttunen, O. Herranen, A. Johansson, H. Jiang, P.R. Mudimela, P. Myllyperkiö, G. Bautista, A.G. Nasibulin, E.I. Kauppinen, M. Ahlskog, M. Kauranen, M. Pettersson, Measurement of optical second-harmonic generation from an individual single-walled carbon nanotube. *New J. Phys.* **15**, 083043 (2013)
95. X. Yin, Z. Ye, D.A. Chenet, Y. Ye, K. O'Brien, J.C. Hone, X. Zhang, Edge nonlinear optics on a MoS<sub>2</sub> atomic monolayer. *Science* **344**(6183), 488–490 (2014)
96. L. Karvonen, A. Säynätjoki, M.J. Huttunen, A. Autere, B. Amirsolaimani, S. Li, R.A. Norwood, N. Peyghambarian, H. Lipsanen, G. Eda, K. Kieu, Z. Sun, Rapid visualization of grain boundaries in monolayer MoS<sub>2</sub> by multiphoton microscopy. *Nat. Commun.* **8**, 15714 (2017)
97. J.C. Jung, M.J. Schnitzer, Multiphoton endoscopy. *Opt. Lett.* **28**(11), 902–904 (2003)
98. M.J. Levene, D. Dombeck, K. Kasischke, R.P. Molloy, W.W. Webb, In vivo multiphoton microscopy of deep brain tissue. *J. Neurophysiol.* **91**, 1908–1912 (2004)
99. D.R. Rivera, C.M. Brown, D.G. Ouzounov, W.W. Webb, C. Xu, Multifocal multiphoton endoscope. *Opt. Lett.* **37**(8), 1349–1351 (2012)
100. D.R. Rivera, C.M. Brown, D.G. Ouzounov, I. Pavlova, D. Kobat, W.W. Webb, C. Xu, Compact and flexible raster scanning multiphoton endoscope capable of imaging unstained tissue. *Proc. Natl. Acad. Sci.* **108**(43), 17598–17603 (2011)
101. B.G. Saar, R.S. Johnston, C.W. Freudiger, X.S. Xie, E.J. Seibel, Coherent Raman scanning fiber endoscopy. *Opt. Lett.* **36**(13), 2396–2398 (2011)
102. G. Ducourthial, P. Leclerc, T. Mansuryan, M. Fabert, J. Brevier, R. Habert, F. Braud, R. Batrin, C. Vever-Bizet, G. Bourg-Heckly, L. Thiberville, A. Druilhe, A. Kudlinski, F. Louradour, Development of a real-time flexible multiphoton microendoscope for label-free imaging in a live animal. *Sci. Rep.* **5**, 18303 (2015)
103. F. Wang, H.S.S. Lai, L. Liu, P. Li, H. Yu, Z. Liu, Y. Wang, W.J. Li, Super-resolution endoscopy for real-time wide-field imaging. *Opt. Express* **23**(13), 16803–16811 (2015)
104. M. Rehberg, F. Krombach, U. Pohl, S. Dietzel, Label-free 3D visualization of cellular and tissue structures in intact muscle with second and third harmonic generation microscopy. *PLoS One* **6**(11), e28237 (2011)
105. H. Segawa, M. Okuno, H. Kano, P. Leproux, V. Couderc, H.-O. Hamaguchi, Label-free tetra-modal molecular imaging of living cells with CARS, SHG, THG and TSFG (coherent anti-Stokes Raman scattering, second harmonic generation, third harmonic generation and third-order sum frequency generation). *Opt. Express* **20**(9), 9551–9557 (2012)
106. I. Pope, W. Langbein, P. Watson, P. Borri, Simultaneous hyperspectral differential-CARS, TPF and SHG microscopy with a single 5 fs Ti: Sa laser. *Opt. Express* **21**(6), 7096–7106 (2013)
107. J. Zhang, E. Moradi, M.G. Somekh, M.L. Mather, Label-free, high resolution, multi-modal light microscopy for discrimination of live stem cell differentiation status. *Sci. Rep.* **8**(1), 697 (2018)
108. B. Wen, K.R. Campbell, K. Tilbury, O. Nadiarnykh, M.A. Brewer, M. Patankar, V. Singh, K.W. Eliceiri, P.J. Campagnola, 3D texture analysis for classification of second harmonic generation images of human ovarian cancer. *Sci. Rep.* **6**, 35734 (2016)

# Chapter 13

## Super-Resolution Microscopy Techniques Based on Plasmonics and Transformation Optics



Igor I. Smolyaninov and Vera N. Smolyaninova

**Abstract** Traditionally the resolution of conventional optical microscopes, which rely on optical waves that propagate into the far field, has been limited because of diffraction to a value on the order of a half-wavelength of the light used. Several nonlinear optical microscopy techniques overcome this limit using photo-switching and saturation of fluorescence. Very recently it was demonstrated that considerable resolution enhancement may also be achieved in linear far-field microscopy by making use of recent progress in plasmonics, metamaterials and transformation optics. We will review theoretical foundations of these techniques and present our recent proof of principle experiments.

### 13.1 Introduction

Although various electron and scanning probe microscopy techniques have long surpassed the conventional optical microscope in resolving power, optical microscopy remains invaluable in many fields of science. The practical limit to the resolution of an optical microscope is determined by diffraction: a wave cannot be localized to a region much smaller than half of its vacuum wavelength  $\lambda_0/2$ . Immersion microscopes introduced by Abbé in the 19th century have slightly improved resolution, on the order of  $\lambda_0/2n$ , because of the shorter wavelength of light,  $\lambda_0/n$ , in a medium with refractive index  $n$ . However, immersion microscopes are limited by the small range of refractive indices  $n$  of available natural transparent materials. For a while it was believed that the only way to achieve nanometer-scale spatial resolution in an optical

---

I. I. Smolyaninov (✉)

Department of Electrical and Computer Engineering, University of Maryland, College Park, MD 20742, USA

e-mail: [smoly@umd.edu](mailto:smoly@umd.edu)

Saltenna LLC, 1751 Pinnacle Drive #600, McLean, VA 22102, USA

V. N. Smolyaninova

Department of Physics Astronomy and Geosciences, Towson University, 8000 York Rd, Towson, MD 21252, USA

© Springer Nature Switzerland AG 2019

V. Astratov (ed.), *Label-Free Super-Resolution Microscopy*,

Biological and Medical Physics, Biomedical Engineering,

[https://doi.org/10.1007/978-3-030-21722-8\\_13](https://doi.org/10.1007/978-3-030-21722-8_13)

microscope was to detect evanescent optical waves in very close proximity to a studied sample using a near-field scanning optical microscope (NSOM) [1]. Although many fascinating results are being obtained with NSOM, such microscopes are not as versatile and convenient to use as regular far-field optical microscopes. For example, an image from a near-field optical microscope is obtained by point-by-point scanning, which is an indirect and a rather slow process, and can be affected by artifacts of the sample.

Over the past twenty years two major new thrusts have developed in optical microscopy, which are quickly demolishing the resolution barrier due to the diffraction limit. The first one is making use of nonlinear optics. A comprehensive review of this major research thrust has been published recently by Hell [2]. Broadly speaking, these techniques rely on photo-switching and/or saturation of fluorescence from individual molecules. They demonstrate far-field resolution of 20–30 nm, which is limited by light collection. Unfortunately, this technique also relies on scanning, which is a slow process. A parallel revolutionary development in usual linear optical microscopy was inspired by seminal paper by Pendry [3] and the following extraordinary progress in the optics of metamaterials. According to the Pendry's idea of a flat "perfect lens" made from an artificial negative refractive index metamaterial, a high resolution optical image could be obtained by amplified evanescent waves (surface plasmon polaritons) which live at the interface between the positive and negative index media. However, according to the original proposal, such an image would be observable only in the near-field of a perfect lens, and would require an auxiliary near-field microscope. Indeed, imaging of this kind has been reported in 2005 in two independent experiments performed by Zhang's group [4] and Blaikie's group [5]. Nevertheless, this technique is limited by the fact that magnification of the planar superlens is equal to 1.

An important early step to overcome this limitation was made in surface plasmon-assisted microscopy experiments [6], in which two-dimensional (2D) image magnification has been achieved in the "geometric optics" mode, as shown in Fig. 13.1b. The increased spatial resolution of microscopy experiments performed with surface plasmon polaritons [7] is based on the "hyperbolic" dispersion law of such waves, which may be written in the form

$$k_{xy}^2 - |k_z|^2 = \frac{\varepsilon_d \omega^2}{c^2} \quad (13.1)$$

where  $\varepsilon_d$  is the dielectric constant of the medium bounding metal surface,  $k_{xy} = k_p$  is the wave vector component in the plane of propagation, and  $k_z$  is the wave vector component perpendicular to the plane. This form of the dispersion relation originates from the exponential decay of the surface wave field away from the propagation plane. Negative refractive index behavior of surface plasmons was also shown to play a very important role in these early experiments [8].

On the theoretical side, various new geometries exhibiting image magnification beyond the usual diffraction limit were proposed [9–11], which make use of newly developed optical metamaterials. For example, in the "optical hyperlens" design

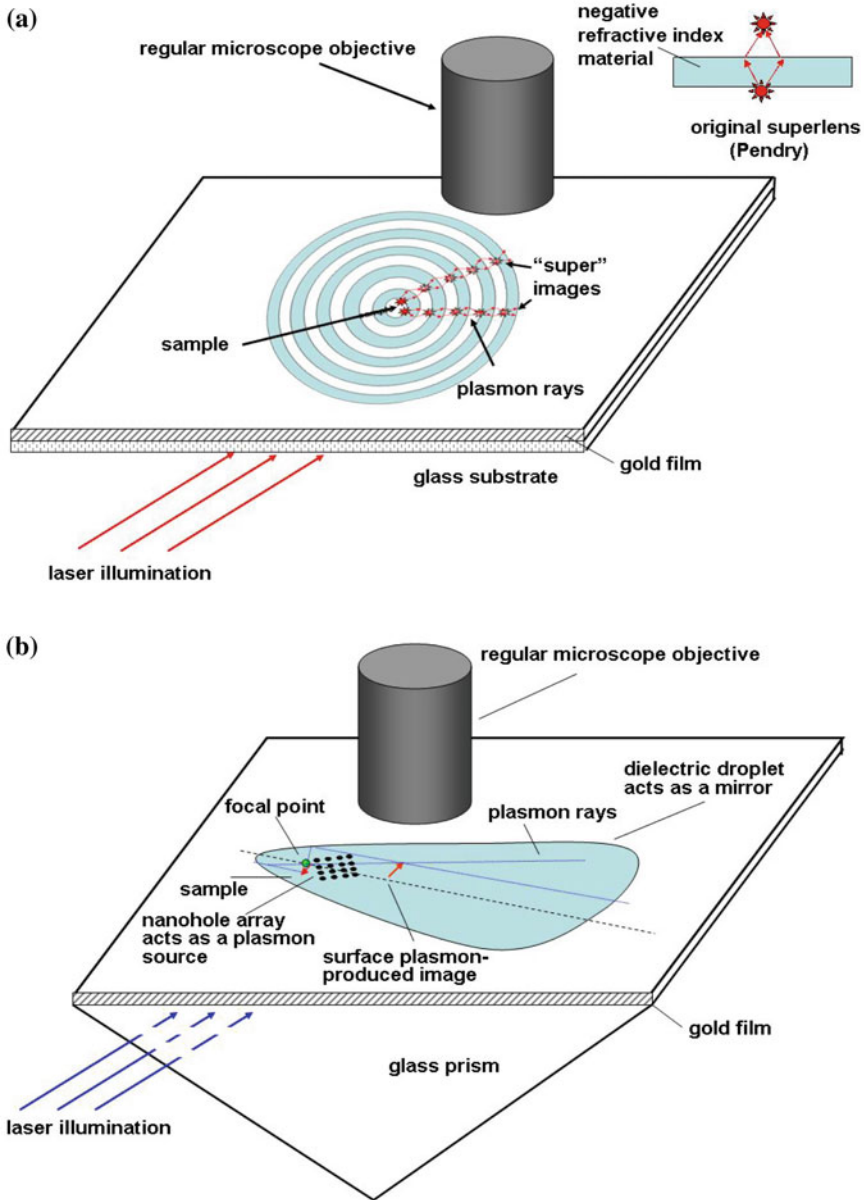


**Fig. 13.1** Two modes of operation of a 2D plasmonic microscope. **a** Plasmon microscope operating in the hyperlens mode: the plasmons generated by the sample located in the center of the hyperlens propagate in the radial direction. The lateral distance between plasmonic rays grows with distance along the radius. The images are viewed by a regular microscope. **b** Plasmon microscope operating in the geometrical optics mode: nanohole array illuminated by external laser light acts as a source of surface plasmons, which are emitted in all directions. Upon interaction with the sample positioned near the focal point of the parabolically shaped dielectric droplet, and reflection off the droplet edge, the plasmons form a magnified planar image of the sample. The image is viewed by a regular microscope. The droplet edge acts as an efficient plasmon mirror because of total internal reflection

developed by Narimanov's group [10] an optical metamaterial made of a concentric arrangement of metal and dielectric cylinders may be characterized by a strongly anisotropic dielectric permittivity tensor in which the tangential  $\varepsilon_\theta$  and the radial  $\varepsilon_r$  components have opposite signs. The resulting hyperbolic dispersion relation

$$\frac{k_r^2}{\varepsilon_\theta} - \frac{k_\theta^2}{|\varepsilon_r|} = \frac{\omega^2}{c^2} \quad (13.2)$$

does not exhibit any lower limit on the wavelength of propagating light at a given frequency. Thus, similar to the 2D optics of surface plasmon polaritons, there is no usual diffraction limit in this metamaterial medium. Abbe's resolution limit simply does not exist. Optical energy propagates through such metamaterial in the form of radial rays. If point sources are located near the inner rim of the concentric metamaterial structure, the lateral separation of the rays radiated from these sources would increase upon propagation towards the outer rim. Resolution of an "immersion" microscope based on such a metamaterial structure is defined by the ratio of inner to outer radii. Resolution appears limited only by losses, which can be compensated by optical gain. Following these theoretical ideas, magnifying superlenses (or hyperlenses) were independently realized in two experiments [12, 13]. Far-field optical resolution of at least 70 nm has been demonstrated using a magnifying superlens based on a 2D plasmonic metamaterial design shown in Fig. 13.1a [12]. Using the experimentally measured point spread function of the microscope, resolution of plasmon microscopy may be further improved to ~30 nm scale by implementing digital resolution enhancement techniques [14].

Thus, it appears that both major thrusts in far-field optical microscopy: the non-linear super-resolution techniques [2], and the linear techniques based on plasmonic and optical metamaterials are quickly moving the resolution scale of far-field optical microscopy towards the 10 nm level.

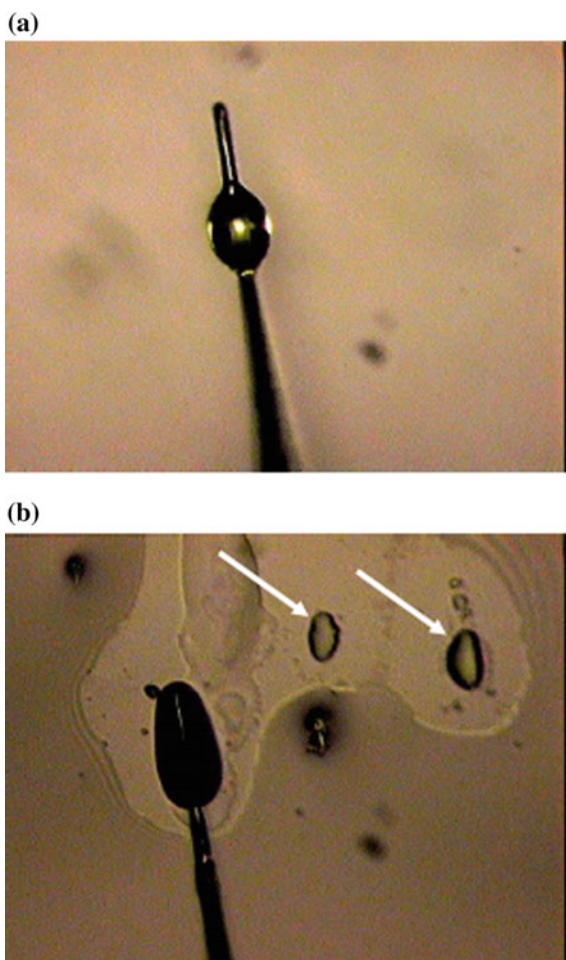
Another interesting recent development indicates that metamaterials may not be necessary to achieve super-resolution microscopy. For example, Wang et al. [15] reported a new 50-nm-resolution microscopy scheme that uses optically transparent micrometer scale SiO<sub>2</sub> microspheres as far-field superlenses to overcome the diffraction limit, while Leonhardt [16] and Minano [17] also indicate that super-resolution imaging may be achieved using various optical configurations, which emulate two-dimensional light propagation over a spherical surface. It is interesting that such imaging devices may be made of regular optical materials or emulated by curvilinear waveguides [18]. The goal of this chapter is to review these recent theoretical developments and their experimental implementations.

## 13.2 Surface Plasmon Microscopy

As we have mentioned in the Introduction, operation of the plasmonic microscope in the geometric optics mode may lead to increased resolution compared to the conventional 3D optical microscopes. This result is natural since plasmon microscope

operation relies on the hyperbolic dispersion law—see (13.1). In our microscopy experiments the samples were immersed inside glycerin droplets on the gold film surface. The droplets were formed in desired locations by bringing a small probe (Fig. 13.2a) wetted in glycerin into close proximity to a sample. The probe was prepared from a tapered optical fiber, which has an epoxy microdroplet near its apex. Bringing the probe to a surface region covered with glycerin led to a glycerin microdroplet formation under the probe (Fig. 13.2b). The size of the glycerin droplet was determined by the size of the seed droplet of epoxy. The glycerin droplet under the probe can be moved to a desired location under the visual control, using a regular microscope. Our droplet deposition procedure allowed us to form droplet shapes, which were reasonably close to parabolic. In addition, the liquid droplet boundary may be expected to be rather smooth because of the surface tension, which is essential for the proper performance of the droplet boundary as a 2D plasmon mirror. Thus,

**Fig. 13.2** Glycerin droplets used in the geometric optics mode of an SPP microscope were formed in desired locations by bringing a small probe **a** wetted in glycerin into close proximity to a sample. The probe was prepared from a tapered optical fiber, which has an epoxy microdroplet near its apex. Bringing the probe to a surface region covered with glycerin led to glycerin microdroplet formation **b** under the probe in locations indicated by the arrows



the droplet boundary was used as an efficient 2D parabolic mirror for propagating surface plasmons excited inside the droplet by external laser illumination. Since the plasmon wavelength is much smaller than the droplet sizes, the image formation in such a mirror can be analyzed by simple geometrical optics in two dimensions.

The resolution test of the microscope has been performed using a  $30 \times 30 \mu\text{m}^2$  array of triplet nanoholes (100 nm hole diameter with 40 nm distance between the hole edges) shown in Fig. 13.3c. This array was imaged using a glycerine droplet shown in Fig. 13.3a. Periodic nanohole arrays first studied by Ebbesen et al. [19] appear to be ideal test samples for the plasmon microscope. Illuminated by laser light, such arrays produce propagating surface waves, which explains the anomalous transmission of such arrays at optical frequencies. The image of the triplet array obtained at 515 nm using a 100x microscope objective is shown in Fig. 13.3b (compare it with an image in Fig. 13.3d calculated using 2D geometrical optics). Even though some discrepancy between the experimental and theoretical images can be seen (the image pattern observed in Fig. 13.3b looks convex looking from the left compared to the concave pattern observed in the calculation in Fig. 13.3d), the overall match between these images is impressive. The most probable reason for the observed convex/concave discrepancy is the fact that the droplet shape is not exactly parabolic, which produces some image aberrations. Although the expected resolution of the microscope at 515 nm is somewhat lower than at 502 nm, the 515 nm laser line is brighter, which allowed us to obtain more contrast in the 2D image. The least distorted part of the image, Fig. 13.3b (far from the droplet edge, yet close enough to the nanohole array, so surface plasmon decay does not affect resolution), is shown at higher digital zooms of the charge-coupled device (CCD) camera mounted onto our conventional optical microscope in Fig. 13.3e, f. These images clearly visualize the triplet nanohole structure of the sample. Moreover, using the experimentally measured point spread function (PSF) of the SPP microscope, resolution of 2D plasmon microscopy may be further improved to the  $\sim 30$  nm scale (as shown in Fig. 13.6) by implementing digital resolution enhancement techniques [14].

The spatial resolution of the optical images (the PSF of the microscope) may be measured directly by calculating the cross-correlation  $P * E$  between the optical image  $P$  and the scanning electron microscopy (SEM) image  $E$  of the same nanohole:

$$P * E(r) = \int P(r_1)E(r_1 + r)dr_1 \quad (13.3)$$

The results of these calculations in the cases of triplet nanoholes from Figs. 13.3 and 13.4 demonstrate that a resolution of the order of  $\text{PSF} \approx 70$  nm or  $\sim \lambda/8$  is achieved in these particular imaging experiments. Such an improved resolution in an SPP microscopy experiment is due to the fact that the SPP wavelength is shorter than the wavelength of guided modes at the same laser frequency. Photonic crystal effects and the effects of negative refraction also play some role in achieving better resolution.

Even though quite an improvement compared to a regular optical microscope, the  $\sim 70$  nm resolution is not sufficient to achieve clear visibility of many nanoholes in

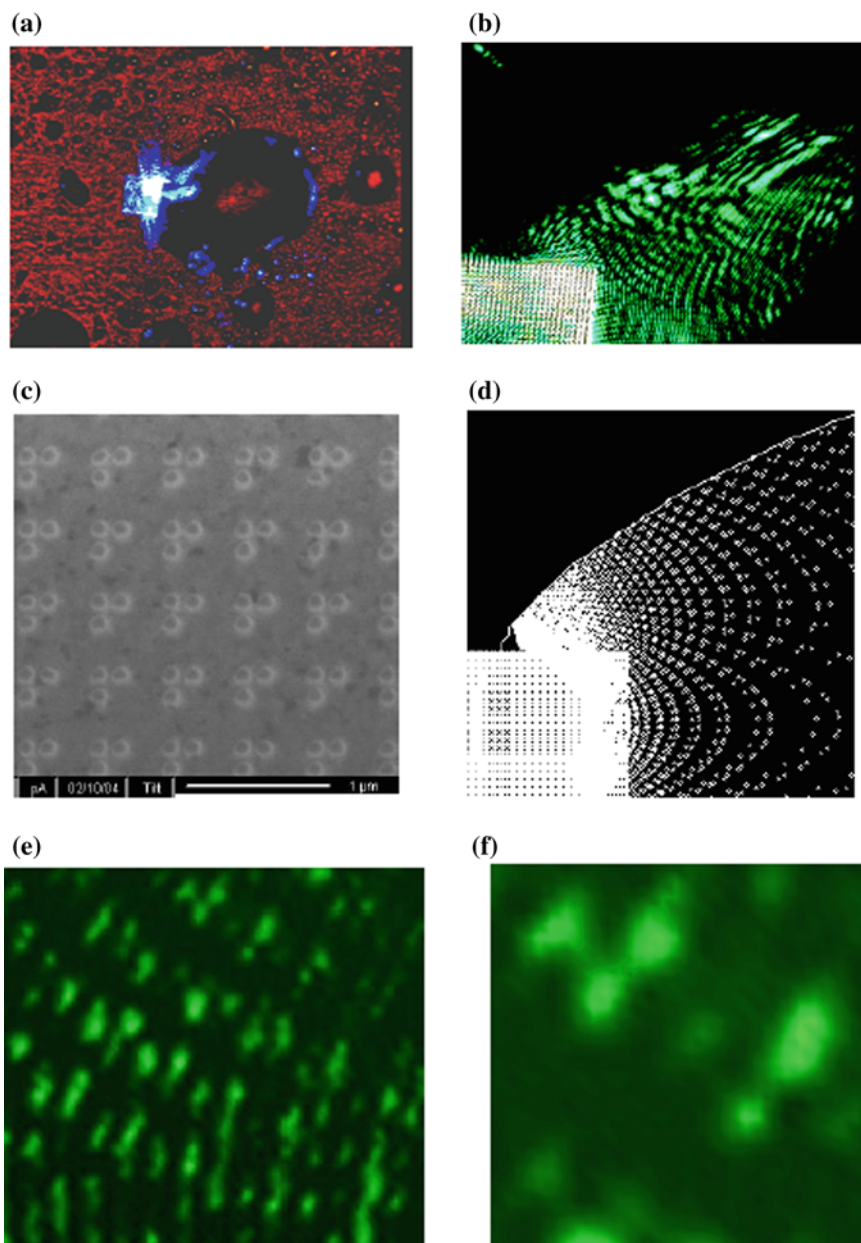


**Fig. 13.3** Resolution test of the 2D plasmonic microscope operated in the geometric optics mode. The array of triplet nanoholes (c) is imaged using a glycerine droplet shown in (a) using a 10x microscope objective. The image of the triplet array obtained using a 100x objective at 515 nm is shown in (b). The least distorted part of the image b is shown at higher digital zooms of the CCD camera mounted onto the microscope in (e) and (f). Comparison of the image (b) with the theoretically calculated image d clearly proves the resolving of the triplet structure

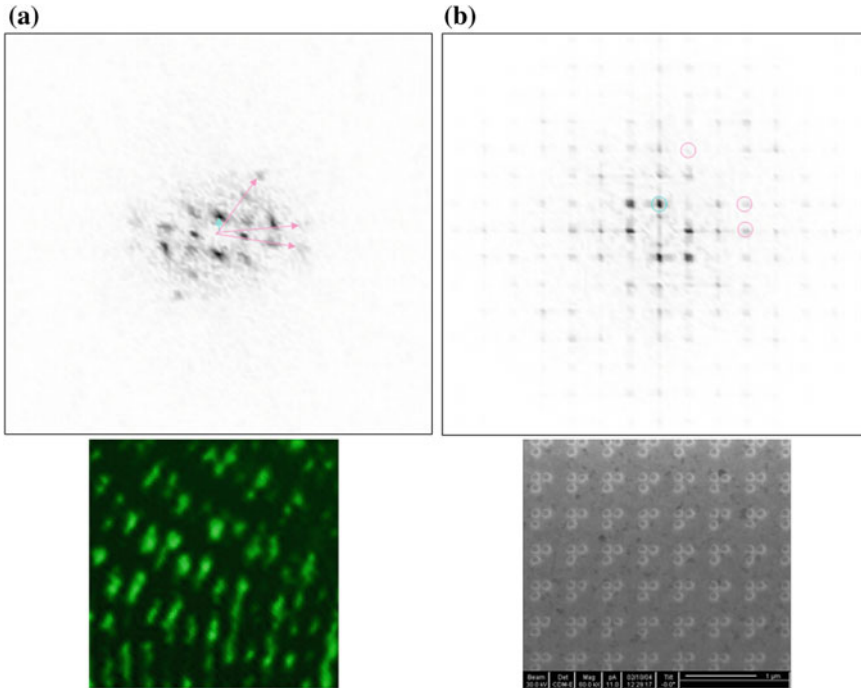


**Fig. 13.4** Comparison of the SPP-produced optical (a) and the SEM (b) images of the test array of triplet nanoholes. Comparison of the Fourier transforms of these images indicates spatial resolution in the optical image of  $\sim 78$  nm. This conclusion may be reached from the apparent visibility of higher harmonics of the triplet structure (indicated by the arrows) in the optical image

the test pattern in Fig. 13.3c. While recognizable, most nanoholes appear quite fuzzy. However, the blurring of optical images at the limits of optical device resolution is a very old problem (one may recall the well-publicized recent problem of Hubble telescope repair). One solution of this problem is also well known. There exists a wide variety of image recovery techniques which successfully fight image blur based on the known PSF of the optical system. One of such techniques is matrix deconvolution based on the Laplacian filter (see Fig. 13.5. as an example). Utilization of such techniques is known to improve resolution by at least a factor of 2. However, precise knowledge of the PSF of the microscope in a given location in the image is absolutely essential for this technique to work, since it involves matrix convolution of the experimental image with a rapidly oscillating Laplacian filter matrix (an example of such  $5 \times 5$  matrix is shown in Fig. 13.5). In our test experiments the PSF of the microscope was measured directly in some particular location of the optical image. This measured PSF was used to digitally enhance images of the neighboring nanohole arrays.

Not surprisingly, the use of such digital filters led to approximately twofold improvement of resolution in the optical images formed by the 2D plasmon micro-

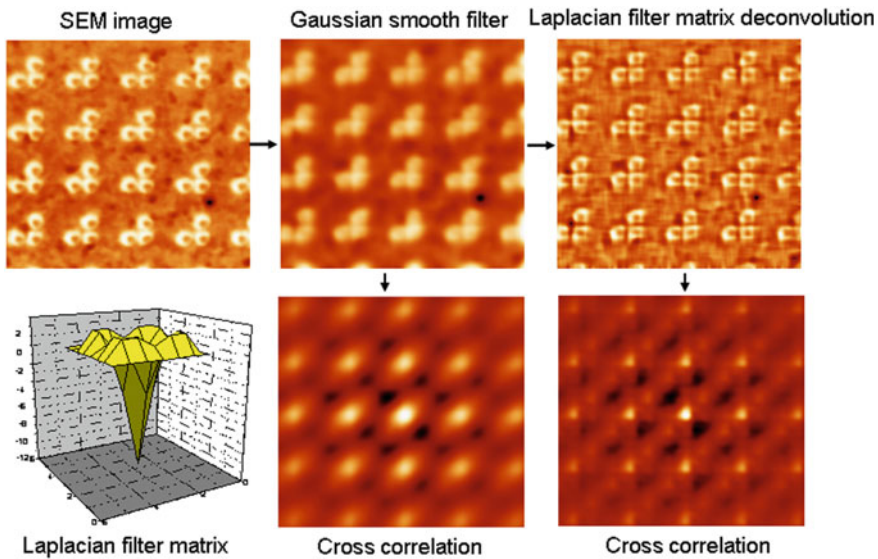


**Fig. 13.5** Theoretical modeling of the image recovery using Laplacian filter matrix deconvolution: Laplacian filter (shown in the inset) allows us to recover image deterioration due to Gaussian blur, which is evidenced via calculation of the cross-correlation of the original SEM image and the image recovered using the Laplacian matrix deconvolution method

scope. This twofold improvement is demonstrated in Fig. 13.6 for both the triplet and the U-shaped nanoholes. The PSF measured as the cross-correlation between the digitally processed optical image and the corresponding SEM image appears to fall firmly into the 30 nm range, which represents improvement of resolution of the SPP-assisted optical microscope down to the  $\sim\lambda/20$  range. This result may bring about direct optical visualization of many important biological systems.

### 13.3 Hyperlenses Based on 2D Hyperbolic Metamaterials

Now let us review imaging results obtained in the hyperlens mode of the 2D plasmonic microscope shown schematically in Fig. 13.1a. The internal structure of the 2D magnifying hyperlens (Fig. 13.7a) consists of concentric rings of PMMA deposited on a gold film surface. The required concentric structures were defined using a Raith e-line electron beam lithography (EBL) system with  $\sim 70$  nm spatial resolutions. The written structures were subsequently developed using a 3:1 IPA/MIBK solution (Microchem) as the developer and imaged using atomic force microscopy (AFM) (see Fig. 13.7a). According to theoretical modeling in [10, 11], optical energy propagates through a hyperbolic metamaterial in the form of radial rays. This behavior is clearly demonstrated in Fig. 5.3b. If point sources are located near the inner rim of the

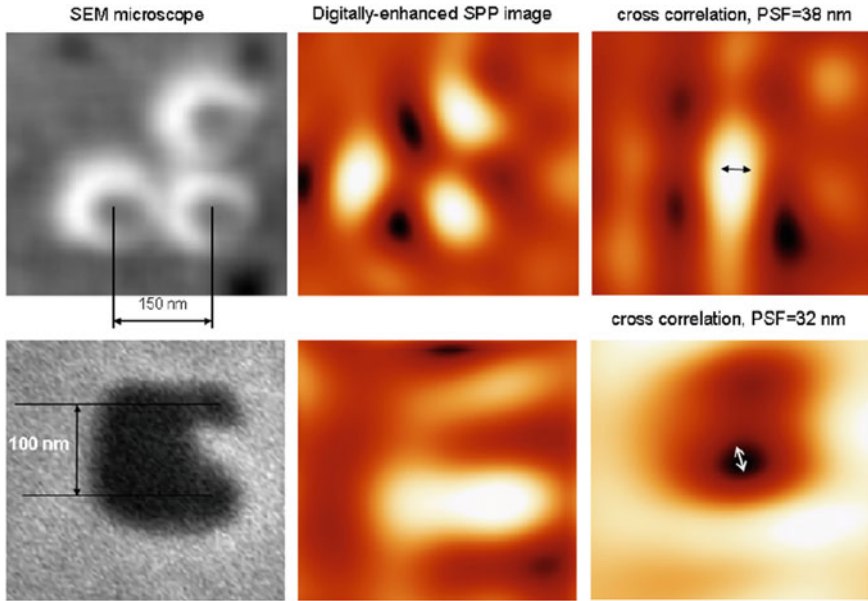


**Fig. 13.6** Calculated cross-correlation functions between the SEM and the digitally enhanced optical images of a triplet and a U-shaped arrangement of nanoholes in a gold film. Calculated point spread function of the digitally enhanced optical images appears to be on the order of 30 nm (from [19])

concentric metamaterial structure, the lateral separation of the rays radiated from these sources increases upon propagation toward the outer rim. Therefore, resolution of an immersion microscope based on such a metamaterial structure is defined by the ratio of inner to outer radii. Resolution appears limited only by losses, which can be compensated by optical gain.

Following these theoretical ideas, magnifying superlenses (or hyperlenses) have been independently realized in two experiments [12, 13]. In particular, experimental data obtained using a 2D plasmonic hyperlens (shown in Figs. 13.7 and 13.8) do indeed demonstrate ray-like propagation of subwavelength plasmonic beams emanated by test samples. A far-field optical resolution of at least 70 nm (see Fig. 13.8f) has been demonstrated using such a magnifying hyperlens based on a 2D plasmonic metamaterial design [12]. Rows of either two or three PMMA dots have been produced near the inner ring of the hyperlens (Fig. 13.8b, c). These rows of PMMA dots had  $0.5 \mu\text{m}$  periodicity in the radial direction so that phase matching between the incident laser light and surface plasmons can be achieved. Upon illumination with an external laser, the three rows of PMMA dots in Fig. 13.8b gave rise to three divergent plasmon rays, which are clearly visible in the plasmon image in Fig. 13.8d obtained using a conventional optical microscope. The cross-sectional analysis of this image across the plasmon rays (Fig. 13.8f) indicates a resolution of at least 70 nm or  $\sim\lambda/7$ . The lateral separation between these rays increased by a

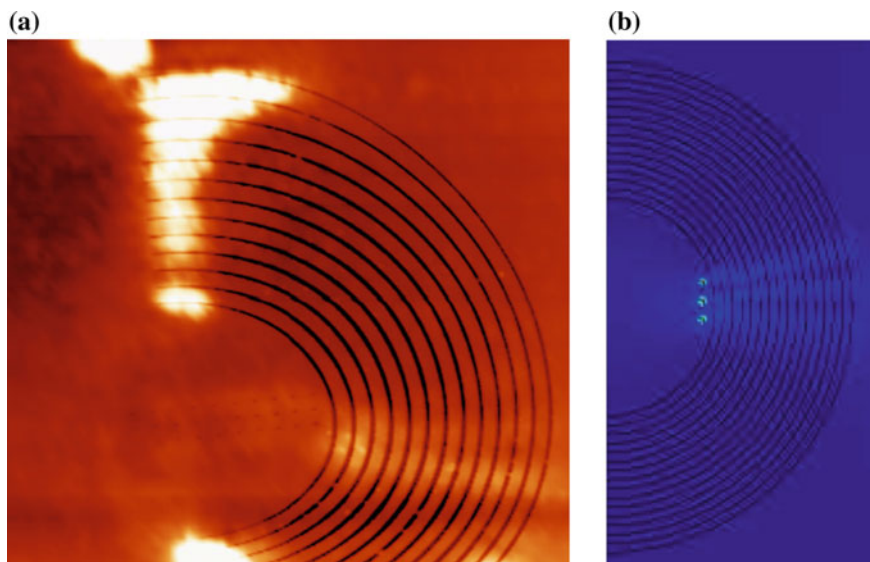


**Fig. 13.7** **a** Superposition image composed of an AFM image of PMMA on a gold plasmonic meta-material structure superimposed onto the corresponding optical image obtained using a conventional optical microscope, illustrating the imaging mechanism of the magnifying hyperlens (from [16]). Near the edge of the hyperlens the separation of three rays is large enough to be resolved using a conventional optical microscope. **b** Theoretical simulation of ray propagation in the magnifying hyperlens microscope

factor of 10 as the rays reached the outer rim of the hyperlens. This increase allowed visualization of the triplet using a conventional microscope. In a similar fashion, two rows of PMMA dots shown in Fig. 13.8c gave rise to two plasmon rays, which are visualized in Fig. 13.8e.

The magnifying action and the imaging mechanism of the hyperlens have been further verified by control experiments presented in Fig. 13.9. The image shown in Fig. 13.9a presents results of two actual imaging experiments (top portion of Fig. 13.9a) performed simultaneously with four control experiments seen at the bottom of the same image. In these experiments, two rows of PMMA dots have been produced near the inner ring of the hyperlens structures seen at the top and at the bottom of Fig. 13.9a (the AFM image of the dots is seen in the inset). These rows of PMMA dots had  $0.5 \mu\text{m}$  periodicity in the radial direction so that phase matching between the incident  $515 \text{ nm}$  laser light and surface plasmons can be achieved. On the other hand, no such PMMA dot structure was fabricated near the control hyperlenses seen in the center of Fig. 13.9a. Upon illumination with an external laser, the two rows of PMMA dots gave rise to the two divergent plasmon rays, which are clearly visible in the top portion of the image in Fig. 13.9a obtained using a conventional optical microscope. No such rays were observed in the four control hyperlenses visible in the bottom portion of the same image. There was no sample to image for the two hyperlenses located in the center of Fig. 13.9a. On the other hand, the PMMA

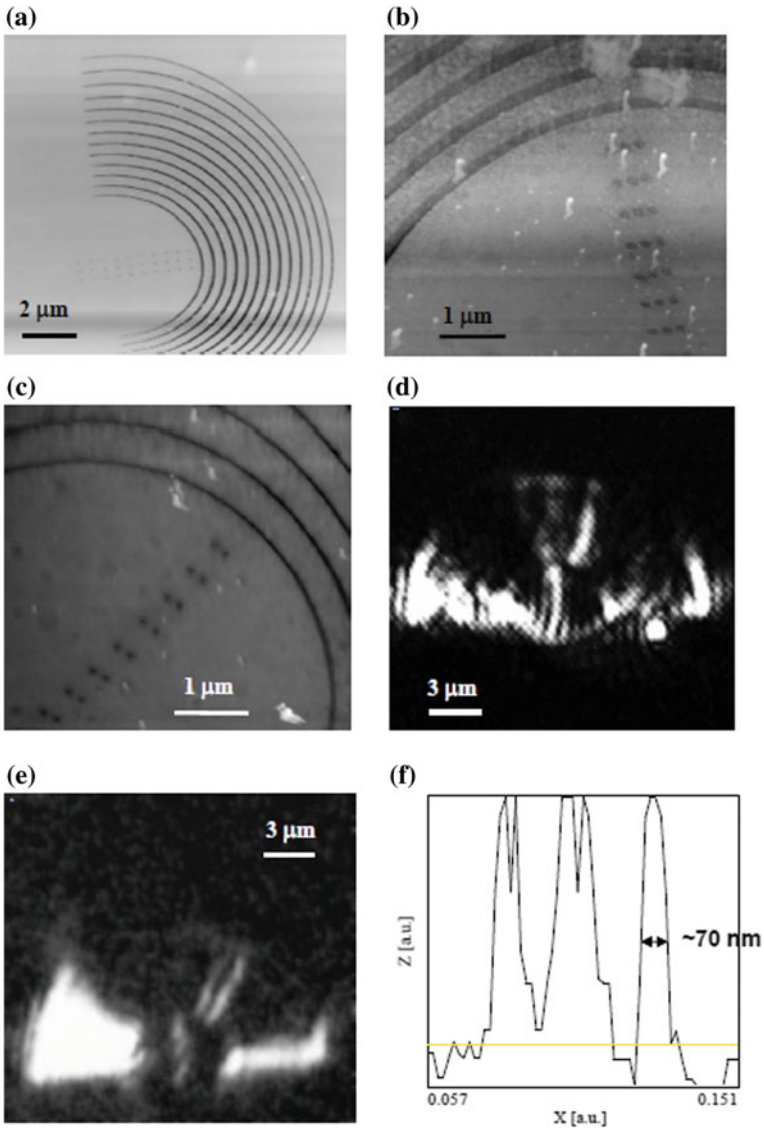
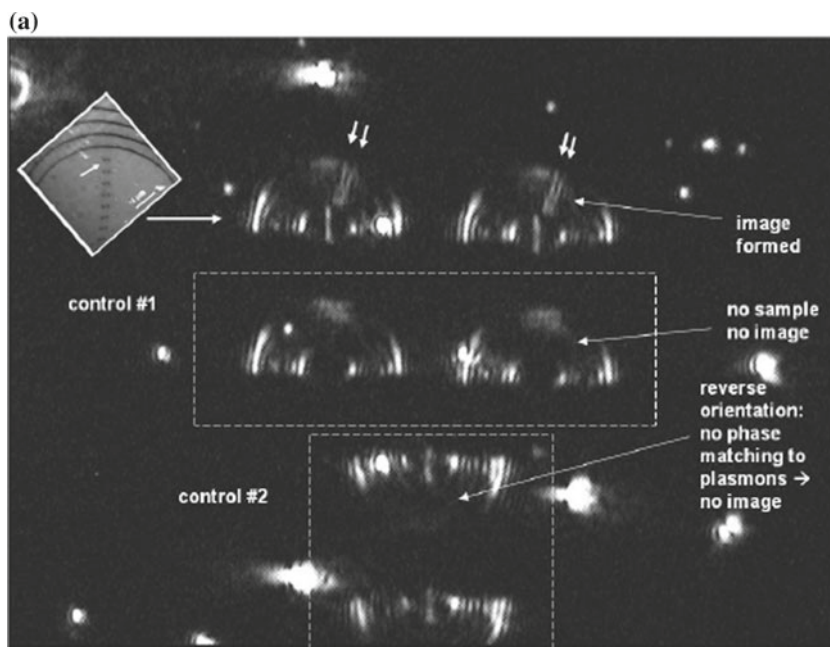


**Fig. 13.8** AFM (a–c) and conventional optical microscope (d, e) images of the resolution test samples composed of three (a, b) and two (c) rows of PMMA dots positioned near the center of the magnifying hyperlens. The conventional microscope images presented in (d and e) correspond to the samples shown in (b and c), respectively. The rows of PMMA dots give rise to either three or two divergent plasmon rays, which are visible in the conventional optical microscope images. **f** Cross section of the optical image along the line shown in (d) indicates a resolution of at least 70 nm or  $\sim\lambda/7$



◀**Fig. 13.9 a** This image obtained using a conventional optical microscope presents the results of two imaging experiments (top portion of the image) performed simultaneously with four control experiments seen at the bottom of the same image. The rows of PMMA dots shown in the inset AFM image were fabricated near the two top and two bottom hyperlenses. No such pattern was made near the two hyperlenses visible in the center of the image. Upon illumination with an external laser, the two rows of PMMA dots separated by a 130 nm gap gave rise to two divergent plasmon rays shown by the arrows, which are clearly visible in the top portion of the image. The four control hyperlenses visible at the bottom do not produce such rays, because there is no sample to image for the two hyperlenses in the center, and the two bottom hyperlenses are inverted. **b** The same pattern produced on an ITO instead of gold film demonstrates a pattern of ordinary light scattering by the structure without any hyperlens imaging effects

dot structure was designed for phase-matched plasmon generation in the upward direction, as seen in the image. That is why no plasmon rays are visible when the hyperlens structures are inverted, as seen in the bottom of Fig. 13.9a. When the gold film was replaced with an ITO film in another control experiment performed using the same experimental geometry, no hyperlens imaging occurred since no surface plasmons are generated on ITO surface (see Fig. 13.9b). These experiments clearly verify the imaging mechanism and increased spatial resolution of the 2D plasmonic hyperlens.

### 13.4 Super-Resolution Microscopy Based on Photon Tunneling

Most of the linear super-resolution microscopy techniques rely on some form of conversion of “fast” normally evanescent Fourier components of the object electromagnetic field into the propagating far field. For example, in scanning photon tunneling microscopy (PSTM) [1] evanescent light tunnels into a small tapered fiber probe, which is scanned over the sample surface. The probe converts evanescent light into photons which propagate inside the fiber. On the other hand, in the 2D and 3D hyperlens geometries [10–13] a similar conversion is achieved using a relatively small volume of hyperbolic material, which typically consists of closely spaced concentric metal-dielectric interfaces, which support surface plasmon polaritons. Therefore, a hyperlens may be understood as a form of photon tunneling device, which relies on radial plasmon tunneling between the adjacent interfaces. Comparison of PSTM and hyperlens techniques indicate that a simple non-scanning super-resolution imaging device may be built based on radial photon tunneling (Fig. 13.10). No metamaterial is necessary for its operation. Similar to our recent cloaking [20] and “trapped rainbow” [21] demonstrations, the “metamaterial properties” needed to observe these effects are emulated by tapered optical waveguides. Similar to PSTM, high spatial resolution of this technique is guaranteed by very strong exponential dependence of tunneling probability on the tunneling distance. This is illustrated in Fig. 13.11, which demonstrates results of numerical simulation of light propagation inside our

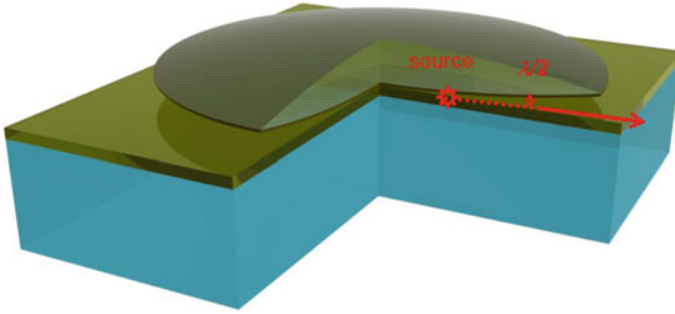


**Fig. 13.10** Experimental geometry of the non-scanning super-resolution microscopy technique based on photon tunneling: light tunnels in the radial direction from the cut-off region of a tapered two-dimensional waveguide formed between metal coated planar and spherical surfaces

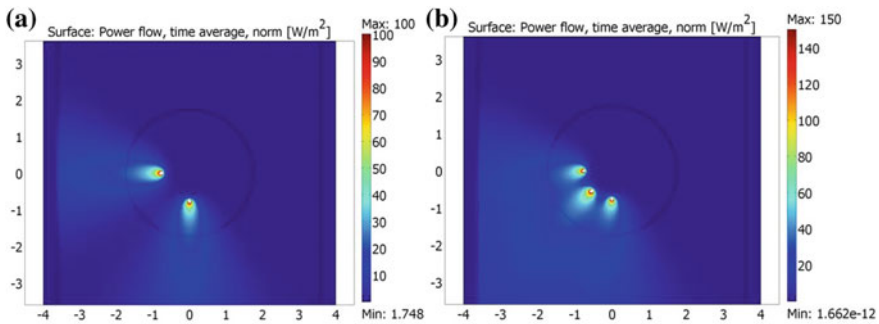
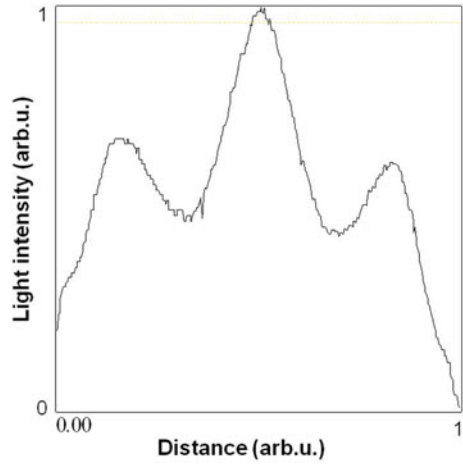


**Fig. 13.11** Numerical simulations of light propagation inside the photon tunneling device show light tunneling from the forbidden region. The cases of two and three point sources located inside the forbidden zone are considered.  $\lambda = 2$  value is used in these simulations. The dark circle shows the forbidden zone boundary

photon tunneling device. Three point sources separated by  $\lambda/4$  distances are clearly resolved inside a vacuum tunneling gap in the case shown in Fig. 13.11b. These simulations were performed via numerical solution of Maxwell equations using COMSOL multiphysics Fig. 3.3a. As expected, light from the point sources located inside the cutoff region of the waveguide tunnels in the radial direction along the shortest distance towards the “allowed region” of the waveguide. Image cross section along the boundary of the cutoff region shown in Fig. 13.12 demonstrates that the three point sources from Fig. 13.11b are indeed clearly resolved. The Rayleigh criterion applied to this image cross section indicates that theoretical resolution of the order of  $\lambda/8$  is obtained in these simulations.

Our experimental observations performed in the geometry shown in Fig. 13.10 indicate validity of the proposed approach. In these experiments we have used a 4.5-mm diameter double convex glass lens which was coated on one side with a 30-nm gold film. The lens was placed with the gold-coated side down on top of a flat glass

**Fig. 13.12** Cross section of Fig. 13.2b along the boundary of the cutoff region demonstrates that the three point sources located at  $\lambda/4$  distances from each other are clearly resolved. The Rayleigh criterion applied to this cross section indicates that theoretical resolution of the order of  $\lambda/8$  is obtained in these simulations



slide coated with a 70-nm gold film. The air gap between these surfaces has been used as an adiabatically changing optical nano waveguide. The dispersion law of light in such a waveguide is

$$\frac{\omega^2}{c^2} = k_r^2 + \frac{k_\phi^2}{r^2} + \frac{\pi^2 l^2}{d(r)^2} \quad (13.4)$$

where  $l = 1, 2, 3 \dots$  is the transverse mode number, and  $d(r)$  is the air gap, which is a function of radial coordinate  $r$ . Gradual tapering of the waveguide leads to mode number reduction. The light in the waveguide is completely stopped at a distance

$$r = \sqrt{R\lambda/2} \quad (13.5)$$

from the point of contact between the gold-coated surfaces, where the optical nano waveguide reaches the cutoff width of  $d = \lambda/2$ . We have used light from an argon ion laser operating at  $\lambda = 514$  nm to illuminate the cutoff region from below. Light distribution inside the cutoff region of the nano waveguide was imaged from the top using an optical microscope (see Fig. 13.4). Our goal was to detect evidence of radial light tunneling from inside the cutoff region. These observations relied on random defects present inside the waveguide. While the area in the immediate vicinity of the point of contact appears bright in Fig. 13.13 (this corresponds to the well-known Newton ring observation conditions), we did observe radial light scattering from the defects located in the dark areas inside the first Newton ring. In addition, data analysis presented in Fig. 13.14 demonstrates that distance dependence of the field scattered by defects is consistent with the tunneling mechanism required for super-resolution microscopy.

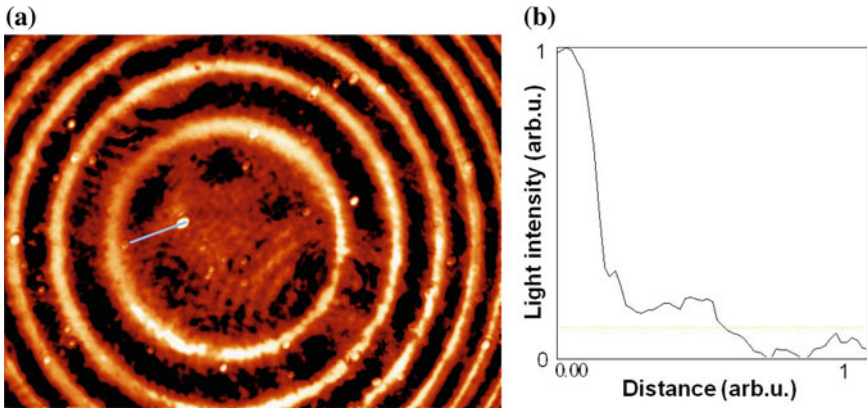
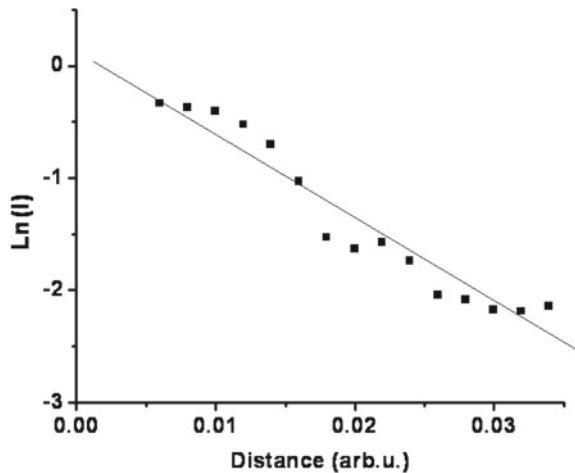


**Fig. 13.13** **a** Experimental image of radial light scattering by random defects located inside the cutoff region of the waveguide. **b** Image cross section along the blue line

**Fig. 13.14** Field decay in the radial direction is consistent with photon tunneling



Thus, suggested super-resolution microscopy scheme appears to be viable.

## 13.5 Microscopy Techniques Based on 2D Transformation Optics

### 13.5.1 Microdroplet-Based Transformation Optics

Current high interest in electromagnetic metamaterials has been motivated by recent work on superlenses, cloaking and transformation optics [3, 22, 23]. This interest has been followed by considerable efforts aimed at introduction of metamaterial

structures that could be realized experimentally. Unfortunately, it appears difficult to develop metamaterials with low-loss, broadband performance. The difficulties are especially severe in the visible frequency range where good magnetic performance is limited. On the other hand, recently we have demonstrated that many transformation optics and metamaterial-based devices, such as electromagnetic cloaks, requiring anisotropic dielectric permittivity and magnetic permeability could be emulated by specially designed tapered waveguides [19]. This approach leads to low-loss, broadband performance in the visible frequency range, which is difficult to achieve by other means. It appears that this approach may be also applied to experimental realization of the Maxwell fisheye and inverted Eaton microlenses [18], which were suggested to act as superb imaging devices even in the absence of negative refraction [16]. Realization of these microlenses using electromagnetic metamaterials would require sophisticated nanofabrication techniques. In contrast, our approach leads to a much simpler design, which involves two-dimensional (2D) imaging using a small liquid microdroplet.

Despite strong experimental and theoretical evidence supporting superresolution imaging based on microlenses and microdroplets, imaging mechanisms involved are not well understood. Magnification of near-field image components has been suggested in recent experiments with self-assembled plano-spherical nanolenses [24, 25] and high-index liquid-immersed microspheres [26] which demonstrated resolution of the order of  $\lambda/4$  to  $\lambda/7$ . Our analysis in terms of the effective metamaterial parameters indicates that the shape of microlenses and microdroplets provides natural realization of the effective refractive index distribution in the fisheye and inverted Eaton microlenses.

The starting point of our analyses is the dispersion law of guided modes in a tapered waveguide. In case of the metal-coated dielectric waveguide it can be written in a simple analytical form:

$$\frac{\omega^2 n_d^2}{c^2} = k_x^2 + k_y^2 + \frac{\pi^2 l^2}{d(r)^2} \quad (13.6)$$

where  $n_d$  is the refractive index of the dielectric,  $d(r)$  is the waveguide thickness, and  $l$  is the transverse mode number. We assume that the thickness  $d$  of the waveguide in the  $z$ -direction changes adiabatically with radius  $r$ . A photon launched into the  $l$ th mode of the waveguide stays in this mode as long as  $d$  changes adiabatically [27]. If we wish to emulate refractive index distribution  $n(r)$  of either 2D fisheye or 2D inverted Eaton lens:

$$\frac{\omega^2 n^2(r)}{c^2} = k_x^2 + k_y^2 \quad (13.7)$$

we need to produce the following profile of the microdroplet:

$$d = \frac{l\lambda}{2\sqrt{n_d^2 - n^2(r)}} \quad (13.8)$$

This is easy to do for some particular mode  $l$  of the waveguide. Typical microdroplet/microlens profiles which emulate the fisheye lens described by equation:

$$n = 2n_1 \left( 1 + \frac{r^2}{R^2} \right)^{-1} \quad (13.9)$$

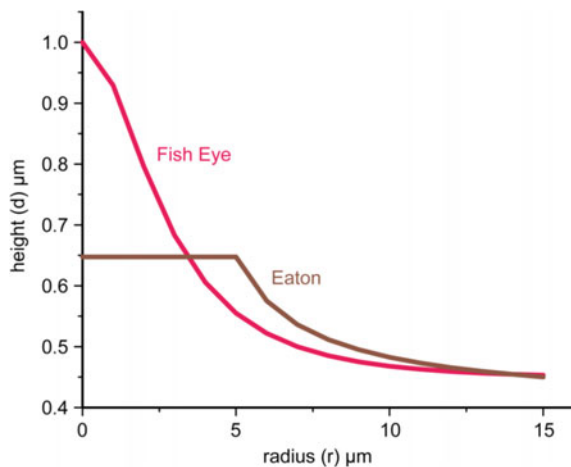
(where  $2n_1$  is the refractive index at the center of the lens, and  $R$  is the scale) or the inverted Eaton lens [17] described by:

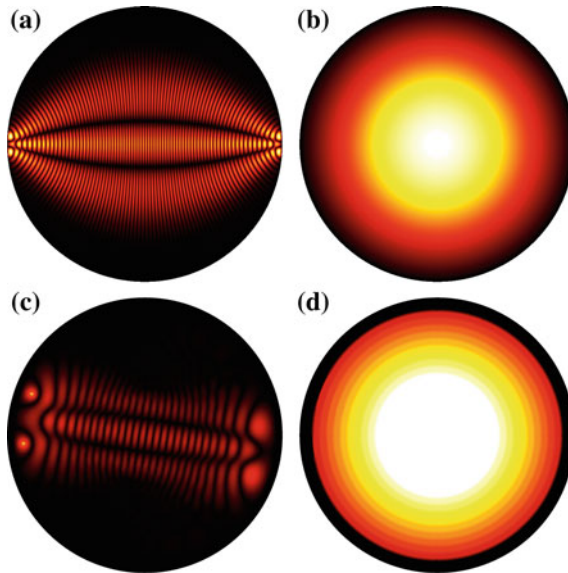
$$n = 1 \text{ for } r < R, \text{ and } n = \sqrt{\frac{2R}{r}} - 1 \text{ for } r > R \quad (13.10)$$

are shown in Fig. 13.15. Real glycerin microdroplets have shapes, which are somewhere in between these cases. Since the refractive index distribution in the fisheye lens is obtained via the stereographic projection of a sphere onto a plane [16], points near the droplet edge correspond to points located near the equator of the sphere. Therefore, these points are imaged into points located near the opposite droplet edge, as shown in Fig. 13.16a. The inverted Eaton lens has similar imaging properties, as shown in Fig. 13.16c. Each droplet depicted in Fig. 13.16 was simulated using scattered field finite element formulation. The continuity of the tangential field components was enforced at the host-droplet interface. The host with the droplet was surrounded by a perfectly matched (absorbing) layer to suppress reflection from the exterior boundaries of the simulation domain.

We have tested this imaging mechanism using glycerin microdroplets formed on the surface of gold film, which were illuminated near the edge using tapered fiber tips of a near-field scanning optical microscope (NSOM), as shown in Fig. 13.17. As expected from the numerical simulations, an image of the NSOM tip was easy to observe at the opposite edge of the microdroplet.

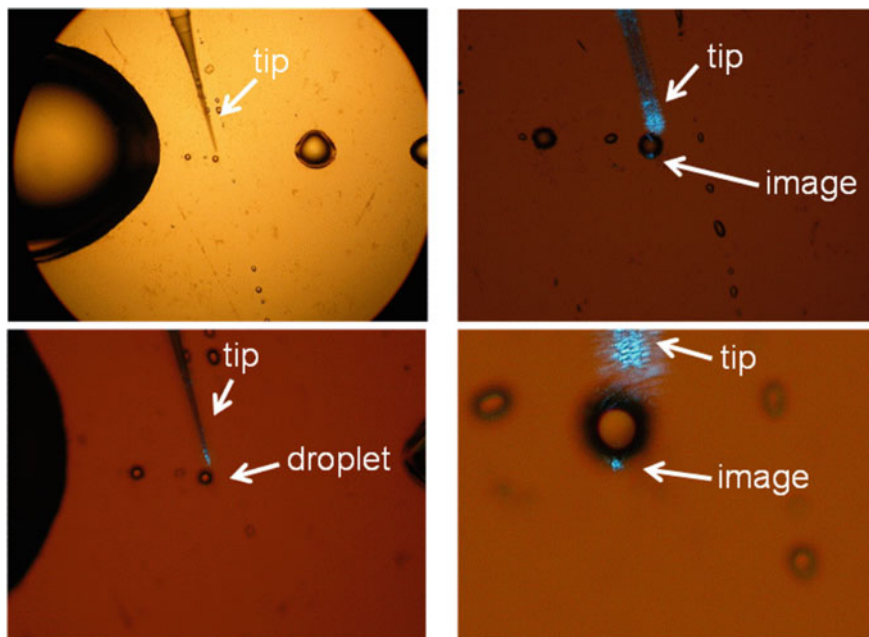
**Fig. 13.15** Typical profiles of a microdroplet which emulates either the fisheye lens ( $R = 7 \mu\text{m}$ ) or the inverted Eaton lens ( $R = 5 \mu\text{m}$ ) for the following set of parameters:  $l = 1$ ,  $\lambda = 1.5 \mu\text{m}$ ,  $n_d = 1.5$ , and  $n_l = 0.65$





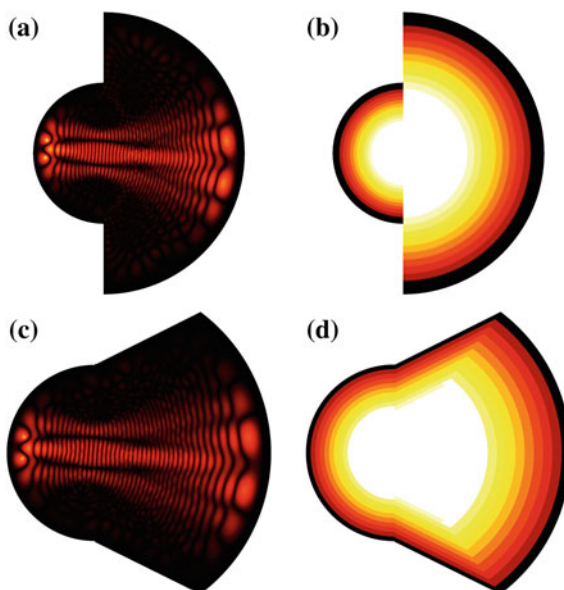
**Fig. 13.16** Numerical simulations of imaging properties of the fisheye (a) and inverted Eaton (c) lenses. Points near the edge of the fisheye and Eaton lenses are imaged into opposite points. Refractive index distributions in these lenses are shown to their right in panels (b) and (d)

While the fisheye lens design is difficult to modify to achieve image magnification, modification of the Eaton lens is straightforward. As shown in Fig. 13.18, two halves of the Eaton lens having different values of parameter  $R$  can be brought together to achieve image magnification. The image magnification in this case is  $M = R_1/R_2$ . Our numerical simulations in the case of  $M = 2$  are presented. Since the sides of the lens play no role in imaging, the overall shape of the imaging device can be altered to achieve the shape of a “deformed droplet”. Using experimental technique described below, we have created glycerin droplets with shapes, which are very close to the shape of the “deformed droplet” used in the numerical simulations. Image magnification of the “deformed droplet” has been tested by moving the NSOM probe tip along the droplet edge, as shown in Fig. 13.19. It appears to be close to the  $M = 2$  value predicted by the simulations. Thus, we have demonstrated that small dielectric microlenses may behave as two-dimensional imaging devices, which can be approximated by 2D fisheye or inverted Eaton lenses. Deformed microlenses/microdroplets are observed to exhibit image magnification, which is consistent with numerical predictions.



**Fig. 13.17** Experimental testing of the imaging mechanism of the glycerin microdroplets shown at different magnifications. The droplet is illuminated near the edge with a tapered fiber tip of a near-field scanning optical microscope (NSOM). Image of the NSOM tip is clearly seen at the opposite edge of the droplet

**Fig. 13.18** Numerical simulations of image magnification ( $M = 2$ ) using the inverted Eaton lens. Since the sides of the lens play no role in imaging, the overall shape of the imaging device can be altered to achieve the shape of a “deformed droplet”



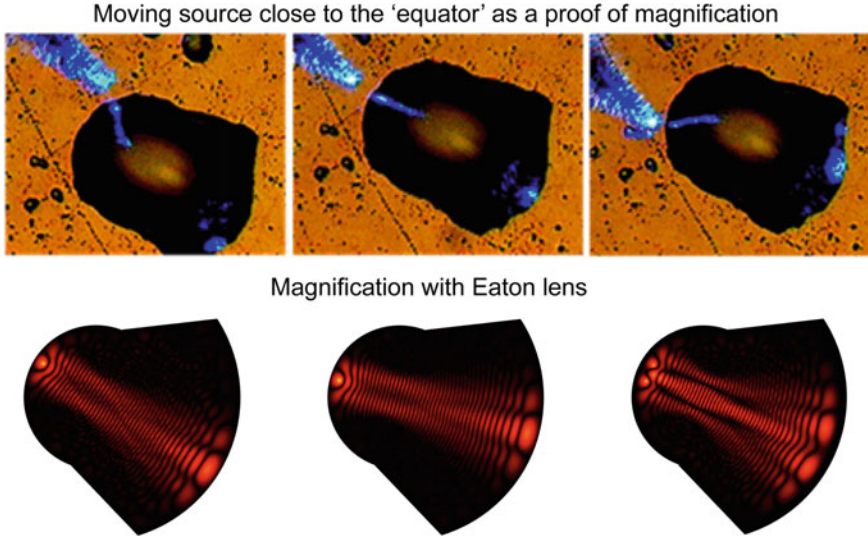


**Fig. 13.19** Experimental testing of image magnification of the “deformed droplet”. The NSOM probe tip was moved along the droplet edge. Bottom row presents results of our numerical simulations in the case of one and two point sources. The shape of the “deformed droplet” used in numerical simulations closely resembles the shape of the actual droplet

### 13.5.2 Lithographically Defined Transformation Optics Devices

While the experimental results obtained using the microdroplet-based imaging are interesting, such devices are difficult to control and fabricate reproducibly. Therefore, it is useful to try and develop lithographically-defined metal/dielectric waveguide-based imaging devices. Since adiabatic variations of the waveguide shape are easier to achieve using lithographic techniques, this method enables much better control of the effective refractive indices experienced by the TE and TM modes propagating inside the waveguides, which is illustrated in Fig. 13.20a.

The effective refractive indices for the TE and TM modes may be defined as  $n_{\text{eff}} = k\omega/c$  for each respective polarization, where the  $k$  vector is calculated via the boundary conditions at the media interfaces as:

$$\left(\frac{k_1}{\varepsilon_m} - \frac{ik_2}{\varepsilon}\right)\left(k_3 - \frac{ik_2}{\varepsilon}\right)e^{-ik_2d} = \left(\frac{k_1}{\varepsilon_m} + \frac{ik_2}{\varepsilon}\right)\left(k_3 + \frac{ik_2}{\varepsilon}\right)e^{ik_2d} \quad (13.11)$$

for the TM, and

$$(k_1 - ik_2)(k_3 - ik_2)e^{-ik_2d} = (k_1 + ik_2)(k_3 + ik_2)e^{ik_2d} \quad (13.12)$$

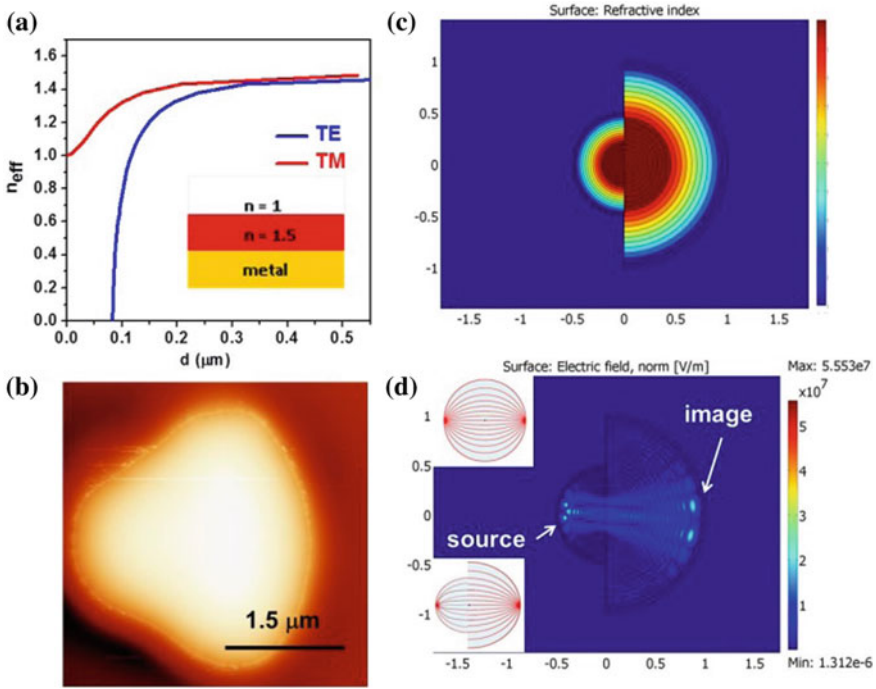


**Fig. 13.20** **a** Effective refractive index plotted as a function of thickness of a tapered waveguide for TM and TE polarizations. The waveguide geometry is shown in the inset. **b** AFM image of a lithographically defined individual magnifying fish-eye lens made of two half-lenses of different radii. **c** Corresponding spatial distribution of the effective refractive index. **d** COMSOL Multiphysics simulation of the fish-eye lens image magnification. The insets illustrate ray propagation in the original and the magnifying fish-eye lenses

for the TE polarized guided modes, respectively, and  $\omega$  is the light frequency. In these expressions the vertical components of the wavevector  $k_i$  are defined as:

$$k_1 = \left( k^2 - \varepsilon_m \frac{\omega^2}{c^2} \right)^{1/2} \quad (13.13)$$

$$k_2 = \left( \frac{\omega^2}{c^2} \varepsilon - k^2 \right)^{1/2} \quad (13.14)$$

$$k_3 = \left( k^2 - \frac{\omega^2}{c^2} \right)^{1/2} \quad (13.15)$$

in metal, dielectric, and air, respectively. The calculated effective birefringence for the lowest guided TM and TE modes is shown in Fig. 13.20a. The effective birefringence is very strong at waveguide thickness  $d < 0.4 \mu\text{m}$ . In addition, both polarizations experience very strong effective refractive index dependences on the waveguide

thickness. If the lithographically-defined waveguide thickness  $d(r)$  is well controlled as a function of the radial coordinate  $r$ , this behavior may be used to build non-trivial birefringent transformation optics devices.

As illustrated in Fig. 13.20b, we were able to develop novel lithography techniques which provide the required precise shape control  $d(r)$  of the dielectric photoresist on a gold film substrate. We have used Shieply S1811 photoresist with refractive index  $n \sim 1.5$  for our device fabrication. Since we wanted to create a gradual edge profile, we have disregarded the typical procedures, which are employed to make the photoresist edges sharp. Instead of contact printing, we have used the soft contact lithographic mode in which a gap is left between the mask and the substrate. Due to diffraction effects, this gap provided a gradient of UV light exposure at the mask edges. This gradient in turn has led to a gradual change of the developed photoresist thickness. During the experiments we have tried different degrees of separation between the mask and the substrate, which produced progressively softer photoresist profile. Underexposure and underdevelopment were also used to provide further variations of sharpness of the waveguide profile edge.

Note that these techniques were also used previously to fabricate such TO-based devices as a modified Luneburg lenses [28] (while, no image magnification has been demonstrated in these experiments). However, as noted in [18], the transformation optics designs of the Eaton and Maxwell fisheye lenses allow straightforward modification to incorporate image magnification.

Equation (13.9) defines the refractive index distribution in a Maxwell fisheye lens, while an inverted Eaton lens is defined by (13.10). The refractive index distribution in the fisheye lens is obtained via the stereographic projection of a sphere onto a plane [16]. Therefore, points near the lens edge correspond to points located near the equator of the sphere. As a result, as shown in the inset in Fig. 13.20d, these points are imaged into points located near the opposite edges of the lens. The imaging properties of the inverted Eaton lens are similar. As illustrated in Fig. 13.20c, d, two halves of either Maxwell fisheye or inverted Eaton lens may be brought together, so that the difference in their R parameter will lead to increased magnification. The image magnification in these cases may be defined as  $M = R_1/R_2$ . We have performed numerical simulations of image magnification in the case of  $M = 2$ , which are presented in Fig. 13.20d. The sides of the lens appear not to play much role in the imaging properties of the resulting structure. Therefore, the overall shape of the lens may be altered to smooth the sharp corners. The resulting magnifying fisheye lens shape is shown in Fig. 13.20b. Such lenses were fabricated using the lithographic technique described above, which is illustrated in the experimental images in Fig. 13.21. In these experiments a near-field scanning optical microscope (NSOM) fiber tip was scanned in close proximity to the lithographically formed magnifying lenses. The point of the tip was used as an illumination source. Similar to the numerical simulations, an image of the NSOM tip was observed near the opposite edge of the lens. The studied angular and polarization performance of the individual lenses in the array agreed well with the theoretical prediction presented in Fig. 13.20c, d.

We should also point out [28] that a fisheye lens for TM light will operate as a spatial filter for TE light due to near zero effective refractive index near the device

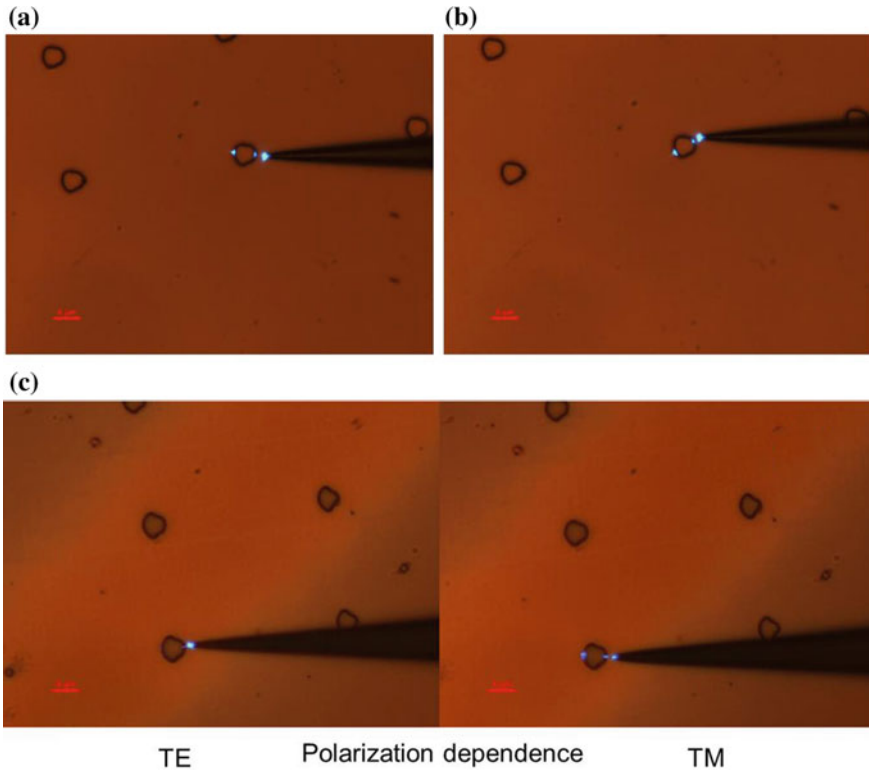


**Fig. 13.21** a Experimental testing of angular (a, b) and polarization (c) performance of the magnifying fisheye lenses at  $\lambda = 488$  nm. The scale bar length is  $5 \mu\text{m}$  in all images

edge. While the near field fiber tip emits unpolarized light, polarization properties of the images produced by these lenses can be separated into the TM and TE contributions with respect to the plane of incidence of the source light. These polarization properties are illustrated in Fig. 13.21. They demonstrate excellent agreement with theoretical predictions.

Based on the images of lens testing presented in Fig. 13.22, we may evaluate image resolution and magnification of the fabricated magnifying Maxwell fisheye lenses. The optical resolution appears to be almost diffraction-limited ( $\sim 0.6\lambda$  at 488 nm), while the measured magnification is very close to the design values.

The theoretically predicted broadband performance of the Maxwell fisheye lenses has been verified in the  $\lambda = 488\text{--}633$  nm range, as illustrated in Fig. 13.23. It is similar to the broadband cloaking performance demonstrated in [19], since the

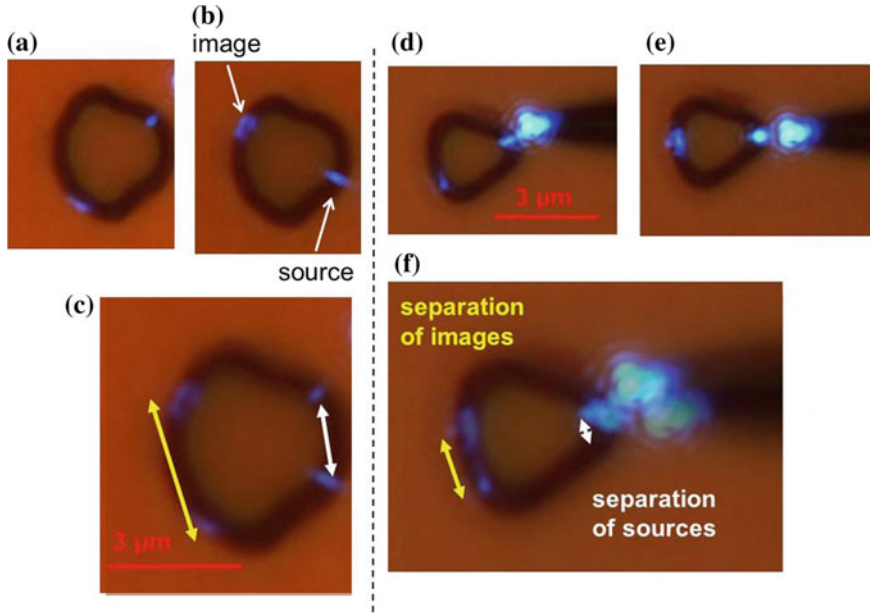


**Fig. 13.22** Experimental testing of image magnification at  $\lambda = 488$  nm of two fisheye lenses with different  $M = R_1/R_2$  ratio: **a, b** Original magnified images obtained at different source positions. The location of image and source are indicated by the arrows. **c** Digital overlap of the images in **(a and b)** indicates that image magnification is close to the design value  $M = 2$ . **d, e** Similar original images and **f** the digital overlap image obtained with a different magnifying lens designed for  $M = 3$

effective refractive index of the tapered waveguide scales as  $d/\lambda$  at small  $d$ . The guided light in these waveguides perceives the waveguide edge as having similar distribution of the effective refractive index. We have also verified that the reverse operation of the same lens may be utilized to achieve image reduction, as illustrated in Fig. 13.24. Therefore, such a “reverse” arrangement of the magnifying fisheye lens may find applications in lithography.

We should also point out that the high spatial magnification and the very compact design of the magnifying Maxwell fisheye lenses are highly suitable in waveguide mode sorting applications. On-chip mode-division multiplexing [29] and sensing [30] applications require compact and efficient mode sorter designs. Our numerical simulations of a Maxwell fisheye mode sorter are presented in Fig. 13.25. In this geometry the signal is sent in through a single multimode waveguide from the left and out-coupled through three different single mode output waveguides on the right.

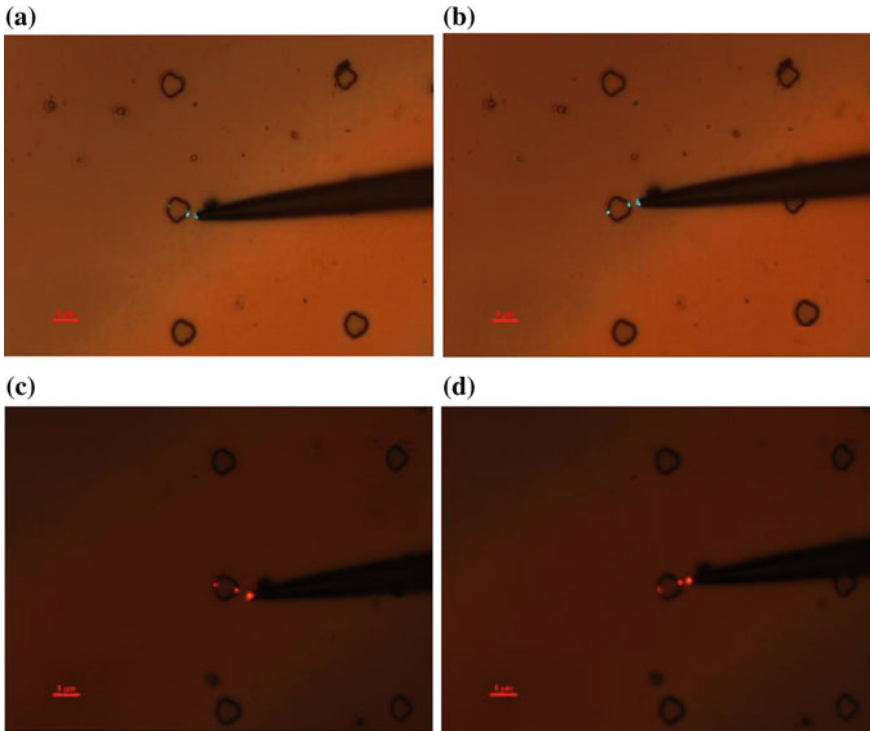


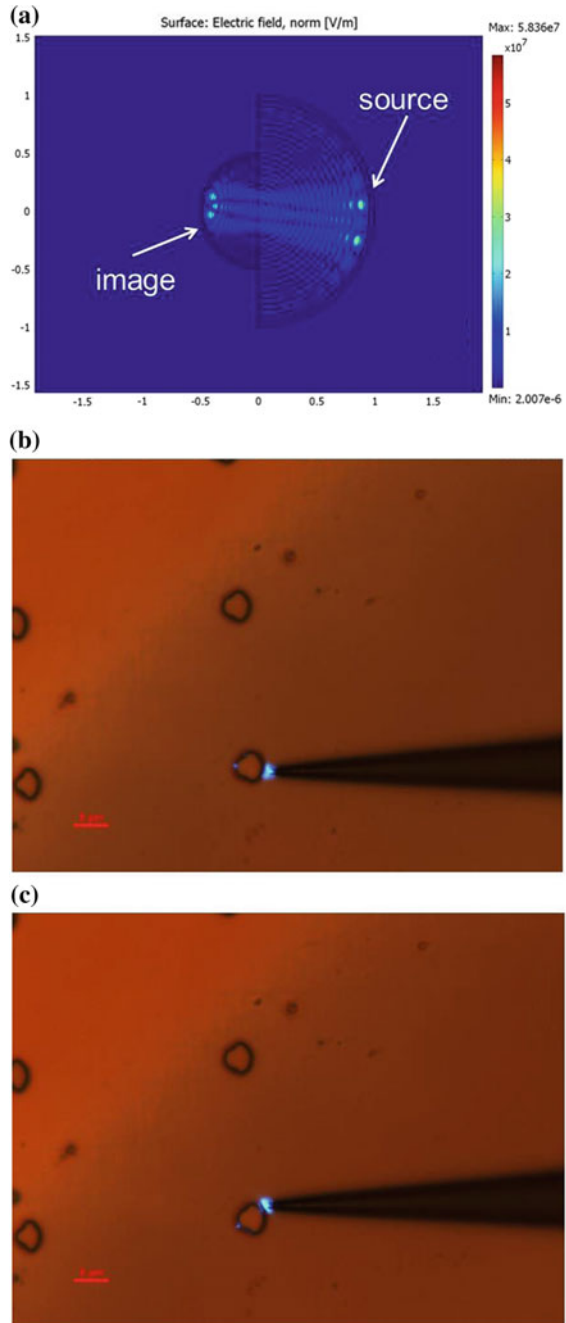
**Fig. 13.23** Experimental verification of broadband performance of the magnifying Maxwell fisheye lens. **a, b** Images taken at  $\lambda = 515$  nm. **c, d** Images taken at  $\lambda = 633$  nm. The scale bar length is  $5 \mu\text{m}$  in all images

These simulations demonstrate excellent mode-sorting performance of a micrometer-scale Maxwell fisheye lens. As illustrated in Fig. 13.25a, symmetric excitation of the input waveguide mostly couples the output power to the central single mode waveguide on the right side of the structure. On the other hand, as shown in Fig. 13.25b, asymmetric excitation of the input waveguide leads to propagation of higher spatial modes, which are channeled primarily into the side output waveguides.

## 13.6 Conclusion

Experimental and theoretical results discussed in this chapter strongly indicate that both major recent developments in far-field optical microscopy—nonlinear super-resolution techniques and linear techniques based on plasmonic and optical metamaterials—are quickly moving the resolution scale of far-field optical microscopy down toward the 10 nm level. While fabrication of 3D photonic metamaterials faces numerous technological challenges, many concepts and ideas in the optics of meta-

**Fig. 13.24** Operation of the magnifying Maxwell fisheye lens in reverse direction, which leads to image reduction. **a** COMSOL Multiphysics simulation of the fisheye lens image reduction using refractive index distribution corresponding to the experimental variation of the waveguide thickness. **b**, **c** Experimental testing of angular performance of the fisheye lens used in reverse direction.  $\lambda = 488$  nm. Image reduction factor  $M = 1/2$  is observed. The scale bar length is  $5 \mu\text{m}$  in all images



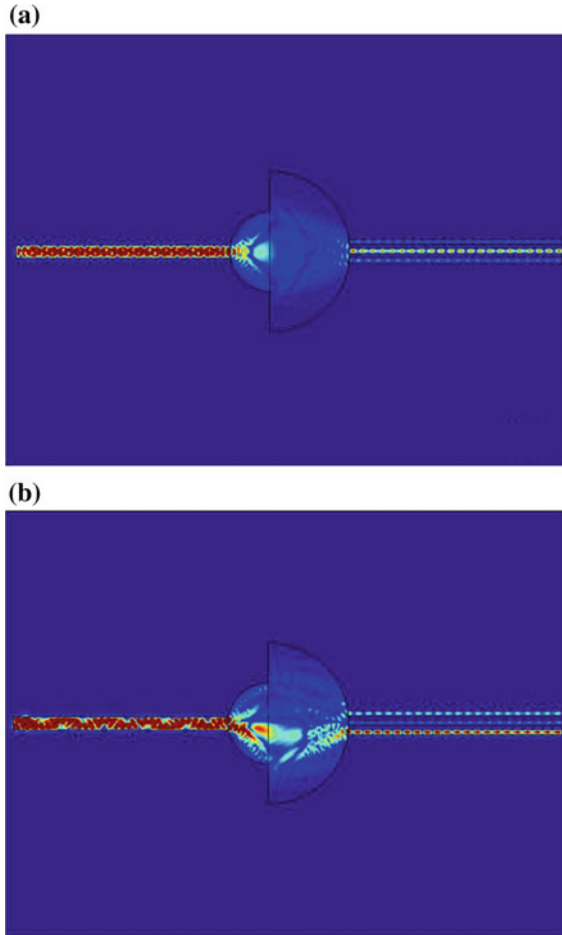


**Fig. 13.25** COMSOL Multiphysics simulations of a Maxwell fisheye-based mode sorter. **a** Symmetric excitation of the multimode input waveguide leads to the output power being channeled into the central single mode output waveguide. **b** Asymmetric excitation of the multimode waveguide leads to propagation of higher spatial modes, which are channeled preferentially into the side single mode waveguides. The spatial dimensions of the magnifying Maxwell fisheye lens in these simulations are the same as in Fig. 13.1

materials may be tested much easier in two spatial dimensions using planar optics of SPPs and the lithographically defined tapered waveguide geometries. The 2D geometries and devices described above may be used in various superresolution microscopy, waveguiding, and laser cavity schemes. We have reviewed various examples of 2D super-resolution imaging devices, which are reasonably easy to fabricate and study. These devices exhibit spatial resolution of at least 70 nm, which far exceed resolution of conventional optical microscopy. Moreover, utilization of well-known digital image recovery techniques enables further improvement of resolution of far-

field optical microscopy down to the  $\sim 30$  nm scale. Unlike more time-consuming near-field optical techniques, the described far-field 2D imaging allows very simple, fast, robust, and straightforward image acquisition. Widespread availability of these techniques to the research community should bring about numerous advances in imaging, lithography, and sensing. However, metamaterial losses remain an important performance-limiting issue. It remains to be seen if loss compensation using gain media [31] will be able to overcome this problem.

## References

1. D.W. Pohl, D. Courjon (eds.), *Near Field Optics* (Kluwer Academic Publishers, Dordrecht, 1993)
2. S.W. Hell, Far field optical nanoscopy. *Science* **316**, 1153–1158 (2007)
3. J.B. Pendry, Negative refraction makes a perfect lens. *Phys. Rev. Lett.* **85**, 3966–3969 (2000)
4. N. Fang, H. Lee, C. Sun, X. Zhang, Sub-diffraction-limited optical imaging with a silver superlens. *Science* **308**, 534–537 (2005)
5. D.O.S. Melville, R.J. Blaikie, Super-resolution imaging through a planar silver layer. *Opt. Express* **13**, 2127–2134 (2005)
6. I.I. Smolyaninov, J. Elliott, A. Zayats, C.C. Davis, Far-field optical microscopy with a nanometer-scale resolution based on the in-plane image magnification by surface plasmon polaritons. *Phys. Rev. Lett.* **94**, 057401 (2005)
7. A.V. Zayats, I.I. Smolyaninov, Near-field photonics: surface plasmon polaritons and localized surface plasmons. *J. Opt. A Pure Appl. Opt.* **5**, S16–S50 (2003)
8. I.I. Smolyaninov, C.C. Davis, J. Elliott, G. Wurtz, A.V. Zayats, Super-resolution optical microscopy based on photonic crystal materials. *Phys. Rev. B* **72**, 085442 (2005)
9. S.A. Ramakrishna, J.B. Pendry, Spherical perfect lens: solutions of Maxwell's equations for spherical geometry. *Phys. Rev. B* **69**, 115115 (2004)
10. Z. Jakob, L.V. Alekseyev, E. Narimanov, Optical Hyperlens: Far-field imaging beyond the diffraction limit. *Opt. Express* **14**, 8247–8256 (2006)
11. A. Salandrino, N. Engheta, Far-field subdiffraction optical microscopy using metamaterial crystals: theory and simulations. *Phys. Rev. B* **74**, 075103 (2006)
12. I.I. Smolyaninov, Y.J. Hung, C.C. Davis, Magnifying superlens in the visible frequency range. *Science* **315**, 1699–1702 (2007)
13. Z. Liu, H. Lee, Y. Xiong, C. Sun, X. Zhang, Far-field optical hyperlens magnifying sub-diffraction-limited objects. *Science* **315**, 1686 (2007)
14. I.I. Smolyaninov, C.C. Davis, J. Elliott, G. Wurtz, A.V. Zayats, Digital resolution enhancement in surface plasmon microscopy. *Appl. Phys. B – Lasers Opt.* **84**, 253–256 (2006)
15. Z. Wang et al., Optical virtual imaging at 50 nm lateral resolution with a white-light nanoscope. *Nat. Commun.* **2**, 218 (2011)
16. U. Leonhardt, Perfect imaging without negative refraction. *New J. Phys.* **11**, 093040 (2009)
17. J.C. Minano, Perfect imaging in a homogeneous three dimensional region. *Opt. Express* **14**, 9627–9635 (2006)
18. V.N. Smolyaninova, I.I. Smolyaninov, A.V. Kildishev, V.M. Shalaev, Maxwell fisheye and Eaton lenses emulated by microdroplets. *Opt. Lett.* **35**, 3396–3398 (2010)
19. T.W. Ebbesen, H.J. Lezec, H.F. Ghaemi, T. Thio, P.A. Wolff, Extraordinary optical transmission through sub-wavelength hole arrays. *Nature* **391**, 667–669 (1998)
20. I.I. Smolyaninov, V.N. Smolyaninova, A.V. Kildishev, V.M. Shalaev, Anisotropic metamaterials emulated by tapered waveguides: application to electromagnetic cloaking. *Phys. Rev. Lett.* **102**, 213901 (2009)

21. V.N. Smolyaninova, I.I. Smolyaninov, A.V. Kildishev, V.M. Shalaev, Experimental observation of the trapped rainbow. *Appl. Phys. Lett.* **96**, 211121 (2010)
22. J.B. Pendry, D. Schurig, D.R. Smith, Controlling electromagnetic fields. *Science* **312**, 1780–1782 (2006)
23. U. Leonhardt, Optical conformal mapping. *Science* **312**, 1777–1780 (2006)
24. J.Y. Lee, B.H. Hong, W.Y. Kim, S.K. Min, Y. Kim, M.V. Jouravlev, R. Bose, K.S. Kim, I. Hwang, L.J. Kaufman, C.W. Wong, P. Kim, K.S. Kim, Near-field focusing and magnification through self-assembled nanoscale spherical lenses. *Nature* **460**, 498–501 (2009)
25. D.R. Mason, M.V. Jouravlev, K.S. Kim, Enhanced resolution beyond the Abbe diffraction limit with wavelength-scale solid immersion lenses. *Opt. Lett.* **35**, 2007–2009 (2010)
26. A. Darafsheh, G.F. Walsh, L. Dal Negro, V.N. Astratov, Optical super-resolution by high-index liquid-immersed microspheres. *Appl. Phys. Lett.* **101**, 141128 (2012)
27. L.D. Landau, E.M. Lifshitz, *Quantum Mechanics* (Reed, Oxford, 1988)
28. V.N. Smolyaninova, H.K. Ermer, A. Piazza, D. Schaefer, I.I. Smolyaninov, Experimental demonstration of birefringent transformation optics devices. *Phys. Rev. B* **87**, 075406 (2013)
29. S. Martínez-Garaot, S.-Y. Tseng, J.G. Muga, Compact and high conversion efficiency mode-sorting asymmetric Y junction using shortcuts to adiabaticity. *Opt. Lett.* **39**, 2306–2309 (2014)
30. G.Z. Racz, N. Bamiedakis, R. Penty, Mode-selective optical sensing using asymmetric waveguide junctions. *Sens. Actuators A* **233**, 91–97 (2015)
31. S. Xiao, V.P. Drachev, A.V. Kildishev, X. Ni, U.K. Chettiar, H.-K. Yuan, V.M. Shalaev, Loss-free and active optical negative-index metamaterials. *Nature* **466**, 735–738 (2010)

# Chapter 14

## Label-Free Super-Resolution Imaging with Hyperbolic Materials



Emroz Khan and Evgenii Narimanov

**Abstract** Optical imaging systems based on hyperbolic materials, offer the potential to combine subwavelength resolution with the advantage of an inherently label-free approach. The chapter reviews recent developments in this field, in both direct imaging and structured illumination configurations.

### 14.1 Introduction

Deeper understanding of biological processes generally relies on detailed information about the dynamics in cellular structures, from the micrometer size down to the nanoscale. However, ordinary light microscopes constrained by the diffraction limit [1] can not resolve features that are substantially smaller than the light wavelength. On the other hand, high energy methods such as X-ray [2] and electron microscopy, [3] and nonlinear optical imaging, [4, 5] though offering high resolution, generally degrade biological samples. The resulting demand for a nondestructive, low-energy imaging methods led to the development of several new imaging systems operating at visible wavelengths [6, 7] that can surpass the conventional diffraction limit, culminating in 2014 Nobel Prize in chemistry for “the development of super-resolved fluorescence microscopy.”

However, in many of these novel imaging methods, the biological sample must first be “labelled” with the fluorescent molecules, [7] and it is the fluorescent “component” of the sample and not the original biological tissue that is actually imaged with super-resolution accuracy. While the methods of “tacking” a fluorescent label such as the green fluorescent protein GFP, onto other cellular proteins, are now well developed (and acknowledged by the 2008 Nobel Prize in biology for “the discovery and development of the green fluorescent protein, GFP”), forcing a biological protein “to hold a glow stick” brings its own set of problems. Not only are the fluorescence-

---

E. Khan · E. Narimanov (✉)  
Department of Electrical and Computer Engineering, Birck Nanotechnology Center,  
Purdue University, West Lafayette, IN 47907, USA  
e-mail: [evgenii@purdue.edu](mailto:evgenii@purdue.edu)

© Springer Nature Switzerland AG 2019  
V. Astratov (ed.), *Label-Free Super-Resolution Microscopy*,  
Biological and Medical Physics, Biomedical Engineering,  
[https://doi.org/10.1007/978-3-030-21722-8\\_14](https://doi.org/10.1007/978-3-030-21722-8_14)

based imaging methods inherently slow, but the fluorescent labels may modify the dynamics of the process that is being investigated, induce an unwanted chemical reaction or may even be toxic to the biological sample.

As a result, there is an increasing demand in an alternative approach to optical imaging that is inherently label-free but offers the resolution comparable to that of the fluorescent microscopy. One possible solution for this objective is offered by the imaging systems that are based on metamaterials—artificial composite structures with the emergent properties that are different from conventional media. The present chapter reviews recent progress in this line of research.

## 14.2 Super-Resolution Microscopy

When an object is illuminated, its fine structure information is carried by evanescent waves [1] which rapidly decay away from the target and therefore do not reach a detector in the far field. Originally proposed in 1928, [8] near-field scanning optical microscopy (NSOM) techniques [9] capture these evanescent waves or scatter them into the far field, using a probe with a subwavelength tip, positioned at a very short distance from the object [10]. Even though high lateral resolution can be achieved, the shallow depth of field and long scanning time limit the applicability of this approach.

An alternative imaging method of the structured illumination [6, 11], uses a coherent grid pattern formed by light through interference, that is superimposed on the object. The resulting scattered signal is detected in the far field, followed by computational reconstruction of the structure of the original object from these data. This approach can be understood as the optical analogue of the detection and “reconstruction” of the signal that was encoded in the modulation of a carrier wave [12]. In this approach, the resulting reconstructed image involves high spatial frequency information outside the diffraction limit, with the extended range that is defined by the periodicity of the illumination pattern. In the standard implementation of structured illumination approach, the diffraction-limited resolution can be improved by the factor of two, [6, 11] down to one-quarter of the light wavelength in the medium surrounding the object,  $\lambda_0/4$ .

Super-resolution can also be achieved by bandwidth extrapolation techniques [13, 14]. Electromagnetic field scattered by a finite object, can be represented as a Fourier transform of a function with a finite spatial support, [1] and is therefore an analytical function of the wavevector. As a result, by virtue of its convergent Taylor series that only involves the derivatives at a single point (albeit of exceedingly high orders), the entire spectrum can be obtained from its finite part, no matter how limited in range. In the actual implementation of this approach, the necessary data post-processing can be facilitated by finding the point spread function of the optical system and deconvolving the image and using multiple images of the same object, with certain a priori information about the target, such as sparsity [15, 16]. While this approach can lead to retrieval of information not originally captured by the imaging sensors,

it is exponentially sensitive to any noise in the system, and as a result so far only produced a limited success.

A number of super-resolution methods rely on the nonlinear response of the dyes that are used to label biological samples in fluorescence imaging. Stimulated emission depletion (STED) microscopy [5] accomplishes so by selectively deactivating part of the illumination region by an additional light and localizing the final excitation spot for the fluorophores to a very small region. However, this optical technique is inherently nonlinear, and suffers from additional stray excitation in the dyes leading to photobleaching [17].

Another super-resolution method in fluorescence imaging is stochastic optical reconstruction microscopy (STORM), [18] which surpasses the diffraction limit by allowing the dyes to fluoresce not all at once, but sequentially, so that very few active molecules are emitting light at any given time. The problem of resolving two closely spaced objects are therefore eliminated, and a complete image of the sample can be formed by superimposing multiple time-resolved recordings of the individual emitters. Apart from having the same drawbacks as those of fluorescence imaging like phototoxicity, photobleaching etc., this method suffers in addition in that it is not a deterministic method and can not capture a biological process in real time [19].

While fluorescence-based methods offer a remarkable improvement of the resolution, as compared to the conventional diffraction-limited optical imaging, fluorescent dyes can induce an unwanted chemical reaction in the sample, or they can only be attached to a certain part of the specimen. The resulting quest for a label-free super-resolution imaging, led to the emergence of an alternative approach that is based on the novel concept of electromagnetic metamaterials.

### 14.3 Metamaterials-Based Super-Resolution

Metamaterials [20] are artificial composites having properties that are usually not available in nature. The constituents are arrayed on a scale much smaller than the wavelength, so that the incoming radiation cannot fully distinguish between the grainy variation, and the medium as a whole shows a response that can be substantially different from the properties of the individual material components. These new emergent properties can be controlled by engineering the geometric structure of the metamaterial unit cell.

One of the earliest examples of these new emergent properties of metamaterials is the negative index which leads to negative refraction, reversed Cherenkov radiation and the possibility of realizing a flat lens [21]. When an object is placed close to a slab of such a medium, the evanescent waves scattered by the object excite surface states at the metamaterial interfaces. For the surface state at the “right” metamaterial–air interface (see Fig. 14.1a), its decay into the negative index slab manifests itself as the effective growth of the field in the metamaterial when viewed from the position of the source at the “left” of the slab. This effective “amplification” of the evanescent field that carries the subwavelength information on the structure of object, is what

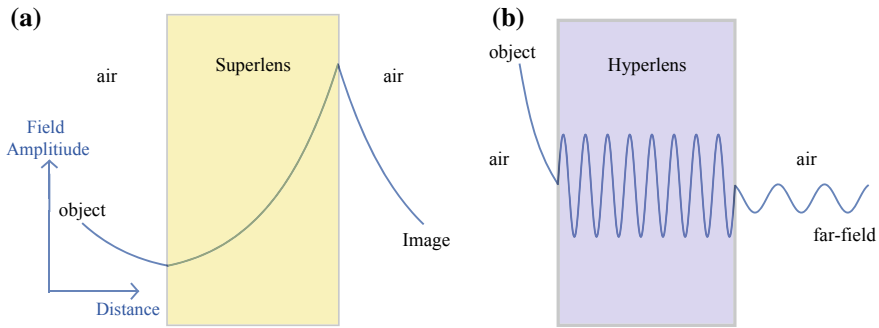


**Fig. 14.1** Super-resolution methods using metamaterials: **a** the superlens “amplifies” the evanescent field using a negative index medium, and **b** the hyperlens converts evanescent waves to propagating field by the use of a hyperbolic material

makes the “superlens”—a slab of a negative refractive index medium operating at the resonance condition when the incident evanescent field is resonantly coupled to the surface states—possible. With the exponential increase of the evanescent field in the negative index medium at this resonance (see Fig. 14.1a), the superlens [22] offers a way to compensate for the decay of evanescent waves in free space by “amplifying” them in the negative index material and combining them with the propagating waves, so that a nearly perfect image is formed at the image plane [22].

However, the actual fabrication of negative index media in the optical domain poses major engineering challenges [20]. Furthermore, the presence of material loss severely limits the subwavelength performance of the superlens, effectively reducing it to the near-field and thus making this imaging method essentially “near-sighted.” [23–25].

The hyperlens [26, 27] represents an alternative metamaterials-based approach to super-resolution that is not as sensitive to loss. It utilizes “hyperbolic” metamaterials (HMM) [26, 27] which are strongly anisotropic media with (the real parts of) the permittivities in two orthogonal directions opposite in sign. The hyperlens essentially “converts” the evanescent field to propagating waves (see Fig. 14.1b) so that the subwavelength information about the object can reach the far field and may be further manipulated with usual optical components. In the original proposal, [26, 27] the hyperlens employs a cylindrical geometry with the object placed in the hollow core. The emitted evanescent waves propagate through the hyperbolic shell and because of device curvature, by the time these waves reach the outer surface, the fine features of the object that they carry, get magnified and become resolvable by an ordinary (diffraction-limited) microscope.

However, the curved geometry, although possible in practical fabrication [28], is not trivial to implement. Furthermore, due to the use of metallic components common in hyperbolic metamaterials, the hyperlens is inherently lossy—which substantially reduces the brightness of the image and reduces the corresponding signal-to-noise ratio.

These difficulties with the limited signal-to-noise ratio in metamaterial imaging systems based on direct imaging, can be addressed in the structured illumination setting, using hyperbolic medium as the substrate [29]. This “hyper-structured illumination” approach employs planar geometry and does not require a thick substrate. As a result, the effect of loss can be offset by raising the illumination intensity, without increasing the optical power density in the sample, since the object in a structured illumination set up is placed “after” the metamaterial, not “before.” Furthermore, as the hyperbolic medium can support illumination patterns having subwavelength features, the resulting resolution is also dramatically improved in comparison to the conventional structural illumination.

In the next sections, we review the relevant properties of the hyperbolic media, and describe the actual implementation of the hyperlens and the hyperstructured illumination in practical imaging systems.

## 14.4 Hyperbolic Media

An isotropic dielectric material is described by a positive (real part of the) permittivity  $\epsilon$ . Its iso-frequency surface (the constant frequency surface in the wavevector space  $\mathbf{k} \equiv (k_x, k_y, k_z)$ ), with the corresponding circular iso-frequency curve in  $(k_x \equiv (k_x^2 + k_y^2)^{1/2} \text{ sign}[k_x], k_n \equiv k_z)$  coordinates,

$$\frac{k^2}{\epsilon} = \frac{\omega^2}{c^2}, \quad (14.1)$$

where  $\omega$  is the frequency and  $c$  is the speed of light, characterizes the available states for light propagation within the medium. For a uniaxial anisotropic dielectric medium with  $\epsilon_\tau \neq \epsilon_n$  (where  $\hat{\mathbf{n}}$  represents the direction of the remaining symmetry axis), the iso-frequency curve is circular for the ordinary ( $\mathbf{E} \perp \hat{\mathbf{n}}$ ), or  $s$ , and elliptic for the extraordinary ( $\hat{\mathbf{n}} \cdot \mathbf{E} \neq 0$ ), or  $p$ , polarizations:

$$\frac{k_\tau^2 + k_n^2}{\epsilon_\tau} = \frac{\omega^2}{c^2}, \quad s\text{-polarization}, \quad (14.2)$$

$$\frac{k_\tau^2}{\epsilon_n} + \frac{k_n^2}{\epsilon_\tau} = \frac{\omega^2}{c^2}, \quad p\text{-polarization}. \quad (14.3)$$

As a result, in the the dielectric there is a bound on the maximum wavenumber that can be supported in the material, which leads to diffraction-limited light propagation.

In contrast to this behavior, a metal, with its negative (real part of the) permittivity, does not support any propagating waves, and the corresponding phase space is empty.

The situation, however, is dramatically different in the uniaxial medium that is so anisotropic that it shows metallic (highly conducting) behavior in one direction and dielectric (low conductivity) in the other (such as graphite)—with the corresponding

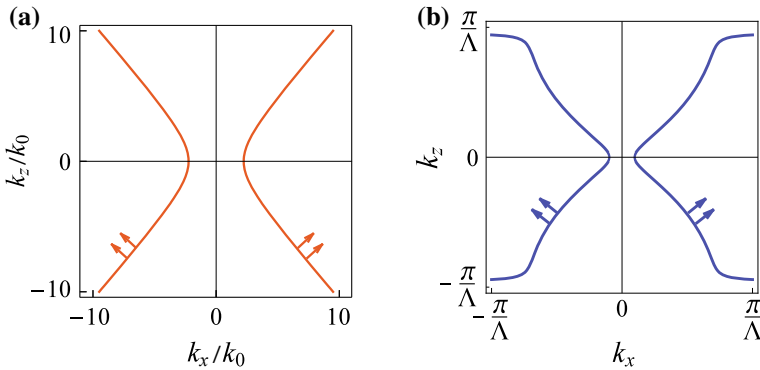


**Fig. 14.2** The iso-frequency curve for a hyperbolic material, in the effective medium limit **(a)** and for a planar metal–dielectric metamaterial with a finite unit cell size  $\Lambda$  **(b)**. In both panels, the arrows indicate the direction of the group velocity (normal to the iso-frequency curve) at the corresponding wavevector. Even though in the case of the planar metamaterial, the normal to the layers component of the wavevector  $k_z$  is limited to the interval  $(-\pi/\Lambda, \pi/\Lambda)$ , the dispersion retains hyperbolic shape for most of this range. The resulting illumination pattern from a point source inside or at the boundary of the hyperbolic metamaterial, while distorted in comparison to the case of natural hyperbolic medium, still shows narrow (sub-diffraction) beams that contain high wavenumber components which are key to hyperstructured illumination

dielectric permittivities opposite in the sign (of their real parts),  $\text{Re}[\epsilon_\tau] \text{Re}[\epsilon_n] < 0$ . For the propagation of the extraordinary ( $p$ -polarized) wave whose components probe the material response in both directions, such medium will behave as neither a metal nor a dielectric, but as an entirely different kind of material.

Due to the opposite signs of the permittivity components parallel and perpendicular to the symmetry axis in such material,  $\epsilon_n$  and  $\epsilon_\tau$ , the corresponding wave equation for the  $p$ -polarized field ( $\hat{\mathbf{n}} \cdot \mathbf{E} \neq 0, \hat{\mathbf{n}} \cdot \mathbf{B} = 0$ ) now belongs to the hyperbolic, rather than elliptic, class of partial differential equations, and the resulting iso-frequency curve [26, 27]

$$k_\tau^2 - \left[ \begin{matrix} \epsilon_n \\ -\epsilon_\tau \end{matrix} \right] k_n^2 = \epsilon_n \frac{\omega^2}{c^2} \quad \text{with} \quad \frac{\text{Re}[\epsilon_n]}{\text{Re}[\epsilon_\tau]} < 0, \tag{14.4}$$

is now a hyperbola—see Fig. 14.2.

Hyperbolic media, although seemingly exotic, are widely available in nature, [32] even in the visible range [33]—see Fig. 14.3. However, natural hyperbolic materials are often relatively lossy, as evident from the imaginary parts of the dielectric permittivities of sapphire and hexagonal boron nitride shown as dashed lines in Fig. 14.3.

Metamaterials having high-quality conducting and dielectric components embedded in subwavelength nanostructure in a strongly anisotropic geometry, can also act as hyperbolic materials, and may offer a significant reduction of the effective loss. A number of different realizations of this approach have now been demonstrated [28, 34–37] using layered structures and the nanorod arrays, as shown in Fig. 14.4. In the

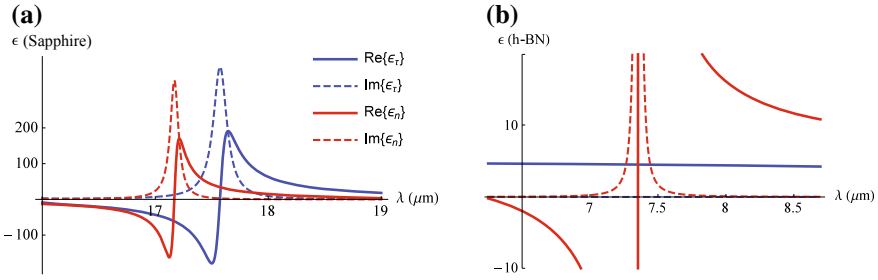


**Fig. 14.3** Permittivities of two naturally occurring hyperbolic materials: **a** sapphire ( $\text{Al}_2\text{O}_3$ ) [30] and **b** hexagonal boron nitride (h-BN) [31]. Note the presence of substantial material loss in the hyperbolic bands (where  $\text{Re}[\epsilon_\tau] \text{Re}[\epsilon_n] < 0$ )

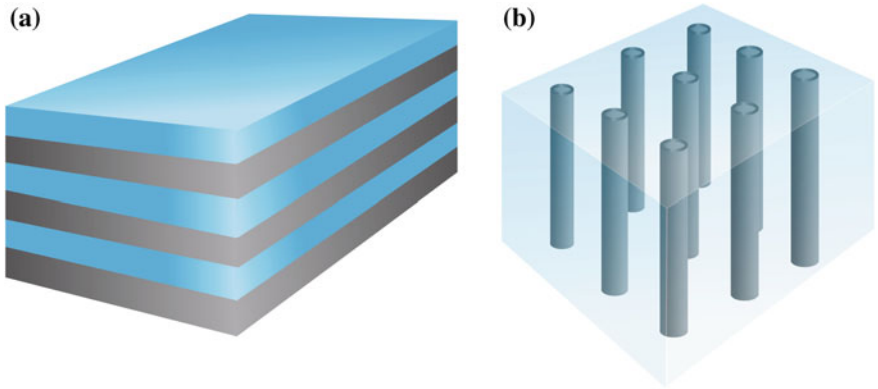


**Fig. 14.4** Metamaterial realizations of hyperbolic medium: **a** layered structure and **b** nanorod array

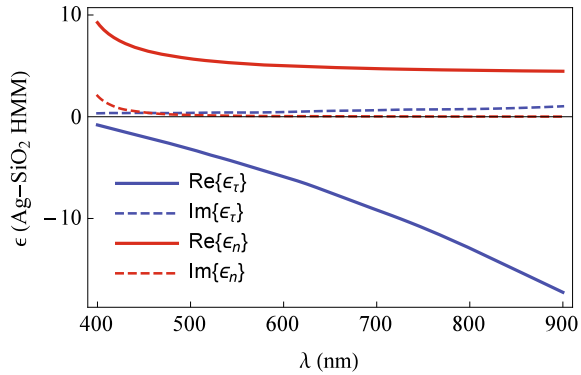
multilayer geometry, when the metal and dielectric components with the permittivities  $\epsilon_m$  and  $\epsilon_d$ , have the corresponding thickness values of  $h_m$  and  $h_d$ , the effective medium theory [38] yields

$$\epsilon_\tau = \epsilon_m \cdot \frac{h_m}{h_m + h_d} + \epsilon_d \cdot \frac{h_d}{h_m + h_d}, \quad (14.5)$$

$$\frac{1}{\epsilon_n} = \frac{1}{\epsilon_m} \cdot \frac{h_m}{h_m + h_d} + \frac{1}{\epsilon_d} \cdot \frac{h_d}{h_m + h_d}. \quad (14.6)$$

In Fig. 14.5, we show the resulting permittivities for a silver-silica-layered structure, with equal thicknesses of the metal and dielectric components of the composite. Note the relatively small amount of loss in this structure.

**Fig. 14.5** The dielectric permittivity components of the planar silver-silica hyperbolic metamaterial (see Fig. 14.4a) calculated using effective medium approach of (14.5) and (14.6). Note that this composite has  $\text{Re}\{\epsilon_r\} \text{Re}\{\epsilon_n\} < 0$  and relatively small loss ( $\text{Im}\{\epsilon\} \ll \text{Re}\{\epsilon\}$ ) in the entire visible range



## 14.5 The Hyperlens

With the wavenumber no longer limited by the frequency, the hyperbolic media are no longer subject to the conventional diffraction limit of optical imaging [39–41]. However, a simple slab of a hyperbolic (meta)material, with its translation symmetry in the object plane, will not allow image magnification. Furthermore, a propagating wave with a large wavenumber that can be supported by the hyperbolic medium, will immediately become evanescent once it escapes into the surrounding dielectric. The hyperlens allows to resolve both of these issues.

### 14.5.1 Hyperlens: The Concept

The main purpose of the hyperlens is to “convert” the evanescent fields that carry the subwavelength information, to propagating waves (see Fig. 14.1b), which would then allow for their processing with standard optical components. This “conversion” however must be accomplished without any loss of information, as this would otherwise prevent the accurate image recovery.

In other words, this means that the new waves that were formed by the hyperlens from the incident evanescent field, must not “mix” with the “original” propagating components of the incident signal. As a result, a straightforward approach based on a subwavelength grating on the surface or in the bulk of the hyperbolic medium, [42–44] cannot be a basis for the hyperlens.

To understand how one can avoid the “mixing” of the outgoing waves that originate from the incident propagating waves and the incident evanescent field that was “converted” by the hyperlens, optical imaging should be considered as a scattering experiment in the angular momentum basis. The incident plane wave that illuminates the object, can then be expressed as

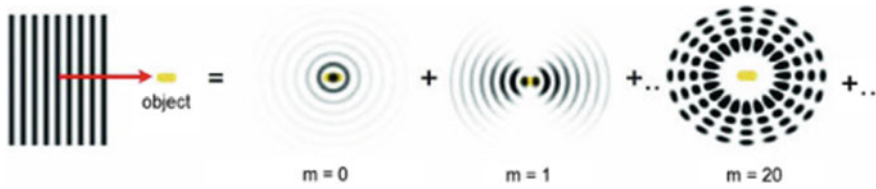


**Fig. 14.6** Imaging with an incident plane wave can be represented as scattering of various angular momentum modes, with the target shown as a yellow object near the origin. The gray scale represents the field intensity. Note that high angular momentum modes are exponentially small close to the object (Reproduced with permission from [26], Copyright 2006 Optical Society of America)

$$\exp(ikx) = \sum_{m=-\infty}^{\infty} i^m J_m(kr) \exp(im\phi), \quad (14.7)$$

where  $J_m$  is the Bessel function of the first kind and  $m$  is the angular momentum mode number of the cylindrical wave (see Fig. 14.6). In this representation, the reconstruction of the image is achieved from the retrieved scattering amplitudes and phase shifts of the various constituent angular momentum modes—which can therefore be considered as distinct information channels through which the information about the object near the origin is conveyed to the far field.

However, even though the number of these channels is infinite, very little information is carried over the high- $m$  channels—as the overlap between a high- $m$  mode and an object placed at the origin is exponentially small. Semiclassically, this corresponds to the parts of an illuminating beam that have a high impact parameter, which therefore misses the scatterer. Furthermore, the standard diffraction limit on the resolution of optical imaging [39–41] can be expressed in terms of the number of angular momentum waves with the impact parameter that’s smaller than the size of the object. As the propagating waves coming from the imaging target, do not involve high angular momentum components, the hyperlens can take advantage of these “un-used” high- $m$  channels as it transforms the evanescent field scattered by the object into propagating waves.

While this transformation can be accomplished by different means (using the spatial variation of the dielectric permittivity tensor components introduced in the design of the system), it’s most readily understood in the cylinder geometry where the angular momentum is a conserved quantity and thus a natural mode index.

In an isotropic dielectric medium, the exponential decay of high- $m$  modes at the center can also be seen as a result of conservation of angular momentum,

$$m = k_\tau r, \quad (14.8)$$

where  $k_\tau$  is the tangential component of the wavevector, and  $r$  is the distance from the origin, leading to  $k_\tau \propto 1/r$ . However, the corresponding dispersion relation

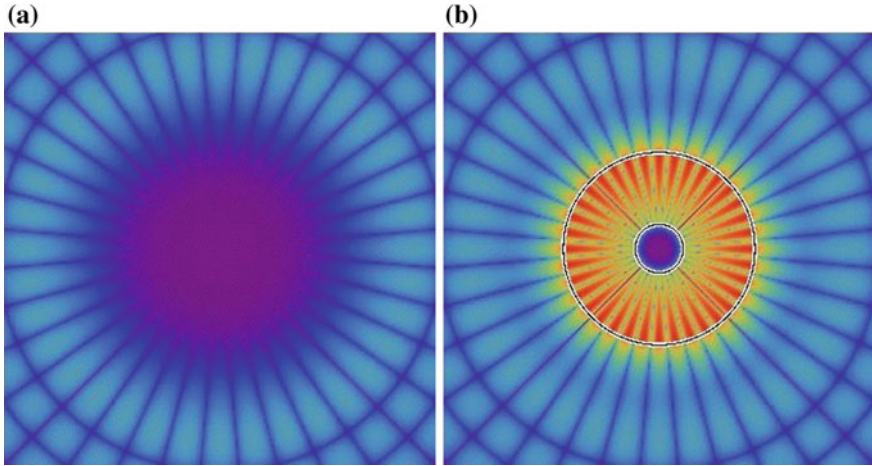


**Fig. 14.7** **a** High angular momentum states in a dielectric medium **(a)**, and in a hollow cylinder formed from a hyperbolic metamaterial with the opposite sign of the radial and tangential permittivities **(b)**. Thin black lines in panel **b** indicate the boundaries of the cylinder. Note that in the case of the hyperbolic system, the field penetrates to the center core, and couples propagating waves outside the cylinder to the subwavelength field pattern in the hollow core

$$\frac{k_n^2 + k_\tau^2}{\epsilon} = \frac{\omega^2}{c^2}, \quad (14.9)$$

limits  $k_\tau$  to the value of  $\sqrt{\epsilon} \omega/c$ . Together with (14.8), this defines the cylindrical caustic with the radius

$$R_c = \frac{mc}{\sqrt{\epsilon} \omega}, \quad (14.10)$$

with the classically inaccessible space  $r < R_c$  where the corresponding mode shows rapid exponential decay. This pattern is clearly seen in Fig. 14.7a.

Introducing the hyperbolic medium in this region, however, dramatically changes the behavior. With the opposite signs of the (real parts of the) permittivity in the radial and tangential directions, the hyperbolic dispersion relation (see also (14.4) of the previous section)

$$\frac{k_n^2}{\epsilon_\tau} + \frac{k_\tau^2}{\epsilon_n} = \frac{\omega^2}{c^2}, \quad (14.11)$$

does not set an upper bound on the magnitude of the tangential wavevector component, and the angular momentum constraint (that is still preserved as the system retains cylinder symmetry) no longer limits the wave propagation to the space outside the critical radius (14.10). Instead, any angular momentum mode can now reach all the way down to the inner boundary of the hyperbolic medium, as shown in

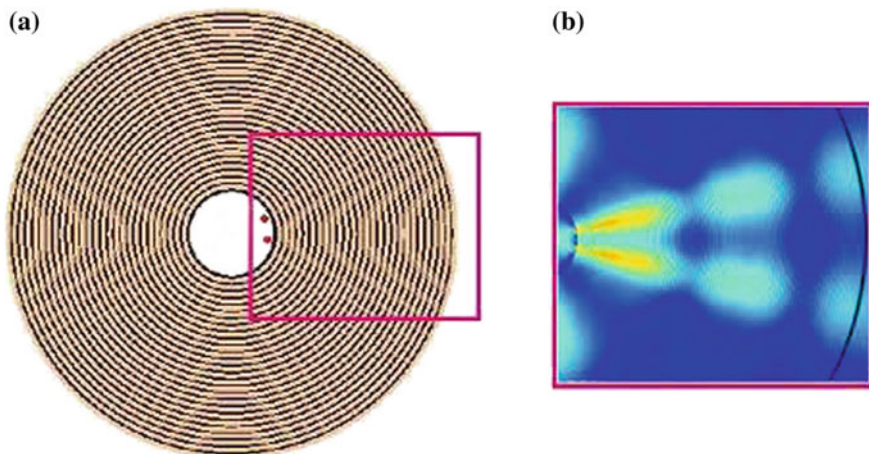


**Fig. 14.8** **a** Imaging by the hyperlens, as envisioned in [26]. **a** Two point sources separated by  $\lambda_0/3$  are placed within the hollow core of the hyperlens consisting of 160 alternating layers of metal ( $\epsilon = -1 + 0.01i$ ) and dielectric ( $\epsilon = 1.1$ ) each 10 nm thick. The radius of the hollow core is 250 nm, the outer radius 1840 nm, the operating wavelength is 300 nm and the distance between the sources is 100 nm. **b** False color plot of intensity in the region bounded by the red rectangle showing the highly directional nature of the beams from the two-point sources. At the outer boundary of the hyperlens (shown in black) the separation between the beams is substantially larger than the free-space wavelength  $\lambda_0$  (Reproduced with permission from [26], Copyright 2006 Optical Society of America)

Fig. 14.7b. As the cylinder hyperlens guides a high angular momentum mode toward its core, the distance between its nodes is progressively reduced—see Fig. 14.7b, and the field undergoes adiabatic compression. As a result, such high angular momentum states can now act as subwavelength probes for an object placed inside the core, while emerging outside the hyperlens as propagating waves that can be imaged by a regular optical microscope.

The resolution of the cylindrical hyperlens is determined by the effective (compressed) wavelength at the core and is given by the ratio of the outer and inner radii of the device,

$$\Delta = \frac{R_{\text{in}}}{R_{\text{o}}} \frac{\lambda_0}{2}, \quad (14.12)$$

as long as the unit cell size of the metamaterial forming the hyperlens, is much smaller than the inner radius  $R_{\text{in}}$ . Here,  $\lambda_0$  is the wavelength in the medium in the core of the device.

The imaging performance of the hyperlens is illustrated in Fig. 14.8, taken from the original hyperlens proposal in [26]. There, the “target” is represented by two line sources kept inside the core of the hyperlens, separated by a distance that is well below the diffraction limit—and the false color plot shows the resulting field

intensity. In the hyperbolic medium, light from the point sources propagates in highly directional beams. When they emerge from the outer boundary of device, they are now separated by the distance that is substantially above the standard diffraction limit, thereby allowing for subsequent processing by conventional optics, in full agreement with (14.12).

### ***14.5.2 Hyperlens: The Experimental Demonstration***

The actual fabrication of the hyperlens can take full advantage of the methods originally developed in the context of planar hyperbolic metamaterials, e.g., using a hollow core (half-)cylinder that consists of alternating sectors or concentric layers of metal and dielectric. This straightforward design allowed the first experimental demonstration of the hyperlens [28] within a single year from the original theoretical proposal of [26, 27].

Over the next 10 years that followed [26, 27], applications of the hyperlens were extended to a broad range of frequencies—from MHz [49] and GHz [50] all the way to visible [47, 51] and UV light, [28] and even to ultrasound imaging [46]—see Fig. 14.9. The original hyperlens design [26, 27] was adapted from the cylinder to spherical geometry, [45] which allowed for subwavelength imaging in both directions of the object plane. Furthermore, hyperlens arrays (see Fig. 14.10) were shown to offer a practical approach to dramatically extend the field of view of these imaging systems [52].

More recently, the concept of the hyperlens operating in “reverse” (i.e., in the demagnification regime) was applied to optical lithography, [48] offering the fabrication of subwavelength patterns with a diffraction-limited optical mask.

### ***14.5.3 Hyperlens: The Limitations***

While offering a unique capability of label-free optical imaging with the magnified image formation in the far field, the hyperlens suffers from three major drawbacks that severely limit its application to biological imaging.

First, to take advantage of the full resolving power of the hyperlens, the object must be placed in the near-field zone of its “inner” interface. While one can still image the target at a further distance from the hyperlens, with its increase the corresponding resolution rapidly deteriorates to the value typical for a diffraction-limited system.

Second, substantial material losses in the hyperbolic medium lead to a noticeable reduction of the signal intensity, with the resulting loss of the signal-to-noise ratio. While not a serious issue for nonbiological structures (such as semiconductor circuits) with their large index contrast and high tolerance for large incident intensity, this represents a major challenge for imaging non-labeled biological structures that can

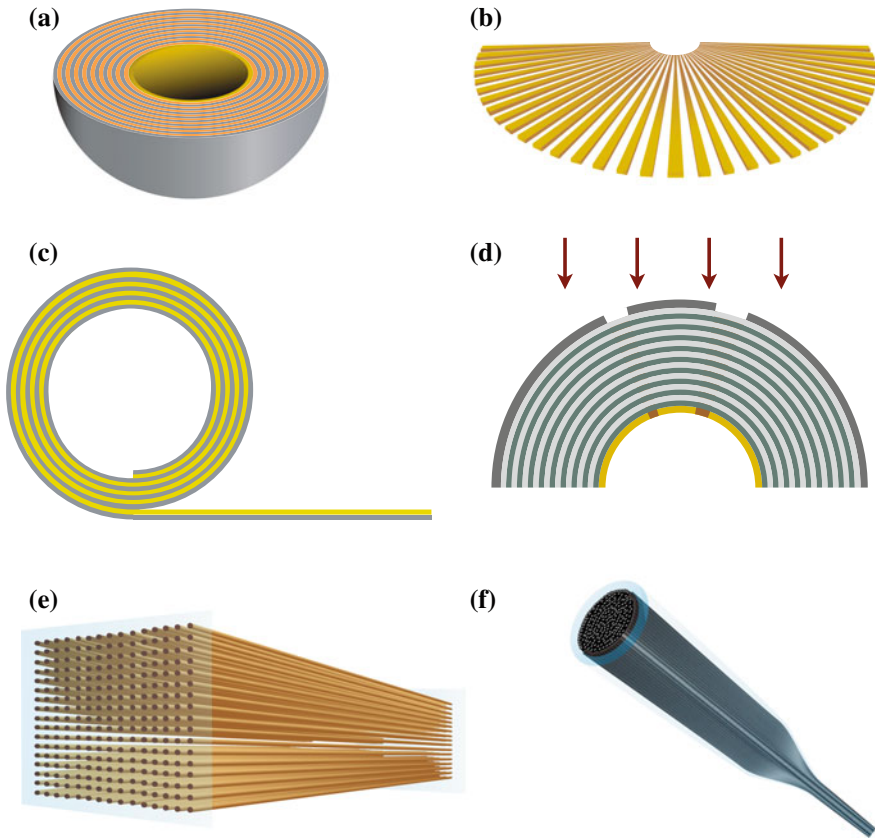


**Fig. 14.9** **a** Spherical hyperlens operating at visible wavelength [45]; **b** acoustic hyperlens made of brass fins [46]; **c** rolled up hyperlens made with metal and semiconductor layers also at visible range [47]; **d** de-magnifying hyperlens for lithography [48]; **e** an endoscope hyperlens made of tapered array of brass wires operating at MHz range [49]; **f** a GHz hyperlens made of a fiber containing long continuous array of metal microwires [50]

be damaged by strong optical fields and generally show relatively small refractive index variations, leading to the correspondingly weak optical signals.

Finally, the cylinder geometry of the original hyperlens, with its curved “object plane” is far from ideal for biological imaging. Even though the hyperlens can in principle be adapted to a planar geometry (with the role of the cylinder geometry taken over by the spatial variations of the local dielectric permittivity), [54] the resulting device retains a limited field of view of the original proposal. The hyperlens arrays—based approach [53] partially ameliorates this problem (see Fig. 14.10), but leads to multiple “dead zones” between the individual hyperlenses.

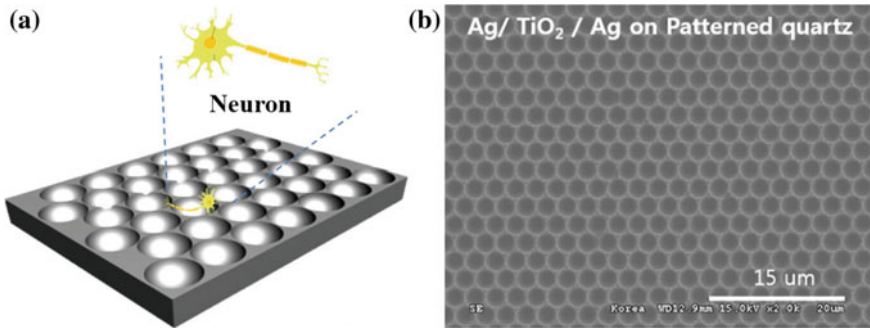


**Fig. 14.10** a The schematic of the hexagonal array of 3D hyperlenses with a neuron on it (a), and (b) the SEM image of the actually fabricated hyperlens array (Adapted with permission from [53], Copyright 2016 SPIE)

The last two issues, however, can be fully addressed by an alternative approach, that combines the concepts of the diffraction-free propagation in hyperbolic media and of the structured illumination.

## 14.6 Hyperstructured Illumination

As opposed to the “direct” imaging where the objective is the formation of a (magnified) image on a physical screen, a detector or the retina of an observer’s eye, the structured illumination approach [6] relies on the computational reconstruction of the object’s shape from optical scattering measurements. In this technique, the object is exposed to a controlled illumination pattern, which can be (rapidly) modified during the imaging. As a result, with sufficient “degrees of freedom” in the illumination pattern, the computational reconstruction becomes possible even with a single stationary detector [55]. Furthermore, even when the illumination pattern is composed entirely of propagating waves, the maximum change of the wavevector in optical scattering is now twice that of the conventional (“direct”) microscopy,  $2k_{\max}$ , where  $k_{\max}$  corresponds to the largest propagating wavenumber that is supported by the surrounding medium. Here, the factor of two originates from the simple fact that the maximum momentum transfer in optical scattering now corresponds to a photon with the incident momentum nearly in the plane of the object,  $\mathbf{k} = (k_{\tau}, k_n)$ , with  $k_n \ll k_{\tau} \leq k_{\max}$ , scattered into  $\mathbf{k}' = (-k_{\tau}, k_n)$ , so that  $k - k' = 2k_{\tau} \leq 2k_{\max}$ . As a result, already the conventional structured illumination approach, while still diffraction-limited, substantially improves upon Abbe’s limit, from  $\lambda_0/2$  to  $\lambda_0/4$ .

This result can be further improved if the object is in direct contact with a high-index substrate that is used for illumination. The maximum optical momentum transfer is now  $(1 + n)k_{\max}$  with the corresponding imaging resolution  $\lambda_0/(2 + 2n)$ , where  $n$  is the relative refractive index of the substrate.

In this sense, the *hyperstructured illumination* (HSI) [29] where the illumination substrate is fabricated from a hyperbolic medium, with the maximum supported wavenumber only limited by the inverse of the material unit cell size  $\Lambda$ , represents the ultimate example of the latter approach—leading to the optical resolution on the order of  $\Lambda$ .

### 14.6.1 HSI: The Concept

As was pointed out earlier (see (14.1)–(14.3)), a transparent dielectric material having a positive permittivity  $\epsilon$ , limits the wavenumber of propagating waves by a magnitude threshold of  $\sqrt{\epsilon} \omega/c$ . A hyperbolic medium, on the other hand, having opposite signs of (the real part of) the permittivity, say along  $x$  and  $z$  directions, so that  $\text{Re}[\epsilon_x] \text{Re}[\epsilon_z] < 0$ , does not have this limitation, because its hyperbolic dispersion for  $p$ -polarized light described by

$$\frac{k_x^2}{\epsilon_z} + \frac{k_z^2}{\epsilon_x} = \frac{\omega^2}{c^2}, \quad (14.13)$$

does not put any upper bound on the magnitude of propagating wavevector  $\mathbf{k} = (k_x, k_z)$  (see Fig. 14.2).

Since the direction of light propagation is along the normal to the iso-frequency surface, at large wavenumbers the direction makes an angle of  $\theta_c = \arctan \text{Re} \sqrt{-\epsilon_x/\epsilon_z}$  with the material symmetry axis  $\hat{\mathbf{z}}$  (see Fig. 14.11). If the light is injected in the medium through an illumination slit at the “bottom” (see Fig. 14.11a), most of the injected energy will be distributed to high wavenumber region ( $|k_x| \gg \omega/c$ ) of the spatial spectrum, and as a result, two bright beams will emerge from the slit and

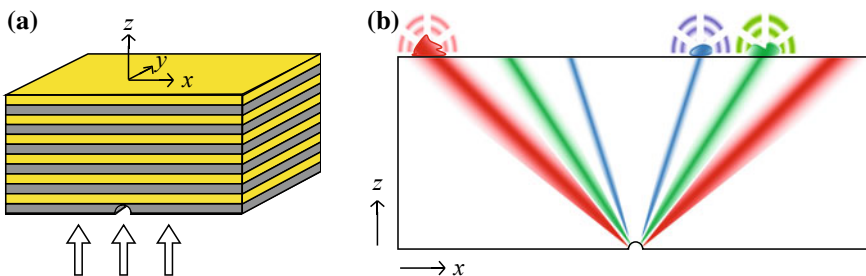


**Fig. 14.11** The schematic setting of the hyperbolic metamaterial substrate for hyperstructured illumination (a) and its operation (b). The object plane at the top of the hyperbolic media is illuminated by the beams with subwavelength width coming from an illumination slit at the bottom. Different parts of the object plane are scanned as the illumination wavelength is varied. As a result, objects which have subwavelength spacing between them are illuminated by different wavelengths, and become resolvable in the far field

illuminate the top surface. Since the spatial spectra of the beams are dominated by high wavenumber components, the beamwidth, as well as the illumination spot size, are subwavelength.

Due to the presence of loss, hyperbolic medium has strong material dispersion  $\epsilon(\omega)$  owing to Kramers–Kronig relations [10]. As a result, a change in frequency will lead to variation of the emission angle of the beams  $\theta_c(\omega)$ , as illustrated in Fig. 14.11b. This allows one to selectively illuminate different subwavelength regions of the top surface. Therefore by sweeping through the frequency of the illuminating light, the entire object plane situated at the top of the hyperbolic substrate can be scanned and a deep subwavelength image can be obtained. This hyperbolic metamaterial assisted hyperspectral imaging process is the main idea of hyperstructured illumination [29]. Note that material dispersion, which is generally considered an engineering limitation for many optical systems designed for a particular resonant condition, here forms a key element to the imaging process.

Although a finite unit cell size of the metamaterial  $\Lambda$  will add a quantitative correction to the dispersion, the topology of the iso-frequency surface (see Fig. 14.2b) along with its wavelength dependence is essentially preserved, and therefore, the beam pattern of hyperstructured illumination retains its subwavelength structure that evolves with the wavelength variation. However, since the size of the unit cell limits the wavenumbers in the object plane to  $\sim 1/\Lambda$ , the final resolution attainable from this imaging process becomes on the order of  $\Lambda$ , which in the current fabrication technology [56] can reach down to a few nanometers.

However, the hyperstructured illumination approach involves an inherent trade-off between the imaging resolution and the depth of view. In this technique, for a given resolution  $\Delta$  the corresponding depth of field also scales as  $\sim \Delta$ , since the high- $k$  waves which are propagating within the hyperbolic substrate, become evanescent outside and rapidly decay away. As a result, the corresponding resolution deteriorates

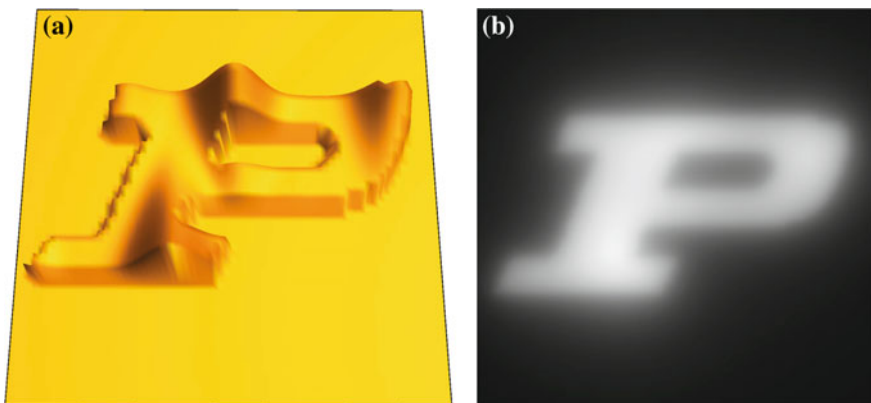


**Fig. 14.12** **a** A target and **b** its Mott projection [29] (shown in gray scale). Note that parts of the object with increased height have a brighter projection

with the increase of the separation between the object and the top surface, eventually approaching the diffraction-limited value of a quarter of a wavelength as in the conventional structured illumination. This prevents the use of HSI as an optical tomography technique.

Furthermore, imaging based on the hyperstructured illumination will show substantial aberrations in the case of the objects that are highly dispersive in the wavelength range of illumination.

### 14.6.2 HSI: Theoretical Description

Hyperstructured illumination imaging relies on the information carried out by the light scattered from the object at various wavelengths. When both the amplitude and the phase information can be measured of the far field, the resulting mathematical problem is linear, well defined and allows a highly efficient numerical solution in real time. In the present section, we describe the corresponding mathematical framework for image reconstruction.

We note however that coherent detection is not necessary for accurate image reconstruction. With a trade-off in efficiency, hyperstructured illumination imaging can also be used in the case when only the amplitude (or intensity) of the far field is available [57].

The object profile can be represented by its permittivity contrast  $\epsilon(\mathbf{r})$ . Since the field outside the hyperbolic substrate is exponentially decaying away from the object plane at the surface of the hyperbolic metamaterial, different parts of the object that is located at different “height”  $z$  (see Fig. 14.11), are illuminated at different intensities. As a result, the information sent to the far field is not of a full 3D hologram of the object but its Motti projection [29]. While this projection contains contributions from all portions of the object, their relative weights decrease with the corresponding height  $z$ . Figure 14.12 shows an example of a target and its Motti projection.

When the object at the “top” surface of the hyperbolic substrate is illuminated by a slit in the “bottom” (see Fig. 14.11), for the amplitudes of the  $s$ - and  $p$ -polarized components of the scattered light we obtain [29]

$$\mathbf{E}_s(\mathbf{k}; \omega) = \frac{4\pi^2\omega^2}{c^2k_nk_\tau} (\mathbf{p}_\mathbf{k} \cdot [\hat{\mathbf{n}} \times \mathbf{k}] + r_s(\mathbf{k}') \mathbf{p}_{\mathbf{k}'} \cdot [\hat{\mathbf{n}} \times \mathbf{k}']), \quad (14.14)$$

$$\mathbf{E}_p(\mathbf{k}; \omega) = \frac{4\pi^2\omega}{ck_nk_\tau} ([\mathbf{p}_\mathbf{k} \times \mathbf{k}] \cdot [\hat{\mathbf{n}} \times \mathbf{k}] - r_p(\mathbf{k}') [\mathbf{p}_{\mathbf{k}'} \times \mathbf{k}'] \cdot [\hat{\mathbf{n}} \times \mathbf{k}']), \quad (14.15)$$

respectively. Here  $k_n$  and  $k_\tau$  are the normal and tangential component (with respect to hyperbolic substrate) of the far-field wavevector  $\mathbf{k} \equiv (\mathbf{k}_\tau, k_n)$ ,  $\hat{\mathbf{n}} = \hat{\mathbf{z}}$  is the surface-normal unit vector,  $r_s$  and  $r_p$  are reflection coefficients from the air–substrate interface for  $s$  and  $p$ -polarizations,  $\mathbf{k}' \equiv (\mathbf{k}_\tau, -k_n)$ , and  $\mathbf{p}_\mathbf{k}$  is the spatial Fourier transform of

the object polarization  $\mathbf{p}(\mathbf{r}) = (1/4\pi)(\epsilon(\mathbf{r}) - 1)\mathbf{E}_i(\mathbf{r}; \omega)$ , with  $\mathbf{E}_i(\mathbf{r}; \omega)$  being the incident field.

When the object is placed close to the substrate and has a vertical dimension that is small compared to the free-space wavelength, the polarization can be written as

$$\mathbf{p}_{\mathbf{k}} = \frac{1}{8\pi^2} \int d^2\mathbf{q} \mathbf{E}_i(\mathbf{k} + \mathbf{q}; \omega) \Delta_M \epsilon(\mathbf{q})$$

where  $\Delta_M \epsilon(\mathbf{q})$  is the spatial Fourier transform of the Motti projection of the object profile,

$$\Delta_M \epsilon(x, y) \equiv \int \frac{d^3\mathbf{r}' (z'/2\pi) (\epsilon(\mathbf{r}') - 1)}{((x - x')^2 + (y - y')^2 + z'^2)^{3/2}}. \quad (14.16)$$

This integral transform above averages out the axial profile of the target in such a way that the resulting Motti projection primarily contains information near the object plane  $z = 0$  (“top” of the hyperbolic substrate).

Once the far field  $\mathbf{E}(\mathbf{k}, \omega)$  is measured, this system of linear equations can be solved to calculate the Motti projection of the object  $\Delta_M \epsilon(x, y)$ . On a standard processor, the resulting numerical complexity can be handled in sub-millisecond time period, which allows real time imaging for a variety of dynamic processes.

In practice, to extend the field of view of the imaging method the object can be illuminated through more than one aperture at the bottom. The positions of the holes can be either random [29, 59] or periodic, [29] with a substantial reduction of the numerical complexity of the image reconstruction in the periodic case [29].

### 14.6.3 HSI Performance

To illustrate the performance of the hyperstructured illumination, we consider the target composed of several silica nanowires intersecting at different angles, each with about 10 nm width—see Fig. 14.13a that shows the top view of a sample target. As expected, even in the presence of substantial noise the reconstructed image (Fig. 14.13b) shows the subwavelength resolution of  $\lambda_0/20$  (where  $\lambda_0$  is the shortest illumination wavelength used), consistent with the limit given by the unit cell size of the hyperbolic metamaterial.

### 14.6.4 HSI: The Effect of Disorder

As every composite media, hyperbolic metamaterials are susceptible to disorder (due to fabrication imperfections, etc). The disorder will reduce the coherence of the

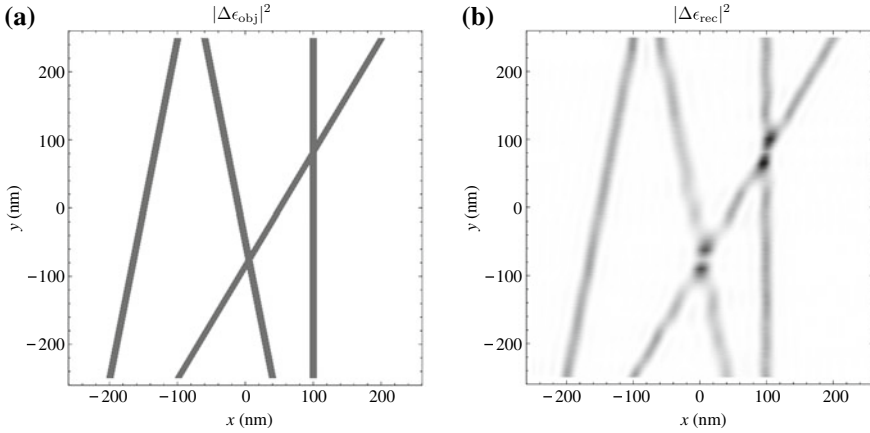


**Fig. 14.13** The performance of hyperstructured illumination. **a** Top view of the object  $|\Delta\epsilon_{\text{obj}}|^2$  and **b** the reconstructed image  $|\Delta\epsilon_{\text{rec}}|^2$ . The object consists of 4 silica nanowires with about 10 nm width. The hyperbolic substrate consists of 11 silica and 10 silver layers, with a layer thickness of 5 nm for both metal and dielectric. Illumination slits are arrayed with spacings of 350 nm. The illumination wavelength varies from 400 to 600 nm in 2 nm steps. The corresponding permittivities are taken with actual losses from [58]. Additive noise with a signal-to-noise ratio of 10 dB is assumed

illumination field, but will not eliminate the subwavelength structure of the intensity pattern in the object plane. Due to the uncertainty in the details in the illumination pattern, this incoherent version of hyperstructured illumination will reduce amount of information that can be determined about the object profile. This setting, however, offers a number of practical advantages such as reduced noise sensitivity, relaxed constraints on fabrication quality, etc.

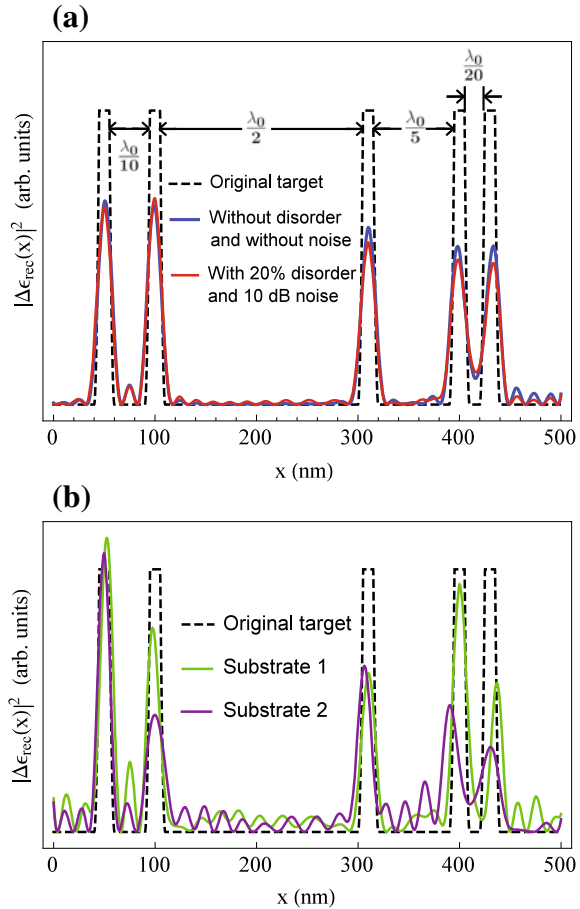
The effect of disorder on the performance of hyperstructured illumination imaging was considered in [60]. Even in the presence of substantial disorder (see Fig. 14.14), accurate image reconstruction using HSI imaging was demonstrated with the resolution of  $\lambda_0/20$ .

### 14.6.5 HSI: Experimental Demonstration

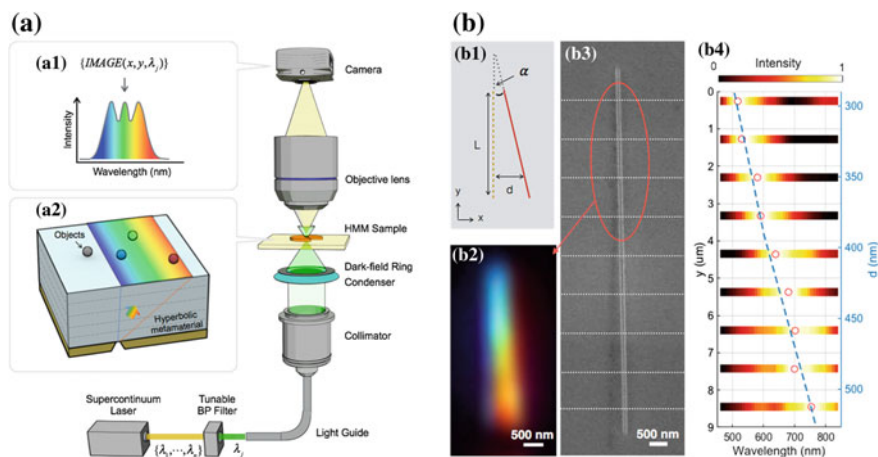
Super-resolution hyperstructured illumination imaging has been recently experimentally demonstrated, [57] and the resolution of about 80 nm has been achieved for an illumination wavelength range of 460–700 nm and a numerical aperture of 0.5, surpassing the diffraction limit by a factor of  $\sim 6$ .

Figure 14.15a shows the experimental set up for the measurements of [57], where a silver-SiO<sub>2</sub> hyperbolic substrate was imaged in a transmission mode dark-field microscope. The illumination and wavelength selection was performed by a broadband light source and a tunable bandpass filter, respectively. The hyperbolic substrate

**Fig. 14.14 a** Imaging performance of the hyperstructured illumination when no disorder (blue) and 20% disorder (red) is present. For the case of the existing disorder, the resolution of  $\lambda_0/20 = 20$  nm can be obtained. **b** The performance when no information about disorder is available. A similar resolution of  $\lambda_0/20$  can still be achieved for two random realizations of the disordered substrate (green and purple). In both **a** and **b** the target (shown by the black dashed line) is a group of silica nanowires with 10 nm width. The results are obtained for the same imaging system as described in Fig. 14.13



was formed by six pairs of alternating silver and silica layers, each layer 14 nm thick. The metamaterial structure was placed on top of a 40 nm thick chromium layer which had a slit of about 27 nm width and a few microns length milled into it. The insets in Fig. 14.15a show that for a broadband source the slit allows a rainbow-like illumination pattern on the substrate top. This spatial-spectral mapping was experimentally verified by milling an artificial object (30 nm wide and a few micrometers long slit) in a 50 nm thick  $\text{Si}_3\text{N}_4$  layer deposited on top of the hyperbolic substrate (see Fig. 14.15b). There, since the target was not aligned with the illumination slit, different parts of the object were illuminated by different wavelengths, forming a color variation in the diffraction-limited image that can be used for accurate determination of the actual object geometry.



**Fig. 14.15** Panel **a**: the experimental set up for hyperstructured illumination. The hyperbolic meta-material (HMM) sample is imaged under a conventional microscope in dark-field configuration. A supercontinuum laser, equipped with a tunable bandpass filter, which serves as a light source, scans its output wavelength from 460 to 840 nm in series, while the HMM sample is imaged by a camera to form a hyperspectral image  $I(x, y, \lambda)$ . The HMM projects a nanoscale rainbow on its top surface to illuminate the object, and the scattering signal (a1) from particles, that are illuminated from the “bottom” slit of the HMM, has different wavelengths at different positions on the surface (a2). Panel **b** shows actual imaging of the single subwavelength line object. Subpanel (b1) illustrates the relative location between the illumination slit and the object. The object parameters are  $\alpha = 1.51^\circ$ ,  $L = 10 \mu\text{m}$ . Subpanel (b2) shows the experimental diffraction-limited RGB image of the object. The three channels (RGB) are acquired in series by setting the tunable bandpass filter to [460 nm: 500 nm], [510 nm: 570 nm], and [580 nm: 700 nm], respectively. Subpanel (b3) presents the scanning electron microscope (SEM) image of the object. Subpanel (b4) shows the spectral response along the  $y$  direction versus distance  $d$  along the  $x$  direction at indicated locations (white dashed lines in (b3)). Red circles correspond to the peak positions of each measured spectrum, while the blue dashed line shows the corresponding theoretical full wave simulation (Adapted with permission from [57], Copyright 2018 American Chemical Society)

Figure 14.16 shows the super-resolution performance of hyperstructured illumination for a pair of tilted line objects, each having a width of about 35 nm. The reconstructed image (middle panel) clearly resolves the two targets—see Fig. 14.16. Three intensity cross sections of the SEM and HSI images (right panel) show that optical image from hyperstructured illumination closely captures the fine object details within the field of view.

As seen from the measurements in [57], the resolution of hyperstructured illumination imaging can rival the accuracy of scanning electron microscopy.

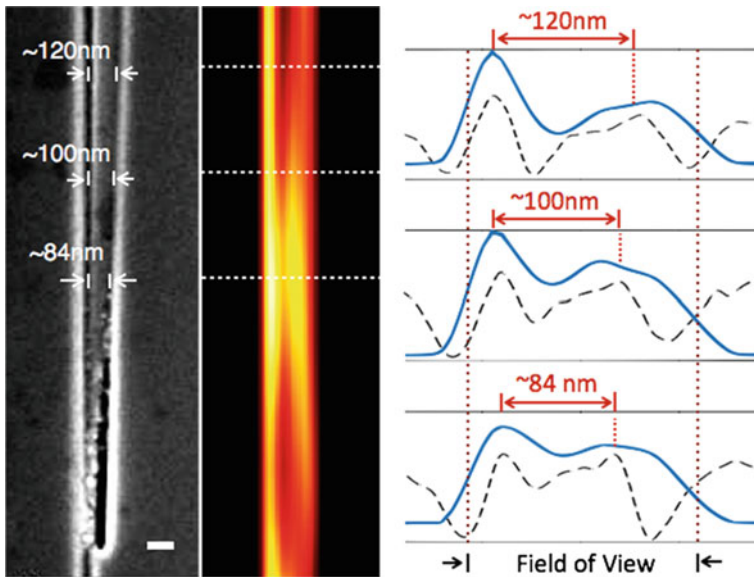


**Fig. 14.16** The experimental demonstration of super-resolution in HSI. Left: SEM image of a tilted pair of line objects. The object line width is 35 nm. Middle panel shows the super-resolution image obtained with the HSI. Right panel presents the cross section of the image at indicated locations, where the blue solid line is the optical image, and the black dashed line is the SEM image. The scale bar in the figure corresponds to 100 nm, and the optical wavelength range in this experiment was from 460 to 700 nm (Adapted with permission from [57], Copyright 2018 American Chemical Society)

## 14.7 Conclusions

In conclusion, active research of the last decade has demonstrated the potential of hyperbolic metamaterials, as a practical tool for super-resolution imaging. Experimentally demonstrated in a variety of setups and at different frequencies, from GHz to UV, hyperbolic metamaterials-based systems allow for both the direct imaging setups and structured illumination implementations. Inherently label-free, super-resolution imaging with hyperbolic metamaterials offers a viable alternative to fluorescence microscopy.

**Acknowledgements** This work was partially supported by the Army Research Office, Grant No. ARO W911NF-14-1-0639, the National Science Foundation, Grant No. DMREF-1629276, and the Gordon and Betty Moore Foundation.

## References

1. M. Born, E. Wolf, *Principles of Optics: Electromagnetic Theory of Propagation, Interference and Diffraction of Light*, 7th edn. (Cambridge University Press, Cambridge, 1999)
2. A. Sakdinawat, D. Attwood, Nanoscale x-ray imaging. *Nat. Photonics* **4**(12), 840–848 (2010)
3. J. Goldstein, D.E. Newbury, P. Echlin, D.C. Joy, A.D. Romig Jr., C.E. Lyman, C. Fiori, E. Lifshin, *Scanning Electron Microscopy and X-Ray Microanalysis: A Text for Biologists, Materials Scientists, and Geologists* (Springer Science & Business Media, New York, 2012)
4. A. Pliss, A.N. Kuzmin, A.V. Kachynski, P.N. Prasad, Nonlinear optical imaging and Raman microspectrometry of the cell nucleus throughout the cell cycle. *Biophys. J.* **99**(10), 3483–3491 (2010)
5. S.W. Hell, J. Wichmann, Breaking the diffraction resolution limit by stimulated emission: stimulated-emission-depletion fluorescence microscopy. *Opt. Lett.* **19**(11), 780–782 (1994)
6. M.G. Gustafsson, Surpassing the lateral resolution limit by a factor of two using structured illumination microscopy. *J. Microsc.* **198**(2), 82–87 (2000)
7. E. Betzig, J. Trautman, T. Harris, J. Weiner, R. Kostelak, Breaking the diffraction barrier: optical microscopy on a nanometric scale. *Science* **251**(5000), 1468–1470 (1991)
8. E. Sygne, Xxxviii. a suggested method for extending microscopic resolution into the ultra-microscopic region. *Lond. Edinb. Dublin Philos. Mag.* **6**(35), 356–362 (1928)
9. B. Hecht, B. Sick, U.P. Wild, V. Deckert, R. Zenobi, O.J. Martin, D.W. Pohl, Scanning near-field optical microscopy with aperture probes: fundamentals and applications. *J. Chem. Phys.* **112**(18), 7761–7774 (2000)
10. L. Novotny, *Principles of Nano-Optics* (Cambridge University Press, Cambridge, 2012)
11. A. Jost, R. Heintzmann, Superresolution multidimensional imaging with structured illumination microscopy. *Annu. Rev. Mater. Sci.* **43**, 261–282 (2013)
12. S. Haykin, *Communication Systems* (Wiley, New York, 2008)
13. S. Borman, R. Stevenson, Spatial resolution enhancement of low-resolution image sequences - a comprehensive review with directions for future research. Technical report, Laboratory for Image and Signal Analysis, University of Notre Dame (1998)
14. E.J. Candès, J. Romberg, T. Tao, Robust uncertainty principles: exact signal reconstruction from highly incomplete frequency information. *IEEE Trans. Inf. Theory* **52**(2), 489–509 (2006)
15. S. Gazit, A. Szameit, Y.C. Eldar, M. Segev, Super-resolution and reconstruction of sparse sub-wavelength images. *Opt. Express* **17**(26), 23920–23946 (2009)
16. Y. Shechtman, Y.C. Eldar, A. Szameit, M. Segev, Sparsity based sub-wavelength imaging with partially incoherent light via quadratic compressed sensing. *Opt. Express* **19**(16), 14807–14822 (2011)
17. J.-I. Hotta, E. Fron, P. Dedecker, K.P. Janssen, C. Li, K. Mullen, B. Harke, J. Buckers, S.W. Hell, J. Hofkens, Spectroscopic rationale for efficient stimulated-emission depletion microscopy fluorophores. *J. Am. Chem. Soc.* **132**(14), 5021–5023 (2010)
18. M.J. Rust, M. Bates, X. Zhuang, Sub-diffraction-limit imaging by stochastic optical reconstruction microscopy (STORM). *Nat. Methods* **3**(10), 793 (2006)
19. D. Kamiyama, B. Huang, Development in the storm. *Dev. Cell* **23**(6), 1103–1110 (2012)
20. W. Cai, V. Shalaev, *Optical Metamaterials: Fundamentals and Applications* (Springer Science & Business Media, New York, 2009)
21. V.G. Veselago, The electrodynamics of substances with simultaneously negative values of  $\epsilon$  and  $\mu$ . *Phys.-Uspekhi* **10**(4), 509 (1968)
22. J.B. Pendry, Negative refraction makes a perfect lens. *Phys. Rev. Lett.* **85**(18), 3966–3969 (2000)
23. J.B. Pendry, Left-handed materials do not make a perfect lens. *Phys. Rev. Lett.* **91**(9), 099701 (2003)
24. R. Merlin, Analytical solution of the almost-perfect-lens problem. *Appl. Phys. Lett.* **84**(8), 1290–1292 (2004)
25. V.A. Podolskiy, E.E. Narimanov, Near-sighted superlens. *Opt. Lett.* **30**(1), 75–77 (2005)

26. Z. Jacob, L.V. Alekseyev, E. Narimanov, Optical hyperlens: far-field imaging beyond the diffraction limit. *Opt. Express* **14**(18), 8247–8256 (2006)
27. A. Salandrino, N. Engheta, Far-field subdiffraction optical microscopy using metamaterial crystals: theory and simulations. *Phys. Rev. B Condens. Matter* **74**(7), 075103 (2006)
28. Z. Liu, H. Lee, Y. Xiong, C. Sun, X. Zhang, Far-field optical hyperlens magnifying subdiffraction-limited objects. *Science* **315**(5819), 1686 (2007)
29. E. Narimanov, Hyperstructured illumination. *ACS Photonics* **3**(6), 1090–1094 (2016)
30. M. Schubert, T. Tiwald, C. Herzinger, Infrared dielectric anisotropy and phonon modes of sapphire. *Phys. Rev. B Condens. Matter* **61**(12), 8187 (2000)
31. M. Autore, P. Li, I. Dolado, F.J. Alfaro-Mozaz, R. Esteban, A. Atxabal, F. Casanova, L.E. Hueso, P. Alonso-González, J. Aizpurua et al., Boron nitride nanoresonators for phonon-enhanced molecular vibrational spectroscopy at the strong coupling limit. *Light Sci. Appl.* **7**(4), 17172 (2018)
32. E.E. Narimanov, A.V. Kildishev, Metamaterials: naturally hyperbolic. *Nat. Photonics* **9**(4), 214 (2015)
33. M. Esslinger, R. Vogelgesang, N. Talebi, W. Khunsin, P. Gehring, S. De Zuani, B. Gompf, K. Kern, Tetradymites as natural hyperbolic materials for the near-infrared to visible. *ACS Photonics* **1**(12), 1285–1289 (2014)
34. D. Smith, D. Schurig, Electromagnetic wave propagation in media with indefinite permittivity and permeability tensors. *Phys. Rev. Lett.* **90**(7), 077405 (2003)
35. A.J. Hoffman, L. Alekseyev, S.S. Howard, K.J. Franz, D. Wasserman, V.A. Podolskiy, E.E. Narimanov, D.L. Sivco, C. Gmachl, Negative refraction in semiconductor metamaterials. *Nat. Mater.* **6**(12), 946–950 (2007)
36. W. Dickson, G. Wurtz, P. Evans, D. OConnor, R. Atkinson, R. Pollard, A. Zayats, Dielectric-loaded plasmonic nanoantenna arrays: a metamaterial with tuneable optical properties. *Phys. Rev. B Condens. Matter* **76**(11), 115411 (2007)
37. L.V. Alekseyev, V.A. Podolskiy, E.E. Narimanov, Homogeneous hyperbolic systems for terahertz and far-infrared frequencies. *Adv. OptoElectron.* **2012** (2012)
38. G.W. Milton, *The Theory of Composites* (Cambridge University Press, Cambridge, 2002)
39. J.-L. Lagrange, *Sur une Loi generale d'Optique* (Memoires de l'Academie de Berlin, 1803)
40. H. von Helmholtz, On the limits of the optical capacity of the microscope. *Proc. Bristol Nat. Soc.* **1**, 435–440 (1874)
41. E.K. Abbe, *Archiv für mikroskopische Anatomie* **9**(1), 413–468 (1873); *Proc. Bristol Naturalists' Soc.* **1**, 200–261 (1874)
42. S. Durant, Z. Liu, J.M. Steele, X. Zhang, Theory of the transmission properties of an optical far-field superlens for imaging beyond the diffraction limit. *J. Opt. Soc. Am. B* **23**(11), 2383–2392 (2006)
43. Z. Liu, S. Durant, H. Lee, Y. Pikus, N. Fang, Y. Xiong, C. Sun, X. Zhang, Far-field optical superlens. *Nano Lett.* **7**(2), 403–408 (2007)
44. Y. Xiong, Z. Liu, C. Sun, X. Zhang, Two-dimensional imaging by far-field superlens at visible wavelengths. *Nano Lett.* **7**(11), 3360–3365 (2007)
45. J. Rho, Z. Ye, Y. Xiong, X. Yin, Z. Liu, H. Choi, G. Bartal, X. Zhang, Spherical hyperlens for two-dimensional sub-diffractive imaging at visible frequencies. *Nat. Commun.* **1**, 143 (2010)
46. J. Li, L. Fok, X. Yin, G. Bartal, X. Zhang, Experimental demonstration of an acoustic magnifying hyperlens. *Nat. Mater.* **8**(12), 931 (2009)
47. S. Schwaiger, A. Rottler, M. Bröll, J. Ehlermann, A. Stemmann, D. Stickler, C. Heyn, D. Heitmann, S. Mendach, Broadband operation of rolled-up hyperlenses. *Phys. Rev. B Condens. Matter* **85**(23), 235309 (2012)
48. J. Sun, T. Xu, N.M. Litchinitser, Experimental demonstration of demagnifying hyperlens. *Nano Lett.* **16**(12), 7905–7909 (2016)
49. P.A. Belov, G.K. Palikaras, Y. Zhao, A. Rahman, C.R. Simovski, Y. Hao, C. Parini, Experimental demonstration of multiwire endoscopes capable of manipulating near-fields with sub-wavelength resolution. *Appl. Phys. Lett.* **97**(19), 191905 (2010)

50. A. Tuniz, K.J. Kaltenecker, B.M. Fischer, M. Walther, S.C. Fleming, A. Argyros, B.T. Kuhlmei, Metamaterial fibres for subdiffraction imaging and focusing at terahertz frequencies over optically long distances. *Nat. Commun.* **4**, 2706 (2013)
51. J. Sun, M.I. Shalaev, N.M. Litchinitser, Experimental demonstration of a non-resonant hyperlens in the visible spectral range. *Nat. Commun.* **6**, 7201 (2015)
52. D. Lee, Y.D. Kim, M. Kim, S. So, H.-J. Choi, J. Mun, D.M. Nguyen, T. Badloe, J.G. Ok, K. Kim, H. Lee, J. Rho, Realization of wafer-scale hyperlens device for sub-diffractive biomolecular imaging. *ACS Photonics* **5**(7), 2549–2554 (2018)
53. M. Kim, D. Lee, J. Rho, High-throughput super-resolution hyperlens imaging. *SPIE Newsroom* (2016) <https://doi.org/10.1117/2.1201604.006407>
54. A.V. Kildishev, V.M. Shalaev, Engineering space for light via transformation optics. *Opt. Lett.* **33**(1), 43–45 (2008)
55. R. Horisaki, H. Matsui, J. Tanida, Single-pixel compressive diffractive imaging with structured illumination. *Appl. Opt.* **56**(14), 4085–4089 (2017)
56. H. Shen, D. Lu, B. VanSaders, J.J. Kan, H. Xu, E.E. Fullerton, Z. Liu, Anomalous weak scattering in metal-semiconductor multilayer hyperbolic metamaterials. *Phys. Rev. X* **5**(2), 021021 (2015)
57. Q. Ma, H. Qian, S. Montoya, W. Bao, L. Ferrari, H. Hu, E. Khan, Y. Wang, E.E. Fullerton, E.E. Narimanov, Experimental demonstration of hyperbolic metamaterial assisted illumination nanoscopy. *ACS Nano* (2018). <https://doi.org/10.1021/acsnano.8b06026>
58. X. Ni, Z. Liu, A.V. Kildishev, PhotonicsDB: Optical Constants (2008). <https://doi.org/10.4231/D35H7BV58>
59. Q. Ma, H. Hu, E. Huang, Z. Liu, Super-resolution imaging by metamaterial-based compressive spatial-to-spectral transformation. *Nanoscale* **9**(46), 18268–18274 (2017)
60. E. Khan, E.E. Narimanov, Hyperstructured illumination in disordered media. *Appl. Phys. Lett.* **111**(5), 051105 (2017)

# Chapter 15

## Super-Resolution Imaging and Microscopy by Dielectric Particle-Lenses



Zengbo Wang and Boris Luk'yanchuk

**Abstract** Imaging by microspheres and dielectric particle-lenses emerged recently as a simple solution to obtaining super-resolution images of nanoscale devices and structures. Calibrated resolution of  $\sim\lambda/6-\lambda/8$  has been demonstrated, making it possible to directly visualize 15–50 nm scale objects under a white light illumination. The technique has undergone rapid developments in recent years. Major advances such as the development of surface scanning functionalities, higher resolution metamaterial superlens, biological superlens and integrated bio-chips as well as new applications in interferometry, endoscopy and others, have been reported. This chapter aims to provide an overall review of the technique including its background, fundamentals and key progresses. The outlook of the technique is finally discussed.

### 15.1 Introduction

#### 15.1.1 Background

The history of optical microscope dates at least to 1595, when Hans and Zaccharis Janssen (1580–1638) of Holland invented a compound optical microscope. Subsequent improvements by Galileo Galilei (1564–1642), Robert hook (1635–1703) and Anthony Leeuwenhoek (1632–1723) has led to the revolution of the entire field of science and technology, especially when biological specimens such as bacteria and blood cells become visible to human eyes.

---

Z. Wang (✉)

School of Computer Science and Electronic Engineering, Bangor University, Bangor LL57 1UT, UK

e-mail: [z.wang@bangor.ac.uk](mailto:z.wang@bangor.ac.uk)

B. Luk'yanchuk

Division of Physics and Applied Physics, School of Physical and Mathematical Sciences, Nanyang Technological University, Singapore 637371, Singapore

Faculty of Physics, Lomonosov Moscow State University, Moscow 119991, Russia

© Springer Nature Switzerland AG 2019

V. Astratov (ed.), *Label-Free Super-Resolution Microscopy*,

Biological and Medical Physics, Biomedical Engineering,

[https://doi.org/10.1007/978-3-030-21722-8\\_15](https://doi.org/10.1007/978-3-030-21722-8_15)

The resolution of optical microscope was first described by German physicist Ernst Abbe in 1873 [1]: The minimum distance,  $d'$ , between two structural elements to be imaged as two objects instead of one, is given by  $d' = K\lambda/\text{NA} = 0.5\lambda/\text{NA}$  ( $K = 0.5$ ), where  $\lambda$  is the wavelength of light and NA the numerical aperture of the objective lens. Other ways of resolution definition, such as Sparrow [2], Houston [3] or Rayleigh [4] criteria, with  $K = 0.473$ , 0.515, or 0.61 respectively, has since been developed in the history. The underlying physics of resolution limit is optical diffraction and loss of evanescent wave components when light travels into far-field from objects; Subwavelength spatial information of an object was carried by the high-frequency evanescent waves which decay exponentially with distance from the object. For a white light microscope, the resolution limit is about 200–250 nm. The Abbe resolution limit was considered the fundamental limit of optical microscope resolution for a century.

The emerge of near-field optics breaks the resolution limit. In 1984, German-Swiss physicist Dieter Pohl and colleagues invented Near-field Scanning Optical Microscopy (NSOM or SNOM), the first optical instrument that provided optical resolution far beyond Abbe's limit, e.g. 20 nm at wavelength 515 nm [5]. Here, a super-resolution image of a structure is constructed by scanning a tiny tip with nano-sized aperture in the proximity (~tens nanometres) of an illuminated specimen. From late 1990s, stimulated by the rapid advancements of plasmonics, nanophotonics and metamaterials, new super-resolution microscopy/nanoscopy techniques have emerged, including metal-based metamaterial superlens [6], STED (stimulated emission depletion microscopy) [7], optical superoscillatory lens [8], SIM (structured illumination microscopy) [9] and more [10].

In 2000, British scientist John Pendry proposed the intriguing 'metamaterial superlens' (also known as Pendry superlens) concept, which uses a slab of NIM (negative-index medium) as superlens to enhance and transfer the evanescent waves for perfect imaging [6]. The fascinating 'perfect lens' proposal sparked a real surge in metamaterials and plasmonics research. Based on Pendry's recipe, several variations of metal-based metamaterial superlenses were developed and demonstrated by groups across the world [11–14]. Among them the hyperlens [12, 13] received most attention. Hyperlens is engineered such that the evanescent waves of objects are converted into propagating waves forming a magnified image of the sample on a distant screen. It is plausible to think it is a far-field imaging device. However, projection to a distant screen does not alert the fact that the hyperlens relies on the sample's near-field to achieve super-resolution. Therefore, it is still a near-field imaging device. Due to intrinsic losses in metals and nanofabrication challenges, superlenses constructed with metal elements show a limited resolution about 70 ~ 100 nm at visible frequencies and being seldom used in biomedical imaging.

Another major route to super-resolution is fluorescent microscopy, which seeks super-resolution from the labelling of samples rather than the lenses. The super-resolution fluorescence microscopy techniques can be divided into two categories: spatially patterned excitation (STED, SSIM, RESOLFTs) [15] and single-molecule localization (STORM, PALM, FPALM) [15] of fluorescence molecules. The techniques have been widely used in biological sciences, like microbiology, cell biology

and neurobiology. It has potential to revolutionize the entire fields of biology and medicine. In 2014, Nobel Prizes in Chemistry were awarded to the three leading scientists (Stefan W. Hell, Erik Betzig and W. E. Moerner) of the techniques. One practical limit is that these techniques are not applicable to imaging non-fluorescence samples, including for example the semiconductor chip devices and biological viruses and sub-cellular structures which cannot be labelled using existing fluorophores. Moreover, using of fluorescence could also alter original function and dynamic processes of biological specimens. As a result, strong needs still exist to develop a super-resolution lens which can offer high-resolution and label-free imaging of samples.

Recently, through manipulation of the diffraction of light with binary masks or gradient met surfaces, several miniaturized and planar lenses have been reported with intriguing functionalities such as subdiffraction-limit focusing in far-field, ultrahigh numerical aperture and large depth of focus, which provides a viable solution for the label-free super-resolution imaging. The most well-known example is possibly the ‘superoscillatory lens (SOL)’ by Zheludev’s group in Southampton [8]. The basic idea, which has root connection with Toraldo di Francia’s proposal in 1956 [16], is to use a carefully-designed amplitude or phase zone plate to modulate the beam to achieve a super-resolution spot in the far-field, through constructively and destructive interference without evanescent waves being involved. The key disadvantage in the technique is the appearance of giant sidelobes near to the central spot, which affected the practical adoption of the technology. The central spot resolution can, in theory, range from infinite small to  $0.38\lambda/\text{NA}$  (known as ‘super-oscillation criteria’ in [17], NA: Numerical Aperture). More recently, Qin et al. reported the development of supercritical lens (SCL), a planar diffraction component which has a focusing spot smaller than  $0.61\lambda/\text{NA}$  but slightly larger than SOL ( $0.38\lambda/\text{NA}$ ), and a needle-like focal region with its Depth of Focus (DOF)  $z = 2\lambda/\text{NA}^2$  that differs from traditional spherical lens, Fresnel Zone Plate, SOL, and others [18]. The main advantage of SCL is its 3D imaging capability (DOF:  $12\lambda$ ) in axial direction with modest super-resolution ( $0.41\lambda$ ) in lateral direction. For more information on latest development of planar diffractive lens, please refer to a latest review by Huang and co-workers [17].

### ***15.1.2 Microsphere Super-Resolution Imaging***

Wang and co-workers published their pioneering work on microsphere nanoscopy in 2011 [19]. The technique employs micro-sized spheres as super-resolution lenses (superlens) to magnify underlying objects before projecting them into the objective lens of a conventional microscope (see Fig. 15.1). The spheres generate subdiffraction illumination on the underlying object, excite and collect the near-field evanescent object information and form virtual images that are subsequently captured by the conventional lens. This is a label-free and real-time imaging technique, which can directly resolve  $\sim 50$  nm features under white light illumination. Such resolving power corresponds to a calibrated resolution of  $\sim \lambda/6 - \lambda/8$  based on convolution

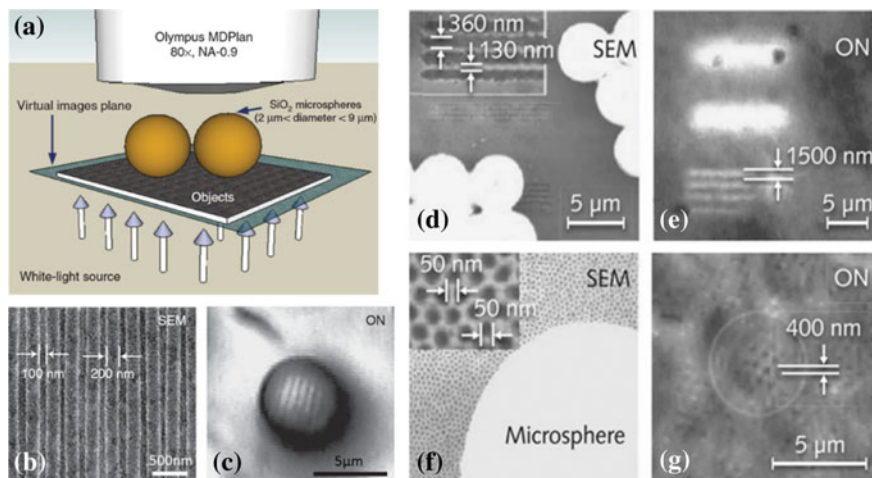


**Fig. 15.1** Microsphere nanoscope. **a** Schematic setup. **b** SEM image of a Blu-ray disc. **c** Nano-imaging by microsphere. **d** SEM image of a diffraction grating. **e** Super-resolved lines by microsphere (mag: 4.17X). **f** SEM image of 50 nm gold-coated fishnet membrane sample. **g** Microsphere imaging of 50 nm sample (mag: 8X) (reproduced from [19], with permission from Springer Nature)

calculation [20]. These intriguing features are unique and attractive for achieving low-intensity high-resolution imaging of any objects [19, 21–24] in nanometre sizes and has been successfully demonstrated for both biological (cells, viruses, etc. [23, 25]) and non-biological samples (semiconductor chips, nanoparticles etc.).

Figure 15.1a depicts the setup of ‘*microsphere nanoscope*’, which can operate in both transmission and reflection mode. SiO<sub>2</sub> microspheres are used as super lenses, with diameter 2–9 μm. The as-received SiO<sub>2</sub> microsphere suspension was diluted and applied to sample surface by drop or dip coating, and the samples are left to dry in air. A white light halogen lamp (with peak wavelength 600 nm) was used as the illumination source. The microspheres collect sample’s near-field information and magnify it before it is projected to an 80X Olympus objective lens (MDPlan, NA = 0.9) of an Olympus microscope (MX-850). The combination of microscope’s objective lens and microsphere-superlenses (MSL) forms a compound-imaging lens system.

Super-resolution images of subdiffraction objects have been captured by the microsphere nanoscope. Figure 15.1b, c shows that a Blu-ray disc (200-nm-wide lines and 100-nm-wide grooves) are clearly imaged by a 4.7 μm microsphere in reflection mode. In another example (Fig. 15.1d, e), the diffraction gratings (coated with 30-nm thick chrome-film, 360-nm-wide lines spaced 130 nm apart on fused silica substrates) were imaged in transmission mode. Only lines with microsphere particles placed on top were resolved. The lines without the particles mix together and form a bright spot that cannot be directly resolved by the optical microscope because of the diffraction limit. The virtual image plane was 2.5 μm beneath the sample surface. These images are in super-resolution, because the best diffraction-limited

resolution (for 400 nm wavelength) is estimated to be 215 nm in air [26], and 152 nm when considering the solid-immersion effect of a particle. At peak wavelength of 600 nm, the limits are 333 nm in air and 228 nm with solid-immersion effect, respectively. Here, it is noted that the focal planes for the lines with and without particles on top are different.

In another example (Fig. 15.1f, g), a fishnet 20-nm-thick gold-coated anodic aluminium oxide (AAO) membrane fabricated by two-step anodizing in oxalic acid (0.3 mol/l) under a constant voltage of 40 V is imaged with 4.7- $\mu$ m-diameter microspheres. The pores are 50 nm in diameter, spaced 50 nm apart. The microsphere nanoscope resolves these tiny pores clearly, obtaining an impressive resolution of  $\lambda/8$  in the visible. Note that the magnification in this case is around 8X—almost two times that of the earlier grating example, implying that the performance of the microsphere super lens is affected by the near-field interaction between the particle and the substrate. The sample-dependent resolution brings in complexity in clarifying the physical mechanism of the technique, nevertheless the resolution range is between 50 and 100 nm, far exceeding the classical limit of  $\sim$ 200 nm.

### 15.1.3 From Microsphere to Metamaterial Particle-Lens

The simplicity and high resolution of the microsphere imaging technique have attracted considerable interests. The technique was validated and resolution levels of  $\sim\lambda/6$ – $\lambda/8$  was repeated by other groups [21, 27]. New microspheres including Polystyrene [28, 68] and BaTiO<sub>3</sub> microspheres [29, 30, 69] (immersed in liquid or solid encapsulated; mostly used particle now) were soon introduced and became widely used in the field. Great efforts have since been devoted to the following areas: (1) scanning functionality development and complete super-resolution image construction. This is driven by the need of overcoming limitations of microsphere lenses whose imaging window is too small for many applications. (2) Mechanism exploration. Exact mechanisms have been debated in literature and considerable efforts were devoted to developing a complete theoretical model for the technique. (3) Development of next generation dielectric superlenses with improved resolution and imaging quality, new physics and fabrication method were explored. This has led to the development of all-dielectric metamaterial solid-immersion lens and nano hybrid lens. Because these lenses are metamaterial-based whose working mechanisms are completely different from previous counterparts, we would classify them as the ‘second-generation particle-lens’ and the previous microspheres the ‘first-generation particle-lens’. (4) Easier access of superlens. Efforts also went to developing simpler version of superlens which layman or general public can access. Biological superlens based on naturally occurring spider silks was developed for this purpose. (5) New applications, including for example three-dimensional interferometry, endoscopy, and Lab-on-Chip (LoC) devices were developed.

In the following, fundamentals about optical super-resolution in microspheres and metamaterial particle-lenses will be firstly presented. The key progresses will then be reviewed, followed by the outlook of the field.

## 15.2 Super-Resolution Mechanisms: Photonic Nanojet, Super-Resonance and Evanescent Jets

The super-resolution mechanisms for microsphere and metamaterial particle-lens are fundamentally different; they are thus presented separately below. Briefly speaking, for microspheres, the super-resolution is a combined result of several super-resolution effects, including photonic nanojet effect (weak super-resolution, non-resonant), super-resonance effect (strong super-resolution, resonant) and others including substrate effect and partial and inclined illumination effect, etc. For the second-generation metamaterial lens, strong super-resolution is a result of a new nanophotonic effect: nanocomposite media made of high refractive index nanoparticles can effectively convert evanescent waves into propagating waves, and vice versa.

### 15.2.1 *Microsphere and Microcylinder*

Optical resolution can be measured and calibrated by different means. In fluorescent imaging, 'point' source objects like fluorescent molecules are readily available. The system resolution can be precisely determined by measuring the point source function of the sources. In contrast, 'point' objects are rarely available in label-free imaging. To circumvent this issue, researchers often use finite size nanostructures and the resolution was measured based on observability of minimal discernible feature sizes which can be represented by the widths of the stripes, diameters of nanopores, edge-to-edge separations in dimers and clusters, etc. This has resulted in the resolution claims spanning the range from  $\lambda/6$  to  $\lambda/17$  [31]. However, such claims were questioned and the resolution should be calibrated. A calibration procedure was suggested by Allen et al. by convolution imaging object with a two-dimension PSF and compare with experimental results. The calibrated resolution for microsphere imaging is about  $\sim\lambda/6\text{--}\lambda/8$  [20, 27, 32], instead of  $\lambda/17$  as claimed by Lin [31]. It is important to note that a  $\lambda/7$  resolution optical system can resolve  $\lambda/25$  features, e.g. 15 nm gap in a bowtie sample as in [20]. In the following, we proceed to explain why a  $\lambda/6\text{--}\lambda/8$  resolution is possible in microsphere-assisted imaging.

Despite of simplicity, the underlying physical mechanism for microsphere imaging is quite complex. A complete theoretical model should consist of three elements: focusing of the incident light by microsphere, interaction of the incident light with the sample, and imaging of the scattered light in virtual mode. These processes are

interlinked and coupled, and complete model is still missing to date. Most existing theoretical studies are based on one or two processes above, leading to incomplete conclusions and debates [19, 20, 23, 31, 33–42]. At the beginning, Photon nanojet (PNJ) was considered as the main super-resolution mechanism [19]. However, it was soon realized that the resolution of PNJ (typically between  $\lambda/2$  and  $\lambda/3$  for  $n = 1.5$  microsphere) is insufficient to explain the experimentally observed resolution of  $\sim\lambda/7$ . Consequently, other mechanisms were discussed and investigated. Duan and co-workers reported that classical Whispery Gallery Modes (WGM) in microsphere can help boost imaging resolution up to  $\sim\lambda/4$ . Besides PNJ and classical WGM, a new physical mechanism, *super-resonance effect (SRE)*, was recently discovered by Wang et al. and Hoang et al. [43, 44]. The SRE is caused by internal particle partial wave modes (not by scattering waves as in PNJ) and surface wave modes; it can generate super-resolution focusing with lateral resolution  $\sim\lambda/5$ – $\lambda/6$ . This new effect helped bridge the resolution gap between PNJ/WGM theories ( $\sim\lambda/4$ ) and experiments ( $\sim\lambda/7$ ). On the other hand, experimental resolution can be enhanced by substrate effect [33, 45], partial and inclined illumination [27], microsphere partial immersion [46] and coherent illumination effect [20] as demonstrated by various authors. In the following, we briefly review the key properties of PNJ, SRE, broadband lighting source effect, substrate and partial and inclined illumination effect on super-resolution imaging. For more information on the basics of related theory (e.g. Mie theory) and PNJ (e.g. how PNJ evolves with respect to size and refractive index, medium effect, PNJ by other shaped particles, etc.), please refer to previous reviews written by us [33, 36].

### 15.2.1.1 Photonic Nanojet

PNJ is a narrow, high-intensity electromagnetic beam that propagates into the background medium from the shadow-side surface of a plane-wave illuminated lossless dielectric microcylinder or microsphere of diameter greater than the illuminating wavelength,  $\lambda$  [19]. The PNJ is attained via light scattering by micro-sized particles (spheres, cylinders, cubes, prisms and others, typical diameter between 1 and 50  $\mu\text{m}$ ) [47, 48, 49–57]. This is an important effect which is now widely used for subwavelength imaging, sensing, patterning, nanoparticle trapping and manipulation, and more. The earliest study relating to PNJ can be dated back to year 2000 by one of the present author: Luk'yanchuk and co-worker first demonstrated that enhanced optical near-fields of a 500-nm silica sphere can be used as super-resolution lens (superlens) for subwavelength structuring of silicon surface [57]. Since then, the technique grows rapidly [58]. Without knowing the initial work by Luk'yanchuk et al., in 2004 Chen et al. coined the terminology PNJ—'*photonic nanojet*' [47], which is now widely used [47, 59–70].

Figure 15.2 shows an example of PNJ subwavelength focusing, where a 1  $\mu\text{m}$ -diameter Polystyrene particle ( $n = 1.6$ ) is illuminated in air by a plane wave laser beam from the top ( $\lambda = 248$  nm); these parameters equivalents to size parameter  $q = 2\pi a/\lambda = 12.67$ , where  $a$  is particle radius and  $\lambda$  the incident wavelength.

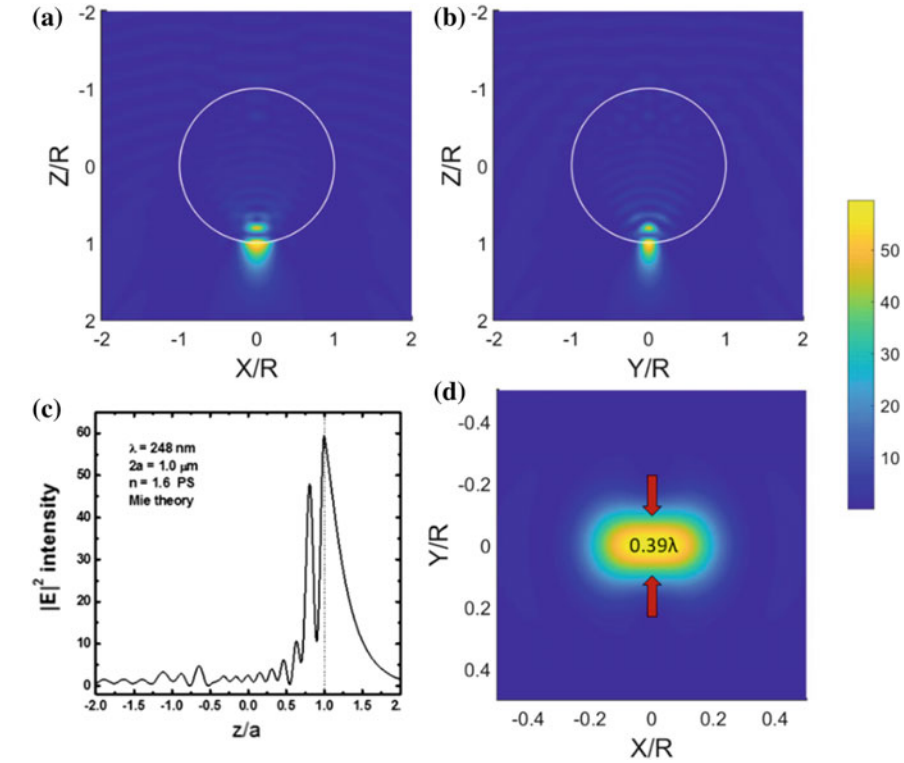


**Fig. 15.2** Demonstration of near-field PNJ effect. Spatial electric field intensity distribution,  $I = |E|^2$ , inside and outside the  $1.0 \mu\text{m}$  PS particle, illuminated by a laser pulse at  $\lambda = 248 \text{ nm}$  ( $q = 12.67$ ), and **a** polarization parallel and **b** perpendicular to the image plane. The maximum intensity enhancement in calculations is about 60 for both regions. **c** Intensity along  $z$ -axis.  $z = 1.0$  is the position under the particle. **d** Super-resolution spot in at  $z = a$ , the tangent plane right under the particle

The results show the electric field intensity is enhanced in particle’s near-field zone, with peak intensity located at  $z = a$  with an enhancement factor 59.6. This value drops exponentially to 1.57 at position  $z = 2a$ , confirming a near-field nature of the focusing. Within the  $z = a$  focusing plane, the laser focus spot manifests an elongated elliptical shape, with super-resolution ( $0.39\lambda$ ) being observed in the cross-polarization direction. The elliptical focusing is caused by the radial component of the electric field,  $E_r$ , which scales with  $r$  as  $E_r \propto 1/r^2$ , in the near-field. As distance increase  $r \geq \lambda$ , the  $E_r$  field quickly decays to zero [71]. In other words, the optical near-field contains both transverse and longitudinal components but in far-field the wave is purely transverse.

The key properties of PNJ can be summarized as [48, 65]:

- Resolution: in most cases the lateral resolution of the jet is slightly better than diffraction limit in air ( $0.5\lambda$ ). However, in some cases the resolution could reach the solid immersion limit  $\lambda/2n$  [72], where  $n$  is the refractive index of particle.
- PNJ usually appears for diameter  $d$  of the dielectric microsphere or microcylinder from  $2\lambda$  to about  $40\lambda$  with the refractive index contrast relative to the background medium less than 2:1.
- PNJ could maintain a subwavelength focusing jet along the path that can extend more than  $2\lambda$  beyond the dielectric cylinder or sphere. This has led to a widespread but misleading claim that PNJ is a non-evanescent propagating beam within which evanescent wave doesn't contribute [73]. In fact, evanescent waves could play strong role in near-field PNJ as demonstrated in Fig. 15.2.

Besides, PNJ engineering has also been extended to other shapes and configurations of dielectric particles (spheroids [74, 75], disks [76], cones [77], cubes [78], multilayer [79] and others [80–82]), incident beam modulation [83], phase masks [84–86], photonic hook [87, 88], reflective PNJ [89–91] and applications in second harmonic generation. For more information on these please refer to our previous review article [36].

### 15.2.1.2 Super-Resonance Effect (SRE)

Besides PNJ, strong resonant modes can be excited in micro spherical cavity. For example, at  $n = 1.5$ ,  $q = 26.94163$ , a super-resonance mode (i.e. a new type WGM mode) can be excited. We define 'super-resonance' as a giant field enhancement mode caused by microsphere's internal partial waves. In contrast, PNJ are induced by scattering waves outside the particle. Unlike WGM which can be excited in both microsphere and microcylinder, SRE only exist in microspheres. Figure 15.3 demonstrates a typical SRE mode field distribution and its giant field enhancement amplitude.

In SRE mode, two near-symmetrical hotspots were generated near the top and bottom apex points (points T, B) of the particle (see Fig. 15.3a). The enhancement factor can be extremely large at these points, reaching the order of  $10^4$  (peak value: 43,774), two orders higher than those in PNJ (typically on order of several tens or hundreds, Fig. 15.3c vs. Fig. 15.1). Importantly, the SRE hotspot spot has a super resolution of  $0.22\lambda$  which exceeds resolution limit of PNJ and WGM. The SRE is caused by the excitation of special order of internal partial waves in Mie theory, e.g.  $L = 43$  for  $q = 26.94163$ . It is very sensitive to the size parameter. For example, when  $q$  changes by  $1e-4$  from 26.94163 to 26.94153, the peak drops by more than 20,000 (see Fig. 15.3c). The top four strongest SRE modes for  $n = 1.5$  particle are seen at  $q = 38.6203$  (*with  $L = 51$  electric partial wave mode excited,  $|E|^2 = 939286$ ,  $|H|^2 = 1793371$* ), 66.5555 ( *$L = 80$  electric mode,  $|E|^2 = 773375$ ,  $|H|^2 = 351073$* ), 32.5623 ( *$L = 43$  magnetic mode,  $|E|^2 = 621863$ ,  $|H|^2 = 55113$* ), and 31.8619 ( *$L = 42$  magnetic mode,  $|E|^2 = 263386$ ,  $|H|^2 = 24880$* ), respectively. Details on SRE are outside the scope of this review and will be presented in a separate publication

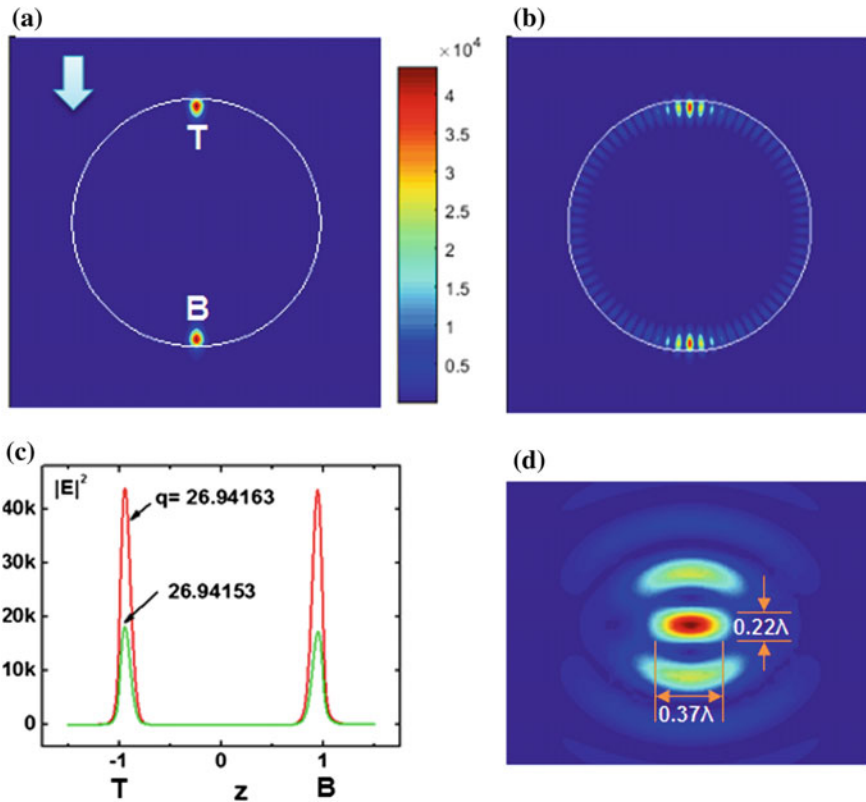


**Fig. 15.3** Demonstration of SRE. **a** Giant electric field intensity  $|E|^2$  distribution in XZ plane and **b** YZ plane, for a linearly incident beam polarized along  $x$ -direction. **c** Intensity across two hotspots (Points T, B), measured from top T to bottom B. **d** The FWHM spot size is  $0.22\lambda$  ( $\sim\lambda/5$ ) at position B

elsewhere. It is noted that Haong et al. also reported super-resonance effect using same experimental parameters as in Fig. 15.1 ( $a = 2.37 \mu\text{m}$ ,  $n = 1.46$ ), they found that a  $\sim 0.24\lambda$  resolution can be achieved at wavelength 402.292 nm, in excess of solid immersion resolution limit of  $\lambda/(2*1.46) = 0.34\lambda$  [43]. We believe SRE is vital to microsphere super-resolution imaging.

### 15.2.1.3 Broadband Illumination Effect

In microsphere imaging, a white lighting source (e.g. halogen lamp) is often used. theoretical analysis of resolution is often carried out by using illumination's peak wavelength (e.g. 550 or 600 nm). This neglects the broadband nature of illumination source. In fact, the application of white light will lead to the simultaneous excitation of various focusing field distribution across a wide size parameter range. Considering a

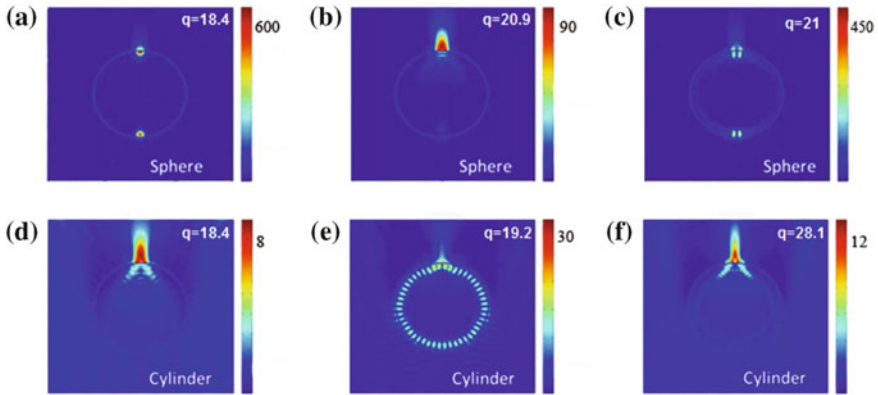


**Fig. 15.4** Typical  $|E|^2$  field distributions of **a–c** spheres and cylinders **d–f** with refractive index  $n = 1.5$  at varying size parameter  $q$  with calculation step size  $\Delta q = 0.1$ . **a** Super-resonance mode of sphere, **b** usual jet mode of sphere, **c** whispery gallery mode of sphere, **d** usual jet mode of cylinder, **e** strong whispery gallery mode of cylinder, **f** weakly excited whispery gallery mode of cylinder. See supplementary video for details

3- $\mu\text{m}$ -diameter glass sphere, when illuminated by a white light with  $400 \leq \lambda \leq 700$ , the size parameter  $q$  will fall within  $13.46 \leq q \leq 23.56$ . The calculated XZ-plane  $|E|^2$  field distribution for  $q$  with step size accuracy  $\Delta q = 0.1$  for both spheres and cylinder, as shown in Fig. 15.4. For spheres, it shows the co-existence of at least three different field modes or patterns, i.e. SRM at  $q = 18.4$  (Fig. 15.4a), a typical PNJ at  $q = 20.9$  (Fig. 15.4b) and WGM at  $q = 21$  (Fig. 15.4c) when excited by white light. For cylinder, the results are slightly different, no the super-resonance modes were observed but we see evidence of more pronounced WGM mode at  $q = 19.2$  (Fig. 15.4e). Please check online movies [92, 93] for complete details on light focusing by an  $n = 1.5$  particle and cylinder when size parameter increases varies from 0 to 600. The flicking phenomena in the movie indicate the modes swapping between PNJ, WGM and SRM. In a complete theoretical model, one should consider spectrum profile of lighting source and integrate all modes contribution.

#### 15.2.1.4 Substrate Effect

Substrate effect is clearly observed in experiments, i.e. imaging magnification and resolution vary for different samples. This is, however, less studied and understood. Sundaram and co-workers performed imaging analysis using full-wave FEM simulation of the light propagation from the target through a microsphere, an objective lens and then to the imaging plane, as shown in Fig. 15.5 [45]. The results show that longitudinally polarized dipole can achieve better resolution than transverse dipole (Fig. 15.5b, c). More importantly, it was shown that substrate plays an important role in imaging magnification and resolution. For example, as shown in Fig. 15.5d,

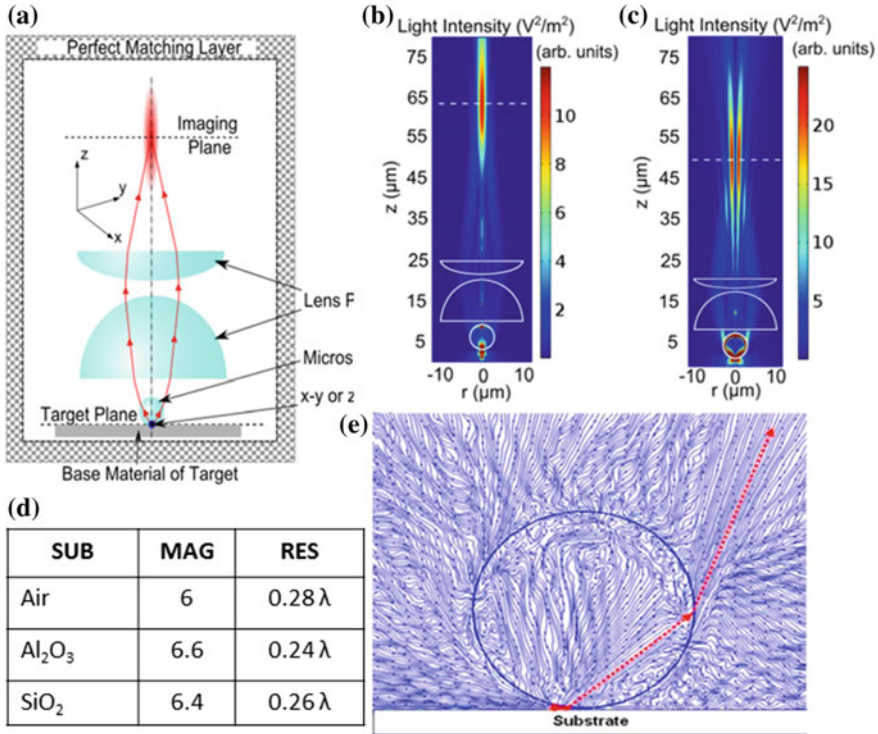


**Fig. 15.5** **a** Schematic of the simulation setup consisting of the substrate target, microsphere, and lens pair. **b** Light intensity ( $|E|^2$ ) distribution induced by a transverse dipole ( $x$ - $y$  dipole), and **c** a longitudinal dipole ( $z$ -dipole), in air with a microsphere lens of diameter  $6 \mu m$  and refractive index  $n = 1.4$ . The dashed lines indicate the imaging plane (reproduced from [45], with permission from AIP Publishing). **d** Table of magnification and resolution for different substrates. SUB: Substrate, MAG: magnification, RES: resolution. **e** Numerically simulated point dipole parallel-to-surface evanescent wavevector decoupling process, from near-field to far-field

imaging resolution for air (without substrate), aluminium oxide ( $Al_2O_3$ ) and fused silica ( $SiO_2$ ) are  $0.28\lambda$ ,  $0.24\lambda$  and  $0.26\lambda$ , and magnification 6, 6.6 and 6.4, respectively. Another numerical simulation performed by us, as shown in Fig. 15.5e, reveals complex nature of high spatial frequency evanescent wave decoupling process from sample surface [33]. A parallel-to-surface wave vector, marked by the red solid line, was scattered by the particle, converting into propagating beam transferring to the far-field (red dashed line). Very recently, Brettin and Astratov et al. demonstrated the resolution can be enhanced by coupling of fluorescent objects to plasmonic metasurfaces (engineered substrate) [94].

## 15.2.2 Dielectric Nanoparticle-Based Metamaterial Superlens

As many studies reveal that most metal-based metamaterials suffer from intrinsic loss at high optical frequencies, which cause them to be unfavorable in near-infrared and visible region [95–98]. Moreover, metal-based plasmonic components have low transmission efficiency at optical frequencies, thus making them less useful for optical waveguiding over long distances or through bulk three-dimensional (3D) structures [99, 100]. Unlike the metal-based metamaterials, dielectric metamaterials use the near-field coupling between transparent (low absorption), high-refractive index dielectric building blocks, which perform similar optical phenomena to metallic nano-resonators, but with much lower energy dissipation [101–104]. Meanwhile, high transmission and diffraction efficiencies of dielectric components make it possible to move optical metamaterials from current 2D metasurfaces or layered metamaterials to truly 3D metamaterials [99]. New types of particle-lens—metamaterial solid immersion lens (mSIL)—has recently been proposed and developed by us [105]. This is based on metamaterial concept and a new super-resolution mechanism. The mSIL is a 3D metamaterial formed by densely stacking of high-index  $\text{TiO}_2$  nanoparticles (Fig. 15.6a). Here, the resolution is determined by the particle size instead of wavelength. This new nanophotonic effect is shown in Fig. 15.6 by a full-wave numerical simulation.

The artificial media is a closely stacked 15-nm anatase  $\text{TiO}_2$  nanoparticle composite, with tiny air gaps between the particles, which forms a dense scattering media.

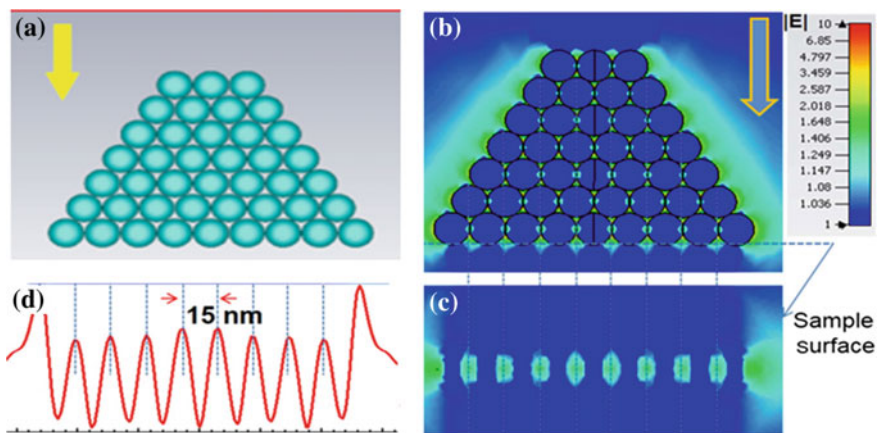


**Fig. 15.6** Propagating wave scattering by densely packed all-dielectric nanoparticles medium. **a** schematic drawing of a nanoparticle stacked media. **b** Plane wave ( $\lambda = 550$  nm) passing through the stacked  $\text{TiO}_2$  nanoparticles. Electric field hotspots are generated in the gaps between contacting particles, which guides light to the underlying sample. **c** Large-area nanoscale evanescent wave illumination can be focused onto the sample surface because of the excitation of nanogap mode. **d** The size of the illumination spots is equal to the particle size of 15 nm [105]

Figure 15.6 shows the calculation results of electric field distribution in the artificial media illustrated by a plane wave ( $\lambda = 550$  nm). Clear field confinements are observed within particles gaps, confirming the ability of the composite media to modulate and confine incident radiation at the nanoscale, as shown in Fig. 15.6b. Since  $\text{TiO}_2$  is loss-free at visible wavelengths, this near-field coupling effect can effectively propagate through the media over long distances, forming an arrayed “patterned illumination” landscape on the substrate surface, as shown in Fig. 15.6c. Note these illumination spots are evanescent, containing high-spatial frequency components. Their sizes are mainly determined by the particle size, having a full width at half maximum (FWHM) resolution of  $\sim 8$  nm, as shown in Fig. 15.6d. Therefore, it is expected that nanoparticle composite media will have the intriguing ability to transform incident illumination into a large array of nanoscale evanescent wave illumination focused on the object surface within the nearfield region. This novel nanophotonic effect has similarity with that of near-field scanning optical microscopy (NSOM), in which resolution is not limited by the incident wavelength but by the aperture size [106, 107]. However, NSOM suffers from several limitations, such as low optical throughput, long scanning time, and insufficient contact between aperture probe and object surface. In contrast, an array of  $\text{TiO}_2$  nanoparticles can act as parallel array of near-field probes to simultaneously (thousands) illuminate the sample surface, and the strength of the focused evanescent wave illumination can be maximized owing to the near perfect solid immersion of imaging object by  $\text{TiO}_2$  nanoparticles. Moreover, theoretically, the size of the evanescent wave illumination spots can be further reduced by using smaller anatase  $\text{TiO}_2$  nanoparticles or higher refractive index rutile ( $n = 2.70$ )  $\text{TiO}_2$  nanoparticles, and this near-field illumination may also be useful for other applications such as nanoscale light harvesting and sensing.

According to the reciprocal principle [108], the conversion process in nanoparticle composite media (Fig. 15.7) from propagating waves to evanescent waves can be optically reversed. In other words, an array of evanescent wave source located on the bottom surface of the nanoparticles composite media will be converted back into propagating waves by the media. This is confirmed by two-point source calculation. For comparison purposes, both conventional media (homogeneous anatase  $\text{TiO}_2$  material) and our metamaterial media (stacked 15 nm anatase  $\text{TiO}_2$  nanoparticle) were simulated. Using slab geometry, we demonstrate in Fig. 15.7 that evanescent waves behave differently when interacting with conventional media, Fig. 15.7a, and composite metamaterial media, Fig. 15.7b, d. As shown in Fig. 15.7c, in homogeneous media the evanescent waves decay exponentially as expected when the distance to sources increases. The loss of evanescent waves causes reduced resolution. Figure 15.7e demonstrates the inability of conventional media to resolve two-point sources (separated by 45 nm) in far-field zone (e.g.  $z = 650$  nm  $>$   $\lambda = 550$  nm). The two points are only resolvable in near-fields when distance to source is extremely small, typically smaller than 50 nm in present case. In nanoparticle composite media, however, the evanescent waves experience strong interaction with  $\text{TiO}_2$  nanoparticles, which causes effective conversion of evanescent waves into propagation waves. The converted waves are mainly guided through the gaps between particles. As shown in Fig. 15.7d, electric field received at far-field region ( $z > \lambda$ ) is about  $|E| \sim 0.45$  (since

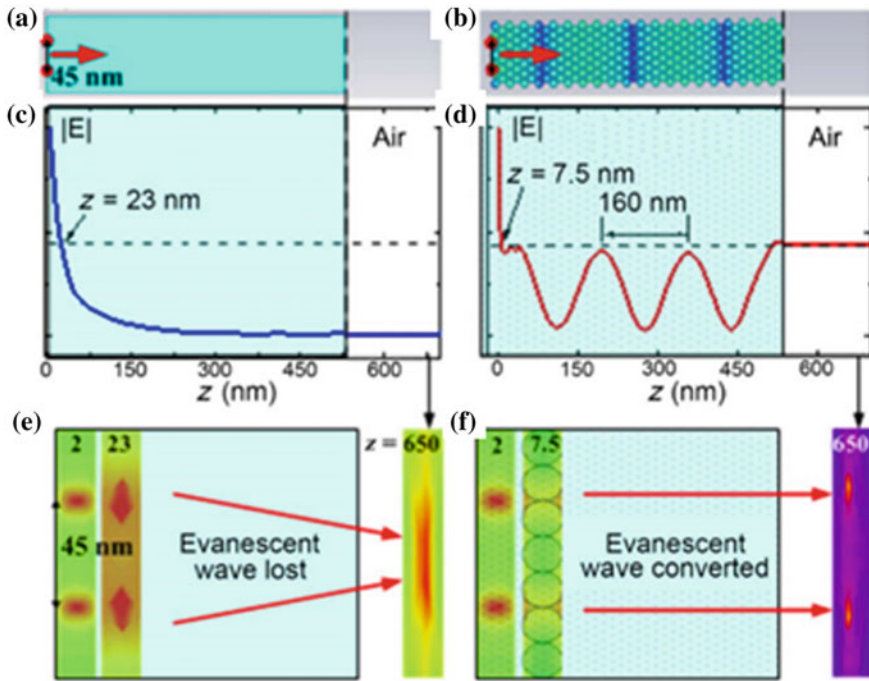


**Fig. 15.7** Comparisons between homogeneous and nanoparticle composite media. **a** Mean electric field amplitude as a function of distance from point sources (*y*-polarised, incoherent). The amplitude decays exponentially. Most evanescent wave energy was lost within 50 nm distance. **b** In nanoparticle composite material, evanescent waves interact with TiO<sub>2</sub> nanoparticles and turn into propagation waves which travel outward to far-field. A periodicity of 160 nm was observed. **c–f** Two-point sources (45 nm separation) imaged with **c** homogeneous and **d** composite material, at positions *z* = 2 nm (near source), *z* = 23 nm (near-field, inside slab) and *z* = 650 nm (far-field, outside slab). In far-field, **e** the homogenous media fails to resolve the two points while **f** the composite media can successfully resolve them [105]

source amplitude  $|E| = 1$ , this corresponds to  $|E|^2 = 20\%$  of total evanescent energy), which is comparable to the field strength at  $z = 7.5$  nm (near-field). This means near-field energies are indeed converted and transported to the far-field. It is also interesting to notice the periodic modulation effects of E-field inside the composite media, which is a signature of this design. Since there is no material loss in composite media, the periodic propagation experiences an un-damped modulation, showing an effective period of 160 nm. These waves propagate outwards from near-fields into far-fields and contribute to super-resolution. In Fig. 15.7f, it is demonstrated that at far-field (e.g.  $z = 650$  nm), the two-point sources are reconstructed and clearly discernible. Comparing to metal-based superlens and hyperlenses whose resolution is limited by material losses in metal [12, 109, 110, 111], the proposed all-dielectric nanoparticles media is free from loss problems; its resolution is mainly affected by the excitation of evanescent waves and the conversion efficiency of evanescent waves

into propagating waves, as well as the effective capture of the subwavelength information in the far field. This makes it possible to design a perfect imaging device using dielectric nanoparticles as building block. In section below, we will show our experimental demonstration of a fabricated  $\text{TiO}_2$  nanoparticle-based metamaterial solid immersion lens (mSIL) and its super-resolution imaging performance (45 nm).

### 15.3 Microsphere Nanoscopy: Key Progresses

In this section, we review key progress in the field, including microsphere-assisted confocal microscopy, integrated superlensing microscope objective, scanning imaging, holography and endoscopy

#### 15.3.1 Confocal Imaging and Resolution Quantification

In widefield, the imaging contrasts are often low and unsatisfactory due to the presence of out-of-focus light in the final image. To enhance the contrast, efforts were required to optimize the microscope lighting and image capturing settings. In contrast, confocal microscopy generally has much better optical contrast and improved resolution; this is achieved by placing a tiny pinhole before the detector to eliminate the out-of-focus light in the final image. Several groups evaluated the imaging performance of microsphere-assisted confocal imaging by integrating microsphere superlens with a 405 nm laser scanning confocal microscope (e.g. Olympus OLS4000). Wang et al. imaged 140 nm nanolines separated 40 nm away using PS particle in air, and emphasised the importance of using single isolated particle in confocal imaging where artefacts could arise when two neighbouring microspheres interferences with each other [33]. Yan et al. imaged 136 nm gold nanodots separated 25 nm away, using PS and fused silica particle in air as well [31]. Using BTG particle, Allen and co-workers imaged 120 nm gold nanocylinders separated 60 nm away (Fig. 15.8a) and a 185 nm nanobowtie separated 15 nm away (Fig. 15.8e) [20]. They also argued that defining the resolution based on observation of minimal discernible features can lead to misleading results if, for example, interpreting the 15 nm gap in nanobowtie (Fig. 15.8e) would imply the resolution over  $\lambda/27$ . They suggested an approach to compute the resolution based on the analogy with the classical theory where the image,  $I(x, y)$ , is considered as a convolution of a point spread function (PSF) and the object's intensity distribution function,  $O(u, v)$ . This can be expressed in the standard integral form [20]:

$$I(x, y) = \int_{-\infty}^{\infty} \int_{-\infty}^{\infty} O(u, v) \text{PSF}\left(\frac{x}{M} - u, \frac{y}{M} - v\right) du dv, \quad (15.1)$$

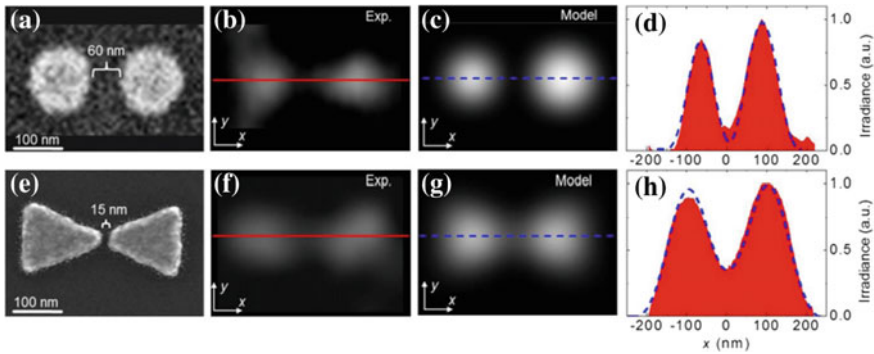


**Fig. 15.8** SEM image of the Au dimer and bowtie, respectively. The dimer is formed by 120 nm nanocylinders with 60 nm separation. **b, f** confocal Images of dimer and bowtie in **a, e** obtained through the 5 and 53  $\mu\text{m}$  BTG microsphere, respectively. **c, g** Calculated images by convolution method at PSF resolution of  $\lambda/7$  and  $\lambda/5.5$ , respectively. **d, h** Comparison of the measured (red background) and calculated (dashed blue curves) irradiance profiles through the cross-section of the Au dimers ( $x$ -axis) (reproduced from [21], with permission from John Wiley and Sons)

in which the integration is performed in the object plane where the coordinates  $(x_o, y_o)$  are linearly related to the image plane via the magnification  $M$  as:  $(x_o, y_o) = (x_i/M, y_i/M)$ . A Gaussian function for PSF  $(x_o, y_o)$  with the full width at half maximum (FWHM) being a fitting parameter. Based on the Houston criterion, fitted values of FWHM in the object plane were considered as resolution of the system. Based on this, the image reconstruction with the  $\lambda/5.5$  PSF resolution allows obtaining a high-quality fit to the experimental results, as illustrated in Fig. 15.8g, h. This means that the resolution for 15 nm gap sample in Fig. 15.8e is  $\lambda/5.5$ , instead of  $\lambda/27$ . Similarly, it was shown the 60 nm gap sample in Fig. 15.8a is  $\lambda/7$  (Fig. 15.8c, d).

### 15.3.2 Scanning Microsphere Super-Resolution Imaging

Microsphere has a viewing window around a quartz size of its diameter. Considering particles with diameter 1–100  $\mu\text{m}$ , the viewing window is less than 25  $\mu\text{m}$  which is too small for many practical applications. Controlling the position of the microspheres is required for generating a complete image of sample. Scanning functionalities are, hence, highly sought by the researchers working the field. There are several proposals existing in the literature, including for example the microsphere-embedded coverslip, superlensing microscope objective, swimming lens and AFM-style scanning microsphere-lens.

### 15.3.2.1 Microsphere-Embedded Coverslip

One of the earliest but important developments is the use of liquid-immersed BTG microspheres for super-resolution imaging (compatible with bio-samples). This configuration is still widely used today, with resolution between  $\lambda/4$  and  $\lambda/7$  depending on the particle size, as demonstrated experimentally [29, 69]. The liquid-immersion design was soon extended to solid-immersion design in a coverslip form [20, 112, 113], as shown in Fig. 15.9a. The fabrication steps are illustrated in Fig. 15.9f: first, BTG spheres were spread on a flat surface. Second, a liquid PDMS (or other resins) was casted and cured, producing a solid thin film coverslip whose thickness can be varied from hundred micrometres to millimetres. Finally, the coverslip film was separated and used for imaging experiments. The coverslip can be attached to a moving stage (Fig. 15.9a) for performing super-resolution imaging at specific site. The motion of the coverslip can be provided by a metallic probe inserted in PDMS and connected to a micromanipulator (Fig. 15.9b). Figure 15.9c–e shows an example of translation of coverslip assisted by IPA lubricant for imaging. The imaging quality and stability are both improved by using coverslip design.

### 15.3.2.2 Superlensing Microscope Objective

The coverslip lens discussed above can be manually manipulated in a way like classical coverslip, offering the freedom to position particle-lens at desired location. Scanning of microsphere superlens, however, requires synchronisation with microscope objective for full super-resolution image construction. We proposed an improved

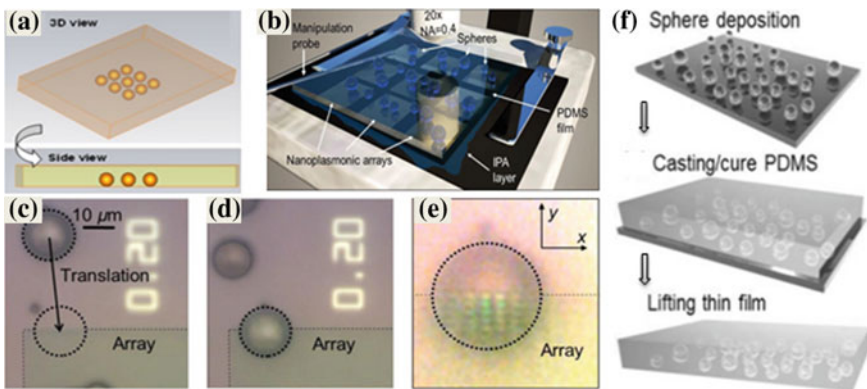


**Fig. 15.9** **a** Microsphere-embedded coverslip design **b** setup and translation of the coverslip lubricated with IPA. **c** The embedded BTG sphere is  $\sim 40 \mu\text{m}$  away from the edge of an Au nanoplasmonic Nanoplasmonics array. **d** The same sphere is at the border of array. **e** By changing the depth of focus, the dimers are seen near the array's edge. **f** Coverslip fabrication steps, sphere deposition on a flat surface, PDMS casting and curing, lifting thin film to obtain the coverslip (reproduced from [21], with permission from John Wiley and Sons)

design which solves the synchronisation problem of coverslip superlens and objective lens. The idea is to use a custom-made lens adaptor to integrate these two lenses to form a superlensing microscope objective lens.

The key concept and design of superlensing microscope objective is illustrated in Fig. 15.10b, c. A conventional microscope objective (OB) lens with magnification factor between  $40\times$  and  $100\times$ , NA between 0.7 and 0.95 was selected. A lens adaptor was designed in CAD software (e.g. Solidworks) and then printed with a 3D plastic printer. The adaptor has a tube size fit to the objective lens tube, with reasonable friction allowing up-down adjustment. A coverslip superlens (Fig. 15.10a) was bounded to the bottom end of the adaptor using high-adhesive glue. This results in an integrated objective lens consisting of conventional OB and a Coverslip Microsphere Superlens (CMS). The imaging resolution will be determined by the coverslip superlens while the conventional objective lens provides necessary condition for illumination. The obtained superlensing lens can be easily fitted to any existing conventional microscopes; The scanning was performed using a high-resolution nano-stage. In experiments, the superlensing objective lens was kept static and the underlying

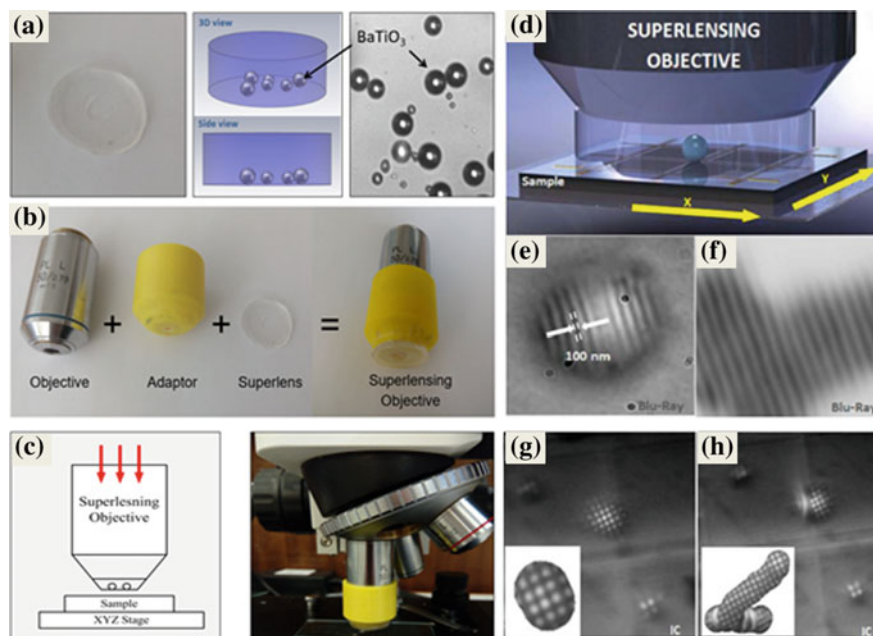


**Fig. 15.10** Superlensing objective lens. **a** The BTG superlens was fabricated by encapsulating a monolayer of BTG microsphere inside a PDMS material. **b** The super objective was made by integrating a conventional microscope objective lens (e.g.  $50\times$ , NA: 0.70, or  $100\times$ , NA: 0.95) with a BTG microsphere superlens using a 3D printed adaptor. **c** Experimental configuration for super-resolution imaging using developed objective which was fitted onto a standard white light optical microscope. **d** Scanning illustration. **e** Single particle imaging. Of Blu-ray. **f** Scanning generated full Blu-ray image. **g** Nanochip imaging. **h** Scanning nanochip imaging [42]

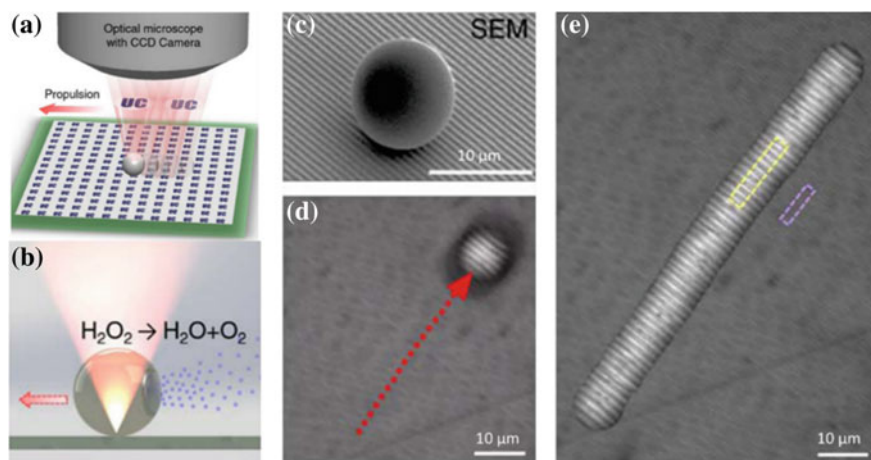


**Fig. 15.11** Swimming lens design. **a** Schematic illustration. **b** Schematic illustration of the chemically powered propulsion and light illumination through the microsphere. **c** SEM of  $10 \mu m$  PS microsphere on a  $320 \text{ nm}$  grating structure. **d** Microsphere imaging and arrow shows the scanning motion. **e** Reconstructed image by stitching from individual video frame (reproduced from [114], with permission from American Chemical Society)

nano-stage moves and scans the samples across the objective lens. The imaging process was video recorded using a high-resolution camera and images were constructed from the video. Figure 15.11e–h demonstrates the scanning super-resolution imaging by the integrated objective lens, which makes large-area super-resolution imaging possible.

### 15.3.2.3 Swimming Lens

Li et al. designed a “swimming lens” technique in which the microsphere lens was propelled and scanned across the sample surface by chemical reaction force in a liquid [114]. This approach enables large-area, parallel and non-destructive scanning with sub-diffraction resolution. Figure 15.11 illustrates the schematic diagram and scanning imaging process.

### 15.3.2.4 AFM-Style Scanning Microsphere Lens

Most recently, Wang et al. introduced a non-invasive, environmentally compatible and high-throughput imaging technique called scanning superlens microscopy (SSUM), which applying the AFM principle by attaching microsphere onto AFM tip for scanning imaging (Fig. 15.12) [75]. This system has high precision in maintaining distance between microsphere and the objects. It has capabilities of operating in contact scanning mode and constant-height scanning mode, therefore variety of sam-

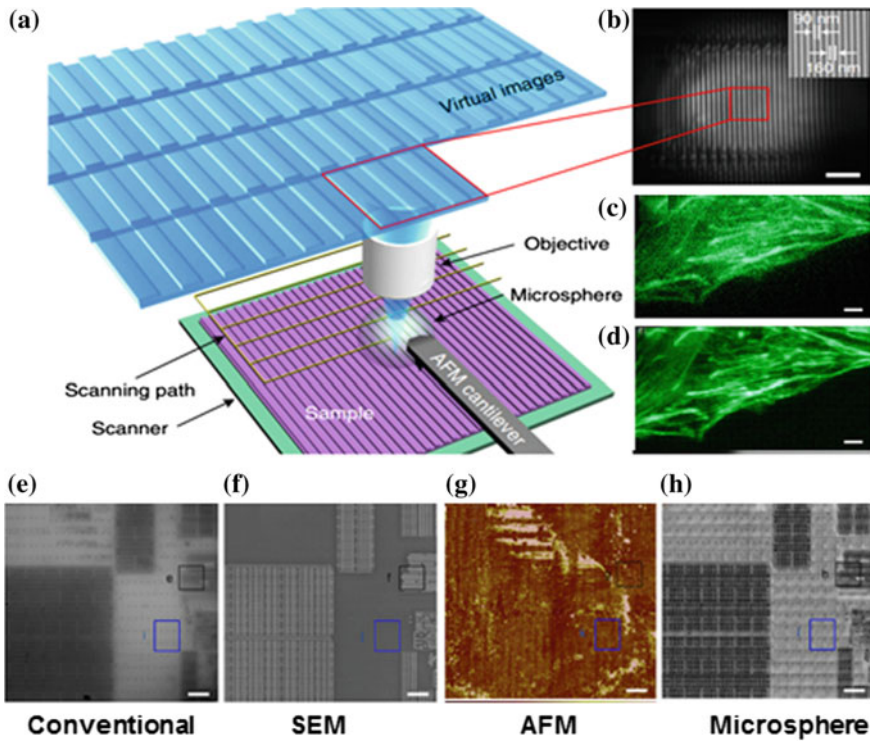


**Fig. 15.12** AFM-style scanning microsphere imaging system. **a** Schematic of the construction of a microsphere-based Microsphere-based scanning superlens microscopy (SSUM) that integrates a microsphere superlens into an AFM scanning system by attaching the microsphere to an AFM cantilever. The objective picks up the virtual images containing sub-diffraction-limited object information and simultaneously focuses and collects the laser beam used in the cantilever deflection detection system. **b** An original virtual image observed using the microsphere superlens. The inset shows an SEM image. **c, d** Backside and frontside images, respectively, of the AFM cantilever with an attached microsphere superlens. Scale bars,  $2\ \mu\text{m}$  (**b**);  $50\ \mu\text{m}$  (**c, d**) [27]

ples such as stiff sample and sensitive specimens can be efficiently imaged. Besides, Krivitsky et al. attached a fine glass micropipette to the microsphere lens to scan the particle [73]. The method allows precisely controlling the microsphere position in three dimensions as well.

### 15.3.3 Endoscopy Application

In vitro nano-scale imaging by super-resolution fluorescence microscopy techniques, such as STED, STORM and PALM has achieved significant development in recent years. However, in vivo endoscopy observation of deep and dense tissues inside

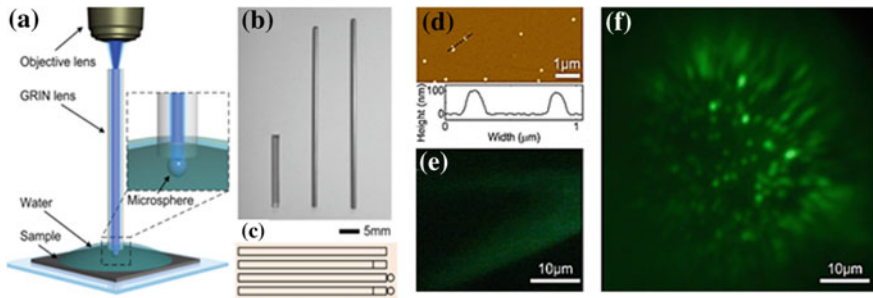


**Fig. 15.13** Microsphere Super-resolution endoscopy. **a** Schematic of microsphere super-resolution endoscopy. **b** Three GRIN lens based endoscope probes, a 1.8 mm diameter singlet ( $NA = 0.46$ ), a 1 mm diameter singlet ( $NA = 0.11$ ) and a 1 mm diameter compound doublet (objective lens  $NA = 0.42$ , relay lens  $NA = 0.11$ ). The second and third probes are covered by protective metal sleeves. **c** Schematic of singlet, doublet and microsphere-functionalized singlet or doublet super-resolution endoscopes. **d** AFM image of 100 nm fluorescent nanoparticle. **e** Fluorescent image obtained by using a conventional doublet endoscopy probe. **f** Super-resolution image obtained using microsphere ( $80 \mu\text{m}$  BTG particle) super endoscope

body has limited by its optical resolution at  $\sim 1 \mu\text{m}$ . Wang and co-workers developed a new endoscopy method by functionalizing graded-index (GRIN) lens with microspheres ( $30\text{--}100 \mu\text{m}$  BTG particle) for real-time white-light or fluorescent super-resolution imaging [38]. The capability of resolving objects with feature size of  $\sim \lambda/5$ , which breaks the diffraction barrier of traditional GRIN lens-based endoscopes by a factor of two, has been demonstrated by using this super-resolution endoscopy method. Figure 15.13 shows the experimental step and imaging test results. The conventional endoscope cannot resolve 100-nm sized fluorescent nanoparticles while new endoscope containing microspheres can clearly resolve them in super-resolution. The super-resolution strength could be further improved by new metamaterial particle-lenses with better resolution. Further development of such a super-resolution endoscopy technique may provide unprecedented new opportunities for in vivo diagnostics and therapy as well as other life sciences studies.

### 15.3.4 3D Interferometry and Optical Profiling

3D super-resolution profiling and imaging was recently demonstrated by integrating a microsphere with a white-light Interferometry system (Linnik [39] or Mirau system [115]). This near-field assisted white-light interferometry (NFWLI) method takes advantage of topography acquisition using white-light interferometry and lateral super-resolution enhancement by microsphere. The ability to discern structures in central processing units (CPUs) with minimum feature sizes of approximately 50 nm in the lateral dimensions and approximately 10 nm in the axial dimension within 25 s

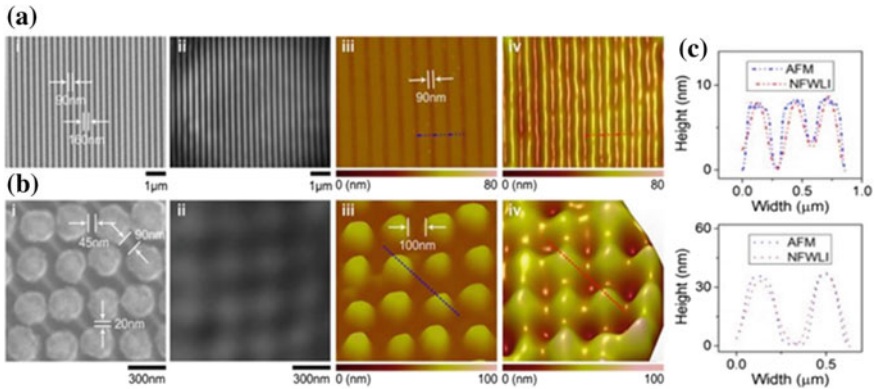


**Fig. 15.14** Near-field assisted white-light interferometry (NFWLI). **a** 90 nm features, **b** 20–90 nm features in a CPU chip. (i) SEM images. (ii) Virtual images generated by 69 μm and 19 μm BTG microspheres in (a) and (b), respectively. (iii) AFM images. (iv) NFWLI images. **c** Comparisons of the cross-sections marked by lines in (a (iii, iv)–b (iii, iv)), respectively [39]

(40 times faster than atomic force microscopes) was demonstrated by Wang and co-workers [39], as shown in Fig. 15.14.

The ability of discerning structures in super-resolution along vertical direction could be explained by the conversion of evanescent waves into propagating waves mediated by the microsphere; the converted beam reaching the far-field interferes with reference beam and produce super-resolution vertical profiling. The technique has great potential for applications in fields where fluorescence technology cannot be utilized and where detection of nanoscale structures with a large aspect ratio is needed, i.e., in cases where the tip of a scanning probe microscope cannot reach.

## 15.4 Metamaterial Dielectric Superlens

Based on metamaterial concept and new super-resolution mechanisms, two types of metamaterial dielectric superlenses were developed, i.e. metamaterial solid immersion lens (mSIL) and nanohybrid lens (nHL).

### 15.4.1 mSIL

A new “nano–solid–fluid assembly (NSF)” method was developed by using 15-nm TiO<sub>2</sub> nanoparticles as building blocks to fabricate the three-dimensional (3D) all-dielectric metamaterial at visible frequencies (see Fig. 15.15). As for its optical transparency, high refractive index, and deep-subwavelength structures, this 3D all-dielectric metamaterial-based solid immersion lens (mSIL) can produce a sharp

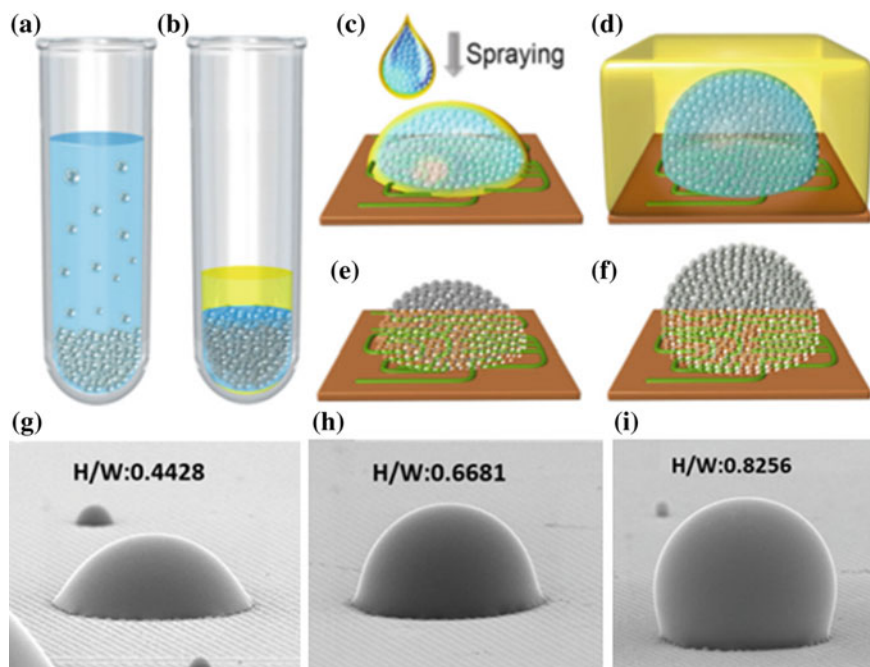


**Fig. 15.15** Nano-solid-fluid (NSF) assembly method for fabrication of mSIL. **a** Anatase  $\text{TiO}_2$  nanoparticles were centrifuged into a tightly packed precipitate. **b** The supernatant was replaced by an organic solvent mixture consisting of hexane and tetrachloroethylene to form a  $\text{TiO}_2$  NSF. **c** To prepare a hemispherical Hemispherical mSIL, the NSF was directly sprayed onto the sample surface. **d** To prepare a superhemispherical mSIL, the NSF was sprayed onto the sample surface covered by a thin layer of organic solvent mixture. **e, f** After evaporation of the solvents, the nanoparticles underwent a phase transition to form a more densely packed structure of mSIL. **g, h, i** Different height to width (H/W) ratio mSIL

image with a super-resolution of at least 45 nm under a white-light optical microscope, significantly exceeding the classical diffraction limit and previous near-field imaging techniques.

The super-resolution imaging performance of mSIL was illustrated in Fig. 15.16. The magnification factor sharply increases with the height-to-width ratio of the mSIL approaching unity (a spherical shape) and reaches 5.3 at a height to-width ratio of 0.82. With the further increase of this ratio, the contrast of the virtual image gradually disappears. Using geometrical ray tracing, we theoretically fit the experimental magnification curve and inversely derived that the mSIL media has an effective index of 1.95 and a high particle volume fraction of 61.3%. This packing fraction is close to the random close packing limit (~64%) of monodisperse hard spheres (46), indicating an intimate contact between  $\text{TiO}_2$  nanoparticles throughout the media. Moreover, the mSIL presented here exhibits a wide field of view, which is approximately linearly proportional to the width of the mSIL. In (c, d) and (e, f), super-resolution imaging was demonstrated; both 60 and 45 nm features can be clearly resolved with

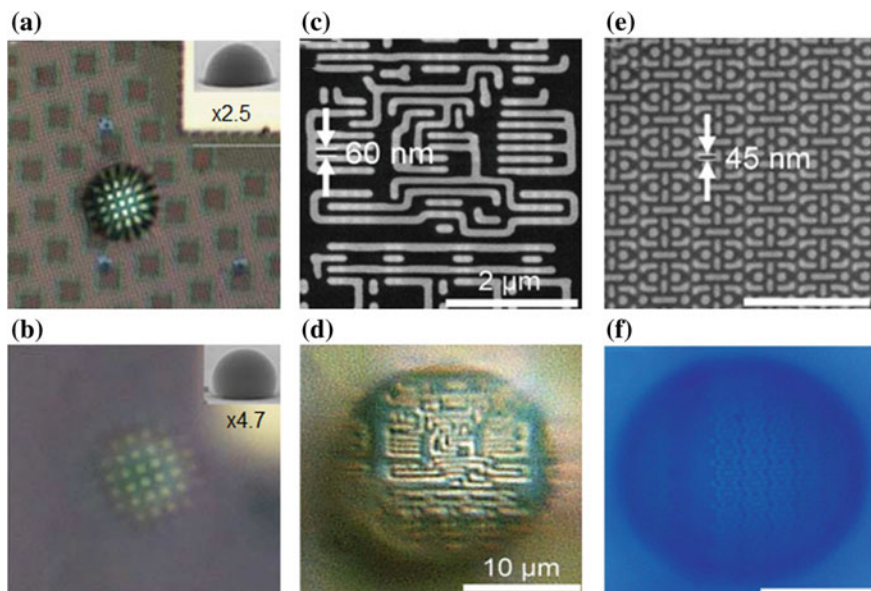


**Fig. 15.16** Super-resolution imaging performance of mSIL. **a** Magnified image ( $\times 2.5$  times) by a mSIL shown in inset. **b** Magnification factor of  $\times 4.7$  for a larger height/width ratio mSIL. **c** SEM, **d** mSIL images of 60 nm features. **e** SEM and **f** mSIL images of 45 nm features

mSIL. The imaging quality, compared to 1st generation microsphere lens, has been greatly improved and being consistent when imaging different types of samples, no matter it is metal, semiconductor or dielectric samples. This indicates the new physical mechanism is robust and dominant in mSIL imaging. Figure 15.17 shows another successful example of mSIL unpublished previously, where 60 nm diameter Polystyrene nanoparticles were clearly imaged by the mSIL, directly under white light. In contrast, microsphere lenses fail to resolve these particles.

The NSFA method we have described is simple and versatile and can be readily extended to assemble  $\text{TiO}_2$  nanoparticles or even other dielectric nanoparticles into arbitrarily shaped metamaterial-based photonic devices (for example, a  $\text{TiO}_2$  wire used as an optical fiber; see Fig. s9 in [105]). Further combining techniques such as nano-imprinting and nanofluidics may lead to compact and inexpensive nanophotonic devices for cloaking, optical interconnect networks, near-field sensing, solar energy utilization, etc.

### 15.4.2 Nanohybrid Lens

Nanohybrid lens is a new class of metamaterial lens with controllable refractive index. This is achieved by uniformly distributing high refractive-index (RI)  $\text{ZrO}_2$  material



**Fig. 15.17** Direct super-resolution of 60-nm-diameter PS nanosphere deposited on a grating sample surface

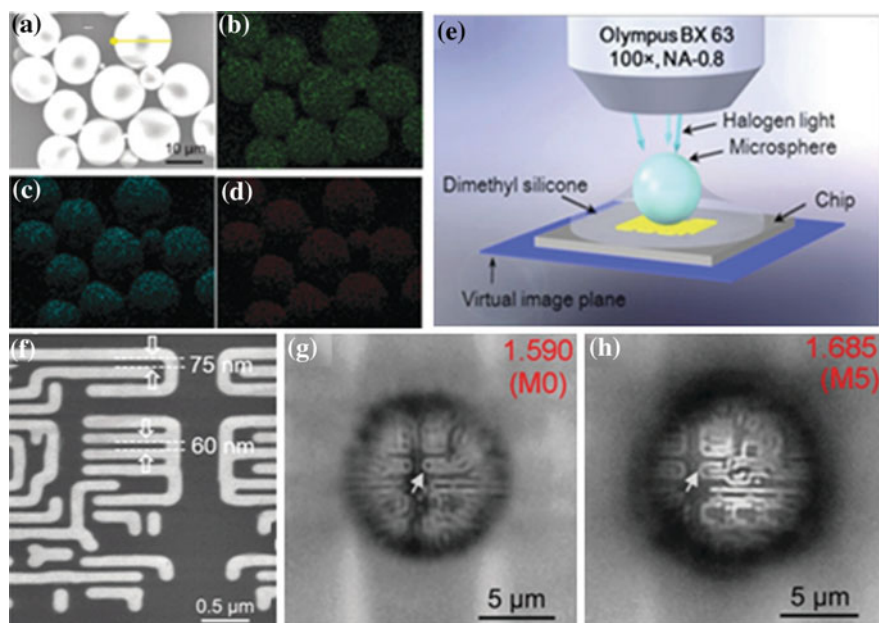


**Fig. 15.18**  $\text{ZrO}_2/\text{PS}$  nanohybrid particle-lens. **a** SEM image and SEM mapping photographs of **b** Zr, **c** C and **d** O in the nanohybrid microspheres. **e** Schematic of the dimethyl-silicone semi-immersed microsphere for super-resolution imaging. **f** Nanochip sample with 75 and 60 nm features. **g** Imaging by  $n = 1.590$  particle. **h** Imaging by  $n = 1.685$  particle [116]

into polystyrene matrix. A nanoparticle-hybrid suspension polymerisation approach was developed for such purpose; high-quality microspheres  $\text{ZrO}_2/\text{PS}$  hybrid microspheres have been synthesized with highly controllability in shape and refractive index ( $n_p = 1.590\text{--}1.685$ ) [116]. Figure 15.18 shows nanohybrid particle-lens (a–d) and its super-resolution imaging performance configured in a semi-immersed liquid environment (e). Comparing (g) and (h), it is obvious that increasing the refractive index of microspheres from 1.590 to 1.685 improve both the imaging resolution and quality. A 60 nm resolution has been obtained in the wide-field imaging mode and a 50 nm resolution in the confocal mode. The synthesis of hybrid microspheres is feasible, easily repeatable and designable in shape, size and refractive index. Accordingly, the approach is quite general, and can be readily extended to prepare a series of hybrid microspheres with various refractive index and optical transparency, by changing the types of polymers and nanoparticles. The as-synthesized nanohybrid colloidal microspheres can be used not only in optical nanoscope for super-resolution imaging with visible frequency, but also in some potential fields of nanolithography, optical memory storage, and optical nano-sensing.

## 15.5 Biological Superlens

Fabrication of superlenses is often complex and requires sophisticated engineering processes. Clearly an easier model candidate, such as a naturally occurring superlens, is highly desirable. Recently, Monks et al. reported a biological superlens provided by nature: the minor ampullate spider silk spun from the *Nephila* spider [117]. This natural biosuperlens can distinctly resolve 100 nm features under a conventional white-light microscope with peak wavelength at 600 nm, obtaining a resolution of  $\lambda/6$  that is well beyond the classical limit.

Figure 15.19 shows Spider silk biological superlens and its imaging performance. The used spider silk is from *Nephila edulis* spider, with diameter about  $6.8\ \mu\text{m}$  (Fig. 15.19a). The spider silk was placed directly on top of the sample surface by using a transparent cellulose-based tape. The gaps between silk and sample was filled with IPA which improves imaging contrast. The silk lens collects the underlying near-field object information and projects a magnified virtual image into a conventional objective lens ( $100\times$ , NA: 0.9, Fig. 15.19b). The spider silk magnifies objects about  $2.1\times$  times (Fig. 15.19c), allowing subdiffraction object to be seen. Blu-ray disc with 100 nm features were clearly resolved by the spider silk (Fig. 15.19d), under an angular beam incident at around  $30^\circ$ . Simulated intensity field in Fig. 15.19g reveals how the samples was illuminated by the angular jet. In Fig. 15.19h, it was also shown that the spider silk produced similar quality of super-resolution image as BTG microspheres, despite the image was slightly rotated by approximately four degree due to fibre direction is not parallel to grating direction (like case in d). This research provides a solid foundation for the development of bio-superlens technology, and it is the first expose of spider silk in this context. It is expected more biological superlenses to be discovered. Indeed, interesting and important recent work by other researchers

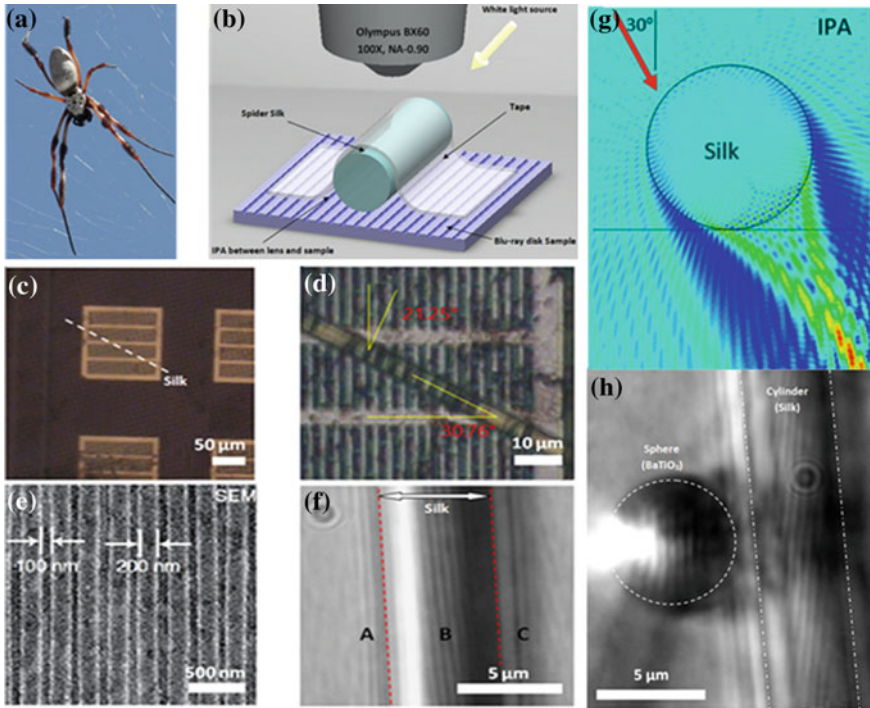


**Fig. 15.19** Spider silk biological superlens and super-resolution imaging. **a** *Nephila edulis* spider, **b** schematic drawing imaging setup. **c** Silk on test pattern, in an angle. **d** Imaging by silk showing magnification and image rotation effect. **e** SEM image of Blu-ray disc with 100 nm features, **f** 100 nm features were resolved, magnified  $2.1\times$  by the spider silk cylinder lens. **g** Simulated optical near-field distribution around the silk lens, with beam incident at an angle of  $30^\circ$ . **h** A BTG microsphere positioned beside the minor ampullate spider silk for imaging comparison experiments [117]

is heading in that direction. For example, Schuergers et al. reported that spherically shaped cyanobacteria *Synechocystis* cells can focus light like a micro-lens, which contributes to the cell's ability to sense the direction of lighting source. These cells might work also as a superlens suitable for super-resolution imaging. Very recently, it was reported that live cyanobacteria can form an aggregated metamaterial-style biological lens which focuses light; however, its imaging performance hasn't been evaluated yet which worth being studied in next-step.

## 15.6 Devices with Integrated Microsphere Superlens

Due to tiny size of microspheres, it has advantage of being integrated in other microsystems, such as microfluidics and optical fiber system, to form a multifunctional on-chip device. For example, Yang et al. demonstrated a microfluidic device

with an integrated microsphere-lens-array, as shown in Fig. 15.20a–c [118]. The microspheres are patterned in a microwell array template, acting as lenses focusing the light originating from a microscope objective into photonic nanojets that expose the medium within a microfluidic channel. When a NP is randomly transported through a nanojet, its backscattered light (for a bare Au NP) or its fluorescent emission is instantaneously detected by video microscopy. Au NPs down to 50 nm in size, as well as fluorescent NPs down to 20 nm in size, are observed by using a low magnification/low numerical aperture microscope objective in bright-field or fluorescence mode, respectively. Compared to the NPs present outside of the photonic nanojets, the light scattering or fluorescence intensity of the NPs in the nanojets is typically enhanced by up to a factor of  $\sim 40$ . The experimental intensity is found to be proportional to the area occupied by the NP in the nanojet. The technique is also used for immunodetection of biomolecules immobilized on Au NPs in buffer and, in future, it may develop into a versatile tool to detect nanometric objects of environmental or biological importance, such as NPs, viruses, or other biological agents. In another work by Li and co-workers, microsphere lenses were attached onto an optical fibre

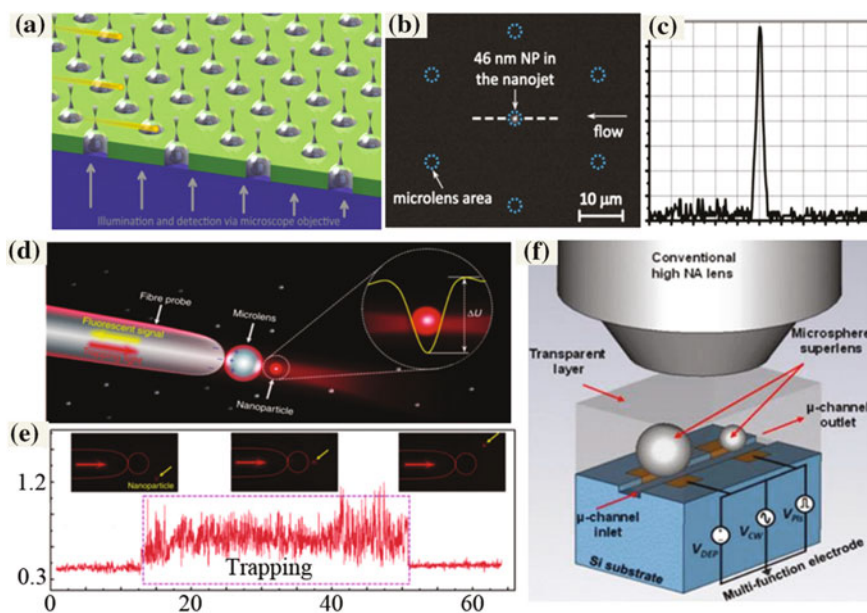


**Fig. 15.20** Device with integrated microspheres. **a** Schematic of microsphere-array-assisted nanoparticle sensing platform. **b** 46 nm fluorescent nanoparticle was detected by microsphere-generated PNJ (reproduced from [118] with permission from American Chemical Society). **c** Corresponding backscattering signal. **d** Schematic illustration of fiber-microsphere-bonded probe detection and trapping of nanoparticles. **e** The real-time trace of the reflected signal in the trapping process of an 85-nm fluorescent PS nanoparticle. The insets show the fluorescent images b1 before trapping, b2 during trapping and b3 in the release. **f** A multifunction biochip device with integrated sensing, trapping and super-resolution imaging functionalities

probe [119]; the generated PNJ focus was used for real-time manipulation (trapping and releasing) and detection of 85 nm objects like nanoparticles and biomolecules, as shown in Fig. 15.20d, e. A multifunctional Lab-on-Chip (LoC) device capable of delivering real-time trapping, detection and super-resolution imaging functionalities was recently proposed and partially experimentally demonstrated by Yan et al., where a coverslip-style microsphere superlens was bonded onto a microfluidic chip on silicon. The trapping function was realized by dielectrophoretic (may also with PNJ effect). When bio-samples flowing through the channel, the objects will be trapped by the dielectrophoretic force at locations beneath the particles, super-resolution images were then obtained through microsphere imaging. The successful realization of proposed device may lead to fundamental changes to biomedical analysis with accuracy in nanometre scales.

## 15.7 Outlook and Conclusions

Compared to other super-resolution techniques, the microsphere nanoscopy technique has several distinct features—simple, easy to implement, label-free, high-resolution and compatible with conventional white-lighting imaging. The scanning superlens system has generated possible opportunities for commercialization, a few start-up companies were recently setup using first-generation dielectric superlenses (PS or BTG particles) technology. These systems are likely to suffer from low imaging contrast and quality compared to second-generation particle superlenses based on metamaterials. Development of commercially viable prototype of metamaterial dielectric superlens is of considerable interests in the next-step development of the technique.

For microsphere imaging, one possible way to further improve the system resolution is to use *microfiber* to evanescently illustrate the specimen [120]. Imaging contrast in this case can be greatly improved owing to the limited illumination depth (typical  $< 200$  nm) of the evanescent waves; sharp and clear images of nanostructures have been achieved [120]. This idea may worth further exploration for sub-50 nm resolution imaging in the future, by extending the evanescence wave illumination approach to microspheres; either prism-style or objective-style TIRM (Total Internal Reflection microscopy) setup can be used [121].

On application side, the breakthrough is likely to come from in vivo endoscopy application where other super-resolution techniques (STED) cannot be applied. The super-resolution endoscope can provide real-time high-resolution image of internal cells and tissues for the early diagnostics of cancers and other diseases.

On the other hand, studies on new effects generated by particles are emerging and growing, including nanoparticle super-resolution, microsphere super-resonance, microsphere array Talbot effect [122], and micro-prism ‘photonic hook’ [123], etc. The ‘photonic hook’ effect may be used for nanoscale light switching and guiding in a Photonic Integrated Chip. The factual Talbot effect of a microsphere lens array may be used to develop a far-field particle-lens super-resolution imaging system.

On theoretical side, building a complete theoretical model is still highly desired. Effects such as multi-wavelengths effects and partial and inclined illumination should also be included in the developments. In a long term, we envisage that every microscope user will have the dielectric superlenses in their hand for daily use of microscopes. Besides imaging, the dielectric particle superlens can find applications in nano-focusing, nanolithography, nano-solar energy concentrator, nanochemistry, nanomedicine and more.

## References

1. E. Abbe, Beitrage zur Theorie des Mikroskops und der mikroskopischen Wahrnehmung. *Archiv Microskop. Anat.* **9**, 413 (1873)
2. C. Sparrow, On spectroscopic resolving power. *Astrophys. J.* **44**, 76 (1916)
3. W.V. Houston, A compound interferometer for fine structure work. *Phys. Rev.* **29**, 478 (1927)
4. L. Rayleigh, XXXI. Investigations in optics, with special reference to the spectroscope, Lond. *Edinb. Dublin Philos. Mag. J. Sci.* **8**, 261–274 (1879)
5. D.W. Pohl, W. Denk, M. Lanz, Optical stethoscopy: image recording with resolution lambda/20. *Appl. Phys. Lett.* **44**, 651–653 (1984)
6. J.B. Pendry, Negative refraction makes a perfect lens. *Phys. Rev. Lett.* **85**, 3966 (2000)
7. S.W. Hell, J. Wichmann, Breaking the diffraction resolution limit by stimulated emission: stimulated-emission-depletion fluorescence microscopy. *Opt. Lett.* **19**, 780–782 (1994)
8. E.T. Rogers, J. Lindberg, T. Roy, S. Savo, J.E. Chad, M.R. Dennis, N.I. Zheludev, A super-oscillatory lens optical microscope for subwavelength imaging. *Nat. Mater.* **11**, 432–435 (2012)
9. M. Gustafsson, Surpassing the lateral resolution limit by a factor of two using structured illumination microscopy. *J. Microsc.* **198**, 82–87 (2000)
10. J. Cartwright, Defeating diffraction. *Phys. World* **25**, 29–34 (2012)
11. X. Zhang, Z.W. Liu, Superlenses to overcome the diffraction limit. *Nat. Mater.* **7**, 435–441 (2008)
12. Z.W. Liu, H. Lee, Y. Xiong, C. Sun, X. Zhang, Far-field optical hyperlens magnifying sub-diffraction-limited objects. *Science* **315**, 1686 (2007)
13. Z. Jacob, L.V. Alekseyev, E. Narimanov, Optical hyperlens: far-field imaging beyond the diffraction limit. *Opt. Express* **14**, 8247–8256 (2006)
14. N. Fang, H. Lee, C. Sun, X. Zhang, Sub-diffraction-limited optical imaging with a silver superlens. *Science* **308**, 534–537 (2005)
15. B. Huang, M. Bates, X. Zhuang, Super-resolution fluorescence microscopy. *Annu. Rev. Biochem.* **78**, 993–1016 (2009)
16. G.T.D. Francia, Super-gain antennas and optical resolving power. *Nuovo Cimento* **9**(Suppl.), 426–435 (1952)
17. K. Huang, F. Qin, H. Liu, H. Ye, C.W. Qiu, M. Hong, B. Luk'yanchuk, J. Teng, Planar diffractive lenses: fundamentals, functionalities, and applications. *Adv. Mater.* **30**, e1704556 (2018)
18. F. Qin, K. Huang, J. Wu, J. Teng, C.W. Qiu, M. Hong, A supercritical lens optical label-free microscopy: sub-diffraction resolution and ultra-long working distance. *Adv. Mater.* **29**, 1602721 (2017)
19. Z. Wang, W. Guo, L. Li, B. Luk'yanchuk, A. Khan, Z. Liu, Z. Chen, M. Hong, Optical virtual imaging at 50 nm lateral resolution with a white-light nanoscope. *Nat. Commun.* **2**, 218 (2011)
20. K.W. Allen, N. Farahi, Y. Li, N.I. Limberopoulos, D.E. Walker, A.M. Urbas, V. Liberman, V.N. Astratov, Super-resolution microscopy by movable thin-films with embedded microspheres: Resolution analysis. *Ann. Phys. (Berl.)* **527**, 513–522 (2015)

21. A. Darafsheh, N.I. Limberopoulos, J.S. Derov, D.E. Walker, V.N. Astratov, Advantages of microsphere-assisted super-resolution imaging technique over solid immersion lens and confocal microscopies. *Appl. Phys. Lett.* **104**, 061117 (2014)
22. L.A. Krivitsky, J.J. Wang, Z.B. Wang, B. Luk'yanchuk, Locomotion of microspheres for super-resolution imaging. *Sci. Rep.* **3**, 3501 (2013)
23. L. Li, W. Guo, Y. Yan, S. Lee, T. Wang, Label-free super-resolution imaging of adenoviruses by submerged microsphere optical nanoscopy. *Light Sci. Appl.* **2**, e104 (2013)
24. Z.B. Wang, L. Li, White-light microscopy could exceed 50 nm resolution. *Laser Focus World* **47**, 61–64 (2011)
25. H. Yang, N. Moullan, J. Auwerx, M.A.M. Gijs, Super-resolution biological microscopy using virtual imaging by a microsphere nanoscope. *Small* **10**, 1712–1718 (2014)
26. B. Richards, E. Wolf, Electromagnetic diffraction in optical systems. II. Structure of the image field in an aplanatic system. *Proc. R. Soc. Lond. Ser. A* **253**, 358 (1959)
27. F.F. Wang, L.Q. Liu, H.B. Yu, Y.D. Wen, P. Yu, Z. Liu, Y. C. Wang, W.J. Li, Scanning superlens microscopy for non-invasive large field-of-view visible light nanoscale imaging. *Nat. Commun.* **7**(2016)
28. A. Vlad, I. Huynen, S. Melinte, Wavelength-scale lens microscopy via thermal reshaping of colloidal particles. *Nanotechnology* **23**, 285708 (2012)
29. A. Darafsheh, G.F. Walsh, L. Dal Negro, V.N. Astratov, Optical super-resolution by high-index liquid-immersed microspheres. *Appl. Phys. Lett.* **101**, 141128 (2012)
30. S. Lee, L. Li, Z. Wang, W. Guo, Y. Yan, T. Wang, Immersed transparent microsphere magnifying sub-diffraction-limited objects. *Appl. Opt.* **52**, 7265–7270 (2013)
31. Y. Yan, L. Li, C. Feng, W. Guo, S. Lee, M.H. Hong, Microsphere-coupled scanning laser confocal nanoscope for sub-diffraction-limited imaging at 25 nm lateral resolution in the visible spectrum. *ACS Nano* **8**, 1809–1816 (2014)
32. A.N. Cartwright, D.V. Nicolau, D. Fixler, V.N. Astratov, A.V. Maslov, K.W. Allen, N. Farahi, Y. Li, A. Brettin, N.I. Limberopoulos, D.E. Walker, A.M. Urbas, V. Liberman, M. Rothschild, Fundamental limits of super-resolution microscopy by dielectric microspheres and microfibers, in *Nanoscale Imaging, Sensing, and Actuation for Biomedical Applications XIII* (2016)
33. Z.B. Wang, Microsphere super-resolution imaging, in *Nanoscience*, ed. by J.T. Paul O'Brien (Royal Society of Chemistry, 2016), pp. 193–210
34. A.V. Maslov, V.N. Astratov, Optical nanoscopy with contact Mie-particles: resolution analysis. *Appl. Phys. Lett.* **110**(2017)
35. S. Lee, L. Li, Z. Wang, Optical resonances in microsphere photonic nanojets. *J. Opt.* **16**, 015704 (2014)
36. B.S. Luk'yanchuk, R. Paniagua-Domínguez, I. Minin, O. Minin, Z. Wang, Refractive index less than two: photonic nanojets yesterday, today and tomorrow, *Opt. Mater. Express* **7**, 1820–1847 (2017)
37. H. Yang, N. Moullan, J. Auwerx, M.A.M. Gijs, Super-resolution biological microscopy using virtual imaging by a microsphere nanoscope. *Small* **10**, 1712–1718 (2013)
38. F. Wang, H.S.S. Lai, L. Liu, P. Li, H. Yu, Z. Liu, Y. Wang, W.J. Li, Super-resolution endoscopy for real-time wide-field imaging. *Opt. Express* **23**, 16803–16811 (2015)
39. F. Wang, L. Liu, P. Yu, Z. Liu, H. Yu, Y. Wang, W.J. Li, Three-dimensional super-resolution morphology by near-field assisted white-light interferometry. *Sci. Rep.* **6**, 24703 (2016)
40. A. Darafsheh, C. Guardiola, A. Palovcak, J.C. Finlay, A. Cárabe, Optical super-resolution imaging by high-index microspheres embedded in elastomers. *Opt. Lett.* **40**, 5–8 (2015)
41. H. Yang, R.I. Trouillon, G. Huszka, M.A. Gijs, Super-resolution imaging of a dielectric microsphere is governed by the waist of its photonic nanojet, *Nano Lett.* **16**, 4862–4870 (2016)
42. B. Yan, Z. Wang, A.L. Parker, Y.-K. Lai, P.J. Thomas, L. Yue, J.N. Monks, Superlensing microscope objective lens. *Appl. Opt.* **56**, 3142–3147 (2017)
43. T.X. Hoang, Y. Duan, X. Chen, G. Barbastathis, Focusing and imaging in microsphere-based microscopy. *Opt. Express* **23**, 12337–12353 (2015)

44. Z.B. Wang, Y. Zhou, B. Luk'yanchuk, Near-field focusing of dielectric microspheres: super-resolution and field-invariant parameter scaling (2013), [arXiv:1304.4139v2](https://arxiv.org/abs/1304.4139v2)
45. V.M. Sundaram, S.B. Wen, Analysis of deep sub-micron resolution in microsphere based imaging. *Appl. Phys. Lett.* **105** (2014)
46. X. Hao, C. Kuang, X. Liu, H. Zhang, Y. Li, Microsphere based microscope with optical super-resolution capability. *Appl. Phys. Lett.* **99**, 203102 (2011)
47. Z.G. Chen, A. Taflove, V. Backman, Photonic nanojet enhancement of backscattering of light by nanoparticles: a potential novel visible-light ultramicroscopy technique. *Opt. Express* **12**, 1214–1220 (2004)
48. Z.B. Wang, *Optical Resonance and Near Field Effects: Small Particles Under Laser Irradiation* (National University of Singapore, Singapore, 2005)
49. W. Guo, Z.B. Wang, L. Li, Z. Liu, B.S. Luk'yanchuk, P.L. Crouse, D.J. Whitehead, Laser parallel nanopatterning of lines and curves by micro-particle lens arrays, in *The 8th International Symposium on Laser Precision Microfabrication* (2007), p. 98
50. W. Guo, Z.B. Wang, L. Li, D.J. Whitehead, B.S. Luk'yanchuk, Z. Liu, Near-field laser parallel nanofabrication of arbitrary-shaped patterns. *Appl. Phys. Lett.* **90**, 243101 (2007)
51. G.X. Chen, M.H. Hong, Y. Lin, Z.B. Wang, D.K.T. Ng, Q. Xie, L.S. Tan, T.C. Chong, Large-area parallel near-field optical nanopatterning of functional materials using microsphere mask. *J. Alloys Compd.* **449**, 265–268 (2008)
52. W. Guo, Z.B. Wang, L. Li, Z. Liu, B. Luk'yanchuk, D.J. Whitehead, Chemical-assisted laser parallel nanostructuring of silicon in optical near fields. *Nanotechnology* **19**, 455302 (2008)
53. L. Li, W. Guo, Z.B. Wang, Z. Liu, D.J. Whitehead, B.S. Luk'yanchuk, Large area laser nano-texturing with user defined patterns, in *The 1st International Conference on Nanomanufacturing (nanoMan2008)* (Singapore, 2008)
54. Y. Zhou, M.H. Hong, J.Y.H. Fuh, L. Lu, B.S. Luk'yanchuk, Z.B. Wang, Near-field enhanced femtosecond laser nano-drilling of glass substrate. *J. Alloys Compd.* **449**, 246–249 (2008)
55. A. Khan, Z. Wang, M.A. Sheikh, L. Li, Laser sub-micron patterning of rough surfaces by micro-particle lens arrays. *Int. J. Manuf. Mater. Mech. Eng. (IJMMME)* **1**, 9 (2011)
56. A. Khan, Z. Wang, M.A. Sheikh, D. Whitehead, L. Li, Laser micro/nano patterning of hydrophobic surface by contact particle lens array. *Appl. Surf. Sci.* **258**, 774–779 (2011)
57. Y.F. Lu, L. Zhang, W.D. Song, Y.W. Zheng, B.S. Luk'yanchuk, Laser writing of a subwavelength structure on silicon (100) surfaces with particle-enhanced optical irradiation. *JETP Lett.* **72**, 457–459 (2000)
58. Z.B. Wang, J. Naveen, L. Li, and B.S. Luk'yanchuk, A review of optical near-fields in particle/tip-assisted laser nanofabrication. *P.I.Mech. Eng. C-J. Mec.* **224**, 1113–1127 (2010)
59. V. Yannopapas, Photonic nanojets as three-dimensional optical atom traps: a theoretical study. *Opt. Commun.* **285**, 2952–2955 (2012)
60. D. McCloskey, J.J. Wang, J.F. Donegan, Low divergence photonic nanojets from Si<sub>3</sub>N<sub>4</sub> microdisks. *Opt. Express* **20**, 128–140 (2012)
61. M.S. Kim, T. Scharf, S. Muhlig, C. Rockstuhl, H.P. Herzig, Gouy phase anomaly in photonic nanojets. *Appl. Phys. Lett.* **98**, 191114 (2011)
62. D. Grojo, L. Charmasson, A. Pereira, M. Sentis, P. Delaporte, Monitoring photonic nanojets from microsphere arrays by femtosecond laser ablation of thin films. *J. Nanosci. Nanotechnol.* **11**, 9129–9135 (2011)
63. C.M. Ruiz, J.J. Simpson, Detection of embedded ultra-subwavelength-thin dielectric features using elongated photonic nanojets. *Opt. Express* **18**, 16805–16812 (2010)
64. Y.E. Geints, E.K. Panina, A.A. Zemlyanov, Control over parameters of photonic-nanojets of dielectric microspheres. *Opt. Commun.* **283**, 4775–4781 (2010)
65. A. Heifetz, S.C. Kong, A.V. Sahakian, A. Taflove, V. Backman, Photonic nanojets. *J. Comput. Theor. Nanosci.* **6**, 1979–1992 (2009)
66. P. Ferrand, J. Wenger, A. Devilez, M. Pianta, B. Stout, N. Bonod, E. Popov, H. Rigneault, Direct imaging of photonic nanojets. *Opt. Express* **16**, 6930–6940 (2008)
67. M. Gerlach, Y.P. Rakovich, J.F. Donegan, Nanojets and directional emission in symmetric photonic molecules. *Opt. Express* **15**, 17343–17350 (2007)

68. X. Li, Z.G. Chen, A. Taflove, V. Backman, Optical analysis of nanoparticles via enhanced backscattering facilitated by 3-D photonic nanojets. *Opt. Express* **13**, 526–533 (2005)
69. A.V. Itagi, W.A. Challeger, Optics of photonic nanojets. *J. Opt. Soc. Am. A Opt. Image Sci.* **22**, 2847–2858 (2005)
70. Z.G. Chen, A. Taflove, V. Backman, Photonic nanojets, in *IEEE Antennas and Propagation Society Symposium*, vols. 1–4, Digest 1923–1926 (2004)
71. M. Born, E. Wolf, *Principles of Optics*, 7th edn. (Cambridge University Press, Cambridge, 1999)
72. H. Guo, Y. Han, X. Weng, Y. Zhao, G. Sui, Y. Wang, S. Zhuang, Near-field focusing of the dielectric microsphere with wavelength scale radius. *Opt. Express* **21**, 2434–2443 (2013)
73. Z. Chen, A. Taflove, V. Backman, Photonic nanojet enhancement of backscattering of light by nanoparticles: a potential novel visible-light ultramicroscopy technique. *Opt. Express* **12**, 1214 (2004)
74. C.H. Li, G.W. Kattawar, P.W. Zhai, P. Yang, Electric and magnetic energy density distributions inside and outside dielectric particles illuminated by a plane electromagnetic wave. *Opt. Express* **13**, 4554–4559 (2005)
75. B.S. Luk'yanchuk, N.V. Voshchinnikov, R. Paniagua-Dominguez, A.I. Kuznetsov, Optimum forward light scattering by spherical and spheroidal dielectric nanoparticles with high refractive index. *ACS Photonics* **2**, 993–999 (2015)
76. C.Y. Liu, C.C. Li, Photonic nanojet induced modes generated by a chain of dielectric microdisks. *Optik* **127**, 267–273 (2016)
77. Y.E. Geints, A.A. Zemlyanov, E.K. Panina, Characteristics of photonic jets from microcones. *Opt. Spectrosc.* **119**, 849–854 (2015)
78. I.V. Minin, O.V. Minin, Y.E. Geints, Localized EM and photonic jets from non-spherical and non-symmetrical dielectric mesoscale objects: brief review. *Ann. Phys. (Berl.)* **527**, 491–497 (2015)
79. Y. Huang, Z.S. Zhen, Y.C. Shen, C.J. Min, G. Veronis, Optimization of photonic nanojets generated by multilayer microcylinders with a genetic algorithm. *Opt. Express* **27**, 1310–1325 (2019)
80. I. Mahariq, I.H. Giden, H. Kurt, O.V. Minin, I.V. Minin, Strong electromagnetic field localization near the surface of hemicylindrical particles. *Opt. Quant. Electron.* **49** (2017)
81. Y.E. Geints, A.A. Zemlyanov, O.V. Minin, I.V. Minin, Systematic study and comparison of photonic nanojets produced by dielectric microparticles in 2D-and 3D-spatial configurations. *J. Opt.* **20** (2018)
82. C.Y. Liu, O.V. Minin, I.V. Minin, First experimental observation of array of photonic jets from saw-tooth phase diffraction grating. *EPL* **123** (2018)
83. L.Y. Yue, B. Yan, J.N. Monks, R. Dhama, Z.B. Wang, O.V. Minin, I.V. Minin, Intensity-enhanced apodization effect on an axially illuminated circular-column particle-lens. *Ann. Phys. (Berl.)* **530** (2018)
84. B. Yan, L.Y. Yue, Z.B. Wang, Engineering near-field focusing of a microsphere lens with pupil masks. *Opt. Commun.* **370**, 140–144 (2016)
85. L.Y. Yue, B. Yan, J.N. Monks, Z.B. Wang, N.T. Tung, V.D. Lam, O. Minin, I. Minin, Production of photonic nanojets by using pupil-masked 3D dielectric cuboid. *J. Phys. D Appl. Phys.* **50** (2017)
86. L.Y. Yue, B. Yan, J.N. Monks, R. Dhama, Z.B. Wang, O.V. Minin, I.V. Minin, A Millimetre-wave cuboid solid immersion lens with intensity-enhanced amplitude mask apodization. *J. Infrared Millim. Terahertz Waves* **39**, 546–552 (2018)
87. L.Y. Yue, O.V. Minin, Z.B. Wang, J.N. Monks, A.S. Shalin, I.V. Minin, Photonic hook: a new curved light beam. *Opt. Lett.* **43**, 771–774 (2018)
88. I.V. Minin, O.V. Minin, G.M. Katyba, N.V. Chernomyrdin, V.N. Kurlov, K.I. Zaytsev, L. Yue, Z. Wang, D.N. Christodoulides, Experimental observation of a photonic hook. *Appl. Phys. Lett.* **114** (2019)
89. B.S. Luk'yanchuk, Z.B. Wang, W.D. Song, M.H. Hong, Particle on surface: 3D-effects in dry laser cleaning. *Appl. Phys. A* **79**, 747–751 (2004)

90. I.V. Minin, O.V. Minin, V. Pacheco-Pena, M. Beruete, Localized photonic jets from flat, three-dimensional dielectric cuboids in the reflection mode. *Opt. Lett.* **40**, 2329–2332 (2015)
91. L.Y. Yue, B. Yan, J.N. Monks, R. Dhama, Z.B. Wang, O.V. Minin, I.V. Minin, Photonic jet by a near-unity-refractive-index sphere on a dielectric substrate with high index contrast. *Ann. Phys. (Berl.)* **530** (2018)
92. Z. Wang,  $n = 1.5$  nano microsphere light focusing (2017), <https://www.youtube.com/watch?v=YSsEeVqjXSrg>
93. Z. Wang,  $n = 1.5$  cylinder (2017) <https://www.youtube.com/watch?v=rkmyQD55QuQ>
94. A. Brettin, F. Abolmaali, K.F. Blanchette, C.L. McGinnis, Y.E. Nesmelov, N.I. Limberopoulos, D.E. Walker, I. Anisimov, A.M. Urbas, L. Poffo, A.V. Maslov, V.N. Astratov, Enhancement of resolution in microspherical nanoscopy by coupling of fluorescent objects to plasmonic metasurfaces. *Appl. Phys. Lett.* **114** (2019)
95. A.V. Kildishev, A. Boltasseva, V.M. Shalaev, Planar photonics with metasurfaces. *Nat. Mater.* **339**, 1232009 (2013)
96. N.I. Zheludev, Obtaining optical properties on demand. *Science* **348**, 973–974 (2015)
97. N. Yu, F. Capasso, Flat optics with designer metasurfaces. *Nat. Mater.* **13**, 139–150 (2014)
98. Y. Liu, X. Zhang, Metamaterials: a new frontier of science and technology. *Chem. Soc. Rev.* **40**, 2494 (2011)
99. C.M. Soukoulis, M. Wegener, Past achievements and future challenges in the development of three-dimensional photonic metamaterials. *Nat. Photonics* **5**, 524–530 (2011)
100. C.M. Soukoulis, M. Wegener, Optical metamaterials—more bulky and Less lossy. *Science* **330**, 1633–1634 (2010)
101. Q. Zhao, J. Zhou, F. Zhang, D. Lippens, Mie resonance-based dielectric metamaterials. *Mater. Today* **12**, 60–69 (2009)
102. J.B. Khurgin, How to deal with the loss in plasmonics and metamaterials. *Nat. Nanotechnol.* **10**, 2–6 (2015)
103. S. Jahani, Z. Jacob, All-dielectric metamaterials. *Nat. Nanotechnol.* **11**, 23–36 (2016)
104. S.J. Corbitt, M. Francoeur, B. Raeymaekers, Implementation of optical dielectric metamaterials: a review. *J. Quant. Spectrosc. Radiat. Transfer* **158**, 3–16 (2015)
105. W. Fan, B. Yan, Z.B. Wang, L.M. Wu, Three-dimensional all-dielectric metamaterial solid immersion lens for subwavelength imaging at visible frequencies. *Sci. Adv.* **2** (2016)
106. D.W. Pohl, W. Denk, M. Lanz, Optical stethoscopy: image recording with resolution  $\lambda/20$ . *Appl. Phys. Lett.* **44**, 651–653 (1984)
107. R.C. Dunn, Near-field scanning optical microscopy. *Chem. Rev.* **99**, 2891–2928 (1999)
108. R.J. Potton, Reciprocity in optics. *Rep. Prog. Phys.* **67**, 717–754 (2004)
109. N. Fang, H. Lee, C. Sun, X. Zhang, Sub-diffraction-limited optical imaging with a silver superlens. *Science* **308**, 534–537 (2005)
110. Z. Liu, H. Lee, Y. Xiong, C. Sun, X. Zhang, Far-field optical hyperlens magnifying sub-diffraction-limited objects. *Science* **315**, 1686 (2007)
111. D. Lu, Z. Liu, Hyperlenses and metalenses for far-field super-resolution imaging. *Nat. Commun.* **3**, 1205 (2012)
112. Z. Wang, Improvements in and Relating to Lenses, PCT/GB2014/052578 (priority date: 2013-AUG-23) (2014)
113. V.N. Astratov, A. Darafsheh, Methods and systems for super-resolution optical imaging using high-index of refraction microspheres and micro-cylinders, US patent application 2014/0355108 A1 published on December 4, 2014 (2014)
114. J. Li, W. Liu, T. Li, I. Rozen, J. Zhao, B. Bahari, B. Kante, J. Wang, Swimming microbot optical nanoscopy. *Nano Lett.* **16**, 6604–6609 (2016)
115. I. Kassamakov, S. Lecler, A. Nolvi, A. Leong-Hoi, P. Montgomery, E. Hægström, 3D super-resolution optical profiling using microsphere enhanced Mirau interferometry. *Sci. Rep.* **7**, 3683 (2017)
116. H. Zhu, B. Yan, Z. Wang, L. Wu, Synthesis and super-resolution imaging performance of refractive-index-controllable microsphere superlens. *J. Mater. Chem. C* **3**, 10907–10915 (2015)

117. J.N. Monks, B. Yan, N. Hawkins, F. Vollrath, Z.B. Wang, Spider silk: mother nature's bio-superlens. *Nano Lett.* **16**, 5842–5845 (2016)
118. H. Yang, M. Cornaglia, M.A.M. Gijs, Photonic nanojet array for fast detection of single nanoparticles in a flow. *Nano Lett.* **15**, 1730–1735 (2015)
119. Y.C. Li, H.B. Xin, H.X. Lei, L.L. Liu, Y.Z. Li, Y. Zhang, B.J. Li, Manipulation and detection of single nanoparticles and biomolecules by a photonic nanojet. *Light Sci. Appl.* **5**, 1–9 (2016)
120. X. Hao, X. Liu, C. Kuang, Y. Li, Y. Ku, H. Zhang, H. Li, L. Tong, Far-field super-resolution imaging using near-field illumination by micro-fiber. *Appl. Phys. Lett.* **102**, 013104 (2013)
121. P.R. Selvin, H. Taekjip, *Single-Molecule Techniques: A Laboratory Manual* (Cold Spring Harbor Laboratory Press, 2007)
122. Z. Wang, T.S. Kao, N. Zheludev, Fractional Talbot effect in a dielectric micro-spheres array, in *CLEO/Europe-EQEC* (2009)
123. L. Yue, O.V. Minin, Z. Wang, J.N. Monks, A.S. Shalin, I.V. Minin, Photonic hook: a new curved light beam. *Opt. Lett.* **43**, 771–774 (2018)

# Chapter 16

## Theoretical Foundations of Super-Resolution in Microspherical Nanoscopy



Alexey V. Maslov and Vasily N. Astratov

**Abstract** A review of recent developments in the emerging area of imaging through contact dielectric microspheres, which we term “microspherical nanoscopy”, is presented. The focus of this review is on the theoretical studies of the mechanisms of super-resolution imaging, which represents a frontier of modern nanophotonics and microscopy with many fascinating concepts proposed in recent years such as photonic nanojets, far-field superlens, localized plasmonic structured illumination microscopy (LPSIM), and coupling of emission of nanoscale objects to localized surface plasmon resonances (LSPRs) in underlying short-period plasmonic metasurfaces. In the first part, we review the main results of the classical imaging theory based on rigorous solutions of the Maxwell equations for point-like sources. The theory accurately describes the near-to-far-field conversion and resonant excitation of whispering-gallery modes in such systems. The point spread functions are calculated and their width is compared with the experimental resolution in microspherical imaging. In the second part, we consider various combinations of microspherical nanoscopy with nanoplasmonics and plasmonic metasurfaces used for illumination or coupling with nanoscale objects. These schemes exemplify the most advanced ways of increasing the resolution far beyond the classical diffraction limit.

---

A. V. Maslov (✉)  
University of Nizhny Novgorod, Nizhny Novgorod, Russia  
e-mail: [avmaslov@rf.unn.ru](mailto:avmaslov@rf.unn.ru)

V. N. Astratov  
Department of Physics and Optical Science, Center for Optoelectronics and Optical  
Communication, University of North Carolina at Charlotte, Charlotte, NC 28223-0001, USA  
e-mail: [astratov@uncc.edu](mailto:astratov@uncc.edu)

© Springer Nature Switzerland AG 2019  
V. Astratov (ed.), *Label-Free Super-Resolution Microscopy*,  
Biological and Medical Physics, Biomedical Engineering,  
[https://doi.org/10.1007/978-3-030-21722-8\\_16](https://doi.org/10.1007/978-3-030-21722-8_16)

## 16.1 Introduction

### 16.1.1 Experimental Results

Since its invention at the end of the sixteenth century, the optical microscope has been continuously improved. At the end of the nineteenth century, several prominent scientists, including Abbe, Helmholtz, and Rayleigh, addressed the question of defining the microscope resolution and finding its ultimate limit. The standard formula for the resolution value  $\delta$  used nowadays states  $\delta = \lambda / (2n \sin \alpha)$ , where  $\lambda$  is the operating wavelength in vacuum,  $n$  is the refractive index of the immersion medium, and  $\alpha$  is the semi-aperture of the objective. In Abbe's approach, the resolution  $\delta$  is the minimal resolvable period of a grating under oblique coherent illumination. Similar expression was obtained by Helmholtz for two self-luminous incoherent points which are more relevant to true imaging [1]. This ultimate resolution corresponds to a finite width of the image of a point source. The finite width appears from the current emission property: the current components with spatial frequency higher than the wavenumber in the surrounding medium cannot emit.

To push the resolution performance beyond  $\lambda/2$ , various new imaging techniques have been proposed and successfully implemented. The last decade of the twentieth century brought super-resolved fluorescence (FL) imaging represented in particular by stimulated emission depletion (STED) [2, 3] and localization microscopies [4, 5], which overperformed the conventional microscopy techniques. Due to extraordinary resolution beyond 20 nm and ability to highlight substructures of interest, these methods pushed the limits of microscopy and resulted in the Nobel Prize in Chemistry awarded in 2014 to the pioneers of these methods. Despite all successes of super-resolved FL microscopy, it has certain drawbacks such as damaging of living biomedical samples by staining them with dyes and photobleaching.

Label-free imaging is, therefore, a preferred method for many applications. However, the arsenal of methods which can be used for increasing the resolution is narrower in this case. In principle, it can be divided into methods which are based on the same far-field linear optics principles, which underlie the classical diffraction limit, and methods involving different physical principles. The examples of the first approach (far-field principles) are based on using solid immersion lenses (SIL) developed [6] in the early 1990s and structured illumination microscopy (SIM) developed [7–11] in the early 2000s. Examples of the second approach include the methods which are based on using the near fields as in near-field scanning optical microscopy (NSOM) [12], nonlinear optics [13–15], and nanostructures with engineered dispersion properties such as nanoplasmonic arrays, metamaterials and metasurfaces. Nanostructure-based optical elements include surface plasmon-polariton lens [16], periodic metallo-dielectric structures [17], far-field superlens [18, 19], hyperlens [20–23], Eaton lens [24], and adiabatic structures [25]. It should be noted, however, that although the nanoplasmonic and metamaterials-based lenses represent exciting new concepts, their deployment faces such barriers as the narrow spectral range of operation, ohmic losses, and challenging fabrication.

In this regard, the miniaturization of SILs that took place around 2009–2011 was an important step in developing super-resolution methods because it demonstrated that the miniature contact microlenses capable of broadband imaging can be fabricated by the standard surface patterning techniques [26–28]. The nanoscale lenses not only can be put in a very close contact with the object, but also give rise to various near field effects related to their nanosize curvature and small focal distance. The use of nano-SILs, however, did not provide any significant resolution improvement over the immersion effect.

In 2011, the imaging through dielectric microspheres in contact with an object was demonstrated [29]. This can be viewed as a natural development of the SIL concept in which the microsphere forms a magnified virtual image of the object with a participation of its near fields. This pioneering work immediately captured the attention of researchers due to significant improvement in quality, optical contrast, and resolution of the images. Silica microspheres in air were used in [29]. After that, it was shown that by using semi-immersed microspheres, one can increase the image contrast [30]. A significant advancement in this area was a proposal [31] of using high-index ( $n > 1.8$ ) microspheres which are fully liquid-immersed [32–34] or embedded in elastomeric slabs [35–39]. It made possible FL imaging of subcellular structures, viruses and proteins in a liquid phase [40–44] and confocal imaging [33, 45] of structures, which cannot be resolved by conventional microscopes. A comparison of SIL and microspherical imaging indeed showed significant resolution improvement in the later regime [33]. Coated high-index microspheres also showed subwavelength resolution [46].

A particularly important aspect of these studies was an experimental quantification of resolution. Initially, it was based on discernibility of small features such as gaps separating metallic nanodisks or nanoholes in plasmonic arrays [29, 32, 47]. In this approach, the resolution was associated with the minimal discernable feature sizes in the optical images of such objects. The problem of this approach can be illustrated, for example, by taking two touching circular objects. Their image calculated by a convolution with the point spread function (PSF) shows that the intensity profile through the centers of the circles actually displays a central dip. If such a dip was observed experimentally, the simplified method based on discernibility of the smallest feature would have suggested an interpretation that the zero gap between the cylinders became “resolved” or “discerned”. This clearly illustrates the contradictions and limitations of this method because it would have meant that the infinite resolution was achieved. It is clear that this simplified method can be used with extreme caution and only for semi-quantitative resolution analysis. This was likely the reason for a broad variation of resolution claims from  $\lambda/7$  [32] to  $\lambda/8 - \lambda/14$  [29] to  $\lambda/17$  [45], which were made during the initial development of microspherical nanoscopy.

A more rigorous resolution quantification method for arbitrarily shaped objects requires taking a convolution with the two-dimensional (2D) PSF. The images need to be calculated for different PSF widths and compared with the experimental images to determine the PSF width providing the best fit for the experimentally observed images. Based on the Houston resolution criterion, such PSF width can be accepted as the resolution of the system. This approach is well known in the far-field optics, but

the similar approach can be used for characterizing the resolution in the case of super-resolution imaging with the difference that the PSF width in the latter case would become narrower than the diffraction-limited resolution. Initially, this approach was realized using simplified convolution with 1D PSF [33]. Soon after it was generalized for arbitrarily shaped objects using convolution with 2D PSF [34, 37].

Experimentally, the resolution depends on many factors: (a) type of the object—near fields can be resonantly enhanced in nanoplasmonic structures, (b) refractive indices of the microlens and surrounding medium—optimal index contrast for virtual imaging is within 1.3–1.7 range, but higher background index can facilitate higher resolution, and (c) type of illumination—confocal can provide a better signal-to-noise ratio compared to widefield, the excitation of Mie resonances in the microsphere and special (oblique or coherent) illumination can favor higher resolution. Since in different experimental studies these conditions and parameters varied greatly, presenting a coherent picture of the developments in this area is rather complicated. We selected only papers which included some resolution quantifications and combined the results in Table 16.1. Besides the resolution values, the table contains the information about the imaged objects, the size and material of the microspheres, the refractive indices of the microspheres and the surrounding media, and the type of illumination used.

The main conclusion of Table 16.1 is that microspherical nanoscopy provides an extremely simple and versatile method of imaging which works similar to SIL, but with somewhat higher resolution. The resolution advantage is particularly well studied for nanoplasmonic objects where the resolution  $\sim \lambda/6 - \lambda/7$  was reproduced in several studies using rigorous resolution criteria. Microspheres provide good near-field coupling conditions with the nanoscale objects (sphere-to-object distance below  $\lambda/2$ ) due to small size of the contact area. The drawback, however, is that the field of view is limited by about a quarter of the sphere diameter [32]. It has been demonstrated that the field of view can be increased by translating the microspheres by a variety of techniques [48–52] followed by stitching the corresponding images.

The simplicity of microspherical imaging implies that it can be combined with practically any other method of resolution enhancement known in standard widefield microscopy. Combination with the confocal microscopy [33, 45] allows increasing the signal-to-noise ratio. Improving the resolution is also possible in confocal microscopy, but it requires a significant reduction of the confocal pinhole with the associated reduction of the signal. Another example is the combination with interferometric measurements which allows increasing the axial resolution [54–56]. One more example is the combination with structured illumination microscopy (SIM) [7–11], especially in the case of plasmonic structures with localized surface plasmon resonances (LSPRs). This idea was implemented for imaging through microspheres, where the resolutions  $\sim \lambda/10$  was reported using localized plasmonic structured illumination microscopy (LPSIM) with post-imaging processing [57]. A different approach was developed for imaging nanoscale objects with emission resonantly coupled to LSPRs in the underlying plasmonic metasurfaces with ultrashort periods [44]. It can be shown that for periods shorter than 150 nm, the coupling to the so-called surface lattice resonances becomes inefficient in the given detection range, and the fluorescence enhancement can be achieved due to coupling to the closest

**Table 16.1** Summary of experimental results of microscope-based imaging. The resolution estimates are based on experimentally discernable minimal feature sizes or on convolution with 1D or 2D PSFs. Notation: minimally resolved features (MRF), barium-titanate glass (BTG), isopropyl alcohol (IPA), polydimethylsiloxane (PDMS), Blu-ray disc (BRD), central processing unit (CPU), localized plasmonic structured illumination microscopy (LPSIM), confocal laser scanning microscopy (CLSM), post-imaging processing (PIP), Appl. Phys. Lett. (APL), Light: Sci. Appl. (LSA), one-dimensional convolution (1D conv.), two-dimensional convolution (2D conv.). Reproduced from [53] with permission of the American Physical Society

| Reference  | Object                               | MS material/ background, size                                  | Illumination  | Modality                            | Estimated resolution                          |
|--|--------------------------------------|--|---|-------------------------------------|---|
| Wang et al., Nat. Commun. <b>2</b> , 218 (2011)  | Gratings, plasmonic structures, BRD  | SiO <sub>2</sub> /air, $D \sim 5 \mu\text{m}$                  | White light, 400–750 nm                             | Widefield: transmission, reflection | $\lambda/8\text{--}\lambda/14$ (MRF)          |
| Darafsheh et al., APL <b>101</b> , 141128 (2012)   | Plasmonic dimers, BRD                | BTG/IPA, $D \sim 2\text{--}220 \mu\text{m}$                    | White light, 400–750 nm                             | Widefield: reflection               | $\lambda/7\text{--}\lambda/4.5$ (MRF)         |
| Li et al., LSA <b>2</b> , e104 (2013)  | Viruses                              | BTG/H <sub>2</sub> O, $D \sim 100 \mu\text{m}$                 | White light: 390–700 nm                             | Widefield: reflection               | $\lambda/6$ (MRF)                             |
| Yang et al., Small <b>10</b> , 1712 (2014)   | FL labeled, nanospheres, subcellular | BTG/H <sub>2</sub> O, $D \sim 60 \mu\text{m}$                  | FL, 680 nm  | FL imaging                          | $\lambda/7$ (MRF)                             |
| Krivitsky et al., Sci. Rep. <b>3</b> , 3501 (2013)   | Plasmonic dimers, grating            | SiO <sub>2</sub> /air, $D \sim 7 \mu\text{m}$                  | White light: 400–750 nm                             | Scanning widefield, reflection      | $\lambda/10\text{--}\lambda/17$ (MRF)         |
| Darafsheh et al., APL <b>104</b> , 061117 (2014)   | Plasmonic dimers                     | BTG/IPA, $D \sim 10\text{--}53 \mu\text{m}$                    | Narrowband, 405 nm                                  | CLSM                                | $\lambda/6$ (1-D conv.)                       |
| Yan et al., ACS Nano <b>8</b> , 1809 (2014)  | Plasmonic nanoholes, nanowires       | Fused SiO <sub>2</sub> /air, $D = 2.5\text{--}7.5 \mu\text{m}$ | Narrowband, 408 nm                                  | CLSM                                | $\lambda/17$ (MRF)                            |
| Allen et al., Ann. Phys. <b>527</b> , 513 (2015)   | Plasmonic dimers                     | BTG/PDMS, $D \sim 5\text{--}53 \mu\text{m}$                    | Narrowband, 405 nm                                  | CLSM                                | $\lambda/6\text{--}\lambda/7$ (2-D conv.)     |
| Allen et al., Opt. Express <b>23</b> , 24484 (2015)  | Plasmonic dimers                     | BTG/IPA, $D \sim 8\text{--}10 \mu\text{m}$                     | Narrowband, 405 nm                                  | CLSM                                | $\lambda/6.6\text{--}\lambda/7.3$ (2-D conv.) |
| Wang et al., Nat. Commun. <b>7</b> , 13748 (2016)  | BRD, CPU, nanowires, FL cells        | BTG/H <sub>2</sub> O, $D \sim 27\text{--}70 \mu\text{m}$       | White light, centered at 550 nm                     | Scanning widefield, reflection      | $\lambda/6.3\text{--}\lambda/8.4$ (2-D conv.) |
| Yang et al., Nano Lett. <b>16</b> 4862 (2016)  | Silicon grating                      | BTG/H <sub>2</sub> O, $D \sim 3\text{--}21 \mu\text{m}$        | White light, 400–700 nm                             | Widefield: reflection               | $\lambda/4\text{--}\lambda/7$ (1-D conv.)     |
| Astratov et al., Proc. SPIE 10077, 100770S (2017), A. Brettin et al., APL 114, 131101 (2019) | FL labeled, proteins or nanospheres  | BTG/plastic, $D \sim 8\text{--}20 \mu\text{m}$                 | FL, 604–644 nm (proteins), 505–555 nm (nanospheres) | Widefield FL, LPSIM, without PIP    | $\lambda/7$ (2-D conv.)                       |
| Bezryadina et al., Nanoscale <b>9</b> , 14907 (2017)   | FL labeled nanospheres               | TiO <sub>2</sub> /H <sub>2</sub> O, $D \sim 20 \mu\text{m}$    | FL, $\sim 570$ nm                                   | Widefield FL, LPSIM, with PIP       | $\lambda/10$ , (2-D conv.)                    |

LSPRs in the underlying array [44] rather than due to collective bandstructure coupling effects. A particularly attractive feature of the latter mechanism is that it does not require post-imaging processing for reconstructing the super-resolved images. Most of this chapter (Sects. 16.2, 16.3, and 16.4) is devoted to the theoretical models of the observed super-resolution and the remaining part (Sect. 16.5) reviews several experimental results related to a combination of microspherical nanoscopy with nanoplasmonics and plasmonic metasurfaces.

### 16.1.2 Theoretical Modeling

The ability to see deeply subwavelength features through dielectric microspheres naturally prompted a search for its physical explanation. It was suggested that the observed super-resolution is related to the ability of microspheres to form photonic nanojets [29]. If the width of photonic nanojets is strongly subwavelength, then the image produced by a point source can also be subwavelength. The sharp focusing as the origin of super-resolution was also used in several subsequent studies [58–68]. However, the quantitative analysis reveals some problems with this analogy, including the fact that the width of photonic nanojets is not significantly smaller than the wavelength [69–73]. When the nanojet maximum is away from the surface, the nanojet width is  $\sim\lambda/2$ . When the nanojet maximum is on the surface, it becomes narrow and its width can be as small as  $\lambda/(2n)$ , where  $n$  is the refractive index of the microsphere. Thus, for typical  $\text{SiO}_2$  microspheres with index  $n = 1.46$ , the width becomes  $\sim\lambda/3$  which is significantly larger than the experimental resolution values. Another issue is that the focusing of light and imaging are two different problems. It was also suggested that the super-resolution can be related to the transformation of the evanescent waves to propagating at the curved surface of the microsphere [74]. If this mechanism works, then the microsphere can perform as a near-field probe similar to that in NSOM.

With the lack of a simple physical explanation of the super-resolution in microspherical nanoscopy, some efforts have been undertaken to model it. The imaging of a point source near a microsphere was addressed using the multipole expansion based on spherical harmonics [75]. The theoretical results for a microsphere with  $D = 4.74 \mu\text{m}$ ,  $n = 1.46$  showed that one cannot reach sub-100 nm resolution using the standard two-point resolution criterion. Slightly higher resolution, but still below the values claimed in the experiments, was achieved using microsphere resonances (the second radial order resonance was considered). The imaging of dipoles near microspheres was also studied using finite element method (FEM) [76]. The resolution and magnification were studied for various refractive indices of the microsphere and the substrate as well as for the different dipole orientations. The resolution of dipoles was found to be in the range  $0.24\lambda - 0.3\lambda$ . It was also suggested that since small metal nanostructures can emit as some effective dipoles located in their centers, then the center-to-center separation of  $0.24\lambda$  between the metal nanostructures can correspond to a much smaller edge-to-edge distance which was perhaps observed

in the experiments. An entire microsphere-based microscope system, including both the focusing (illumination) and imaging subsystems, was studied in [77] using multipole and plane wave expansions. The resolution of about  $\lambda/4$  was obtained in the regime in which the resonant modes of the microsphere are excited.

Coherent effects may affect resolution as well. In the total internal reflection dark-field microscopy, coherent illumination can give rise to the resolution higher than the classical limit [78]. The origin of enhancement is related to the out-of-phase excitation of closely spaced objects and their subsequent re-radiation. Coherent re-radiation, however, introduces image distortions and artifacts [79]. The problem of imaging coherent currents through microspheres was considered in [80], where it was shown that one obtains deeply subwavelength resolution accompanied by image distortion. Modeling of coherent emission of several closely spaced point sources located near a microsphere (in 2D model) using COMSOL Multiphysics also showed the capability of their resolution when the emission phase is shifted by  $\pi$  between the neighbors [81, 82].

Using microspheres that provide a high-index contrast relative to the environment, such as  $n = 2$  microspheres in the air, gives rise to some interesting effects. In particular, one obtains images of objects when focusing the microscope objective just above the particle in the upright system. The resolution can reach about  $\lambda/4$  if the illumination is tuned at the wavelengths of the internal microparticle resonances [83]. This means that the resolution enhancement does not come only from the immersion effect.

In this chapter, we present an analysis of the performance of microspherical nanoscopy using various models. In Sect. 16.2 we begin with a simple geometrical optics. In Sect. 16.3 we move to imaging point sources emitting near microspheres, as in the classical approach used for resolution definition. In Sect. 16.4 we quantify the resolution in terms of the SIL concept. We also discuss the possible role of coherence. In Sect. 16.5, we consider the combinations of microspherical nanoscopy with nanoplasmonics and plasmonic metasurfaces, which represent the most advanced way of increasing the resolution far beyond the classical diffraction limit.

## 16.2 Geometrical Optics of Contact Microspheres

Geometrical optics provides the basic understanding of imaging and, therefore, it is useful to apply it to microspherical nanoscopy. Certainly, its results have to be treated with caution. While the size 2–20  $\mu\text{m}$  of typical microspheres exceeds the typical operating wavelengths  $\lambda \sim 600 \text{ nm}$ , it may not be sufficiently larger than  $\lambda$  for the geometrical optics approximations. On the other hand, rather large microspheres with sizes  $\sim 60 \mu\text{m}$  are also used [58].

In the approximation of geometrical optics, a point-like source near a microsphere emits rays, see Fig. 16.1b. The ray paths can be found directly using the Fresnel refraction formulas. Upon exiting the microsphere, the rays are focused by the lens on the detector. Extending the exiting rays backwards, the location of the virtual

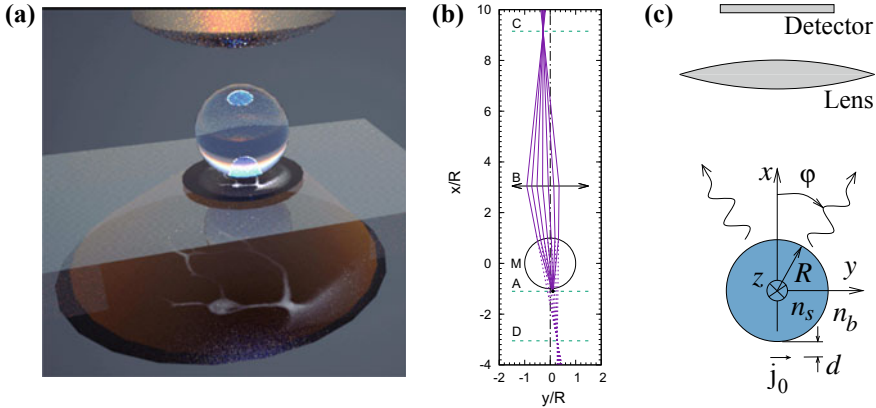


**Fig. 16.1** **a** Illustration of imaging with a microsphere in contact with a sample. **b** Typical ray tracing. The rays originate from the point source in the object plane A separated from the microsphere M by  $d/R = 0.1$ . The source is displaced from the optical axis by  $0.1R$ . The rays undergo refraction at the microsphere surface. Upon exiting the microsphere the rays are collected by the lens B and projected into the detector C. The intersections of the backwardly propagating rays form the location D of the virtual image. **c** Geometry used for the rigorous calculation of the image produced by the current source  $j_0$  emitting near the microsphere. Reproduced from [53] with permission of the American Physical Society

image is obtained. If the plane of focus for the external imaging system (lens and detector) coincides with the plane of the virtual image, exactly the same image (except for possible inversion and magnification) will be formed on the detector. The backward propagated rays do not intersect in one single virtual point. Instead, their multiple intersections lie close to each other and form a spot. This corresponds to the presence of aberration. The spot area depends on the location of the original point source and the angular spread of the rays. For the parameters used in Fig. 16.1b the spot size is quite small.

The dependence of the virtual plane location  $x_v$  on the point-to-microsphere distance  $d$  for several values of the microsphere refractive index  $n_s$  is shown in Fig. 16.2. In all cases, the virtual image location moves from the microsphere quite rapidly with increasing  $d$ . For example, for  $n_s = 1.4$  the relative distance  $|x_v|/R - 1$  of the virtual plane changes from 1.34 to 1.97 when  $d/R$  increases from 0 to only  $d/R = 0.1$ . For higher  $n_s$ , the change is even more rapid. One can also calculate the magnification  $M$  which is defined as the transverse displacement of the virtual point divided by the displacement of the emitting point. Increasing  $d$  also increases magnification, see Fig. 16.2b. However, even for  $d = 0$  and  $n_s = 1.4$  one obtains  $M = 2.3$ . One can also obtain the magnification  $M$  from a simple formula

$$M = -\frac{|x_v|}{R + d}, \tag{16.1}$$

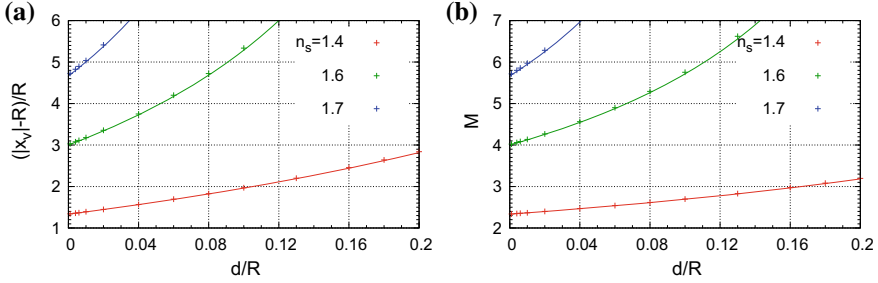


**Fig. 16.2** **a** Relative distance between the virtual image plane position  $x_v$  and the microsphere surface as a function of the source-to-microsphere distance  $d$  for several values of the microsphere refractive index  $n_s$ . **b** Image magnification  $M$  as a function of  $d$ . The dots in both frames show the results of ray tracing obtained for a point object displaced by  $0.01R$  from the optical axis. The lines show the result of (16.2) and (16.1). In all cases the background refractive index is  $n_b = 1$

where  $x_v$  is the position of the virtual plane. The minus sign in (16.1) denotes the image inversion. Calculating  $x_v$  one can arrive at the following formula [37]:

$$M = -\frac{n_r}{2 - n_r - 2(n_r - 1)d/R}, \quad n_r = \frac{n_s}{n_b}. \quad (16.2)$$

As shown in Fig. 16.2, the results of (16.1) agree very well with the values calculated numerically using ray tracing. Note that both  $x_v$  and  $M$  diverge at some  $n_r$ . For  $d/R = 0$ , the divergence takes place at  $n_r = 2$ . For  $d/R > 0$ , the corresponding value of  $n_r$  decreases.

## 16.3 Diffractive Optics of Contact Microspheres

### 16.3.1 Wave Scattering and Focusing

The interaction of microspheres with incident light allows one to understand the role of illumination in microspherical nanoscopy. As a simple theoretical model we can limit the treatment by considering a 2D geometry in which the fields and the dielectric constant do not change along the  $z$  direction, see Fig. 16.1c. We consider the transverse magnetic (TM) field with  $\{E_x, E_y, H_z\}$  components. The 2D case is sufficient to understand the basic wave optics effects.

Assuming a plane wave incident on the particle, we can expand the fields into the cylindrical functions inside and outside the particle. After matching the fields by the boundary conditions we can find the expansion coefficients. This allows one to obtain the scattered fields. The scattering cross section is shown in Fig. 16.3a. It shows large-scale oscillations and small narrow peaks. The large-scale oscillations

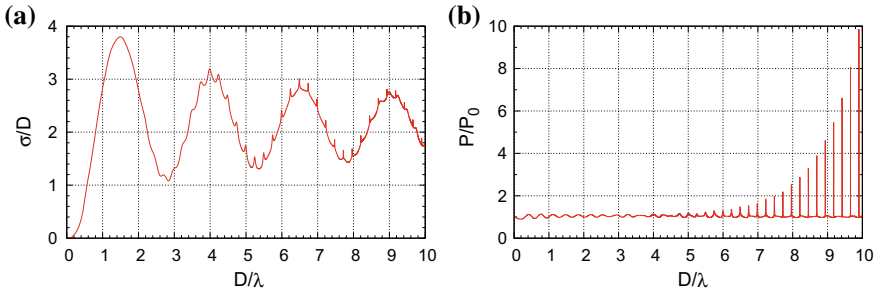


**Fig. 16.3** **a** Scattering cross section  $\sigma$  for a TM polarized wave incident on a cylinder and **b** power  $P$  emitted by a point source separated by  $d/\lambda = 0.1$  from the cylinder as functions of the size parameter  $D/\lambda$ . The power is normalized to the emitted power in free space  $P_0$ . The refractive indices are  $n_s = 1.4$  and  $n_b = 1$

are related to the interference of the light passed through the particle and through the background and have a period of  $D/\lambda \approx 1/(n_s - n_b) = 2.5$ . The small narrow peaks are signatures of various resonances excited in the particle. The resonances are characterized by their radial and azimuthal numbers. For small radial numbers and large azimuthal numbers the resonant fields propagate near the periphery of the particle. Such modes are referred to as whispering-gallery modes (WGMs). Despite quite significant  $Q$ -factors, the resonances are barely seen due to their weak coupling to the incident plane wave. However, emitters in the proximity of the particle can provide a much larger efficiency of WGM excitation, as illustrated in Fig. 16.3b.

Besides the ability of dielectric particles to support resonant modes, they are also capable of focusing the incident light. Such focusing is similar to that of an ordinary lens. The focused field distributions in the case of microspheres are often referred to as photonic nanojets [69, 73, 84]. The focusing properties depend on the relative size parameter  $kR$  and refractive indices  $n_s$  and  $n_b$ . The jets can be formed with or without resonances in the particle [72]. For small particles, the maximum of the jet intensity is located near the particle surface. With growing size parameter  $kR$ , the maximum moves away from the surface. Typically, the transverse width of the field intensity at maximum is about  $\lambda/3 - \lambda/2$ . Initially [29], the ability to form nanojets by microsphere was proposed to be directly related to super-resolution properties based on the analogy with the reciprocity principle in optics. However, the discrepancy between the rather large nanojet width and the imaging resolution of about  $\lambda/6 - \lambda/7$  [34] shows that this analogy is incomplete and that the calculation of photonic nanojets is not a substitute for the resolution analysis.

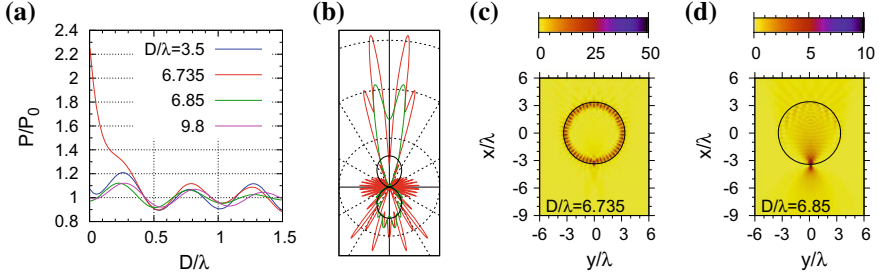


**Fig. 16.4** **a** Power emitted by a point source as a function of distance  $d$ . The case  $D/\lambda = 6.735$  is resonant, the others are nonresonant. **b** Angular distribution of the emitted power  $p(\varphi)$  at  $d/\lambda = 0.1$  for  $D/\lambda = 6.735$  (red),  $D/\lambda = 6.85$  (green) and in free space (black) for the current source with the same amplitude. **c** and **d** Spatial distribution of  $|H_z(x, y)/H_0|^2$ , where  $H_0 = j_0\omega/c^2$ , for  $d/\lambda = 0.1$ . The divergent intensities created by the point sources in frames **c** and **d** were limited to the colorbar ranges

### 16.3.2 Point-Source Emission and Field Distribution

The classical resolution theory is based on finding the images of point-like emitters. It is interesting to apply this model to microspherical imaging by solving rigorously the Maxwell equations. This accounts for various near-field effects related to the subwavelength gaps between the object and particle. To do so within a 2D theory one can take a point-like current source located near the dielectric particle:

$$\mathbf{J}(x, y) = j_0 \hat{y} \delta(x + R + d) \delta(y), \quad (16.3)$$

where  $j_0$  is the amplitude of the current,  $\delta(\xi)$  is the Dirac delta function, and the unit vector  $\hat{y}$  defines the current polarization. To find the field created by current (16.3) we can also apply the standard series expansion into the cylindrical functions. By matching the fields at the particle surface we can find the expansion coefficients. Using the fields, one can calculate the emitted power, which is shown in Fig. 16.4a. For non-resonant frequencies, the power dependence on the gap  $d$  shows some oscillations around  $P/P_0 \sim 1$  related to interference. The corresponding field distribution, see Fig. 16.4d, shows the divergence at the particle location as expected for a point source. At resonance, the emitted power increases very strongly as the source approaches the particle surface. This corresponds to a very efficient excitation of the WGMs which is seen from the field distribution in Fig. 16.4c. Such redirection of power into resonant modes can significantly affect the imaging properties. The asymptotic far-field behavior

$$H_z(x, y) = \frac{f(\varphi)}{\sqrt{k_b \rho}} e^{i k_b \rho - i \pi / 4} \quad (16.4)$$

where  $k_b = n_b k$  and  $k = \omega/c$ , allows one to find the angular distribution function  $f(\varphi)$  from the expansion. The power is emitted at all possible angles and can be

represented as

$$P = \int_0^{2\pi} d\varphi p(\varphi), \quad p(\varphi) = \frac{c^2}{2\pi\omega\varepsilon_b} |f(\varphi)|^2, \quad (16.5)$$

where  $p(\varphi)$  is the angular power density and  $\varphi$  is the angle with respect to the  $x$  axis. Figure 16.4(b) shows  $p(\varphi)$ . In the absence of the particle, the power distribution is  $p(\varphi) \sim \cos^2 \varphi$ . In the nonresonant case, the power emission in the upper half-space becomes narrow and multiple lobes appear. In the resonant case, the emission distribution also shows rather narrow but small peaks, which can be attributed to the reemission of the standing WGMs excited in the particle.

## 16.4 Microsphere as a Solid Immersion Lens: Resolution Analysis

### 16.4.1 Imaging of a Point Source

A basic characteristic of any imaging system is the response to a point source, called the point spread function (PSF). For incoherent imaging, it is sufficient to know the image intensity created by a point source. For coherent imaging, one needs the complex field distribution which includes the magnitude and phase of the created field on the detector. The knowledge of PSF allows one to find the incoherent images created by extended objects by performing the convolution of the PSF and the objects.

Here we discuss the PSF of a microsphere lens within our 2D model. To achieve this we can take the far-field distribution  $f(\varphi)$  created by current source (16.3). The propagating field in the background material can be represented as

$$H_z(x, y) = \int_{|g| < k_b} dg e^{ihx + igy} \tilde{H}_z(g), \quad (16.6)$$

where  $\tilde{H}_z(g)$  is the Fourier component and  $g^2 + h^2 = k_b^2$ . Evaluating the integral in (16.6) asymptotically at  $\rho \rightarrow \infty$  and comparing with (16.4) give us the Fourier component

$$\tilde{H}_z(g) = \frac{f(\varphi)}{\sqrt{2\pi} k_b \cos \varphi}, \quad g = k_b \sin \varphi. \quad (16.7)$$

An objective lens collects the far field and forms an image on the detector. For an ideal objective lens with  $\text{NA} = 1$  and without magnification the image is equivalent to the intensity distribution of the backpropagated far field in the plane of focus (defined by  $x$ ). The knowledge of  $\tilde{H}_z$  allows us to formally backpropagate the field to any point in space and find the image intensity

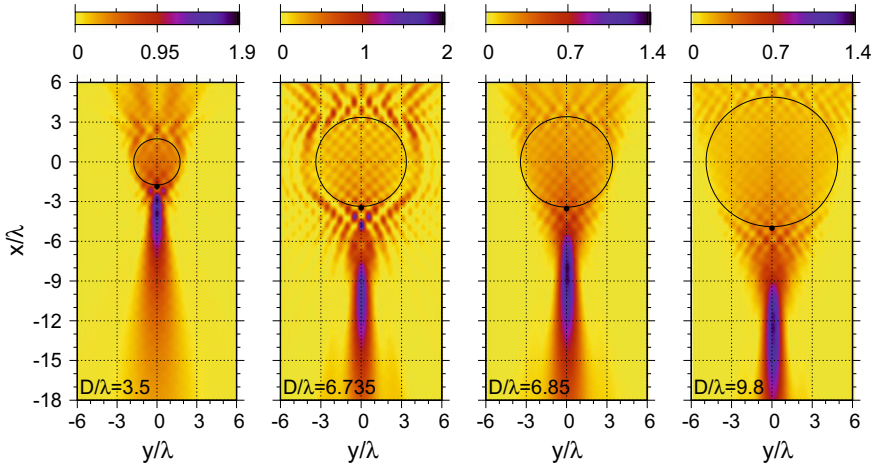


**Fig. 16.5** Images of point sources separated by  $d/\lambda = 0.1$  from the particle for four values of  $D/\lambda$  (shown in the frames). The case  $D/\lambda = 6.735$  is resonant, the others are nonresonant. The vertical axis  $x$  is the plane-of-focus coordinate and the horizontal axis  $y$  is the location in that plane. The black dots show the sources and the circles show the microparticles

$$I(x, y) = |H_z(x, y)|^2. \quad (16.8)$$

The backpropagated field at some location differs from the actual field there since this procedure is equivalent to image formation and is not a solution of an inverse scattering problem. If the far field is generated by some sources in free space, the sharpest image is observed when the plane of focus passes through the sources. Thus, by scanning over various positions  $x$  of the plane of focus we search for the location of the far-field sources. Generally, such scanning mimics finding the sharpest image in experimental microscopy. Any magnification of the objective lens only scales the image on the detector, i.e., along  $y$ .

Typical images of point objects are shown in Fig. 16.5. The geometrical optics formulas for  $d/\lambda = 0.1$  predict the virtual images at  $x_v/\lambda = 4.67$  for  $D/\lambda = 3.5$ , at  $x_v/\lambda = 8.56$  for  $D/\lambda = 6.85$ , and  $x_v/\lambda = 12.0$  for  $D/\lambda = 9.8$ . These numbers agree rather well with the maxima of the virtual images in Fig. 16.5. The resonant case,  $D/\lambda = 6.735$ , shows rather significant deviation from the geometrical optics result  $x_v/\lambda = 8.42$ .

To evaluate the resolution qualitatively Fig. 16.6 shows the cuts through the PSFs in Fig. 16.5. For the plane-of-focus values near the particle, the images show multiple lobes which significantly reduce the image recognition. Rather away from the particle, near the locations of the virtual images, the PSF consists of a single peak. The resolution can be found as the width of the peak  $\mathcal{W}$  divided by the magnification  $M$ . The results of image analysis at various plane-of-focus positions are collected in Table 16.2. The resolution  $\mathcal{W}/(M\lambda)$  is around 0.42 – 0.45 and is comparable for small  $D/\lambda = 3.5$  and larger  $D/\lambda = 6.85, 9.8$  particles. In the resonant case, one

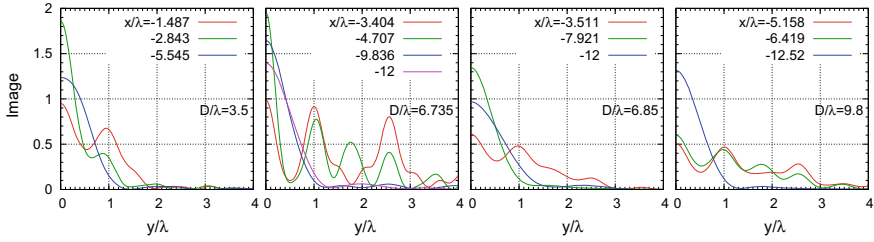


**Fig. 16.6** Cuts through the images shown in Fig. 16.5

**Table 16.2** Properties of images shown in Fig. 16.6 at various sizes  $D/\lambda$  and plane-of-focus (virtual plane) positions  $x$  for a fixed  $d/\lambda = 0.1$ .  $\mathcal{W}$  is the width of the image,  $M$  is the magnification

|   | $D/\lambda$ | $-x/\lambda$ | $\mathcal{W}/\lambda$ | $M$  | $\mathcal{W}/(M\lambda)$ |
|---|-------------|--------------|-----------------------|------|--------------------------|
| 1 | 3.5         | 2.843        | 0.635                 | 1.54 | 0.413                    |
| 2 | 3.5         | 5.545        | 1.30                  | 3.00 | 0.433                    |
| 3 | 6.735       | 4.707        | 0.435                 | 1.36 | 0.320                    |
| 4 | 6.735       | 9.836        | 0.998                 | 2.84 | 0.352                    |
| 5 | 6.735       | 12           | 1.21                  | 3.46 | 0.348                    |
| 6 | 6.85        | 7.921        | 1.04                  | 2.25 | 0.462                    |
| 7 | 6.85        | 12           | 1.49                  | 3.40 | 0.438                    |
| 8 | 9.8         | 12.52        | 1.12                  | 2.50 | 0.446                    |

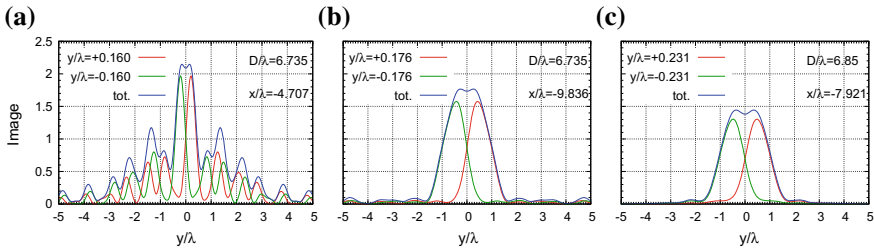


**Fig. 16.7** Images created by two incoherent point sources individually and their superposition for several parameter sets listed in Table 16.2. In the legends, the values  $y/\lambda$  are the displacements of the sources from the optical axis and  $x/\lambda$  are the plane-of-focus locations

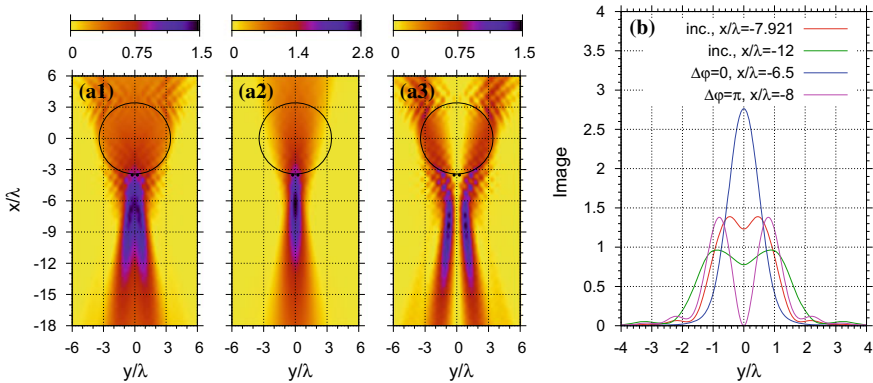
can obtain some enhancement up to  $\mathcal{W}/(M\lambda) \sim 0.32$  but multiple sidelobes may significantly reduce the image quality. This value can be further increased if imaging performed in immersion mode  $\epsilon_b \neq 1$  using high-index microparticle. With the immersion enhancement equal to  $\sqrt{\epsilon_b} \approx 1.3 - 1.5$  the resolution values obtained from the classical incoherent theory change from  $\sim \lambda/4$  to  $\sim \lambda/5.6$  (for the same index contrast 1.4). However, they still remain worse than the resolution of  $\lambda/7$  estimated from the experiments.

Figure 16.7 shows the images obtained for several cases listed in Table 16.2 when the two incoherent sources are separated by the corresponding values of  $\mathcal{W}/(M\lambda)$  which are defined as resolution. In all cases, the images form a weak but noticeable dip in the center indicating the possibility to resolve the sources. However, in the resonant case, Fig. 16.7a, the image of the two sources have significant artifacts in the form of the sidelobes.

### 16.4.2 Coherent Versus Incoherent Imaging

The results of the classical imaging theory based on point emission near the microparticle predicts resolution which is worse than the experimental values even if we take into account the increase of the background index in the case of high-index liquid immersed microspheres. However, there can be factors that may play a significant role in microspherical imaging and yet are left out of this basic theory. One of such factors is the presence of coherence. Coherent illumination in total internal reflection dark-field microscopy results in subwavelength resolution of 190 nm fluorescent polystyrene beads [78]. However, the resolution enhancement comes at a price as the images become distorted [79]. In [80], the role of coherence in microspherical imaging was also studied using the model of coherent current sources emitting near a microsphere. References [81, 82] studied the imaging of multiple point sources which emit in some specific phases.

To illustrate the role of coherence, Fig. 16.8 compares the images of two sources separated by  $\lambda$  and emitting incoherently and coherently. The incoherent sources can



**Fig. 16.8** **a** Images of incoherent (a1) and coherent (a2, a3) point emitters. The coherent sources oscillate in phase ( $\Delta\phi = 0$ ) in (a2) and out of phase ( $\Delta\phi = \pi$ ) in (a3). The particle size is  $D/\lambda = 6.85$ , the separation between the sources is  $\lambda/2$ , the distance from the particle to the object plane is  $d/\lambda = 0.1$ . The vertical axis  $x$  is the plane-of-focus coordinate and the horizontal axis  $y$  is the location in that plane. **b** Cuts at some fixed values of  $x$  through the images shown in frames (a1, a2, a3)

be resolved if the plane of focus is below  $x/\lambda \approx -7$ . The in-phase source cannot be resolved at all for the given parameters. The out-of-phase sources clearly create images with the best resolution. In fact, the resolution persists if one moves the out-of-phase sources significantly closer but the emission intensity reduces quite drastically and the peak-to-peak distance will not be equal to the distance between the sources. The coherent emission is likely to be present when imaging plasmonic structures.

## 16.5 Beyond Solid Immersion Lens: Plasmonic Contributions

Previous analysis in this Chapter is based on exact numerical solution of the Maxwell equations and the textbook definition of resolution introduced for incoherent point sources. Perhaps not surprisingly, we showed that the classical resolution in MN is reasonably well described by the SIL concept. It should be noted that the SIL concept has been introduced in the beginning of the 1990s for hemispherical and superspherical lens shapes which have the advantage of collecting the light from the object in half of the space with index  $n > 1$ , meaning that  $\theta$  approaching  $\pi/2$  in the Abbe's limit  $\lambda/(2n \sin \theta)$ . These lenses are represented by hemispheres and truncated spheres, respectively, and they have a flat base which should be closely attached to the substrate to provide the optical near-field coupling conditions with the object located on this substrate. Similar concept can be applied for imaging by dielectric microspheres. Due to their compact size, however, they have much smaller near-field coupling region with the substrate. At first glance, it can be viewed as a disadvantage of microspheres due to the resulting field of view being limited by a quarter of their diameters. However, the smallness of the contact region simplifies the minimization of the object-to-lens distance enabling better near-field coupling. Also, the spheres can be translated along the substrate by a variety of techniques, and the corresponding super-resolved images can be stitched increasing the field of view. Another potential concern regarding the resolution comparison of MN with hemispherical and superspherical SILs is related to spherical aberrations of microspheres. However, for mesoscale spheres, the problem of imaging can be solved exactly using numerical methods which means that the images are calculated taking into account all aberrations.

The results of resolution quantification for microspheres obtained by numerical solution of the Maxwell equations are found to be in a reasonable agreement with the SIL model. The classical resolution of mesoscale silica spheres with  $n \sim 1.5$  was found to be close to  $\sim \lambda/3$ . The resolution of high-index ( $n \sim 2$ ) liquid-immersed or slab-embedded microspheres with the same index contrast as silica in air can be increased up to  $\sim \lambda/5.6$  in the case of imaging performed under resonance with WGMs. The nonresonant resolution is slightly lower, but it is still rather close to the estimations ( $\sim \lambda/4$ ) based on the SIL model. Coherent imaging under oblique

incidence or other conditions allow resolving much finer features, but this type of imaging should not be confused with the classical resolution defined for incoherent point sources.

It is important to note that although the enhancement of the classical resolution offered by high-index ( $n = 2$ ) microspheres can be viewed as modest, there are many straightforward techniques to increase the resolution much further by combining MN with a series of ideas and methods developed for increasing the resolution in conventional microscopy. As we discussed above, the MN drawback related to its limited field of view can be solved by developing the surface scanning technologies. On the other hand, for each fixed position of dielectric microsphere MN represents a simplest widefield and white light imaging technique similar to standard microscopy. Another limitation in comparison with the standard microscopy is the fact that MN works for imaging objects located at  $\sim\lambda/2$  proximity to the surface of the spheres. This condition can be realized by reducing the thickness of the samples (by pressing slightly the spheres or slabs with embedded spheres into the substrate). In the case of thick samples, it can be achieved by depositing the investigated biomedical samples directly on the surface of the microspheres. This can be viewed as a disadvantage or a “price to pay” in comparison with the convenience of conventional microscopy. However, from the pure imaging point of view, MN has all other advantages of conventional microscopy including parallel acquisition with a low-intensity level not damaging for the biomedical objects. Another advantage is related with its millisecond dynamical range enabling real-time study of dynamical processes. Most importantly, it opens a possibility to increase the MN resolution further by combining this technique with the whole series of label-free super-resolution imaging techniques developed in standard microscopy.

The use of nanostructured plasmonic objects represent the first step on this path, and from the very beginning MN was applied for imaging nanoholes fabricated in metal sheets, plasmonic dimers, etc., that resulted in resolution values  $\sim\lambda/7$  which far exceeded the resolution limits determined by the classical resolution theory developed for incoherent point sources. The reasons for increased resolution of nanoplasmonic objects include stronger near fields with much larger  $k$ -vectors which are intrinsic for plasmons compared to photons in air, especially in the case of resonant excitation of localized surface plasmon resonances. Another important factor is connected with a coherent excitation of out-of-phase plasmonic oscillations in such structures which can contribute to the observation of subdiffraction features.

The use of confocal microscopy represents the next step which was taken at the initial stage of developing MN [33, 45]. Due to the effect of the confocal pinhole, it allowed to increase the optical contrast and signal-to-noise ratio of the images obtained through the microspheres which was an important factor in improving the experimental quantification of resolution in this method. Initially, the resolution of confocal microscopy was overestimated at  $\sim\lambda/17$  level [45], however eventually the resolution  $\sim\lambda/7$  was demonstrated using convolution with PSF for imaging nanoplasmonic structures. Another technique was based on nonlinear reduction of PSF using MN integration with two-photon photoluminescence [85]. This method was used for imaging dimer gap region where the resolution of  $\sim\lambda/7$  was demon-

strated. One more technique includes integration with interferometric methods which allowed achieving axial resolution on the order of few nanometers still keeping the lateral resolution around 112 nm for visible light illumination [56].

In this section, we concentrate on one more approach which can be viewed as the most natural way of enhancing the resolution capability of MN based on integration with structured illumination microscopy (SIM). At this point, we will move away from imaging the nanoplasmonic structures themselves and switch to imaging nanoscale objects, for example, dielectric nanospheres or biomedical structures placed at the top of such arrays. We are primarily interested in situations where different periodic (or not periodic) nanoplasmonic structures are used in near-field proximity to the objects of interests to increase the amount of information which can be used for reconstructing images with high spatial frequencies exceeding the classical diffraction limit. To this end, we will use examples of using dye-doped fluorescent objects as opposed to label-free imaging. We need to clarify that the physical mechanisms of super-resolution considered in this Section are not based on special nonlinear properties of such FL objects. They were selected only to increase the brightness and contrast of nanoscale objects selected for the resolution quantification.

We begin in Sect. 16.5.1 with introducing a basic principle of SIM in which the illumination with an interference pattern is used. After that, we consider a series of techniques where a similar principle is realized using plasmon-assisted SIM (PSIM), localized PSIM (LPSIM), and eventually, LPSIM integrated with MN. These methods can be viewed as far-field techniques based on out-of-plane diffraction caused by periodic surface modulation. These methods require obtaining multiple images and post-imaging processing. After that, in Sect. 16.5.2 we consider a method based on plasmon coupled leakage radiation (PCLR) which allowed a modest twofold increase of resolution compared to standard microscopy without post-imaging processing. Finally, in Sect. 16.5.3 we suggest a novel way of near-field illumination of objects using plasmonic “hot spots” in short-period nanoplasmonic arrays which cannot be resolved in the far field, but can contribute to super-resolution imaging of objects placed in contact with such arrays. For arrays with sufficiently short periods ( $<150$  nm) the coupling to surface lattice resonances becomes inefficient, and more likely mechanism of imaging is the coupling to the closest LSPRs or “hot spots” containing near fields with very large in-plane  $k$ -vectors. We believe that in the latter case the super-resolution stems from the coupling of the emission of nanoscale objects to the closest LSPRs in the underlying plasmonic metasurface. In its turn, such highly localized, plasmonic-mediated emitters are evanescently coupled into high-index microspheres and form magnified virtual images of such nanoscale objects with the participation of their optical near fields.

### 16.5.1 Principles of SIM, PSIM, and LPSIM

In classical SIM the objects are illuminated with a periodically modulated interference pattern and their high spatial frequency information gets “smeared across

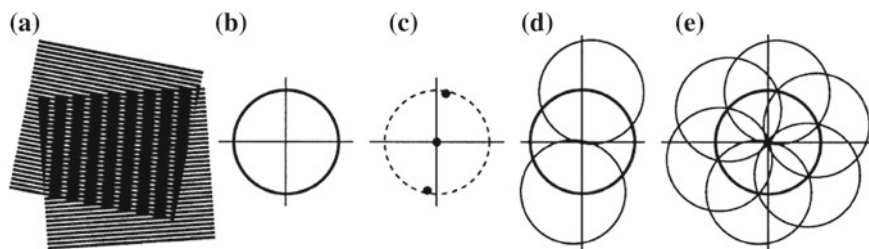


**Fig. 16.9** SIM concept: **a** If two line patterns are superposed (multiplied), their product will contain moiré fringes. **b** Region of reciprocal space observable by a diffraction-limited microscope objective. **c** A sinusoidally striped illumination pattern has only three Fourier components. The positions of the two side components are determined by the period of the illumination pattern. **d** The observable region will thus contain, in addition to the normal information, moved information that originates in two offset regions. **e** From a sequence of such images with different orientation and phase of the pattern, it is possible to recover information from an area twice the size of the normally observable region in  $k$ -space, corresponding to twice the normal resolution. Reproduced from [7] with permission of the Royal Microscopical Society

frequency space” by the Fourier transform of the excitation pattern [7–9], as illustrated in Fig. 16.9. The super-resolution stems from the multiple ( $m$ ) images acquired at different phase shifts ( $m\varphi$ ) and different directions of illumination fringes. There are as many equations (images) as there are unknowns (information components) that allow finding components by inverting an  $m \times m$  matrix (equivalent to a discrete Fourier transform with respect to  $\varphi$ ). In this sense, all modifications of SIM including blind reconstruction [10, 11] use post-imaging processing.

In a more detailed way, such imaging is shown in Fig. 16.10, where several important modifications of this method are also illustrated [86, 87]. The escape cone is represented by the blue circle in Fig. 16.10b showing the range of  $k$ -vectors responsible for a diffraction-limited resolution. The radius of this circle is determined by NA of the imaging system such as a microscope objective or a microsphere operating in combination with the microscope objective in the case of virtual imaging through contact spherical microlens. Under structured illumination, the moiré fringes are formed due to  $k$ -vector shift ( $k_{sp}$ ) determined by the period of the interference pattern. This means that the information about higher spatial frequencies (larger  $k$ -vectors) of the object is transformed into an escape cone accessible for the far-field imaging [7–9]. Thus, the principle underlying the super-resolution imaging is a  $k$ -vector shift due to illumination with the interference pattern.

The advantage of plasmonic SIM method (PSIM) [88] is based on much larger  $k$ -vectors ( $k_{SPP}$ ) of surface plasmon polaritons (SPPs) compared to that for free photons ( $k_{ex}$ ), as illustrated in Fig. 16.10a. This allows for larger  $k$ -vector shift to improve the resolution compared to SIM.

The amount of  $k$ -vector shift can be further increased in localized PSIM method (LPSIM) where instead of using SPPs the illumination is provided by much smaller plasmonic nanodisks supporting localized surface plasmon resonances (LSPRs) which can be coherently coupled giving rise to collective surface lattice resonances

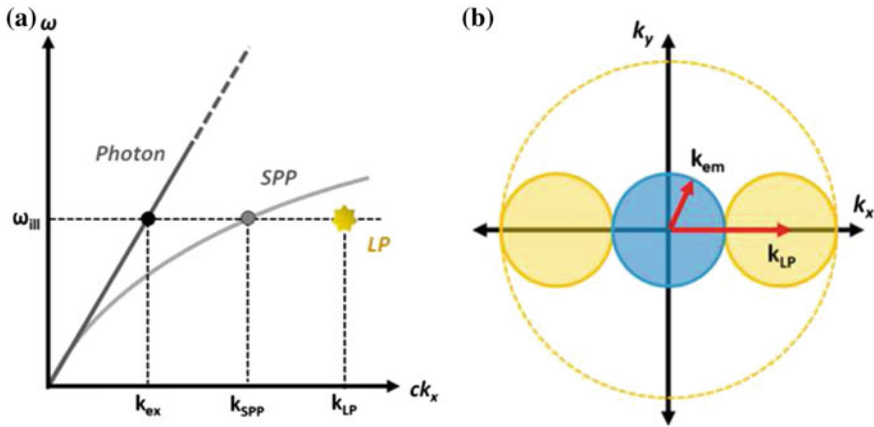


**Fig. 16.10** **a** Illustrative plot of temporal frequency versus wavenumber for the illuminating laser, the PSIM method (light gray curve), and the localized plasmonic field (gold star). Here,  $k_{LP}$  is the spatial frequency generated by the nanoantenna array, which can be tuned as desired, within fabrication capabilities. **b** Reciprocal space diagram: The collected wavevectors in a traditional image are limited by the emission wavenumber  $k_{em}$  (blue circle). With structured illumination via localized plasmonic fields, this imaging resolution is enhanced dramatically in a controllable manner (gold dashed circle, in this specific example). Reproduced from [86] with permission of American Chemical Society

(SLRs). Besides applications in LPSIM super-resolution imaging, such SLR resonances determine reflection [89, 90], transmission, and emission [91, 92] properties of such arrays. The amount of  $k$ -vector shift is  $k_{LP} = 2\pi/a$ , where  $a$  is the period along a given direction. Such  $k$ -vector shift by  $k_{LP}$  is illustrated in Fig. 16.10b. Thus, the amount of the  $k$ -vector shift in LPSIM is controlled by the period  $a$ , as schematically illustrated in Fig. 16.10b.

When the array periodicity is on the order of particle resonance wavelength, the coupling between the diffractive orders of the array and the LSPRs in each individual particle will result in a collective SLR [93]. SLRs in plasmonic nanoparticle arrays show angle-dependent dispersions and have significantly narrower linewidths compared to LSPRs in the individual particles. Not only the emission can couple to diffraction orders of grating, but also the incident light in the case of measurements of reflection or transmission spectra can couple to the band structure of various periodic structures such, for example, as photonic crystal waveguides determining their resonant optical properties [94, 95].

Principle of LPSIM closely resembles the mechanism of resonant enhancement of the emission due to SLRs [91, 92] schematically illustrated by the photon dispersion diagram in Fig. 16.11. The emission energy of interest,  $E = hc/\lambda$ , is represented by the horizontal red line corresponding to the emission wavelength  $\lambda = 620$  nm. The slope of photonic dispersions is determined by the effective index,  $n_{eff}$ , of the medium surrounding the array with the corresponding  $k$ -vector represented by  $n_{eff}2\pi/\lambda$ . The enhanced emission takes place at the points where the red line intersects the folded

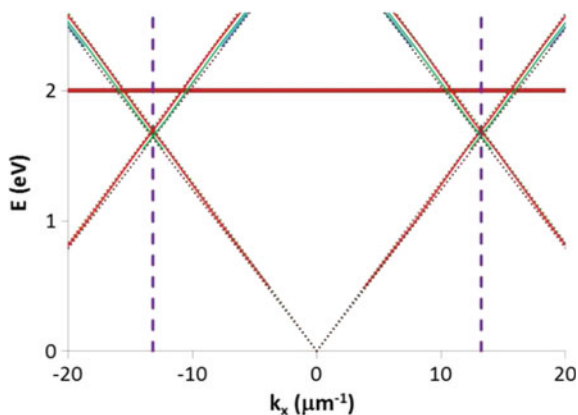


**Fig. 16.11** Diagram of energy versus parallel wave vector showing the dispersion of Rayleigh anomalies and guided modes for a waveguide with refractive index  $n_2 = 1.59$  coupled to a lattice with period  $a = 238$  nm between media with  $n_1 = 1$  and  $n_3 = 1.52$ . Dotted lines: Rayleigh anomalies for  $n = 1.52$  and  $1.59$ , thin solid lines: waveguide modes. Vertical purple lines: border of 1st Brillouin zone. The horizontal red line shows the emission energy of interest. Reproduced from [92] with permission from the Optical Society of America

dispersions. However, the case shown in Fig. 16.11 illustrates enhanced emission not in air, but in an adjacent waveguide with index  $n_2 = 1.59$  because the corresponding crossing points actually located outside the light escape cone in the air (this cone is not shown in Fig. 16.11). This situation is determined by the period  $a = 238$  nm of the array [92]. It is easy to show that by slightly increasing  $a$  the emission at 620 nm would be provided in the light escape cone and this structure would be suitable for developing LPSIM. For 1D grating, the corresponding enhancement of surface emission due to coupling to the band structure takes place under condition  $a > \lambda / (1 + n_{\text{eff}})$ . This means that an attempt to increase the resolution of LPSIM by reducing  $a$  faces a cutoff condition. In 2D case, this condition should be reformulated taking into account the symmetry of corresponding array supporting LSRs [93].

Combination of LPSIM with microspherical nanoscopy was recently reported for imaging dye-doped 40 nm nanospheres (570 nm emission) placed at the top of the hexagonal array of silver nanodisks with 60 nm diameters and 150 nm pitch [57]. The virtual imaging was achieved through 46  $\mu\text{m}$  polystyrene ( $n = 1.59$ ) microspheres and through 21  $\mu\text{m}$   $\text{TiO}_2$  ( $n = 2.1$ ) microspheres. In both cases the spheres were immersed in water leading to refractive index contrasts 1.2 and 1.58 for virtual imaging, respectively. The microspheres were manipulated in water by the optical tweezers. The magnification of  $\text{TiO}_2$  microsphere was measured to be  $M = 3.6$ . The effective NA of the system increased to 1.45 and the diffraction-limited FWHM of the image of FL nanosphere under the sphere decreased from 625 to 240 nm, see Fig. 16.12. After LPSIM post-imaging processing, the FWHM decreased, from 240 nm under the microlens, to 57 nm ( $\sim \lambda / 10$ ), which provided an additional 4.2 times improvement of the  $\text{TiO}_2$  microlens, as illustrated in Fig. 16.12.

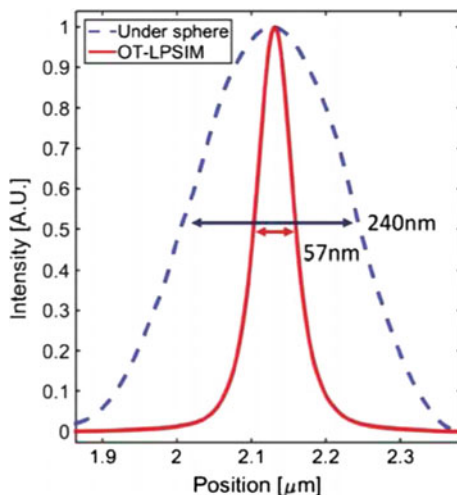


**Fig. 16.12** Quantification of the experimental resolution using the intensity profile of the magnified FL image of 40 nm diameter beads under 21  $\mu\text{m}$   $\text{TiO}_2$  microsphere through  $60\times$  (0.8NA) objective lens before (blue dashed) and after (red) LPSIM post-imaging processing. The virtual image is magnified 3.6 times under a  $\text{TiO}_2$  sphere. The FWHM after LPSIM reconstruction drops to 57 nm. Reproduced from [57], with permission from The Royal Society of Chemistry

### 16.5.2 Plasmon-Coupled Leakage Radiation (PCLR)

Besides SIM, another inspiration for achieving the optical super-resolution imaging came from the far-field superlens idea proposed in 2007 [18]. The detailed review of this idea goes beyond the scope of this Chapter. The principle of far-field superlens is based on using a thin (several tenths nanometers) metallic layer adjacent to the object where the evanescent fields containing high spatial frequency information are amplified. After that, the evanescent waves are converted into propagating waves by the surface grating [18]. The proposal of far-field superlens brought interesting new physics insight in this area and it was inspirational for many groups. It should be noted, however, that the far-field superlens is narrowband, rather difficult in fabrication, and, potentially, requires the post-imaging processing.

Recently, a more practical approach termed plasmon-coupled leakage radiation (PCLR) method was developed to obtain true subwavelength resolution images in the far field [96]. The principle underlying the PCLR technique is the enhancement of the FL intensity that is transmitted through a 50 nm uniform Au layer via coupling with evanescent waves and the subsequent collection of the transmitted evanescent-coupled fluorescence by the oil immersion objective lens of a microscope. The physical mechanism relies on the fact that the wavevector of the surface plasmon-polaritons ( $k_{\text{spp}}$ ) is subtracted from the in-plane  $k$ -vector which is added to the light diffracted by the object, allowing information from smaller features to be transmitted into the substrate. The PCLR advantages are related to the fact that it is

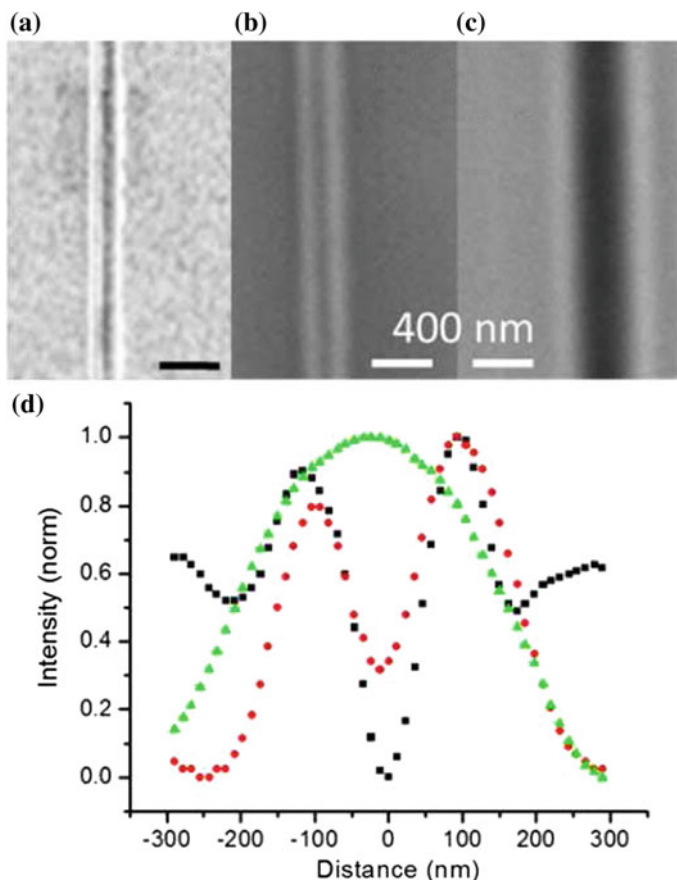


**Fig. 16.13** SEM **a**, PCLR **b**, and WL **c** images of 35 nm thick and 120 nm wide Cr double lines defined on the top of the gold 50 nm thick layer. The double-line center-to-center ( $p$ ) separation is 200 nm with an 80 nm gap between the lines. **d** Line intensity profiles for the images shown in **(b)** and **(c)**. Reproduced from [96] with permission from the Optical Society of America

a rather broadband method, simple in realization and fabrication, and not requiring the post-imaging processing. Although the experimental quantification of resolution was performed only based on a minimal discernable feature sizes, the theoretical estimations predict two times resolution improvement compared to a standard far-field microscopy for objective with a given NA [96].

The PCLR imaging of two parallel lines (120 nm wide each and 50  $\mu\text{m}$  long) of chromium ( $\sim 35$  nm thick) patterned on the top of the uniform Au layer (50 nm thick), with edge-to-edge line separation ( $\Delta x$ ) of 80 nm is illustrated in Fig. 16.13. The whole sample was then covered with 110 nm thick R6G-PMMA. The Cr metal layer modifies the propagating SPPs in the double-line samples. Figure 16.13 shows repre-

sentative SEM (Fig. 16.13a), PCLR (Fig. 16.13b), and white light (WL) (Fig. 16.13c) images of a Cr/Au double-line sample.

Although PCLR has not been integrated with microsphere-based imaging yet, we believe that this method is highly promising in this regard. The limited resolution advancement in PCLR is related to the absence of the magnification of the image in a near-field zone where the higher spatial frequencies of the object are contained. A combination of MN with PCLR can allow additional image magnification required for further resolution improvement.

### ***16.5.3 Microspherical Nanoscopy Based on Short-Period Arrays with Small Gaps: Super-Resolution Without Post-imaging Processing***

In previous Sects. 16.5.1 and 16.5.2 we considered different situations when the nanoplasmonic layer adjacent to the objects was designed to collect the objects's near-fields that resulted in super-resolution imaging of these objects. In PSIM (Sect. 16.5.1), the illumination of the objects was provided with short-period standing plasmonic waves. In LPSIM (Sect. 16.5.1), the individual LSPRs in nanodisks were arranged with the wavelength-scale periodicity to provide illumination with collective SLRs due to out-of-plane diffraction. In PCLR method (Sect. 16.5.2), the surface plasmon polaritons with large in-plane  $k$ -vectors were used to offset the parallel momentum gained by the diffraction.

The question emerges regarding a principle possibility of using arrays with much shorter periods where the coupling to SLRs becomes inefficient. In a simple 1D model, the cutoff condition for coupling with SLRs is  $a > \lambda/(1 + n_{\text{eff}})$ , where  $n_{\text{eff}}$  is the index of the surrounding medium. If the gaps are sufficiently small ( $<20$  nm), the coupling between the neighboring LSPRs will create regions of very strong electromagnetic field enhancement between the metallic stripes in 1D model or between the nanocylinders in 2D case. Such plasmonic hot spots would not be discernable by the far-field microscopy. If the period of such nanoplasmonic arrays, which can be termed plasmonic metasurfaces, is below the cutoff condition, they would produce illumination of the nanoscale objects located in the vicinity of such arrays with near fields containing extremely high in-plane  $k$ -vectors, however, these illumination peaks would not be resolvable in the far-field region.

In fact, such formation of strong maxima of the plasmonic near fields between the Au nanoparticles was observed almost two decades ago [97] using photon scanning tunneling microscope, see Fig. 16.14. Although this experiment was performed for 1D chains of nanoparticles, similar plasmonic hot spots can be expected in the case of 2D arrays. Theoretically, it is important to know the photon dispersions in such short-period arrays where strong hybridization of LSPRs can take place. In principle, the basic properties can be understood based on a tight-binding approximation in 1D [98] and 2D [99] cases. However, the modeling of LSPR as point dipoles in tight-binding

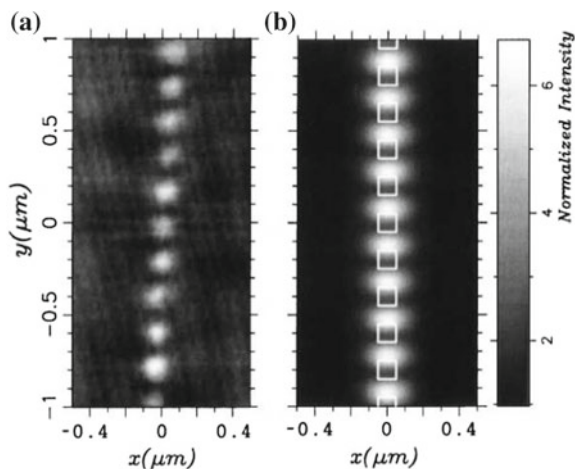


**Fig. 16.14** **a** Constant height photon scanning tunneling microscope image recorded above a chain of Au particles (individual size:  $100 \times 100 \times 40 \text{ nm}^3$ ) separated from each other by a distance of 100 nm and deposited on an ITO substrate. **b** A comparison with a numerical simulation shows that the bright spots are not on top of the Au particles (the surface projections of the particles correspond to the white squares). Reproduced from [97] with permission of the American Physical Society

approximation can be considered only for sufficiently small metallic particles with the radius  $r < a/3$  [99].

Such illumination offers an almost perfect setting for combining with the microspherical nanoscopy where the evanescent waves with high  $k$ -vectors produced by these hot spots are coupled with the objects' emission and can be collected by the high-index microspheres, which in turn can be used for creating the magnified virtual images of these objects formed with the participation of their optical near fields [100].

Recently, this mechanism of imaging based on using short-period nanoplasmonic arrays with small gaps was tested for imaging dye-doped 47 nm polystyrene nanospheres and F-actin protein filaments placed on top of a series of nanoplasmonic arrays with the nanocylinder diameter 60 nm and various periods  $80 < a < 200 \text{ nm}$  [43, 44], as illustrated in Fig. 16.15. For imaging FL nanospheres, the barium-titanate glass microspheres with  $8 - 20 \mu\text{m}$  diameters and  $n = 2.1$  (higher titanium content) were embedded in a cellulose acetate coverslip with an index  $\sim 1.48$  at the plastic softening temperatures. The magnification of the virtual image  $M = 3.4$  was determined experimentally in this case [44]. The SEM images of arrays with periods  $a = 80, 100, 150, \text{ and } 200 \text{ nm}$  are illustrated in Fig. 16.15a. The corresponding  $k$ -vector diagrams are represented in Fig. 16.15b. These diagrams suggest an analogy with LPSIM method, however, it is important to remember that for the peak emission of nanospheres at 530 nm, the folding of the band structure into the escape cone does not take place for the shortest periods  $a < 150 \text{ nm}$  according to a simple 1D model [44]. The folding of the band structure for 2D square arrays requires a more

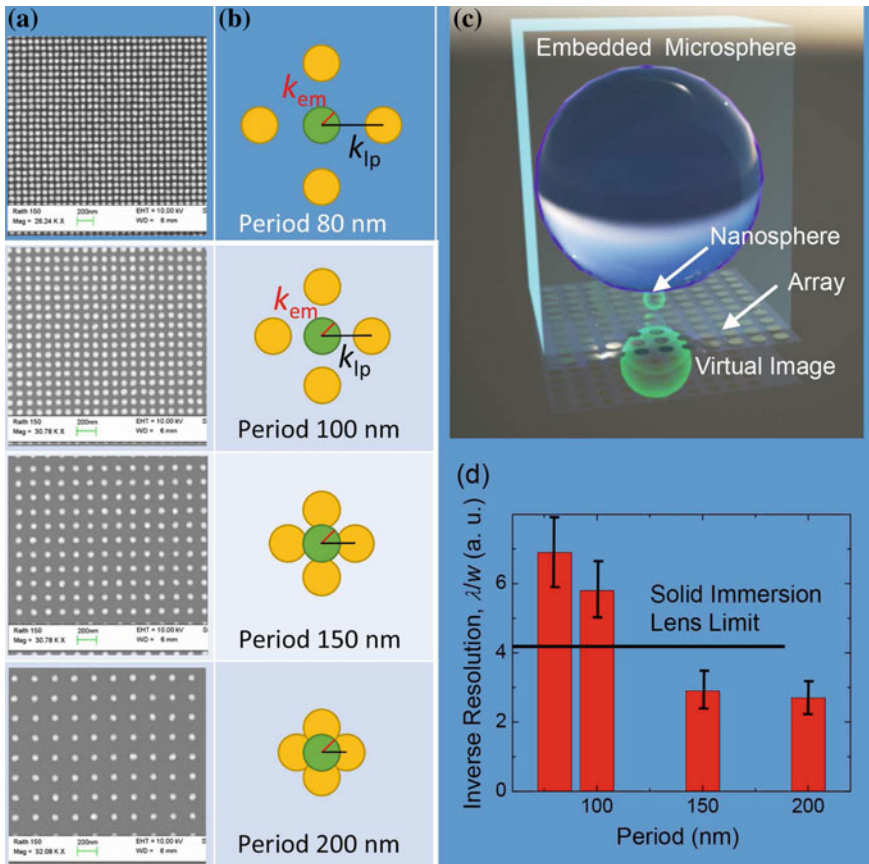


**Fig. 16.15** **a** SEM images and **b**  $k$ -vector diagrams illustrating coupling with a square array with  $a = 80, 100, 150,$  and  $200$  nm from top down, respectively. **c** Setup with the nanoplasmonic array. **d** Inverse resolution,  $\lambda/w$ , presented as a function of  $a$ , where  $w$  is the width of the Gaussian PSF providing the best fit of the images of  $47$  nm nanospheres. The sequence of elements in the vertical direction, microspheres object array, in **c** corresponds to upright microscopy. In the case of using inverted microscope the sequence should be reversed. **a** and **d** reproduced from [44] with permission of the American Physical Society

detailed analysis, however, such periods as  $80$  and  $100$  nm seem to be too short for the coupling into the escape cone to take place, as required by the regular LPSIM [57]. The schematic image of the setup in Fig. 16.15c illustrates an upright version of MN, whereas experimentally an inverted Olympus IX71 microscope with excitation provided by a mercury lamp was used with a  $100\times$  ( $NA = 1.35$ ) silicone oil ( $1.406$  index) immersion objective. In inverted microscope, the order of elements of the setup is reversed in vertical direction compared to that shown in Fig. 16.15c.

The resolution quantification for different array periods is represented in Fig. 16.15d. The solid immersion lens limit,  $\sim\lambda/4.2$ , is shown by the horizontal

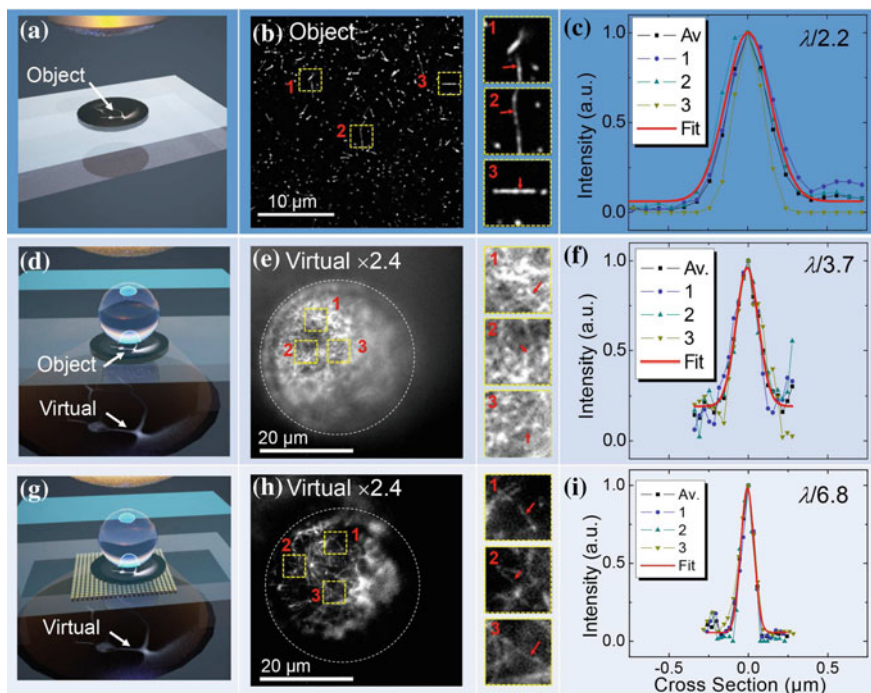


**Fig. 16.16** Comparison of three imaging modalities, **a–c** without microspheres with the resolution  $\sim\lambda/2.2$ , **d–f** through microspheres without nanoplasmonic array with resolution  $\sim\lambda/3.7$ , and **g–i** through microspheres using nanoplasmonic array with resolution  $\sim\lambda/6.8$  obtained without post-imaging processing. Imaging is performed by DeltaVision OMX SR microscope with a  $60\times$  ( $NA = 1.35$ ) silicone oil immersion objective. The barium-titanate glass microspheres with  $45 - 53 \mu\text{m}$  diameters and  $n = 1.9$  were embedded in a cellulose acetate coverslip with index  $\sim 1.48$ . Reproduced from [44] with permission of the American Physical Society

line. It is seen that for longer array periods,  $a = 150$  and  $200 \text{ nm}$ , the resolution is found to be below the solid immersion limit. However, for shorter periods,  $a = 80$  and  $100 \text{ nm}$ , the resolution was found to exceed the solid immersion limit reaching the values about  $\lambda/6 - \lambda/7$  without any post-imaging processing. The experimental quantification of resolution was performed by convolution with PSF taking into account the magnification ( $M$ ) of the virtual image.

The resolution of this method was further tested using F-actin protein filaments as an example of 1D objects with the width on the order of few nanometers and the length of about several microns [43, 44]. For such objects, the width of the image divided by  $M$  directly represents the resolution of the system. For these experiments, barium-titanate glass microspheres with  $45\text{--}53 \mu\text{m}$  diameter and  $n = 1.9$  (higher barium content) were embedded in a cellulose acetate coverslip. The experimentally determined magnification in this case was  $M = 2.4$  [44]. The array with the minimal period  $a = 80 \text{ nm}$  was used. The imaging was performed using DeltaVision OMX

SR microscope with  $60\times$  ( $NA = 1.42$ ) oil immersion objective, FL laser excitation at  $\lambda = 525$  nm and detection at  $604 - 644$  nm.

The comparison of three imaging modalities, (i) without microspheres, (ii) through microspheres without plasmonic arrays, and (iii) through microspheres using plasmonic arrays, is illustrated in Fig. 16.16. The analyses of these results show that in the case (i) represented by Fig. 16.16a–c the resolution  $\sim\lambda/2.2$  is, as expected, below the diffraction limit determined by the microscope objective. In the case (ii) represented by Fig. 16.16d–f the resolution of virtual imaging through microspheres  $\sim\lambda/3.7$  approaches the SIL limit. Finally, in the case (iii) represented by Fig. 16.16g–i the resolution is found to be  $\sim\lambda/6.8$ , similar to imaging of FL nanospheres in Fig. 16.15d.

The results of imaging FL labeled nanospheres and F-actin protein filaments presented in Figs. 16.15, 16.16 cannot be explained by the regular LPSIM mechanism because the post-imaging processing was not used in these experiments [44]. In addition, the bandstructure folding into the escape cone, as it was already mentioned, is not possible for arrays with periods as short as 80 and 100 nm in the range of detection wavelengths selected in these experiments. It has been hypothesized [44] that the mechanism of the observed super-resolution is based on the coupling of the emission on nanoscale objects to the localized surface plasmon resonances (LSPRs) in the adjacent Au nanodiscs. For sufficiently small gaps between the coupled nanodiscs, the maxima of the plasmonic near-fields can be located between the nanodiscs [97]. The resonantly enhanced plasmonic near-field peaks with large in-plane  $k$ -vectors are evanescently coupled to high-index microspheres, thus contributing to the formation of magnified virtual images of FL objects. While the regular LPSIM mechanism leads to the moiré fringes formation with the need to use post-imaging processing, the proposed mechanism does not require post-imaging processing.

## 16.6 Conclusion

Microspherical nanoscopy, or imaging by dielectric microspheres placed in contact with the objects, emerged as amazingly simple and powerful method of increasing the resolution of standard microscopes. The method does not require any complicated hardware or software—just putting the microsphere on the top of the object and finding its virtual image using a standard microscope. Scanning large areas require translating the microsphere. However, the critical difference compared to such methods as NSOM or AFM is that instead of slow point-by-point scanning by a very narrow nanoprobe, the microspherical nanoscopy offers much faster area-by-area scanning followed by stitching the images obtained for each position of microsphere on the sample surface. The translation of microspheres can be easily achieved by a variety of techniques from using movable coverslips with embedded microspheres [35–38, 43, 44] to attaching microspheres to AFM probes [49]. Super-resolved imaging of a broad range of objects such as metallic and semiconductor nanostructures, surfaces of central processing units, biological cells, and proteins has been demonstrated. Microspheres of various sizes and materials located in the air as well as in liquids

or plastics have been used. Super-resolution has been shown to persist under various illumination conditions. This includes transmission and reflection modes with white light and monochromatic light, scanning confocal mode [33, 45], as well as structured illumination [57] and imaging mediated by coupling with plasmonic metasurfaces [43, 44, 100]. These developments should lead to the creation of a new generation of inexpensive, fast, and very simple optical microscopes with resolution laying between that of the standard microscopes ( $\sim\lambda/2$ ) and NSOM or AFM systems ( $\lambda/20$ ).

This consideration suggests that the quantification of the resolution is an important issue for emerging microspherical nanoscopy. Experimental quantification of resolution was performed at various conditions using different criteria and the results vary in a broad range, as illustrated in Table 16.1. The application of rigorous resolution criteria allows one to estimate conservatively that the experimental resolution of nanoplasmonic objects can reach at least  $\sim\lambda/6 - \lambda/7$  for virtual imaging through the microspheres [34, 37, 38]. A similar resolution can be achieved by resonant coupling the FL objects to the localized surface plasmon resonances in the underlying plasmonic metasurfaces [44, 100–102].

In this chapter, we provided a review of theoretical resolution quantification results for imaging incoherent point sources based on the exact numerical solution of the Maxwell equations [74–77, 80, 83]. This accounts for several new, compared to the standard microscopy, effects: near-to-far-field conversion and excitation of WGMs in dielectric microspheres [53]. The results are quite intriguing and puzzling because they predict a lower resolution compared to the experimental values observed in nanoplasmonic structures. For low-index silica microspheres in air, the nonresonant and resonant resolutions can be estimated as  $\sim\lambda/3$  and  $\sim\lambda/4$ , respectively. For high-index ( $n = 2$ ) microspheres immersed in liquids or dielectric slabs, the resolution can be improved by the factor determined by the background index for the same index contrast [53]. This puts the theoretical resolution in the resonant case closer to the experimentally reported values. However, this resolution still remains somewhat lower compared to the experiment and that raises a very interesting question about the fundamental nature of super-resolution in microspherical nanoscopy.

One way to answer this question is to refer to an enhanced fraction of near fields in nanoplasmonic structures under resonance with LSPRs in metallic nanodisks and other similar objects. These objects (or illumination provided in near-field zone of such objects) are fundamentally different from the dipole emission considered in our theoretical consideration. It is quite possible that the super-resolution of such objects is influenced by the increased near fields under resonance with the LSPRs spectral peaks in nanoplasmonic arrays. One fact which points toward this hypothesis is an experimental observation that the super-resolution imaging of FL nanospheres at the top of nanoplasmonic arrays becomes possible only for extremely small gaps and periods of such arrays [44, 101, 102]. Another fact which strongly supports this interpretation is a preliminary observation that the resonance between the FL band of dielectric nanospheres and LSPRs in underlying nanoplasmonic arrays is indeed required for super-resolution imaging of such objects [102]. However, these experiments are in their beginning stage and more work is required to prove the

role of resonantly enhanced LSPRs in achieving super-resolution in microspherical nanoscopy.

Another way to explain the super-resolution of imaging through the microspheres is to consider a possibility of coherent or partly coherent phenomena in illumination or resonant photoexcitation of nanoscale objects. Coherent contributions can stem from two different mechanisms. First, they can be related to illumination similar to ROCS microscopy [78, 103] and other similar methods where, as an example, an oblique illumination is used to produce a certain phase distributions along the objects. Second, they can stem from the resonant properties of two neighboring microdisks or other similar plasmonic objects which can be resonantly coupled producing bonding and antibonding modes. Such coupled systems are well known for their photonic counterparts—photonic molecules [104]. If the objects reemit at the frequencies of these modes, which can take place naturally in the case of broadband excitation, the visibility and resolution of different features should change drastically. In-phase oscillations in closely spaced objects reduce the visibility of the gaps separating these objects below the classical diffraction limit for incoherent point sources, whereas out-of-phase oscillations allow one to observe the zero-intensity point in the center of the gap even for infinitely small gaps [80].

In conclusion, this chapter introduces the basic physical principles of super-resolution mechanisms in microspherical nanoscopy. It is a dynamic area where new concepts such as LPSIM [57] and coupling of FL objects to LSPRs in the underlying plasmonic metasurfaces [44, 100–102] were proposed recently. The fusing of nanoplasmonics with photonics imaging mechanisms underlies the developments in this area toward ever increasing spatial resolution.

**Acknowledgements** The authors would like to thank Aaron Bretin for useful discussions and help with the preparation of Figs. 16.1a and 16.15c. VNA is thankful for support by Center for Metamaterials, an NSF I/U CRC, award number 1068050.

## References

1. C.J.R. Sheppard, Resolution and super-resolution. *Microsc. Res. Tech.* **80**(6), 590–598 (2017)
2. S.W. Hell, J. Wichmann, Breaking the diffraction resolution limit by stimulated emission: stimulated-emission-depletion fluorescence microscopy. *Opt. Lett.* **19**(11), 780–782 (1994)
3. B. Hein, K.I. Willig, S.W. Hell, Stimulated emission depletion (STED) nanoscopy of a fluorescent protein-labeled organelle inside a living cell. *Proc. Natl. Acad. Sci. U.S.A.* **105**, 14271 (2008)
4. E. Betzig, G.H. Patterson, R. Sougrat, O.W. Lindwasser, S. Olenych, J.S. Bonifacino, M.W. Davidson, J. Lippincott-Schwartz, H.F. Hess, Imaging intracellular fluorescent proteins at nanometer resolution. *Science* **313**(5793), 1642–1645 (2006)
5. H. Shroff, C.G. Galbraith, J.A. Galbraith, E. Betzig, Live-cell photoactivated localization microscopy of nanoscale adhesion dynamics. *Nat. Methods* **5**, 417 (2008)
6. S.M. Mansfield, G.S. Kino, Solid immersion microscope. *Appl. Phys. Lett.* **57**(24), 2615–2616 (1990)
7. M.G.L. Gustafsson, Surpassing the lateral resolution limit by a factor of two using structured illumination microscopy. *J. Microsc.* **198**(2), 82–87 (2000)

8. M.G.L. Gustafsson, L. Shao, P.M. Carlton, C.J.R. Wang, I.N. Golubovskaya, W.Z. Cande, D.A. Agard, J.W. Sedat, Three-dimensional resolution doubling in wide-field fluorescence microscopy by structured illumination. *Biophys. J.* **94**, 4957–4970 (2008)
9. F. Ströhl, C.F. Kaminski, Frontiers in structured illumination microscopy. *Optica* **3**(6), 667–677 (2016)
10. E. Mudry, K. Belkebir, J. Girard, J. Savatier, E.L. Moal, C. Nicoletti, M. Allain, A. Sentenac, Structured illumination microscopy using unknown speckle patterns. *Nat. Photonics* **6**, 312–315 (2012)
11. J. Min, J. Jang, D. Keum, S.-W. Ryu, C. Choi, K.-H. Jeong, J.C. Ye, Fluorescent microscopy beyond diffraction limits using speckle illumination and joint support recovery. *Sci. Rep.* **3**, 2075 (2013)
12. D.W. Pohl, W. Denk, M. Lanz, Optical stethoscopy: image recording with resolution  $\lambda/20$ . *Appl. Phys. Lett.* **44**, 651–653 (1984)
13. P. Wang, M.N. Slipchenko, J. Mitchell, C. Yang, E.O. Potma, X. Xu, J.-X. Cheng, Far-field imaging of non-fluorescent species with subdiffraction resolution. *Nat. Photonics* **7**, 449–453 (2013)
14. S.-W. Chu, T.-Y. Su, R. Oketani, Y.-T. Huang, H.-Y. Wu, Y. Yonemaru, M. Yamanaka, H. Lee, G.-Y. Zhuo, M.-Y. Lee, S. Kawata, K. Fujita, Measurement of a saturated emission of optical radiation from gold nanoparticles: application to an ultrahigh resolution microscope. *Phys. Rev. Lett.* **112**(1), 017402 (2014)
15. O. Tzang, A. Pevzner, R.E. Marvel, R.F. Haglund, O. Cheshnovsky, Super-resolution in label-free photomodulated reflectivity. *Nano Lett.* **15**(2), 1362–1367 (2015)
16. I.I. Smolyaninov, J. Elliott, A.V. Zayats, C.C. Davis, Far-field optical microscopy with a nanometer-scale resolution based on the in-plane image magnification by surface plasmon polaritons. *Phys. Rev. Lett.* **94**, 057401 (2005)
17. P.A. Belov, Y. Hao, Subwavelength imaging at optical frequencies using a transmission device formed by a periodic layered metal-dielectric structure operating in the canalization regime. *Phys. Rev. B* **73**, 113110 (2006)
18. Z. Liu, S. Durant, H. Lee, Y. Pikus, N. Fang, Y. Xiong, C. Sun, X. Zhang, Far-field optical superlens. *Nano Lett.* **7**(2), 403–408 (2007)
19. X. Zhang, Z. Liu, Superlenses to overcome the diffraction limit. *Nat. Mater.* **7**, 435–441 (2008)
20. Z. Jacob, L. Alekseyev, E. Narimanov, Optical hyperlens: far-field imaging beyond the diffraction limit. *Opt. Express* **14**(18), 8247–8256 (2006)
21. A. Salandrino, N. Engheta, Far-field subdiffraction optical microscopy using metamaterial crystals: theory and simulations. *Phys. Rev. B* **74**, 075103 (2006)
22. Z. Liu, H. Lee, Y. Xiong, C. Sun, X. Zhang, Far-field optical hyperlens magnifying sub-diffraction-limited objects. *Science* **315**, 1686 (2007)
23. J. Sun, M.I. Shalaev, N.M. Litchinitser, Experimental demonstration of a non-resonant hyperlens in the visible spectral range. *Nat. Comm.* **6**, 7201 (2015)
24. V.N. Smolyaninova, I.I. Smolyaninov, A.V. Kildishev, V.M. Shalaev, Maxwell fish-eye and Eaton lenses emulated by microdroplets. *Opt. Lett.* **35**(20), 3396–3398 (2010)
25. H. Cang, A. Salandrino, Y. Wang, X. Zhang, Adiabatic far-field sub-diffraction imaging. *Nat. Comm.* **6**, 7942 (2015)
26. J.Y. Lee, B.H. Hong, W.Y. Kim, S.K. Min, Y. Kim, M.V. Jouravlev, R. Bose, K.S. Kim, I.-C. Hwang, L.J. Kaufman, C.W. Wong, P. Kim, K.S. Kim, Near-field focusing and magnification through self-assembled nanoscale spherical lenses. *Nature* **460**, 498–501 (2009)
27. D.R. Mason, M.V. Jouravlev, K.S. Kim, Enhanced resolution beyond the Abbe diffraction limit with wavelength-scale solid immersion lenses. *Opt. Lett.* **35**(12), 2007–2009 (2010)
28. M.-S. Kim, T. Scharf, M.T. Haq, W. Nakagawa, H.P. Herzig, Subwavelength-size solid immersion lens. *Opt. Lett.* **36**(19), 3930–3932 (2011)
29. Z. Wang, W. Guo, L. Li, B. Luk'yanchuk, A. Khan, Z. Liu, Z. Chen, M. Hong, Optical virtual imaging at 50 nm lateral resolution with a white-light nanoscope. *Nat. Commun.* **2**, 218 (2011)
30. X. Hao, C. Kuang, X. Liu, H. Zhang, Y. Li, Microsphere based microscope with optical super-resolution capability. *Appl. Phys. Lett.* **99**(20), 203102 (2011)

31. V.N. Astratov, A. Darafsheh, Methods and systems for superresolution optical imaging using high-index of refraction microspheres and microcylinders (2012-06-07). <https://www.google.com/patents/US20140355108>. U.S patent 9726874B2
32. A. Darafsheh, G.F. Walsh, L.D. Negro, V.N. Astratov, Optical super-resolution by high-index liquid-immersed microspheres. *Appl. Phys. Lett.* **101**(14), 141128 (2012)
33. A. Darafsheh, N.I. Limberopoulos, J.S. Derov, D.E. Walker Jr., V.N. Astratov, Advantages of microsphere-assisted super-resolution imaging technique over solid immersion lens and confocal microscopies. *Appl. Phys. Lett.* **104**(6), 061117 (2014)
34. K.W. Allen, N. Farahi, Y. Li, N.I. Limberopoulos, D.E. Walker, A.M. Urbas, V.N. Astratov, Overcoming the diffraction limit of imaging nanoplasmonic arrays by microspheres and microfibers. *Opt. Express* **23**(19), 24484–24496 (2015)
35. K.W. Allen, N. Farahi, Y. Li, N.I. Limberopoulos, D.E. Walker, A.M. Urbas, V.N. Astratov, in *NAECON 2014 - IEEE National Aerospace and Electronics Conference* (2014), pp. 50–52
36. K.W. Allen, Waveguide, photodetector, and imaging applications of microspherical photonics. Ph.D. thesis, University of North Carolina at Charlotte (2014). Chapter 4: Super-resolution imaging through arrays of high-index spheres embedded in transparent matrices, pp. 98-122
37. K.W. Allen, N. Farahi, Y. Li, N.I. Limberopoulos, D.E. Walker, A.M. Urbas, V. Liberman, V.N. Astratov, Super-resolution microscopy by movable thin-films with embedded microspheres: resolution analysis. *Ann. Phys. (Berlin)* **527**(7–8), 513–522 (2015)
38. K.W. Allen, Y. Li, V.N. Astratov, Reply to “Comment on ‘Super-resolution microscopy by movable thin-films with embedded microspheres: Resolution analysis’ [Ann. Phys. (Berlin) 527, 513 (2015)]”, *Ann. Phys. (Berlin)* **528**(11-12), 901–904 (2016)
39. V. Astratov, K. Allen, N. Farahi, Y. Li, N. Limberopoulos, D.W.A. Urbas, V. Liberman, M. Rothschild. Optical nanoscopy with contact microlenses overcomes the diffraction limit. *SPIE Newsroom*, 11 (2016)
40. L. Li, W. Guo, Y. Yan, S. Lee, T. Wang, Label-free super-resolution imaging of adenoviruses by submerged microsphere optical nanoscopy. *Light: Sci. Appl.* **2**, e104 (2013)
41. H. Yang, N. Moullan, J. Auwerx, M.A.M. Gijs, Super-resolution biological microscopy using virtual imaging by a microsphere nanoscope. *Small* **10**(9), 1712–1718 (2014)
42. A. Brettin, K.F. Blanchette, Y. Nesmelov, N.I. Limberopoulos, A.M. Urbas, V.N. Astratov, in *2016 IEEE National Aerospace and Electronics Conference (NAECON) and Ohio Innovation Summit (OIS)* (2016), pp. 269–271
43. V.N. Astratov, A.V. Maslov, A. Brettin, K.F. Blanchette, Y.E. Nesmelov, N.I. Limberopoulos, D.E. Walker, A.M. Urbas, in *Proceedings of the SPIE, Nanoscale Imaging, Sensing, and Actuation for Biomedical Applications XIV*, vol. 10077 (2017), p. 00770S
44. A. Brettin, F. Abolmaali, K.F. Blanchette, C.L. McGinnis, Y.E. Nesmelov, N.I. Limberopoulos, D.E. Walker, Jr., I. Anisimov, A.M. Urbas, L. Poffo, A.V. Maslov, V.N. Astratov, Enhancement of resolution in microspherical nanoscopy by coupling of fluorescent objects to plasmonic metasurfaces. *Appl. Phys. Lett.* **114**(13), 131101 (2019)
45. Y. Yan, L. Li, C. Feng, W. Guo, S. Lee, M. Hong, Microsphere-coupled scanning laser confocal nanoscope for sub-diffraction-limited imaging at 25 nm lateral resolution in the visible spectrum. *ACS Nano* **8**(2), 1809–1816 (2014)
46. P.-Y. Li, Y. Tsao, Y.-J. Liu, Z.-X. Lou, W.-L. Lee, S.-W. Chu, C.-W. Chang, Unusual imaging properties of superresolution microspheres. *Opt. Express* **24**(15), 16479–16486 (2016)
47. E.T.F. Rogers, J. Lindberg, T. Roy, S. Savo, J.E. Chad, M.R. Dennis, N.I. Zheludev, A super-oscillatory lens optical microscope for subwavelength imaging. *Nat. Mater.* **11**, 432–435 (2012)
48. L.A. Krivitsky, J.J. Wang, Z. Wang, B. Luk'yanchuk, Locomotion of microspheres for super-resolution imaging. *Sci. Rep.* **3**, 3501 (2013)
49. F. Wang, L. Liu, H. Yu, Y. Wen, P. Yu, Z. Liu, Y. Wang, W.J. Li, Scanning superlens microscopy for non-invasive large field-of-view visible light nanoscale imaging. *Nat. Commun.* **7**, 13748 (2016)
50. J. Li, W. Liu, T. Li, I.R.J. Zhao, B. Bahari, B. Kante, J. Wang, Swimming microrobot optical nanoscopy. *Nano Lett.* **16**(10), 6604–6609 (2016)

51. M. Duocastella, F. Tantussi, A. Haddadpour, R.P. Zaccaria, A.D.A. Jacassi, G. Veronis, F.D. Angelis, Combination of scanning probe technology with photonic nanojets. *Sci. Rep.* **7**, 3474 (2017)
52. G. Huszka, H. Yang, M.A.M. Gijs, Microsphere-based super-resolution scanning optical microscope. *Opt. Express* **25**(13), 15079–15092 (2017)
53. A.V. Maslov, V.N. Astratov, Resolution and reciprocity in microspherical nanoscopy: Point-spread function versus photonic nanojets. *Phys. Rev. Appl.* **11**(6), 064004 (2019)
54. F. Wang, L. Liu, P. Yu, Z. Liu, H. Yu, Y. Wang, W.J. Li, Three-dimensional super-resolution morphology by near-field assisted white-light interferometry. *Sci. Rep.* **6**, 24703 (2016)
55. P.C. Montgomery, S. Lecler, A. Leong-Hoï, S. Perrin, P. Pfeiffer, in *Proceedings of the SPIE, Optical Measurement Systems for Industrial Inspection X*, vol. 10329 (2017), p. 1032918
56. I. Kassamakov, S. Lecler, A. Nolvi, A. Leong-Hoï, P. Montgomery, E. Hægström, 3D super-resolution optical profiling using microsphere enhanced Mirau interferometry. *Sci. Rep.* **7**, 3683 (2017)
57. A. Bezryadina, J. Li, J. Zhao, A. Kothambawala, J. Ponsetto, E. Huang, J. Wang, Z. Liu, Localized plasmonic structured illumination microscopy with an optically trapped microlens. *Nanoscale* **9**, 14907–14912 (2017)
58. H. Yang, M.A. Gijs, Optical microscopy using a glass microsphere for metrology of sub-wavelength nanostructures. *Microelectron. Eng.* **143**, 86–90 (2015)
59. H. Yang, R. Trouillon, G. Huszka, M.A.M. Gijs, Super-resolution imaging of a dielectric microsphere is governed by the waist of its photonic nanojet. *Nano Lett.* **16**(8), 4862–4870 (2016)
60. B. Du, Y.-H. Ye, J. Hou, M. Guo, T. Wang, Sub-wavelength image stitching with removable microsphere-embedded thin film. *Appl. Phys. A* **122**, 15 (2016)
61. M. Guo, Y.-H. Ye, J. Hou, B. Du, Size-dependent optical imaging properties of high-index immersed microsphere lens. *Appl. Phys. B* **122**(3), 65 (2016)
62. C.A. González Mora, M. Hartelt, D. Bayer, M. Aeschlimann, E.A. Ilin, E. Oesterschulze, Microsphere-based cantilevers for polarization-resolved and femtosecond snom, *Appl. Phys. B* **122**(4), 86 (2016)
63. H.S.S. Lai, F. Wang, Y. Li, B. Jia, L. Liu, W.J. Li, Super-resolution real imaging in microsphere-assisted microscopy. *PLoS ONE* **11**(10), e0165194 (2016)
64. G. Gu, R. Zhou, H. Xu, G. Cai, Z. Cai, Subsurface nano-imaging with self-assembled spherical cap optical nanoscopy. *Opt. Express* **24**(5), 4937–4948 (2016)
65. M. Guo, Y.H. Ye, J. Hou, B. Du, T. Wang, Imaging of sub-surface nanostructures by dielectric planer cavity coupled microsphere lens. *Opt. Commun.* **383**, 153–158 (2017)
66. J. Ling, X. Wang, D. Li, X. Liu, Modelling and verification of white light oil immersion microsphere optical nanoscope. *Opt. Quant. Electron.* **49**(11), 377 (2017)
67. S. Yang, F. Wang, Y. Ye, Y. Xia, Y. Deng, J. Wang, Y. Cao, Influence of the photonic nanojet of microspheres on microsphere imaging. *Opt. Express* **25**(22), 27551–27558 (2017)
68. Y. Zhou, Y. Tang, Q. Deng, L. Zhao, S. Hu, Contrast enhancement of microsphere-assisted super-resolution imaging in dark-field microscopy. *Appl. Phys. Express* **10**(8), 082501 (2017)
69. Z. Chen, A. Taflove, V. Backman, Photonic nanojet enhancement of backscattering of light by nanoparticles: a potential novel visible-light ultramicroscopy technique. *Opt. Express* **12**(7), 1214–1220 (2004)
70. X. Li, Z. Chen, A. Taflove, V. Backman, Optical analysis of nanoparticles via enhanced backscattering facilitated by 3-D photonic nanojets. *Opt. Express* **13**(2), 526–533 (2005)
71. M.-S. Kim, T. Scharf, S. Mühlig, C. Rockstuhl, H.P. Herzig, Engineering photonic nanojets. *Opt. Express* **19**(11), 10206–10220 (2011)
72. Y.E. Geints, A.A. Zemlyanov, E.K. Panina, Photonic jets from resonantly excited transparent dielectric microspheres. *J. Opt. Soc. Am. B* **29**(4), 758–762 (2012)
73. B.S. Luk'yanchuk, R. Paniagua-Domínguez, I. Minin, O. Minin, Z. Wang, Refractive index less than two: photonic nanojets yesterday, today and tomorrow [Invited]. *Opt. Mater. Express* **7**(6), 1820–1847 (2017)

74. Y. Ben-Aryeh, Increase of resolution by use of microspheres related to complex Snell's law. *J. Opt. Soc. Am. A* **33**(12), 2284–2288 (2016)
75. Y. Duan, G. Barbastathis, B. Zhang, Classical imaging theory of a microlens with super-resolution. *Opt. Lett.* **38**(16), 2988–2990 (2013)
76. V.M. Sundaram, S.-B. Wen, Analysis of deep sub-micron resolution in microsphere based imaging. *Appl. Phys. Lett.* **105**(20), 204102 (2014)
77. T.X. Hoang, Y. Duan, X. Chen, G. Barbastathis, Focusing and imaging in microsphere-based microscopy. *Opt. Express* **23**(9), 12337–12353 (2015)
78. P. von Olshausen, A. Rohrbach, Coherent total internal reflection dark-field microscopy: label-free imaging beyond the diffraction limit. *Opt. Lett.* **38**(20), 4066–4069 (2013)
79. R. Horstmeyer, R. Heintzmann, G. Popescu, L. Waller, C. Yang, Standardizing the resolution claims for coherent microscopy. *Nat. Phot.* **10**, 68–71 (2016)
80. A.V. Maslov, V.N. Astratov, Imaging of sub-wavelength structures radiating coherently near microspheres. *Appl. Phys. Lett.* **108**(5), 051104 (2016)
81. V.N. Astratov, F. Abolmaali, A. Brettin, K.W. Allen, A.V. Maslov, N.I. Limberopoulos, D.E. Walker, A.M. Urbas, in *2016 18th International Conference on Transparent Optical Networks (ICTON)* (2016), pp. 1–4
82. S. Perrin, S. Lecler, A. Leong-Hoi, P.C. Montgomery, in *Proceedings of the SPIE, Modeling Aspects in Optical Metrology VI*, vol. 10330 (2017), p. 10330V
83. A.V. Maslov, V.N. Astratov, Optical nanoscopy with contact Mie-particles: resolution analysis. *Appl. Phys. Lett.* **110**(26), 261107 (2017)
84. Y.F. Lu, L. Zhang, W.D. Song, Y.W. Zheng, B.S. Luk'yanchuk, Laser writing of a subwavelength structure on silicon (100) surfaces with particle-enhanced optical irradiation. *JETP Lett.* **72**(9), 457–459 (2000)
85. B. Hou, M. Xie, R. He, M. Ji, S. Trummer, R.H. Fink, L. Zhang, Microsphere assisted superresolution optical imaging of plasmonic interaction between gold nanoparticles. *Sci. Rep.* **7**, 13789 (2017)
86. J.L. Ponsetto, F. Wei, Z. Liu, Localized plasmon assisted structured illumination microscopy for wide-field high-speed dispersion independent super resolution imaging. *Nanoscale* **6**, 5807–5812 (2014)
87. J.L. Ponsetto, A. Bezryadina, F. Wei, K. Onishi, H. Shen, E. Huang, L. Ferrari, Q. Ma, Y. Zou, Z. Liu, Experimental demonstration of localized plasmonic structured illumination microscopy. *ACS Nano* **11**, 5344–5350 (2017)
88. F. Wei, Z. Liu, Plasmonic structured illumination microscopy. *Nano Lett.* **10**(7), 2531–2536 (2010)
89. V.G. Kravets, F. Schedin, A.N. Grigorenko, Extremely narrow plasmon resonances based on diffraction coupling of localized plasmons in arrays of metallic nanoparticles. *Phys. Rev. Lett.* **101**, 087403 (2008)
90. B. Auguié, W.L. Barnes, Collective resonances in gold nanoparticle arrays. *Phys. Rev. Lett.* **101**, 143902 (2008)
91. G. Lozano, G. Grzela, M.A. Verschuuren, M. Ramezani, J.G. Rivas, Tailor-made directional emission in nanoimprinted plasmonic-based light-emitting devices. *Nanoscale* **6**, 9223–9229 (2014)
92. D.K.G. de Boer, M.A. Verschuuren, K. Guo, A.F. Koenderink, J.G. Rivas, S.R.-K. Rodriguez, Directional sideward emission from luminescent plasmonic nanostructures. *Opt. Express* **24**, A388–A396 (2016)
93. R. Guo, T.K. Hakala, P. Törmä, Geometry dependence of surface lattice resonances in plasmonic nanoparticle arrays. *Phys. Rev. B* **95**, 155423 (2017)
94. A.D. Bristow, D.M. Whittaker, V.N. Astratov, M.S. Skolnick, A. Tahraoui, T.F. Krauss, M. Hopkinson, M.P. Croucher, G.A. Gehring, Defect states and commensurability in dual-period  $\text{Al}_x\text{Ga}_{1-x}\text{As}$  photonic crystal waveguides. *Phys. Rev. B* **68**, 033303 (2003)
95. D.M. Whittaker, I.S. Culshaw, V.N. Astratov, M.S. Skolnick, Photonic band structure of patterned waveguides with dielectric and metallic cladding. *Phys. Rev. B* **65**, 073102 (2002)

96. C.J. Regan, R. Rodriguez, S. Gourishetty, L. Grave de Peralta, A.A. Bernussi, Imaging nanoscale features with plasmon-coupled leakage radiation far-field superlenses. *Opt. Express* **20**(19), 20827–20834 (2012)
97. J.R. Krenn, A. Dereux, J.C. Weeber, E. Bourillot, Y. Lacroute, J.P. Goudonnet, G. Schider, W. Gotschy, A. Leitner, F.R. Aussenegg, C. Girard, Squeezing the optical near-field zone by plasmon coupling of metallic nanoparticles. *Phys. Rev. Lett.* **92**, 2590–2593 (1999)
98. M.L. Brongersma, J.W. Hartman, H.A. Atwater, Electromagnetic energy transfer and switching in nanoparticle chain arrays below the diffraction limit. *Phys. Rev. B* **62**, R16356–R16359 (2000)
99. G. Weick, C. Woollacott, W.L. Barnes, O. Hess, E. Mariani, Dirac-like plasmons in honeycomb lattices of metallic nanoparticles. *Phys. Rev. Lett.* **110**, 106801 (2013)
100. V.N. Astratov, N.I. Limberopoulos, A. Urbas. Super-resolution microscopy methods and systems enhanced by dielectric microspheres or microcylinders used in combination with metallic nanostructures. U.S. patent 9835870B2 (5 June 2015)
101. A. Brettin, C.L. McGinnis, F. Abolmaali, N.I. Limberopoulos, D. Walker, A.M. Urbas, L. Poffo, A.V. Maslov, V.N. Astratov, in *NAECON 2018 - IEEE National Aerospace and Electronics Conference* (2018), pp. 536–539
102. F. Abolmaali, L. Poffo, A. Brettin, D.E. Walker, N.I. Limberopoulos, I. Anisimov, A.M. Urbas, A.V. Maslov, V.N. Astratov, in *NAECON 2018 - IEEE National Aerospace and Electronics Conference* (2018), pp. 540–543
103. F. Jünger, P. Olshausen, A. Rohrbach, Fast, label-free super-resolution live-cell imaging using rotating coherent scattering (ROCS) microscopy. *Sci. Rep.* **6**, 30393 (2016)
104. Y. Li, F. Abolmaali, K.W. Allen, N.I. Limberopoulos, A. Urbas, Y. Rakovich, A.V. Maslov, V.N. Astratov, Whispering gallery mode hybridization in photonic molecules. *Laser Phot. Rev.* **11**(2), 1600278 (2017)

# Chapter 17

## Microsphere-Assisted Interference Microscopy



Stephane Perrin, Sylvain Lecler and Paul Montgomery

**Abstract** Microsphere-assisted microscopy is a new two-dimensional super-resolution imaging technique, which allows the diffraction limit to be overcome by introducing a transparent microsphere in a classical optical microscope. This super-resolution technique makes it possible to reach a lateral resolution of up to one hundred nanometres. Furthermore, microsphere-assisted microscopy distinguishes itself from others by being able to perform label-free and full-field acquisitions and requires only slight modifications of a classical white light microscope. Extended to three-dimensional surface measurement through interference microscopy which has the advantage of providing a high-axial sensitivity, super-resolution topography or the volume distribution of objects can thus be reconstructed depending on the interference method employed. This chapter first presents a brief history of optical microscopy and recent advances in optical nanoscopy. Then, the super-resolution phenomenon through microspheres is introduced and its performance is described. Finally, the combination of optical interferometry with nanoscopy based on microspheres, giving microsphere-assisted interference microscopy, is exposed.

### 17.1 Optical Microscopy and Its Advances for Super-Resolution

The discovery of optical microscopy and the principle of the power of optical magnification power using an assembly of lenses are usually attributed to Z. Jansen in the 1590s, despite the fact that this claim reveals a confusion due to the year of

---

S. Perrin (✉) · S. Lecler · P. Montgomery  
ICube, University of Strasbourg - CNRS, 300 Boulevard Sébatien Brant,  
67412 Illkirch, France  
e-mail: [stephane.perrin@unistra.fr](mailto:stephane.perrin@unistra.fr)

S. Lecler  
e-mail: [sylvain.lecler@unistra.fr](mailto:sylvain.lecler@unistra.fr)

P. Montgomery  
e-mail: [paul.montgomery@unistra.fr](mailto:paul.montgomery@unistra.fr)

© Springer Nature Switzerland AG 2019  
V. Astratov (ed.), *Label-Free Super-Resolution Microscopy*,  
Biological and Medical Physics, Biomedical Engineering,  
[https://doi.org/10.1007/978-3-030-21722-8\\_17](https://doi.org/10.1007/978-3-030-21722-8_17)

birth of the Dutch optician being in reality in 1585 [1]. The precise origin of optical microscopy may thus be difficult nowadays to determine. We can, however, assign the observation of biological elements (e.g. bacteria and structures of plants) through an optical lens arrangement, for the first time, to A. van Leeuwenhoek [2]. His work was attested and simultaneously improved by R. Hooke who published the first book on microscopy in 1665 [3]. At that time and right up until the nineteenth century, the performance of the optical microscope was abstract and the notion of resolution was still unknown.

### 17.1.1 From Diffraction-Limited Optical Microscopy

It was only in the mid-1860s that the scientific community took a particular interest in the understanding of the concept of resolution and its limits. For the first time, in 1869, the diffraction of light was explicitly mentioned as a probable reason for the resolution limit [4]. This assumption was further promoted in 1873 by E. Abbe who considered the object to be visualized as a sum of periodic diffraction elements [5]. E. Abbe described in words that at least two orders of a periodic object (e.g. the +1 and -1 orders of a diffraction grating) should be collected by the objective lens in order to resolve its features. In 1876, H. von Helmholtz confirmed the Abbe theory through a mathematical demonstration of the resolution limit [6], leading to the first expression of the spatial resolution of an optical microscope:

$$\delta_{x,y} = \frac{\lambda}{n \sin(\alpha)} \quad (17.1)$$

Where  $\lambda$  is the wavelength of the monochromatic light source in air,  $n$  is the refractive index of the surrounding medium (e.g. in air, in water or in oil) and  $\alpha$  is the diffraction angle of the smallest discernible periodic object, i.e. the half-angle of the light collection cone. According to this theory, the details of the object having a spatial period finer than  $\delta_{x,y}$  are thus not resolved by the microscope and the high-frequency information is thus lost. At the same time, H. von Helmholtz showed that (17.1) requires a factor 1/2 when the illumination light source is incoherent (the term  $\lambda$  could thus be replaced by  $\lambda_0$ , the central wavelength of the broadband light source) [6]. In 1881, the term *numerical aperture* ( $NA$ ) of the objective lens appeared and was introduced as the sine of the angle  $\alpha$  multiplied by the refractive index of the working medium  $n$  [7]. In addition, E. Abbe reported a twofold increase in the lateral resolution by using oblique coherent illumination, yielding the famous definition of the lateral resolution:

$$\delta_{x,y} = \frac{\lambda}{2 NA} \quad (17.2)$$

Here, in (17.2), the angle of the illumination cone is assumed to equal the angle  $\alpha$ . Following this, A. Köhler suggested an enhancement of the illumination conditions

by using an even illumination of the object using an arrangement of lenses and diaphragms [8].

In addition in [6], H. von Helmholtz also discussed a second spatial resolution criterion which was determined previously by Lord Rayleigh in 1874 [9]. Unlike E. Abbe who assumed the object to consist of diffraction gratings, Lord Rayleigh and H. von Helmholtz considered the object as a sum of emitting point light sources. Lord Rayleigh defined the lateral resolution in the focal plane of an imaging system as the distance between the intensity maximum and the first intensity minimum of the diffraction pattern of a bright point source. In 1896, Lord Rayleigh significantly described his criterion of lateral resolution [10] using the previous work of G. B. Airy on the diffraction of light by a circular aperture [11].

$$\delta_{x,y} \approx 1.22 \frac{f \lambda}{D} \approx 0.61 \frac{\lambda}{NA} \quad (17.3)$$

From (17.3),  $NA$  can be retrieved through the focal length of the imaging system  $f$  and its pupil diameter  $D$ . Moreover, Lord Rayleigh highlighted the influence of imperfections on the imaging quality. In reality, the microscopes of the time were not able to reach the theoretical resolution due to the associated optical aberrations. Concurrently with these optical studies occurred the manufacturing of high-quality optical components (e.g. with the development of new types of glass by the German company *Glastechnische Laboratorium Schott & Genossen*). In 1879, O. Schott and E. Abbe achieved in making the first abnormal dispersion glass in order to correct the spherical aberrations for several wavelengths [12] and, in 1886, the first apochromatic microscope objective [13]. Nowadays, the majority of optical microscopes are able to form aberration-free images in the so-called diffraction-limited imaging systems.

Other resolution criteria exist such as the Sparrow criterion based on the contrast response of a photodetector [14] and the Houston criterion based on the full width at half maximum (FWHM) of the point spread function (PSF) of the imaging system [15]. One of them, in particular, became prominent in optical microscopy (and confirmed by the work of E. Abbe): the Fourier criterion through the measurement of the system's frequency response [16]. Introduced in 1946 by P. M. Duffieux, Fourier optics makes the analogy with analogue electronic systems and is based on diffraction as well as the propagation of light [17]. Indeed, this powerful method allows the characterization of an entire imaging system through the measurement of its transfer function, enabling both performance (e.g. the resolution) and imaging quality (e.g. the optical aberrations) retrieval. In 1960, V. Ronchi highlighted the importance of considering both the sensitivity of the sensor and the illumination conditions, in order to determine the resolving power of an imaging system [18] (Fig. 17.1).

Despite a decrease in the wavelength of light  $\lambda$  or an increase in the refractive index of the surrounding medium in order to achieve a better lateral resolution, this key parameter in the classical optical microscope is still limited by the diffraction of light, i.e. a maximum of  $\lambda/2$  in air. Typically, a perfect diffraction-limited optical microscope is able to resolve details with 300 nm of size over a lateral field of view (FOV) of 100  $\mu\text{m}$ . The problem is that the higher frequency components of the details

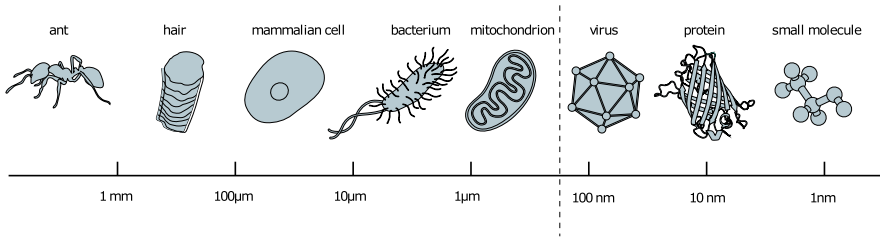


**Fig. 17.1** Lateral resolution limit in classical optical microscopy. Reproduced with permission of The Royal Swedish Academy of Sciences © Johan Jarnestad/The Royal Swedish Academy of Sciences

of the object, i.e. the evanescent waves emanating from it, decay exponentially in the positive refractive index surrounding medium and are thus not collected by a conventional microscope objective.

Fourier optics brought a real enthusiasm to the scientific community since it showed the tantalizing potential of being able to go beyond the optical cut-off frequency [19]. Furthermore, the need to visualize elements that were smaller and smaller made it possible to develop several sub-diffraction-limited techniques [20] which are nowadays identified as *super-resolution* imaging techniques [21], all of those that are able to go beyond  $\lambda/2$ .

### 17.1.2 To Super-Resolution Optical Microscopy

Although the notion of optical nanoscopy arose much earlier, it was only brought to the forefront with the Nobel Prize for Chemistry in 2014 through super-resolved fluorescence microscopy and single molecule localization microscopy [22]. The difference between these two super-resolution imaging techniques are that in the first, there is a real improvement in the resolving power, whereas the second uses super-localization in order to map details to a higher resolution using unresolved molecules. Sub-diffraction-limited techniques can hence be classified in different categories according to their illumination/detection method, i.e. near-field or far-field imaging, and to their linear (or nonlinear) spatial and temporal response of the sample [23, 24] (see classification of nanoscopy techniques in Fig. 17.2).

**Scanning near-field optical microscopy** The concept of super-resolution imaging dates back to the 1920s with the notion of *ultramicroscopy* [25]. E.H. Syngé suggested placing an orifice at a few hundred nanometres from the surface of the sample in order to collect the evanescent waves. Then, the probe or the sample would be laterally displaced to perform a 2D image [26]. It took fifty years for this concept of scanning near-field optical microscopy (SNOM) to emerge [27] and, in the 1980s, the microscopist community became enthusiastic about this sub-diffraction-limit imaging technique, leading to new designs of SNOM devices [28–31], variants

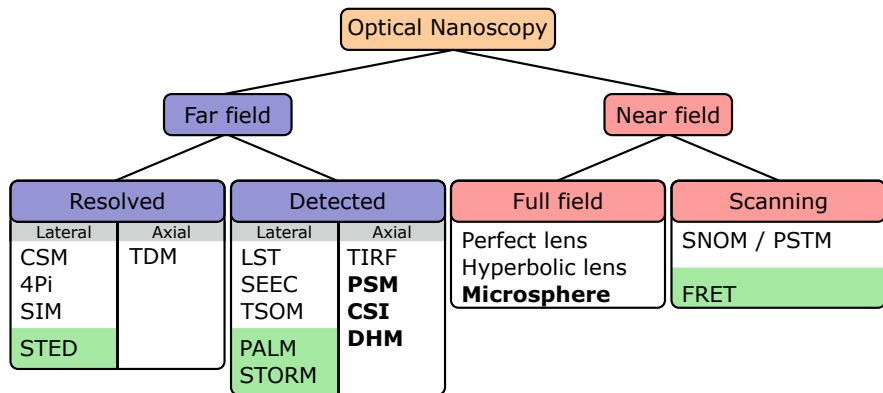


**Fig. 17.2** Classification scheme of optical nanoscopy techniques according to their acquisition method. Lateral or axial improvement in spatial resolution is considered in the classification, as well as the techniques requiring labels or markers (in the green areas). The imaging techniques written in bold characters are used for microsphere-aided interference nanoscopy (see Sect. 17.3). More details on the classification of the optical nanoscopy techniques are reported in [24]

(e.g. of photon scanning tunnelling microscopy (PSTM) [32, 33] or Förster resonance energy transfer (FRET) microscopy [34, 35]), and a better understanding of the principle [36, 37]. The only limit of the lateral resolution of SNOM was the diameter of the probing aperture which can reach around 20 nm in ideal cases [38].

**Confocal microscopy** Shortly before the invention of the LASER, confocal microscopy (CSM) appeared in the patent filed by Minsky [39], despite its principle being previously pointed out in 1940 by H. Goldmann for ophthalmology [40] and in 1951 by Koana [41]. This far-field scanning imaging technique enables an increase of the lateral resolution of 1.5 times compared to standard optical microscopy by spatially filtering both the illumination and imaging rays using point detection. However, the axial resolution was still low. J. C. R. Sheppard (in 1991) [42] and S. Hell (in 1992) [43, 44] proposed thus to illuminate the sample by a coherent light source and then collect the fluorescence beam using two opposing objectives. This double-pass CSM configuration, known as 4Pi confocal fluorescence microscopy, referring to the solid angle in 4Pi holography [45], leads to constructive interference, and reduces the axial PSF by a factor of 5 compared to confocal microscopy. At the beginning of the 2000s, the enhancement of computing power allowed the discovery of the focusing effect in the near field of dielectric particles, i.e. the photonic jet [46, 47]. This phenomenon concentrates light in a sub-diffraction-limit progressive beam. Indeed, the waist of the photonic jet beam has a size of around  $\lambda/3$  in air, enabling the enhancement of the optical performance in confocal microscopy [48], Raman microscopy [49] and photoacoustic microscopy [50].

**Structured illumination microscopy** At the beginning of the 1960s, the principle of structured illumination microscopy (SIM) was reported for the first time by W. Lukosz et al. [51] and reinvented in 1992 by P. C. Sun et al. [52]. Easy to

implement, SIM consists of illuminating the sample with a sinusoidal pattern and recording at least three angle-shifted images. The period of the periodic excitation pattern is chosen to shift the inaccessible high-frequency components within the passband of the conventional optical transfer function (OTF). Using the computation optical sensing and imaging (COSI) approach, the high-resolution information is extracted and the image is then reconstructed using a deconvolution of the sample with the illumination pattern in Fourier space [53]. The first convincing results with linear SIM have shown a real enhancement of the lateral resolution and an overcoming of the diffraction limit by a factor of two [54, 55].

The diffraction of light limits not only the lateral resolution but also the axial resolution of optical microscopes where its limit can be expressed as:

$$\delta_z = \frac{\lambda}{n [1 - \cos(\alpha)]} \quad (17.4)$$

Generating an interference pattern along the third dimension, i.e. above and below the focal plane, thus allowed the axial resolution to be improved [53].

**Metamaterial-superlens-based microscopy** V. G. Veselago reported in 1967 the advantage of the use of materials with negative refractive index in order to record both the near field and the far field from the surface of an object [56]. Thirty years later, J. B. Pendry highlighted electromagnetic resonances to create negative refractive index lenses ( $n = -1$ ) [57] and then (re)proposed the concept of the *perfect lens* by collecting both the propagative and evanescent waves with a flat lens placed close to the object surface [58]. Nevertheless, materials having both a negative dielectric permittivity and a negative magnetic permeability do not exist in the natural state, making it necessary to require metamaterials to create super lenses [59, 60]. The experimental demonstration of this new super-resolution imaging technique appeared shortly afterwards with the enhancement of the near field of microwaves [61, 62]. The limitations of the technique were finally discussed by Smith et al. [63]. Afterwards, metal-based flat super lenses began to emerge [64–66] followed by the hyperbolic metamaterial lenses [67, 68].

**Stimulated emission depletion microscopy** In 1986, stimulated emission depletion (STED) microscopy was introduced through a patent filed by Okhonin [69]. Then, in 1994, S. Hell revealed the principle of STED, enabling a lateral resolution of 30 nm to be reached in the far field [70] and, further, the first experimental implementation of the fluorescent-label-based technique in 1999 [71]. The aim of STED microscopy consists of narrowing the PSF of the point-to-point system by depleting the fluorescence from the outer plane of the focal point and thus leaving the centre active to emit fluorescence [72]. Therefore, a phase mask is placed in the depletion arm so as to make possible the altering of the functions of the pupil. In STED microscopy, the lateral resolution depends not only on the wavelength of the light and the  $NA$  of the imaging system but also on the saturation irradiance of the depletion incident beam. The need for high exposure irradiance ( $\sim 1 \text{ kW/cm}^2$ ) nevertheless damages the sample, as in single-molecule microscopy [73] which can perform a lateral resolution of 20 nm using around  $50 \text{ W/cm}^2$  of surface power density.

**Tomographic diffractive microscopy** With tomographic acquisitions, tomographic diffractive microscopy (TDM) is based on the principle of digital holographic microscopy (DHM) in which interferometry enables the axial resolution to reach a few tens of nanometres [74]. However, the lateral resolution in DHM is still limited by the diffraction of light, and in this case requires a coherent light source, i.e.  $\delta_{x,y} \sim \lambda$  [75]. TDM achieves an improvement in the lateral resolution by varying the illumination angle of the plane wave [76–78]. By performing multiple incident illuminations, the numerical aperture of the interference system appears thus enhanced in the Fourier domain and, further, the coherent noise is averaged, providing a higher SNR [79]. TDM allows the reconstruction of the volume of the sample using an adapted model of diffraction [80, 81] with a lateral resolution that is twice as high as that in DHM. It was shown that a decrease in the wavelength of the light to 405 nm allows TDM to visualize objects 90 nm of size [82].

**Total internal reflection microscopy** In 1981, D. Axelrod used the idea proposed by E. J. Ambrose on total internal reflection [83] in order to increase the axial resolution of biological imaging systems [84]. A transparent prism is placed above the surface of the sample and only the evanescent waves generated at the glass–sample interface allows the illumination of the sample. This method is known as total internal reflection microscopy (TIRFM) and makes it possible to excite an interface to within a few 100 nanometres depth, corresponding to the decay in the evanescent field. This provides the advantage of removing the out-of-focus fluorescence signal, resulting in a higher signal-to-noise ratio [85]. An axial resolution of 100 nm can thus be achieved which is smaller than the diffraction limit. Nevertheless, the gain in resolving power is only along the optical axis. In fact, the lateral resolution is still limited by the diffraction although an immersion objective lens collects the fluorescence far-field information. Exploiting the performance of SNOM, the emanating evanescent waves were therefore recorded with a high-lateral resolution, leading to scanning tunnelling optical microscopy (STOM) [32, 86].

**Laser scanning tomography** At the end of the 1980s, the group of J. P. Fillard at the University of Montpellier (France) was one of the first groups to develop the notion of *optical nanoscopy* [87]. In order to study defects inside silicon and the key semiconductor alloys at the root of the communications and semiconductor light source revolutions, several techniques were developed that allowed the observation and study of nanometre-sized structures without resolving them. For example, laser scanning tomography (LST) [88, 89] used the very high contrast of dark-field illumination with a focused laser beam orthogonal to the viewing direction, now known as light sheet microscopy [90], to map micrometre-sized microprecipitates in 3D. The technique was even able to show distributions of 10 nm-sized microprecipitates within annealed gallium arsenide [91]. By means of image processing, phase contrast microscopy was able to show up the effect of pinning of looped dislocation paths in gallium arsenide by individual microprecipitates [87]. The atomic sized defect was indirectly visible due to it being extended in one direction and forming a stress field that modified the surrounding refractive index sufficiently for the path to be discernible. Since then, many other optical nanoscopy techniques have been developed for studying and measuring nanostructures without resolving them, such as surface-

**Table 17.1** Summary of performance of super-resolution optical techniques

| Technique         | Method                                  | Typical resolution                     | Requirements   |
|-------------------|---|--|--|
| 4Pi microscopy    | Constructive interferences              | 200 nm (laterally)<br>100 nm (axially) | <ul style="list-style-type: none"> <li>• Lateral scanning</li> <li>• Degree of freedom for alignment</li> </ul>  |
| CSM <sup>a</sup>  | Spatial filtering in the far field      | 200 nm (laterally)<br>500 nm (axially) | <ul style="list-style-type: none"> <li>• Lateral scanning</li> <li>• Limitation of the imaging depth</li> </ul>  |
| SIM <sup>b</sup>  | Shift of the object spectral components | 100 nm (laterally)<br>300 nm (axially) | <ul style="list-style-type: none"> <li>• Resolution—SNR trade-off</li> <li>• Sensitive to out-of-focus</li> <li>• Cut-off frequency limit = <math>4 NA/\lambda</math></li> </ul> |
| SNOM <sup>c</sup> | Near-field local probing                | 40 nm (laterally)<br>10 nm (axially)   | <ul style="list-style-type: none"> <li>• Low working distance (<math>&lt; \lambda</math>)</li> <li>• Limitation of the imaging depth</li> <li>• Lateral scanning</li> </ul>      |
| STED <sup>d</sup> | Non linear response of fluorophores     | 40 nm (laterally)<br>200 nm (axially)  | <ul style="list-style-type: none"> <li>• Photo-induced toxicity of sample</li> <li>• Complex to implement</li> <li>• Lateral scanning</li> </ul>                                 |
| Super lens        | Perfect lens with negative index        | 100 nm (laterally)<br>100 nm (axially) | <ul style="list-style-type: none"> <li>• Difficult to fabricate</li> <li>• Monochromatic illumination</li> </ul>   |
| TDM <sup>e</sup>  | Multiple angular illuminations          | 100 nm (laterally)<br>10 nm (axially)  | <ul style="list-style-type: none"> <li>• Slow refractive index gradient</li> <li>• Multiple acquisitions</li> </ul>  |

<sup>a</sup>Confocal scanning microscope, <sup>b</sup>Structured illumination microscopy, <sup>c</sup>Scanning near-field optical microscopy, <sup>d</sup>Stimulated emission depletion microscopy, <sup>e</sup>Tomographic diffractive microscopy

enhanced ellipsometric contrast microscopy [92], and through focus scanning optical microscopy [93] (Table 17.1).

**Microsphere-assisted microscopy** More recently, Wang et al. demonstrated experimentally in 2011 full-field and label-free super-resolution microscopy through glass microspheres [94]. Introducing a transparent microsphere in a classical white light microscope allows the diffraction limit to be overcome and the lateral resolution to reach a couple of 100 nanometres in water. Thus, microsphere-assisted microscopy makes it possible to increase the lateral resolution further than that with confocal microscopy and the solid immersion lens [95]. Moreover, a similar resolving power can be achieved in comparison with structured illumination microscopy and the metamaterial-based lenses while being relatively simpler and easier to implement. Instead of a bead, an optical fibre [96–98] or even a spider’s silk thread [99] can also perform super-resolution imaging along one transversal axis which acts as a cylindrical *superlens*.

## 17.2 Microsphere-Assisted Microscopy for 2D Imaging

### 17.2.1 Principle

The approach of microsphere-assisted microscopy for 2D imaging consists of simply placing a transparent microsphere between the sample to be tested and an optical microscope. A magnified image which is virtual in the case illustrated in Fig. 17.3a, is then generated below the object plane. Finally, the objective lens of the optical microscope which usually cannot resolve the features of the object (see the example in Fig. 17.3b), collects the image which reveals sub-diffraction-limit information (see the example in Fig. 17.3c). Super-resolution label-free imaging can thus be performed using a microscale glass sphere and a moderate NA objective lens which is suitably chosen to resolve the features of the magnified image.

The concept of super-resolution has been proven through experiments (e.g. for the first time by Wang et al. using object features having sub-wavelength sizes as shown in Fig. 17.4 [94]) as well as by simulations. Nonetheless, the fundamental phenomenon behind the technique is up to now not fully explained. At this point, we can attest that the photonic jet phenomenon is not relevant to justify this resolution improvement [100, 101]. Despite overcoming the diffraction limit, the waist size of the near-field beam of the photonic jet is only around a third of the wavelength in air which remains larger than the lateral resolution previously reported in the literature for microsphere imaging of around  $\lambda/6$ . Recently, Y. Ben-Aryeh demonstrated mathematically that the process of super-resolution could be explained by the collection of the evanescent waves by the microsphere using the complex form of Snell's law [102]. The particle thus converts the near-field information from the sample into far-field propagating waves [103]. This near-field to far-field transformation phenomenon can be enhanced

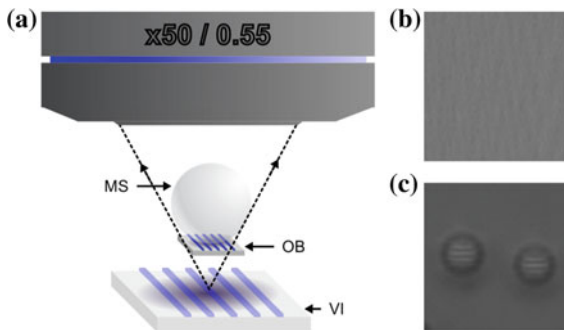


**Fig. 17.3** Principle of microsphere-assisted microscopy. **a** A microsphere MS placed on the surface of the object OB generates here a virtual image VI which is magnified. The MS transforms the near-field information of the OB into far-field propagating waves. Then, a microscope objective collects the VI in the far field. A comparison of the performance in air using, **b** a  $\times 50$  microscope objective alone where the 200-nm-size details of the OB are not resolved, and **c** using the MS-based nanoscope. Here, the diameter of the silica MS is  $6\ \mu\text{m}$

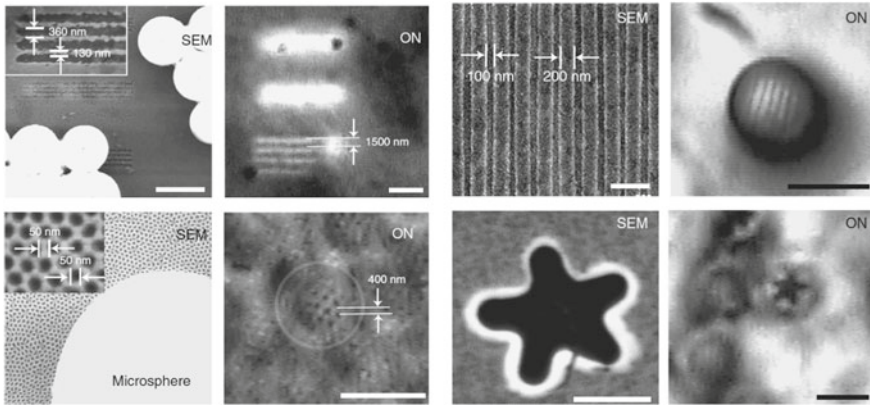


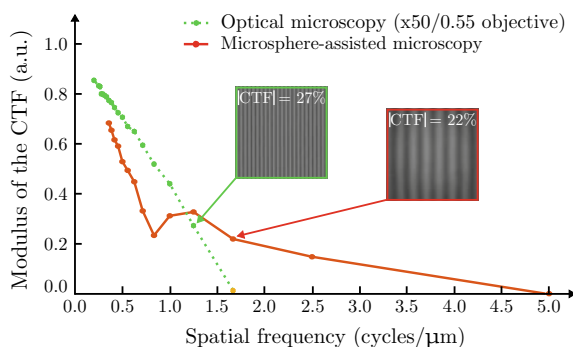
**Fig. 17.4** Experimental demonstration of the super-resolution phenomenon through silica microspheres using white light illumination. The  $5\ \mu\text{m}$ -diameter microsphere is placed on the sample to be measured. The experimental results were performed in the transmission mode using a 490-nm-period grating and 100-nm-period pores (on the left), and also in the reflection configuration using a 300-nm-period Blu-ray disc and a star having corners of 90 nm. Scale bars represent 500 nm (SEM) and  $5\ \mu\text{m}$  (ON). Reproduced with permission from [94]. ©2018 Nature

by considering the whispering-gallery mode resonance within the microsphere [104–106]. Furthermore, the influence of both the excitation of the electromagnetic modes and the coherence of the light on the imaging contrast has also been highlighted [105, 107–109].

### 17.2.2 Performance

A theoretical expression of the super-resolution limit in microsphere-assisted microscopy is thus currently not fully defined. Only experimental and numerical results allow an evaluation of the performance of this imaging technique, showing a resolution limit of around  $\lambda/4$  through simulations [105, 109, 110] and  $\lambda/6$  through experiments [103, 111] in air and in immersion. However, the quantitative evaluation of lateral resolution is often overestimated, ranging from  $\lambda/7$  to  $\lambda/17$  since it is based on the measurement of the object size or the grating groove size (*e.g.*, feature size or inter-distance between two features) [94, 112, 113]. The limit in resolving power of a linear imaging system is usually defined as the period of an object feature having a contrast depending on a criterion (typically, a contrast of 0 being the cut-off frequency of the system) [114]. See, for example, the work of Duocastella et al. with the optical frequency response characterization of a microbead coupled to a bright-field microscope [115]. Figure 17.5 demonstrates the super-resolving power in microsphere-assisted microscopy through an experimental measurement of the contrast transfer function [116].

**Fig. 17.5** Comparison of the modulus of the contrast transfer function (CTF) of microsphere-assisted microscopy with optical microscopy. The frequency response has been measured using positive Ronchi targets. The microsphere has a refractive index of 1.52 and a diameter of 26  $\mu\text{m}$ . The illumination is a white light source [116]



More adapted for experiments in microscopy (far field as well as near field), the FWHM of the PSF of the linear imaging system, i.e. the Houston criterion, could also be used (see Fig. 17.6) [19]. In white light microsphere-aided microscopy, achieving a resolution beyond 100 nm in air is difficult at present despite nanoplasmonic arrays having been used to increase further the super-resolution phenomenon [117].

The performance of microsphere-assisted microscopy depends on geometrical (e.g. the diameter of the microsphere) and optical (e.g. the refractive index of both the surrounding medium and the microsphere, and the wavelength of light) parameters. The super-resolution phenomenon can be achieved using glass microspheres

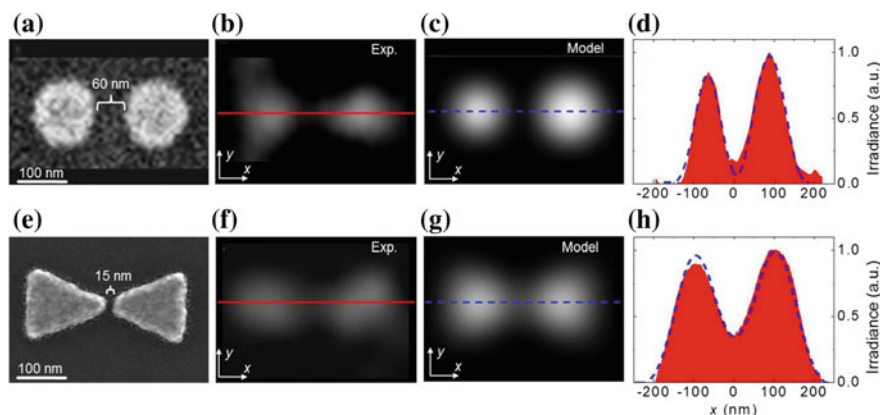


**Fig. 17.6** Calculation of the resolution in microsphere-assisted microscopy using the Houston criterion. SEM images of **a** two Au nanocylinders and **e** two bow tie-shaped nanostructures. Super-resolution imaging of these samples obtained through **b** 5  $\mu\text{m}$ -diameter and **f** 53  $\mu\text{m}$ -diameter BTG microspheres in air. **c, g** Calculated convolutions of the perfect objects (nanocylinders and bow tie-shaped nanostructures) with 2D PSFs having a FWHM of  $\lambda/7$  and  $\lambda/5.5$ , respectively. **d, h** Comparison of the measured (red background) and calculated (dashed blue curves) irradiance profiles along the  $x$  direction. The wavelength of the light source is 405 nm. Reproduced with permission from [127]. ©2018 Wiley

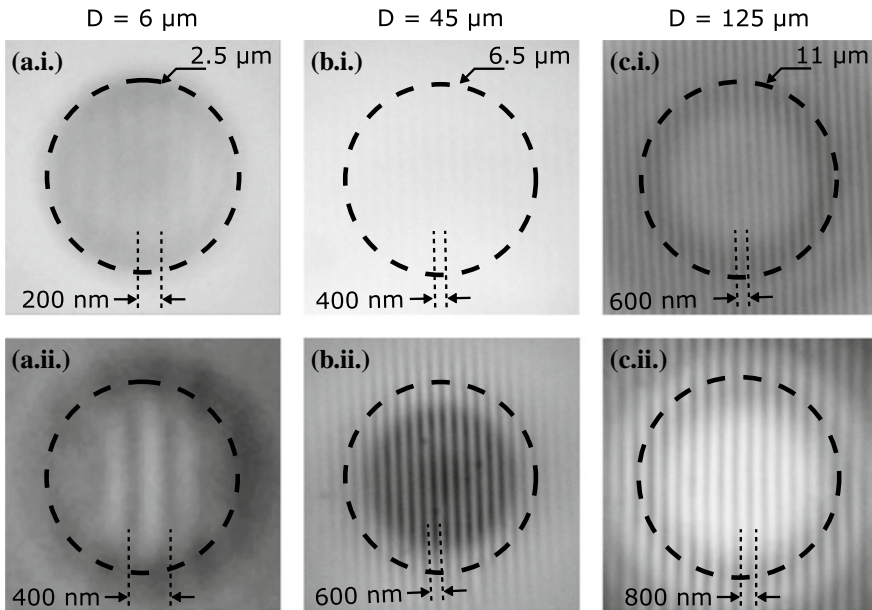


**Fig. 17.7** Influence of the size of the microsphere on the super-resolution phenomenon. Glass microspheres ( $n \sim 1.5$ ) having different diameters were thus placed on periodic Ronchi targets. The dashed black lines represent the calculated lateral FOV. An increase in the microsphere diameter leads to an increase in the lateral FOV, following a root-square function. However, the resolving power appears to be reduced, i.e. the 6- $\mu\text{m}$ , 45- $\mu\text{m}$  and 125- $\mu\text{m}$ -diameter microspheres are able to visualize (a.i) 200-nm, (b.i) 400-nm and (c.i) 600-nm-period features, respectively, with an imaging contrast of 9%. (a.ii), (b.ii) and (c.ii) are the super-resolved images obtained through the three microspheres with larger period gratings and therefore a more acceptable imaging contrast

having diameters ranging from a few micrometers [118] to a few 100 micrometers [119]. The diameter of the microsphere influences not only the lateral resolution but also the lateral FOV: the smaller the microsphere, the higher is the resolution and the smaller is the measurement area (see Fig. 17.7). The FOV of a microsphere-assisted imaging system has been determined to be around the square root of the diameter using white light illumination centred at 500 nm [120]. For example, a 25  $\mu\text{m}$ -diameter microsphere allows the magnification and the FOV to reach around 4.5 and 5  $\mu\text{m}$ , respectively. Beyond this area, the collection of near-field waves by the microsphere decreases dramatically. Nevertheless, using a bigger microsphere decreases the resolving power, as shown in Fig. 17.7 and in Fig. 17.6. Therefore, recent work reported the design and the development of optical heads based on a vertical integration [113, 121–123], AFM cantilevers [115, 124], chemically powered probes [125] or a matrix configuration [126–128] in order to extend the lateral FOV. Furthermore, these implementations allow the performing of contact-less and non-invasive acquisitions by holding the microsphere at a certain distance from the sample while retaining the ability to perform super-resolution measurements. The

refractive index contrast, i.e. the ratio between the refractive indices of the microsphere and the surrounding medium, must also be considered in the super-resolution imaging formation [129]. Indeed, increasing the refractive index ratio makes it possible to improve the super-resolution phenomenon [111, 130]. A partial immersion of the microsphere also contributes to the enhancement of the sub-diffraction-limit imaging [131].

### 17.2.3 Image Formation

Usually, the magnified image generated by the microsphere is virtual as for example in Fig. 17.4. However, the refractive index ratio and the diameter have also an influence on the nature of the image created by the microsphere. The generation of real images in microsphere-assisted microscopy has been experimentally demonstrated (see Fig. 17.8) [132].

Despite the photonic jet phenomenon not being relevant to explain the super-resolution, it plays, however, a critical role in the imaging process [100]. The formation of the real image can hence be explained by considering the photonic jet as the *focal point* of the microsphere [101], which is inside the microsphere when the refractive index contrast is higher than around 1.8 regardless of the size of the microsphere (see Figs. 17.9 and 17.10). Thus, the image can also be virtual or real, depending on the axial position of the object regarding the photonic jet position.

The work reported by R. Ye et al. tends to confirm this assumption [133]. The sample was placed axially between the rear interface of a silica microsphere and the photonic jet, thus giving a virtual image, whereas raising the microsphere beyond the position of the photonic jet provided a real image. It should be noted that a distance between the microsphere and the sample can lead to a loss of the near-field collection

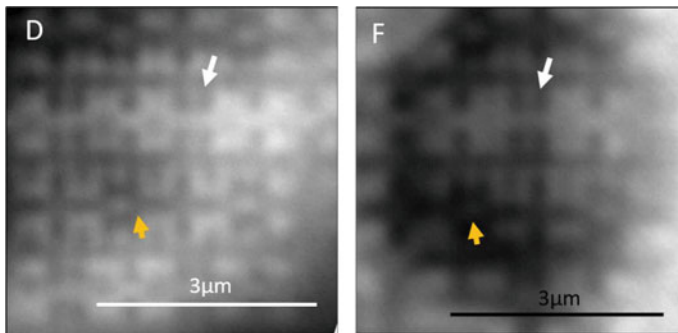


**Fig. 17.8** Formation of (on the left) a virtual image using an 1.59 refractive index microsphere with a radius of  $30\ \mu\text{m}$  and a real image using a 1.9-refractive-index microsphere with a radius of  $35\ \mu\text{m}$  in air. The barium-titanate microspheres are in contact with the CPU features. Reproduced with permission from [132]

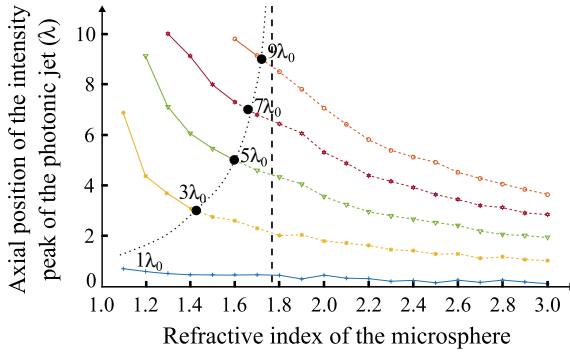


**Fig. 17.9** Evolution of the axial position of the photonic jet intensity peak as a function of the refractive index of the microsphere for different radii in air. The distance and the radii are expressed in wavelengths  $\lambda$ . Five radius-dependent curves are represented, going from  $1 \lambda$  to  $9 \lambda$ , with an increment of  $2 \lambda$ . The black dots represent the position of the photonic jet on the interface of the microsphere. An imaging system having a refractive index contrast higher than around 1.8 will always provide a real image [101]

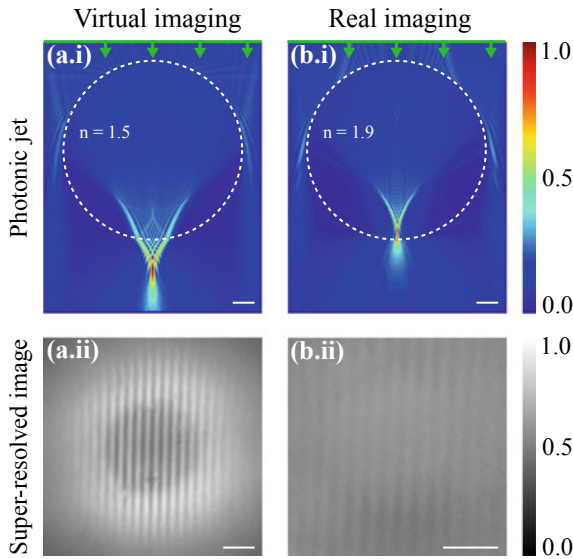


**Fig. 17.10** Image formation depending on the refractive index contrast between the microsphere and the surrounding medium. The microbead is in contact with the object. (a.i) A soda-lime-glass microsphere ( $n = 1.52$ ) generates a photonic jet outside the microsphere in air. (a.ii) A virtual image occurs. (b.i) Using a barium-titanate-glass microsphere ( $n = 1.90$ ) in air, the focus spot appears inside the microsphere. (b.ii) The image is real. In both cases, the super-resolved images were experimentally measured using a 600-nm-period grating placed against the  $32 \mu\text{m}$ -diameter microspheres [101]. White scale bars represent  $2 \mu\text{m}$

due to their exponential irradiance decrease and, thus, the loss in the high-frequency information from the sample.

### 17.2.4 Applications

Full-field microsphere-assisted microscopy has successfully been demonstrated in several imaging approaches in both the transmission and reflexion modes [134] ranging from fluorescence nanoscopy [135] to dark-field nanoscopy [136, 137]. Moreover, the imaging technique was applied in various domains such as biological imaging for the visualization of proteins [117], subcellular structures [135], and medium-sized nonenveloped viruses [138]. After sub-diffraction-limited characterization of materials was first implemented in 2D using microspheres, the technique was then extended to 3D object inspection. This was achieved by combining a microsphere with interference microscopy in order to measure and reconstruct high-spatial-resolution sample profiles in three dimensions (Fig. 17.11).

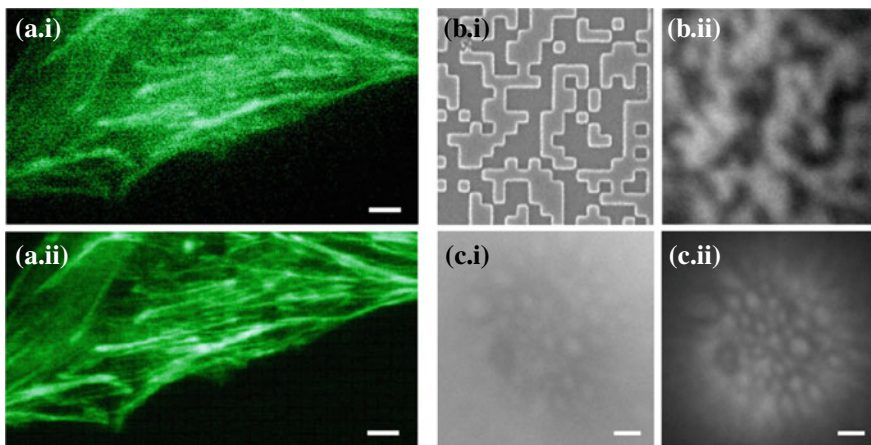


**Fig. 17.11** Biological imaging using microsphere-aided microscopy. (a.i) fluorescent classical microscopy and (a.ii) fluorescent microsphere-aided microscopy of a C2C12 cell. A  $56\ \mu\text{m}$ -diameter microsphere held by an AFM cantilever and combined with a microscope objective ( $\times 100$ ,  $\text{NA} = 0.8$ ) allows the observation of actin filaments. The sample was labelled by Alexa Fluor 488-phalloidin. Scale bars represent  $5\ \mu\text{m}$ . Reproduced with permission from [124]. ©2018 Nature. (b.i) SEM image and (b.ii) dark-field microsphere-assisted microscopy of a random matrix of glass nano-printed squares. A  $25\ \mu\text{m}$ -diameter microsphere combined with a microscope objective ( $\times 20$ ,  $\text{NA} = 0.4$ ) make it possible to resolve the  $250\ \text{nm}$  features. High-contrast super-resolution imaging of myelinated nerve fibres of the mouse brain hippocampus using (c.i) bright-field illumination and (c.ii) dark-field illumination. The smallest translucent cells having a size of around  $300\ \text{nm}$  are now distinguished [137]

## 17.3 Three-Dimensional Microsphere-Assisted Microscopy

Optical interference microscopy is a powerful imaging technique allowing a quantitative measurement and reconstruction of the surface topography [139], the inside tomographic view [140] or the volume [74, 141]. Interferometry consists of superposing two light beams from a unique light source in which the first beam is reflected (or transmitted) by the object and the second beam is reflected from a reference surface. The detection of the interferogram by the detector, resulting from the combination of the two beams, makes it possible to extract the wavefront deformation and, hence, the height distribution. Several interferometric methods and optical interference configurations exist depending on the nature of the illumination light, the measurement mode, i.e. transmission or reflection, and the signal processing.

### 17.3.1 Interference Methods

Mainly used for the characterization of material surfaces and micro-components, coherence scanning interference microscopy (CSI), also called white light interference microscopy is based on the acquisition of the interference signal which is gated by an envelope function when broadband illumination is employed. Optical coherence tomography for biological imaging [142] is based on the same principle, but using a remote fibred interferometer and point detection. The interference signal occurs only when the optical path difference between the two arms of the interferometer is less than the coherence length of the light source. The maximum intensity of the gate function, thus, reveals the exact axial position of the object with respect to the reference mirror at a given pixel. A variation in the optical path difference between the two arms of the interferometer enables the probing of the surface or volume of the object by the fringes from which a height distribution can be retrieved. Different algorithms have been implemented to process the interferogram [143]. In the case of digital holographic microscopy (DHM), spatially and temporally coherent illumination is required (e.g. a laser source), resulting in the need for only one interference pattern acquisition to retrieve the surface topography or the volume distribution of the sample. A numerical processing of the hologram uses 2D fast Fourier transform operators to perform numerical wavefront propagation, allowing the phase distribution of the sample to be retrieved [144]. Enhancements of DHM have been reported through software developments [145] and optical setups [146]. Phase-shifting interference microscopy (PSM) requires the measurement of three or more shifted interference patterns by introducing a known optical delay between the reference and object arms [142]. Depending on the algorithm and the displacement technique, the phase difference distribution can then be recovered through simple mathematical formulas, making possible the point-by-point reconstruction of the wavefront deformation from the object. Coherent as well as low-coherent light sources can be used in PSM. More easier to implement from a software development

point of view than DHM, PSM needs however several acquisition frames compared with just one for DHM.

Other interference imaging techniques exist and also allow non-invasive and label-free imaging to be performed with a high-axial sensitivity. Nevertheless, the theoretical lateral resolving power of interference microscopes is limited by the diffraction of light [147] as in classical light microscopy. For example, the lateral resolution in DHM cannot be better than the wavelength of the monochromatic light source  $\lambda$  or  $\lambda/2$  using oblique illumination [148]. In practice, a lateral resolution of  $\lambda$  is unfortunately never achieved. Indeed, the fabrication of interference objectives having an NA superior to 0.6 is relatively complex. Furthermore, the use of high-numerical aperture microscope objectives in an interferometer are not trivial due to the misalignments of optical components which can occur, leading to wavefront errors. This restriction yields a non-homogeneous spatial resolution along the transverse and axial dimensions, i.e. a non-homogeneous *voxel* size. While the remarkable nanometric axial resolution of automated interference techniques has been recognized and appreciated by optical metrologists for over three decades, it has been frustrating to have to put up with a lateral resolution that is over two orders of magnitude worse. The recent idea of combining interference microscopy with super-resolution imaging aided by a microsphere is thus perceived as a major breakthrough in providing a more uniform 3D resolution of samples.

### 17.3.2 Super-Resolution Interference Methods

The first paper on microsphere-assisted interference microscopy showing a potential increase in lateral resolution was reported using DHM, in 2015 [149]. It was underlined that the super-resolution phenomenon is applicable not only to the amplitude image but also to the phase image. Moreover, a 90  $\mu\text{m}$ -diameter polystyrene microsphere acting as a near-field to far-field transforming optical element allows the diffraction limit to be broken, passing from 1.38 to 1  $\mu\text{m}$ . Here, the magnification factor of the microsphere equals 2.3.

A few months later, F. Wang et al. demonstrated experimentally a concrete and significant enhancement of the lateral resolution in 3D label-free super-resolution imaging using microspheres [150]. Indeed, the lateral resolution was increased by a factor of 2.3 (according to the Abbe criterion). Here, the interferometric method used is CSI and the configuration consists of a Linnik interferometer using a white light lamp and two 0.6-numerical-aperture objectives. Microspheres with different diameters were placed in water (made of barium-titanate glass) and in air (made of polystyrene). F. Wang et al. claim to discern features having a smallest size of 50 nm (in reality, the highest lateral resolution achieved experimentally is around 200 nm) while keeping 10 nm of axial sensitivity. The surface topography of complex-shaped samples (e.g. gratings, nanodot array and structures of a CPU chip) was successfully reconstructed as shown in Fig. 17.12. Furthermore, the influence of the illumination conditions on the image contrast was reported.

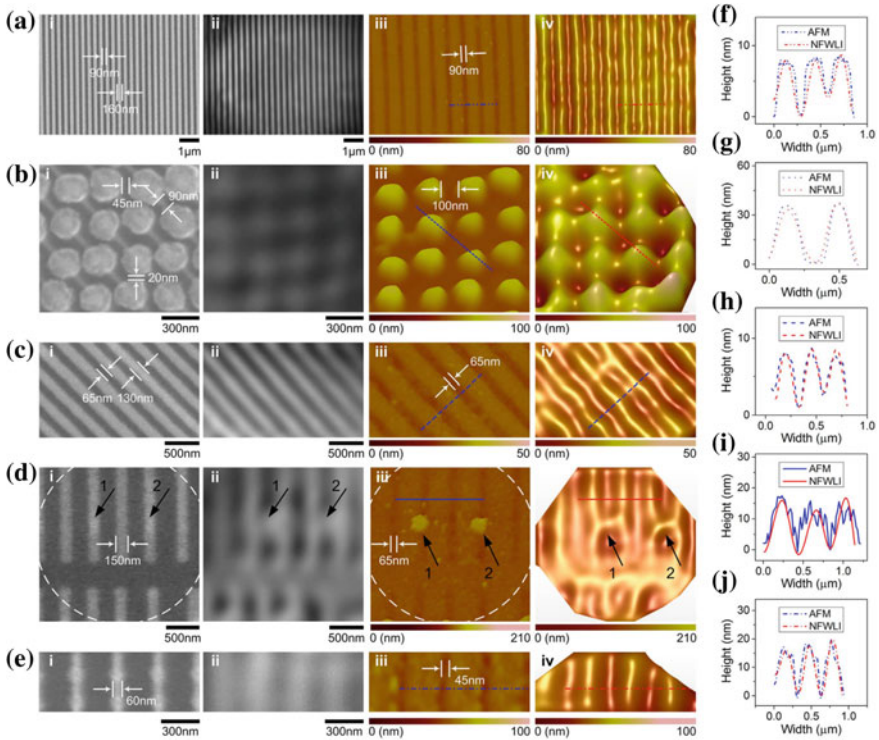


**Fig. 17.12** Experimental results achieved using near-field white light interferometry (NFWLI) which consists of BaTiO<sub>3</sub> microspheres having diameters of **a** 69 μm, **b** 19 μm, **c** 26 μm, **d** 33 μm and **e** 25 μm. (i) SEM images of the sample. (ii) Virtual images of the samples generated by the microspheres. (iii) AFM images. (iv) 3D morphology reconstructed using NFWLI. **f–j** Comparisons of the cross sections marked by lines in (a(iii,iv)–e(iii,iv)). Reproduced with permission from [150]. ©2018 Nature

In 2016, DHM aided by a microsphere was again developed for cell identification [151]. A 230-μm-diameter silica microsphere was placed between the biological sample and a Mirau-microscope objective and held by an optical fibre. The lateral resolution was increased by a factor of 1.5 which appears enough to visualize red blood cells as shown in Fig. 17.13. An enhancement of the super-resolution phenomenon followed in 2017 by using a smaller microsphere diameter [152], and in 2018, an application for 3D surface characterization of polymeric nanocomposites [153]. It should be noted that the use of a coherent illumination in microsphere-assisted microscopy tends to generate coherent noise from the multiple reflections between the microsphere interfaces [154] which can then reduce the image quality. This effect can be reduced by using a rotating diffuser, which reduces the spatial coherence of the illumination.

The Mirau-interference configuration was taken up shortly afterwards by I. Kasamakov et al. for optical profilometry based on CSI [155]. A resolving power of

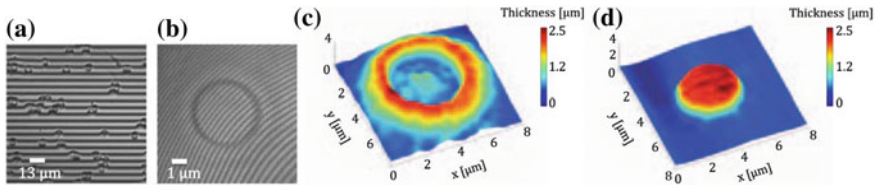


**Fig. 17.13** Experimental results achieved using Mirau-based DHM enhanced by microsphere-assisted microscopy. **a** Hologram of RBC sample through the 0.3-NA Mirau-based objective alone. **b** Hologram of an RBC with the combination of Mirau-DHM and microsphere-assisted microscopy (sphere diameter is around 234  $\mu\text{m}$ ). 3D Phase maps of **(c)** a normal red blood cell and **(d)** a thalassemia minor red blood cell from hologram reconstruction. Reproduced with permission from [151]. ©2018 Optical Society of America

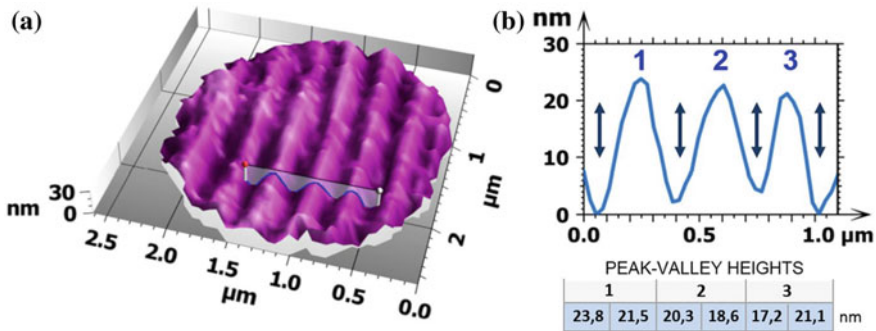


**Fig. 17.14** Experimental results achieved using Mirau-based optical CSI enhanced by microsphere-assisted microscopy. **a** 3D reconstruction topography of a Blu-ray Disc reconstructed using microsphere-assisted interferometry. **b** Cross sectional profile from position indicated in **(a)**, showing the resolved grooves. Reproduced with permission from [155]. ©2018 Nature

300 nm was reported using a melamine formaldehyde ( $n = 1.68$ ) microsphere with a diameter of 11  $\mu\text{m}$ , corresponding to an improvement in the lateral resolution of 1.7 according to the Abbe criterion and enabling the surface reconstruction of a Blu-ray Disc as shown in Fig. 17.14. Moreover, a numerical analysis of the imaging formation (a finite element method simulation using Comsol Multiphysics presented in [109]) allowed us to predict the axial position of the virtual plane and the lateral magnification from the microsphere (Fig. 17.15).

We then demonstrated the combination of PSM with microsphere-assisted microscopy for the first time in 2017 for the topography retrieval of sub-diffraction-limited structures [156]. The experimental Linnik interferometer consisted of a white light source, two 0.3-NA microscope objectives and an 25- $\mu\text{m}$ -diameter glass microsphere. These results were the fruit of a PhD begun in 2013 and defended in 2016 to find a suitable super-resolution technique to enhance the lateral resolution of interference microscopy [157]. We showed a lateral magnification factor of 4.5 from the microsphere and an increase in the lateral resolution of 2.3 in air while maintaining an axial sensitivity of several nanometres. Furthermore, we highlighted the problem of

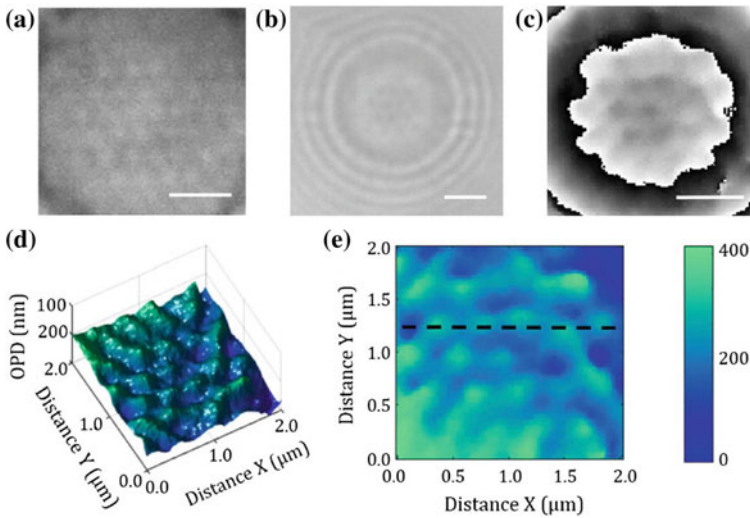


**Fig. 17.15** Experimental results achieved using PSM enhanced by microsphere-assisted microscopy. Super-resolved topography reconstruction of oval-shaped nanodots of Ag covered by a SiON layer using a 25- $\mu\text{m}$ -diameter microsphere. **a** Direct image through the glass microsphere placed in air and illuminated by the white light source. **b** The interference pattern allows the measurement of **(c)** the wrapped phase and then **(d)** the 3D reconstruction of **(e)** the topography surface. White scale bars represent 1  $\mu\text{m}$ . Reproduced with permission from [156]. ©2018 Optical Society of America

wavefront deformation resulting from the use of the microsphere in the object arm, with the circular fringes adding a spherical-like phase error to the measurements. This error can be corrected by applying a 2D fit to the form and subtracting the curvature to reveal the surface shape of the sample or by placing a similar microsphere

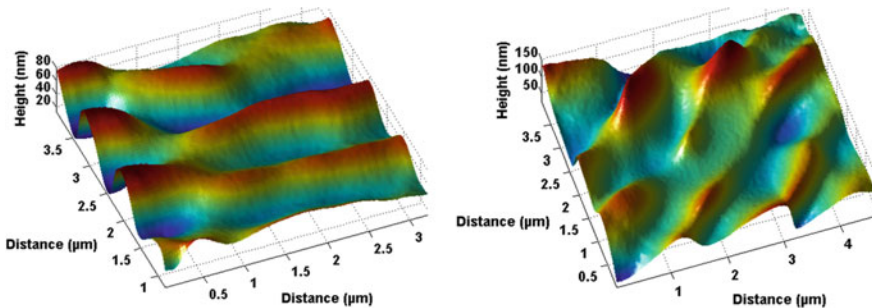


**Fig. 17.16** Experimental results achieved using PSM enhanced by microsphere-assisted microscopy. Measurements of ripples with orientations of 30° and 55° using a 24- $\mu\text{m}$ -diameter microsphere. Reproduced with permission from [158]. ©2018 Wiley

in the reference arm. Finally, an application for the characterization of femtosecond LASER induced nanoripples in stainless steel, spaced by a few 100 nanometres was demonstrated [158] (Fig. 17.16).

## 17.4 Conclusion

Label-free super-resolution imaging techniques are of growing interest in biology for subcellular visualization and in industry for micro- and nanomaterial characterization. Several techniques have been developed in recent years in order to overcome the resolution limit imposed by the diffraction of light which results in the fundamental best values of lateral and axial resolutions as half of the wavelength and the wavelength, respectively. Indeed, a diffraction-limited imaging system, working in the visible range and having a numerical aperture of 1.0, is thus not able to visualize an object having a lateral feature size smaller than around 300 nm and an axial feature size smaller than around 600 nm.

Nowadays, the main full-field super-resolution techniques allow a resolution of up to 100 nm to be reached, compared with the scanning super-resolution techniques which can achieve a few tens of nanometres. By placing a glass microsphere within a classical white light microscope on (or above) the sample makes it possible to visualize sub-diffraction-limited object structures of the sample in 2D. The principle consists of collecting the super-resolution image generated by the microsphere, allowing a lateral resolution of below 100 nm to be achieved in air. Microsphere-assisted microscopy distinguishes itself from the other super-resolution techniques by its easy-to-implement capacity and its low-cost aspect. While the results from experimental measurements and simulations have clearly demonstrated the effect of super resolution, with a lateral resolution limit of  $\lambda/6$  being claimed, the physical principle behind the technique remains unclear to date. The strongest contender for an explanation of the phenomenon is that the microsphere acts as an optical element that transforms the evanescent waves into propagating waves. But then it is also important to consider the geometrical and optical parameters of the imaging system due to their influence on the performance and image formation.

More recently, microsphere-assisted microscopy was further enhanced by introducing a reference arm, so as to superimpose an interference pattern on the super-resolution image and to access the phase of the wavefront. Microsphere-assisted interference microscopy was then implemented using digital holography, coherence scanning interferometry and phase-stepping interferometry so as to be able to reconstruct the surface topography of an object sub-wavelength in size. This new 3D imaging technique appears to be extremely promising for nanometrology and sub-cellular imaging.

**Acknowledgements** The author would like to thank the members of IPP research team of the ICube Laboratory (Strasbourg, France) for their contributions, specially A. Leong-Hoi for her PhD thesis work on super-resolution optical imaging and P. Twardowski for his useful discussions and

advice. Moreover, we thank all partners who have directly or indirectly contributed to the linked associated research projects.

## References

1. M. Rooseboom, The history of the microscope. *Proc. R. Microsc. Soc.* **2**, 266–293 (1967)
2. J. Zuylen, The microscopes of Antoni van Leeuwenhoek. *J. Microsc.* **121**(3), 309–328 (1981)
3. R. Hooke, *Micrographia* (Royal Society, London, 1665)
4. E. Verdet, *Leçons d'optique physique* (Victor Masson et fils, Paris, 1869)
5. E. Abbe, Beiträge zur theorie des Mikroskops und der mikroskopischen Wahrnehmung. *Arch. Mikrosk. Anat.* **9**, 413–418 (1873)
6. H. von Helmholtz, H.E. Fripp, On the limits of the optical capacity of the microscope. *Mon. Microsc. J.* **16**(1), 15–39 (1876)
7. E. Abbe, On the estimation of aperture in the microscope. *J. R. Microsc. Soc.* **1**(3), 388–423 (1881)
8. A. Köhler, Ein neues Beleuchtungsverfahren für mikrophotographische Zwecke. *Zeitschrift für wissenschaftliche Mikroskopie und für Mikroskopische Technik* **10**, 433–440 (1893)
9. J.W. Rayleigh, On the manufacture and theory of diffraction-gratings. *Phil. Mag.* **47**(310), 81–93 (1874)
10. J.W. Rayleigh, On the theory of optical images, with special reference to the microscope. *Phil. Mag.* **42**(255), 167–195 (1896)
11. G.B. Airy, On the diffraction of an object-glass with circular aperture. *Trans. Camb. Philos. Soc.* **5**, 283–291 (1835)
12. E. Abbe, On new methods for improving spherical correction, applied to the construction of wide-angled object-glasses. *J. R. Microsc. Soc.* **2**(7), 812–824 (1879)
13. E. Abbe, Ueber Verbesserungen des Mikroskope mit Hilfe neuer Arten optischen Glases (Sitzber. Jen. Ges. Med, Naturwiss, 1886)
14. C.M. Sparrow, On spectroscopic resolving power. *Astrophys. J.* **44**, 76–87 (1916)
15. W.V. Houston, A compound interferometer for fine structure work. *Phys. Rev.* **29**(3), 478–484 (1927)
16. J.W. Goodman, *Introduction to Fourier Optics*, 2nd edn. (McGraw-Hill companies, 1996)
17. P.M. Duffieux, *L'intégrale de Fourier et ses applications à l'optique* (Faculté des Sciences de Besancon, 1946)
18. V. Ronchi, Resolving power of calculated and detected images. *J. Opt. Soc. Am.* **51**(4), 458–460 (1961)
19. D. Courjon, *Near-Field Microscopy and Near-Field Optics* (Imperial College Press, London, 2003)
20. Editorial, Beyond the diffraction limit. *Nature Photon.* **3**, 361 (2009)
21. A. Neice, Methods and limitations of subwavelength imaging. *Adv. Imaging Electron Phys.* **163**, 117–140 (2010)
22. M. Ehrenberg, *The Nobel Prize in Chemistry 2014*. Press Release, Royal Swedish Academy of Sciences (Published 8 Octo 2014, Accessed 03 July 2019 10:35:35). <http://www.nobelprize.org/>
23. P.C. Montgomery, A. Leong-Hoi, Emerging optical nanoscopy techniques. *Nanotechnol. Sci. Appl.* **8**, 31–44 (2015)
24. P.C. Montgomery, A. Leong-Hoi et al., From superresolution to nanodetection: overview of far field optical nanoscopy techniques for nanostructures. *J. Phys. Conf. Ser.* **682**, 012010 (2016)
25. E.H. Synge, A suggested method for extending microscopic resolution into ultra microscopic region. *Phil. Mag.* **6**(35), 356–362 (1928)

26. E.H. Synge, An application of piezo-electricity to microscopy. *Phil. Mag.* **13**(83), 297–300 (1932)
27. E.A. Ash, G. Nicholls, Super-resolution aperture scanning microscope. *Nature* **237**, 510–512 (1972)
28. D.W. Pohl, W. Denk et al., Optical stethoscopy: image recording with resolution  $\lambda/20$ . *Appl. Phys. Lett.* **44**(7), 651 (1984)
29. G.A. Massey, Microscopy and pattern generation with scanned evanescent waves. *Appl. Opt.* **23**(5), 658–660 (1984)
30. U.T. Dürig, D.W. Pohl et al., Near-field optical-scanning microscopy. *J. Appl. Phys.* **59**(10), 3318 (1986)
31. U.C. Fischer, U.T. Dürig et al., Near-field optical scanning microscopy in reflection. *Appl. Phys. Lett.* **52**(4), 249 (1988)
32. J.M. Vigoureux, C. Girard et al., General principles of scanning tunneling optical microscopy. *Opt. Lett.* **14**(19), 1039–1041 (1989)
33. J.M. Guerra, Photon tunneling microscopy. *Appl. Opt.* **29**(26), 3741–3752 (1990)
34. T. Förster, Zwischenmolekulare Energiewanderung und Fluoreszenz. *Ann. Phys.* **437**, 55–75 (1948)
35. T. Ha, T. Enderle et al., Probing the interaction between two single molecules: fluorescence resonance energy transfer between a single donor and a single acceptor. *Proc. Natl. Acad. Sci. U.S.A.* **93**(13), 6264–6268 (1996)
36. C. Girard, D. Courjon, Model for scanning tunneling optical microscopy: a microscopic self-consistent approach. *Phys. Rev. B* **42**(15), 9340 (1990)
37. C. Girard, M. Spajer, Model for reflection near field optical microscopy. *Appl. Opt.* **29**(26), 3726–3733 (1990)
38. Y. Oshikane, T. Kataoka et al., Observation of nanostructure by scanning near-field optical microscope with small sphere probe. *Sci. Technol. Adv. Mater.* **8**(3), 181–185 (2007)
39. M. Minsky, Microscopy apparatus. U.S. Patent 3,013,467 (1961)
40. H. Goldmann, Spaltlampenphotographie und -photometrie. *Ophthalmologica* **98**, 257–270 (1940)
41. H. Naora, Microspectrophotometry and cytochemical analysis of nucleic acids. *Science* **114**(2959), 279–280 (1951)
42. C.J.R. Sheppard, Y. Gong, Improvement in axial resolution by interference confocal microscopy. *Optik* **87**(3), 129–132 (1991)
43. S. Hell, E.H.K. Stelzer, A 4Pi confocal microscope has an improved axial resolution. in *Presentation at the 4th International Conference on Confocal Microscopy* (Amsterdam, 1992)
44. S. Hell, E.H.K. Stelzer, Properties of a 4Pi confocal fluorescence microscope. *J. Opt. Soc. Am. A* **9**(12), 2159–2166 (1992)
45. C. Cremer, Verfahren zur Darstellung bzw. Modifikation von Objekt-Details, deren Abmessungen außerhalb der sichtbaren Wellenlängen liegen. DE patent DE2116521 (1971)
46. S. Lecler, Y. Takakura, P. Meyrueis, Properties of a three-dimensional photonic jet. *Opt. Lett.* **30**(19), 2641–2643 (2005)
47. A.V. Itagi, W.A. Challener, Optics of photonic nanojets. *J. Opt. Soc. Am. A* **22**(12), 2847–2858 (2005)
48. Z. Chen, A. Taflove, V. Backman, Photonic nanojet enhancement of backscattering of light by nanoparticles: a potential novel visible-light ultramicroscopy technique. *Opt. Express* **12**(7), 1214–1220 (2004)
49. J. Kasim, T. Yu et al., Near-field Raman imaging using optically trapped dielectric microsphere. *Opt. Express* **16**(11), 7976–7984 (2008)
50. P.K. Upputuri, Z.-B. Wen et al., Super-resolution photoacoustic microscopy using photonic nanojets: a simulation study. *J. Biomed. Opt.* **19**(11), 116003 (2014)
51. W. Lukosz, M. Marchand, Optischen Abbildung unter Überschreitung der beugungsbedingten Auflösungsgrenze. *Opt. Acta.* **10**(3), 241–255 (1963)
52. P.C. Sun, E.N. Leith, Superresolution by spatial-temporal encoding methods. *Appl. Opt.* **31**(23), 4857–4862 (1992)

53. M. Saxena, G. Eluru, S.S. Gorthi, Structured illumination microscopy. *Adv. Opt. Photon.* **7**(2), 241–275 (2015)
54. R. Heintzmann, C. Cremer, Laterally modulated excitation microscopy: improvement of resolution by using a diffraction grating. in *Proceedings of the SPIE, SPIE BiOS Europe*, vol. 3568 Stockholm (19 Jan 1999) pp. 185–196
55. M.G. Gustafsson, Surpassing the lateral resolution limit by a factor of two using structured illumination microscopy. *J. Microsc.* **198**(2), 82–87 (2000)
56. V.G. Veselago, The electrodynamics of substances with simultaneously negative values of  $\epsilon$  and  $\mu$ . *Sov. Phys. Usp.* **10**(4), 509–514 (1968)
57. J.B. Pendry, A.J. Holden et al., Extremely low frequency plasmons in metallic mesostructures. *Phys. Rev. Lett.* **76**(25), 4773–4776 (1996)
58. J.B. Pendry, Negative refraction makes a perfect lens. *Phys. Rev. Lett.* **85**(18), 3966 (2000)
59. X. Zhang, Z. Liu, Superlenses to overcome the diffraction limit. *Nat. Mater.* **7**, 435–441 (2008)
60. X.C. Tong, *Advanced Materials for Integrated Optical Waveguides* (Springer International, 2014)
61. R.A. Shelby, D.R. Smith et al., Experimental verification of a negative index of refraction. *Science* **292**(5514), 77–79 (2001)
62. D.R. Smith, W.J. Padilla et al., Composite medium with simultaneously negative permeability and permittivity. *Phys. Rev. Lett.* **84**(18), 4184 (2000)
63. D.R. Smith, D. Schurig et al., Limitations on subdiffraction imaging with a negative refractive index slab. *Appl. Phys. Lett.* **82**(10), 1506 (2003)
64. N. Fang, H. Lee et al., Sub-diffraction-limited optical imaging with a silver superlens. *Science* **308**(5721), 534–537 (2005)
65. R.J. Blaikie, D.O.S. Melville, M.M. Alkaisi, Super-resolution near-field lithography using planar silver lenses: a review of recent developments. *Microelectron. Eng.* **83**(4), 723–729 (2006)
66. W. Srituravanich, N. Fang et al., Plasmonic nanolithography. *Nano Lett.* **4**(6), 1085–1088 (2004)
67. D.R. Smith, D. Schurig, Electromagnetic wave propagation in media with indefinite permittivity and permeability tensors. *Phys. Rev. Lett.* **90**(7), 077405 (2003)
68. Z. Jacob, L.V. Alekseyev, E. Narimanov, Optical hyperlens: far-field imaging beyond the diffraction limit. *Opt. Express* **14**(18), 8247–8256 (2006)
69. V.A. Okhonin, Method of investigating specimen microstructure. U.S. Patent 1,374,922 (1991)
70. S.W. Hell, J. Wichmann, Breaking the diffraction resolution limit by stimulated emission: stimulated-emission-depletion fluorescence microscopy. *Opt. Lett.* **19**(11), 780–782 (1994)
71. T.A. Klar, S.W. Hell, Subdiffraction resolution in far-field fluorescence microscopy. *Opt. Lett.* **24**(14), 954–956 (1999)
72. S.W. Hell, Far-field optical nanoscopy. *Science* **316**(5828), 1153–1158 (2007)
73. R.M. Dickson, A.B. Cubitt et al., On/off blinking and switching behaviour of single molecules of green fluorescent protein. *Nature* **388**, 355–358 (1997)
74. E. Cuche, F. Bevilacqua, C. Depeursinge, Digital holography for quantitative phase-contrast imaging. *Opt. Lett.* **24**(5), 291–293 (1999)
75. Y. Park, W. Choi et al., Speckle-field digital holographic microscopy. *Opt. Express* **17**(15), 12285–12292 (2009)
76. R. Dändliker, K. Weiss, Reconstruction of the three-dimensional refractive index from scattered waves. *Opt. Commun.* **1**(7), 323–328 (1970)
77. V. Lauer, New approach to optical diffraction tomography yielding a vector equation of diffraction tomography and a novel tomographic microscope. *J. Microsc.* **205**(2), 165–176 (2002)
78. M. Debailleul, V. Georges et al., High-resolution three-dimensional tomographic diffractive microscopy of transparent inorganic and biological samples. *Opt. Lett.* **34**(1), 79–81 (2009)
79. O. Haeberlé, K. Belkebir et al., Tomographic diffractive microscopy: basics, techniques and perspectives. *J. Mod. Opt.* **57**(9), 686–699 (2010)
80. M. Born, E. Wolf, *Principles of Optics* (Cambridge University Press, Cambridge, 1999)

81. W. Jueptner, U. Schnars, *Digital Holography Digital Hologram Recording, Numerical Reconstruction, and Related Techniques* (Springer, Berlin, 2005)
82. Y. Cotte, F. Toy et al., Marker-free phase nanoscopy. *Nat. Photon.* **7**, 113–117 (2013)
83. E.J. Ambrose, A surface contact microscope for the study of cell movements. *Nature* **178**, 1194 (1956)
84. D. Axelrod, Cell-substrate contacts illuminated by total internal reflection fluorescence. *J. Cell Biol.* **89**(1), 141–145 (1981)
85. T. Funatsu, Y. Harada et al., Imaging of single fluorescent molecules and individual ATP turnovers by single myosin molecules in aqueous solution. *Nature* **374**, 555–559 (1995)
86. D. Courjon, K. Sarayeddine, M. Spajer, Scanning tunneling optical microscopy. *Opt. Commun.* **71**(1), 23–28 (1989)
87. P.C. Montgomery, Nanoscopy: nanometre defect analysis by computer aided 3D optical imaging. *Nanotechnology* **1**(1), 54 (1990)
88. J.P. Fillard, P.C. Montgomery et al., High resolution and sensitivity infrared tomography. *J. Cryst. Growth* **103**(1), 109–115 (1990)
89. J.P. Fillard, *Near Field Optics and Nanoscopy* (World Scientific, Singapore, 1996)
90. P. Mahou, J. Vermot, E. Beaurepaire, W. Supatto, Multicolor two-photon light-sheet microscopy. *Nat. Methods* **11**(6), 600 (2014)
91. P.C. Montgomery, J.P. Fillard, High-resolution imaging of defects in III–V compound wafers by near-infra-red phase contrast microscopy. *Electron. Lett.* **25**(2), 89–90 (1989)
92. A. Ducret, M.P. Valignat et al., Wet-surface-enhanced ellipsometric contrast microscopy identifies slime as a major adhesion factor during bacterial surface motility. *Proc. Natl. Acad. Sci. U.S.A.* **109**, 10036–10041 (2012)
93. R. Attota, B. Bunday, V. Vartanian, Critical dimension metrology by through-focus scanning optical microscopy beyond the 22 nm node. *Appl. Phys. Lett.* **102**(22), 222107 (2013)
94. Z. Wang, W. Guo et al., Optical virtual imaging at 50 nm lateral resolution with a white-light nanoscope. *Nat. Commun.* **2**, 218 (2011)
95. A. Darafsheh, N.I. Limberopoulos et al., Advantages of microsphere-assisted super-resolution imaging technique over solid immersion lens and confocal microscopies. *Appl. Phys. Lett.* **104**(6), 061117 (2014)
96. K.W. Allen, N. Farahi et al., Overcoming the diffraction limit of imaging nanoplasmic arrays by microspheres and microfibers. *Opt. Express* **23**(19), 24484–24496 (2015)
97. K.W. Allen, N. Farahi et al., Super-resolution by microspheres and fibers—Myth or reality? in *IEEE ICTON Proceedings of the IEEE* (Budapest, 5 July 2015), pp. 1–4
98. C.Y. Liu, W.-C. Lo, Large-area super-resolution optical imaging by using core-shell microfibers. *Opt. Commun.* **399**, 104–111 (2017)
99. J.N. Monks, B. Yan et al., Spider silk: mother nature’s bio-superlens. *Nano Lett.* **16**(9), 5842–5845 (2016)
100. S. Yang, F. Wang et al., Influence of the photonic nanojet of microspheres on microsphere imaging. *Opt. Express* **25**(22), 27551–27558 (2017)
101. S. Lecler, S. Perrin et al., Photonic jet lens. *Sci. Rep.* **9**, 4725 (2019)
102. Y. Ben-Aryeh, Increase of resolution by use of microspheres related to complex Snell’s law. *J. Opt. Soc. Am. A* **33**(12), 2284–2288 (2016)
103. K.W. Allen, N. Farahi et al., Super-resolution microscopy by movable thin-films with embedded microspheres. *Ann. Phys.* **527**(7), 513–522 (2015)
104. A. Heifetz, J.J. Simpson et al., Subdiffraction optical resolution of a gold nanosphere located within the nanojet of a Mie-resonant dielectric microsphere. *Opt. Express* **15**(25), 17334–17342 (2007)
105. V.N. Astratov, A.V. Maslov et al., Fundamental limits of super-resolution microscopy by dielectric microspheres and microfibers. in *Proceedings of the SPIE 97210K, SPIE BiOS*, vol. 9721, San Francisco (22 April 2016)
106. S. Zhou, Y. Deng et al., Effects of whispering gallery mode in microsphere super-resolution imaging. *Appl. Phys. B* **123**, 236 (2017)

107. Y. Duan, G. Barbastathis, B. Zhang, Classical imaging theory of a microlens with super-resolution. *Opt. Lett.* **38**(16), 2988–2990 (2013)
108. A.V. Maslov, V.N. Astratov, Imaging of sub-wavelength structures radiating coherently near microspheres. *Appl. Phys. Lett.* **108**(5), 051104 (2016)
109. S. Perrin, S. Lecler et al., Role of coherence in microsphere-assisted nanoscopy. in *Proceedings of the SPIE, 103300V, SPIE Optical Metrology*, vol. 10330, Munich (26 June 2017)
110. A.V. Maslov, V.N. Astratov, Theoretical resolution of contact microspherical nanoscopy. in *Proceedings of the IEEE, IEEE ICTON*, pp. 1–4, Girona (2 July 2017)
111. A. Darafsheh, C. Guardiola et al., Optical super-resolution imaging by high-index microspheres embedded in elastomers. *Opt. Lett.* **40**(1), 5–8 (2015)
112. Y. Yan, L. Li et al., Microsphere-coupled scanning laser confocal nanoscope for sub-diffraction-limited imaging at 25 nm lateral resolution in the visible spectrum. *ACS Nano* **8**(2), 1809–1816 (2014)
113. B. Yan, Z. Wang et al., Superlensing microscope objective lens. *Appl. Opt. Commun.* **56**(11), 3142–3147 (2017)
114. C.J.R. Sheppard, Resolution and super-resolution. *Microsc. Res. Tech.* **80**(6), 590–598 (2017)
115. M. Duocastella, F. Tantussi et al., Combination of scanning probe technology with photonic nanojets. *Sci. Rep.* **7**, 3474 (2017)
116. S. Perrin, H. Li et al., Illumination conditions in microsphere-assisted microscopy. *J. Microsc.* **274**(1), 69–75 (2019)
117. A. Brettin, C.L. McGinnis et al., Quantification of resolution in microspherical nanoscopy with biological objects. in *Proceedings of the IEEE, IEEE NAECON*, pp. 189–192, Dayton (27 June 2017)
118. X. Hao, C. Kuang et al., Microsphere based microscope with optical super-resolution capability. *Appl. Phys. Lett.* **99**(20), 203102 (2011)
119. H. Yang, M.A.M. Gijs, Optical microscopy using a glass microsphere for metrology of sub-wavelength nanostructures. *Microelectron. Eng.* **143**, 86–90 (2015)
120. Q. Lin, D. Wang et al., Super-resolution imaging by microsphere-assisted optical microscopy. *Opt. Quant. Electron.* **48**, 557 (2016)
121. G. Huszka, H. Yang, M.A.M. Gijs, Microsphere-based super-resolution scanning optical microscope. *Opt. Express* **25**(13), 15079–15092 (2017)
122. S.L. Stanescu1, S. Vilain et al., Imaging with the super-resolution microsphere amplifying lens (SMAL) nanoscope. *J. Phys. Conf. Ser.* **902**, 012014 (2017)
123. L. Chen, Y. Zhou et al., Remote-mode microsphere nano-imaging: new boundaries for optical microscopes. *Opto-Electron. Adv.* **1**(1), 170001 (2018)
124. F. Wang, L. Liu et al., Scanning superlens microscopy for non-invasive large field-of-view visible light nanoscale imaging. *Nat. Commun.* **7**, 13748 (2016)
125. J. Li, W. Liu et al., Swimming microrobot optical nanoscopy. *Nano Lett.* **16**(10), 6604–6609 (2016)
126. K.W. Allen, N. Farahi et al., Super-resolution imaging by arrays of high-index spheres embedded in transparent matrices. in *Proceedings of the IEEE, IEEE NAECON*, pp. 50–52 Dayton (24 June 2014)
127. K.W. Allen, N. Farahi et al., Super-resolution microscopy by movable thin-films with embedded microspheres: resolution analysis. *Ann. Phys.* **527**(7), 513–522 (2015)
128. G. Huszka, M.A.M. Gijs, Turning a normal microscope into a super-resolution instrument using a scanning microlens array. *Sci. Rep.* **8**, 601 (2018)
129. X. Hao, C. Kuang et al., Microsphere-assisted super-resolution imaging with enlarged numerical aperture by semi-immersion. *Appl. Phys. Lett.* **112**(2), 023101 (2018)
130. A. Darafsheh, Influence of the background medium on imaging performance of microsphere-assisted super-resolution microscopy. *Opt. Lett.* **42**(4), 735–738 (2017)
131. Y. Zhou, Y. Tang et al., Effects of immersion depth on super-resolution properties of index different microsphere-assisted nanoimaging. *Appl. Phys. Express* **11**(3), 032501 (2018)
132. H.S.S. Lai, F. Wang et al., Super-resolution real imaging in microsphere-assisted microscopy. *PLoS ONE* **11**(10), e0165194 (2016)

133. R. Ye, Y.-H. Ye et al., Experimental imaging properties of immersion microscale spherical lenses. *Sci. Rep.* **4**, 3769 (2014)
134. P.K. Upputuri, M. Pramanik, Microsphere-aided optical microscopy and its applications for super-resolution imaging. *Opt. Commun.* **404**, 32–41 (2017)
135. H. Yang, N. Moullan et al., Super-resolution biological microscopy using virtual imaging by a microsphere nanoscope. *Small* **10**(9), 1712–1718 (2014)
136. Y. Zhou, Y. Tang et al., Contrast enhancement of microsphere-assisted super-resolution imaging. *Appl. Phys. Express* **10**(8), 082501 (2017)
137. S. Perrin, H. Li et al., Transmission microsphere-assisted dark-field microscopy. *Phys. Status Solidi RRL*. **13**(2), 1800445 (2019)
138. L. Li, W. Guo et al., Label-free super-resolution imaging of adenoviruses by submerged microsphere optical nanoscopy. *Light Sci. Appl.* **2**, e104 (2013)
139. P. de Groot, Principles of interference microscopy for the measurement of surface topography. *Adv. Opt. Photonics* **7**(1), 1–65 (2015)
140. D. Huang, E.A. Swanson et al., Optical coherence tomography. *Science* **254**(5035), 1178–1181 (1991)
141. F. Charriere, A. Mariani et al., Cell refractive index tomography by digital holographic microscopy. *Opt. Lett.* **31**(2), 178–180 (2006)
142. D. Malacara, *Optical Shop Testing*, 3rd edn. (Wiley, New Jersey, 2007)
143. G. Gianto, F. Salzenstein, P.C. Montgomery, Comparison of envelope detection techniques in coherence scanning interferometry. *Appl. Opt.* **55**(24), 6763–6774 (2016)
144. E. Cucho, P. Marquet et al., Simultaneous amplitude-contrast and quantitative phase-contrast microscopy by numerical reconstruction of Fresnel off-axis holograms. *Appl. Opt.* **38**(34), 6994–7001 (1999)
145. E. Cucho, P. Marquet, C. Depeursinge, Spatial filtering for zero-order and twin-image elimination in digital in-line holography. *Appl. Opt.* **39**(23), 4070–4075 (2000)
146. J. Kühn, T. Colomb et al., Real-time dual-wavelength digital holographic microscopy with a single hologram acquisition. *Opt. Express* **15**(12), 7231–7242 (2007)
147. P. Lehmann, W. Xie et al., Coherence scanning and phase imaging optical interference microscopy at the lateral resolution limit. *Opt. Express* **26**(6), 7376–7389 (2018)
148. A. Faridian, D. Hopp et al., Nanoscale imaging using deep ultraviolet digital holographic microscopy. *Opt. Express* **18**(13), 14159–14164 (2010)
149. Y. Wang, S. Guo et al., Resolution enhancement phase-contrast imaging by microsphere digital holography. *Opt. Commun.* **366**, 81–87 (2015)
150. F. Wang, L. Liu et al., Three-dimensional super-resolution morphology by near-field assisted white-light interferometry. *Sci. Rep.* **6**, 24703 (2016)
151. M. Aakhte, V. Abbasian et al., Microsphere-assisted super-resolved Mirau digital holographic microscopy for cell identification. *Appl. Opt.* **56**(9), D8–D13 (2017)
152. Q. Lin, D. Wang et al., Super-resolution quantitative phase-contrast imaging by microsphere-based digital holographic microscopy. *Opt. Eng.* **56**(3), 034116 (2017)
153. V. Abbasiana, E.A. Akhlaghiab et al., Digital holographic microscopy for 3D surface characterization of polymeric nanocomposites. *Ultramicroscopy* **185**, 72–80 (2018)
154. P. Chavel, Optical noise and temporal coherence. *J. Opt. Soc. Am.* **70**(8), 935–943 (1980)
155. I. Kassamakov, S. Lecler et al., 3D super-resolution optical profiling using microsphere enhanced Mirau interferometry. *Sci. Rep.* **7**, 3683 (2017)
156. S. Perrin, A. Leong-Hoi et al., Microsphere-assisted phase-shifting profilometry. *Appl. Opt.* **56**(25), 7249–7255 (2017)
157. A. Leong-Hoi, *Etude des techniques de super-résolution latérale en nanoscopie et développement d'un système interférométrique nano-3D*. Ph.D. thesis, (University of Strasbourg, 2016)
158. A. Leong-Hoi, C. Hairay et al., High resolution microsphere-assisted interference microscopy for 3D characterization of nanomaterials. *Phys. Status Solidi A* **215**, 1700858 (2017)

# Index

## A

Abbe, Ernest, 27, 240, 372, 444, 445  
Abbe law, 16, 142, 182, 240, 290  
Abbe's limit, 290, 316, 358, 372, 422  
Aberrations, 28, 143, 149, 150, 175, 176, 256, 318, 361, 414, 422, 445  
    chromatic, 27, 143, 149, 150, 175, 176  
    spherical, 422, 445  
Ablation, 266  
Absorbance region, 218  
Absorption, 1, 71, 87, 93, 101–103, 128, 132, 137–141, 143, 144, 148–153, 155, 157–159, 161, 162, 171–174, 177, 179–181, 184–186, 188, 196, 215–217, 219, 228, 229, 232, 233, 240–242, 245, 246, 248, 249, 251, 252, 262, 264, 267, 280, 383  
Absorption coefficient, 174, 215, 228, 233  
Absorption cross section, 148, 153, 174, 219, 220, 248, 252  
Absorption saturation, 184  
Acousto-optical deflectors, 49, 70  
Acousto-Optical Modulator (AOM), 177, 267, 268, 270, 273, 281–284  
Actin, 51, 55, 303  
Actin filament, 30, 52, 457  
Adhesion, 29, 56, 92  
Adiabatic compression, 355  
Albumin, 48  
All-optical switching, 239, 245–247, 251–253, 256, 257  
Ambient, 43, 261, 282  
Amino acid, 153  
Amoeba, 89  
Amplitude, 1, 2, 4, 7, 71, 81, 87, 89–91, 103, 113, 116, 117, 119, 122–125,

128, 132, 133, 177–180, 267, 276, 281–284, 373, 379, 385  
Amplitude modulated, 267  
Angular momentum, 352–355  
Angular radiation pattern, 113, 125–128  
Anisotropic geometry, 350  
Anisotropic media, 348  
Antenna, 36, 129, 218, 250, 251  
Antibody, 50, 302  
Aperture, 31, 69, 89–92, 94, 96, 97, 103, 113–115, 119, 121–125, 127, 132, 133, 142, 175, 182–184, 203, 241, 244, 248, 292, 295, 362, 363, 372, 373, 384, 399, 445, 447, 449, 459, 463  
Aperture probe, 113, 119, 121–125, 133  
Apodization, 261, 276  
Arbitrary, 292  
Arbitrary Wave Generator (AWG), 267, 282  
Aspect ratios, 214, 215, 219, 223, 393  
Auger carriers annihilation, 264  
Autofluorescence, 242, 248, 290, 297  
Azimuthal numbers, 416

## B

Back-focal plane, 11, 36, 49, 74, 95, 113, 116  
Background removal, 37, 42, 77, 78  
Backprojection, 89, 305  
Bacteria, 27, 55, 208, 371, 444  
Bacteriophages, 47, 48  
Bandstructure effects, 412  
Bandwidth extrapolation, 346  
Barium-titanate glass, 411, 431, 433  
BaTiO<sub>3</sub> microspheres, 375, 460

- BBO crystal, 176, 177  
 Beam instabilities, 36  
 Beam pointing, 273  
 Beam-shearing, 29  
 Beer-Lambert law, 228  
 Benzene, 200  
 Betula pendula pollen grain, 100  
 Betzig, Eric, 242  
 Bidirectional motions, 79  
 Bilayer membrane, 53, 54  
 Biological samples, 17, 39, 92, 94, 98, 149, 203, 206, 218, 258, 303, 345–347, 374  
 Biology, 17, 31, 47, 51, 68, 82, 85, 138, 139, 156, 157, 162, 257, 307, 345, 372, 373, 463  
 Biomarkers, 214  
 Biomedical, 17, 137–139, 143, 152, 156, 180, 215, 234, 239, 280, 372, 400, 408, 423, 424  
 Biomedical applications, 180, 304  
 Biomedical optics, vii  
 Biosensing, 48, 49  
 Birefringent, 103, 336  
 Blind reconstruction, 425  
 Blood, 13, 14, 27, 92, 94, 98, 181, 304, 371  
 Blue shift, 218, 219, 223  
 Blur, 263, 266, 320, 321  
 Blu-Ray Disc (BRD), 374, 397, 411, 461  
 Born approximation, 2, 91, 103  
 Boron nitride, 350, 351  
 Bright sky, 28  
 Bright-field, 9, 28, 32, 33, 56, 399, 452, 457  
 Brightness of the image, 348
- C**
- Camera, 9, 10, 30, 36, 37, 39, 41, 42, 49, 70, 81, 82, 87, 102, 117, 119, 121, 122, 132, 207, 230, 232, 276, 277, 294, 295, 307, 318, 319, 365, 390  
 Cancer, 28, 181, 304, 400  
 Carbon mesh, 92  
 Carbon nanotube, 31, 161, 180, 304  
 Carrier concentration, 215, 216, 263  
 Catalytic reaction, 52  
 Caustic, 354  
 Cell
  - bacterial, 263
  - cancerous, 92
  - HeLa, 55, 72, 78, 302
  - hepatocyte, 92
  - immune, 51, 150
  - living, 30, 56, 57, 69, 72, 137, 143, 149, 180, 205, 242
  - red blood, 14, 98, 181, 460, 461
  - single, 49, 51, 77
  - white blood, 92, 94
  - yeast, 27
 Cell biology, 55, 138, 156, 372  
 Cell–cell adhesion, 29, 92  
 Cell cycle, 89  
 Cell division, 89  
 Cell identification, 460  
 Cell migration, 89  
 Cell nuclei, 55  
 Cell plasma membranes, 77, 78  
 Cellular membranes, 52, 55  
 Cellular structures, 86, 214, 345  
 Cellulose acetate, 431, 433  
 Charge carrier excitation, 56, 263, 266  
 Charge carriers, 35, 159, 223, 228, 262, 263, 266, 267, 274  
 Chemical reaction, 346, 347, 390  
 Chemical recognition, 263  
 Chemistry, 31, 80, 82, 138, 142, 157, 345, 373, 408, 428, 446  
 Cherenkov radiation, 347  
 Chromatic aberrations, 27, 149, 150, 175  
 Chromium, 364, 429  
 Chromosome, 92  
 Citations, vii  
 Clathrin, 55  
 Coherence, 15, 16, 28, 33, 42, 69, 71, 72, 87, 161, 201, 299, 362, 413, 421, 452, 458, 460, 463  
 Coherence length, 33, 458  
 Coherent Raman effects, 199  
 Colloid, 43, 44, 209  
 Common-path, 9, 11, 81, 103  
 Complex electromagnetic field reconstruction, 119  
 Complex extinction, 33  
 Computational reconstruction, 87, 102, 346, 358  
 Condenser, 12, 28, 69, 70, 89, 94–96, 98, 144, 155, 176  
 Confocal, 14, 29, 36, 41–43, 57, 89, 92, 94, 98, 103, 140, 143, 151, 156, 158, 183, 201, 203, 204, 214, 240, 245, 257, 276, 295, 386, 397, 409, 410, 423, 435, 450  
 Confocal pinhole, 203, 240, 386, 410  
 Contrast enhancement, 30, 42, 81  
 Contrast mechanism, 1, 25, 26, 31, 68, 138, 171, 172, 290

- Controversial, vi
- Conversion of evanescent to propagating, 348, 384, 393, 412, 428, 463
- Convolution, 3, 272, 291, 301, 320, 373, 376, 386, 409–411, 418, 423, 433, 453
- Core–shell, 45
- Critical angle, 36, 119, 124, 127
- Critical radius, 354
- Cross section, 68, 81, 123, 129, 131, 138, 148, 153, 159, 174, 209, 214, 216, 217, 219, 220, 222, 224–227, 248, 249, 252, 271, 272, 324, 327–329, 415, 416
- Cross-correlation, 15, 179, 318, 321, 322
- Cylindrical geometry, 348
- Cylindrical wave, 353
- Cytoskeletal, 29
  
- D**
- Damage, 81, 149, 152, 186, 218, 233, 242, 357, 448
- Danio rerio, 86
- Dark-field, 28, 31, 34–37, 39, 43, 47, 85, 86, 144, 244, 363, 413, 421, 457
- Darkness, 26, 28
- Dark noise, 37
- Decoherence beam, 140, 161, 201, 202
- Deconvolution, 103, 139, 221, 230, 244, 245, 256, 257, 272, 276, 293, 320, 321, 448
- Delay, 1, 4, 5, 7, 8, 10–12, 16, 95, 96, 145, 147, 159, 173, 174, 176, 177, 179–181, 185, 186, 264, 266, 268, 271, 274, 277, 279, 458
- Delay line, 176, 177, 180, 185, 268, 274
- Demodulation, 87, 89, 177, 178, 199, 246, 255
- Density matrix, 203
- Depletion curve, 186, 187
- Deposited energy, 263
- Depth of view, 360
- Detection
  - cell, 89
  - coherent, 86, 197, 361
  - homodyne, 31, 34
  - photothermal, 137, 139, 140, 148, 153
- Detector, 6, 9, 27, 32, 37, 39, 41, 46, 49, 57, 68, 75, 117, 118, 138, 141, 150, 174, 176–178, 203, 205, 207–209, 268, 282, 295, 301, 306, 307, 346, 358, 386, 413, 414, 418, 419, 458
- Detector nonlinearities, 37, 183
- Diamond, 44, 153, 199–202, 242
- Diamond plate, 201, 202
- Diatoms, 89, 92
- Dichroic filter, 268
- Dichroic Mirror (DM), 142, 146, 150, 155, 175, 176, 186, 268, 277, 278, 294, 306
- Dielectric microsphere, 379, 423
- Dielectric permittivity tensor, 316, 353
- Dielectric substrates, 47
- Dielectrophoretic cell rotation, 98
- Differential Interference Contrast (DIC), 1, 12, 29, 34, 85, 86, 96, 103, 257
- Diffraction, 26, 28, 31, 33, 35, 289, 290, 294, 297, 300, 424, 426, 430, 444, 445, 448, 449, 463
- Diffraction limit, 16, 113, 114, 131, 137–140, 142–145, 152, 153, 158, 162, 171, 182, 184, 186, 195, 196, 198, 200, 201, 203, 205, 208, 209, 213, 214, 217, 230, 231, 240, 241, 243, 244, 248, 255, 256, 265, 272, 277, 289, 290, 314, 316, 345–347, 352, 353, 356, 363, 374, 379, 394, 407, 408, 413, 424, 434, 436, 443, 448–451, 459
- Diffraction limited spot, 261, 264, 276
- Diffraction orders, 9, 118–120, 444
- Diffraction optics, 415
- Digital micromirror devices, 103
- Dipole, 36, 39, 113, 115, 116, 121, 123, 124, 126, 127, 130, 133, 216, 217, 222, 381, 412, 430, 435
- Dipole moment, 216
- Directional emission, 125, 128
- Discoveries, 31, 138, 242, 245, 248, 249, 253, 345, 443, 447
- Discrete Dipole Approximation (DDA), 216, 218
- Disordered media, 132, 133
- Dispersion, 213, 314, 316, 317, 328, 330, 350, 353, 354, 360, 426, 427, 430, 445
- DNA, 32, 47, 48, 290
- Doughnut, 92, 99, 137, 139, 140, 158–161, 183–187, 213, 215, 217, 228, 234
- Doughnut-like shaping of the PSF, 228
- Dry mass, 14
- Dual focus, 29
- Dye molecules, 25, 31, 44, 46–48
- Dynamic adaptive feedback algorithm, 281
- Dynamic range, 30, 37

**E**

Effective masses, 216  
 Effective medium theory, 351  
 Effect of disorder, 362, 363  
*e-h* pair, 233  
 Einstein, Albert, 114  
 Electric dipole, 113, 115, 123, 127  
 Electric permittivity, 172, 316  
 Electromagnetic field amplitude, 116, 132  
 Electromagnetic field phase, 116, 132  
 Electromagnetic hotspots, 130  
 Electron-phonon coupling, 271  
 Electro-Optic Modulator (EOM), 87, 177, 294  
 Electrostatic potentials, 44  
 Elliptic, 349, 350, 378  
 Endoscopy, 306, 371, 375, 386, 391, 392, 400  
 Energy, 56, 91, 137, 143, 148, 173, 216, 232, 242, 252, 262–264, 266, 271, 277, 296, 316, 321, 345, 359, 383, 385, 395, 401, 426, 427  
 Energy absorption, 262  
 Energy conservation, 91  
 Energy dissipation, 264, 383  
 Engineering, 17, 74, 81, 82, 148, 162, 196, 198, 256, 282, 347, 348, 360, 379, 397  
 Enhanced electrical field, 222  
 Envelope, 267, 281, 458  
 Escherichia Coli, 139, 263  
 Evanescent jets, 376  
 Evanescent wave, 113, 114, 241, 244, 314, 346–348, 372, 376, 379, 382, 384, 385, 400, 412, 428, 431, 446, 448, 449, 451, 463  
 Ewald sphere, 91  
 Excitation, 35, 56, 116, 124, 127, 130, 132, 137–139, 151, 152, 161, 176, 182, 183, 187, 195–201, 203, 208, 214, 222, 239–242, 244–257, 263–267, 274, 275, 293, 295–297, 303, 304, 306, 339, 341, 347, 372, 379, 380, 385, 407, 417, 423, 425, 432, 434, 435, 448, 452  
 Excitation level, vii  
 Excited state absorption, 173, 179  
 Exosomes, 32  
 Extraordinary waves, 350

**F**

Fabrication imperfections, 362

Fabry–Pérot (FP) resonator, 229  
 F-actin protein, 431, 433, 434  
 Far-field amplitude, 91  
 Far-field methods, 113  
 FCC diffusion, 233  
 Fibroblasts, 29, 79, 80  
 Field of view, 39, 51, 89, 181, 356, 357, 362, 365, 445  
 Filopodia, 55  
 Finite Difference Time Domain (FDTD) simulations, 113, 121, 123  
 Finite-difference time-domain method, 113, 121, 123  
 Finite Element Method (FEM), 412  
 Fluorescence, 25, 35, 37, 39, 40, 44, 45, 47, 49, 52, 55, 296, 297, 347, 410, 428  
 Fluorescence emission, 187, 196, 199, 207, 239, 242, 246–248, 256  
 Fluorescence enhancement, 410  
 Fluorescence-free, 25, 26  
 Fluorescence Recovery After Photobleaching (FRAP), 52, 103  
 Fluorescent dye, 213, 289, 290, 347  
 Fluorescent label, 25, 242, 345, 346  
 Fluorescent labeling, 138, 262  
 Fluorescent molecules, 153, 171, 183, 188, 196, 207, 242, 247, 248, 256, 291, 292, 303, 345, 376  
 Fluorescent polystyrene beads, 421  
 Fluorescent proteins, 25, 68, 138, 242, 345  
 Fluorophore, 17, 39, 68, 86, 138, 158, 159, 180, 181, 214, 241–243, 245, 248, 303, 347, 373  
 Focus, 2, 57, 69, 71, 121, 122, 137, 143, 149, 157, 161, 171, 175, 176, 197, 198, 201, 205, 227, 240, 245–247, 250, 253, 273, 289, 290, 294, 295, 297, 298, 306, 373, 378, 386, 391, 398, 400, 407, 412–414, 418, 419, 447, 456  
 4-f system, 10, 11  
 Fourier coefficient, 91  
 Fourier component, 326, 418, 425  
 Fourier inversion, 95, 103  
 Fourier plane, 9, 10, 96, 116  
 Fourier space, 89, 91, 94, 97, 118, 448  
 Fourier transform algorithm, 118  
 Fourier Transform (FT), 291, 346, 361, 362, 425, 458  
 Fourier Transform Infrared (FTIR) spectroscopy, 149  
 Free carrier concentration, 215, 216

- Free Charge Carriers (FCC), 223, 228, 229, 232–234
- Frequency doubled, 175, 268
- Fresnel refraction, 413
- Frontiers of science and technology, v
- Full field, 6, 113, 132, 133
- Full Width at Half Maximum (FWHM), 145, 159, 160, 242, 255–257, 270–272, 279, 384, 387, 445
- Function
- Bessel, 353
  - Dirac delta, 15, 417
  - Green, 90
  - optical transfer (OTF), 91, 96, 97, 99, 100, 291, 448
  - periodic, 267
  - point spread (PSF), 16, 26, 40, 76, 77, 132, 138, 139, 158, 159, 161, 176, 182, 185, 196, 198, 213–215, 219, 221, 228, 230, 234, 235, 240, 242, 246, 247, 250, 251, 253–256, 261–265, 267, 270–273, 276, 277, 291, 316, 318, 320–322, 346, 376, 386, 387, 407, 409, 418, 445
- G**
- GaAs, 218, 230
- Gabor, Denis, 29, 116
- Galvanometer, 273
- Galvanometric mirrors, 103, 175, 294
- Galvo scanning mirror, 268
- Gaussian, 17, 41, 42, 69, 73, 161, 187, 198–201, 214, 215, 217–221, 228–233, 245, 246, 253, 265, 267, 272, 276, 321, 387, 432
- Gaussian fit, 73
- Gaussian profile, 198, 253
- Genetically modified, 86
- Geometrical optics, 315, 318, 413, 419
- Giant electric field, 380, 381
- Giant Unilamellar Vesicle (GUV), 54, 55
- Glycerol, 148
- Gold, 28, 31, 34, 38, 44, 51, 72, 74, 81, 119, 122–129, 131, 146, 148, 150, 153, 154, 176, 180, 214, 217, 218, 243, 245, 249–251, 261, 270, 274–276, 317, 321–323, 326–328, 331, 336, 374, 375, 386
- Gold bowtie antenna, 250, 251
- Gold core, 217, 218
- Gold nanodisk chains, 129
- Gold Nano Rods (GNRs), 214, 215, 217–221, 225, 227, 250
- Gold Nanosphere (GNS), 249, 250
- Gold stripes, 270, 274
- Gold surfaces, 261
- Gouy phase, 32
- Gradient-Index (GRIN), 10, 306, 392
- Granular film, 271
- Graphene, 138, 155, 159, 161, 177, 178, 180, 181, 184, 186–188, 206, 262
- multi-layer, 180, 181, 186, 188
  - single-layer, 177, 178, 181
- Graphic Processing Unit (GPU), 102
- Graphite, 160, 186, 349
- Green Fluorescent Protein (GFP), 242, 345
- Ground state, 138, 157, 158, 161, 173, 174, 179, 201, 248, 262
- Ground State Depletion (GSD), 138, 139, 158, 159, 161, 173, 174, 179, 185, 248, 262
- Grueneisen parameter, 281
- H**
- Halo artifacts, 87
- Harmonic demodulation, 199, 246
- Harmonic distortion, 267, 268
- Harmonic impurity, 261
- Harmonics, 86, 157, 172, 178, 199, 246, 247, 254, 255, 261, 264–270, 273–275, 281, 283, 284, 320, 379, 412
- Heat, 35, 137, 141, 148, 149, 152, 252, 266
- Heat diffusion, 266
- Heating, 218, 266, 277, 278
- Hell, Stefan W., 241, 248, 314, 373
- Helmholtz equation, 2, 90
- Hemispherical, 394, 422
- Hemoglobin, 148, 181
- Higher-order nonlinear responses, 199
- High-harmonic response, 267
- High harmonics, 261, 264, 266, 267, 281, 283
- High-order nonlinear relations, 199, 265
- Hilbert transform, 8
- Historical, 25, 30, 56, 182
- Hollow pyramidal probe, 115, 130
- Holograms, 85, 87, 89, 102, 113, 116–120, 122, 125, 129, 130, 132, 133
- Holography, 1, 12, 29, 32, 56, 87–89, 113, 116–119, 128, 130, 132, 133, 386, 447
- digital, 56, 113, 116, 119, 128, 130, 132, 449, 458, 463
- Gabor, 29, 87, 88
- off-axis, 87, 88, 113, 117, 118, 121, 133

- phase-shifting, 87–89
  - Hooke, Robert, 27, 371, 444
  - Hotplate, 225
  - Hot spot, 130, 141, 145, 207–209, 244, 251, 379, 424, 430, 431
  - Houston resolution criterion, 372, 387, 409
  - Human hair, 92
  - Hyperbola, 350
  - Hyperbolic dispersion, 314, 316, 317, 354, 359
  - Hyperbolic materials, 326, 345, 350
  - Hyperbolic medium, 349, 350, 352, 354, 356, 358–360
  - Hyperbolic Metamaterial (HMM), 316, 321, 348, 350, 352, 354, 356, 359, 361, 362, 365
  - Hyperlens
    - de-magnifying, 357
    - resolving power of, 356
    - spherical, 357
- I**
- Illumination
    - broadband, 380, 458
    - coherent, 377, 408, 413, 421, 436, 444, 458, 460
    - hyper-structured, 349, 350, 359–361
    - incoherent, 86, 241, 291
    - Köhler, 89, 444
    - non-uniform, 75, 76, 241, 242, 244
    - oblique, 85, 436, 459
    - partially coherent, 103
    - partly coherent, 436
    - patterned, 205, 384
    - uniform wide-field laser, 70
  - Illumination pattern, 70, 183, 205, 349
    - hyper-structured, 349
    - structured, 183, 205, 346
  - Image contrast, 199, 208, 409, 459
  - Image distortions, 283, 413
  - Image formation, 33, 182, 196–198, 207, 291, 301, 318, 356, 419, 456, 463
  - Image inversion, 415
  - Image processing, 57, 139, 449
  - Image reconstruction, 73, 87, 89, 97, 102–104, 361, 363, 387
  - Imaging
    - biological, 1, 14, 28, 69, 85, 153, 181, 356, 397, 449, 458
    - biomedical, 137, 215, 234, 239, 280, 372
    - chemical, 143, 263
    - coherent, 16, 100, 198, 205, 300, 422
    - coherent bright-field (COBRI), 32, 69, 72, 74, 80
    - direct, 43, 67, 69, 157, 188, 345, 349, 358, 462
    - dynamic live cell, 14, 67, 69, 74, 75, 81, 258
    - fluorescence life-time (FLIM), 103, 179, 181
    - full-field, 132
    - ghost, viii
    - high resolution, 280, 375
    - hyperspectral, 103, 156, 360, 365
    - interference plasmonic (iPM), 32
    - label-free, 1, 2, 13, 14, 17, 32, 67, 69, 74, 76, 77, 138, 152, 153, 155, 208, 243, 258, 302–304, 356, 373, 376, 451, 459
    - label-free live cell, 67, 77
    - low-energy, 242, 345
    - microspherical, 407, 410, 417, 421
    - multispectral, 103, 156
    - nanochip, 389
    - nanoscale, 145, 262
    - non-destructive, 181, 345, 390
    - nonlinear optical, 139, 273, 345
    - phase, 1, 2, 56, 87, 104, 133, 459
    - phase-contrast, 1
    - quantitative phase (QPI), 1, 2, 56, 95, 104
    - sensors, 205, 346
    - silicon wafers, 228
    - software, vii
    - sparse, 183
    - speckle, 103, 132, 290
    - sub-wavelength, 214, 215
    - sum frequency, 273
    - super-resolution, 17, 114, 116, 132, 139, 161, 188, 195, 196, 199, 201, 203, 209, 239, 242–245, 253, 256, 258, 316, 326, 341, 366, 371, 373, 377, 380, 386–392, 394, 396–398, 400, 407, 410, 423–426, 428, 430, 446, 448, 450, 453, 455, 457
    - superresolution optical fluctuation (SOFI), 262
    - super-resolved fluorescence, 92, 215, 408
    - suppression of scattering (SUSI), 245, 256
    - three-dimensional, 113, 175, 263, 294, 303
    - ultrasound, 356
    - white-light, 380, 389, 392, 394, 395, 400, 423
    - wide-field, 48, 67, 92, 205, 208, 394, 397

Immersion objective, 70, 122, 151, 384, 428, 432, 434, 449  
 Immunoglobulin G (IgG), 49  
 Incident plane wave, 90, 352, 353, 416  
 Incoherent point sources, 420, 422, 423, 435, 436  
 Index matching oil, 46  
 Information channel, 353  
 Information theory, viii  
 Infrared (IR) spectroscopy, 138, 156  
 Infra-red probe, 213  
 In-phase component, 179  
 Instabilities, 35–37  
 Instantaneous temperature, 262, 269  
 Instrumentation, 2, 7, 39, 86, 289  
 Instruments, 2, 17, 27, 57, 103, 372  
 Insulator-to-metal transition, 261, 270  
 Integrated microsphere, 399  
 Intensity modulator, 176, 185  
 Intensity weighted subtraction, 187  
 Interference, 29, 34, 35, 43, 56, 57, 443, 447–449, 457–459  
 Interference pattern, 115, 116, 244, 424, 425, 458, 462, 463  
 Interference Reflectance Imaging Sensing (IRIS), 32, 149  
 Interferogram, 6, 8, 9, 87, 89, 138, 458  
 Interferometer  
   Jamin, 30  
   Linnik, 392, 459, 461  
   Mirau, 29, 392  
 Interferometric measurements, 87, 97, 410  
 Interferometry, 2, 7, 15, 29, 33, 35, 67, 75, 81, 103, 140, 371, 375, 392, 443, 449, 458, 461, 463  
 Intracellular transportation at nanoscale, 80  
 Invention, 1, 29–31, 85, 149, 240, 408, 447  
 Iso-frequency curve, 349, 350  
 Iso-frequency surface, 349, 359  
 Isopropyl Alcohol (IPA), 227, 321, 388, 397, 411  
 Isotropic dielectric medium, 353  
 ITO, 218, 270, 326, 431

## J

Jamin, Jules, 29  
 Jitter, 230

## K

Kinesin, 51  
 Kramers–Kronig relation, 360

## L

Lab-on-Chip (LoC), 375, 400  
 Label free, 1, 2, 13, 14, 17, 25, 26, 32, 47, 49, 67, 69, 74, 76, 79, 81, 86, 100, 137, 138, 142, 148, 152–155, 171, 184, 186, 188, 213, 215, 234, 240, 243, 258, 261–263, 277, 280, 282, 289, 290, 296, 297, 302–304, 306, 307, 345–347, 356, 366, 373, 376, 400, 423, 424, 443, 450, 451, 459  
 Label-free localization, 26, 208  
 Labeling, 17, 52, 53, 68, 79–81, 86, 93, 94, 138, 203, 214, 262  
 Laser, 29, 34–37, 42, 45, 46, 48, 57, 69–72, 80, 92, 103, 116, 117, 121, 131, 138, 140, 141, 143–152, 154–156, 162, 171, 172, 175–178, 180, 187, 196–203, 205, 215, 217, 218, 228–232, 234, 241, 242, 245–247, 249, 251–257, 261, 264–266, 271, 274, 276–279, 281, 315, 318, 322, 323, 326, 328, 341, 365, 377, 378, 386, 391, 411, 426  
 Laser focus, 197, 201, 378  
 Laser pulse, 232, 261, 274, 277, 302, 378  
 Laser scanning, 146, 196, 199, 203, 241, 242, 247, 249, 253, 254, 256, 257, 386, 449  
 Lattice, 271, 425, 427  
 Layered structure, 13, 350, 351  
 Leaky surface plasmons, 116, 121, 124, 125, 127  
 Lens  
   cylindrical, 97, 355, 450  
   dielectric particle-, 371, 401  
   Eaton, 330–333, 336  
   first-generation particle, 375  
   Fourier, 9, 11, 95  
   Luneburg, 336  
   Maxwell fisheye, 330, 336–341  
   metamaterial, 376, 395, 448, 450  
   metamaterial solid immersion (mSIL), 383, 386, 393  
   nanohybrid lens (nHL), 393, 395  
   objective, 155, 182, 197, 202, 203, 207, 244, 270, 372–374, 381, 389, 390, 397, 428, 444, 451  
   perfect, 314, 372, 448, 450  
   second-generation particle, 375, 400  
   solid immersion (SIL), 203, 383, 386, 393, 408, 432, 450  
   super-, 374, 375, 407, 428, 448, 450  
   superoscillation, 373

swimming, 387, 390  
 tube, 70, 95, 145, 268  
 Lewis, Aaron, v  
 Light escape cone, 427  
 Light-induced, 263  
 Linear absorption, 137–139, 158, 174, 241  
 Linear model, 263  
 Linear translation-invariant system, 291  
 Lipid, 35, 47, 51–54, 68, 79, 86, 155, 156, 303–305  
 Lipid diffusion, 52, 53  
 Lipid membranes, 51  
 Liquid, 95, 98, 131, 140, 141, 145, 148, 150, 172, 261, 282, 317, 330, 375, 388, 390, 397, 409, 434  
 Lister, Joseph Jackson, 28  
 Lister's dark-field stop, 42  
 Localized Surface Plasmon Resonances (LSPRs), 214, 215, 217–219, 244, 245, 407, 425, 426, 430, 434–436  
 Lock-in amplifier, 146, 176–179, 254, 255, 265, 268, 274, 281

## M

Machine learning, 57, 104, 306  
 Magnetic dipole, 115, 121, 124, 130, 133  
 Magnification, 13, 16, 27, 240, 314, 330, 332–338, 352, 375, 381, 382, 387, 389, 394, 398, 399, 412, 414, 415, 418, 419, 427, 430, 431, 433, 443, 454, 459, 461  
 Magnified Image Spatial Spectrum (MISS), 10  
 Mask, 95, 96, 185, 276, 336, 356, 373, 379  
 Material dispersion, 360  
 Material loss, 348, 351, 356, 385  
 Maxwell equations, 327, 407, 417, 435  
 Mechanical oscillators, 49  
 Mechanisms, 1, 32, 68, 137, 138, 157, 158, 171–173, 201, 228, 249–252, 254, 255, 264, 323, 326, 328, 330, 331, 333, 375–377, 383, 393, 395, 407, 424, 436  
 Medical diagnostic, 214  
 Mercury lamp, 432  
 Metal-coated optical fiber, 115  
 Metallic coating, 215  
 Metallic thin films, 116  
 Metals, 34, 115, 120, 121, 123–126, 130, 133, 223, 224, 243, 244, 261, 270, 282, 314, 316, 326, 327, 330, 334, 335, 372, 383, 385, 395

Metamaterials, 313, 314, 316, 321–323, 326, 329, 330, 339, 341, 342, 347, 350, 366, 371, 372, 375, 376, 383, 384, 386, 392, 393, 395, 398, 400  
 Mica, 45  
 Microalgae, 92  
 Microcapillary, 89, 97  
 Microdroplet, 317, 329–334  
 Microfluidic channels, 47, 98, 399  
 Microlenses, 330–332  
 Micron, 56, 139, 214, 364, 433  
 Microorganism, 143, 155  
 Microscope  
   atomic force, 31, 139, 277, 321, 393  
   epi-reflection, 268  
   inverted, 330, 332, 432  
   plasmonic, 315, 316, 319, 321  
   scanning tunneling, 31, 328, 430, 431  
 Microscopy  
   absorption-based, 137, 139, 140, 142, 143, 157, 158, 162, 171, 175  
   atomic force (AFM), 31, 139, 277, 321, 323, 335, 387, 390, 391, 393  
   bright-field, 9, 28, 56, 399, 452  
   coherence scanning interference (CSI), 458  
   coherent brightfield (COBRI), 32, 67, 69–71, 73, 74, 76, 77, 79–82  
   comparison between COBRI and iSCAT, 32, 73, 75  
   confocal, 14, 92, 98, 151, 156, 158, 203, 204, 214, 240, 386  
   confocal fluorescence, 29, 89, 92, 94, 103, 183, 447  
   confocal laser-scanning, 29, 92, 103, 241, 257, 295, 386  
   dark-field, 28, 31, 34–37, 39, 85, 86, 144, 244, 363, 365, 413, 421, 457  
   differential interference contrast (DIC), 1, 12, 29, 85, 86, 96, 103, 257  
   diffraction phase (DPM), 9, 10  
   digital holographic (DHM), 85–87, 90, 91, 116, 121, 458  
   Dot gradient contrast, 85  
   electron, 87, 92, 214, 240, 255, 289, 313, 318  
   far-field, 90, 100, 114, 123, 137–139, 241, 242, 261, 262, 277, 282, 313, 316, 326, 339, 342, 429, 430, 453  
   fluorescence, 25, 29, 44, 80, 86, 103, 138, 148, 171, 183, 195, 199, 203, 205, 207, 214, 235, 240–243, 277, 291, 303, 345, 366, 372, 391, 446

- fluorescence localization, 40, 138, 207
- gradient light interference (GLIM), 12, 15, 56, 96
- hardware, vii
- Hoffman modulation, 85, 86
- image interference ( $I^M$ ), 241
- image-scanning, 203, 204, 295
- interference reflection, 56
- interferometric reflection, 29
- interferometric scattering (iSCAT), 25, 57, 73–75, 81
- label free (LFM), 79, 86, 100, 137, 138, 142, 148, 171, 184, 186, 240, 261, 262, 277, 282
- light, 67, 96, 240–242, 345, 372
- localization, 40, 138, 175, 183, 196, 207, 208, 262, 290, 408, 446
- localized plasmonic structured illumination (LPSIM), 407, 410
- microsphere-assisted, 386, 443, 450, 452, 453, 457, 459–463
- Mirau interference, 34
- multiphoton, 214, 241, 297, 303, 305–307
- near-field scanning optical (NSOM), 31, 409, 450
- nonlinear, 139, 140, 143, 152, 156–158, 161, 172, 175, 178, 182, 198, 199, 203, 241, 261, 264, 266, 273, 294, 302, 304, 313, 316
- nonlinear photo-modulated reflectivity (NPMR), 261, 264, 282
- non-linear (saturated) structured illumination (SSIM), 138
- optical, 28, 31, 68, 85, 86, 92, 100, 104, 113, 114, 119, 156, 161, 172, 183, 184, 195, 196, 214, 241, 262, 273, 289, 290, 295, 305, 313, 314, 316, 339, 341, 342, 346, 372, 384, 408, 435, 443–445
- phase contrast (PCM), 1, 11, 28, 56, 85–87, 95, 96, 257, 444, 449
- phase-shifting interference, 12, 15, 458
- photo-acoustics, 262
- photo-activated localization (PALM), 138, 183, 242, 262, 290, 372, 391
- photothermal (PTM), 139, 142–144, 146, 148–156, 162
- plasmonic structured illumination (PSIM), 244, 407, 410
- polarized, 85
- pump-probe, 139, 157, 160, 171, 174–176, 178, 180–184, 186–188, 279
- quantum emitters, 37, 262
- reversible saturable optical fluorescence transitions (RESOLFT), 157, 183, 184, 372
- saturated absorption, 262
- saturation excitation (SAX), 245
- scanning, 31, 92, 95, 113, 114, 119, 121, 122, 133, 139, 175, 176, 178, 196, 198, 199, 203, 214, 240–242, 249, 251, 253, 262, 265, 272, 273, 276, 277, 279, 313, 314, 318, 321, 322, 331, 372, 384, 386, 390, 450
- scanning electron (SEM), 92, 122, 208, 214, 227, 255, 269, 271, 272, 276, 279, 318, 320–322, 365, 374, 390, 391, 396
- scanning near-field optical (SNOM), 114, 115, 119, 133, 139, 372, 446
- scanning probe, 31, 114, 240, 277, 313, 393
- selective plane illumination (SPIM), 240, 241
- single-molecule localization, 25, 196, 372, 446
- spatial light interference (SLIM), 11, 12, 95, 96
- stimulated emission depletion (STED), 86, 103, 138, 161, 183, 196, 199, 201, 235, 242, 245, 247, 262, 347, 372, 391, 408, 448
- stochastic optical reconstruction (STORM), 138, 183, 262, 347, 372, 391
- structured illumination (SIM), 69, 103, 138, 203, 205, 206, 214, 242, 244, 256, 262, 277, 372, 408, 424, 447, 450
- super-resolution, 114, 116, 132, 137–139, 142, 143, 152, 161, 171, 186, 195, 196, 199, 201, 203, 207, 240–243, 261, 282, 289, 290, 307, 316, 326, 328, 372, 391, 459
- super-resolved, 81, 92, 133, 234, 244, 255, 374, 446
- super-resolved fluorescence, 92, 408, 446
- thermo-reflectance (TR), 263
- tomographic diffractive (TDM), 85, 90–94, 96–104, 449, 450
- total internal reflection fluorescence (TIRFM), 214, 241, 449
- transient absorption, 138, 139, 157, 159, 160, 174, 180, 181
- transmission optical, 86, 92
- ultrahigh-speed, 69, 77–81
- video-enhanced, 30

- widefield, 67, 73, 86, 92, 94, 178, 205–208, 240, 241, 256, 301, 386, 397, 410
- Microspheres
  - high-index, 330, 409, 413, 422–424, 434, 435
  - liquid-immersed, 330, 388, 409, 422
  - slab-embedded, 387, 388, 422
- Microtubules, 30, 32, 38, 51, 55, 303
- Mid-infrared light, 200
- Mid-Infrared (Mid-IR), 139, 143–145, 148–152, 155–157, 162
- Mie resonances, 410
- Mie theory, 153, 377, 379
- Miniature aperture, v
- Minimally Resolved Features (MRF), 411
- Minute hole, v
- Mirror, 87, 103, 142, 146, 150, 155, 175, 176, 186, 268, 273, 277, 278, 315, 317, 318, 458
- Mitochondria, 154
- Mobility, 30, 48, 51, 52, 54, 55, 216
- Model, 14, 34, 52, 54, 55, 86, 113, 121, 123, 124, 133, 140, 152, 153, 161, 263, 272, 277, 304, 305, 375–377, 381, 397, 401, 412, 413, 415, 417, 418, 421, 422, 430
- Modulation, 11, 32, 34, 38, 56, 74, 75, 85, 86, 140–142, 150, 151, 160, 177–180, 185, 228, 246, 247, 253, 254, 256, 261, 264–268, 270, 273, 274, 277, 280–284, 291, 292, 294, 295, 298, 346, 379, 385, 424
- Modulation depth, 253, 273
- Moerner, William E., 31, 242, 373
- Moiré fringes, 242, 425
- Monoclinic, 270, 271
- Motor proteins, 51, 52, 68, 77, 79
- Motti projection, 361, 362
- Mottle, 30
- Multifunctional biochip, 399
- Multi-layer geometry, 351
- Multiphoton absorption, 138, 264, 291, 296
- Multiphoton excitations, 264, 303
- Myosin, 303
  
- N**
- Naked eye, 30
- Nano-Solid-Fluid (NSF), 393, 394
- Nanometer, 30, 37, 41, 47, 48, 55, 67–69, 77–80, 113, 128, 175, 195, 244, 262, 289, 290, 313, 360, 424, 433
- Nanoparticle composite, 383–385
- Nanoparticle sensing, 399
- Nanoparticles, 17, 25, 26, 31, 32, 34–36, 38–45, 47, 57, 67–75, 77–81, 115, 128, 131, 132, 142–144, 148, 152, 153, 180, 200, 205, 214, 215, 217, 222–224, 234, 243, 245, 251–253, 255–258, 266, 271, 272, 374, 376, 377, 383–386, 392–395, 397, 399, 400, 430
  - absorption extinction, 71
  - biological, 67, 68, 78, 79
  - diamond, 199, 200
  - gold, 28, 31, 34, 43, 74, 81, 128, 131, 148, 153, 180, 214, 243, 245
  - silver, 31, 222, 223, 245
  - TiO<sub>2</sub>, 132, 383–386, 393–395
- Nanopipette, 44
- Nanoplasmonics, 388, 389, 407, 412, 413, 436
- Nanorod, 43, 148, 153, 154, 222–226, 250, 350
- Nanorod arrays, 350, 351
- Nanoscale objects, 407, 410, 424, 430, 434, 436
- Nanoscope
  - label-free super-resolved, 234
  - microsphere, 374, 375
  - non-fluorescent, 215, 234
- Nanoscopy
  - dark-field, 86, 244
  - extinction, 26, 71
  - fluorescence, 44, 86, 138
  - microsphere, 373, 386, 400
  - microspherical, 407, 410, 413, 415, 427, 431, 434–436
  - photo-stable optical nanoscopy (PHOTON), 244
  - stimulated emission depletion (STED), 86, 103, 245
- Nanostructured silicon, 261
- Nature of light, 171, 195, 207, 262
- Near-field, far-field signal, 132, 133
- Near-fields, 113–115, 119, 121, 127, 128, 131–133, 139, 214, 241, 243–245, 262, 314, 330, 331, 333, 336, 337, 342, 346, 348, 372–375, 377–379, 383–385, 392, 394, 395, 397, 447, 448
- Near-infrared, 172, 198, 383
- Near-sighted, 348
- Negative index, 314, 347, 348
- Negative lobes, 273

Negative (real part of the) permittivity, 349  
 Negative refraction, 318, 330, 347  
 Neurons, 6, 68, 92, 95, 304  
 Nobel Prize, 28, 29, 116, 345, 373, 408, 446  
 Noise, 9, 28, 36–38, 42, 45, 46, 67, 68, 73, 75–77, 81, 103, 131, 138, 141, 148, 150, 151, 154, 155, 177, 199, 209, 247, 266, 293, 347–349, 362, 363, 449, 460  
 Noise level, 37, 199  
 Nonconducting and conducting silicon nanoparticle, 223  
 Non-invasive, 14, 240, 281, 390, 454, 459  
 Non-linear absorption, 137, 157, 162, 172, 173, 175, 179, 181, 184  
 Nonlinear absorption and emission, 246  
 Nonlinear changes, 266  
 Nonlinear components, 200, 253, 263, 265  
 Nonlinear index, 252  
 Non-linear interaction, 172, 298  
 Nonlinearity of fluorescence emission, 239, 248  
 Nonlinearity order, 261, 265, 267, 273, 282  
 Nonlinear photoacoustic, 280  
 Nonlinear reflectance, 261, 264  
 Nonlinear relation, 197, 199  
 Non-linear response, 158, 214, 251, 254, 255, 261, 262, 266, 267, 270, 271, 277, 278, 347  
 Normanski, Georges, 29  
 Notch filter, 277  
 Numerical aperture, 89–91, 94, 97, 125, 142, 175, 182, 184, 203, 244, 248, 292, 372, 373, 399, 444, 449, 459, 463  
 Numerical complexity, 362  
 Numerical propagation, 113  
 Numerical reconstruction, 87

**O**

Object polarization, 362  
 Off-axis, 7–9, 15, 119, 150, 203  
 Off-axis holography, 87, 88, 113, 117, 118, 133  
 On/off switching, 239, 242  
 Opaque, 132, 148, 261, 282  
 Opaque plate, v  
 Opaque samples, 27, 148  
 Optical contrast, 76, 280, 386, 409, 423  
 Optical lithography, 356  
 Optical microcavities, 49  
 Optical nanoantennas, 128, 130  
 Optical parametric oscillator, 149, 175, 176

Optical pathlength, 2  
 Optical sectioning, 91, 92, 96, 172, 240, 256, 294, 297, 303, 305  
 Optical shadow, 26  
 Optical tweezers, 98, 100, 427  
 Organelles, 56, 67, 75, 79, 138, 258  
 Organic molecules, 42, 45, 155  
 Organisms, 27, 86, 137–139, 149, 152, 214, 263  
 Organizational, vii, viii  
 Organoids, 14, 86  
 Out-of-focus, 240, 273, 386, 449, 450  
 Outgoing waves, 352

## P

Papers, 90, 129, 130, 132, 314, 410  
 Parametric process, 296  
 Particle tracking, 40, 53, 55, 68  
 Patents, 240, 447, 448  
 Path length, 2, 30  
 PDE non-linearity, 234, 235  
 Pendry, John, 314, 372  
 Penetration depth, 172, 228, 233, 240, 257, 296  
 Phase-Contrast (PC), 1, 11, 13, 34, 85–87, 95, 96, 257, 449  
 Phase mask, 42, 95, 96, 185, 448  
 Phase matching condition, 124, 197  
 Phase plate, 28, 42, 161, 185, 234, 256  
 Phase retrieval, 2, 7  
 Phase-shifting, 7, 10–12, 15, 87, 89, 458  
 Phase transition, 270–272  
 Phonon, 159, 180, 263, 266, 267, 271, 274  
 Phospholipids molecules, 51  
 Photoacoustic, 261, 280, 447  
 Photobleaching, 14, 17, 25, 39, 40, 52, 68, 103, 149, 172, 214, 239, 242, 247, 248, 290, 347, 408  
 Photoblinking, 25, 45  
 Photodamage, 39, 89, 144, 149, 152, 161, 248  
 Photodiode detector, 268  
 Photoemission, 25  
 Photo-excitation, 261–264, 270, 436  
 Photography, 30, 116  
 Photo-induced reflectance, 263  
 Photo-induction, 261  
 Photonic hook, 379, 400  
 Photonic jet, 447, 451, 455, 456  
 Photonic nanojet, 376, 377, 399, 407, 412, 416  
 Photonics, 45, 234, 253, 318, 339, 376, 377, 379, 395, 399, 400

- Photopolymer, 101, 102  
 Photostability, 31, 45, 242, 243, 245  
 Photo-thermal effect, 251, 252, 258  
 Photothermal (PT) lens effect, 139–141, 143  
 Phototoxicity, 14, 81, 82, 86, 242, 248, 303, 347  
 Physical principles, 408, 436, 463  
 Physics, 1, 2, 28, 29, 31, 32, 34, 46, 52, 56, 116, 372, 375, 428  
 Piezoelectric actuators, 49  
 Piezoelectric driven mirror, 87  
 Pinhole, 9, 10, 36, 203, 240, 295, 386  
 Planar geometry, 349, 357  
 Plasma Dispersion Effect (PDE), 213–215, 217, 219, 229, 232–235  
 Plasmon-Coupled Leakage Radiation (PCLR), 424, 428–430  
 Plasmonic antennas, 44, 49  
 Plasmonic media, 113, 133  
 Plasmonic metasurface, 382, 407, 410, 412, 413, 424, 430, 435, 436  
 Plasmonic nanostructures, 239, 243, 255, 423  
 Plasmonic near-fields, 430, 434  
 Plasmonic oscillations, 423  
 Plasmonics, 31, 43, 243, 245, 250, 251, 313, 372  
 Plasmonic substrates, 51  
 Plasmonic wavelength, vii  
 Pohl, Dieter, 372  
 Point-by-point, 314, 434, 458  
 Point-like source, 116, 122, 132, 133, 407, 413  
 Point-source, 16, 123, 182, 316, 321, 327, 328, 334, 350, 355, 356, 376, 384, 385, 408, 412–414, 416–419, 421, 445  
 Point-source emission, 417  
 Point Spread Function (PSF) shaping, 40, 196, 346, 407, 409, 418, 445  
 Poisson distribution, 37  
 Polarizability, 34, 47, 54, 172  
 Pollen grain, 100, 101  
 Pollens, 89, 92  
 Poly-Methyl-Methacrylate (PMMA), 144, 203, 225, 227, 321–324, 326  
 Polydimethylsiloxane (PDMS), 388, 389, 411  
 Polymer, 138, 155, 206, 263, 397  
 Polymer films, 263  
 Polystyrene, 72, 145, 152, 198, 204, 263, 375, 395, 397, 427, 431, 459  
 Polystyrene beads, 72, 145, 198, 204, 263  
 Porous structures, 92  
 Positive (real part of the) permittivity, 349, 359  
 Post-Imaging Processing (PIP), 410–412, 424, 425, 427, 428, 433, 434  
 Power, 12, 34, 36, 39, 45, 49, 51, 87, 121, 138, 140, 141, 145, 148–150, 161, 172, 179, 181, 182, 186, 195, 197, 199, 202, 223, 228, 239, 245, 246, 252, 254, 256, 265, 267, 271, 283, 284, 313, 339, 341, 349, 356, 373, 390, 416–418  
 Power fluctuations, 36  
 Precision, 25, 29, 40, 43, 47, 51–53, 55, 67–69, 73, 77–80, 87, 97, 138, 176, 183, 243, 390  
 Principles, 1, 6, 12, 15–17, 25, 26, 28, 29, 32, 33, 39, 49, 74, 76, 85, 87, 88, 91, 95, 98, 116, 132, 140, 145, 157, 160, 177, 183, 184, 195, 229, 235, 240, 242, 246, 247, 264, 265, 304, 313, 357, 384, 390, 408, 416, 424–426, 428, 430, 443, 447–449, 451, 458, 463  
 Prism dimer, 224, 226  
 Probe, 14, 43, 44, 52, 53, 79, 80, 113–116, 119–128, 130–133, 139–151, 154, 155, 157–160, 171–188, 196, 207, 209, 213, 215, 217, 218, 220, 227–235, 240, 241, 248, 252, 261–266, 268–271, 273–279, 282, 290, 297, 313, 317, 326, 332, 334, 346, 350, 355, 384, 388, 393, 399, 400, 412, 434, 446, 454  
 Probe beam, 139–151, 155, 157–160, 173–179, 183, 185–187, 213, 215, 217, 218, 227–235, 252, 264, 273, 274, 276, 277  
 Probe intensity, 154, 158, 173, 177, 178, 185, 262  
 Probe laser, 147, 229, 230, 264, 277, 279  
 Propagating beam, 379, 382  
 Propagating field wavefronts, 123  
 Proteins, 14, 30, 32, 35, 36, 38, 43, 47–49, 51, 52, 55–57, 68, 77, 79, 81, 138, 148, 153, 154, 242, 290, 303, 305, 345, 409, 434, 457  
 Protozoans, 27  
 Ptychography, 87  
 Pulsed laser, 171, 172, 175, 180, 202, 218, 302  
 Pulse duration, 233, 234, 268, 274  
 Pulse train, 160, 175, 177, 178, 266, 280, 281

- Pump, 56, 137, 139–146, 148–152, 154, 157–160, 171–188, 197–202, 205, 213, 215–221, 223–235, 261–279, 282, 296
- Pump and probe beams, 140, 142, 143, 145, 148, 159, 160, 175–178, 183, 187, 227, 261, 264, 274
- Pump beam, 137, 139–144, 146, 148–152, 157, 158, 160, 174, 177, 178, 185, 186, 213, 215–221, 228–235, 261, 267, 268, 271, 273, 277
- Pump fluence, 264, 269–271
- Pump intensity, 173, 177, 185, 219, 223–226, 266
- Pump pulse, 174, 186, 232–234, 261, 264–267, 269, 271, 274
- Q**
- Quadrature component, 179
- Quantum Cascade Laser (QCL), 138, 150, 151
- Quantum dots, 25, 35, 44, 45, 47, 48
- Quantum emitter, 37, 45, 262
- R**
- Radial numbers, 416
- Radon transform, 89
- Rainbow, 326, 364, 365
- Raman scattering
  - coherent anti-stokes (CARS), 86, 157, 196–200, 205, 263, 296
  - resonant, 201
  - spontaneous, 195, 197, 201
  - stimulated, 138, 140, 157, 177, 195–197, 201, 263, 273
  - surface enhanced-, 196, 205
  - tip-enhanced (TERS), 196, 262, 277
- Rate equations, 203
- Rayleigh, Lord (John William Strut), 240, 445
- Ray tracing, 394, 414, 415
- Real image, 118, 120, 413, 455, 456
- Red shift, 219, 223
- Reflectance, 32, 149, 261–264, 271, 274, 275
- Reflection interference, 34, 56
- Reflectivity, 34, 233, 261, 263–270, 274, 275, 282
- Refraction index change, 124, 140, 215
- Refraction maps, 89
- Refractive index, 2, 4–7, 14, 17, 28, 30, 34, 35, 38, 43, 48, 56, 68, 90, 98, 140, 141, 172, 182, 197, 198, 214–217, 219, 224, 228, 229, 233, 313, 314, 330–332, 335, 336, 338, 340, 348, 357, 358, 376, 377, 379, 383, 384, 393, 395, 397, 408, 412, 414, 415, 427, 444, 445, 448–450, 453, 455, 456
- Relative permittivity, 90, 91
- Repetition rate, 180, 230, 266, 281
- Research-grade microscopes, 27
- Resistivity, 229
- Resolution
  - axial, 41, 99, 100, 182, 203, 241, 242, 290, 297–299, 306, 410, 424, 447–449, 459, 463
  - diffraction-limited, 81, 129, 142, 143, 146, 300, 337, 346, 374, 410, 425
  - lateral, 91, 92, 99, 100, 144, 205, 214, 240–242, 248, 289–293, 297, 298, 301, 302, 346, 377, 379, 392, 424, 443–452, 454, 459–461, 463
  - spatial, 16, 17, 26, 67, 68, 81, 139, 142–144, 146, 149, 151–153, 155, 156, 161, 162, 171, 176, 178, 180, 182, 183, 186, 188, 195–203, 205, 206, 208, 209, 239–241, 243, 245–248, 251, 253, 254, 256, 257, 262, 265, 273, 306, 313, 314, 318, 320, 321, 326, 341, 436, 444
  - spatio-temporal, 25, 53, 67, 68, 76, 77, 79
  - subwavelength, 215, 322, 345, 362, 372, 377, 428
  - super-, 17, 25, 43, 114, 116, 132, 137–139, 142, 143, 146, 147, 152, 156, 158, 161, 171, 183, 186, 188, 195, 196, 199, 201, 203, 207–209, 213–215, 220, 231, 234, 239–246, 248, 253–258, 261, 262, 275, 282, 289, 290, 295, 297, 303, 304, 306, 316, 326–329, 339, 341, 346–348, 365, 366, 371–380, 383, 385–394, 396–398, 400, 407, 412, 416, 423–426, 428, 430, 434–436, 443, 446, 452–455, 459, 463
  - temporal, 17, 25, 26, 52, 53, 67–69, 78, 80–82, 171, 174–177, 180
  - ultrahigh-, 79, 262
- Resolution criteria, 16, 372, 410, 435, 445
- Resolution limit, 17, 182, 196, 207, 239–241, 262, 316, 372, 379, 380, 423, 444, 452, 463
- Retina, 358
- Retrieval, 2, 7, 15, 346, 445, 461
- Reverse saturation, 239, 249–251, 253, 254, 257

- Richard Adolf Zsigmondy, 28  
 Richardson-Lucy algorithm, 221  
 Rotation axis, 97, 99, 100  
 Rutile, 270, 271, 384  
 Rytov approximation, 96
- S**
- Sample staining, vi  
 Sapphire, 175, 269, 270, 273, 274, 278, 279, 350, 351  
 Sapphire substrate, 270, 274, 278, 279  
 Saturable and reverse saturable absorption, 161, 186, 188, 248  
 Saturation, 25, 39, 40, 68, 81, 139, 160, 161, 181, 184–187, 199, 201, 239, 245–254, 257, 313, 314, 448  
 Saturation effects, 37, 160  
 Scalar approximation, 90  
 Scanning microsphere, 387, 390, 391, 450  
 Scanning translator, 268, 434  
 Scattered electromagnetic field, 116, 128, 133, 346  
 Scattering  
   apertureless, 114, 115  
   back, 2, 3, 5–7, 33, 73, 245, 254  
   carrier–carrier, 263  
   carrier–phonon, 263  
   elastic, 91, 132  
   interferometric, 25, 71, 73, 74, 81  
   light, 68, 70, 73, 132, 149, 326, 328, 329, 361, 377, 399, 435  
   linear, 2, 34, 68, 306  
   Mie, 251  
   nonlinear, 138, 172, 199, 203, 205, 239, 248–254, 258, 261, 269, 277, 281  
   plasmonic, 124, 127, 199, 243, 245, 248–251, 253, 254, 256, 257  
   Rayleigh, 31, 35, 37, 243  
   reverse saturation of, 239, 249–251, 253, 257  
   rotating coherent (ROCS), 32  
   saturation of, 68, 199, 201, 239, 245, 249–251, 253, 254, 257  
   stroboscopic interference (strobeSCAT), 32  
   wave, 132, 377, 379, 415  
 Scattering angle, pattern, directional, 122, 127–130  
 Scattering background estimation and correction, 69, 77, 79  
 Scattering cross section, 68, 81, 129, 131, 216, 217, 219, 249, 415, 416  
 Scattering media, 57, 132, 280, 281, 383  
 Scattering potential, 2–4  
 Scattering surface, 31, 47, 269  
 Second Harmonic Generation (SHG), 86, 157, 172, 178, 296, 297, 300, 302–306, 379  
 Semiconductor, 9, 35, 44, 45, 56, 138, 187, 243, 261, 269, 282, 357, 373, 374, 395, 434  
 Semiconductor circuits, 356  
 Semiconductor nanocrystals, 45  
 Semi-transparent, 74, 261, 282  
 Sensitivity, 2, 12, 13, 25–29, 31, 35–37, 42, 43, 45, 46, 49, 51, 53–57, 67–69, 71–74, 77, 79, 81, 82, 86, 89, 137–142, 148, 149, 152, 153, 155, 162, 171, 177, 178, 180, 273, 279, 282, 363, 443, 445, 459  
 Shot noise, 37, 67, 68, 73, 76, 81, 177  
 Shot-noise-limited sensitivity, 67, 68, 73, 81, 177  
 Side lobes, 199, 253, 254, 373  
 Siedentopf, Henry, 28  
 Signal-to-Noise Ratio (SNR), 26, 35, 37, 45, 77, 131, 138, 141, 142, 146, 148, 150, 151, 154, 177, 179, 181, 184, 247, 266, 270, 279–281  
 Silica, 363, 374, 377, 382, 386, 422, 451, 452  
 Silica nanowires, 362–364  
 Silicon, 449  
 Silicon coated gold nano-particles, 219  
 Silicon coated nano structures, 217, 218  
 Silicon coating, 217–219, 225, 227  
 Silicon layers, 269, 273  
 Silicon nanorod, 223–226  
 Silicon nanostructures, 215, 269  
 Silicon On Insulator (SOI), 225  
 Silicon oxide, 225  
 Silicon photonics, 234  
 Silicon shell, 215, 218–220  
 Silicon stripes, 269, 279  
 Silicon substrate, 180, 271  
 Silicon wafer, 214, 215, 228, 229, 235, 264  
 Silicone oil, 432, 433  
 Silva, 161, 201  
 Silver nanorods, 223–226  
 Silver Nanosphere (SNS), 250, 251  
 Sine intensity-modulated, 264  
 Sine modulation, 261, 264  
 Single cell vesicle nanoscopic dynamics, 67  
 Single molecule, 25, 26, 34, 44–46, 86, 137, 138, 142, 148, 152–154, 183, 196, 207, 372, 448

- Single-particle tracking
  - microsecond temporal resolution, 67, 69, 80
  - nanometer localization precision, 80
  - three-dimensional, 69
  - ultrahigh-speed, 67, 69, 77, 78
- Single viral nanoscopic dynamics, 78, 79
- Sirks, Jacobus Laurens, 29
- Small Unilamellar Vesicle (SUV), 54
- Spacing, 266, 269, 359
- Sparsity, 346
- Spatial coherence, 15, 16, 69, 71, 460
- Spatial filtering, 118
- Spatial frequency, 2, 6, 16, 69, 132, 199, 205, 206, 214, 215, 228, 235, 243, 244, 291–294, 301, 346, 382, 384, 408, 424, 426, 428
- Spatial frequency components, 199, 243, 292, 384
- Spatial Light Interference Tomography (SLIT), 96
- Spatial Light Modulator (SLM), 9, 11, 96, 159, 185, 208
- Spatial modulation, 75, 246, 247, 261, 268, 273, 292, 294
- Spatial overlap, 293
- Spatial overlap modulation, 273, 274, 282
- Spatial profile, 217, 263
- Spatial-spectral mapping, 364
- Spatiotemporal, 67, 68, 76, 77, 79, 195
- Specimen, 1, 2, 5, 9, 12–14, 17, 27, 28, 38, 40, 52, 57, 85–87, 89, 96, 97, 99, 153, 172, 177, 217, 227, 240–242, 347, 371–373, 391, 400
- Specimen plane, 29, 240
- Speckle, 6, 12, 103, 132, 133, 281, 290
- Speckle-free, 12
- Speed of light, 215, 349
- Spherical aberrations, 422, 445
- Spider silk, 375, 397, 398, 450
- Spider web, 28
- Spiral phase plate, 234
- Spontaneous emission, 35, 195, 199, 247, 248
- Spot, 26, 41, 43, 71, 73, 76, 89, 137, 139, 146, 158–160, 176, 182–185, 197–201, 203, 205, 209, 244–248, 261, 262, 264, 276, 295, 347, 360, 373, 374, 378, 379, 384, 414, 431, 456
- Spurious background, 37
- Stage, 71, 122, 175, 176, 277, 282, 283, 388, 389, 423, 435
- Staining, 1, 13, 29, 408
- State-of-the-art, 180
- Steady state heating, 266
- Steady state temperature, 269
- Stepwise motions, 77, 79, 80
- Stimulated emission, 347, 408
- Stimulated Emission Depletion (STED), 86, 103, 138, 161, 183, 196, 199–201, 203, 213, 234, 235, 242, 245–248, 253, 256, 258, 262, 347, 372, 391, 400
- Stitching images, 390
- Stochastic optical probes, 131, 183
- Stochastic switching and read-out, 183
- Stokes beams, 161, 197–201, 205
- Stokes scanning, 279
- Sub-diffraction, 137, 140, 143, 145, 159, 160, 184, 186, 187, 205, 244, 350, 373, 374, 390, 391, 397
- Subnanometer, vi
- Substrate, 30, 34, 38, 43, 45, 48, 51, 52, 54, 74, 119, 123–128, 148, 180, 205, 208, 270, 271, 274, 278, 279, 336, 349, 358–364, 374–377, 381, 382, 384, 412, 422, 423, 428, 431
- Substrate effect, 376, 377, 381
- Subwavelength features, 412
- Subwavelength grating, 352
- Subwavelength information, 347, 348, 352, 386
- Subwavelength light-matter interaction, 137
- Subwavelength nanostructure, 350
- Subwavelength tip, 116, 346
- Sum-frequency generation, 172, 176, 177, 186
- Sunlight, 28
- Supercontinuum, 34, 44, 365
- Superlens
  - biological, 371, 375, 397
  - coverslip microsphere (CMS), 389
  - far-field, 316, 428
  - metamaterial, 348, 371, 372, 383, 448
  - near-sighted, 348
- Superlensing objective, 389
- Super resolution, 17, 81, 103, 114, 116, 132, 137–139, 142, 143, 146, 147, 152, 158, 161, 171, 183, 186, 188, 195, 196, 199, 201, 203, 207–209, 213–215, 220, 231, 234, 239, 241–246, 248, 253–258, 261, 262, 275, 282, 316, 326–330, 339, 341, 371–380, 383, 385–388, 390–394, 396–400, 443, 463
- Super-resolution endoscopy, 306, 392, 400

Super-resonance, 376, 377, 379–381, 400  
 Superspherical, 422  
 Surface lattice resonances, 410, 424, 425  
 Surface plasmon, 49, 51, 114–116, 121, 124, 125, 127, 153, 154, 186, 187, 239, 243, 244, 250, 314–316, 318, 322, 323, 326, 407, 410, 423, 425, 430, 435  
 Surface Plasmon Polaritons (SPP), 114–116, 186, 187, 239, 244, 314, 316, 318, 321, 326, 341, 425  
 Surface Plasmon Resonance (SPR), 154, 239, 243, 244, 250–252, 407  
 Surface profilometry, 29  
 Surface states, 347, 348  
 Susceptibility tensor, 172  
 Synergistic interplay, v  
 Synge, E. H., 114, 446  
 Synthetic aperture, 92, 103  
 Synthetic lipid bilayers, 47

## T

Targeted switching and read-out, 183  
 Taylor series, 266, 346  
 Temperature, 44–46, 140, 148, 153, 251, 253, 261–266, 269, 271, 277–279, 431  
 Temporal focusing, 297, 298, 306  
 Temporal median filtering, 76  
 Temporal modulation, 246, 254, 256  
 Thermal, 36, 67, 76, 137, 139–141, 144, 145, 147, 149, 152, 153, 251, 252, 263, 266  
 Thermalization, 180, 263, 279  
 Thermal properties, 153, 263, 271  
 Thermal relaxation, 266  
 Thermal transport, 263  
 Thermo Reflectance (TR), 266  
 Third Harmonic Generation (THG), 86, 157, 172, 296, 297, 300  
 3D image, 119  
 Three-dimensional speckle, 132  
 Three-dimensional wavefield, 116  
 3D interferometry, 392  
 Three-photon fluorescence, 291  
 Tight-binding approximation, 430, 431  
 Time, 27, 29, 38–40, 42, 43, 48, 52, 54, 290, 295, 297, 301, 302, 306, 346–348, 362, 427, 428, 444, 445, 447, 451, 461  
 Time scale, 159, 176, 263, 266  
 Time-domain thermoreflectance, 263

Timeframe, 266  
 Time-resolved spectroscopy, 157, 174  
 Time reversal, viii  
 Time-reversal symmetry, 132  
 Timescale, 52  
 Ti:sapphire, 175  
 Tissue, 1, 4, 12–14, 17, 47, 96, 139, 145, 154, 155, 177, 180, 240, 250, 256, 258, 262, 280, 299, 303, 304, 345, 391, 400  
 Tomography, 361, 392, 449, 458  
 Topography surface, 462  
 Toraldo-style pupil filter, 198  
 Transformation optics, 313, 329, 330, 334, 336  
 Transient Absorption (TA), 138, 139, 156–161, 174, 180, 181, 186  
 Translation symmetry, 352  
 Transparent, 1, 2, 6, 70, 359, 443, 449–451  
 Transparent media, 70, 89, 96, 113, 122, 124, 125, 133, 148, 150, 177, 240, 313, 316, 383, 397  
 Trap stiffness, 44  
 Truncated spheres, 422  
 Tubulin, 49, 302  
 Turbid media, 103, 133  
 Two-arm, 29  
 Two layers nanorod dimer, 223, 226  
 Two layers structure, 223, 224  
 Two-photon absorption, 173, 174, 179, 217  
 Two-photon fluorescence, 157, 178

## U

Ultra-fast photo-excitation, 270  
 Ultrahigh-resolution Optical Coherence Tomography (OCT), viii  
 Ultramicroscope, 28  
 Ultrashort pulses, 172, 174, 175, 297  
 Ultra-short pump pulse, 261, 264, 266, 277  
 Uncertainty principle, 16, 17  
 Uniaxial, 349  
 Uniaxial anisotropic dielectric medium, 349  
 Unit cell, 347, 350, 355, 359, 360, 362  
 UV light, 201, 242, 336, 356

## V

Vacuum, 215, 261, 282, 313, 327, 408  
 Vanadium dioxide (VO<sub>2</sub>), 261, 270–272  
 Van Leeuwenhoek, Antonie, 27, 444  
 Vertex, 223, 224  
 Vesicle membranes, 30  
 Vibrational coherence, 161, 201

- Vibrational excitation, 195, 199  
Vibrational frequency, 199  
Vibrational spectroscopy, 161  
Viral-mimetic particles, 55  
Virtual image, 117, 118, 120, 373, 374, 391, 394, 397, 409, 414, 415, 419, 424, 428, 431, 433, 434, 451, 455, 456, 460  
Viruses, 32, 35, 47, 48, 51, 52, 67–69, 71, 73, 76–80, 373, 374, 399  
Visible pump, 56, 146, 148  
Visible wavelengths, 213, 263, 345, 384  
Voltage, 37, 267, 280, 282, 375
- W**  
Wafer, 213–215, 225, 228, 229, 235, 264  
Wavefront analyzers, 87, 103  
Wavefront modulation, 273  
Wavefront shaping, 280  
Wavelength, 2, 9, 14, 25, 26, 34, 35, 38, 39, 45, 46, 72, 74, 80, 89, 90, 94, 95, 100, 103, 124, 128–130, 137–139, 141–143, 149–152, 159, 161, 172–176, 178, 180–184, 186, 188, 195–197, 205, 213–215, 217, 218, 220–222, 228, 229, 233, 240, 241, 244, 245, 247–252, 255, 256, 263, 266, 274, 280, 282, 313, 316, 318, 345–347, 355, 357, 359, 372, 374, 375, 377, 380, 383, 384, 397, 401, 408, 412, 413, 415, 426, 434, 444, 445, 448, 449, 451, 453, 456, 459, 463  
Weak high-order nonlinearities, 261  
Whispering-Gallery Mode (WGMs), 407, 416, 452  
White-light diffraction tomography, 14, 95, 96  
Wide-field, 36, 38, 40–42, 48, 54, 56, 67, 70, 73, 86, 92, 94, 178, 205–208, 240, 241, 256, 297, 299, 386, 394, 397  
Wide-field interferometry in transmission, 73  
Wiener filter, 230, 293
- X**  
X-ray, 345
- Z**  
Zernike phase plate, 42  
Zernike, Frits, 1, 11, 28  
Zinc oxide, 161  
Z-scan, 249